

Topics in Organometallic Chemistry 64

Vadapalli Chandrasekhar  
Fabrice Pointillart *Editors*

# Organometallic Magnets

 Springer

**Series Editors**

- M. Beller, Rostock, Germany  
P. H. Dixneuf, Rennes, France  
J. Dupont, Porto Alegre, Brazil  
A. Fürstner, Mülheim, Germany  
F. Glorius, Münster, Germany  
L. J. Gooßen, Kaiserslautern, Germany  
S. P. Nolan, Ghent, Belgium  
J. Okuda, Aachen, Germany  
L. A. Oro, Zaragoza, Spain  
M. Willis, Oxford, United Kingdom  
Q.-L. Zhou, Tianjin, China

## **Aims and Scope**

The series *Topics in Organometallic Chemistry* presents critical overviews of research results in organometallic chemistry. As our understanding of organometallic structure, properties and mechanisms increases, new ways are opened for the design of organometallic compounds and reactions tailored to the needs of such diverse areas as organic synthesis, medical research, biology and materials science. Thus the scope of coverage includes a broad range of topics of pure and applied organometallic chemistry, where new breakthroughs are being achieved that are of significance to a larger scientific audience.

The individual volumes of *Topics in Organometallic Chemistry* are thematic. Review articles are generally invited by the volume editors. All chapters from Topics in Organometallic Chemistry are published Online First with an individual DOI. In references, Topics in Organometallic Chemistry is abbreviated as Top Organomet Chem and cited as a journal.

More information about this series at <http://www.springer.com/series/3418>

Vadapalli Chandrasekhar • Fabrice Pointillart  
Editors

# Organometallic Magnets

With contributions by

J. Autschbach • H. Bolvin • O. Cador • V. Chandrasekhar •  
E. Colacio • A. Dey • S. Gao • F. Gendron • T. Gupta •  
M. J. Heras Ojea • S.-D. Jiang • P. Kögerler • T. Korzeniak •  
R. A. Layfield • L. C. H. Maddock • R. S. Narayanan •  
B. Nowicka • F. Pointillart • G. Rajaraman •  
M. Shanmugam • B. Sieklucka • M. K. Singh •  
M. Speldrich • J. Tang • S. Tripathi • J. van Leusen •  
B.-W. Wang • Z. Zhu

 Springer



*Editors*

Vadapalli Chandrasekhar  
Department of Chemistry  
Indian Institute of Technology  
Kanpur, India

Fabrice Pointillart  
Institut des Sciences Chimiques de Rennes  
Equipe Organométalliques : Matériaux et  
Catalyse  
Rennes Cedex, France

ISSN 1436-6002

ISSN 1616-8534 (electronic)

Topics in Organometallic Chemistry

ISBN 978-3-030-26008-8

ISBN 978-3-030-26009-5 (eBook)

<https://doi.org/10.1007/978-3-030-26009-5>

© Springer Nature Switzerland AG 2019

This work is subject to copyright. All rights are reserved by the Publisher, whether the whole or part of the material is concerned, specifically the rights of translation, reprinting, reuse of illustrations, recitation, broadcasting, reproduction on microfilms or in any other physical way, and transmission or information storage and retrieval, electronic adaptation, computer software, or by similar or dissimilar methodology now known or hereafter developed.

The use of general descriptive names, registered names, trademarks, service marks, etc. in this publication does not imply, even in the absence of a specific statement, that such names are exempt from the relevant protective laws and regulations and therefore free for general use.

The publisher, the authors, and the editors are safe to assume that the advice and information in this book are believed to be true and accurate at the date of publication. Neither the publisher nor the authors or the editors give a warranty, expressed or implied, with respect to the material contained herein or for any errors or omissions that may have been made. The publisher remains neutral with regard to jurisdictional claims in published maps and institutional affiliations.

This Springer imprint is published by the registered company Springer Nature Switzerland AG.  
The registered company address is: Gewerbestrasse 11, 6330 Cham, Switzerland

# Preface

The discovery, in the 1990s, that the polynuclear mixed valent complex  $[\text{Mn}_{12}\text{O}_{12}(\text{OAc})_{16}(\text{H}_2\text{O})_4]$  was a single-molecule magnet (SMM) created a new interdisciplinary field in the area of molecular magnets. Contributions and collaborations from chemists, physicists, and materials scientists and between theorists and experimentalists are allowing this field to grow vigorously, being motivated by not only academic questions but also potential applications in high density storage, quantum computing, and spintronic devices. These joint efforts have led to the use of 4f lanthanide ions and the discovery of the first mononuclear complex of  $\text{Tb}^{\text{III}}$  which behaves as an SMM in 2003. Researchers also developed strategies to combine the advantages of both 3d and 4f elements in designing heterobimetallic compounds. More recently this is being extended to systems containing 4d/5d and 5f actinide ions. Now, more than ever before, molecular magnets are in the race for high density storage applications since their design uses organometallic chemistry and the observation of magnetic memory up to 80 K.

This book aims to illustrate different strategies to design molecular magnets through the recent achievements of the contributors and how brain storming between experimental chemists, theoreticians as well as physicists increased the understanding and performance of the molecular magnets. To do so, this volume is divided into eleven chapters. In the chapter “Hybrid Organic-Inorganic Cyanide-Bridged Networks,” Korzeniak, Nowicka, and Sieklucka reveal strategies to design hybrid organic-inorganic cyanide-bridged networks as molecular magnets. In the chapter “Cobalt(II) Complexes as Single-Ion Magnets”, Tripathi, Dey, Shanmugam, Narayanan, and Chandrasekhar present recent achievements about Co(II) single-ion magnets and in the chapter “Cobalt(II)/(III)–Lanthanide(III) Complexes as Molecular Magnets”, the same authors show how Co(II) can be associated with 4f ions to observe slow magnetic relaxation. In the chapter “Mannich Base Ligands as Versatile Platforms for SMMs”, Colacio highlights the usefulness of Mannich-base ligands to assemble homometallic 4f complexes and heterometallic 3d/4f complexes as SMMs. Utility of a specific ligand, viz. the tetrathiafulvalene-based ligand, is shown in the chapter “[Tetrathiafulvalene-Based Magnets of Lanthanides](#)” by Cadore

and Pointillart to rationally design and assemble mono- and polynuclear SMMs. In the chapter “Geometry and Magnetism of Lanthanide Compounds”, Zhu and Tang demonstrate the importance of the coordination geometries on the magnetic behavior. In the chapter “[Single-Ion Anisotropy: An Insight to Complicated Magnetic Molecules](#)”, Gao, Jiang, and Wang overviewed the theoretical and experimental considerations in constructing mononuclear SMM. Organometallic approach is treated in the chapter “[Lanthanide Organometallics as Single-Molecule Magnets](#)” by Ojea, Maddock, and Layfield as a powerful tool to achieve magnetic bistability above liquid-nitrogen temperatures. In the chapter “[Role of Ab Initio Calculations in the Design and Development of Lanthanide Based Single Molecule Magnets](#)”, Gupta, Singh, and Rajaraman highlight the crucial role of the ab initio approach in the understanding of the magnetic properties and the development of future coordination and organometallic molecular magnets while the chapter “[Complete Active Space Wavefunction-Based Analysis of Magnetization and Electronic Structure](#)” by Autschbach, Bolvin, and Gendron addresses the complete Active Space Wavefunction-Based Analysis of Magnetization and Electronic Structure for the entire transition metals, lanthanides, and actinides. Finally in the chapter “[Magnetism of Actinide Coordination Compounds](#)”, Leusen, Speldrich, and Kögerler introduce a model focused on the interpretation of the magnetic properties of a recent class of coordination complexes involving actinides.

The editors hope that the reader will be convinced about the fast progress in the understanding of the magnetic properties of molecular magnets thanks to the collaborative work between experimental researchers (chemists, spectroscopists, and physicists) and theoreticians. Obviously the challenges that remain are still huge including minimizing fast magnetic relaxation (mainly through quantum effects), grafting of most promising systems on surfaces without alteration of the properties, and addressing properties from such systems.

The editors are extremely thankful to all the authors for their contributions to this book.

# Contents

<b>Hybrid Organic–Inorganic Cyanide-Bridged Networks . . . . .</b>	<b>1</b>
Tomasz Korzeniak, Beata Nowicka, and Barbara Sieklucka	
<b>Cobalt(II) Complexes as Single-Ion Magnets . . . . .</b>	<b>35</b>
Shalini Tripathi, Atanu Dey, Maheswaran Shanmugam, Ramakirushnan Suriya Narayanan, and Vadapalli Chandrasekhar	
<b>Cobalt(II)/(III)–Lanthanide(III) Complexes as Molecular Magnets . . . . .</b>	<b>77</b>
Atanu Dey, Shalini Tripathi, Maheswaran Shanmugam, Ramakirushnan Suriya Narayanan, and Vadapalli Chandrasekhar	
<b>Mannich Base Ligands as Versatile Platforms for SMMs . . . . .</b>	<b>101</b>
Enrique Colacio	
<b>Tetrathiafulvalene-Based Magnets of Lanthanides . . . . .</b>	<b>163</b>
Olivier Cador and Fabrice Pointillart	
<b>Geometry and Magnetism of Lanthanide Compounds . . . . .</b>	<b>191</b>
Zhenhua Zhu and Jinkui Tang	
<b>Single-Ion Anisotropy: An Insight to Complicated Magnetic Molecules . . . . .</b>	<b>227</b>
Shang-Da Jiang, Bing-Wu Wang, and Song Gao	
<b>Lanthanide Organometallics as Single-Molecule Magnets . . . . .</b>	<b>253</b>
María José Heras Ojea, Lewis C. H. Maddock, and Richard A. Layfield	
<b>Role of Ab Initio Calculations in the Design and Development of Lanthanide Based Single Molecule Magnets . . . . .</b>	<b>281</b>
Tulika Gupta, Mukesh Kumar Singh, and Gopalan Rajaraman	
<b>Complete Active Space Wavefunction-Based Analysis of Magnetization and Electronic Structure . . . . .</b>	<b>355</b>
Frédéric Gendron, H�el�ene Bolvin, and Jochen Autschbach	

<b>Magnetism of Actinide Coordination Compounds</b> . . . . .	391
Jan van Leusen, Manfred Speldrich, and Paul Kögerler	
<b>Correction to: Cobalt(II) Complexes as Single-Ion Magnets</b> . . . . .	411
Shalini Tripathi, Atanu Dey, Maheswaran Shanmugam, Ramakirushnan Suriya Narayanan, and Vadapalli Chandrasekhar	
<b>Correction to: Cobalt(II)/(III)–Lanthanide(III) Complexes as Molecular Magnets</b> . . . . .	413
Atanu Dey, Shalini Tripathi, Maheswaran Shanmugam, Ramakirushnan Suriya Narayanan, and Vadapalli Chandrasekhar	
<b>Index</b> . . . . .	415

# Hybrid Organic–Inorganic Cyanide-Bridged Networks



Tomasz Korzeniak, Beata Nowicka, and Barbara Sieklucka

## Contents

1	Introduction .....	2
2	Magnetic Systems .....	3
2.1	Magnetic Interactions .....	3
2.2	Magnetic Clusters .....	4
2.3	Magnetic Chains .....	8
2.4	Magnetic Layers and 3-D Networks .....	10
3	Interaction with Light .....	11
3.1	Photomagnetism .....	11
3.2	Luminescence .....	17
3.3	Non-linear Effects .....	19
4	Interaction with Molecules .....	21
4.1	Release of Coordinated Solvent .....	21
4.2	Guest Molecules .....	23
4.3	Guest-Controlled CT and Spin-Crossover .....	25
4.4	Guest Ions .....	26
5	Summary .....	27
	References .....	28

**Abstract** Hybrid organic–inorganic CN-bridged networks are an important and versatile group of molecular magnets. Cyanide ligands mediate relatively strong magnetic interactions and at the same time allow easy design of polynuclear assemblies via building block approach. Introduction of organic ligands allows effective manipulation of topology and dimensionality, enabling formation of discrete polynuclear structures, chains and layers as well as intricate 3D architectures. Organic molecules in hybrid systems can act as blocking or bridging ligands as well as guest molecules. Most importantly, apart from directing the structure formation, organic ligands can be used to induce additional desired properties. In this chapter, we present numerous examples of hybrid CN-bridged assemblies to illustrate their diverse functionalities. They include single molecule (SMMs) and single chain magnets (SCMs),

magnetic sponges, multi-switchable spin-crossover (SCO) and charge-transfer systems as well as materials combining magnetic ordering with optical activity or luminescence. Current efforts in the research of CN-bridged systems concentrate on several topics connected with their potential applications, like search for materials with high critical temperature of magnetic ordering, development of bistable systems responsive to multiple stimuli, or surface deposition and formation of heterostructures.

**Keywords** Cyanide ligand · Luminescence · Multifunctionality · Photomagnetism · Solvatomagnetism · Spin crossover

## 1 Introduction

The cyanide ligand is one of the best choices for the construction of molecular magnetic systems based on paramagnetic metal centres. Magnetic interactions mediated by bridging ligands are usually weaker than the interactions in classical metallic or oxide-based magnets, which arise either from direct overlap of magnetic orbitals or from superexchange through the mononuclear  $O^{2-}$  ion. For that reason, molecular magnets are usually characterised by low ordering temperatures. The cyanido-ligand due to its small size and presence of low-lying antibonding  $\pi$  orbitals affords relatively strong magnetic coupling and there are cyanido-bridged systems, which order magnetically above room temperature [1]. At the same time, cyanide ligands allow easy and effective design of polynuclear assemblies of different dimensionality and topology, incorporating organic fragments. The cyanido-bridged networks are usually obtained in self-assembly processes from appropriate cyanidometallates and metal cations or preformed cationic complexes as building blocks. The reactions are carried out in water or organic solvents under mild conditions, which is a great advantage of this class of compounds over classical metallic or oxide-based magnets that are obtained in high-temperature energy-consuming processes. Moreover, the cyanido-bridged networks are usually quite robust. Most of the polymeric structures are practically insoluble and, depending on the metal centres, the evolution of the toxic HCN gas requires harsh conditions: high temperature or exposure to strong acids. Because of the above-mentioned properties, the cyanido-bridged assemblies constitute an important class of molecular magnets.

Prussian blue, the purely inorganic cyanido-bridged compound obtained at the beginning of the eighteenth century and widely used as a pigment, was the first known coordination network. Its dark blue colour [2] and magnetic properties [3] arise from charge delocalisation between Fe(II) and Fe(III) centres. Development of studies into molecular magnetism brought renewed interest in Prussian blue and numerous analogous cyanido-bridged networks of regular cubic structure based on different metal ions have been widely investigated. Some of the Prussian blue analogues (PBAs) show high critical temperature of magnetic ordering [4, 5]. However, the non-stoichiometric character of these networks and difficulties in their crystallisation were a serious drawback in establishing magneto-structural correlations. In order to better understand magnetic exchange through the bridging cyanido-ligands, discrete systems with restricted number of metal centres were created. These included

dinuclear molecules as well as squares and cubes, which served as models for PBAs and allowed quantitative analysis and theoretical modelling of magnetic interactions [1, 6]. In that way, blocking organic ligands were introduced into cyanido-bridged networks enabling engineering of dimensionality and topology.

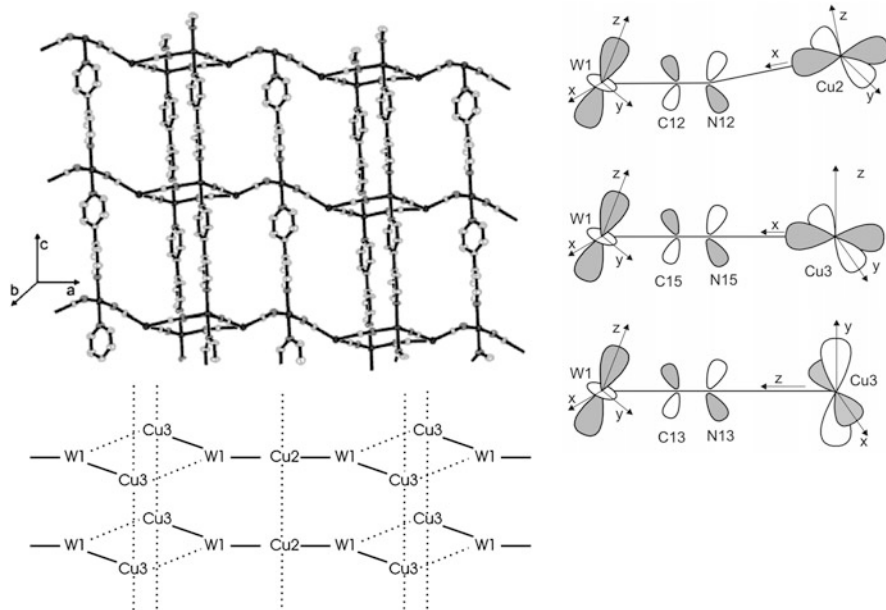
The design of hybrid organic–inorganic cyanido-bridged networks based on the building block principle is amazingly effective, even though the serendipity factor must always be taken into account in the crystallisation processes. Organic molecules and ions can be introduced to replace some of the cyanido groups in cyanidometallates or bound as ligands to cationic building blocks. They can act as blocking or bridging ligands as well as guest molecules. Most importantly, apart from directing the structure formation, organic ligands can be used to induce additional desired properties, thus bringing out the strongest asset of molecular magnets – multifunctionality. Blocking organic ligands allow formation of low-dimensionality structures, among which numerous single molecule magnets (SMMs) and single chain magnets (SCMs) were found. Additionally, specially designed ligands can be used to enforce unusual coordination geometry and enhance magnetic anisotropy. By the use of appropriate blocking or bridging ligands, porous networks can be constructed, which show sorption properties and guest-dependent magnetism. Incorporation of chiral ligands into cyanido-bridged networks may lead to coexistence of optical activity and magnetic ordering resulting in non-linear magneto-optical effects, like magnetisation-induced second harmonic generation (MSHG), or magneto-chiral dichroism (MChD). Other properties that can be achieved in cyanido-bridged networks with organic components include luminescence, photomagnetism and bistability connected with spin-crossover (SCO) or charge-transfer (CT) effects. In this chapter, we present several examples of hybrid cyanido-bridged networks to illustrate their diverse functionalities.

## 2 Magnetic Systems

### 2.1 Magnetic Interactions

The deliberate design of molecular magnetic polynuclear assemblies requires at the first step, the planning of the coordination geometry of the metal centres. This accounts not only for the splitting pattern of the d-orbitals but also determines the “magnetic orbital”, i.e. the singly occupied molecular orbital (SOMO). The important aspect of the super-exchange mechanism is the dependence of molecular interaction on the direction as well as on the type of ligand, as seen in the case of 2-D hybrid system [Cu( $\mu$ -4,4'-bpy)(DMF)<sub>2</sub>][Cu( $\mu$ -4,4'-bpy)(DMF)<sub>2</sub>][W<sup>V</sup>(CN)<sub>8</sub>]<sub>2</sub>·2DMF·2H<sub>2</sub>O [7]. The molecular structure of this assembly is shown in Fig. 1 and reveals two types of bridging ligands, namely cyanido and 4,4'-bipyridine. The simultaneous presence of the organic and inorganic bridging ligands qualifies this system as an inorganic–organic hybrid network. Both ligands are able to transmit the magnetic coupling due to  $\sigma$ -donation and  $\pi$ -acceptor properties, but the bipyridine spacer is much longer than the cyanido one, resulting in an 11.1 Å Cu–Cu distance of 11.1 Å compared to 5.2–5.6 Å in the cyanido-bridged Cu–W linkage. This leads to the assumption that the magnetic interaction





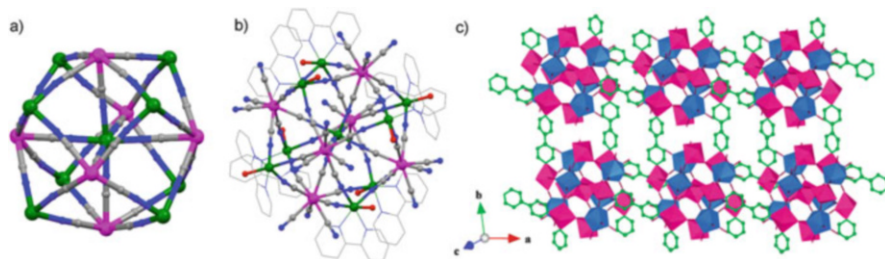
**Fig. 1** The view on the molecular structure of  $[\text{Cu}(\mu\text{-}4,4'\text{-bpy})(\text{DMF})_2][\text{Cu}(\mu\text{-}4,4'\text{-bpy})(\text{DMF})_2][\text{W}^{\text{V}}(\text{CN})_8]_2 \cdot 2\text{DMF} \cdot 2\text{H}_2\text{O}$ , the scheme of the mutual orientation of magnetic orbitals and the model of the magnetic interactions within the cyanido-bridged structure. Reprinted with permission from Ref. [7]. Copyright 2004 American Chemical Society

between the  $\text{Cu}_3\text{W}_2$  chains is weaker than between the  $[\text{Cu}(\mu\text{-}4,4'\text{-bpy})(\text{DMF})_3]_n^{2n+}$  ions that form the chain. However, the pathways of magnetic coupling can be estimated taking into account the mutual orientation of the magnetic orbitals of the paramagnetic centres of  $\text{Cu}^{\text{II}}$  and  $\text{W}^{\text{V}}$  based on the coordination geometry at these metal centres as well as their overlapping with the  $\pi^*$  orbitals of the cyanido-ligand as shown in Fig. 1. Thus, this two-dimensional hybrid network reveals the presence of pentametallic  $\text{Cu}_3\text{W}_2$  units coupled ferromagnetically ( $J = +35 \text{ cm}^{-1}$ ) and the interactions between the units are of antiferromagnetic nature ( $J' = -0.05 \text{ cm}^{-1}$ ). The magnetic dimensionality of this system (i.e. the dimensionality of the magnetic sublattice) is lower than the dimensionality of the coordination network (Fig. 1).

Due to the fact that the magnetic phenomena displayed by the molecular systems depend strongly on the dimensionality of the coordination system as well as its topology, we will show classes of molecular assemblies which display some intriguing properties.

## 2.2 Magnetic Clusters

Magnetic clusters are discrete cyanido-bridged molecules, whose geometry is controlled mainly by blocking, usually chelating ligands. The employment of the



**Fig. 2** The molecular structures of the pentadecanuclear  $M_9M'_6$  core: (a) with terminal aqua ligands, (b) with terminal bpy ligands, and (c) acting as a secondary building block (SBB) unit in the supramolecular hybrid network. Reprinted with permission from Ref. [23]. Copyright 2008 American Chemical Society

preprogrammed ligands prevents the formation of extensive cyanido-bridges and stops the formation of polymeric systems. The structure and the topology of the resulting assembly depends heavily on the building blocks used as well as the reaction conditions and even with the same coordination core different clusters can be obtained as shown in Fig. 2. The self-assembly of the solvated  $M^{2+}$  ions ( $M = Mn, Fe, Co, Ni$ ) with the  $[M'(CN)_8]^{3-}$  ( $M' = Mo, W, Re$ ) leads to the formation of the pentadecanuclear  $M_9M'_6$  cluster units [8–16]. The rational design allows the exchange of the terminal solvent ligands with the bis-chelate diimine ligands [17–22]. Further work enabled to use the pentadecanuclear cluster units as the preprogrammed secondary building blocks (SBBs) and to connect them into the supramolecular network of the higher dimensionality [23–25].

The second family of clusters based on octacyanidometallates employs the  $[M'(CN)_8]^{4-}$  unit, namely the diamagnetic octacyanidomolybdate(IV) and octacyanidotungstate(IV) complexes, which can be substituted with the isostructural paramagnetic octacyanidoniobate(IV). The self-assembly of these complexes with the diimine complexes of divalent cations of transition metals allows the formation of hexanuclear clusters revealing an  $M_4M'_2$  structural motif [26–29]. Due to the presence of the photoactive  $[Mo^{IV}(CN)_8]^{4-}$  ion, these clusters are able to display photomagnetic effect and are discussed in Sect. 3.1.

### 2.2.1 Pentadecanuclear Clusters $M_9M'_6$

Due to the presence of paramagnetic centres connected with a large number of cyanido-bridges, the pentadecanuclear  $M_9M'_6$  molecules are known to reveal a high value of spin, resulting in HSMs (high spin molecules). In the case of highly anisotropic systems, SMM behaviour can be observed.

Typical examples of the HSMs based on the octacyanidometallates are the members of the  $[M^{II}\{M(MeOH)_3\}_8(\mu-CN)_{30}\{M'^V(CN)_3\}_6]\cdot 5MeOH\cdot 2H_2O$  ( $M = Mn^{II}, Fe^{II}, Co^{II}, Ni^{II}$ ;  $M' = Mo^V, W^V$ ) pentadecanuclear clusters revealing the structure of the six-capped body centred cube as shown in Fig. 2a. The geometry of this cluster

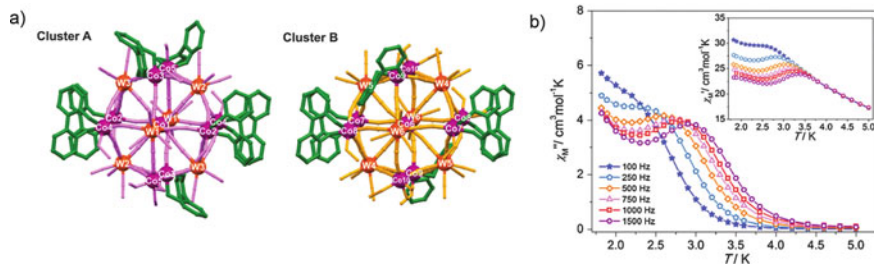
can be described as built of octacyanidometallate units occupying the vertices of an octahedron. All the walls of the octahedron are capped by the eight  $M^{2+}$  units and the ninth  $M^{2+}$  ion occupies the centre of the octahedron.

The first systems of this kind were reported in the year 2000 by the research groups of Decurtins [8] and Hashimoto [9]. Due to the presence of the high-spin  $Mn^{II}$  with  $S = 5/2$  each, which are connected through the cyanido-bridges with the  $Mo^V$  or  $W^V$  centres ( $S = 1/2$ ), the whole molecule reveals antiferromagnetic interaction. Thus, the total spin of the molecule reaches a value of  $S = 39/2$  for the whole  $Mn_9W_6$  unit.

Apart from  $Mn^{II}$  systems, numerous structural analogues were reported. The magnetic properties revealed by the molecules depend on the metal centres used. The substitution of  $Mn^{II}$  centres for  $Ni^{II}$  ions resulted in the formation of  $[Ni\{Ni(MeOH)_3\}_8(\mu-CN)_{30}\{Mo(CN)_3\}_6]$  HSMs displaying  $S = 12$  due to the ferromagnetic interaction between the paramagnetic centres [10]. The incorporation of anisotropic  $Co^{II}$  ions into the pentadecanuclear core gives rise to the SMM behaviour [11], revealing a relaxation energy barrier of  $\Delta E/k_B = 27.8$  K. Further investigation on these class of systems unveiled the presence of thermally induced charge transfer in a series of iron-containing molecules [15, 16]. The  $Fe_9W_6$  cluster obtained by the self-assembly reaction between  $Fe^{2+}$  and  $[W(CN)_8]^{3-}$  ions shows some degree of charge transfer at room temperature, as it displays the  $Fe^{II}_7Fe^{III}_2W^{IV}_2W^V_4$  composition of the pentadecanuclear core. The electron transfer from  $Fe^{II}$  towards  $W^V$  occurs in one step leading to the formation of  $Fe^{II}_3Fe^{III}_6W^{IV}_6$  phase. This thermal charge-transfer phenomenon reveals a hysteresis, with the  $T_{1/2}$  HT  $\rightarrow$  LT equalling 208 K and  $T_{1/2}$  LT  $\rightarrow$  HT, 215 K. The thermal hysteresis seen on the  $\chi_M T$  vs. T plot shows an untypical shape, as the value of the  $\chi_M T$  for the LT phase is higher than that for the HT one. The versatility and the tunability of the  $M_9M'_6$  cluster systems is confirmed by the results of the systematic research of the  $Co_xFe_{9-x}W_6$  series where  $x = 0-9$  [16]. All the members of this series reveal a systematic change in their properties. The iron-rich systems display the thermal CT phenomena due to the aforementioned  $^{HS}Fe^{II}W^V \rightleftharpoons ^{HS}Fe^{III}W^{IV}$  process, which is accompanied by the  $^{HS}Co^{II}W^V \rightleftharpoons ^{LS}Co^{III}W^{IV}$  channel. As the  $Co_9W_6$  system shows an SMM behaviour, the same is observed in the series of  $Co_6Fe_3W_6-Co_9W_6$  systems, which display an increasing value of the blocking energy.

As the original pentadecanuclear clusters contained solvent molecules of methanol to complete the coordination spheres of the metal ions involved, the logical extension of this synthetic strategy was the employment of blocking chelate ligands in order to influence the electronic structure of the metal centres.

The implementation of the 2,2'-bpdo (2,2-bipyridine *N,N'*-dioxide) ligand in the coordination sphere of the external cobalt ions building the  $Co_9W_6$  cluster allowed for modification of the SMM behaviour [22]. The molecular structure of the systems built of pentadecanuclear  $\{Co_9W_6(2,2'-bpdo)_7\}$  cluster molecules (2,2'-bpdo = 2,2-bipyridine *N,N'*-dioxide), which co-crystallise with the  $\{Co_9W_6(2,2'-bpdo)_6\}$  molecules is shown in Fig. 3. This system is formed by a self-assembly process and allows for the increase of the relaxation energy barrier. Due to the induction of the structural anisotropy brought by the coordination of the seven bpdo ligands, the relaxation energy barrier increased to 30.0 K compared to 27.8 K in the case of  $Co_9W_6$  unit with methanol ligands.



**Fig. 3** (a) The molecular structures of  $\{\text{Co}_9\text{W}_6(2,2'\text{-bpdo})_7\}$  (Cluster A) and  $\{\text{Co}_9\text{W}_6(2,2'\text{-bpdo})_6\}$  (Cluster B) units; (b) the plots of the real (inset) and imaginary components of the magnetic susceptibility vs. temperature. Reprinted with permission from Ref. [22]. Copyright 2016 Royal Society of Chemistry

Several pentadecanuclear clusters containing the  $\text{Ni}_9\text{M}'_6$  ( $\text{M}' = \text{Mo}, \text{W}$ ) core bearing coordinated diimine ligands have been reported [17–21]. These molecules display a ferromagnetic interaction within the cyanido-bridged cluster, leading to a spin value  $S = 12$ . However, in several cases the coordination of the chelate ligand allows the induction of the slow relaxation of the magnetic moment. The 2,2'-bipyridine substituted compound of the formula  $[\text{Ni}\{\text{Ni}(\text{bpy})(\text{H}_2\text{O})\}_8\{\text{W}(\text{CN})_8\}_6] \cdot 23\text{H}_2\text{O}$  was found to display substantial anisotropy that allows the induction of the SMM behaviour contrary to the unsubstituted molecule [17]. Such functionalisation of the molecule by the bidentate ligand was reported in the systems bearing tetramethylphenanthroline. The  $\{\text{Ni}[\text{Ni}(\text{tmphen})(\text{MeOH})]_6[\text{Ni}(\text{H}_2\text{O})_3]_2[\text{W}^{\text{V}}(\text{CN})_8]_6\} \cdot 6\text{DMF}$  molecule reveals slow relaxation of the magnetic moment [20], characterised by the relaxation energy barrier of 5.6 K.

The modification of the parent pentadecanuclear unit with the peripheral ligands can introduce new properties, as in the case of chiral  $\{\text{M}^{\text{II}}[\text{M}^{\text{II}}(\text{R/S-mpm})(\text{MeOH})]_8[\text{W}^{\text{V}}(\text{CN})_8]_6\} \cdot 14\text{MeOH}$  ( $\text{M} = \text{Co}, \text{Ni}$ ) containing the chiral mpm ligand (mpm = 2-(1-hydroxyethyl)pyridine) [30]. The presence of the chiral ligands lowers the molecular symmetry of the pentadecanuclear moiety. The cobalt-based system reveals a relaxation energy barrier of 19 K. The SMM behaviour is not observed in the case of the nickel analogue, presumably due to the lower magnetic anisotropy of the  $\text{Ni}^{\text{II}}$  compared to  $\text{Co}^{\text{II}}$ .

The modification of the coordination sphere with ligands can modify the parameters of the SCO phenomena. A comparison of  $\{\text{Fe}^{\text{II}}_9[\text{Re}^{\text{V}}(\text{CN})_8]_6(\text{MeOH})_{24}\}$  with its analogue  $\{\text{Fe}^{\text{II}}_9[\text{Re}^{\text{V}}(\text{CN})_8]_6(\text{Me}_3\text{tacn})_8\} \cdot 14\text{MeOH}$  containing the triamine ligands  $\text{Me}_3\text{tacn}$  (1,4,7-trimethyl-1,4,7-triazacyclononane) shows the effect of ligand [31]. The first system reveals SCO at the central  $\text{Fe}^{\text{II}}$  ion, whereas the eight terminal iron(II) centres are SCO-silent due to the  $\text{N}_3\text{O}_3$  coordination sphere. However, the facial coordination of the triaza ligands to the terminal  $\text{Fe}^{\text{II}}$  centres allows the observation of the gradual SCO process involving all of the iron(II) centres.

The pentadecanuclear  $\text{M}_9\text{M}'_6$  molecules can act as SBBs. Taking into account the high tunability of the properties of these units, these can serve as building units that allow the formation of molecular materials with more advanced features. Depending on the type of molecular bridges formed, these systems reveal different topologies of

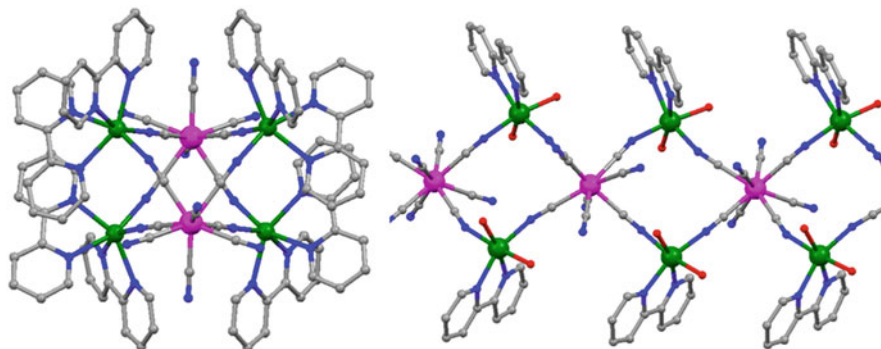
inorganic–organic hybrid networks. The use of the 4,4′-bipyridine molecular bridge causes the formation of organic bridges between the  $\text{Mn}_9\text{W}_6$  cluster units, leading to the formation of the hybrid system of  $1^0\text{O}^2$  dimensionality [23]. On the other hand, the use of the *N,N*-dioxide derivative, namely 4,4′-bipyridine *N,N*-dioxide, to connect the  $\text{Co}_9\text{W}_6$  units resulted in the formation of two systems where the role of 4,4′-bpdo is different [25]. In the molecular structure of  $\{\text{Co}^{\text{II}}[\text{Co}^{\text{II}}(4,4′\text{-bpdo})_{1,5}(\text{MeOH})]_8[\text{W}^{\text{V}}(\text{CN})_8]_6\} \cdot 2\text{H}_2\text{O}$  system, the 4,4′-bpdo molecule connects the  $\text{Co}^{\text{II}}$  centres, leading to formation of the coordination strands of  $1^0\text{O}^1$  dimensionality. Due to the presence of weak antiferromagnetic interaction along the organic bridge, the magnetic isolation of  $\text{Co}_9\text{W}_6$  clusters is counteracted. This leads to a weakening of the SMM behaviour pronounced by the shifting of  $\chi''$  frequency-dependent maxima below 1.8 K. However, the 4,4′-bpdo molecules can act also as supramolecular guest molecules, as in the  $\{\text{Co}^{\text{II}}_9(\text{MeOH})_{24}[\text{W}^{\text{V}}(\text{CN})_8]_6\} \cdot 4,4′\text{-bpdo} \cdot \text{MeOH} \cdot 2\text{H}_2\text{O}$  system. In this case, the pentadecanuclear units are relatively well isolated from each other, resulting in SMM behaviour characterised by the energy barrier of 10.3 K, which is significantly lower than the value of 27.8 K for the totally isolated  $\text{Co}_9\text{W}_6$  units.

The concept of connecting the cluster units can also be realised by the use of inorganic bridges. The  $\{\text{Mn}^{\text{II}}_9[\text{W}^{\text{V}}(\text{CN})_8]_6(\text{dpe})_5(\text{MeOH})_{10}\}_3 \cdot 14\text{MeOH}$  (*dpe* = *trans*-1,2-di(4-pyridyl)ethylene) system consists of two types of bridging ligands: the organic spacers as well as the cyanido-ligands, resulting in the formation of  $1^1\text{O}^2$  hybrid network [24]. The cyanido-bridged chains reveal a superparamagnetic behaviour due to strong magnetic interaction within the chains. The chains are connected by the long organic spacer, which leads to weak antiferromagnetic interactions between the chains.

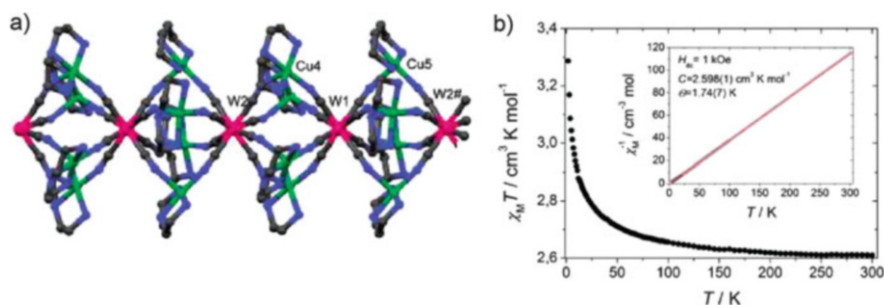
### 2.3 Magnetic Chains

From the structural point of view, the formation of the cyanido-bridged chain structure requires, generally, a similar number of cyanido linkages as in the case of 0-D assemblies. However, the design of the coordination sphere of cationic metal centre requires careful planning. A good example is a pair of systems obtained in the self-assembly between  $\text{Mn}^{2+}$  ions, 2,2′-bipyridine and  $[\text{W}(\text{CN})_8]^{4-}$  ions shown in Fig. 4. Depending on the reaction conditions, 0-D  $\text{Mn}(\text{bpy})_4\text{W}_2$  or 1-D chains containing vertex-sharing squares can be obtained [26, 32].

The polymetallic chain system built of the paramagnetic metal centres bridged by the cyanido-ligand cannot exhibit long-range magnetic ordering (LRMO). However, in the presence of the strong intrachain magnetic coupling and weak interaction between the chains (interchain), the system reveals an Ising chain behaviour, also known as the easy-axis magnetisation system. An interesting topology is displayed by the  $(\text{H}_3\text{O})\{[\text{Cu}^{\text{II}}(\text{dien})_4[\text{W}^{\text{V}}(\text{CN})_8]]_4[\text{W}^{\text{V}}(\text{CN})_8]_2\} \cdot 6.5\text{H}_2\text{O}$  system [33] (*dien* = diethylenetriamine) shown in Fig. 5. Here, all the cyanido-ligands act as bridging ligands. The magnetic interaction between the  $\text{Cu}^{\text{II}}$  and  $\text{W}^{\text{V}}$  centres is ferromagnetic. The magnetic properties of this system have been analysed by the use of DFT methods. Based on the structural data, a model was built, taking into account two types of cyanido-bridges that reveal different geometrical arrangements. The values of *J* coupling constants



**Fig. 4** The structures of 0-D hexanuclear cluster and 1-D chain of vertex-sharing squares obtained in the  $\text{Mn}^{2+}/\text{bpy}/[\text{W}(\text{CN})_8]^{4-}$  systems



**Fig. 5** The molecular structure of  $(\text{H}_3\text{O})\{[\text{Cu}^{\text{II}}(\text{dien})]_4[\text{W}^{\text{V}}(\text{CN})_8]\}[\text{W}^{\text{V}}(\text{CN})_8]_2 \cdot 6.5\text{H}_2\text{O}$  (a); the thermal dependence of the magnetic susceptibility of the assembly as  $\chi_{\text{M}}T$  and  $\chi_{\text{M}}^{-1}$  (inset) plots (b). Reprinted with permission from Ref. [3]. Copyright 2011 American Chemical Society

were found to be  $+2.9 \text{ cm}^{-1}$  and  $+1.5 \text{ cm}^{-1}$  in the case of the axial and equatorial bridges, respectively.

In the case of strong magnetic interaction within the isolated chains (i.e. the absence of interchain interactions), an SCM behaviour can be observed. This phenomenon shows basically similar magnetic characteristics. One of the systems that display such properties is the 1-D helical  $[\{(\text{H}_2\text{O})\text{Fe}(\text{L}^1)\}\{\text{Nb}(\text{CN})_8\}\{\text{Fe}(\text{L}^1)\}]$  chain [34]. The  $\text{Fe}^{\text{II}}$  centres reveal an unusual coordination number of 7, which is the reason for the high anisotropy in the system. The magnetic interaction within the helical chain is of anti-ferromagnetic nature, revealing  $J = -20 \text{ cm}^{-1}$ . What is interesting is that the chains are well isolated, so that the slow relaxation of magnetisation is observed. The energy of the blocking barrier is relatively high,  $\Delta/k_B = 74 \text{ K}$ . The values of blocking barrier energies in the case of SCM systems are higher than that of SMM materials, as the reorientation of a chain of spins is a collective process. In other words, the propagation of the wall domain reversal needs more energy. The magnetisation vs. field recorded at 0.38 K reveals a sharp coercive loop due to the tunnelling effect upon the external magnetic field.



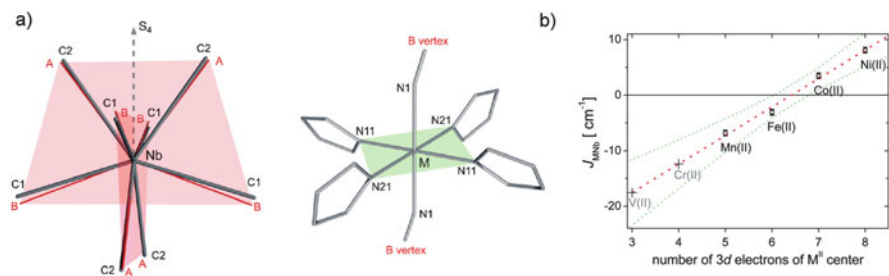
## 2.4 Magnetic Layers and 3-D Networks

The construction of two-dimensional layered structures does not require a high number of blocking ligands in the coordination sphere of the metal centre as the number of cyanido-bridges is higher. Generally, two types of coordination spheres' arrangements are observed. The metal centres can act as linkers or nodes in the resulting coordination network. The application as a linker is typical for the metal complex with macrocyclic ligands such as cyclam [35–38], where two coordination sites are available for substitution with the cyanido-bridges in the apical positions. Systems of this kind usually reveal a honeycomb topology with wide channels available for solvent molecules. On the other hand, the nodal role of the cationic metal complex demands the formation of more molecular bridges which results in the preference of square-grid-type topologies.

The formation of a two-dimensional layer and the increased cross-linking by the cyanido-bridges allows long-range magnetic interactions. This can give rise to the formation of the layered systems with the presence of LRMO, such as in the case of  $\text{Cs}^{\text{I}}[\text{Mn}^{\text{II}}(3\text{-cyanopyridine})_2\{\text{W}^{\text{V}}(\text{CN})_8\}\cdot\text{H}_2\text{O}$  [39]. The molecular structure of the system is formed by cyanido-bridging at the  $\text{Mn}^{\text{II}}$  centres in the equatorial positions. The magnetic moments of  $\text{Mn}^{\text{II}}$  and  $\text{W}^{\text{V}}$  interact antiferromagnetically, resulting in the final ferrimagnetic behaviour below the temperature of 35 K. It is worth noting that the analogous system consisting  $\text{Co}^{\text{II}}$  ions reveals photomagnetic properties shown in Sect. 3.1.

Other 2-D systems revealing high number of linkages such as Cu–W, Cu–Mo double-layered systems display relatively high values of the long-range ordering temperatures in the range of 28–35 K [40–42]. These can be compared with the cyanido-bridged layers, but with the lower cross-linking, such as  $[\text{Ni}^{\text{II}}(\text{cyclam})]_3[\text{W}^{\text{V}}(\text{CN})_8]_2$  system [35]. On the other hand, the presence of the flexible coordination skeleton allows for the modification of the  $T_C$  temperature in the range of 4.9–11.2 K upon solvation/desolvation processes as shown in the Sect. 4.2.

The 3-D cyanido-bridged systems are generally built of metal centres linked by the cyanido-bridges and the networks with blocking ligands are rare. The typical systems of this kind are PBAs revealing the regular structure due to the presence of the regular coordination geometries of the building blocks. The octacyanidometallate-based coordination networks display a lower geometry as the  $[\text{M}(\text{CN})_8]^{n-}$  ion adopts a coordination geometry that is intermediate between dodecahedral, square antiprismatic and bicapped trigonal prism [43, 44]. The typical values of  $T_C$  for the PBA based on octacyanidometallate ions are in the range 40–50 K [45], which is unfortunately lower compared to hexacyanidometallate-based systems. The similarity of these types of systems is seen also in the non-stoichiometric systems consisting  $\text{V}^{\text{II}}/\text{V}^{\text{III}}$  ions. The employment of the ions possessing occupied  $t_{2g}$  orbitals and one empty  $e_g$  orbital was predicted to allow obtaining exceptionally high critical temperature values for the 3-D networks that reveal ferromagnetic coupling. Presumably due to the experimental difficulties of working with Cr ions, attention has been devoted to vanadium ions. Indeed, the V–Cr<sup>III</sup> 3-D Prussian blue has been confirmed to order ferromagnetically above room temperature [46]. The respective analogue V–Nb<sup>IV</sup> system reveals



**Fig. 6** (a) The coordination geometries of the Nb<sup>IV</sup> and M<sup>II</sup> centres in the molecular structure of [M<sup>II</sup>(pyrazole)<sub>4</sub>]<sub>2</sub>[Nb<sup>IV</sup>(CN)<sub>8</sub>]-4H<sub>2</sub>O; (b) the correlation of the  $J$  coupling constant with the number of 3d-electrons. Reprinted with permission from Ref. [48]. Copyright 2010 American Chemical Society

significantly lower  $T_C = 210$  K; however, it is still the highest reported  $T_C$  for the octacyanidometallate systems [47].

The other ways to increase the ordering temperature of 3-D systems is the implementation of a molecular bridge, namely an organic ligand due to the reversible removal of solvent molecules. This type of behaviour is called “magnetic sponge” and was demonstrated for the first time in the {[Mn<sup>II</sup>(pydz)(H<sub>2</sub>O)<sub>2</sub>][Mn<sup>II</sup>(H<sub>2</sub>O)<sub>2</sub>][Nb<sup>IV</sup>(CN)<sub>8</sub>]-2H<sub>2</sub>O} system described in Sect. 4.1.

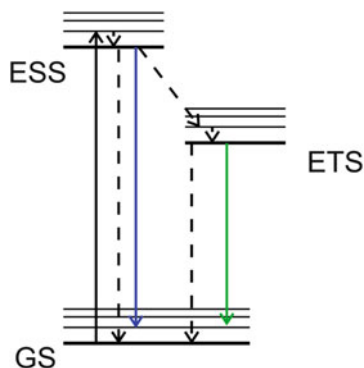
The 3-D networks with terminal ligands, such as pyrazole, reveal the analogous trends in the change of magnetic properties as the PBAs do. A systematic analysis of the magnetic properties in the isostructural series {[M<sup>II</sup>(pyrazole)<sub>4</sub>]<sub>2</sub>[Nb<sup>IV</sup>(CN)<sub>8</sub>]-4H<sub>2</sub>O} (M = Mn, Fe, Co, Ni) [48] reveals the correlation of the  $J$  coupling constant with the metal centre as shown in Fig. 6.

## 3 Interaction with Light

### 3.1 Photomagnetism

The basic idea of the photomagnetic effect can be briefly summarised in just one sentence: it is the modification of the magnetic properties of the molecular systems upon interaction with light. Following this simple definition, one can distinguish two main types of the photomagnetic phenomena found in the cyanido-bridged systems. The first group relies on the SCO phenomena that occur on a specific metal centre. Due to the fact that the SCO phenomenon can also be induced by different external stimuli such as pressure or temperature, the photogenerated change of the spin state has been ascribed a name of LIESST (Light Induced Excited Spin State Trapping). The second group of the photomagnetic systems exhibits an electron transfer between the metal centres and is named as MMCT (metal-to-metal charge transfer) systems. Before we proceed towards a more detailed description of the two mechanisms, the prerequisite conditions to design the photomagnetic systems need to be specified. Regardless of the mechanism, the following necessary conditions need to be fulfilled:





**Fig. 7** The Jablonski diagram showing the pathways of the photomagnetic effect and luminescence. *GS* ground singlet state, *ESS* excited singlet state, *ETS* excited triplet state, black solid line – absorption of light, colour lines – luminescence (blue – fluorescence and green – phosphorescence), dot lines – non-radiative transitions: relaxation, intersystem crossing, etc.

- The presence of a band in the visible range, which is connected with the transition between different spin states (in the case of the LIESST-type systems) or an intermetallic charge-transfer band (for systems that reveal photoinduced MMCT). However, the excitation wavelength should be selected carefully – although sometimes it is possible to detect the photomagnetic effect with the white light, it is advisable to check the different wavelengths separately. This is especially important in the case of photoswitchable on–off systems, such as  $\text{Cu}^{\text{II}}[\text{Mo}^{\text{IV}}(\text{CN})_8] \cdot 8\text{H}_2\text{O}$ , that reveal photoinduced transfer of the electron  $\{\text{Cu}^{\text{II}}\text{Mo}^{\text{IV}}\} \rightarrow \{\text{Cu}^{\text{I}}\text{Mo}^{\text{V}}\}$  upon irradiation with 430 nm light and the reversed photoprocess upon irradiation with 600 nm [49].
- The possibility to stabilise the excited (i.e. photogenerated) state. This is a metastable state, so the relaxation occurs as shown in the Fig. 7. There are two main pathways of relaxation. The first is the thermal pathway, where the ground state is recovered after heating up to a certain temperature – in the case of the photomagnetic systems based on octacyanidometallates this thermal threshold falls usually in the range of 50–200 K. The second pathway is the emission of the light of the energy lower than the one used in the excitation, which leads to fluorescence or phosphorescence, depending on whether the system retains the value of the spin or changes its value, respectively. The luminescence studies on the cyanido-bridged coordination systems are presented in Sect. 3.2.

### 3.1.1 The Light Induced Excited Spin State Trapping Systems

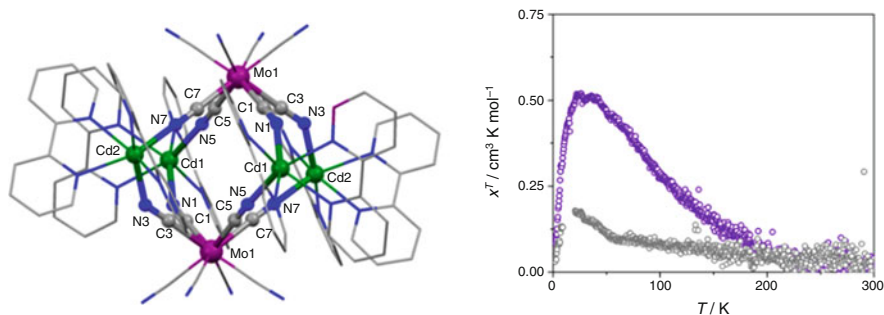
The change of the spin state upon irradiation with light is known as the LIESST effect. In this phenomenon, light induces the spin transition. Due to the fact that the change of the spin occurs within the one metal centre, it can be observed also in monometallic complexes, such as  $[\text{Fe}(\text{ptz})_6](\text{BF}_4)_2$  ( $\text{ptz} = 1\text{-propyl-tetrazole}$ ) [50] as

well as in polynuclear networks. Due to the irradiation with the 514 nm light, the HS state is populated (LIESST effect), which undergoes a back transition to the LS state upon irradiation with 820 nm light, which is called reverse-LIESST.

Polynuclear cyanido-bridged systems based on octacyanidometallates are able to display photomagnetic transition. A detailed analysis of the mechanism of photoinduction of magnetisation in the cyanido-bridged systems containing the  $[\text{Mo}(\text{CN})_8]^{4-}$  units possessing metal ions with a  $d^2$  electronic configuration revealed the presence of the singlet–triplet transition upon irradiation with 436 nm light [51–53]. The selected wavelength falls within the d-d band of the octacyanidomolybdate(IV) ion. The conditions necessary for such a transition to occur involve the structural deformation of the octacyanidometallate ion. Due to the fact that the energies of the d orbitals depend on the coordination geometry around the Mo(IV) ion, the most favourable geometry is the distorted square antiprism geometry as in this case the difference of the energies of the first two d-orbitals of the lowest energy is minimised [54]. The investigation of the photomagnetic effect in the model trimetallic system  $[\text{Zn}(\text{tren})]_2\text{Mo}(\text{CN})_8$  led to the first unequivocal assignment of the singlet–triplet mechanism in the octacyanidomolybdate(IV)-based molecular system. The asymmetric unit consists of two types of trimetallic  $\text{Zn}_2\text{Mo}$  units of a slightly distorted square antiprism coordination geometry of the molybdenum centre. Irradiation of the single crystal of the diamagnetic sample with the 436 nm light led to the display of a paramagnetic signal, due to the transition of 50% of molybdenum centres towards the triplet state. The photomagnetic effect was connected with the change of the sample colour as the original yellow crystal became red. The molecular structure was examined with the use of XRD at the photoinduced state of the sample and revealed the presence of structural deformation of the  $\text{Zn}_2\text{Mo}$  moieties. A detailed analysis of the molecular shape revealed that the coordination geometry of one of the  $[\text{Mo}(\text{CN})_8]^{4-}$  moieties undergoes a significant distortion towards the dodecahedral geometry. Theoretical predictions on the energy of d-orbitals in the octacoordinate systems indicate that the distortion of the square antiprismatic coordination geometry towards the dodecahedral one stabilises the triplet state, as the energies of the two lowest d-orbitals are close to each other.

An example of the system that reveals the LIESST mechanism is the  $[\text{Cd}(\text{bpy})_2]_4[\text{Mo}(\text{CN})_8]_2$  hexanuclear cluster unit [29]. As the starting material is diamagnetic, the irradiation of the clusters induces the emergence of the magnetic signal. The photogenerated state undergoes a thermal relaxation as shown in Fig. 8. The SCO phenomenon in the  $[\text{M}(\text{CN})_8]^{4-}$  systems was attributed only to the  $\text{Mo}^{\text{IV}}$  systems. Moreover, this system reveals the reversible single-crystal to single-crystal dehydration–rehydration phenomenon.

The singlet–triplet photoinduced transition on the octacyanidometallate(IV) moieties has been observed in the polynuclear systems built from  $[\text{Mo}(\text{CN})_8]^{4-}$  ions. Very recently, such phenomenon has been observed in the octacyanidotungstate-based  $\{[\text{Mn}^{\text{II}}(\text{bpy})_2][\text{Mn}^{\text{II}}(\text{bpy})(\text{H}_2\text{O})_2][\text{W}^{\text{IV}}(\text{CN})_8] \cdot 5\text{H}_2\text{O}\}$  chain system [55]. In this case, irradiation with 436 nm light caused an increase of the magnetic signal. Due to the fact that the saturation magnetisation of the photoexcited sample is higher than that of the pristine one and the excitation energy falls within the d-d band of the  $[\text{W}(\text{CN})_8]^{4-}$  ion, photomagnetic effect is due to the singlet–triplet transition. The



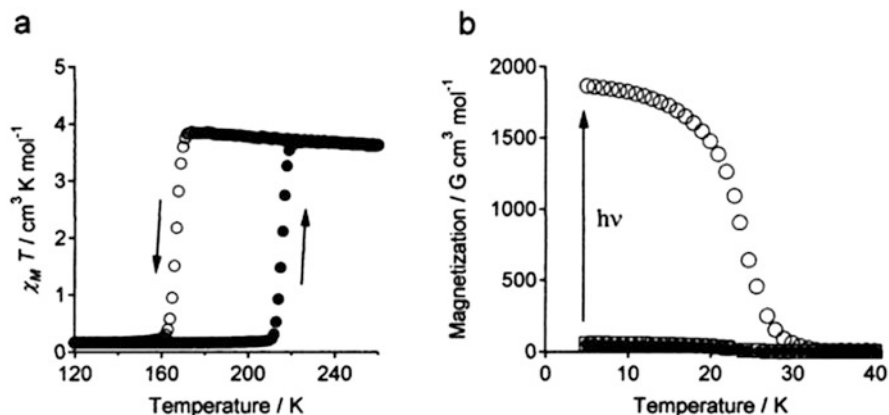
**Fig. 8** The molecular structure of the  $[\text{Cd}^{\text{II}}(\text{bpy})_2]_4[\text{Mo}^{\text{IV}}(\text{CN})_8]_2 \cdot 10\text{H}_2\text{O}$ ; the magnetic susceptibility after irradiation (magenta) and after thermal relaxation (grey) of the  $\text{Cd}_4\text{Mo}_2$  system. Reprinted with permission from Ref. [29]. Copyright 2017 American Chemical Society

photoinduced state reveals weak antiferromagnetic interactions between  $\text{Mn}^{\text{II}}$  and  $\text{W}^{\text{IV}}_{\text{HS}}$  centres. A similar behaviour has been observed for the molybdenum analogue.

Taking into account the other octacyanidometallate(IV) ions, no effect related to its S–T transition can be observed for the  $[\text{Nb}^{\text{IV}}(\text{CN})_8]^{4-}$  as  $\text{Nb}^{\text{IV}}$  has a  $d^1$  electron configuration. However, the LIESST effect can be observed provided that it occurs on the cationic metal centre, as revealed on  $\text{Fe}^{\text{II}}$  in the hexametallic cluster  $[\text{Fe}(\text{tmphen})_2]_4[\text{Nb}(\text{CN})_8]_2 \cdot 6\text{H}_2\text{O} \cdot 15\text{MeOH}$  (tmphen = 3,4,7,8-tetramethyl-1,10-phenanthroline) possessing an octahedral topology [56]. Irradiation with 740 nm light causes an increase of the magnetic signal due to photoinduced SCO on the  $\text{Fe}^{\text{II}}$  centres and the photoexcited state is relaxed thermally at 60 K.

### 3.1.2 Metal-to-Metal Charge Transfer Systems

The second type of the phenomena is the charge transfer between the metal centres. This mechanism involves an inner-sphere redox reaction, namely transfer of an electron mediated by the cyanido-bridge. This is common for the cyanido-bridged coordination networks of a high dimensionality, such as the 3-D networks. In order to observe such a transition, the systems need to be irradiated in the MMCT band. Due to the high intensity of the charge-transfer bands, the cross-section of the process is relatively high. In the case of the redox or spin state bistability of one or two metal centres, the charge-transfer phenomena can be accompanied by other effects such as SCO at one (or two) metal centres that are involved in bridging. One of the examples is the 2-D coordination network  $\text{Cs}^+[\{\text{Co}^{\text{II}}(\text{3-cyanopyridine})_2\}\{\text{W}^{\text{V}}(\text{CN})_8\}] \cdot \text{H}_2\text{O}$  [57] shown in Fig. 9. The system at its ground state reveals  $\text{Co}^{\text{II}}$  LS ( $S = 1/2$ ) and  $\text{W}^{\text{V}}$  ( $S = 1/2$ ) spin states. On cooling, the low-temperature phase is formed due to the thermal process, resulting in the diamagnetic system  $\text{Co}^{\text{III}}\text{LS}$  ( $S = 0$ ) –  $\text{W}^{\text{IV}}$  ( $S = 0$ ). The irradiation of the sample with the red light causes a dramatic increase of the magnetic signal, as the  $\text{Co}^{\text{II}}\text{HS}$  ( $S = 3/2$ ) –  $\text{W}^{\text{V}}$  ( $S = 1/2$ ) phase is



**Fig. 9** (a) Thermal spin-crossover (SCO) loop for  $\text{Cs}^{\text{I}}\{[\text{Co}^{\text{II}}(3\text{-cyanopyridine})_2]\{\text{W}^{\text{V}}(\text{CN})_8\}\}\cdot\text{H}_2\text{O}$  system; (b) the photoinduced magnetisation of the sample (empty circles) compared with the magnetisation before irradiation (full circles). Reprinted with permission from Ref. [57]. Copyright 2003 American Chemical Society

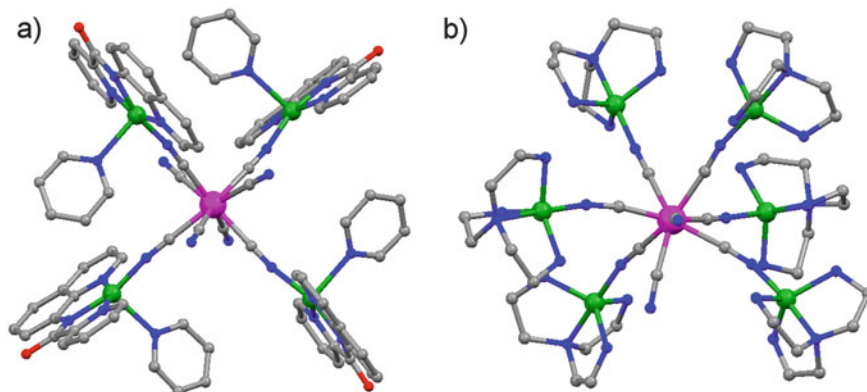
formed. The system reveals ferromagnetic coupling through the cyanido-bridge and both charge-transfer transitions are reversible with the thermal relaxation procedure.

The cyanido-bridged systems that reveal the MMCT-based photomagnetic effect can also exhibit the opposite electron transfer (i.e. from the excited state to the ground state) upon irradiation with a different wavelength of lower energy. Such a phenomenon is exhibited by the  $\text{Cu}^{\text{II}}_2[\text{Mo}^{\text{IV}}(\text{CN})_8]\cdot 8\text{H}_2\text{O}$  coordination network [49]. This system reveals the highly bridged 3-D structure. Irradiation with the 480 nm CT band causes the formation of the paramagnetic  $\text{Mo}^{\text{V}}$  centres at the expense of  $\text{Cu}^{\text{II}}$  ions. Due to the Cu:Mo stoichiometry of 2:1 even at the completed transformation, the moiety consists of paramagnetic centres linked by the cyanido-bridges. The dominant ferromagnetic interaction in the excited state accounts for the increase of the magnetic signal.

The photomagnetic effect is also exhibited by cyanido-bridged systems of lower dimensionality. One of the interesting systems is the pentametallic complex  $[\text{Cu}(\text{L}1_0)(\text{pyridine})]_4[\text{Mo}^{\text{IV}}(\text{CN})_8]\cdot 14\text{H}_2\text{O}$  ( $\text{L}1_0 = N\text{-}(\text{quinolin-8-yl})\text{pyridine-2-carboximidate}$ ) possessing a star topology [58] as shown in Fig. 10a. The  $\text{Cu}_4\text{Mo}$  core reveals a paramagnetic behaviour due to the presence of the diamagnetic  $\text{Mo}^{\text{IV}}$  node connecting the four paramagnetic  $\text{Cu}^{\text{II}}$  centres. Irradiation at 436 nm leads to a charge transfer between the  $\text{Mo}^{\text{IV}}$  and  $\text{Cu}^{\text{II}}$  centres, resulting in the photogenerated state  $\text{Cu}^{\text{I}}\text{Cu}^{\text{II}}_3\text{Mo}^{\text{V}}$  that reveals a ferromagnetic interaction within the molecule.

### 3.1.3 Mixed Mechanisms

Investigations of the photomagnetic effect in the cyanido-bridged molecular systems are still in progress. Some of the systems reveal more complex behaviour, which can be ascribed to the simultaneous processes connected with SCO and charge-transfer



**Fig. 10** The molecular core structures of  $\text{Cu}_4\text{Mo}$  (left) and  $\text{Cu}_6\text{Mo}$  (right) systems (see descriptions in the text). Colours: Mo – magenta, Cu – green, C – grey, N – blue, O – red

phenomena. One such system is the 1-D chain  $[\text{Cu}^{\text{II}}(\text{bapa})_2][\text{Mo}^{\text{IV}}(\text{CN})_8] \cdot 7\text{H}_2\text{O}$  (bapa = bis(3-aminopropyl)amine) [59]. The photomagnetic response of this compound can be obtained by irradiation at 405, 532 nm as well as with white light. However, no photogenerated magnetisation was observed upon using the 647, 843 and 980 nm wavelengths. The relaxation of the photoexcited state occurs upon heating above 250 K, which is one of the highest values in this kind of systems and it enables the detection of the photomagnetic effect upon irradiation in the temperature of 100 K. The explanation of the photomagnetic effect in this compound should take into account the complexity of the molecular structure of the 1-D chain as well as the simultaneous occurrence of the charge-transfer and SCO processes.

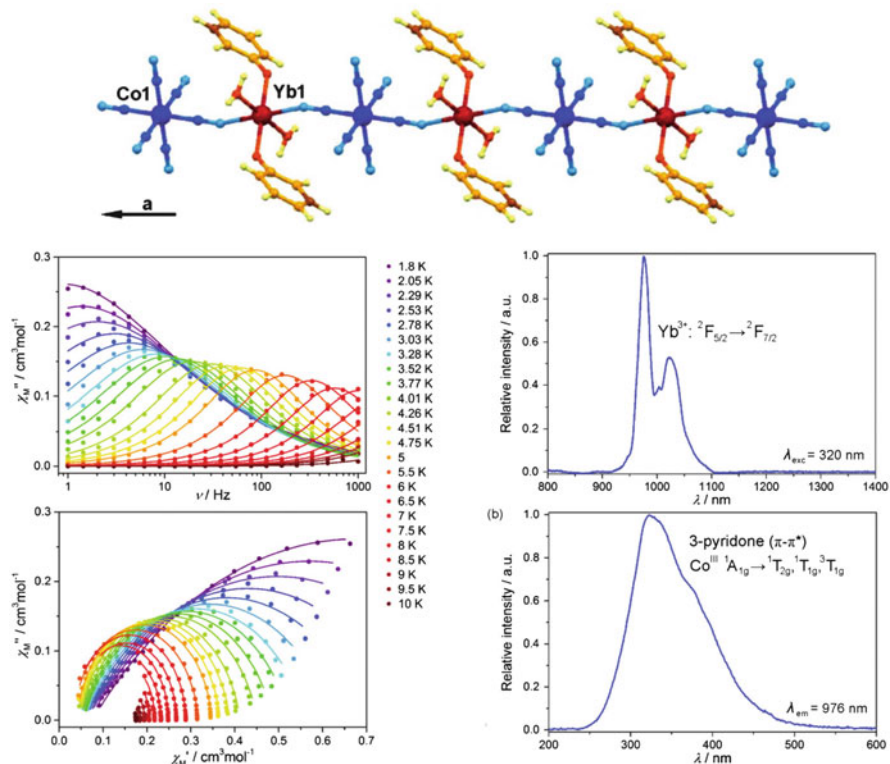
One of the thoroughly investigated photomagnetic systems that exhibits the coexistence of the two mechanisms of the photogenerated magnetisation is the heptametallic molecule  $\{[\text{Cu}(\text{tren})(\mu\text{-NC})]_6\text{Mo}(\text{CN})_2\}(\text{ClO}_4)_2$  of the star topology [52, 60] shown in Fig. 10b. The magnetic properties of this system are typical for paramagnetic compound, as the six paramagnetic  $\text{Cu}^{\text{II}}$  complexes are linked to the diamagnetic  $\text{Mo}^{\text{IV}}$  centre. This system reveals the photomagnetic effect upon the irradiation with the 406 nm light. The first elucidation of the origin of the photoinduced magnetisation assumed the electron transfer from  $\text{Mo}^{\text{IV}}$  to one of the  $\text{Cu}^{\text{II}}$  centres, leading to formation of  $\text{Cu}^{\text{I}}\text{Cu}^{\text{II}}_5\text{Mo}^{\text{V}}$  system containing the six  $S = 1/2$  spins connected by the cyanido-bridging ligands. The  $[\text{Cu}(\text{tren})(\text{NC})]$  moieties reveal the trigonal bipyramidal geometry enforced by the geometry of the ligand, which leads to the coordination of the cyanido-bridge at the axial position. This leads to the presence of a strong ferromagnetic interaction. The system undergoes thermal relaxation with recovering of the original state. However, the mechanism of the photoinduced magnetisation in this system has been recently revised with the employment of the second-order perturbation theory and the DFT calculations, pointing out the simultaneous occurrence of the d-d excitation on the Mo centre. Based on the results of the calculations, it is expected that the photomagnetic effect is accompanied by the distortion of the octacyanidomolybdate moiety and dissociation of one

of the terminal cyanido-ligands. This approach shows the trend in resolving the complexity of the mechanism of photogenerated magnetisation in the cyanido-bridged  $\text{Cu}^{\text{II}}\text{--Mo}^{\text{IV}}$  systems.

### 3.2 Luminescence

The incorporation of the luminescent building units containing lanthanoid centres into the cyanido-bridged system gives rise to the formation of multifunctional molecular materials. As the luminescence is displayed by certain  $\text{Ln}^{3+}$  ions, the coordination of the ligands can lead to the enhancement of the luminescence or even effectively tune the energy of the emitted light. In order to design the extended polynuclear systems, polycyanidometallate ions can be used. Depending on the building blocks used, the different properties can be obtained. Recently, a decent review concerning the luminescence in the cyanidometallate-based systems has been published [61].

An example of a luminescent system is  $[\text{Nd}(\text{phen})_2(\text{DMF})_2(\text{H}_2\text{O})\text{Mo}(\text{CN})_8]\cdot 2\text{H}_2\text{O}$  which is present as a 1-D chain, the same as the structurally related polymers  $[\text{Nd}(\text{phen})(\text{DMF})_5(\text{H}_2\text{O})\text{M}(\text{CN})_8]\cdot x\text{H}_2\text{O}$  ( $\text{M} = \text{Mo}, \text{W}$ ) [62]. All the three systems reveal photoluminescence in the near-infrared region with the maximum of emission at 1,060 nm and display ferromagnetic interactions within the chain. The combination of the slow magnetic relaxation with light emitting properties leads to a luminescent SCM. These phenomena have been successfully combined in the 1-D cyanido-bridged chain system  $\{[\text{Yb}^{\text{III}}(3\text{-pyridone})_2(\text{H}_2\text{O})_2][\text{Co}^{\text{III}}(\text{CN})_6]\}$  [63], which displays the slow relaxation typical for the SCM systems with the emission of the near-infrared light, shown in Fig. 11. The observed properties are not just the sum of the phenomena brought by the building blocks as the coordination of the pyridone ligand and hexacyanidocobaltate(III) to the ytterbium ion enhances the yield of the luminescence. On the other hand, the SCM-like behaviour has been made available upon the chain formation, which shows clearly the synergic effect of combined magnetic and optical properties. The other example of the luminescent chain system that reveals slow relaxation is  $\{[\text{Dy}^{\text{III}}(3\text{-OHpy})_2(\text{H}_2\text{O})_4][\text{Co}^{\text{III}}(\text{CN})_6]\}\cdot \text{H}_2\text{O}$ , (3-OHpy = 3-hydroxypyridine) [64]. This system reveals the SMM behaviour with relaxation energy value  $\Delta E = 266(12) \text{ cm}^{-1}$ , which is exceptionally high among this class of systems. Irradiation with the UV light induces the emission of white light, with the peaks centred at 481 and 576 nm. The use of the 3-hydroxypyridine ligand and the  $[\text{Co}^{\text{III}}(\text{CN})_6]^{3-}$  metalloligand facilitates the energy transfer, thus enhancing the luminescence. As the 2-D cyanido-bridged systems cannot exhibit SMM nor SCM behaviour, the combination of LRMO is possible. The molecular structure of  $\{[\text{Nd}^{\text{III}}(\text{pmmo})_2(\text{H}_2\text{O})_3][\text{Cr}^{\text{III}}(\text{CN})_6]\}$  (pmmo = pyrimidine N-oxide) reveals a square-grid layer topology [65]. This system displays magnetic ordering below 2.8 K due to the presence of ferromagnetic interactions between the paramagnetic metal centres. This molecular assembly emits light in the NIR region, namely at the energies of 895 and 1,060 nm, as the energy transfer from the organic ligand and the hexacyanidochromate(III) ion occurs. Due to the coexistence and



**Fig. 11** The fragment of  $\{[\text{Yb}^{\text{III}}(3\text{-pyridone})_2(\text{H}_2\text{O})_2][\text{Co}^{\text{III}}(\text{CN})_6]\}$  coordination polymer; AC magnetic susceptibility at  $H_{\text{ac}} = 3$  Oe,  $H_{\text{dc}} = 1,000$  Oe; room temperature solid-state emission in the near-infrared range. Reprinted with permission from Ref. [63]. Copyright 2017 Royal Society of Chemistry

interplay between the magnetic interactions and the luminescence, this system can be classified as a magneto-luminescent coordination polymer.

Control over the emitted light energy has been demonstrated in the series of 1-D chains  $\{[\text{Eu}^{\text{III}}_x\text{Tb}^{\text{III}}_{1-x}(3\text{-OHpy})_2(\text{H}_2\text{O})_4][\text{Co}^{\text{III}}(\text{CN})_6]\} \cdot \text{H}_2\text{O}$  (3-OHpy = 3-hydroxypyridine) [66]. The presence of the diamagnetic spacer does not allow for the magnetic interactions between the metal centres. However, it causes the magnetic separation of the lanthanoid ions. Due to this, an SMM behaviour is expected in the case of  $\text{Tb}^{3+}$ -rich systems. Indeed, the terbium-only system characterised by  $x = 0$  reveals characteristic magnetic features for SMMs. The interesting case is the increase of the energy barrier value upon increasing the concentration of  $\text{Eu}^{3+}$  ions with the highest value of  $\Delta E/k_B = 35$  K for systems characterised by  $x = 0.8$ . This can be rationalised with the presence of the additional fast relaxation mechanism. The colour of the emitted light changes gradually with the composition of the lanthanoid ions. In the case of the Eu-only system, red light is emitted. Upon increasing the concentration



of  $Tb^{3+}$  ions, the colour of the luminescence shifts to orange and finally green light is emitted.

The application of chirality to the luminescent systems can lead to circularly polarised luminescence (CPL), as observed in the series of 1-D systems  $\{[Ln^{III}(L)(dmf)_4]_3[W^V(CN)_8]_3\}_n \cdot dmf \cdot 4H_2O$  [67] ( $Ln = Gd, Nd$ ). These compounds crystallise in a non-centrosymmetric space group due to presence of the chiral derivatives of pyridine bis(oxazoline) as ligands. These compounds show selective absorption of the polarised light revealing the presence of natural circular dichroism (NCD). The combination of chiral ligands with luminescent lanthanoid ions and the paramagnetic octacyanidometallate ions results in the formation of a family of systems that can exhibit the luminescence upon irradiation with the circularly polarised light. Due to the presence of the CPL effect, the emission spectra of both enantiomorphs are different.

The combination of chirality and luminescence can lead to the emerging of the new phenomena, as the thermally switchable luminescence in the enantiomorphic pair  $\{[Eu^{III}(iPr-Pybox)(dmf)_4]_3[W^V(CN)_8]_3\}_n \cdot dmf \cdot 8H_2O$ , where  $iPr-Pybox = 2,2'-(2,6\text{-pyridinediy})bis(4\text{-isopropyl-2-oxazoline})$  in RR or SS form [68]. The compounds crystallise in the chiral space groups as 1-D helical chains. In this system, the energy of the emitted light depends strongly on the temperature. The luminescence at room temperature displays the dominating blue colour due to the luminescence of the ligand, whereas lowering the temperature increases the red emissions due to increasing the antenna effect and electron transfer from the ligand towards lanthanoid centre.

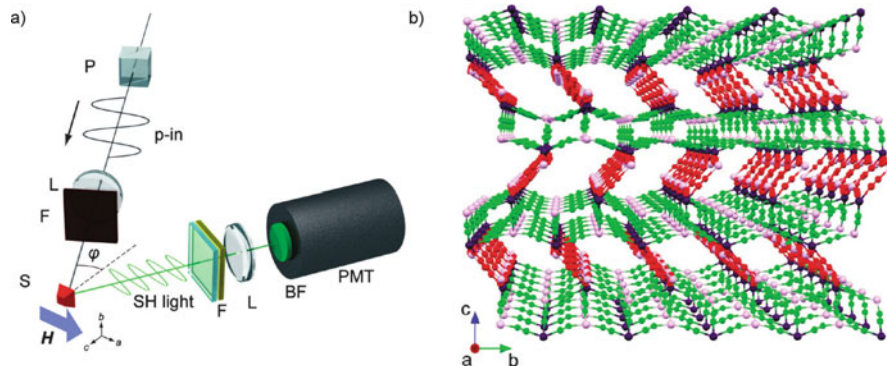
The implementation of the chirality into the luminescent and magnetic systems can lead to new magneto-optical effects such as MChD. This effect consists on the dependence of the absorption of the polarised light upon the applied magnetic field.

### 3.3 Non-linear Effects

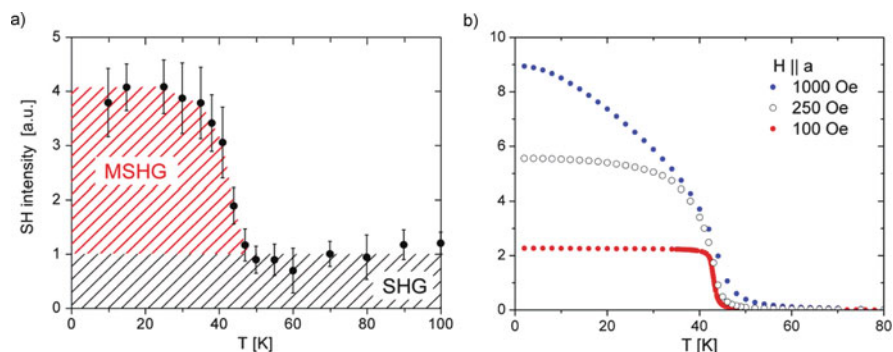
The molecular materials that crystallise in the non-centrosymmetric space groups can reveal the non-linear optical effects, such as SHG (second harmonic generation) or MSHG. These phenomena are studied with the use of the experimental setup shown in Fig. 12a.

The 3-D coordination network  $\{[Mn^{II}(H_2O)(urea)_2][Nb^{IV}(CN)_8]\}_n$  crystallises in two polymorphic forms: chiral and centric [69]. The chiral polymorph, denoted  $\alpha$ , is shown in Fig. 12b. Due to the existence of the 3-D cyanido-bridged network, the system reveals the ferrimagnetic behaviour below 43 K due to the antiferromagnetic interactions between  $Mn^{II}$  and  $Nb^{IV}$  centres. Based on the presence of prerequisites such as LRMO and the non-centrosymmetric space group, the SHG behaviour was expected. In order to check the presence of the effect, the monocrystal of the sample was irradiated with the optical amplifier pumped by the 775 nm laser. The generated light of 532 nm was collected at the angle of  $30^\circ$ . The energy of the generated light corresponds to the electronic transition in the coordination sphere of  $Nb^{IV}$ . After applying the external magnetic field, the intensity of the generated light multiplied





**Fig. 12** (a) The schematic illustration of the setup used for magnetisation-induced second harmonic generation (MSHG) detection: *P* polariser, *L* lens, *F* colour filter, *S* single crystal of the sample, *BF* bandpass filter, *PMT* photomultiplier tube. (b) The packing diagram of  $\alpha\text{-Mn}^{\text{II}}(\text{H}_2\text{O})(\text{urea})_2[\text{Nb}^{\text{IV}}(\text{CN})_8]_n$ . Reprinted with permission from Ref. [69]. Copyright 2011 American Chemical Society



**Fig. 13** (a) Thermal variation in the second harmonic generation (SHG) signal for a single crystal in a 500 G magnetic field applied along the *a*-axis, and (b) magnetisation vs. temperature measured for magnetic field applied along the easy *a* axis. At 1 kOe applied field, the moment saturates in low temperature and the data represent magnetisation of a single domain sample. At smaller fields, demagnetisation and multidomain effects cut the measured moment (blue points, 1 kOe; circles, 250 Oe; red points, 100 Oe). Reprinted with permission from Ref. [69]. Copyright 2011 American Chemical Society

by the factor of 4 due to the presence of MSHG effect below the critical temperature of 43 K is shown in Fig. 13.

The molecular systems based on octacyanidometallate that reveal the chiral space groups and LRMO can combine the functionalities that arise from their acentric structure. The important case is the hybrid organic–inorganic  $\{[\text{Mn}^{\text{II}}(\text{H}_2\text{O})_2]\{\text{Mn}^{\text{II}}(\text{pyrazine})(\text{H}_2\text{O})_2\}\{\text{Mn}^{\text{II}}(\text{pyrazine})(\text{H}_2\text{O})_2\}\{\text{Nb}^{\text{IV}}(\text{CN})_8\}\cdot 4\text{H}_2\text{O}$  3-D network [70, 71]. This system crystallises in the chiral space group and consists of two types of bridging ligands, namely cyanido- and pyrazine ligands, and reveals a ferrimagnetic behaviour below 48 K

due to the presence of long-range antiferromagnetic ordering. The presence of spontaneous electric polarisation is connected with the magnetic ordering, which enables the classification of this system as pyroelectric ferrimagnet. However, it can generate the second harmonic of the incident light, which was tested by the irradiation of the monocrystal of the sample with YAG laser emitting 1,064 nm light. The generated beam of 532 nm wavelength was recorded and its intensity increases below 48 K, due to enhancement of the effect by the magnetic ordering, confirming the presence of the MSHG effect. This simultaneous presence of these phenomena enables to classify this system as a molecular multiferroic.

The isostructural analogue based on the diamagnetic  $[\text{Mo}(\text{CN})_8]^{4-}$  ion also displays the pyroelectric effect as well as the SHG [72]. However, due to the lack of LRMO, there is no possibility of observing the MSHG effect.

## 4 Interaction with Molecules

The possibility of inducing structural and magnetic changes by the sorption of small molecules is one of the important features of molecular magnetic materials that make them different from classical magnets which are characterised by a rigid metallic or ionic structure [73]. Sorption-sensitive magnetic materials may find potential applications as molecular switches or small molecule sensors. Moreover, the study of structural transformations in connection with magnetic properties provides valuable insight into the relation between magnetic superexchange and structural features, like connectivity, coordination and bonding geometry as well as supramolecular interactions. Solvatomagnetic materials comprise systems with weakly coordinated ligands, which can be reversibly detached [74–81], as well as networks with elastic coordination frameworks, where removal of solvent of crystallisation causes deformation of the structure [35, 36, 82–87].

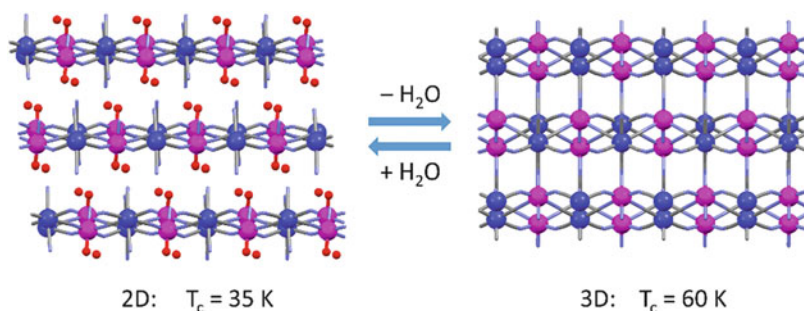
Compounds changing magnetic characteristics upon reversible dehydration were first observed by Oliver Kahn and co-workers in late 1990s and named as magnetic sponges [74]. Later, the term solvatomagnetic effect was introduced to cover the phenomena of magnetic-property modification upon reversible or irreversible sorption, desorption or exchange of solvent molecules in the structure of molecular magnetics [88].

### 4.1 Release of Coordinated Solvent

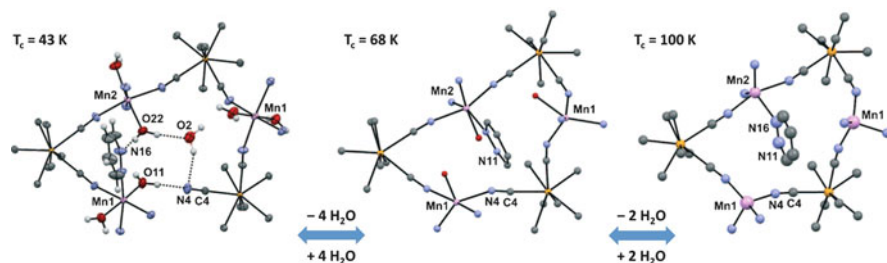
Typical magnetic sponges contain weakly coordinated solvent molecules, usually water. When these ligands are detached, pronounced structural transformations take place, including changes of coordination number and/or formation of new bonds resulting in increased connectivity between metal centres. Many examples of this type of behaviour can be found among cyanido-bridged networks [75–81].

The structural transformations with retention of crystallinity are particularly beneficial for the understanding of magneto-structural correlations. Reversible single-crystal-to-single-crystal (SCSC) transition upon loss of coordinated water is shown by the 2D  $[\text{Mn}^{\text{II}}(\text{NNdmenH})(\text{H}_2\text{O})][\text{Cr}^{\text{III}}(\text{CN})_6] \cdot \text{H}_2\text{O}$  network (NNdmen = *N,N*-dimethylethylenediamine) composed of corrugated square-grid layers [75]. Upon reversible dehydration, it loses both coordinated and lattice water molecules to form anhydrous  $[\text{Mn}^{\text{II}}(\text{NNdmenH})][\text{Cr}^{\text{III}}(\text{CN})_6]$ . As a result, the vacated coordination site on  $\text{Mn}^{\text{II}}$  is taken by a closely located cyanide ligand and an additional bridge is formed by linking adjacent layers to give a 3D network (Fig. 14). Higher connectivity and dimensionality of the network leads to a considerable increase of critical temperature of the ferrimagnetic ordering from 35 to 60 K.

Very interesting sponge-like behaviour was observed for two compounds based on octacyanidonioabate(IV) and manganese(II) with heterocyclic *N*-donating ligands. Both networks undergo reversible dehydration, which causes not only formation of new bridges and increased connectivity but also reduced coordination number and change of geometry at the Mn(II) ion. The 3D  $\{[\text{Mn}^{\text{II}}(\text{imH})(\text{H}_2\text{O})_2][\text{Nb}^{\text{IV}}(\text{CN})_8] \cdot 4\text{H}_2\text{O}\}_n$  (imH = imidazole) network [76] can be transformed into anhydrous  $\{[\text{Mn}^{\text{II}}(\text{imH})_2][\text{Nb}^{\text{IV}}(\text{CN})_8]\}_n$ . The  $\text{Mn}^{\text{II}}$  ions originally in an octahedral environment are bound to three CN bridges, one imH and two water molecules. After release of the aqua ligands, one of the  $\text{Mn}^{\text{II}}$  centres adopts tetrahedral geometry and the other forms one additional CN bridge changing shape to trigonal bipyramid. This structure transformation is reflected in the increase of  $T_C$  from 25 to 62 K. In the related  $\{[\text{Mn}^{\text{II}}(\text{pydz})(\text{H}_2\text{O})_2][\text{Mn}^{\text{II}}(\text{H}_2\text{O})_2][\text{Nb}^{\text{IV}}(\text{CN})_8] \cdot 2\text{H}_2\text{O}\}_n$  (pydz = pyridazine) compound [77], fully reversible two-step dehydration is observed. In the first step, the lattice water and one aqua ligand from each  $\text{Mn}^{\text{II}}$  ion are released. An additional CN bridge is formed to one of the  $\text{Mn}^{\text{II}}$  centres, while the other adopts a coordination number of 5 with a distorted square pyramid geometry (Fig. 15). At the same time, an interesting effect of pydz ligand migration between cations is observed. In the second step, both  $\text{Mn}^{\text{II}}$  centres loose the remaining water molecules and change coordination geometry to tetrahedral and trigonal bipyramid, respectively. The increase in  $T_C$  is observed in both steps, reaching the value of 100 K for the anhydrous  $\{[\text{Mn}^{\text{II}}(\text{pydz})]\text{Mn}^{\text{II}}[\text{Nb}^{\text{IV}}(\text{CN})_8]\}_n$ .



**Fig. 14** Formation of interlayer CN-bridges upon reversible dehydration in the  $[\text{Mn}^{\text{II}}(\text{NNdmenH})(\text{H}_2\text{O})][\text{Cr}^{\text{III}}(\text{CN})_6] \cdot \text{H}_2\text{O}$  network



**Fig. 15** Structural changes in the  $\{[\text{Mn}^{\text{II}}(\text{pydz})(\text{H}_2\text{O})_2][\text{Mn}^{\text{II}}(\text{H}_2\text{O})_2][\text{Nb}^{\text{IV}}(\text{CN})_8]\cdot 2\text{H}_2\text{O}\}_n$  magnetic sponge

An example of cyanido-bridged magnetic sponge with a relatively high ordering temperature is the 3D  $[\text{Mn}^{\text{II}}(\text{HL})(\text{H}_2\text{O})_2]\text{Mn}^{\text{II}}[\text{Mo}^{\text{III}}(\text{CN})_7]\cdot 2\text{H}_2\text{O}$  ( $\text{L} = N,N$ -dimethylalaninol) network [78]. The crystallisation as well as weakly coordinated water molecules occupy parallel channels in the structure and can be reversibly removed. Both hydrated and anhydrous forms of the network are ferrimagnets with  $T_{\text{CS}}$  of 85 and 106 K, respectively.

## 4.2 Guest Molecules

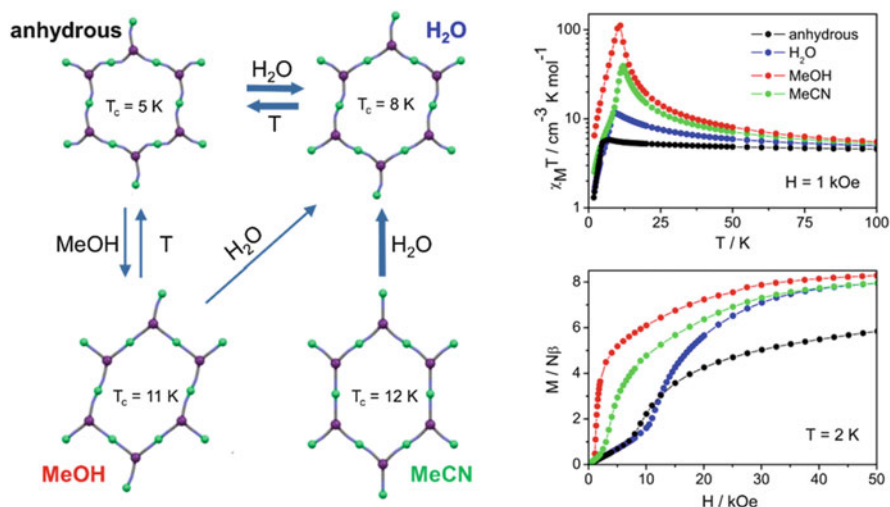
Magnetic properties of molecular materials can also be influenced by removal or introduction of non-coordinated guest molecules. The bonding geometry of non-rigid coordination polymers can be affected by the release of solvent of crystallisation resulting in modification of magnetic characteristics. This problem was often disregarded in the past and sometimes structural data obtained for crystals protected from the loss of solvent were used to interpret magnetic properties of samples dried in air or under vacuum. It is exemplified by several compounds, which upon re-examination have shown marked solvatomagnetic behaviour that originally went unnoticed [89–91]. Cyanido-bridged networks are particularly suited for the construction of flexible frameworks and observation of guest-influenced magnetism. The CN bridges may be strongly distorted (the  $\text{M}-\text{N}-\text{C}$  angle in known systems ranges from  $130^\circ$  to  $180^\circ$ ) [92], which allows the structures to adapt to changing amounts of solvent of crystallisation. For hepta- and octacyanidometallates, this effect is additionally enhanced by the non-rigid coordination geometry [45]. Most importantly, for several metal ions the strength and character of magnetic superexchange through the CN ligand strongly depends on the bridging geometry [93].

One of the first well-documented cases of the influence of the water of crystallisation on magnetic properties of CN-bridged networks was a 3D coordination polymer  $\{[\text{Ni}^{\text{II}}(\text{dipn})]_2[\text{Ni}^{\text{II}}(\text{dipn})(\text{H}_2\text{O})][\text{Fe}^{\text{III}}(\text{CN})_6]\cdot 11\text{H}_2\text{O}\}_n$  ( $\text{dipn} = N,N$ -di(3-aminopropyl) amine) [82]. Its microporous structure contains water-filled channels. In a reversible first dehydration step, 10 lattice water molecules are removed to give an amorphous

phase characterised by weaker Ni–Fe ferromagnetic coupling. This compound can be further irreversibly dehydrated to an anhydrous  $\{[\text{Ni}^{\text{II}}(\text{dipn})]_3[\text{Fe}^{\text{III}}(\text{CN})_6]\}_n$ .

As mentioned earlier, existence of SCSC transformation pathways is beneficial for the understanding of magneto-structural correlations. It is particularly important in the case of the guest-induced solvatomagnetism, where often only subtle deformation of the coordination framework is observed. The 2D  $\{[\text{Ni}(\text{cyclam})]_3[\text{W}(\text{CN})_8]_2\}_n$  (cyclam = 1,4,8,11-tetraazacyclotetradecane) network of honeycomb topology is an exceptional CN-bridged assembly for which four different solvates could be obtained as single crystals and fully structurally and magnetically characterised [35, 36, 83]. The microporous channels of this compound can be stretched to accommodate several types of small molecules. The forms containing water, methanol or mixed acetonitrile and ethanol as guests as well as an anhydrous form can be interconverted into one another along the pathways shown in Fig. 16, three of which (marked with bold arrows) are of SCSC character. The study of solvatomagnetic effect in this network allowed direct observation of the switching in the character of magnetic superexchange from antiferromagnetic to ferromagnetic with the increasing value of the Ni–N–C cyanido-bridge angle [35]. Re-examination of two related 2D networks based on hexacyanidometallates  $\{[\text{Ni}(\text{cyclam})]_3[\text{M}(\text{CN})_6]_2 \cdot n\text{H}_2\text{O}\}_n$  ( $\text{M} = \text{Cr}$  or  $\text{Fe}$ ) [90, 91] revealed similarly rich solvatomagnetic behaviour with the existence of different hydrates and MeOH-modified forms [84].

Reversible dehydration accompanied by changes in magnetic properties can also be observed in non-porous structures, containing localised hydrogen-bound water of crystallisation. For chiral pentanuclear  $\{[\text{Co}^{\text{II}}(\text{mpm})_2]_3[\text{W}^{\text{V}}(\text{CN})_8]_2\} \cdot 9\text{H}_2\text{O}$  (mpm =  $\alpha$ -methylpyridinemethanol) clusters, significant weakening of intracluster ferromagnetic



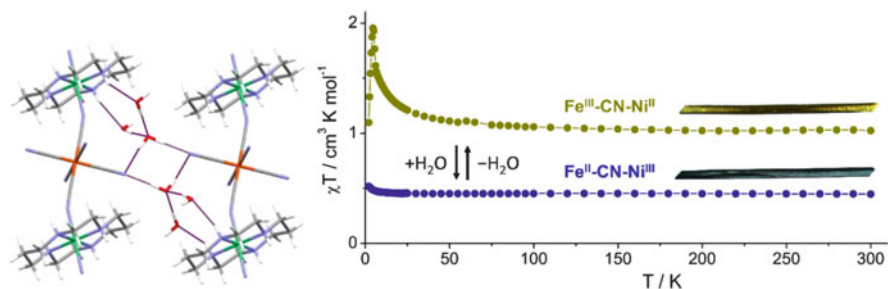
**Fig. 16** Structural and magnetic changes upon guest sorption in the 2D  $\{[\text{Ni}(\text{cyclam})]_3[\text{W}(\text{CN})_8]_2\}_n$  network; only bridging ligands are shown for clarity; wide arrows mark single-crystal-to-single-crystal (SCSC) transformations

interactions was noted upon partial dehydration [85]. In  $\{[\text{Ni}^{\text{III}}(\text{cyclam})][\text{M}^{\text{III}}(\text{CN})_6] \cdot 6\text{H}_2\text{O}\} (\text{M} = \text{Cr or Fe})$  chains, employing an unusual  $\text{Ni}^{\text{III}}$  cation [86] and a  $\{[\text{Ni}^{\text{II}}(\text{en})_2]_3[\text{Fe}^{\text{III}}(\text{CN})_6]_2 \cdot 3\text{H}_2\text{O}\}_n$  ( $\text{en} = \text{ethylenediamine}$ ) system of rope-ladder topology [87] the loss of crystallisation water leads to changes in critical temperature of antiferromagnetic ordering and critical field of the metamagnetic transition.

### 4.3 Guest-Controlled CT and Spin-Crossover

The drawback of most of the magnetic sponges is the fact that switching between different forms and registration of magnetic response cannot be realised at the same temperature. Desolvation usually requires room or elevated temperature, while magnetic ordering is observed under cryogenic conditions. There are, however, some examples of solvatomagnetic compounds, where the electronic state of the metal centres is affected by the sorption process and changes in magnetic moment and sample colour can be observed in a wide temperature range. This effect can be realised by charge-transfer (CT) or SCO or combination of both processes – charge-transfer induced spin-crossover (CTIST).

MMCT upon dehydration was observed for several PBAs containing combinations of redox-active centres including  $\text{Co}^{\text{II/III}}$ ,  $\text{Fe}^{\text{II/III}}$  and  $\text{Ni}^{\text{II/III}}$  [94, 95]. For hybrid organic–inorganic CN-bridged networks, sorption-induced CT is very rare. It was observed in the  $\{(\text{H}_3\text{O})[\text{Ni}^{\text{III}}(\text{cyclam})][\text{Fe}^{\text{II}}(\text{CN})_6] \cdot 5\text{H}_2\text{O}\}_n$  chain [96], where the presence of the  $\text{H}^+$  cation stabilises unusual oxidation states of the metal centres. Reversible partial dehydration of this compound causes electron transfer from  $\text{Fe}^{\text{II}}$  to  $\text{Ni}^{\text{III}}$ . As a result, the change of colour and magnetic susceptibility is observed in the entire temperature range (Fig. 17).



**Fig. 17** Structure of the  $\{(\text{H}_3\text{O})[\text{Ni}^{\text{III}}(\text{cyclam})][\text{Fe}^{\text{II}}(\text{CN})_6] \cdot 5\text{H}_2\text{O}\}_n$  chains and magnetic susceptibility vs. temperature graphs together with photographs of the crystals of the hydrated and dehydrated forms

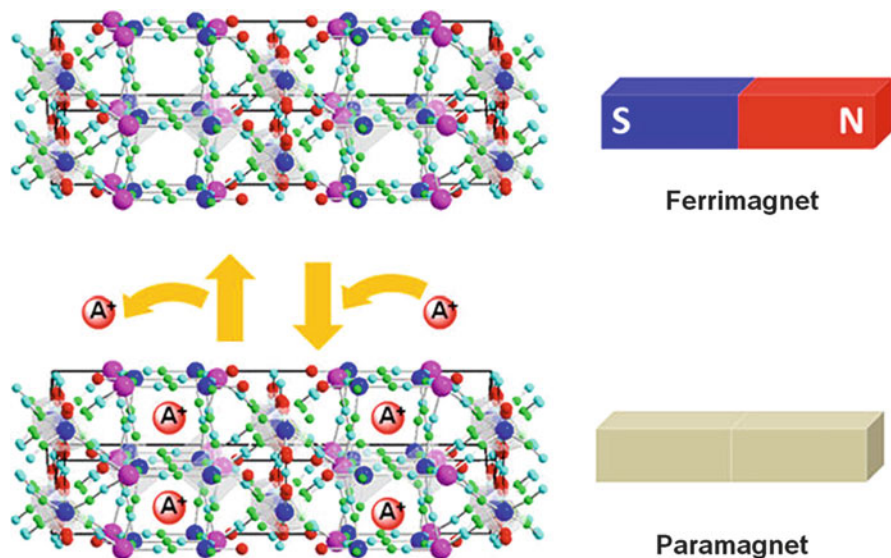


The characteristics of thermally induced SCO can be modified by guest molecules. Synergetic effect of host–guest chemistry and SCO was observed in Hofmann-type compounds composed of CN-bridged square-grid bimetallic layers bound by organic ligands into 3D hybrid networks [97, 98]. Various guests including water, organic solvents and aromatic heterocycles can be incorporated in their porous structure, either during synthesis or by post-synthetic modifications, affecting the SCO process.

Cyanido-bridged systems containing cobalt ions coupled with redox-active polycyanidometallates can undergo thermal or optical CTIST. In several cases, this process was found to be modified by removal or exchange of solvent of crystallisation [99–101]. The trigonal bipyramid  $\{[\text{Co}(\text{tmphen})_2]_3[\text{Fe}(\text{CN})_6]_2\}$  (tmphen = 3,4,7,8-tetramethyl-1,10-phenanthroline) clusters were found to exist in three different oxidation state configurations:  $\{\text{Co}^{\text{II}}\text{Co}^{\text{III}}_2\text{Fe}^{\text{II}}_2\}$ ,  $\{\text{Co}^{\text{II}}\text{Co}^{\text{III}}\text{Fe}^{\text{II}}\text{Fe}^{\text{III}}\}$  and  $\{\text{Co}^{\text{II}}_3\text{Fe}^{\text{III}}_2\}$ , depending on the crystallisation solvent and temperature [99]. Well-documented effect of dehydration on the CTIST process was presented for  $\{[\text{Co}_3(4\text{-methylpyridine})_2(\text{pyrimidine})_2(\text{H}_2\text{O})_2][\text{W}(\text{CN})_8]_2 \cdot 4\text{H}_2\text{O}\}_n$  [101]. This compound undergoes a thermal transition from HT  $\{\text{Co}^{\text{II}}_3\text{W}^{\text{V}}_2\}$  phase to LT  $\{\text{Co}^{\text{II}}\text{Co}^{\text{III}}_2\text{W}^{\text{IV}}_2\}$  phase with a hysteresis between 147 and 242 K. Reversible stepwise dehydration causes gradual increase of the HT  $\rightarrow$  LT transition temperature up to 191 K and narrowing of the bistability range.

#### 4.4 Guest Ions

Apart from guest molecules, coordination polymers may incorporate non-coordinated ions, both organic and inorganic, which are often introduced to direct the self-assembly process towards desired topology. Guest ions can also modify network properties, like redox potentials of metal centres in the case of the  $\text{Ni}^{\text{III}}\text{--Fe}^{\text{II}}$  chain mentioned in Sect. 4.3 [96]. Presence of s-block metal cations is common in non-stoichiometric PBAs, where their type and content is known to influence magnetic properties [1]. Mobile guest ions may result in ionic conductivity, which is a desired feature of materials designed for the development of battery-related technologies [102]. Among hybrid organic–inorganic CN-bridged assemblies, ionic conductivity was observed for a 2D  $\{(4\text{-aminopyridinium})_2[\text{Mn}^{\text{II}}(4\text{-aminopyridine})_4]_2[\text{Mn}^{\text{II}}(4\text{-aminopyridine})_2(\text{H}_2\text{O})_2][\text{Nb}^{\text{IV}}(\text{CN})_8]_2 \cdot 10\text{H}_2\text{O}\}$  network [103]. An interesting post-synthetic modification by ion guest incorporation was presented for the 3D  $[\text{Mn}^{\text{II}}(\text{H}_2\text{O})][\text{Mn}^{\text{II}}(\text{HCOO})_{2/3}(\text{H}_2\text{O})_{2/3}]_{3/4}[\text{Mo}^{\text{V}}(\text{CN})_8] \cdot \text{H}_2\text{O}$  network [104]. In this coordination polymer, reversible electrochemical alkali ion insertion causes reduction of  $\text{Mo}^{\text{V}}$  to  $\text{Mo}^{\text{IV}}$  with a ferrimagnet to paramagnet switching (Fig. 18).



**Fig. 18** Magnetic switching caused by reversible reduction of Mo<sup>V</sup> upon electrochemical ion insertion into the  $[\text{Mn}^{\text{II}}(\text{H}_2\text{O})][\text{Mn}^{\text{II}}(\text{HCOO})_{2/3}(\text{H}_2\text{O})_{2/3}]_{3/4}[\text{Mo}^{\text{V}}(\text{CN})_8] \cdot \text{H}_2\text{O}$  network. Reprinted with permission from Ref. [104]. Copyright 2013 American Chemical Society

## 5 Summary

As shown by examples presented above, hybrid organic–inorganic CN-bridged assemblies constitute an important and versatile group of molecular magnets. Introduction of organic ligands allow effective manipulation of topology and dimensionality, as well as modification and introduction of new properties. The structures vary from clusters to 3D architectures. Among the discrete assemblies, the largest groups are represented by pentanuclear clusters of trigonal bipyramid topology, formed by cyanido complexes with coordination numbers from 6 to 8 and pentadecanuclear clusters of body-centred six-capped cube shape characteristic for octacyanido-metallates. The latter clusters, which are formed in alcoholic media without any blocking ligands, were successfully used as SBBs to construct extended hybrid structures with organic bridges. Apart from slow magnetic relaxation and SMM characteristics, which appear for some of the larger clusters, the discrete assemblies were used as platforms for the introduction of SCO thermal switchability, optical activity and photomagnetic effects. The 1D structures apart from linear alternating bimetallic chains comprise ladder and vertex-sharing squares as well as more complicated architectures. Among the chain structures, there are examples of SCM behaviour, photoluminescence and sorption-induced MMCT. The 2D assemblies may show simple square-grid or honeycomb topology as well as more complicated structures. The layered polymers often show metamagnetic behaviour, with long-



range antiferromagnetic or ferrimagnetic ordering. For some 2D structures, magnetic characteristics can be modified by guest molecules. The 3D assemblies include classical hybrid Hofmann-type networks as well as other structures with mixed organic–inorganic connectivity. However, the largest group constitute cyanido-bridged polymers with blocking organic ligands. The 3D networks are also most versatile group among CN-bridged compounds. Most of them exhibit LRMO, though due to lower connectivity the critical temperatures of magnetic ordering for hybrid networks are usually lower than for corresponding purely inorganic compounds like PBAs based on the same metal centres. However, by involving organic fragments, exciting new functions could be achieved, like MChD, MSHG or magnetic-sponge-like behaviour.

Current efforts in the research of CN-bridged assemblies concentrate on several topics connected with their potential applications. The search for systems with high critical temperature of magnetic ordering is probably the most important issue. The achievement of magnetic ordering at ambient conditions would enable wide technological applications of molecular magnetics. A very promising pathway is the development of bistable systems, based on SCO or CT effects. Particularly interesting are multi-switchable materials that can respond to different stimuli, like irradiation, temperature and pressure changes or the presence of particular guest molecules. Considerable efforts are also directed at the development of heterostructures, deposition of magnetic molecules on surfaces or arranging them into extended structures.

## References

1. Verdager M, Bleuzen A, Marvaud V et al (1999) Molecules to build solids: high  $T_C$  molecule-based magnets by design and recent revival of cyano complexes chemistry. *Coord Chem Rev* 190–192:1023–1047
2. Robin MB (1962) The color and electronic configurations of Prussian blue. *Inorg Chem* 1:337–342
3. Ito A, Suenaga M, Ono K (1968) Mossbauer study of soluble Prussian blue, insoluble Prussian blue, and Turnbull's blue. *J Chem Phys* 48:3597–3599
4. Ferlay S, Mallah T, Ouahes R, Veillet P, Verdager M (1995) A room-temperature organo-metallic magnet based on Prussian blue. *Nature* 378:701–703
5. Holmes SM, Girolami GS (1999) Sol-gel synthesis of  $KV^{II}[Cr^{III}(CN)_6] \cdot 2H_2O$ : a crystalline molecule-based magnet with a magnetic ordering temperature above 100 °C. *J Am Chem Soc* 121:5593–5594
6. Newton GN, Nihei M, Oshio H (2011) Cyanide-bridged molecular squares – the building units of Prussian blue. *Eur J Inorg Chem* 2011:3031–3042
7. Korzeniak T, Stadnicka K, Rams M, Sieklucka B (2004) Grid-type two-dimensional magnetic multinuclear metal complex: strands of  $\{[Cu^{II}(\mu-4,4'-bpy)]^{2+}\}_n$  cross-linked by Octacyanotungstate(V) ions. *Inorg Chem* 43:4811–4813
8. Larionova J, Gross M, Pilkington M, Andres H, Stoeckli-Evans H, Güdel HU, Decurtins S (2000) High-spin molecules: a novel Cyano-bridged  $Mn^{II}_9Mo^V_6$  molecular cluster with a  $S = 51/2$  ground state and ferromagnetic intercluster ordering at low temperatures. *Angew Chem Int Ed* 39:1605–1609
9. Zhong ZJ, Seino H, Mizobe Y, Hidai M, Fujishima A, Ohkoshi S, Hashimoto K (2000) A high-spin cyanide-bridged  $Mn_9W_6$  cluster ( $S = 39/2$ ) with a full-capped cubane structure. *J Am Chem Soc* 122:2952–2953

- Bonadio F, Gross M, Stoeckli-Evans H, Decurtins S (2002) High-spin molecules: synthesis, X-ray characterization, and magnetic behavior of two new cyano-bridged  $\text{Ni}^{\text{II}}_9\text{Mo}^{\text{V}}_6$  and  $\text{Ni}^{\text{II}}_9\text{W}^{\text{V}}_6$  clusters with a  $S = 12$  ground state. *Inorg Chem* 41:5891–5896
- Song Y, Zhang P, Ren X-M, Shen X-F, Li Y-Z, You X-Z (2005) Octacyanomometallate-based single-molecule magnets:  $\text{Co}^{\text{II}}_9\text{M}^{\text{V}}_6$  ( $\text{M} = \text{W}, \text{Mo}$ ). *J Am Chem Soc* 127:3708–3709
- Freedman DE, Bennett MV, Long JR (2006) Symmetry-breaking substitutions of  $[\text{Re}(\text{CN})_8]^{3-}$  into the centered, face-capped octahedral clusters  $(\text{CH}_3\text{OH})_{24}\text{M}_9\text{M}'_6(\text{CN})_{48}$  ( $\text{M} = \text{Mn}, \text{Co}$ ;  $\text{M}' = \text{Mo}, \text{W}$ ). *Dalton Trans*:2829–2834
- Ma SL, Ren S, Ma Y, Liao DZ, Yan SP (2009) A high-spin cyanide-bridged  $\text{Mo}_6\text{Mn}_9$  cluster: crystal structure and magnetism. *Struct Chem* 20:161–167
- Podgajny R, Chorazy S, Nitek W, Rams M, Majcher AM, Marszałek B, Żukrowski J, Kapusta C, Sieklucka B (2013) Co–NC–W and Fe–NC–W electron-transfer channels for thermal bistability in trimetallic  $\{\text{Fe}_6\text{Co}_3[\text{W}(\text{CN})_8]_6\}$  cyanido-bridged cluster. *Angew Chem Int Ed* 52:896–900
- Chorazy S, Podgajny R, Nogaś W, Nitek W, Kozieł M, Rams M, Juszyńska-Gałązka E, Żukrowski J, Kapusta C, Nakabayashi K, Fujimoto T, Ohkoshi S (2014) Charge transfer phase transition with reversed thermal hysteresis loop in the mixed-valence  $\text{Fe}_9[\text{W}(\text{CN})_8]_6 \cdot x\text{MeOH}$  cluster. *Chem Commun* 50:3484–3487
- Chorazy S, Stanek JJ, Nogaś W, Majcher AM, Rams M, Kozieł M, Juszyńska-Gałązka E, Nakabayashi K, Ohkoshi S, Sieklucka B, Podgajny R (2016) Tuning of charge transfer assisted phase transition and slow magnetic relaxation functionalities in  $\{\text{Fe}_{9-x}\text{Co}_x[\text{W}(\text{CN})_8]_6\}$  ( $x = 0\text{--}9$ ) molecular solid solution. *J Am Chem Soc* 138:1635–1646
- Lim JH, Yoo JH, Kim HC, Hong CS (2006) Surface modification of a six-capped body-centered cube  $\text{Ni}_9\text{W}_6$  cluster: structure and single-molecule magnetism. *Angew Chem Int Ed* 45:7424–7426
- Lim JH, Yoo HS, Kim JI, Yoon JH, Yang N, Koh EK, Park J-G, Hong CS (2008) A facially capped body-centered  $\text{Ni}_9\text{W}_6$  cubane modified with sulfur-containing bidentate ligands: structure and magnetic properties. *Eur J Inorg Chem*:3428–3431
- Lim JH, Yoo HS, Yoon JH, Koh EK, Kim HC, Hong CS (2008) Structure and magnetic properties of cyanide-bridged  $\text{Ni}^{\text{II}}_9\text{Mo}^{\text{V}}_6$  cluster modified by bidentate capping ligands. *Polyhedron* 27:299–303
- Hilfiger MG, Zhao H, Prosvirin A, Wernsdorfer W, Dunbar KM (2009) Molecules based on M (V) ( $\text{M} = \text{Mo}, \text{W}$ ) and Ni(II) ions: a new class of trigonal bipyramidal cluster and confirmation of SMM behavior for the pentadecanuclear molecule  $\{\text{Ni}^{\text{II}}[\text{Ni}^{\text{II}}(\text{tmphen})(\text{MeOH})_6][\text{Ni}(\text{H}_2\text{O})_3]_2[\text{m-CN}]_{30}[\text{W}^{\text{V}}(\text{CN})_3]_6\}$ . *Dalton Trans*:5155–5163
- Nowicka B, Stadnicka K, Nitek W, Rams M, Sieklucka B (2012) Geometrical isomerism in pentadecanuclear high-spin  $\text{Ni}_9\text{W}_6$  clusters with symmetrical bidentate ligands detected. *CrystEngComm* 14:6559–6564
- Chorazy S, Rams M, Hoczek A, Czarnecki B, Sieklucka B, Ohkoshi S, Podgajny R (2016) Structural anisotropy of cyanido-bridged  $\{\text{Co}^{\text{II}}_9\text{W}^{\text{V}}_6\}$  single-molecule magnets induced by bidentate ligands: towards the rational enhancement of energy barrier. *Chem Commun* 52:4772–4775
- Podgajny R, Nitek W, Rams M, Sieklucka B (2008) Testing the high spin  $\text{Mn}^{\text{II}}_9\text{W}^{\text{V}}_6$  cluster as building block for three-dimensional coordination networks. *Cryst Growth Des* 8:3817–3821
- Podgajny R, Chorazy S, Nitek W, Rams M, Bałanda M, Sieklucka B (2010)  $\{\text{Mn}^{\text{II}}_9\text{W}^{\text{V}}_6\}_n$  nanowires organized into 3D hybrid network of  $\text{I}^{\text{O}2}$  topology. *Cryst Growth Des* 10:4693–4696
- Chorazy S, Podgajny R, Nitek W, Rams M, Ohkoshi S, Sieklucka B (2013) Supramolecular chains and coordination nanowires constructed of high-spin  $\text{Co}^{\text{II}}_9\text{W}^{\text{V}}_6$  clusters and 4,4'-bpdo linkers. *Cryst Growth Des* 13:3036–3045
- Sieklucka B, Szklarzewicz J, Kemp TJ, Errington W (2000) X-ray evidence of CN bridging in bimetallic complexes based on  $[\text{M}(\text{CN})_8]^{4-}$  ( $\text{M} = \text{Mo}, \text{W}$ ). The crystal structure of  $[\{\text{Mn}(\text{bpy})_2\}_2(\mu\text{-NC})_2][\text{Mo}(\text{CN})_6]_2(\mu\text{-CN})_2[\text{Mn}(\text{bpy})_2]_2 \cdot 8\text{H}_2\text{O}$ . *Inorg Chem* 39:5156–5158

27. Mathonière C, Podgajny R, Guionneau P, Labrugere C, Sieklucka B (2005) Photomagnetism in cyano-bridged hexanuclear clusters  $[\text{Mn}^{\text{II}}(\text{bpy})_2]_4[\text{M}^{\text{IV}}(\text{CN})_8]_2 \cdot x\text{H}_2\text{O}$  ( $M = \text{Mo}$ ,  $x = 14$ , and  $M = \text{W}$ ,  $x = 9$ ). *Chem Mater* 17:442–449
28. Venkatakrishnan TS, Rajamani R, Ramasesha S, Sutter JP (2007) Synthesis, crystal structure, and magnetic properties of hexanuclear  $\{[\text{MnL}_2]_4\{\text{Nb}(\text{CN})_8\}_2\}$  and nonanuclear  $\{[\text{MnL}_2]_6\{\text{Nb}(\text{CN})_8\}_3\}$  heterometallic clusters ( $L = \text{bpy}$ ,  $\text{phen}$ ). *Inorg Chem* 46:9569–9574
29. Korzeniak T, Jankowski R, Koziel M, Pinkowicz D, Sieklucka B (2017) Reversible single-crystal-to-single-crystal transformation in photomagnetic cyanido-bridged  $\text{Cd}_4\text{M}_2$  octahedral molecules. *Inorg Chem* 56:12914–12919
30. Chorazy S, Reczyński M, Podgajny R, Nogaś W, Buda S, Rams M, Nitek W, Nowicka B, Mlyński J, Ohkoshi S, Sieklucka B (2015) Implementation of chirality into high-spin ferromagnetic  $\text{Co}^{\text{II}}\text{W}^{\text{V}}_6$  and  $\text{Ni}^{\text{II}}\text{W}^{\text{V}}_6$  cyanido-bridged clusters. *Cryst Growth Des* 15:3573–3581
31. Chorazy S, Stanek JJ, Kobylarczyk J, Ohkoshi S, Sieklucka B, Podgajny R (2017) Modulation of the  $\text{Fe}^{\text{II}}$  spin crossover effect in the pentadecanuclear  $\{\text{Fe}_9[\text{M}(\text{CN})_8]_6\}$  ( $M = \text{Re}$ ,  $\text{W}$ ) clusters by facial coordination of tridentate polyamine ligands. *Dalton Trans* 46:8027–8036
32. Ozaki N, Yamada R, Nakabayashi K, Ohkoshi S (2011) Catena-poly[[tetrakis(cyanido-kC)-tungstate(IV)]-di-m-cyanido-k<sup>4</sup>C:N-bis-[diaqua(2,2'-bipyridyl-k<sup>2</sup>N,N')-manganese(II)]-di-m-cyanido-k<sup>4</sup>N:C]hexahydrate]. *Acta Cryst E* 67:m702–m703
33. Podgajny R, Pełka R, Desplanches C, Ducase L, Nitek W, Korzeniak T, Stefańczyk O, Rams M, Sieklucka B, Verdager M (2011) W-knotted chain  $\{[\text{Cu}^{\text{II}}(\text{dien})_4[\text{W}^{\text{V}}(\text{CN})_8]_6\}^{\infty}$ : synthesis, crystal structure, magnetism, and theory. *Inorg Chem* 2011:3213
34. Venkatakrishnan TS, Sahoo S, Brefuel N, Duhayon C, Paulsen C, Barra AL, Ramasesha S, Sutter JP (2010) Enhanced ion anisotropy by nonconventional coordination geometry: single-chain magnet behavior for a  $\{[\text{Fe}^{\text{II}}\text{L}]_2\{\text{Nb}^{\text{IV}}(\text{CN})_8\}\}$  helical chain compound designed with heptacoordinate  $\text{Fe}^{\text{II}}$ . *J Am Chem Soc* 132:6047–6056
35. Nowicka B, Rams M, Stadnicka K, Sieklucka B (2007) Reversible guest-induced magnetic and structural single-crystal-to-single-crystal transformation in microporous coordination network  $\{[\text{Ni}(\text{cyclam})]_3[\text{W}(\text{CN})_8]_2\}_n$ . *Inorg Chem* 46:8123–8125
36. Nowicka B, Bałanda M, Gaweł B, Cwiak G, Budziak A, Łasocha W, Sieklucka B (2011) Microporous  $\{[\text{Ni}(\text{cyclam})]_3[\text{W}(\text{CN})_8]_2\}_n$  affording reversible structural and magnetic conversions. *Dalton Trans* 40:3067–3073
37. Lim JH, You YS, Yoo HS, Yoon JH, Kim JI, Koh EK, Hong CS (2007) Bimetallic  $\text{M}^{\text{V}}_2\text{Cu}^{\text{II}}_3$  ( $M = \text{Mo}$ ,  $\text{W}$ ) coordination complexes based on octacyanometalates: structures and magnetic variations tuned by chelated tetradentate macrocyclic ligands. *Inorg Chem* 46:10578–10586
38. Long J, Chamoreau LM, Mathoniere C, Marvaud V (2009) Photoswitchable heterotrimetallic chain based on octacyanomolybdate, copper, and nickel: synthesis, characterization, and photomagnetic properties. *Inorg Chem* 48:22–24
39. Arimoto Y, Ohkoshi S, Zhong ZJ, Seino H, Mizobe Y, Hashimoto K (2002) Crystal structure and magnetic properties of two-dimensional cyanide-bridged bimetallic assembly composed of  $\text{Cs}^+[\text{Mn}^{\text{III}}(3\text{-cyanopyridine})_2\{\text{W}^{\text{V}}(\text{CN})_8\}]\cdot\text{H}_2\text{O}$ . *Chem Lett* 31:832–833
40. Podgajny R, Korzeniak T, Bałanda M, Wasiutyński T, Errington W, Kemp TJ, Alcock NW, Sieklucka B (2002) 2-D soft ferromagnet based on  $[\text{W}^{\text{V}}(\text{CN})_8]^{3-}$  and  $\text{Cu}^{\text{II}}$  with a  $T_c$  of 34 K. *Chem Commun* 2:1138–1139
41. Korzeniak T, Podgajny R, Alcock NW, Lewiński K, Bałanda M, Wasiutyński T, Sieklucka B (2003) A new family of magnetic 2D coordination polymers based on  $[\text{M}^{\text{V}}(\text{CN})_8]$  ( $M = \text{Mo}$ ,  $\text{W}$ ) and pre-programmed  $\text{Cu}^{2+}$  centres. *Polyhedron* 22:2183–2190
42. Sieklucka B, Korzeniak T, Podgajny R, Bałanda M, Nakazawa Y, Miyazaki Y, Sorai M, Wasiutyński T (2004) Ferromagnetic ordering in new layered copper octacyanometalates. *J Magn Mater* 272–276:1058–1059
43. Sieklucka B, Podgajny R, Przychodzeń P, Korzeniak T (2005) Engineering of octacyanometalate-based coordination networks towards functionality. *Coord Chem Rev* 249:2203–2221

44. Przychodzeń P, Korzeniak T, Podgajny R, Sieklucka B (2006) Supramolecular coordination networks based on octacyanometalates: from structure to function. *Coord Chem Rev* 250:2234–2260
45. Nowicka B, Korzeniak T, Stefańczyk O, Pinkowicz D, Chorąży S, Podgajny R, Sieklucka B (2012) The impact of ligands upon topology and functionality of octacyanidometallate-based assemblies. *Coord Chem Rev* 256:1946–1971
46. Hatlevik Ø, Buschmann WE, Zhang J, Manson JL, Miller JS (1999) Enhancement of the magnetic ordering temperature and air stability of a mixed valent vanadium hexacyanochromate(III) magnet to 99°C (372 K). *Adv Mater* 11:914–918
47. Imoto K, Takemura M, Tokoro H, Ohkoshi S (2012) A cyano-bridged vanadium-niobium bimetal assembly exhibiting a high curie temperature of 210 K. *Eur J Inorg Chem* 16:2649–2652
48. Pinkowicz D, Pełka R, Drath O, Nitek W, Bałanda M, Majcher AM, Ponetti G, Sieklucka B (2010) Nature of magnetic interactions in 3D  $\{[M^{II}(\text{pyrazole})_4]_2[\text{Nb}^{IV}(\text{CN})_8] \cdot 4\text{H}_2\text{O}\}_n$  ( $M = \text{Mn, Fe, Co, Ni}$ ) molecular magnets. *Inorg Chem* 49:7565–7576
49. Ohkoshi S, Hashimoto K (2001) Photo-magnetic and magneto-optical effects of functionalized metal polycyanides. *J Photochem Photobiol C* 2:71–88
50. Decurtins S, Gütllich P, Köhler CP, Spiering H, Hauser A (1984) Light-induced excited spin state trapping in a transition-metal complex: the hexa-1-propyltetrazole-iron (II) tetrafluoroborate spin-crossover system. *Chem Phys Lett* 105:1–4
51. Carvajal MA, Reguero M, de Graaf C (2010) On the mechanism of the photoinduced magnetism in copper octacyanomolybdates. *Chem Commun* 46:5737–5739
52. Carvajal MA, Caballol R, de Graaf C (2011) Insights on the photomagnetism in copper octacyanomolybdates. *Dalton Trans* 40:7295–7303
53. Bunău O, Arrio MA, Sainctavit P, Paulatto L, Calandra M, Juhin A, Marvaud V, Cartier dit Moulin C (2012) Understanding the Photomagnetic behavior in copper octacyanomolybdates. *J Phys Chem A* 116:8678–8683
54. Bridonneau N, Long J, Cantin JL, von Bardeleben J, Pillet S, Bendeif EE, Aravena D, Ruiz E, Marvaud V (2015) First evidence of light-induced spin transition in molybdenum(IV). *Chem Commun* 51:8229
55. Magott M, Stefańczyk O, Sieklucka B, Pinkowicz D (2017) Octacyanidotungstate(IV) coordination chains demonstrate a light-induced excited spin state trapping behavior and magnetic exchange photoswitching. *Angew Chem Int Ed* 56:13283–13287
56. Arczyński M, Rams M, Stanek J, Fitta M, Sieklucka B, Dunbar KR, Pinkowicz D (2017) A family of octahedral magnetic molecules based on  $[\text{Nb}^{IV}(\text{CN})_8]^{4-}$ . *Inorg Chem* 56:4021–4027
57. Arimoto Y, Ohkoshi S, Zhong ZJ, Seino H, Mizobe Y, Hashimoto K (2003) Photoinduced magnetization in a two-dimensional cobalt octacyanotungstate. *J Am Chem Soc* 125:9240–9241
58. Korzeniak T, Pinkowicz D, Nitek W, Dańko T, Pełka R, Sieklucka B (2016) Photoswitchable  $\text{Cu}^{II}_4\text{Mo}^{IV}$  and  $\text{Cu}^{II}_2\text{Mo}^{IV}$  cyanido-bridged molecules. *Dalton Trans* 45:16585–16595
59. Stefańczyk O, Majcher AM, Rams M, Nitek W, Mathoniere C, Sieklucka B (2015) Photo-induced magnetic properties of the  $[\text{Cu}^{II}(\text{bapa})]_2[\text{Mo}^{IV}(\text{CN})_8] \cdot 7\text{H}_2\text{O}$  molecular ribbon. *J Mater Chem C* 3:8712–8719
60. Herrera JM, Marvaud V, Verdager M, Marrot J, Kalisz M, Mathoniere C (2004) Reversible photoinduced magnetic properties in the heptanuclear complex  $[\text{Mo}^{IV}(\text{CN})_2(\text{CN}-\text{CuL})_6]^{8+}$ : a photomagnetic high-spin molecule. *Angew Chem Int Ed* 43:5468–5471
61. Chorazy S, Wyczesany M, Sieklucka B (2017) Lanthanide photoluminescence in heterometallic polycyanidometallate-based coordination networks. *Molecules* 22:1902
62. Long J, Chelebaeva E, Larionova J, Guari Y, Ferreira RAS, Carlos LD, Almeida Paz FA, Trifonov A, Guérin C (2011) Near-infrared luminescent and magnetic cyano-bridged coordination polymers  $\text{Nd}(\text{phen})_n(\text{DMF})_m[\text{M}(\text{CN})_8]$  ( $M = \text{Mo, W}$ ). *Inorg Chem* 50:9924–9926
63. Chorazy S, Rams M, Wang J, Sieklucka B, Ohkoshi S (2017) Octahedral Yb(III) complexes embedded in  $[\text{Co}^{III}(\text{CN})_6]$ -bridged coordination chains: combining sensitized near-infrared fluorescence with slow magnetic relaxation. *Dalton Trans* 46:13668–13672

64. Chorazy S, Rams M, Nakabayashi K, Sieklucka B, Ohkoshi S (2016) White light emissive Dy III single-molecule magnets sensitized by diamagnetic  $[\text{Co}^{\text{III}}(\text{CN})_6]^{3-}$  linkers. *Chem Eur J* 22:7371–7375
65. Chorazy S, Sieklucka B, Ohkoshi S (2016) Near-infrared photoluminescence in hexacyanido-bridged Nd–Cr layered ferromagnet. *Cryst Growth Des* 16:4918–4925
66. Chorazy S, Kumar K, Nakabayashi K, Sieklucka B, Ohkoshi S (2017) Fine tuning of multicolored photoluminescence in crystalline magnetic materials constructed of trimetallic  $\text{Eu}_x\text{Tb}_{1-x}[\text{Co}(\text{CN})_6]$  cyanido-bridged chains. *Inorg Chem* 56:5239–5252
67. Chorazy S, Nakabayashi K, Arczynski M, Peřka R, Ohkoshi S, Sieklucka B (2014) Multifunctionality in bimetallic  $\text{Ln}^{\text{III}}[\text{W}^{\text{V}}(\text{CN})_8]^{3-}$  (Ln=Gd, Nd) coordination helices: optical activity, luminescence, and magnetic coupling. *Chem Eur J* 20:7144–7159
68. Chorazy S, Nakabayashi K, Ozaki N, Peřka R, Fic T, Mlynski J, Sieklucka B (2013) Thermal switching between blue and red luminescence in magnetic chiral cyanido-bridged  $\text{Eu}^{\text{III}}\text{--W}^{\text{V}}$  coordination helices. *RSC Adv* 3:1065–1068
69. Pinkowicz D, Podgajny R, Nitek W, Rams M, Majcher AM, Nuida T, Ohkoshi S, Sieklucka B (2011) Multifunctional magnetic molecular  $\{[\text{Mn}^{\text{II}}(\text{urea})_2(\text{H}_2\text{O})_2][\text{Nb}^{\text{IV}}(\text{CN})_8]\}_n$  system: magnetization-induced SHG in the chiral polymorph. *Chem Mater* 23:21–31
70. Kosaka W, Hashimoto K, Ohkoshi S (2007) Three-dimensional manganese octacyanoniobate-based pyroelectric ferrimagnet. *Bull Chem Soc Jpn* 81:992–994
71. Tsunobuchi Y, Kosaka W, Nuida T, Ohkoshi S (2009) Magnetization-induced second harmonic generation in a three-dimensional manganese octacyanoniobate-based pyroelectric ferrimagnet. *CrystEngComm* 11:2051–2053
72. Kosaka W, Nuida T, Hashimoto K, Ohkoshi S (2007) Crystal structure, magnetic properties, and second harmonic generation of a three-dimensional pyroelectric cyano-bridged Mn–Mo complex. *Bull Chem Soc Jpn* 80:960–962
73. Dechambenoit P, Long JR (2011) Microporous magnets. *Chem Soc Rev* 40:3249–3265
74. Kahn O, Larionova J, Yakhmi JV (1999) Molecular magnetic sponges. *Chem Eur J* 5:3443–3449
75. Kaneko W, Ohba M, Kitagawa S (2007) A flexible coordination polymer crystal providing reversible structural and magnetic conversions. *J Am Chem Soc* 129:13706–13712
76. Pinkowicz D, Podgajny R et al (2008) Magnetic sponge-like behavior of 3D ferrimagnetic  $\{[\text{Mn}_{\text{II}}(\text{imH})_2][\text{Nb}^{\text{IV}}(\text{CN})_8]\}_n$  with  $T_c = 62$  K. *Inorg Chem* 47:9745–9747
77. Pinkowicz D, Podgajny R et al (2011) Double switching of a magnetic coordination framework through intraskeletal molecular rearrangement. *Angew Chem Int Ed* 50:3973–3977
78. Milon J, Daniel MC, Kaiba A, Guionneau P, Brandes S, Sutter JP (2007) Nanoporous magnets of chiral and racemic  $\{[\text{Mn}(\text{HL})]_2\text{Mn}\{\text{Mo}(\text{CN})_7\}_2\}$  with switchable ordering temperatures ( $T_c = 85$  K  $\leftrightarrow$  106 K) driven by  $\text{H}_2\text{O}$  sorption (L = N,N-dimethylalaninol). *J Am Chem Soc* 129:13872–13878
79. Zhang YJ, Liu T, Kanegawa S, Sato O (2009) Reversible single-crystal-to-single-crystal transformation from achiral antiferromagnetic hexanuclears to a chiral ferrimagnetic double zigzag chain. *J Am Chem Soc* 131:7942–7943
80. Ohkoshi S, Tsunobuchi Y, Takahashi H, Hozumi T, Shiro M, Hashimoto K (2007) Synthesis and alcohol vapor sensitivity of a ferromagnetic copper–tungsten bimetallic assembly. *J Am Chem Soc* 129:3084–3085
81. Wang QL, Southerland H, Li JR, Prosvirin AV, Zhao H, Dunbar KR (2012) Crystal-to-crystal transformation of magnets based on heptacyanomolybdate(III) involving dramatic changes in coordination mode and ordering temperature. *Angew Chem Int Ed* 51:9321–9324
82. Yanai N, Kaneko W, Yoneda K, Ohba M, Kitagawa S (2007) Reversible water-induced magnetic and structural conversion of a flexible microporous Ni(II)Fe(III) ferromagnet. *J Am Chem Soc* 129:3496–3497
83. Nowicka B, Reczyński M, Rams M, Nitek W, Kozieł M, Sieklucka B (2015) Larger pores and higher  $T_c$ :  $\{[\text{Ni}(\text{cyclam})]_3[\text{W}(\text{CN})_8]_2\text{solv}\}_n$  – a new member of the largest family of

- pseudo-polymorphic isomers among octacyanometallate-based assemblies. *CrystEngComm* 17:3526–3532
84. Nowicka B, Reczyński M, Bałanda M, Fitta M, Gawel B, Sieklucka B (2016) The rule rather than the exception: structural flexibility of  $[\text{Ni}(\text{cyclam})]^{2+}$ -based cyano-bridged magnetic networks. *Cryst Growth Des* 16:4736–4743
  85. Chorazy S, Podgajny R et al (2015) Optical activity and dehydration-driven switching of magnetic properties in enantiopure cyanido-bridged  $\text{Co}^{\text{II}}_3\text{W}^{\text{V}}_2$  trigonal bipyramids. *Inorg Chem* 54:5784–5794
  86. Nowicka B, Heczko M, Reczyński M, Rams M, Nitek W, Gawel B, Sieklucka B (2016) Exploration of a new building block for the construction of cyano-bridged solvatomagnetic assemblies:  $[\text{N}(\text{cyclam})]^{3+}$ . *CrystEngComm* 18:7011–7020
  87. Herchel R, Tuček J, Trávníček Z, Petridis D, Zbořil R (2011) Crystal water molecules as magnetic tuners in molecular metamagnets exhibiting antiferro-ferro-paramagnetic transitions. *Inorg Chem* 50:9153–9163
  88. Maspoch D et al (2007) Structural and magnetic modulation of a purely organic open framework by selective guest inclusion. *Chem Eur J* 13:8153–8163
  89. Ohba M, Maruono N, Okawa H, Enoki T, Latour JM (1994) A new bimetallic ferromagnet,  $[\text{Ni}(\text{en})_2]_3[\text{Fe}(\text{CN})_6]_2 \cdot 2\text{H}_2\text{O}$ , with a rare rope-ladder chain structure. *J Am Chem Soc* 116:11566–11567
  90. Ferlay S, Mallah T, Vaissermann J, Bartolome F, Veillet P, Verdagner M (1996) A chromium (III) nickel(II) cyanide-bridged ferromagnetic layered structure with corrugated sheets. *Chem Commun* 1996:2481–2482
  91. Colacio E, Dominguez-Vera JM, Ghazi M, Kivekas R, Lloret F, Morenoa JM, Stoeckli-Evans H (1999) A novel two-dimensional honeycomb-like bimetallic iron(III)–nickel(II) cyanide-bridged magnetic material  $[\text{Ni}(\text{cyclam})]_3[\text{Fe}(\text{CN})_6]_2 \cdot n\text{H}_2\text{O}$  (cyclam = 1,4,8,11-tetraazacyclodecane). *Chem Commun* 1999:987–988
  92. Marvaud V, Decroix C, Scullier A, Guyard-Duhayon C, Vaissermann J, Gonnet F, Verdagner M (2003) Hexacyanometalate molecular chemistry: heptanuclear heterobimetallic complexes; control of the ground spin state. *Chem Eur J* 8:1677–1691
  93. Tuyères F, Scullier A, Duhayon C, Hernandez-Molina M, Fabrizi de Biani F, Verdagner M, Mallah T, Wernsdorfer W, Marvaud V (2008) Hexacyanidometalate molecular chemistry, part III: di-, tri-, tetra-, hexa- and hepta-nuclear chromium–nickel complexes: control of spin, structural anisotropy, intra- and inter-molecular exchange couplings. *Inorg Chim Acta* 361:3505–3518
  94. Gu ZZ, Einaga Y, Sato O, Fujishima A, Hashimoto K (2001) Photo- and dehydration-induced charge transfer processes accompanied with spin transition on  $\text{CoFe}(\text{CN})_5\text{NH}_3 \cdot 6\text{H}_2\text{O}$ . *J Solid State Chem* 159:336–342
  95. Liu M, Bian XF, Xia YF, Bao Z, Wu HS, Xu MX (2011) Variation of magnetic properties with different annealed temperatures in the  $\text{Ni}_3[\text{Fe}(\text{CN})_6]_2 \cdot \text{XH}_2\text{O}$ . *Curr Appl Phys* 11:271–275
  96. Nowicka B, Reczyński M, Rams M, Nitek W, Żukrowski J, Kapusta C, Sieklucka B (2015) Hydration-switchable charge transfer in the first bimetallic assembly based on the  $[\text{Ni}(\text{cyclam})]^{3+}$  – magnetic CN-bridged chain  $\{(\text{H}_3\text{O})[\text{Ni}^{\text{III}}(\text{cyclam})][\text{Fe}^{\text{II}}(\text{CN})_6] \cdot 5\text{H}_2\text{O}\}_n$ . *Chem Commun* 51:11485–11488
  97. Ohba M et al (2009) Bidirectional chemo-switching of spin state in a microporous framework. *Angew Chem Int Ed* 48:4767–4771
  98. Bartual-Murgui C et al (2012) Synergetic effect of host-guest chemistry and spin crossover in 3D Hofmann-like metal-organic frameworks  $[\text{Fe}(\text{bpac})\text{M}(\text{CN})_4]$  (M=Pt, Pd, Ni). *Chem Eur J* 18:507–516
  99. Berlinguette CP, Dragulescu-Andrasi A, Sieber A, Güdel HU, Achim C, Dunbar KR (2005) A charge-transfer-induced spin transition in a discrete complex: the role of extrinsic factors in stabilizing three electronic isomeric forms of a cyanide-bridged  $\text{Co}/\text{Fe}$  cluster. *J Am Chem Soc* 127:6766–6779
  100. Ozaki N, Tokoro H, Miyamoto Y, Ohkoshi S (2014) Humidity dependency of the thermal phase transition of a cyano bridged  $\text{Co}$ – $\text{W}$  bimetal assembly. *New J Chem* 38:1950–1954

101. Koumoussi ES et al (2014) Metal-to-metal electron transfer in co/Fe Prussian blue molecular analogues: the ultimate miniaturization. *J Am Chem Soc* 136:15461–15464
102. Horike S, Umeyama D, Kitagawa S (2013) Ion conductivity and transport by porous coordination polymers and metal-organic frameworks. *Acc Chem Res* 46:2376–2384
103. Imoto K, Nakagawa K, Miyahara H, Ohkoshi S (2013) Super-ionic conductive magnet based on a cyano-bridged Mn–Nb bimetal assembly. *Cryst Growth Des* 13:4673–4677
104. Okubo M (2013) Reversible solid state redox of an octacyanometallate-bridged coordination polymer by electrochemical ion insertion/extraction. *Inorg Chem* 52:3772–3779

# Cobalt(II) Complexes as Single-Ion Magnets



Shalini Tripathi, Atanu Dey, Maheswaran Shanmugam,  
Ramakirushnan Suriya Narayanan, and Vadapalli Chandrasekhar

## Contents

1	Introduction .....	36
2	Coordination Number 2 .....	40
2.1	Linear Geometry .....	40
3	Coordination Number 3 .....	42
3.1	Trigonal Planar Geometry .....	42
4	Coordination Number 4 .....	44
4.1	Tetrahedral Geometry .....	44
4.2	Square Planar and Trigonal Pyramidal Geometry .....	51
5	Coordination Number 5 .....	55
5.1	Trigonal Bipyramidal Geometry .....	55
5.2	Square Pyramidal Geometry .....	57
6	Coordination Number 6 .....	61
6.1	Octahedral Geometry .....	61
6.2	Trigonal Prismatic Geometry .....	67
7	Complexes with Extended Structures .....	69
8	Seven- and Eight-Coordinated Co(II) Complexes .....	70
9	Summary and Outlook .....	72
	References .....	73

**Abstract** This book chapter is mainly devoted to the recent findings about the cobalt(II) single-ion magnets (SIMs). Influence of various coordination numbers (from 2 to 8) around Co(II) in determining the spin Hamiltonian (SH) parameters of

---

The original version of this chapter was revised. A correction to this chapter is available at DOI [10.1007/3418\\_2019\\_32](https://doi.org/10.1007/3418_2019_32).

All the authors contributed equally to this work.

---

S. Tripathi and M. Shanmugam (✉)

Department of Chemistry, Indian Institute of Technology Bombay, Mumbai, Maharashtra, India  
e-mail: [eswar@chem.iitb.ac.in](mailto:eswar@chem.iitb.ac.in)

A. Dey and R. S. Narayanan

Tata Institute of Fundamental Research Hyderabad, Hyderabad, Telangana, India

V. Chandrasekhar

Tata Institute of Fundamental Research Hyderabad, Hyderabad, Telangana, India

Department of Chemistry, Indian Institute of Technology Kanpur, Kanpur, Uttar Pradesh, India



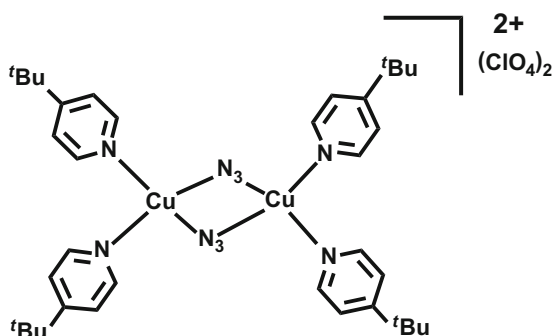
the complexes is reviewed. This chapter also discloses the importance of proper ligand design for stabilizing Ising or uniaxial anisotropy in mononuclear Co(II) complexes.

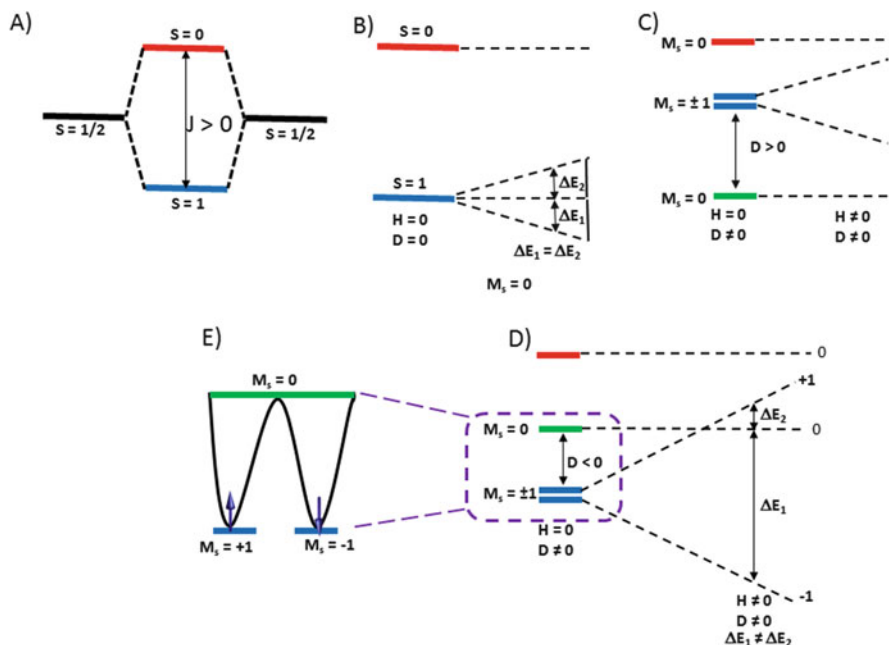
**Keywords** Cobalt complexes · EPR · Magnetism · Single-ion magnets · X-ray diffraction

## 1 Introduction

Single-molecule magnets (SMMs) are now known for nearly two decades, yet this field continues to grow exponentially. The first example of a SMM is the dodecanuclear complex  $[\text{Mn}_{12}(\text{O})_{12}(\text{CH}_3\text{CO}_2)_{12}(\text{H}_2\text{O})_4] \cdot 4\text{H}_2\text{O} \cdot 2\text{CH}_3\text{COOH}$  (**1**) which has led to interest in polynuclear transition metal complexes. Subsequent studies revealed that heterometallic 3d/4f complexes as well as homometallic complexes containing certain 3d or 4f metal are equally effective. Studies on transition metal complexes have shown that a high-spin ground state ( $S$ ) and a negative magnetic anisotropy ( $D$ ) should be present to achieve high anisotropic energy barriers ( $U_{\text{eff}}$ ) for magnetization reversal [1, 2]. The concept of  $S$  and  $D$  can be clarified by considering two dimeric complexes,  $[\text{Cu}_2(t\text{-Bu-Py})_4(\text{N}_3)_2]$  (**2**) and  $[\text{Cu}_2(\text{CH}_3\text{CO}_2)_4(\text{H}_2\text{O})_2]$  (**3**, Fig. 1) [3, 4]. In **2** and **3**, the two Cu(II) ions are bridged by two azide and carboxylate ligands, respectively. The temperature-dependent magnetic susceptibility of both the complexes reveals that the Cu(II) ions in **2** and **3** are coupled ferromagnetically and antiferromagnetically, respectively. For both the complexes,  $S = 1/2$  is not a valid quantum number anymore (either  $S = 1$  or  $0$  is the valid quantum number). In **2**,  $S = 1$  will be the ground state, and it has the lowest energy compared to the excited state of  $S = 0$ . The depopulation of the diamagnetic excited state and population of the paramagnetic ground state upon decreasing the temperature causes the magnetic susceptibility to increase progressively before it gets saturated at some temperature for **2**. A reverse trend is observed in the case of **3**, as the antiferromagnetic interaction becomes dominant in this complex. The energy

**Fig. 1** Line diagram of complex **2**





**Fig. 2** (a) Energy level diagram of a ferromagnetically coupled system. (b) Splitting pattern of  $M_s$  levels in the absence of an external magnetic field. (c) Splitting pattern of  $M_s$  levels in the presence of an external magnetic field giving  $D > 0$ . (d) Splitting pattern of  $M_s$  levels in the presence of an external magnetic field giving  $D < 0$ . (e) Double-well potential showing barrier for spin reversal

gap between the ground state and the excited state is determined by the extent of interaction between the Cu(II) centers via the azide or carboxylate bridges. Such an interaction via closed shell ligands is called the super-exchange interaction ( $J$ ). The larger the exchange interaction, the larger is the separation between the ground and the excited state. In molecular magnets it is preferable to have a large exchange interaction.

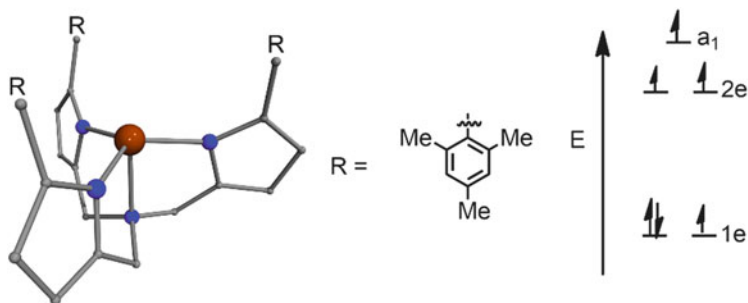
When these paramagnetic complexes are kept in the magnetic field, all the energy levels will split further ( $2S + 1$  multiplicity), i.e.,  $S = 1$  state will split into three  $m_s$  levels ( $\pm 1$  and 0) and  $S = 0$  will be unaffected by the external magnetic field. Assuming that the three  $m_s$  levels arising due to the Zeeman interaction are degenerate, the energy gap between the  $m_s$  levels  $-1$  to 0 ( $\Delta E_1$ ) and 0 to  $+1$  ( $\Delta E_2$ ) at a given field will be always the same (Fig. 2b). Nevertheless, this is not the scenario in a majority of the complexes, i.e., the degeneracy of these  $m_s$  levels is lifted due to the orbital angular momentum (spin-orbit coupling) and spin-spin interaction even in the absence of external field. The extent of splitting between the  $m_s$  levels of  $\pm 1$  and 0 is called magnetic anisotropy or zero-field splitting (in the zero dc magnetic field,  $D$ ), i.e., now the magnetization vector prefers to orient in a particular direction (conventionally z-axis or easy axis). Now, there are two situations, either the largest  $m_s$  level  $\pm 1$  will be lowest in energy and the smallest  $m_s$  value "0" will be higher in energy or

vice versa. The former situation is described by convention as negative anisotropy or easy axis ( $-D$ ), and the latter situation is represented as positive or easy-plane anisotropy ( $+D$ ). In general, large  $D$ -values arise from systems with large orbital angular momenta than merely spin-spin interactions. The system with negative anisotropy presents a barrier for the magnetization reversal (see Fig. 2e), while changing the magnetization vector direction is a barrierless process for positive anisotropy containing systems. Nevertheless, there are some exceptions found for the latter statement, i.e., certain complexes show field-induced slow relaxation of magnetization even with a positive  $D$ -value (see below).

After the discovery of **1**, several polynuclear transition metal complexes containing metal centers such as  $\text{Mn}^{\text{II}}$ ,  $\text{Fe}^{\text{II}}$ ,  $\text{Co}^{\text{II}}$ ,  $\text{Ni}^{\text{II}}$ , and  $\text{V}^{\text{II}}$  have been widely investigated [5–11]. Discussing about these is beyond the scope of this chapter. There are several excellent reviews that deal with polynuclear metal complexes ([12] and references there in). In this chapter, we have exclusively covered the single-ion magnetic behavior of Co(II) complexes possessing various geometric features. Interest in these complexes stems from the fact that Co(II) has a large spin-orbit coupling which could be harnessed under suitable conditions to reveal new generation of molecular magnets. In this chapter we will deal with Co(II) single-ion magnets (SIMs). The following chapter in this book will deal with hybrid Co(II)/4f heterometallic complexes.

Based on two decades of intense research investigation, it's been realized that in larger oligomeric clusters, the magnetic anisotropy is proportional to  $1/S^2$  [13, 14] while realizing that controlling the anisotropic axes in multinuclear cluster is an extremely challenging task. Hence, research was focused to control the  $D$ -value of mononuclear metal complexes. In this line of interest, the first ever transition metal-based SIM was reported by Long and co-workers in 2010 with the molecular formula of  $\text{K}[\text{Fe}(\text{tpa}^{\text{Mes}})]$  (**4**) ( $\text{tpa}^{\text{Mes}}$  = mesityltripyroleamine) [15]. The central divalent iron has four nitrogen donors in its coordination environment. While three of these occupy the corners of a trigonal plane, the fourth nitrogen occupies the apical position affording a trigonal pyramidal geometry about Fe(II). Temperature-dependent magnetic susceptibility reveals the contribution of the orbital angular momentum to the total magnetic moment. The magnetization data were fitted using ANISOFIT 2.0 using the parameters  $D = -39.6 \text{ cm}^{-1}$ ,  $E = -0.4 \text{ cm}^{-1}$ , and  $g = 2.21$  ( $S = 2$ , Fig. 3).

The presence of first-order orbital angular momentum due to the electronically degenerate levels facilitates the stabilization of a large single-ion magnetic anisotropy (Fig. 3, right). AC measurements performed in the presence of an optimum external magnetic field reveal  $\chi_M''$  signals. The analysis of the data leads to an estimation of an anisotropic energy barrier of  $42 \text{ cm}^{-1}$ . This is significantly lower than the expected energy barrier value of  $148 \text{ cm}^{-1}$ , suggesting that there are other relaxation pathways apart from the Orbach relaxation process. In transition metal ion-based SIMs, the ground state of the complex is always fixed, and the only parameter that can modulate the effective energy barrier is the single-ion magnetic



**Fig. 3** Crystal structure of the Fe(II) complex **4** (left) and the splitting of 3d orbitals for high-spin Fe(II) complex (right). Color code: Fe, brown; N, blue; and C, gray

anisotropy. Various methodologies have been proposed in the literature to fine-tune the  $D$ -value. These include (1) reducing the coordination number [16–19], (2) increasing the covalency of the donor atoms [20–22], (3) heavier halide ion-induced ground state to excited state mixing via spin-orbit coupling [23], (4) varying the substituent on the ligand [24, 25], (5) anion or cation influence on  $D$ -value, (6) in-plane or out-of-plane orientation of the Co(II) ions [26], etc. Not only the first coordination sphere but also the secondary coordination sphere has a non-zero influence on determining not only the sign but also the magnitude of single-ion magnetic anisotropy [27, 28]. Unlike the magnitude of magnetic anisotropy in large oligomeric clusters, the  $D$ -value of single-ion complexes is usually large; often the conventional methods such as electron paramagnetic resonance [EPR (X and Q-band)] employed to predict quantitatively the sign and magnitude of  $D$  would not be useful. Other sophisticated techniques are required (such as cantilever torque measurement [29], inelastic neutron scattering [30, 31], paramagnetic NMR methods [24, 32] and high frequency, high-field EPR measurements [33, 34], etc.) to compliment the spin Hamiltonian parameters extracted from magnetic data fit. Often, quantum chemical calculations add further understanding of the electronic structure and origin of magnetic anisotropy in mononuclear metal complexes.

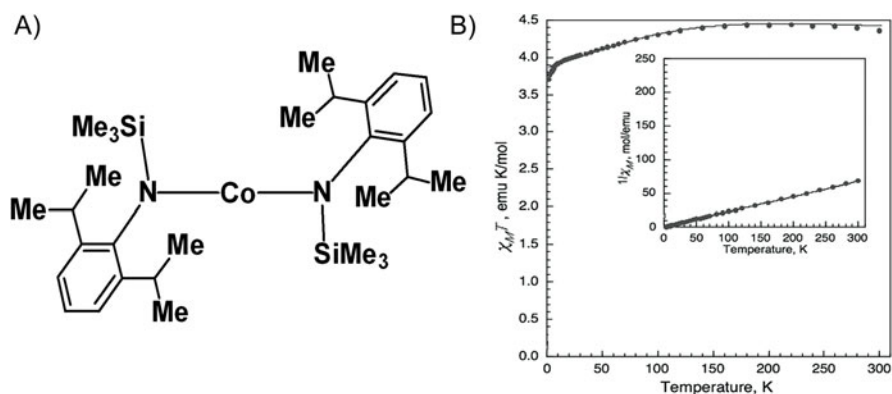
In general, for a given metal ion, the origin of magnetic anisotropy arises due to the first-order orbital angular momentum. The ground state electronic configuration of certain metal ions (such as tetrahedral Co(II) ion) does not give rise to first-order orbital angular momentum, in such cases the origin of magnetic anisotropy is due to the second-order orbital angular momentum, i.e., spin-orbit coupling induced mixing of isotropic ground state with the anisotropic excited states. The mixing of ground state to the excited states is totally governed by the geometry. In general, the geometry around transition metal complexes has a significant influence on both the sign and magnitude of  $D$ . In the following section, we have given an overview of SIM behavior of Co(II) complexes that possess various coordination geometries.

## 2 Coordination Number 2

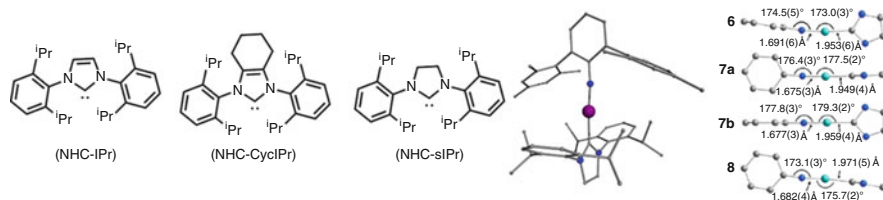
### 2.1 Linear Geometry

Non-zero orbital angular momentum provided by the low-coordinate metal complexes is helpful to increase the  $D$ -value significantly. The reaction of cobalt halides with  $(\text{LiN}(\text{SiMe}_3)\text{Dipp})$  (where Dipp = 2,6-diisopropylphenyl) results in the isolation of a linear Co(II) complex (**5**, Fig. 4) [16]. Dc magnetic susceptibility data collected on a polycrystalline sample of **5** is shown in Fig. 4. The room temperature  $\chi_{\text{M}}T$  value of  $4.2 \text{ cm}^3 \text{ K mol}^{-1}$  is significantly larger than the expected value for a simple paramagnetic complex with  $S = 3/2$ . The magnetic data  $\chi_{\text{M}}T(T)$  and  $M(H)$  were fitted (from 10 K to 300 K) simultaneously by considering  $S = 3/2$  and  $L = 2$  to yield,  $B_2^0 = -161 \text{ cm}^{-1}$ ;  $\lambda = -183 \text{ cm}^{-1}$ ,  $g_{x,y} = 2.15$ , and  $g_z = 2.37$ . The sharp decrease in  $\chi_{\text{M}}T$  value below 10 K is likely due to the antiferromagnetic ordering and is consistent with the negative value of Curie-Weiss constant. Unfortunately, relaxation dynamics studies were not reported for this and the other two-coordinate Co(II) complexes.

Although two-coordinate cobalt complexes can be ideal candidates to harvest the large orbital angular momentum of Co(II), there appear to be some disadvantages to achieve a high anisotropic barrier. These include (1) the dynamic distortion associated with two-coordinate complexes and (2) long M-N  $\sigma$  bond lengths. Further, dynamic distortion will introduce unwanted vibronic coupling, which will enhance faster relaxation. Long and co-workers have suggested that increasing the metal-ligand covalency can lead to a reduction in vibronic coupling which in turn can facilitate the increase of single-ion magnetic anisotropy [17].



**Fig. 4** (a) Line diagram of complex **5**. (b) Temperature-dependent  $\chi_{\text{M}}T$  data recorded on a polycrystalline sample of **5** (inset: the temperature dependence of  $1/\chi_{\text{M}}$  and the corresponding fits) between 2 and 300 K. Reprinted with permission from [16], Copyright (2013) The American Chemical Society



**Fig. 5** Representative structure of the ligands and their designation. Molecular structure of **6**. Structure of the two-coordinate cores of **6–8** (**7** contains crystallographically distinct molecule labeled as **7a** and **7b**). Color code: magenta and sky blue = Co; blue = N; and gray = C. Reprinted with permission from [18] The American Chemical Society

Based on this proposal, Gao and co-workers have reported two-coordinate linear cobalt complexes,  $[\text{Co}(\text{NHC-R})(\text{NDmp})]$  [ $\text{Dmp} = 2,6\text{-dimesitylphenyl}$ ;  $\text{R} = \text{IPr}$  (**6**) or  $\text{cyIPr}$  (**7**) and  $\text{sIPr}$  (**8**)], where the coordination sites were completed by *N*-heterocyclic carbene (NHC) and an imido ligand [18]. In all the cases, the NHC plane was orthogonal to the aryl group of the imido ligand. Depending on the derivative employed, the N-Co-C linearity varies which is depicted in Fig. 5. The Co-N bond distance in all the cases falls in the range 1.675–1.691 Å which is significantly shorter than Co-N(amido) bond distance. Dc magnetic susceptibility data were performed on all the samples with the room temperature  $\chi_{\text{MT}}$  value of 3.86, 3.72, and 3.74  $\text{cm}^3 \text{K mol}^{-1}$ , respectively, for (**6–8**), suggesting that there is a sizable orbital angular momentum contribution to the magnetic moment. Considering the HDVV Hamiltonian with *D* and *E* terms, dc magnetic data could not be modeled. This is understandable since the Hamiltonian applies the precondition that orbital angular momentum is quenched, i.e., the Hamiltonian does not project the realistic situation.

Ac relaxation dynamics measurements revealed out-of-phase susceptibility signals with a high anisotropic barrier of 413  $\text{cm}^{-1}$  ( $\tau_0 = 1.2 \times 10^{-10}$ ) for **8**. The anisotropic barrier for **6** [288  $\text{cm}^{-1}$  ( $H_{\text{dc}} = 0$ )] and **7** [297  $\text{cm}^{-1}$  ( $H_{\text{dc}} = 0$ )] is slightly lower than **8**. In addition, all the complexes reveal hysteresis at 2 K (sweep rate of 700 Oe  $\text{s}^{-1}$ ).

To understand the electronic structure of these complexes, MOLCAS 7.8 and ORCA suite software were employed. Calculations were performed on two different model complexes (1) considering  $S = 3/2$  state for Co(II) ion where the spins are localized on the metal ion (2) a spin delocalized model, i.e., an unpaired electron on the metal transferred to an imido ligand (due to its extensive covalent nature). The calculation results based on case study 1 were as follows: (1) the ground to first excited Kramers state energy gap was  $\sim 280 \text{ cm}^{-1}$ , and (2) there is no difference in the energy gap between the ground and the first excited Kramers state across all the complexes. The later scenario is not realistic because the experimentally extracted energy barrier shows significant energy difference. For the same case, calculations were performed with the extended CAS (7,10) which reveals an energy difference between the ground and first excited Kramers state. The energy gap was also found to be sensitive to the Co-N distance confirmed by detailed computational studies. In

order to assess another possible situation where there is charge transfer from metal to ligand, calculations were performed on model complexes with  $S = 1$  and  $1/2$  on the cobalt and the ligand, respectively. This particular situation still reflects the overall ground state of  $S = 3/2$  for the entire molecule. Overall, one can conclude that increasing covalency in the metal-ligand bond reduces vibronic coupling and leads to a high anisotropic barrier.

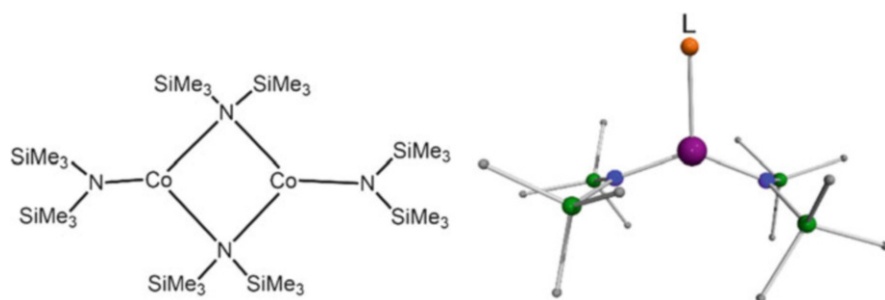
### 3 Coordination Number 3

#### 3.1 Trigonal Planar Geometry

The bis(trimethylsilyl)amide complex of cobalt was believed to be monomeric for quite some time in solid state, but recently Power and co-workers revealed that it exists as a dimer in the solid state [16]. The structure of this complex  $[\text{Co}_2(\{\text{N}(\text{SiMe}_3)_2\}_4)]$  (**9**) was unmistakably determined by single-crystal X-ray diffraction (Fig. 6). In **9** both the cobalt ions exist in divalent oxidation states. The coordination geometry is trigonal planar, and the Co(II) ions are surrounded by one terminal amido and two bridging amido group. Reaction of **9** with Lewis base results in the formation of monomeric tri-coordinate complexes  $[\text{Co}(\{\text{N}(\text{SiMe}_3)_2\}_2)(\text{L})]$  where  $\text{L} = \text{THF}$  (**10**) or  $\text{PMe}_3$  (**11**) or pyridine (Py) (**12**) (Fig. 6). Analysis of the dc magnetic data afforded the following parameters:  $[D = -73(2) \text{ cm}^{-1}, E = \pm 14.6 \text{ cm}^{-1}, g = 3.038$  (**10**),  $D = -74(2) \text{ cm}^{-1}, E = \pm 9.6(5) \text{ cm}^{-1}, g = 2.435$  (**11**);  $D = -82(2) \text{ cm}^{-1}, E = \pm 21.0 \text{ cm}^{-1}, g = 2.722$  (**12**)].

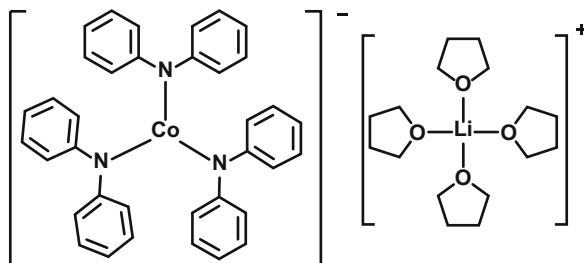
Although all these complexes possess an easy-axis anisotropy, studies related to the magnetization relaxation dynamics have not been reported.

Investigation of  $\text{Li}(15\text{-crown-5})[\text{Co}\{\text{N}(\text{SiMe}_3)_2\}_3]$  (**13**) and  $[\text{Co}(\text{N}(\text{SiMe}_3)_2)_2(\text{P}(\text{C}_6\text{H}_{11})_3)]$  (**14**) also revealed an easy-axis anisotropy  $[D = -57 \text{ cm}^{-1}, E = \pm 12.7 \text{ cm}^{-1}, g = 2.79$  (**13**);  $D = -82 \text{ cm}^{-1}, E/D = 0, g_{x,y} = 2.58,$



**Fig. 6** Line diagrams of  $[\text{Co}_2(\{\text{N}(\text{SiMe}_3)_2\}_4)]$  (**9**) (left panel) and X-ray structure of  $[\text{Co}\{\text{N}(\text{SiMe}_3)_2\}_2(\text{L})]$  where  $\text{L} = \text{THF}$  (**10**),  $\text{PMe}_3$  (**11**), and Py (**12**) (right panel). Color code: Co, purple; N, blue; Si, green; and C, gray

**Fig. 7** Line diagram of complex **15**



$g_z = 2.90$  (**14**)] with non-zero rhombic terms. The spin Hamiltonian (SH) parameters for all these complexes have been reported based on the dc magnetic data fit, which is often insensitive to the sign and magnitude of  $D$ -value. Hence, these values need to be taken cautiously.

The out-of-phase susceptibility signal intensity of all the three complexes, in the absence of an external magnetic field, was found to be extremely weak compared to the in-phase susceptibility signals. Ac measurements in the presence of an optimum external magnetic field revealed well-resolved  $\chi_M''$  signals with maxima. Replacement of the alkyl amide ligands with aryl amides such as diphenyl amide (DPA) afforded  $\text{Li}(\text{THF})_4[\text{Co}(\text{DPA})_3]$  (**15**, Fig. 7). **15** shows an easy-plane anisotropy upon magnetic data modeling. This is corroborated from HF-EPR measurements where  $g_{\parallel}$  and  $g_{\perp}$  signals arise from the lowest Kramers doublet  $\pm 1/2$  of a ground state  $3/2$ . Linear dependency of  $g_{\parallel}$  and  $g_{\perp}$  signals with frequency and simulation of EPR spectral features unequivocally ascertains the sign and magnitude of  $D$ -value for **15** (Fig. 7).

Ac relaxation dynamics study performed on a polycrystalline sample of **15** in the absence of an external magnetic field shows no  $\chi_M''$  signals. This indicates that quantum-tunneling mechanism (QTM) drives the magnetization relaxation predominantly. Ac relaxation dynamics in the presence of a bias field opens up the Orbach relaxation process by arresting QTM to some extent. But the Arrhenius plot deviates from linearity below 4 K indicative of a non-zero contribution of other relaxation process such as Raman and direct processes. The spin-lattice relaxation time was fitted by considering Orbach ( $\tau_0 = 2.5 \times 10^{-8}$  s), Raman ( $C = 0.02 \text{ K}^{-8.23} \text{ s}^{-1}$ ,  $n = 8.23$ ), and direct process ( $A = 2.56 \text{ K}^{-1} \text{ s}^{-1}$ ) to yield an excellent fit to the experimental data with an anisotropic barrier of  $30 \text{ cm}^{-1}$ .

Ab initio calculations on **15** reveal among other things that the 3d-orbital splitting follows the order of  $d_{xz} \approx d_{yz} < d_z^2 < d_{xy} < d_{x^2-y^2}$ . The lowest energy transition in this scenario, between any orbital, will cause change in  $\Delta m_l = \pm 1$ ; hence positive  $D$ -value prevails.

Representative spin Hamiltonian (SH) parameters obtained for other three-coordinate Co(II) complexes reported in literature are summarized in Table 1.



**Table 1** Spin Hamiltonian parameters for three-coordinated Co(II) complexes

Compound	$D$ (cm <sup>-1</sup> )	$E$ (cm <sup>-1</sup> )	$g$	$U_{\text{eff}}$ (cm <sup>-1</sup> )	Ref
[Co{N(SiMe <sub>3</sub> ) <sub>2</sub> } <sub>2</sub> (THF)] ( <b>10</b> )	-73	±14.6	$g_x = g_y = 2.7$ ; $g_z = 3.2$	18.1	[16, 19]
[Co{N(SiMe <sub>3</sub> ) <sub>2</sub> } <sub>2</sub> (PMe <sub>3</sub> )] ( <b>11</b> )	-74	±9.6	$g_x = g_y = 2.1$ ; $g_z = 2.8$	-	[16]
[Co{N(SiMe <sub>3</sub> ) <sub>2</sub> } <sub>2</sub> (Py)] ( <b>12</b> )	-82	±21.0	$g_x = g_y = 2.5$ ; $g_z = 2.8$	-	[16]
[Li(15-crown-5)] [Co{N(SiMe <sub>3</sub> ) <sub>2</sub> ] <sub>3</sub> ] ( <b>13</b> )	-57	±12.7	$g_x = g_y = 2.7$ ; $g_z = 2.7$	16.1	[19]
[Co{N(SiMe <sub>3</sub> ) <sub>2</sub> } <sub>2</sub> (PCy <sub>3</sub> )] ( <b>14</b> )	-82	0	$g_x = g_y = 2.5$ ; $g_z = 2.9$	19.1	[19]
[Li(THF) <sub>4</sub> ][Co(DPA) <sub>3</sub> ] ( <b>15</b> )	40.2	±0.06	$g_x = g_y = 2.5$ ; $g_z = 2.0$	29.2	[35]
[Na(12-crown-4) <sub>2</sub> ] [Co{N(SiMe <sub>3</sub> ) <sub>2</sub> ] <sub>2</sub> ] <sub>3</sub> ] ( <b>16</b> )	-62	±10	$g_x = g_y = 2.9$ ; $g_z = 2.7$	-	[16]

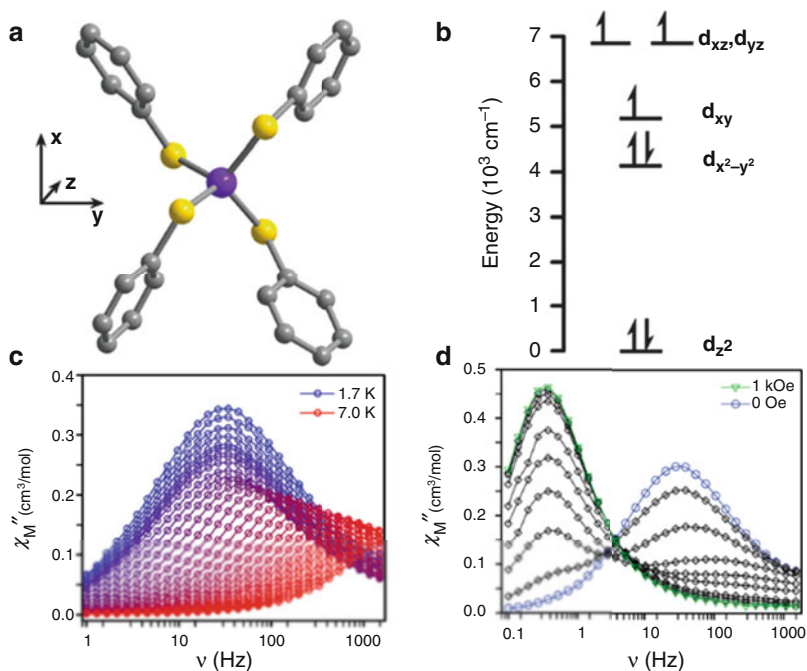
*PMe<sub>3</sub>* trimethylphosphine, *Py* pyridine, *THF* tetrahydrofuran, *DPA* diphenylamine

## 4 Coordination Number 4

### 4.1 Tetrahedral Geometry

Long et al. studied the anionic complex, (PPh<sub>4</sub>)<sub>2</sub>[Co(SPh)<sub>4</sub>] (**17**) (Fig. 8). In this complex, Co(II) is present in a distorted tetrahedral geometry in an approximate D<sub>2d</sub> symmetry. Dc magnetic susceptibility data and its fitting using ANISOFIT 2.0 software reveals the SH parameters ( $D = -74$  cm<sup>-1</sup>;  $E \leq 0.01$ ) associated with these complexes. Based on the angular overlap model (AOM) calculations, the d-orbital splitting of **17** was computed (Fig. 8). The geometry around Co(II) brings near degeneracy between the d<sub>x<sup>2</sup>-y<sup>2</sup></sub> and d<sub>xy</sub> orbitals, and the spin-orbit coupling leads to a mixing of the ground and excited states to stabilize a large negative  $D$ -value. Ac relaxation dynamics on **17** reveal frequency-dependent out-of-phase susceptibility signals even in zero applied dc magnetic field with an estimated anisotropic energy barrier of 21 cm<sup>-1</sup>. This value is significantly lower compared to the expected barrier value  $2D \sim 140$  cm<sup>-1</sup>, implying that other faster relaxation of magnetization processes such as QTM is operational. To quench the QTM, ac data was measured in the presence of 1 kOe (Fig. 8). The  $\chi_M''$  signal intensity at higher frequency gradually decreases as a function of external magnetic field with concomitant increase in lower frequency suggesting that QTM is predominant in **17**.

Variation of the ligand environment in the complexes A<sub>2</sub>[Co(Ph-X)<sub>4</sub>] [A = PPh<sub>4</sub>, X = O (**18**); A = K, X = O (**19**); A = PPh<sub>4</sub>, X = S (**17**); and A = PPh<sub>4</sub>, X = Se (**20**)] [21] leads to some structural modifications. In all the complexes, tetragonal elongation geometry was observed, except **18** where tetragonal compression was observed. The  $D$ -values range from -11 to -83 cm<sup>-1</sup> in these



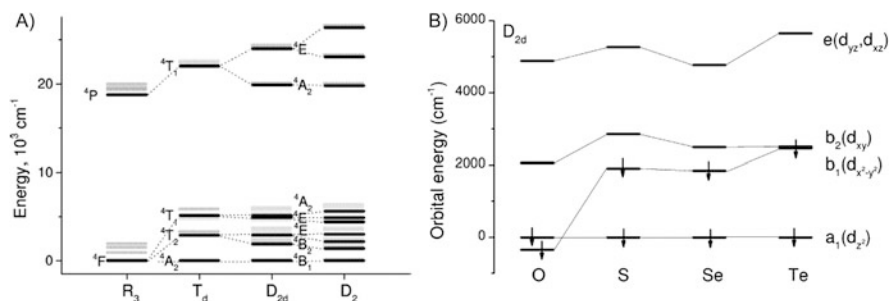
**Fig. 8** (a) Crystal structure of **17**. (b) Electronic configuration and d-orbital energy level splitting for complex **17**. (c) Frequency dependence of the molar out-of-phase ac susceptibility of **17** (zero DC field) collected at temperature intervals of 0.1 K between 1.7 and 2.4 K and intervals of 0.2 K between 2.4 and 7.0 K. (d) Molar out-of-phase ac susceptibility ( $\chi_M''$ ) at 2 K for **17** under applied dc fields from 0–1 kOe in 100 Oe increments. Reprinted with permission from [36], Copyright (2011) The American Chemical Society. Color code: Co, lilac; S, yellow; and C, gray

**Table 2** Spin Hamiltonian parameters for **18–20**

	$g_z$	$g_{x,y}$	$D$ ( $\text{cm}^{-1}$ )	$U_{\text{eff}}$ ( $\text{cm}^{-1}$ )	$\tau_0$ (s)
<b>18</b>	2.222(9)	2.118(6)	−11.1(3)	21(1)	$7(1) \times 10^{-10}$
<b>19</b>	2.958(3)	2.701(2)	−23.8(2)	–	–
<b>17</b>	2.960(3)	2.285(4)	−62.0(1)	21(1)	$1.0(3) \times 10^{-7}$
<b>20</b>	2.953(3)	2.165(5)	−83.0(1)	19(1)	$3(1) \times 10^{-6}$

complexes which increase as the ligand field strength decreases and covalency increases (Table 2).

Detailed ac relaxation dynamics revealed that except **18**, all the complexes show zero-field SIM behavior. The anisotropic barrier estimated for all the complexes is in range of 19–21  $\text{cm}^{-1}$  indicating that an increase of  $D$ -value does not guarantee an increasing the anisotropy barrier. This implies that apart from the Orbach process, other faster relaxation processes are operational. Recently, Neese and co-workers through more accurate quantum chemical calculations elegantly explained the rationale for the trend in the observed  $D$ -values in this family of complexes [37].



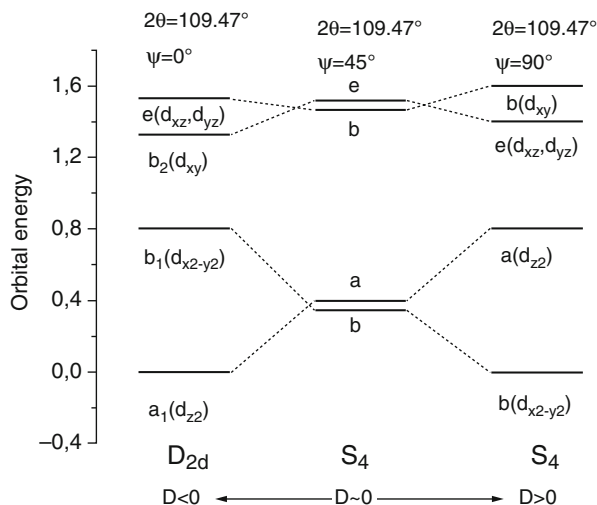
**Fig. 9** (a) Co(II) ion (spherical symmetry,  $R_3$ ) showing CASSCF(7,5) computed quartet terms and terms for a hypothetical Co(II) ion surrounded by four negative charges forming  $T_d$  symmetric,  $D_{2d}$  symmetric, and  $D_2$  symmetric crystal field. In gray the result of additional SOC splitting is shown. (b) Energies computed by ab initio LFT based on the CASSCF(7,5) solution for 10 quartet and 40 doublet states of d-orbitals of the  $D_{2d}$  symmetrized complexes. Reprinted with permission from [37], Copyright (2015) The American Chemical Society

An interesting study on  $A[\text{Co}^{\text{II}}(\text{L}_1)]$  [ $\text{L}_1 =$  thiophenolate anion and  $A = \text{PPh}_4$  (**17**) or  $\text{Et}_4\text{N}$  (**21**)] revealed that while the Co-S bond lengths in both of these are similar, the S-Co-S bond angles vary. Among the six different S-Co-S bond angles in **17**, four S-Co-S bond angles are greater than  $109.5^\circ$  while two other are smaller. A reverse trend was observed in the case of **21**. While **17** has been suggested to have a  $D_{2d}$  symmetry (elongated tetrahedron), **21** has a  $S_4$  symmetry (compressed tetrahedron) indicating the influence of the cation on the structure. Due to the elongated tetrahedral geometry in **17**, the Co(II) ion possesses a very large easy-axis anisotropy ( $D = -55 \text{ cm}^{-1}$ ;  $E/D = 0$ ), while in **21** the magnetization vector prefers to orient along the xy plane ( $D = +11 \text{ cm}^{-1}$ ;  $E/D = 0.18$ ).

The estimated  $D$ -values were confirmed by other techniques including magnetic circular dichroism (MCD), EPR, and theoretical studies. In order to probe the sensitivity of the SH parameters with respect to the structural conformations, Neese and co-workers have developed a magneto-structural correlation to understand the electronic structure and rationalize the origin of  $D$ -value in pseudo-tetrahedral complexes. It has been shown that the e-orbital splitting pattern for a four-coordinate Co(II) complex in a  $D_{2d}$  geometry is as indicated in Fig. 9.

In all the situations, the doubly degenerate  $d_{xz}$  and  $d_{yz}$  orbitals are highest in energy, while the  $d_z$  orbital is lowest. By varying the ligand field strength, the energy gap between the  $d_{xy}$  and  $d_{x^2-y^2}$  orbitals is most affected. In fact, this lowest transition between the orbitals ( $d_{xy}$  and  $d_{x^2-y^2}$ ) contributes to a negative  $D$  for the global  $D$ -value of the complex. The transition between  $d_{x^2-y^2} \rightarrow d_{xz}$  (or  $d_{yz}$ ) contributes to a positive  $D$  for the overall  $D$ -value of the complex. Hence, to stabilize a large Ising or easy-axis magnetic anisotropy, the energy gap between  $d_{xy}$  and  $d_{x^2-y^2}$  should be small, and a large energy gap between the  $d_{x^2-y^2} \rightarrow d_{xz}$  (or  $d_{yz}$ ) orbitals is needed. Soft donors (S, Se, or Te) are hence best suitable for stabilizing the  $d_{xy}$  orbital and increasing the energy of the  $d_{x^2-y^2}$  orbital.

**Fig. 10** Energy level diagram of 3d orbitals for a model complex with fully  $\pi$ -anisotropic metal-ligand bonds relating the limited  $D_{2d}$  geometries ( $\Psi = 0^\circ$  left and  $\Psi = 180^\circ$  right) with pseudo-tetrahedral  $S_4$  geometry ( $\Psi = 45^\circ$ ). Reprinted with permission from [37], Copyright (2015) The American Chemical Society



Co(II) complexes possessing a compressed tetrahedral geometry, on the other hand, would have a different situation (Fig. 10). Since transitions between orbitals with two different  $m_l$  values contribute to a positive  $D$  (while the transition between orbitals with  $\Delta m_l = 0$  contributes to negative  $D$ ) in the compressed situation, the lowest energy transition from  $d_x^2 - y^2 (m_l = |2|) \rightarrow d_{xz}$  (or  $d_{yz}$ ;  $m_l = |1|$ ) leads to a positive  $D$  contribution. The negative contribution given by  $d_x^2 - y^2 (m_l = |2|) \rightarrow d_{xy}$  ( $m_l = |2|$ ) will not be able to compensate the positive  $D$ ; hence, an overall easy-plane anisotropy will be stabilized.

Based on the above, the easy-axis anisotropy reported for Co(II) complexes  $[\text{Co(II)}(\text{L}_2)_2]^{2-}$  (**22**) and  $[\text{Co(II)}(\text{L}_3)_2]^{2-}$  (**23**;  $\text{L}_2 = \text{C}_3\text{S}_5^{2-} = 4,5\text{-dimercapto-1,3-dithiole-2-thione}$ ;  $\text{L}_3 = \text{carborane dithiolate}$ ) can be rationalized [38, 39]. In these complexes, Co(II) ion possesses a pseudo-tetrahedral geometry in a  $D_{2d}$  symmetry and consequently has an easy-axis anisotropy [ $D = -161 \text{ cm}^{-1}$  (**22**);  $D = -71.6 \text{ cm}^{-1}$  (**23**)] with negligible rhombicity [ $E = 0$  (**22**);  $E = 0.27 \text{ cm}^{-1}$  (**23**)]. As expected, both these complexes show zero-field SIM behavior.

It is not always necessary that only the soft donors will tend to stabilize the easy-axis anisotropy. Slageren and co-workers have reported a tetrahedral Co(II) complex  $[\text{Co}^{\text{II}}(\text{L}_4)_2]^{2-}$  (**24**), whose coordination sites are occupied by nitrogen donors of the dianion of bis(1,2-sulfonamide)benzene ligand ( $\text{L}_4$ ) [40]. The  $\text{L}_4$  ligand is an excellent axial ligand, which minimizes the energy gap between the  ${}^4B_1$  and  ${}^4B_2$  states, where the transition between these two states contributes to negative  $D$  for the global  $D$ -value. Dc magnetic data fitting reveals that these complexes possess large single-ion easy-axis anisotropy ( $D = -115 \text{ cm}^{-1}$ ). This represents a theoretical anisotropic energy barrier for the magnetization reversal of  $230 \text{ cm}^{-1}$ . The ac relaxation dynamics performed on these complexes show out-of-phase signal in zero applied magnetic field with an extracted energy barrier of  $U_{\text{eff}} = 118 \pm 5 \text{ cm}^{-1}$ . The lower value suggests that other relaxation mechanisms are operational.

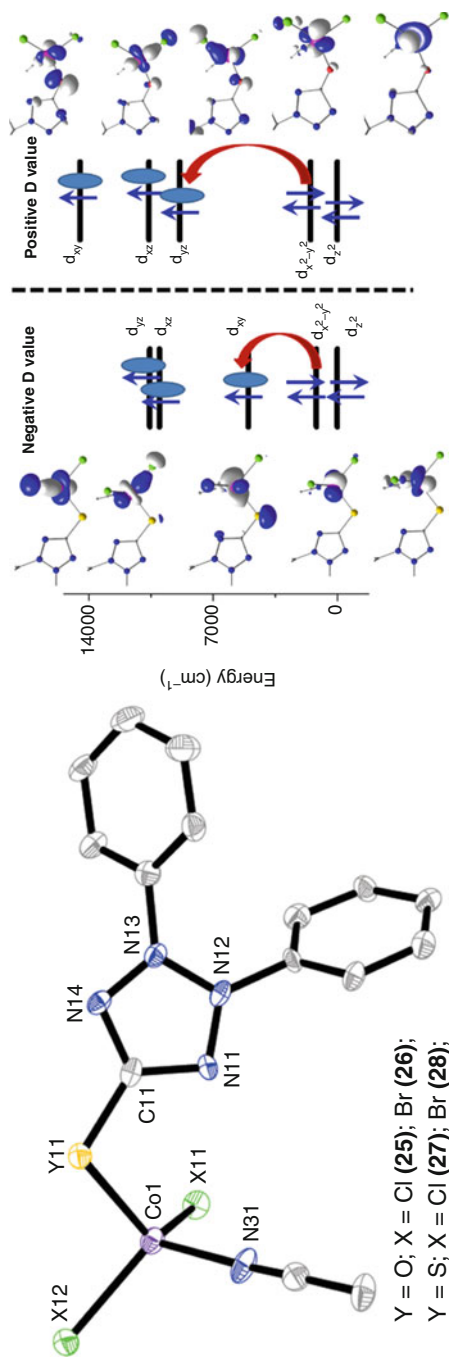
Far-infrared transmission spectra recorded in different magnetic field for **24** unambiguously prove that the energy gap between the two lowest Kramers' states is in fact  $230\text{ cm}^{-1}$ , reaffirming the  $D$ -value extracted ( $-115\text{ cm}^{-1}$ ). This is well supported by EPR and MCD measurements.

All the examples discussed above contain a similar donor environment around Co (II). Shanmugam and co-workers have shown that even a single soft donor around  $\text{Co}^{\text{II}}$  is sufficient for modulating the  $D$ -value [20]. The complexes involved were  $[\text{Co}(\text{L}_5\text{-O})(\text{MeCN})(\text{X})_2]$  [ $\text{L}_5\text{-O} = 2,3$ -diphenyl-1,2,3,4-tetrazolium-5-olate  $\text{X} = \text{Cl}$  (**25**) or  $\text{Br}$  (**26**)] and  $[\text{Co}(\text{L}_5\text{-S})(\text{MeCN})(\text{X})_2]$  [ $\text{L}_5\text{-S} = 2,3$ -diphenyl-1,2,3,4-tetrazolium-5-thiolate,  $\text{X} = \text{Cl}$  (**27**) or  $\text{Br}$  (**28**)] (Fig. 11). The coordination environment in all these complexes is similar except that while **27** and **28** have one sulfur donor atom, **25** and **26** have an oxygen donor.

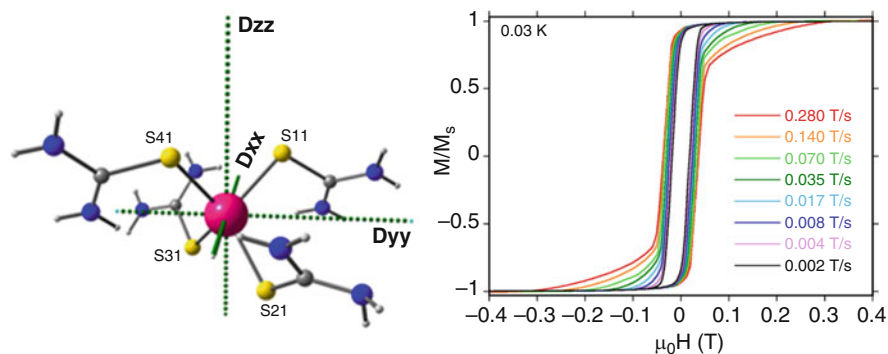
Simultaneous fitting of  $\chi_{\text{M}}T(T)$  and  $M(H)$  data reveals that **25** ( $D = +15.61\text{ cm}^{-1}$ ) and **26** ( $D = +11.16\text{ cm}^{-1}$ ) are stabilized with an easy-plane anisotropy, while **27** ( $D = -11.30\text{ cm}^{-1}$ ) and **28** ( $D = -10.32\text{ cm}^{-1}$ ) possess an easy-axis anisotropy. As discussed above, the lowest energy transition between the  $d$ -orbitals having the same  $|m_l|$  value will contribute to a negative  $D$  to the overall  $D$ -value of the complex. For example, transition between  $d_x^2 - y^2$  ( $m_l = +2$ )  $\rightarrow d_{xy}$  ( $m_l = -2$ ) and  $d_{xz}$  ( $m_l = +1$ )  $\rightarrow d_{yz}$  ( $m_l = -1$ ) will contribute to the negative  $D$  (Fig. 11). On the other hand, transition between the orbitals with  $\Delta m_l = 1$  (e.g.,  $d_x^2 - y^2$  or  $d_{xy} \rightarrow d_{xz}$  or  $d_{yz}$  ( $\Delta m_l = \pm 1$ )) will contribute to positive  $D$  for the global  $D$ -value of the complex. Usually the lowest energy transition contributes to the overall  $D$  substantially. In the case of **25**, the lowest energy transition corresponds to  $d_x^2 - y^2 \rightarrow d_{yz}$ ; hence, the complex is stabilized with a global positive  $D$ . In contrast to this in **27**, the lowest energy transition is between the orbitals with same  $m_l$  value ( $d_x^2 - y^2 \rightarrow d_{xy}$ ); hence in **27** or **28**, the magnetization vector preferentially orients along the  $z$ -axis (easy axis).

The concept that soft donors stabilize easy-axis anisotropy was further corroborated in  $[\text{Co}(\text{L}_6)_4](\text{NO}_3)_2 \cdot \text{H}_2\text{O}$  (**29**,  $\text{L}_6 =$  thiourea). In **29**, the  $\text{Co}(\text{II})$  ion is surrounded by four sulfur donor atoms in a distorted tetrahedral geometry (elongated tetrahedron). The simultaneous fit of the dc magnetic data discloses the easy-axis anisotropic ( $D = -61.7\text{ cm}^{-1}$ ) nature of the complex, as expected. The fourfold increase in  $D$  combined with small rhombic distortion results in slow magnetization of relaxation ( $H_{\text{dc}} = 0$ ). Interestingly, this compound also shows hysteresis with a blocking temperature of 3 K at the indicated sweep rate (Fig. 12). The role of intermolecular dipolar interactions and hydrogen bonding in impacting the magnetic behavior was probed. Upon dilution, coercivity and zero-field quantum tunneling of magnetization dominates at  $H = 0$  in hysteresis loop measurements. In contrast, 100% pure samples show large coercivity, and quantum tunneling of magnetization is quenched at zero field (Fig. 12b). In fact, the first steps found near 0.03 T (in hysteresis loop) are indicative of ferromagnetic ordering that act as a bias field. This pushes the tunneling step to higher field (0.03 T) rather at zero field. Such a scenario arises due to strong supramolecular interaction, a situation opposite to the trend observed in the literature.

The role of halides in modulating the  $D$  parameters was investigated in  $[\text{Co}(\text{L}_6)_2\text{X}_2]$  where  $\text{L}_6 =$  thiourea;  $\text{X} = \text{Cl}$  (**30**),  $\text{Br}$  (**31**), or  $\text{I}$  (**32**). In this series, it was



**Fig. 11** Thermal ellipsoid crystal structure picture of **25–28**. Eigenvalue plots computed through DFT of the five d-orbitals for complex **27** (left panel) and **25** (right panel). Figures adopted from [20]. Copyright (2015) The Royal Chemical Society. (Color code: Co, lilac; N, blue; and C, gray)



**Fig. 12** (a) Schematic representation of **29** along with ab initio computed  $D$ -tensor orientation. (b) Sweep-rate-dependent hysteresis loop measurements of a single crystal (100% sample) where magnetic field applied in the average easy-axis directions of **29**. Reprinted with permission from [41], Copyright (2016) The American Chemical Society. (Color code: Co, magenta; S, yellow; N, blue; and C, gray)

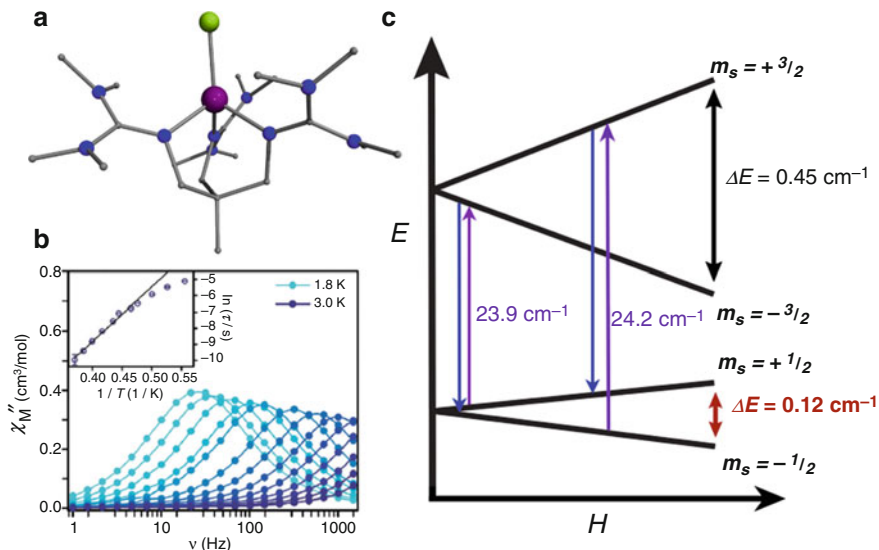
noticed that **30** was stabilized with a positive  $D$ , while in **31** and **32**, the magnetization vector preferentially orients toward the  $z$ -axis (negative  $D$ ). All the three complexes show field-induced SIM behavior. The large spin-orbit coupling and weak  $\pi$ -donation associated with heavier halides have been suggested [15] as being responsible for the easy-axis anisotropy observed in **31** and **32**.

Duan and co-workers utilized 2,9-dimethyl-1,10-phenanthroline (dmph) as a chelating ligand and obtained  $[\text{Co}(\text{dmph})\text{Br}_2]$  (**33**) [42] which showed a field-induced slow relaxation of magnetization with an energy barrier of  $22.88 \text{ cm}^{-1}$ .

The above conclusions regarding the sign of  $D$  and its relation to the symmetry of the tetra-coordinate Co(II) complexes while appearing to be obeyed in many cases have exceptions. Thus in  $[\text{Co}(\text{L}_7)_2\text{Cl}_2]$  (**34**) [33] ( $\text{L}_7$  = heterocyclic  $N$ -donor ligands), the sign and magnitude of  $D$ -value seem to suggest that complexes with a flattened tetrahedral geometry stabilize an easy-axis anisotropy, and an elongated tetrahedron tends to stabilize positive  $D$ -value.

This is opposite to what has been discussed previously and probably needs a reinvestigation.

It was found that a tridentate donor ligand, in the complex  $[\text{Co}(\text{L}_8)\text{Cl}]$  (**35**) [ $\text{L}_8$  = 1,1,1-tris-[2*N*-(1,1,3,3-tetramethylguanidino)methyl]ethane)], stabilizes an easy-plane anisotropy [43]. The three nitrogen donors derived from  $\text{L}_8$  occupy one face of the tetrahedron, while a chloride ion completes the coordination site of Co(II) ions. **35**, thus, possesses an approximate  $C_3$  symmetry where the  $C_3$  axis passes through the cobalt ion. EPR experiments reveal that **35** is rhombic ( $D = +12.7 \text{ cm}^{-1}$ ;  $E = 1.27 \text{ cm}^{-1}$ ;  $g_x = 2.30$ ;  $g_y = 2.30$ ;  $g_z = 2.17$ ). Magnetization relaxation dynamics, in the presence of 1.5 kOe external magnetic field, revealed an anisotropic barrier of  $24 \text{ cm}^{-1}$ . The authors determined the energy gap between the  $\pm 3/2$  and  $\pm 1/2$  states ( $25 \text{ cm}^{-1}$  and  $23 \text{ cm}^{-1}$  from magnetization fit [ $D = 11.4 \text{ cm}^{-1}$ ]) and suggest that spin reaches an equilibrium via  $S = \pm 3/2$  Kramers level and propose a mechanism of relaxation as shown in Fig. 13.



**Fig. 13** (a) Crystal structure of complex **35**. (b) Variable temperature ac magnetic susceptibility data for **35** in a 1,500 Oe dc field. (Inset: Arrhenius plot). (c) Zeeman energy diagram for an  $S = 3/2$  spin center. All energies correspond to  $H = 1,500$  Oe. (Red, slow direct relaxation; purple, excitation utilized by Orbach relaxation pathways; and blue, relaxations involved in magnetic relaxation pathways). Adapted with permission from [40] The Royal Society of Chemistry. Color code: Co, violet; N, blue; Cl, green; and C, gray

The spin Hamiltonian parameters for four-coordinate Co(II) complexes in tetrahedral/distorted tetrahedral geometry are summarized in Table 3.

## 4.2 Square Planar and Trigonal Pyramidal Geometry

Compared to the common tetrahedral and octahedral geometry reported for Co(II) complexes, complexes having square planar and trigonal pyramidal geometry are extremely rare. Perhalobenzene anion-containing complexes,  $[\text{Co}^{\text{II}}(\text{PFB})_4]^{2-}$  (**70**) and  $[\text{Co}^{\text{II}}(\text{PCB})_4]^{2-}$  (**71**), (PFB and PCB denote pentafluorobenzene and pentachlorobenzene anion, respectively) were shown to possess a square planar geometry (Fig. 14) [54]. Magnetic measurements indicated the presence of only one unpaired electron in the metal center. EPR spectrum of **70** revealed two well-resolved  $g_{\parallel}$  and  $g_{\perp}$  transitions with Co(II) hyperfine interaction. In the X-band the hyperfine lines  $g_{\parallel}$  and  $g_{\perp}$  tend to mix with each other; however, the same is well resolved in Q-band measurement.

The EPR spectral features were simulated using  $g$ -axial anisotropy and hyperfine coupling constants considering a  $S = 1/2$  ground state, i.e., low-spin Co(II) ion in



**Table 3** Spin Hamiltonian parameters for selected four-coordinated Co(II) complexes in tetrahedral/distorted tetrahedral geometry

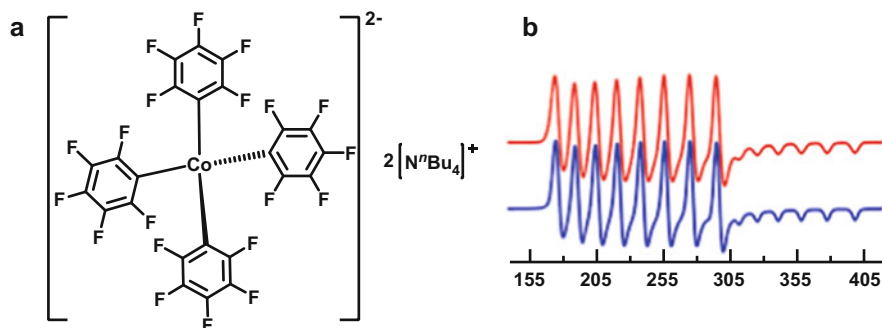
Compound	$D$ (cm <sup>-1</sup> )	$E$ (cm <sup>-1</sup> )	$g$	$U_{\text{eff}}$ (cm <sup>-1</sup> )	Ref
(Ph <sub>4</sub> P) <sub>2</sub> [Co(SPh) <sub>4</sub> ] ( <b>17</b> )	-74	<0.01	-	21	[26]
	-55	0	$g_{xy} = 2.08$ $g_z = 2.59$	-	[34]
(Ph <sub>4</sub> P) <sub>2</sub> [Co(OPh) <sub>4</sub> ].(CH <sub>3</sub> CN) ( <b>18</b> )	-11.1	-	$g_{xy} = 2.11; g_z = 2.22$	21	[21]
K(Ph <sub>4</sub> P)[Co(OPh) <sub>4</sub> ] ( <b>19</b> )	-23.8	-	$g_{xy} = 2.70; g_z = 2.95$	-	[21]
(Ph <sub>4</sub> P) <sub>2</sub> [Co(SePh) <sub>4</sub> ] ( <b>20</b> )	-83	-	$g_{xy} = 2.16; g_z = 2.95$	19	[21]
(NEt <sub>4</sub> ) <sub>2</sub> [Co(SPh) <sub>4</sub> ] ( <b>21</b> )	11	1.98	$g_{xy} = 2.11; g_z = 2.07$	-	[34]
(Ph <sub>4</sub> P) <sub>2</sub> [Co(C <sub>3</sub> S <sub>5</sub> ) <sub>2</sub> ] ( <b>22</b> )	-161	0	$g_{\text{iso}} = 3.24$	33.9	[38]
[Co(C <sub>2</sub> S <sub>2</sub> ) <sub>2</sub> ].2NEt <sub>3</sub> H ( <b>23</b> )	-71.6	0.27	$g_{x,y} = 2.48; g_z = 2.75$	26.8	[39]
(HNEt <sub>3</sub> ) <sub>2</sub> [Co(L <sub>4</sub> ) <sub>2</sub> ] <sup>2-</sup> ( <b>24</b> )	-115	-	$g_{\perp} = 2.20; g_{\parallel} = 3.03$	230	[40]
[Co <sup>II</sup> (L <sub>5</sub> -O)(Cl) <sub>2</sub> (MeCN)] ( <b>25</b> )	15.61	2.80	$g_x = 2.47; g_y = 2.39$ $g_z = 2.21$	10.3	[20]
[Co <sup>II</sup> (L <sub>5</sub> -O)(Br) <sub>2</sub> (MeCN)] ( <b>26</b> )	11.16	2.67	$g_x = 2.49; g_y = 2.38$ $g_z = 2.23$	8.2	[20]
[Co <sup>II</sup> (L <sub>5</sub> -S)(Cl) <sub>2</sub> (MeCN)] ( <b>27</b> )	-11.30	2.26	$g_x = 2.28; g_y = 2.36$ $g_z = 2.50$	20.2	[20]
[Co <sup>II</sup> (L <sub>5</sub> -S)(Br) <sub>2</sub> (MeCN)] ( <b>28</b> )	-10.32	1.65	$g_x = 2.31; g_y = 2.38$ $g_z = 2.54$	13.8	[20]
[Co(L <sup>tu</sup> ) <sub>4</sub> ](NO <sub>3</sub> ) <sub>2</sub> ( <b>29</b> )	-61.7	3.14	$g_x = 2.16; g_y = 2.26;$ $g_z = 2.93$	19.5	[41]
[Co(L <sup>tu</sup> ) <sub>2</sub> Cl <sub>2</sub> ] ( <b>30</b> )	10.8	1.18	$g_1 = 2.2; g_2 = 2.2$ $g_3 = 2.4$	4.23	[23]
[Co(L <sup>tu</sup> ) <sub>2</sub> Br <sub>2</sub> ] ( <b>31</b> )	-18.7	5.98	2.2	-	[23]
[Co(L <sup>tu</sup> ) <sub>2</sub> I <sub>2</sub> ] ( <b>32</b> )	-19.3	4.82	2.3	-	[23]
[Co(dmPh)Br <sub>2</sub> ] ( <b>33</b> )	10.62	-0.01	$g_x = 2.92; g_y = 2.05$ $g_z = 3.67$	22.8	[42]
[CoL <sup>dmn</sup> <sub>2</sub> Cl <sub>2</sub> ] ( <b>34</b> )	11.40	0.11	$g_x = 2.37; g_y = 2.09$ $g_z = 2.16$	-	[33]
[L <sub>8</sub> CoCl](CF <sub>3</sub> S <sub>3</sub> ) ( <b>35</b> )	12.7	1.2	2.17	24	[43]
[CoL <sup>bi</sup> <sub>2</sub> Cl <sub>2</sub> ] ( <b>36</b> )	-3.15	0.50	$g_x = 2.22; g_y = 2.24$ $g_z = 2.23$	-	[33]
[Co(L <sup>tmu</sup> ) <sub>4</sub> ](ClO <sub>4</sub> ) <sub>2</sub> ( <b>37</b> )	-21.3	3.01	$g_x = 2.27; g_y = 2.35;$ $g_z = 2.56$	18.7	[41]
[Co(L <sup>btu</sup> ) <sub>4</sub> ](ClO <sub>4</sub> ) <sub>2</sub> ( <b>38</b> )	-80.7	1.61	$g_x = 2.11; g_y = 2.16;$ $g_z = 3.09$	62.0	[41]
[Co(L <sup>Phu</sup> ) <sub>4</sub> ](ClO <sub>4</sub> ) <sub>2</sub> ( <b>39</b> )	-63.8	1.91	$g_x = 2.16; g_y = 2.23;$ $g_z = 2.92$	32.7	[41]
[CoL <sup>ap</sup> <sub>2</sub> Cl <sub>2</sub> ] ( <b>40</b> )	12.20	2.40	$g_x = 2.24; g_y = 2.22$ $g_z = 2.22$	-	[33]
[CoL <sup>c</sup> <sub>2</sub> Cl <sub>2</sub> ] ( <b>41</b> )	-5.23	0.51	$g_x = 2.23; g_y = 2.22$ $g_z = 2.25$	-	[33]
[Co{ <sup>t</sup> Pr <sub>2</sub> P(E)NP(S) <sup>t</sup> Pr <sub>2</sub> } <sub>2</sub> ] ( <b>42</b> )	24	-1.2	$g_x = 1.62; g_y = 2.38$ $g_z = 6.44$	-	[44]

(continued)

**Table 3** (continued)

Compound	$D$ (cm <sup>-1</sup> )	$E$ (cm <sup>-1</sup> )	$g$	$U_{\text{eff}}$ (cm <sup>-1</sup> )	Ref
[Co( <sup>i</sup> Pr <sub>2</sub> P(E)NP(Se) <sup>i</sup> Pr <sub>2</sub> ) <sub>2</sub> ] ( <b>43</b> )	30	-9.9	$g_{xy} = 0.3; g_z = 7.12$	-	[44]
Co(quinoline) <sub>2</sub> I <sub>2</sub> ( <b>44</b> )	9.2	0.01	-	-	[22]
Co(PPh <sub>3</sub> ) <sub>2</sub> I <sub>2</sub> ( <b>45</b> )	-36.9	0.2	-	30.6	[22]
Co(AsPh <sub>3</sub> ) <sub>2</sub> I <sub>2</sub> ( <b>46</b> )	-74.7	-0.82	-	32.6	[22]
[Co(biq)Cl <sub>2</sub> ] ( <b>47</b> )	10.5	0	2.40	29.6	[45]
[Co(biq)Br <sub>2</sub> ] ( <b>48</b> )	12.5	0	2.39	27.5	[45]
[Co(biq)I <sub>2</sub> ] ( <b>49</b> )	10.3	4.1	2.09	39.6	[45]
[Co(bcp)Cl <sub>2</sub> ] ( <b>50</b> )	-5.62	-	$g_x = 2.50; g_z = 2.21$	33.22	[46]
[Co(bcp)Br <sub>2</sub> ] ( <b>51</b> )	-6.72	-	$g_z = 2.31$	-	[46]
[Co(bcp)I <sub>2</sub> ] ( <b>52</b> )	-7.03	-	$g_z = 2.34$	-	[46]
[Co(L <sup>Br</sup> ) <sub>2</sub> ] ( <b>53</b> )	-36.7	0	2.55	36	[47]
[Co(L <sup>Ph</sup> ) <sub>2</sub> ]-CH <sub>2</sub> Cl <sub>2</sub> ( <b>54</b> )	-39.8	1.7	2.67	43	[47]
[Co(dmphen)Cl <sub>2</sub> ] ( <b>55</b> )	11.9	-	2.31	-	[48]
[Co(dmphen)Br <sub>2</sub> ] ( <b>56</b> )	13.8	-	$g_x = 2.41; g_z = 2.07$	44.8	[48]
[Co(dmphen)I <sub>2</sub> ] ( <b>57</b> )	16.6	-	$g_x = 2.37; g_z = 2.24$	48.37	[48]
[Co(PPh <sub>3</sub> ) <sub>2</sub> Cl <sub>2</sub> ] ( <b>58</b> )	-16.2	0.9	-	25.8	[49]
[Co(DPEphos)Cl <sub>2</sub> ] ( <b>59</b> )	-14.4	1.7	-	24.3	[49]
[Co(Xantphos)Cl <sub>2</sub> ] ( <b>60</b> )	-15.4	1.3	-	20.7	[49]
[Co(Bc <sup>tBu</sup> ) <sub>2</sub> ] ( <b>61</b> )	-3.86	0.53	$g_{xy} = 2.13; g_z = 2.15$	-	[50]
[Co{(N <sup>t</sup> Bu) <sub>3</sub> SMe} <sub>2</sub> ] ( <b>62</b> )	-58	8.7	$g_x = 2.17; g_y = 1.90$ $g_z = 2.94$	75	[51]
[Co(PPh <sub>3</sub> ) <sub>2</sub> Br <sub>2</sub> ] ( <b>63</b> )	-13	-	$g_{xy} = 2.00; g_z = 2.16$	25.7	[52]
Co[(SPPH <sub>2</sub> ) <sub>2</sub> N] <sub>2</sub> ( <b>64</b> )	-11.9	0.59	-	25.3	[52]
Co[(SePPH <sub>2</sub> ) <sub>2</sub> N] <sub>2</sub> ( <b>65</b> )	-15.8	1.61	2.37	29.2	[52]
Co[(TePPH <sub>2</sub> ) <sub>2</sub> N] <sub>2</sub> ( <b>66</b> )	-45.1	-	2.94	22	[52]
(PPh <sub>4</sub> ) <sub>2</sub> [Co(OPh) <sub>4</sub> ] ( <b>67</b> )	-11.1	0	$g_x = 2.11; g_y = 2.29;$ $g_z = 2.22$	-	[37]
(PPh <sub>4</sub> ) <sub>2</sub> [Co(SPh) <sub>4</sub> ] ( <b>68</b> )	-62	0	$g_x = 2.28; g_y = 2.23;$ $g_z = 2.96$	-	[37]
(PPh <sub>4</sub> ) <sub>2</sub> [Co(SePh) <sub>4</sub> ] ( <b>69</b> )	-83	0	$g_x = 2.16; g_y = 2.19;$ $g_z = 2.95$	-	[37]

*SPh* thiophenolate, *OPh* phenolate, *SePh* benzeneselenolate, C<sub>3</sub>S<sub>5</sub><sup>2-</sup> 4,5-dimercapto-1,3-dithiole-2-thione (L<sub>2</sub>), C<sub>2</sub>S<sub>2</sub> carborane dithiolate (L<sub>3</sub>), L<sub>4</sub> dianion of bis(1,2-sulfonamide)benzene, L<sub>5</sub>-O 2,3-diphenyl-1,2,3,4-tetrazolium-5-olate, L<sub>5</sub>-S 2,3-diphenyl-1,2,3,4-tetrazolium-5-thiolate, L<sup>tu</sup> thio-urea (L<sub>6</sub>), L<sup>tmu</sup> tetramethylthiourea, L<sup>btu</sup> 1,3-dibutylthiourea, L<sup>Phiu</sup> 1,3-phenylethylthiourea, *dmph* 2,9-dimethyl-1,10-phenanthroline, L<sub>8</sub> 1,1,1-tris-[2N-(1,1,3,3-tetramethylguanidino)methyl]ethane, *biq* 2,2'-biquinoline, *bcp* bathocuproine = 4,7-diphenyl-2,9-dimethyl-1,10-phenanthroline, *HL<sup>Br</sup>* 1-[N-(4-bromophenyl)carboximidoyl]naphthalen-2-ol, *HL<sup>Ph</sup>* 1-[N-(2-phenylphenyl)carboximidoyl]naphthalen-2-ol, *dmphen* 2,9-dimethyl-1,10-phenanthroline neocuproine, *PPh<sub>3</sub>* triphenylphosphine, *DPEphos* 2,2'-bis(diphenylphosphino) diphenyl ether, *xantphos* 9,9-dimethyl-4,5-bis(diphenylphosphino), *Bc<sup>tBu</sup>* bis(3-tert-butylimidazol-2-ylidene)-borate, *SPPH<sub>2</sub>* mercaptodiphenyl phosphine, *SePPH<sub>2</sub>* selenodiphenyl phosphine, *TePPH<sub>2</sub>* tellurodiphenyl phosphine



**Fig. 14** (a) Schematic diagram of **70**. (b) EPR spectra of polycrystalline powder sample of **70** in X-band. Blue traces correspond to calculated spectra. Reprinted with permission from [53], Copyright (2014) American Chemical Society

square planar geometry. From a detailed analysis, it was concluded that the unpaired electron resides in the  $d_z^2$  orbital.

Cyclic voltammogram performed on these complexes (**70** and **71**) in dichloromethane shows a reversible oxidation peak with redox potential of  $-0.29$  V and  $-0.36$  V, respectively, which upon chemical oxidation with  $\text{Br}_2$  diluted in  $\text{CCl}_4$  led the authors to isolate the  $[\text{Co}^{\text{III}}(\text{PCB})_4]^-$  (**72**) and  $[\text{Co}^{\text{III}}(\text{PCB})_4]^-$  (**73**). The structures of **72** and **73** are characterized by single crystal X-ray diffraction.

$^{19}\text{F}$  and  $^{13}\text{C}$  NMR studies performed on **72** and **73** fail to show the NMR peaks suggesting that Co(III) ion in these complexes is paramagnetic in nature. On the other hand, both **72** and **73** remain EPR silent in both X- and Q-band EPR spectroscopy. Both NMR and EPR do not provide any conclusive answers to study the electronic structure of **72** and **73**. Nevertheless, variable temperature magnetic susceptibility measurement not only unravels the paramagnetic signature but also reveals the number of unpaired electron associated with these complexes. The room temperature cMT value of  $\sim 2.1 \text{ cm}^3 \text{ K mol}^{-1}$  is close to the expected value for  $S = 1$  system and the cMT drops as temperature decreases suggests that complexes should have considerably large magnetic anisotropy.

The integer spin nature and large magnetic anisotropy associated with **72** ( $D = +208 \text{ cm}^{-1}$ ) and **73** ( $D = +134 \text{ cm}^{-1}$ ) is responsible for the EPR silent nature of them. The  $D$ -value observed for these complexes is significantly larger than other square planar complexes reported in the literature (see Table 4). It appears that all the Co(III) square planar complexes are stabilized in intermediate spin state ( $S = 1$ ) and possess easy plane anisotropy (Table 4). Among these complexes, a large magnetic anisotropy is found to be associated with **72** ( $D = +208 \text{ cm}^{-1}$ ) (Table 4).

Among the four-coordinate Co(II) complexes, trigonal pyramidal geometry is even rarer than the square planar geometry. In the complexes,  $[\text{Co}_2(\text{L}_9)_2] \cdot 2(\text{CH}_3\text{CN})$  (**88**) and  $[\text{Co}_2(\text{L}_{10})_2] \cdot 6(\text{CH}_3\text{CN})$  (**89**) [ $\text{L}_9 = \text{bis}(N\text{-salicylidene-4,4'-diaminodiphenyl)methane}$ ;  $\text{L}_{10} = \text{bis}(N\text{-pyridyl-4,4'-diaminodiphenyl)}$ ], each

**Table 4** Spin Hamiltonian parameters for four-coordinated Co(II) square planar complexes

Compound	$D$ (cm <sup>-1</sup> )	$E$ (cm <sup>-1</sup> )	$g$	$U_{\text{eff}}$ (cm <sup>-1</sup> )	Ref
(NBu <sub>4</sub> ) <sub>2</sub> [Co <sup>II</sup> (PFB) <sub>4</sub> ] ( <b>70</b> )	–	–	3.20	–	[54]
(NBu <sub>4</sub> ) <sub>2</sub> [Co <sup>II</sup> (PCB) <sub>4</sub> ] ( <b>71</b> )	–	–	2.62	–	[54]
(NBu <sub>4</sub> ) [Co <sup>III</sup> (PFB) <sub>4</sub> ] ( <b>72</b> )	208	–	$g_{\parallel}=1.93$ ; $g_{\perp}=2.82$	–	[54]
(NBu <sub>4</sub> ) [Co <sup>III</sup> (PCB) <sub>4</sub> ] ( <b>73</b> )	134	–	$g_{\parallel}=1.95$ ; $g_{\perp}=2.74$	–	[54]
[Co(bpe)(Cl)] ( <b>74</b> )	35	–	–	2.27	[53]
[Co(bpe)(Br)] ( <b>75</b> )	26	–	–	2.17	[53]
[Co(bpe)(I)] ( <b>76</b> )	18	–	–	2.28	[53]
[Co(TC <sub>-3,3</sub> ) <sup>+</sup> ] ( <b>77</b> )	–	–	–	–	[55]
[Co(TC <sub>-4,4</sub> ) <sup>+</sup> ] ( <b>78</b> )	–	–	–	–	[55]
[(C <sub>6</sub> H <sub>5</sub> ) <sub>3</sub> (CH <sub>3</sub> )As] [Co(tdt) <sub>2</sub> ] ( <b>79</b> )	–	–	–	–	[56]
KCo(bi) <sub>2</sub> ( <b>80</b> )	–	–	–	–	[57]
(Bu <sub>4</sub> N)[Co(bi) <sub>2</sub> ] ( <b>81</b> )	–	–	–	–	[57]
(Bu <sub>4</sub> N)[Co(bdt) <sub>2</sub> ] ( <b>82</b> )	37.4	–	$g_{\perp} = 2.31$ ; $g_{\parallel} = 2.19$	–	[58]
(Bu <sub>4</sub> N)[Co(tdt) <sub>2</sub> ] ( <b>83</b> )	39.4	–	$g_{\perp} = 2.27$ ; $g_{\parallel} = 2.09$	–	[58]
[Co(S <sub>2</sub> C <sub>2</sub> Ph <sub>2</sub> ) <sub>2</sub> ] <sup>2-</sup> ( <b>84</b> )	–	–	2.33	–	[59]
(Bu <sub>4</sub> N) [Co(S <sub>2</sub> C <sub>6</sub> H <sub>4</sub> )] ( <b>85</b> )	–	–	–	–	[59]
[KCo(3-propbi) <sub>2</sub> ] ( <b>86</b> )	–	–	–	–	[60]
[K[Co(3-prbi) <sub>2</sub> ].2H <sub>2</sub> O] ( <b>87</b> )	–	–	–	–	[61]

*PFB* pentafluorobenzene, *PCB* pentachlorobenzene, *bpe* 2,2'-(2,2'-bipyridine-6,6'-diyl)bis(1,1-diphenylethanethiolate), *TC<sub>-3,3</sub>* H<sub>2</sub>tropocoronand-3,3, *TC<sub>-4,4</sub>* H<sub>2</sub>tropocoronand-4,4, *tdt* toluene-3,4-dithiolate, *S<sub>2</sub>C<sub>6</sub>H<sub>4</sub>* benzene-1,2-dithiolate, *S<sub>2</sub>C<sub>2</sub>Ph<sub>2</sub>* cis-stilbenedithiolate, *1-propbiH<sub>2</sub>* Pr<sup>n</sup> HN-CO-NHCO-NH<sub>2</sub>, *3-prbi* 3-propylbiuret

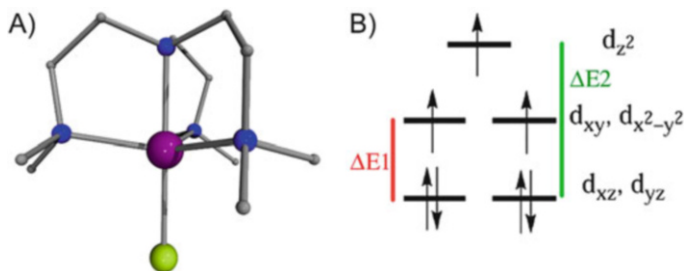
Co(II) is surrounded by a 2N,2O coordination environment. Based on the angular index analysis, the geometry around cobalt ion has been described as a trigonal pyramid.

Analysis of the magnetic data afforded the following parameters:  $D = +19.5$  cm<sup>-1</sup>;  $g = 2.35$  ( $E = 0$ ) for **88** and  $D = +16.2$  cm<sup>-1</sup>;  $g = 2.22$  ( $E = 0.019$  cm<sup>-1</sup>) for **89**. For both the complexes, an easy-plane anisotropy is indicated. Both **88** and **89** exhibit field-induced slow magnetization relaxation with anisotropic energy barrier of 14.6 cm<sup>-1</sup> and 8.0 cm<sup>-1</sup>, respectively.

## 5 Coordination Number 5

### 5.1 Trigonal Bipyramidal Geometry

A trigonal bipyramidal geometry around Co(II) is sought after because by enforcing the C<sub>3</sub> geometry, an easy-axis or Ising-type anisotropy can be enforced and also the



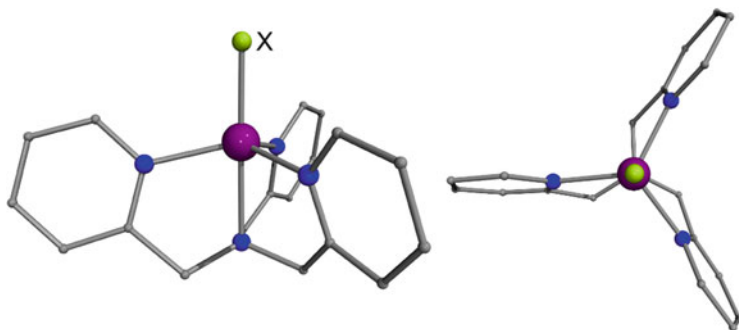
**Fig. 15** (a) Crystallographic structure of **90** (X = Cl and Y = ClO<sub>4</sub>); **91** (X = Br and Y = Br). (b) In a trigonal pyramidal crystal field (C<sub>3v</sub>) removal of degeneracy in d-orbitals. Figures adapted from [63]. Color code: Co, purple; N, blue; and C, gray

rhombic symmetry is potentially avoided. Hence, even complexes with small easy-axis anisotropy show well-defined and well-resolved out-of-phase susceptibility signals as QTM induced by rhombicity is completely quenched. As the volume of the complexes reported in the literature is considerably large, only selected examples are discussed below.

Mallah and co-workers designed a complex where the ligand imposed an axial symmetry and allowed the stabilization of a large negative anisotropy. The complexes [Co(Me<sub>6</sub>tren)X](Y) [Me<sub>6</sub>tren = hexamethyl tris(aminoethyl)amine; X = Cl and Y = ClO<sub>4</sub> (**90**); X = Br and Y = Br (**91**)] [62] were prepared and characterized (Fig. 15).

In **91** the Co(II) ion is surrounded by four nitrogen donors derived from neutral Me<sub>6</sub>Tren ligand and a chloride ion. Three of the four nitrogen donors occupy the equatorial plane, while the fourth is at the axial position. The magnetic data could be modeled, and the resultant extracted parameters are  $D = -6.2 \text{ cm}^{-1}$ ,  $g = 2.24$  ( $D = -2.5 \text{ cm}^{-1}$ ,  $g = 2.22$  for **91**). For **90**, EPR signals at near zero field appear in 475 GHz suggesting an energy gap of  $\sim 15.8 \text{ cm}^{-1}$  between the two Kramers levels which actually amounts to  $2|D|$  value, hence  $D = -7.9 \text{ cm}^{-1}$ . This value is closer to the value predicted from dc magnetic data. Simulation of variable frequency and variable temperature EPR spectral features of **90** results in the parameters  $g_x = g_y = 2.15 \pm 0.10$ ,  $g_z = 2.2 \pm 0.2$ , and  $D = -8.12 \pm 0.06 \text{ cm}^{-1}$ . The presence of hysteresis loop with several steps in 5% diluted samples unmistakably demonstrates the SIM behavior of these complexes.

A weak  $\sigma$ -donor ligand in the equatorial position (which will reduce the energy of  $d_{x^2-y^2}$ ,  $d_{xy}$ ) and strong  $\sigma$ -donors in the axial position (which will destabilize the  $d_{xz}$  and  $d_{yz}$ ) are anticipated to enhance the single-ion anisotropy of the Co(II) ion. The complex [Co(NS<sub>3</sub><sup>iPr</sup>)Cl]BPh<sub>4</sub> (**92**) conforms to this design and has a sulfur ligand, a weak  $\sigma$ -donor, in the equatorial plane. This causes stabilization of  $d_{xy}$  and  $d_{x^2-y^2}$  orbitals while raising the energy of the  $d_{xz}$  and  $d_{yz}$  orbitals. A weak  $\sigma$ -donation coupled with  $\pi$ -donor ability of sulfur in the equatorial plane will further reduce the energy gap ( $\Delta E_1$ ) between  $d_{xy}$  and  $d_{x^2-y^2}$  orbital and  $d_{xz}$  and  $d_{yz}$  which will facilitate to enhance the  $D$ -value further. Moreover, due to the strong axial Co(II)-N bond



**Fig. 16** Crystal structure of  $[\text{Co}(\text{TPMA})\text{X}]$  in two different view (where  $\text{X} = \text{CH}_3\text{CN}$  (**96**) or  $\text{Cl}$  (**97**) or  $\text{Br}$  (**98**) or  $\text{I}$  (**99**)). Color code: Co, purple; N, blue; and C, gray

length in **92**, the energy gap between the ground state orbitals ( $d_{xz}$  and  $d_{yz}$ ) to the  $d_z^2$  orbital increases ( $\Delta E_2$ ). Decreasing  $\Delta E_1$  and increasing  $\Delta E_2$  are more favorable for stabilizing a large negative anisotropy. These hypotheses were realized, and **92** is stabilized with an easy-axis anisotropy of  $-19 \text{ cm}^{-1}$ . However, although the complex possesses a large negative  $D$ , it has a non-zero rhombic term, since the complex does not possess a strict  $C_3$ -symmetry. As a result, combination with other transverse fields is enabled to facilitate a faster relaxation.

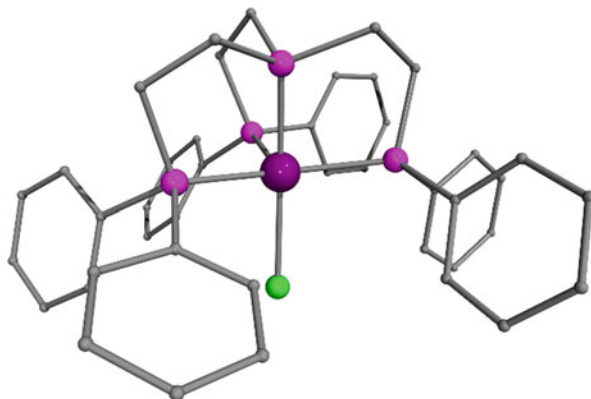
A series of complexes,  $[\text{Co}^{\text{II}}(\text{NS}_3\text{Bu-}t)\text{X}]$  where  $\text{X} = \text{Cl}$  (**93**) or  $\text{Br}$  (**94**) or  $\text{SCN}$  (**95**), were studied to learn more about the influence of the ligands in the equatorial vs axial positions [64]. All the three complexes possess a distorted pentagonal bipyramidal geometry. In fact **95** crystallizes in the cubic space group which ensures that the molecule itself possesses a crystallographically imposed  $C_3$ -symmetry. However, **93** and **94** possess pseudo  $C_3$ -symmetry. The dc magnetic data modeling reveals the  $D$ -value associated with these complexes [**93** ( $g = 2.29$ ;  $D = -21.4$ ) and **94** ( $g = 2.29$ ;  $D = -20.2$ ); **95** ( $g = 2.29$ ;  $D = -11.0$ )].

Tris(pyridylmethyl)amine (TPMA) was employed by Dunbar and co-workers to enforce an axial symmetry around  $\text{Co}(\text{II})$  in the complexes,  $[\text{Co}(\text{TPMA})\text{CH}_3\text{CN}](\text{BF}_4)_2$  (**96**);  $[\text{Co}(\text{TPMA})\text{X}](\text{X})$  [where  $\text{X} = \text{Cl}$  (**97**),  $\text{Br}$  (**98**),  $\text{I}$  (**99**)] (Fig. 16) [65].

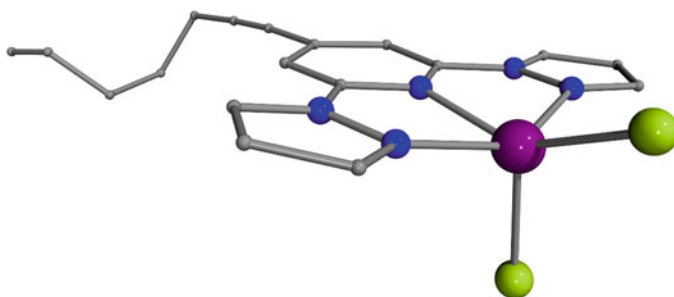
Ac susceptibility measurements performed for all the samples reveal that SIM behavior is not shown in the absence of dc magnetic field suggesting that QTM is active. However, all the complexes show field-induced SIM behavior.

## 5.2 Square Pyramidal Geometry

Unlike the trigonal bipyramidal geometry,  $\text{Co}(\text{II})$  complexes that possess square pyramidal geometry are relative sparse. A phosphorus-based tripodal ligand analogous to tren facilitated the isolation of complexes,  $[\text{Co}(\text{PP}_3)\text{X}]$  [ $\text{X} = \text{Cl}$  (**100**) or  $\text{Br}$  (**101**)] where  $\text{Co}(\text{II})$  is in a distorted square pyramidal geometry (Fig. 17) [66]. Two of the tripodal arms and the central P-atoms of the  $\text{PP}_3$  ligand and a halide ion



**Fig. 17** Crystal structure of  $[\text{Co}(\text{PP}_3)\text{X}]$  [ $\text{X} = \text{Cl}$  (**100**) or  $\text{Br}$  (**101**)]. Color code: Co, purple; P, magenta; and C, gray

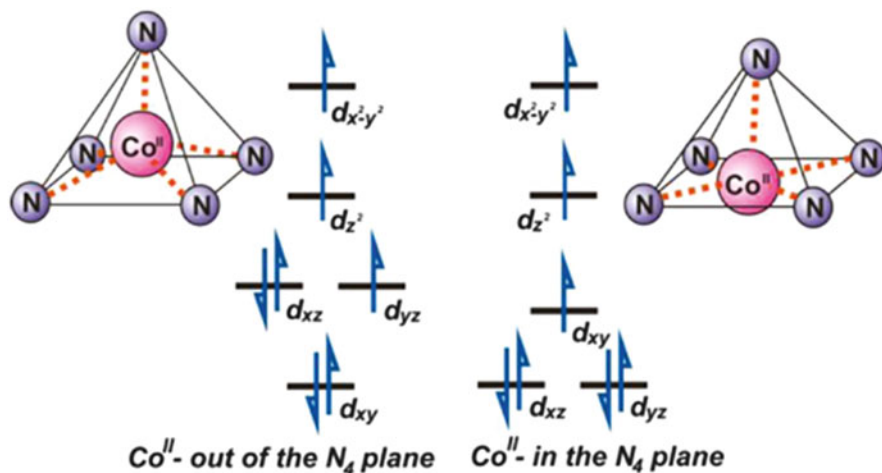


**Fig. 18** Crystal structure of **102**. Color code: Co, purple; N, blue; Cl, green; and C, gray

occupy the basal plane of the square pyramid; the third arm of the tripodal  $\text{PP}_3$  ligand is present at the apical position. Both **100** and **101** possess an easy-plane anisotropy value ( $D = +46.4 \text{ cm}^{-1}$ ,  $E = 10.1 \text{ cm}^{-1}$ ,  $g = 2.31$  for **100** and  $D = +40.7 \text{ cm}^{-1}$ ,  $E = 9.3 \text{ cm}^{-1}$ ,  $g = 2.28$  for **101**).

The origin of the positive  $D$ -value in **100** and **101** has been studied in detail using ORCA suite software and MOLCAS which revealed that the lowest energy transition between the orbitals results in a change in the  $\Delta m_l$  value of  $\pm 1$  leading to a positive contribution to the overall  $D$ . As expected, zero-field SIM behavior was not observed for these complexes.

Use of a pyrazole-decorated pyridine ligand ( $\text{NNN}^{\text{pyr}}$ ) stabilizes a tetragonal pyramid geometry in  $[\text{Co}^{\text{II}}(\text{NNN}^{\text{pyr}})\text{Cl}_2]$  (**102**) (Fig. 18) [67]. Due to the planar nature of the ligand, strong head-to-head  $\pi$ - $\pi$  interactions prevail within the crystal lattice resulting in a dimer motif for **102** in the solid state. The dc data collected on a polycrystalline sample of **102** could not be fit by considering the  $S = 3/2$  ground state. Only upon inclusion of the isotropic exchange interaction ( $J = +1.4 \text{ cm}^{-1}$ ) with a large single-ion anisotropy ( $D/hc = 151 \text{ cm}^{-1}$ ;  $E/hc = 11.6$ ), the authors



**Fig. 19** d-orbital splitting for a square-based pyramid with the metal out of the basal plane (left) and in the basal plane (right). Reprinted with permission from [26], Copyright (2011) American Chemical Society

could model the data reasonably well with anisotropic g-values ( $g_z = 2.0$  and  $g_x = g_y = 3.28$ ). Slow magnetization relaxation is observed for **102** in the presence of an optimum external magnetic field.

Use of bis(imino)pyridine NNN-pincer ligand (NNN<sup>ip</sup>) afforded the complexes,  $[\text{Co}^{\text{II}}(\text{NNN}^{\text{ip-R}})(\text{SCN})_2]$  R = Me (**103**) or Ph (**104**) [26]. The coordination environment in **103** or **104** reveals three nitrogen donors and a monodentate –SCN at the corners of the basal plane while the fifth ligating SCN is at the axial position. The Co(II) in **103** is placed 0.39 Å above the basal plane, while in **104** it is above 0.52 Å. It has been suggested that the out-of-plane shift of the Co(II) ion ensures a large spin-orbit coupling which can be potentially exploited to fine-tune the magnetic anisotropy. The resultant electronic structure due to the out-of-plane shift is shown in Fig. 19.

These complexes possess an easy-axis anisotropy ( $D = -28.8 \text{ cm}^{-1}$  for both **103** and **104**). This observation is an absolute contrast with other square planar complexes reported to date where only an easy-plane anisotropy is registered. For both complexes ac relaxation measurements were performed, but there were no  $\chi_M''$  signals in the absence of an external dc field.

The spin Hamiltonian parameters for five-coordinated Co(II) complexes are summarized in Table 5.



**Table 5** Spin Hamiltonian parameters for five-coordinated Co(II) complexes

Compound	$D$ (cm <sup>-1</sup> )	$E$ (cm <sup>-1</sup> )	$g$	$U_{\text{eff}}$ (cm <sup>-1</sup> )	Ref
<i>Trigonal bipyramid</i>					
[Co(Me <sub>6</sub> tren)Cl]ClO <sub>4</sub> ( <b>90</b> )	-6.2	-	2.24	-	[62]
[Co(Me <sub>6</sub> tren)Br]Br ( <b>91</b> )	-2.5	-	2.22	-	[62]
[Co(NS <sub>3</sub> <sup>iPr</sup> )Cl]BPh <sub>4</sub> ( <b>92</b> )	-19.1	1.5	2.43	32	[68]
[Co(NS <sub>3</sub> <sup>tBu</sup> )Cl]ClO <sub>4</sub> ( <b>93</b> )	-21.4	-	2.29	-	[64]
[Co(NS <sub>3</sub> <sup>tBu</sup> )Br]ClO <sub>4</sub> ( <b>94</b> )	-20.2	-	2.29	21	[64]
[Co(NS <sub>3</sub> <sup>tBu</sup> )NCS]ClO <sub>4</sub> ( <b>95</b> )	-11.0	-	2.29	20	[64]
[Co(TPMA)(CH <sub>3</sub> CN)](BF <sub>4</sub> ) <sub>2</sub> ·CH <sub>3</sub> CN ( <b>96</b> )	9.6	0.2	2.29		[65]
[Co(TPMA)Cl]Cl·2.4(H <sub>2</sub> O) triclinic ( <b>97t</b> )	-6.9	-1.78	2.35		[65]
[Co(TPMA)Cl]Cl cubic ( <b>97c</b> )	-8.4	0	2.30		[65]
[Co(TPMA)Br]Br·2.0(H <sub>2</sub> O) ( <b>98t</b> )	-6.3	1.6	2.34		[65]
[Co(TPMA)Br]Br ( <b>98c</b> )	-7.1	0			[65]
[Co(TPMA)I]I ( <b>99</b> )	-7.5	1			[65]
<i>Square pyramid</i>					
[Co(PP <sub>3</sub> )Cl]ClO <sub>4</sub> ( <b>100</b> )	46.4	10.1	2.31	37.8	[66]
[Co(PP <sub>3</sub> )Br]ClO <sub>4</sub> ( <b>101</b> )	40.7	9.3	2.28	34.5	[66]
[Co <sup>II</sup> (NNN <sup>PvT</sup> )Cl <sub>2</sub> ] ( <b>102</b> )	150	11.6	$g_z = 2.00$ $g_{x,y} = 3.28$		[67]
[Co <sup>II</sup> (NNN <sup>ip-Me</sup> )SCN <sub>2</sub> ] ( <b>103</b> )	-28.8	-	-	11.1	[26]
[Co <sup>II</sup> (NNN <sup>ip-Ph</sup> )SCN <sub>2</sub> ] ( <b>104</b> )	-28.8	-	-	16.7	[26]
[Co(Me <sub>4</sub> cyclam)N <sub>3</sub> ] <sup>+</sup> ( <b>105</b> )	30	9.8	$g_{xy} = 2.35$ $g_z = 2.03$	2.3	[69]
[Co <sup>II</sup> (NNN <sup>bim</sup> )Cl] ( <b>106</b> )	14.5	0	$g_x = 2.41$ ; $g_y = 2.25$ ; $g_z = 2.01$	19.6	[70]
[Co <sup>II</sup> (NNN <sup>bim</sup> )Br] ( <b>107</b> )	8.4	0	$g_x = 2.30$ ; $g_y = 2.20$ $g_z = 1.99$	8.2	[70]
[Co(tpa)Cl]ClO <sub>4</sub> ( <b>108</b> )	-10.1	1.8	-	12	[71]
[Co(tpa)Br]ClO <sub>4</sub> ( <b>109</b> )	-7.8	2.1	-	8.7	[71]
[Co(tbta)Cl](ClO <sub>4</sub> )(MeCN) <sub>2</sub> (H <sub>2</sub> O) ( <b>110</b> )	-7.5	0.4	-	8.1	[71]
[Co(tbta)Br]ClO <sub>4</sub> ( <b>111</b> )	-4.3	0.03	-	5	[71]
[Co(N <sub>3</sub> LH <sub>3</sub> ) <sup>4+</sup> ] ( <b>112</b> )	-7.1	-	$g_{x,y} = 2.36$ ; $g_z = 2.24$	14.2	[72]
[Co(terpy)Cl <sub>2</sub> ] ( <b>113</b> )	-	-	$g_x = 1.35$ ; $g_y = 1.93$ $g_z = 7.75$	19.5 2.8	[73]
[Co(terpy)(NCS) <sub>2</sub> ] ( <b>114</b> )	-	-	-	11.8 2.1	[73]

(continued)

**Table 5** (continued)

Compound	$D$ (cm <sup>-1</sup> )	$E$ (cm <sup>-1</sup> )	$g$	$U_{\text{eff}}$ (cm <sup>-1</sup> )	Ref
[Co(bzimpy)Cl <sub>2</sub> ] ( <b>115</b> )	71.7	1.4	$g_x = 2.50$ ; $g_y = 2.62$ $g_z = 1.47$		[74]
[CoL <sup>1</sup> Cl <sub>2</sub> ] ( <b>116</b> )	71.7	0	$g_{x,y} = 2.50$ ; $g_z = 2.00$		[75]
[CoL <sup>2</sup> Cl <sub>2</sub> ] ( <b>117</b> )	46.8	0	$g_{x,y} = 2.35$ ; $g_z = 2.00$		[75]

*Me<sub>6</sub>tren* hexamethyl tris(aminoethyl)amine, *NS<sub>3</sub><sup>IPr</sup>* tris-(2-(isopropylthio)ethyl)amine, *NS<sub>3</sub><sup>IBu</sup>* tris-(2-(tertbutyl)thio)ethyl)amine, *Me<sub>4</sub>cyclam* tetramethylcyclam, *N<sub>3</sub>* azido, *PP<sub>3</sub>* tris [2-(diphenylphosphino) ethyl]-phosphine, *NNN<sup>IPr</sup>* 4-hept-1-ynyl-2,6-dipyrazol-1-ylpyridine, (*NNN<sup>IPr</sup>*) bis(imino)pyridine, *terpy* terpyridine, *bzimpy* 2,6-bis(benzimidazol-2-yl)pyridine, *L<sup>1</sup>* 4'-iodo-2',6'-dipyrazolyl-pyridine, *LH<sub>3</sub>* 6,16,2,5-tribenzena(1,4)-1,4,8,11,14,18,23,27-octaazabicyclo[9.9.9]nonacosaphane, *N<sub>3</sub>* azide

## 6 Coordination Number 6

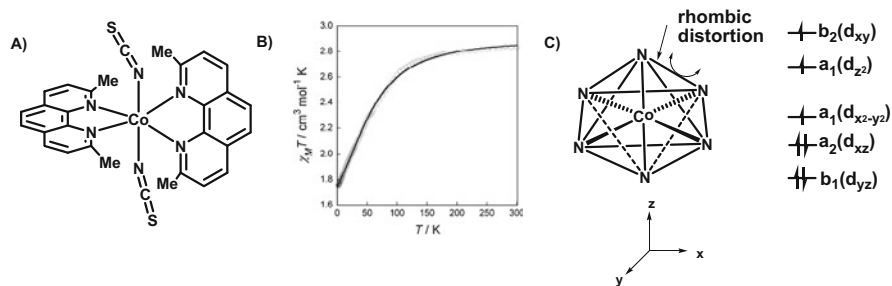
### 6.1 Octahedral Geometry

Octahedral Co(II) complexes predominantly stabilize a non-uniaxial magnetic anisotropy. For example, Pardo and co-workers have reported an octahedral Co(II) complex [*cis*-[Co<sup>II</sup>(dmphen)<sub>2</sub>(NCS)<sub>2</sub>]-0.25EtOH] (**118**) (Fig. 20) (dmphen = 2,9-dimethyl-1,10-phenanthroline) with an easy-plane anisotropy ( $D = +98$  and  $E = 8.4$  cm<sup>-1</sup>). This complex exhibited a slow relaxation of magnetization in the presence of an applied magnetic field [76]. In this complex Co(II) ion exists in a distorted octahedral geometry. The equatorial positions are occupied by two *cis*-thiocyanate (*N*-donor) ligands with the other two being derived from the nitrogen atoms of the chelating dmphen ligand. The remaining two pyridyl nitrogen donors complete the coordination sites of Co(II) in the axial position (Fig. 20). The variable temperature  $\chi_M T$  data on polycrystalline sample of **118** shown in Fig. 20b. As expected for a paramagnetic Co(II) ion, the room temperature  $\chi_M T$  value is significantly larger than the expected spin-only value due to the unquenched orbital angular momentum. The magnetic data were fitted using the following HDVV Hamiltonian.

$$H = D \left[ S_z^2 + \frac{S(S+1)}{3} \right] + E \left( S_x^2 + S_y^2 \right) + g\beta H \cdot S \quad (1)$$

The best fit to the  $\chi_M T(T)$  data were obtained using the parameters  $D = +98$  cm<sup>-1</sup>,  $E = +8.4$  cm<sup>-1</sup>, and  $g = 2.78$ . The sign of single-ion magnetic anisotropy of **118** was unambiguously confirmed by low-temperature X-band EPR measurements (polycrystalline at 9 K) which also strongly corroborate the large rhombicity associated with the cobalt complex ( $g_x = 6.1$ ,  $g_y = 3.8$ ,  $g_z = 2.4$ ).

The ac susceptibility measurement on polycrystalline sample of **118** does not show frequency-dependent out-of-phase susceptibility signals in the absence of dc bias field. This is not surprising for a complex with positive  $D$ -value. On the other hand, ac



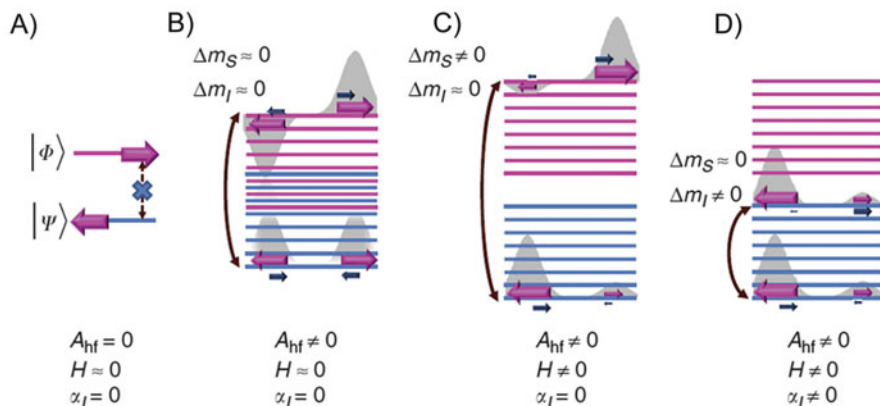
**Fig. 20** (a) Line diagram of complex **118**. (b) Temperature-dependent magnetic susceptibility of **118** in the presence of an external magnetic field of 0.1 ( $\leq 20$  K) and 1.0 kOe ( $> 20$  K). The solid line represents the best fit obtained for the parameters described in main text. (c) The d-orbital splitting pattern of an octahedral geometry after the application of a rhombic distortion. Reprinted with permission from [75], Copyright (2012) American Chemical Society

measurements performed in the presence of an optimum external magnetic field (1, 2.5 and 5 kOe) indeed shows frequency-dependent slow magnetization of relaxation. The barrier for the magnetization reversal was estimated to be  $16.2 \text{ cm}^{-1}$  which is an order of magnitude less than the theoretically predicted anisotropic barrier ( $U_{\text{eff}} = 2D = 196 \text{ cm}^{-1}$ ). Pardo and co-workers proposed for the first time that the origin of energy barrier in this complex (**118**) is not due to the classical axial anisotropy ( $U_{\text{eff}} = 2D$ ) but due to the transverse anisotropy and hence  $U_{\text{eff}} = ES^2 - 1/4 \cong 2E$ . Since the maximum limit of rhombic distortion associated with the molecule is dictated by  $E$  [ $|E| \leq D/3$ ], the barrier will always be lower than the anisotropic barrier.

Ruiz and co-workers studied the microscopic mechanism of slow relaxation of magnetization in molecules with positive  $D$ -values [77]. For this study, they have chosen an octahedral elongated molecule  $[\text{Co}(\text{acac})_2(\text{H}_2\text{O})_2]$  (**119**) and its magnetically diluted sample in a diamagnetic matrix  $[\text{Co}_{0.05}\text{Zn}_{0.95}(\text{acac})_2(\text{H}_2\text{O})_2]$  (**119-Zn**). The Co(II) ion in **119** is surrounded by six oxygen donor atoms and exhibits a distorted octahedral geometry. Four out of the six coordination sites are occupied by the two acac ligands in the equatorial positions. The two terminal water molecules reside in the axial positions; the Co-O distances involved are slightly larger than the Co-O(acac) distance. The magnetic behavior could be described with the following effective spin Hamiltonian.

$$H = D \left[ S_z^2 - \frac{S(S+1)}{3} \right] + E(S_x^2 - S_y^2) - g\beta H \cdot S + S \cdot A \cdot I \quad (2)$$

In the above equation,  $A$ ,  $I$ , and  $g$  represent hyperfine tensor, nuclear spin moment, and gyromagnetic ratio, respectively. The complex **119** was found to possess very large positive  $D$ -value ( $\approx 57 \text{ cm}^{-1}$ ) which was substantiated by X-band EPR spectroscopy and ab initio calculations. The theoretical calculation predicts that the two Kramers levels in **119** are separated by more than  $130 \text{ cm}^{-1}$  with a significantly large rhombic distortion. The presence of rhombic anisotropy in **119** and **119-Zn** is authenticated by the spin Hamiltonian parameters extracted from



**Fig. 21** (a) Electronic states ( $\Psi$  and  $\phi$ ) related by time reversal symmetry; transition between these states are forbidden under zero applied field due to Van-Vleck cancellation. (b) Hyperfine interaction breaks down the Kramers degeneracy (breaking the time reversal spin-phonon operator) and allows the phonon-induced transition between the states possessing same  $m_I$  value ( $\Delta m_I = 0$ ). (c) Zeeman interaction with the external magnetic field further splits the energy level. (d) A non-zero probable spin-lattice relaxation constant breaks down the selection rule ( $\Delta m_I \approx 0$ ), thus makes all the transition probability allowed

X-band EPR spectrum (i.e.,  $E/D = 0.31$ ). Spin-lattice relaxation time investigation for **119-Zn** was performed using the ac magnetization susceptibility studies. As expected, due to zero-field tunneling,  $\chi_M''$  signals could not be observed. The extracted magnetization reversal barrier was observed to be significantly lower ( $14 \text{ cm}^{-1}$ ) than the energy gap predicted between the two Kramers states ( $130 \text{ cm}^{-1}$ ). In order to explain these experimental results involving the slow relaxation of a complex with a positive  $D$ , Ruiz and co-workers carried out detailed theoretical studies, the summary of which is presented below.

According to the “Van-Vleck cancellation” rule for the spin-lattice relaxation, the modulation of crystal field by phonons cannot induce transition between  $m_S = \pm 1/2$  Kramers levels with a positive  $D$ -value, i.e., spin cannot change its magnetization direction. The presence of nuclear hyperfine interaction, however, enhances the transition probabilities between any pair of states. This can be understood by the cartoon given in Fig. 21. However, hyperfine interaction induces the transition from one state to the other state which induces a vanishingly small magnetic moment within the states and hence cannot be detected in the ac magnetic field ( $H_{dc} = 0$ ). However, upon applying an external magnetic field ( $H_{dc} \neq 0$ ), due to Zeeman interaction, the energy levels further split, and the transition probability between the states associated with large magnetic moment changes [77].

Hence, the relaxation dynamics can be followed through ac measurements. In such complexes, the magnetization relaxation is predominantly governed by the direct and Raman processes. The former appears to be dominant below 3 K, while above 3 K, two-phonon, temperature-dependent Raman process prevails. Based on

the detailed experimental and theoretical observations, Ruiz and co-workers further proposed that complexes with non-integer spin states with a high anisotropy (either positive or negative) are the ideal candidates for developing single-ion spin memories. But, besides the two criteria mentioned above (half-integer and large  $D$ -value), hyperfine interaction needs to be minimized to prevent the single-phonon direct process (which will reduce the blocking temperature) to stabilize well-defined spin projection. Hence, complexes containing Cr(III), Ni(III), and Fe(I) can stabilize large magnetization reversal barrier.

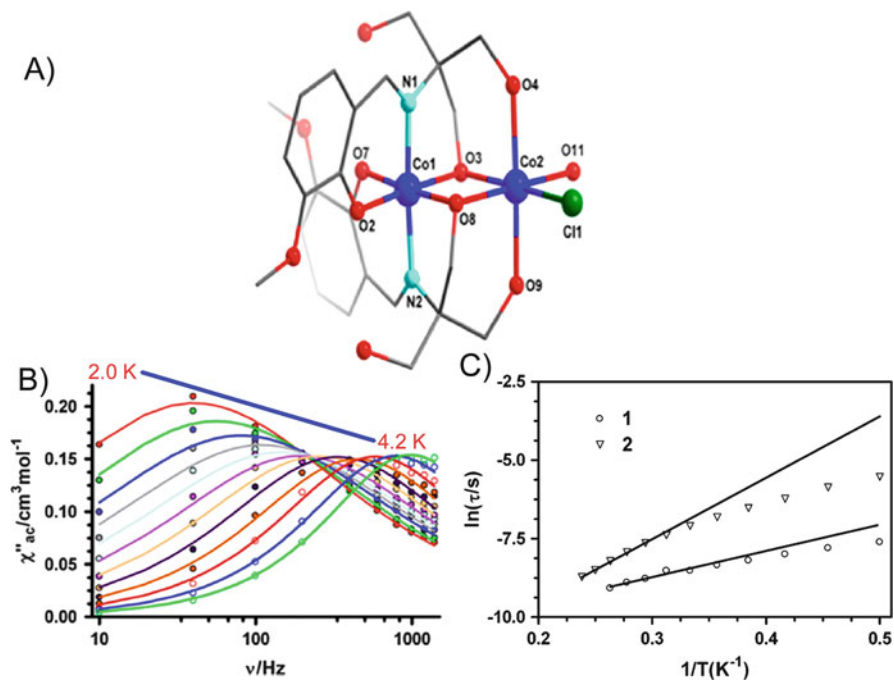
Travnicek and co-workers prepared a  $[\text{Co}(\text{abpt})_2(\text{tcm})_2]$  (**120**) [abpt = 4-amino-3,5-bis(2-pyridyl)-1,2,4-triazole; tcm = tricyanomethanide anion]. Here also the tcm ligand occupies the axial position similar to the case in **119** [78]. However, Co-N (tcm) axial distance in **120** is smaller than Co-OH<sub>2</sub> in **119**, and therefore the geometry is compressed octahedron. The experimental magnetic data can be fitted with both isotropic  $g$ -value [ $g = 2.461$ ;  $D = +48(2) \text{ cm}^{-1}$ ;  $E/D = 0.27(2)$ ] and anisotropic  $g$ -value which results in slightly different  $D$  and  $E$  values. In both situations, however, the sign of  $D$  was predicted to be positive. This complex showed only a field-induced SIM behavior. However, in contrast to the observation in **118** and **119**, incorporation of Orbach process (third term in Eq. 3) is mandatory for the fitting of Arrhenius plot in the entire temperature region, apart from direct (first term in Eq. 3) and Raman process (second term in Eq. 3).

$$\tau^{-1} = AB^2T + CT^n + \tau_0^{-1} \exp\left(-\frac{U_{\text{eff}}}{kT}\right) \quad (3)$$

This is likely due to the change in electronic structure brought by the compressed octahedral geometry. Nevertheless, the computed energy barrier ( $123.6 \text{ cm}^{-1}$ ) between the two lowest Kramers levels of **120** and the theoretically expected energy barriers ( $U_{\text{eff}} = 2(D^2 + E^2)^{1/2} = 109.2 \text{ cm}^{-1}$ ) are approximately twice as large as the experimentally extracted barrier ( $61.6 \text{ cm}^{-1}$ ) from ac measurements. The extracted magnetization reversal barrier ( $61.6 \text{ cm}^{-1}$ ) is the largest among the non-uniaxial barrier reported for the complexes.

It has been observed in the literature that irrespective of the nature of the donor atoms (oxygen or nitrogen predominantly), Co(II) complexes present in a regular or distorted octahedral geometry (elongated or compressed) are stabilized with a non-uniaxial single-ion magnetic anisotropy. A few exceptions exist where negative zero-field splitting is witnessed such as in a mixed-valent complex,  $[\text{Co}^{\text{III}}\text{Co}^{\text{II}}(\text{LH}_2)_2(\text{X})(\text{H}_2\text{O})](\text{H}_2\text{O})_4$  ( $\text{X} = \text{Cl}$  (**121**) or  $\text{Br}$  (**122**);  $\text{LH}_2 =$  dianionic 2-[(2-hydroxy-3-methoxyphenyl)methylene]amino)-2-(hydroxymethyl)-1,3-propanediol) which was reported by Chandrasekhar and co-workers (Fig. 22) [79].

The room temperature  $\chi_{\text{M}}T$  value of all the three complexes (**121–122**) is above the expected value for a paramagnetic Co(II) ion with an average value of 2.0 due to the non-zero orbital contribution to the magnetic moment. Due to the unquenched orbital angular momentum, the degeneracy of  $m_s$  levels of ground state Co(II) ion is lifted resulting in a non-zero magnetic anisotropy. The best fit of the magnetic data revealed the following parameters:  $g = 2.32$ ,  $D = -7.4 \text{ cm}^{-1}$ ,  $E/D < 0.001$  for **121**;  $g = 2.52$ ,



**Fig. 22** (a) Single crystal structure of complex **121** (left). (b) Frequency-dependent out-of-phase signals for **122** at 0.1 KOe (middle). (c) Arrhenius plot constructed from ac data of **121** and **122**. Solid black line represents the linear fit of the data (“triangle” represents **121** and “circle” represents **122**) (right). Reprinted with permission from [79], Copyright (2013) The American Chemical Society

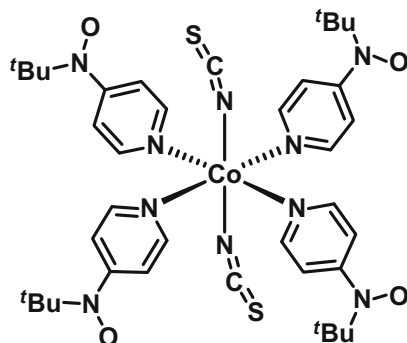
$D = -9.7 \text{ cm}^{-1}$ ,  $E/D < 0.0001$  for **122**. These complexes exhibit a field-induced (1 kOe) slow relaxation of magnetization. The barrier for the magnetization reversal was estimated to be  $7.9 \text{ cm}^{-1}$  and  $14.5 \text{ cm}^{-1}$  for **121** and **122**, respectively. To unravel the details of the origin of the negative  $D$ , theoretical studies may be necessary.

So far we have discussed six coordinate octahedral Co(II) complexes surrounded by diamagnetic ligands. In the following, we will discuss octahedral Co(II) complexes containing paramagnetic ligands. Also, magnetization relaxation dynamics and strategies to increase  $S$  and  $D$ -values by employing suitable paramagnetic ligand design are discussed.

The influence of radical ligands on the magnetic properties of Co(II) complexes has been studied. The complexes,  $[\text{Co}(\text{X})_2(4\text{NOpy})_4]$  ( $\text{X} = \text{NCO}$  (**123**),  $\text{NCS}$  (**124**), and  $\text{Br}$  (**125**)) (Fig. 23), containing the aminoxyl radical were synthesized and characterized [80].

These complexes possess a distorted compressed octahedral geometry with the NCO, NCS, or Br ligands occupying the axial positions. Interestingly, an antiferromagnetic ordering is observed at low temperatures in the solid state resulting in the absence of SMM behavior. On the other hand, in a frozen solution of THF, slow

Fig. 23 Line diagram of **124**

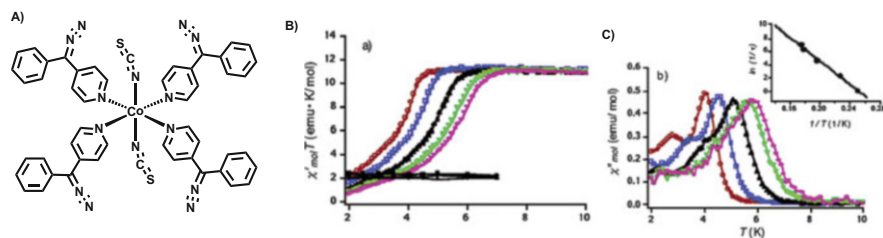


magnetization of relaxation is reinstated in all the three complexes. Detailed analysis of the packing diagram of **123** and **124** reveals that **123** does not possess short contact between the radicals; rather these radicals interact with the adjacent molecule of pyridine ring ( $\beta$ -carbon). On the other hand, complex **124** shows, in addition to the radical-pyridine ring interaction as in **123**, that there are short contacts between the radicals of one molecule with the adjacent molecule. The latter interaction leads to a linear dimer structure, while the former supramolecular interaction leads to the formation of a ribbon-like structure.

Based on the discussion made thus far, it may be noted that in general, octahedral Co(II) coordination complexes seemed to be predominantly stabilized with positive  $D$ -value (except complexes **121**, **122**, and **123** or when paramagnetic ligands are involved).

The complex  $[\text{Co}(\text{SCN})_2(\text{DAPy})_4]$  (**126**) encapsulated by 4-( $\alpha$ -diazobenzyl)pyridine (DAPy) possesses compressed octahedral geometry; the two monodentate thiocyanate reside in the axial sites. Irradiation of the complex results in a triplet state for the photoactive ligand which ferromagnetically interacts with Co(II) ion resulting in a ground state of  $S_{\text{tot}} = 9/2$  ( $S = 1$  from four DAPy ligands and an effective ground state  $1/2$  from Co(II); Fig. 24). Ac relaxation dynamics performed on frozen solution of **126** after photolysis shows a well-defined out-of-phase susceptibility signals in the absence of zero dc field.

A barrier height of  $63.6 \text{ cm}^{-1}$  could be extracted from the Arrhenius plot. Modifying the diaza group by a carbene allows a similar phenomenon, in  $[\text{Co}(\text{NCS})_2(\text{CAPy})_4]$  (**127**). In all of these complexes, the tuning of the anisotropy barrier by the axial ligand was also demonstrated:  $\text{NCS}^-$  ( $63.6 \text{ cm}^{-1}$ , **128**)  $<$   $\text{Cl}^-$  ( $65 \text{ cm}^{-1}$ , **129**)  $<$   $\text{NCO}^-$  ( $92.9 \text{ cm}^{-1}$ , **130**). An interesting observation is that all the Co(II) complexes either with a stable radical ligand (4NOPy) or with a diazo or carbene derivative of pyridine (in triplet state) are coupled ferromagnetically. Not only that, all the complexes are stabilized with a negative zero-field splitting exhibit SMM ( $H_{\text{dc}} = 0$ ) behavior (negligibly small  $E$  as well), although Co(II) ion in an octahedral (compressed) geometry.



**Fig. 24** (a) Line diagram of complex **126**. Plots of (b)  $\chi'T$  vs  $T$  and (c)  $\chi''$  vs  $T$  obtained after irradiation of 1:4 mixture (10 mM) of **126** in frozen THF-EtOH solution with a 5 Oe ac field oscillating at 1,000 (square), 500 (triangle), 100 (inverted triangle), 10 (diamond), and 1 (circle) Hz. The blackfilled marks in (a) are the data before irradiation, and the inset is an Arrhenius plot. Reprinted with permission from [81], Copyright (2003) The American Chemical Society

## 6.2 Trigonal Prismatic Geometry

Enforcing a trigonal prism geometry in six-coordinated Co(II) complexes is a synthetic challenge. This has been realized in the complexes,  $[\text{Co}(\text{R-L})]$  (L = clathrochelate ligand<sup>2-</sup>; R =  $\text{C}_{16}\text{H}_{33}$  (**131**); 3,5-bis(trifluoromethyl)phenyl (**132**) or F (**133**) (Fig. 25) [32].

In situ condensation of dichloroglyoxime with various organoboronic acids in the presence of metal halides results in the isolation of various Co(II) (**131–133**) or Fe(II) (**131a–132a**) complexes with trigonal prism geometry (Fig. 25). An approximate  $D_3$  symmetry is associated with these complexes with the  $C_3$ -axis passing through B-M-B axis. Complexes **131** and **132** experience spin crossover behavior and exist in the high-spin state (**131** and **132**) above 190 K. The following parameters could be extracted ( $g_{\parallel} = 2.4$ ,  $g_{\perp} = 2.2$  and  $D = -65 \text{ cm}^{-1}$ ). These were corroborated by EPR measurements, and it appears that if suitable Co(II) complexes in a trigonal prismatic geometry are isolated, they would have large negative  $D$ -values.

In accordance with above, the complex  $[\text{Co}(\text{R-L-Pzo})]$  (Pzo = pyrozoloximate and R = Ph (**134**)) (Fig. 26) was prepared which was a high-spin complex in the entire temperature range 2–300 K. This complex was analyzed to have the following SH parameters ( $g_{\parallel} = 2.9$ ,  $g_{\perp} = 2.2$  and  $D = -82 \text{ cm}^{-1}$ ;  $E/D = 0.003$ ). A  $D$  of  $-109 \text{ cm}^{-1}$  was obtained through analysis from paramagnetic NMR. In order to understand the electronic structure of **134**, CASSCF-NVEPT2 calculations were performed using ORCA suite software. As expected, SOC splits the ground state in four pairs of Kramers states, which span within  $6,883 \text{ cm}^{-1}$ . The energy gap between the ground state and the first excited Kramers level was computed to be  $220 \text{ cm}^{-1}$ . Ac magnetization relaxation dynamics revealed out-of-phase susceptibility signals with anisotropic barriers of  $71 \text{ cm}^{-1}$  ( $H_{\text{dc}} = 0$ ) and  $101 \text{ cm}^{-1}$  ( $H_{\text{dc}} = 1.5 \text{ kOe}$ ) by considering only the thermally assisted Orbach relaxation process. Upon inclusion of Raman and direct processes in addition to the Orbach



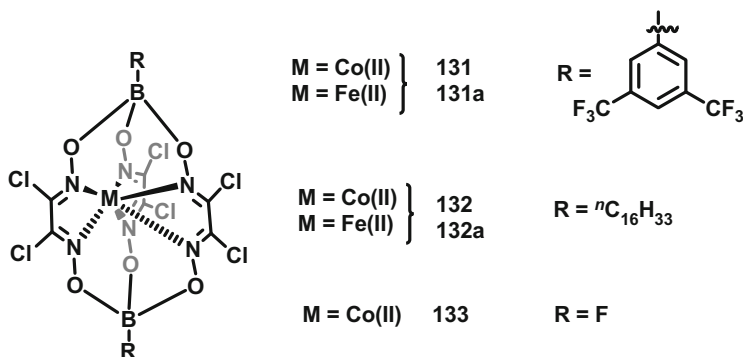


Fig. 25 Schematic diagrams of 131–133

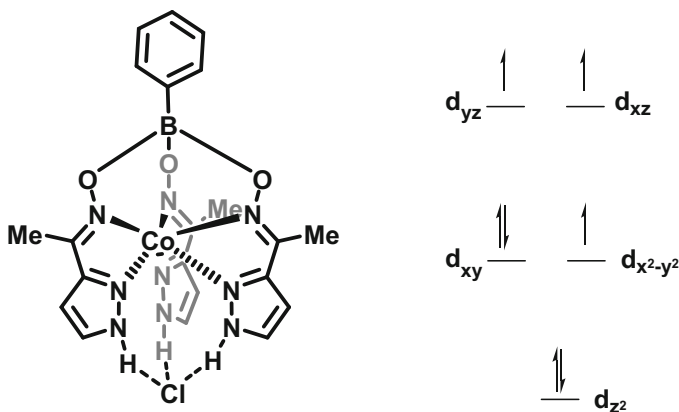


Fig. 26 (a) Line diagram of 134. (b) Splitting of d-orbitals in a trigonal prismatic crystal field

process for Arrhenius data fitting, the estimated barrier improved significantly ( $152 \text{ cm}^{-1}$ ) and is much more closer to the theoretically expected barrier of  $164$  ( $\sim 2D = 2 \times 82$ ).

A star-shaped complex,  $\text{HNEt}_3[\text{Co}^{\text{II}}\text{Co}^{\text{III}}\text{L}_6]$  (**135**), was isolated using a chiral ligand ( $\text{H}_2\text{L}$ , *R*-4-bromo-2-((2-hydroxy-1-phenylethylimino)methyl)phenol) [25]. The chirality of the ligand has been transferred to the metal complex, which crystallizes in the orthorhombic  $P2_12_12_1$  space group. Three of the cobalt centers are at the vertices of an equilateral triangle, while the fourth cobalt ion is located above the triangular plane. The latter has been shown to be in a distorted trigonal prism geometry. The experimental magnetic data could be fitted by using  $D$ ,  $E$ , and  $g$  as  $115 \text{ cm}^{-1}$ ,  $2.8 \text{ cm}^{-1}$ , and  $3.05$ , respectively. Frequency-dependent magnetic susceptibility performed on these samples shows well-resolved  $\chi_M''$  signals at higher temperature (slow relaxation) while below  $6 \text{ K}$ , another fast relaxation is observed which is due to the QTM in the absence of zero bias field. The anisotropic barrier

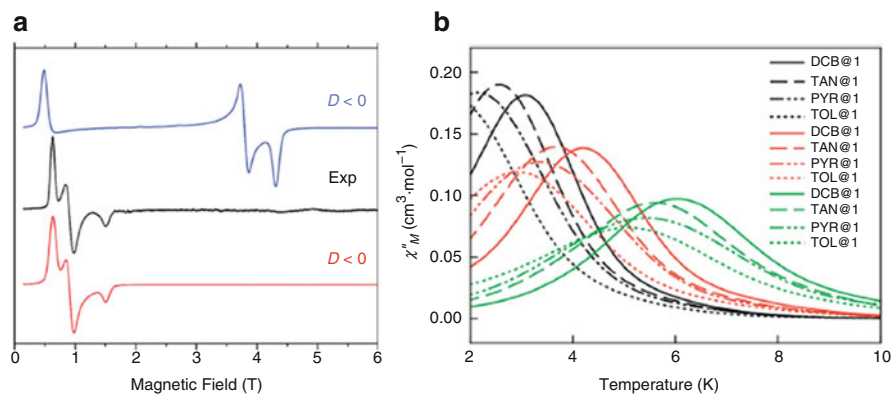
estimated for the slow relaxation process was  $77.9 \text{ cm}^{-1}$ . Upon measuring the ac data under the influence of external magnetic field (1.5 kOe), the barrier height is marginally increased to  $88.6 \text{ cm}^{-1}$ . Theoretical calculation performed on **135** and the computed SH parameters are consistent with the experimental data. The computed  $D$ -value ( $-107 \text{ cm}^{-1}$ ) is slightly lower than the experimental value. Similarly the experimentally extracted anisotropic barrier of  $77.9 \text{ cm}^{-1}$  is significantly lower than the theoretically expected one ( $214 \text{ cm}^{-1}$ ), implying that apart from the thermally assisted Orbach process, other relaxation mechanisms are operational. It was found that while introducing an electron-donating substituent on the  $p$ -position of the phenolic ring reduces the anisotropic barrier, the presence of an electron withdrawing group has the opposite effect.

In contrast to the complexes discussed above, those possessing a trigonal antiprism geometry are even rare. In fact the distinction between this geometry and a distorted octahedral is very subtle, and the reader is referred to the original work [82]. The complexes,  $[\text{Co}^{\text{II}}(\text{Tpzm})_2][\text{X}]_2$  [ $\text{X} = \text{ClO}_4$  (**136**) or  $\text{BPh}_4$  (**137**)], were formulated as possessing the trigonal antiprism geometry and the magnetic data of these complexes could be modeled by considering negative magnetic anisotropy ( $g_x = 2.04$ ,  $g_y = 2.20$ ,  $g_z = 2.89$ ,  $D = -92 \text{ cm}^{-1}$ , and  $E = 10.5 \text{ cm}^{-1}$  for **136**;  $g_x = 2.07$ ,  $g_y = 2.23$ ,  $g_z = 2.83$ ,  $D = -93 \text{ cm}^{-1}$ , and  $E = 11.5 \text{ cm}^{-1}$  for **137**). In spite of a negative  $D$ , both the complexes did not show slow relaxation of magnetization in the absence of external magnetic field.

## 7 Complexes with Extended Structures

Using long-chained spacer ligands Co(II), complexes possessing extended structures can be isolated. A square-grid metal-organic framework containing octahedral Co(II) at the nodes was accordingly prepared (**138**) [83]. Interestingly, all the Co(II)-MOF systems reveal a positive  $D$ . Surprisingly, variation of guest molecules within the pores of the MOF seemed to cause a change in the magnetization relaxation dynamics (Fig. 27).

By changing the linear organic linker to 2,4,6-tris(4-pyridyl)-1,3,5-triazine (TPT), a 3D-MOF,  $[\{(\text{Co}(\text{NCS})_2)_3(k^3\text{-TPT})_4\}(\text{H}_2\text{O})(\text{MeOH})]_n$  (**139**), was isolated [84]. The Co(II) present in the nodes contain thiocyanate ligands in the axial positions, while pyridyl nitrogen atoms occupy the equatorial plane. The extracted energy barrier ( $5 \text{ cm}^{-1}$ ) is several orders of magnitude less than the energy gap between the ground and first excited state ( $280 \text{ cm}^{-1}$ ); hence, the participation of Orbach relaxation mechanism to the spin reversal can be precluded. Apart from these aforementioned examples, other 1D, 2D, and 3D extended structures are known [85–87].



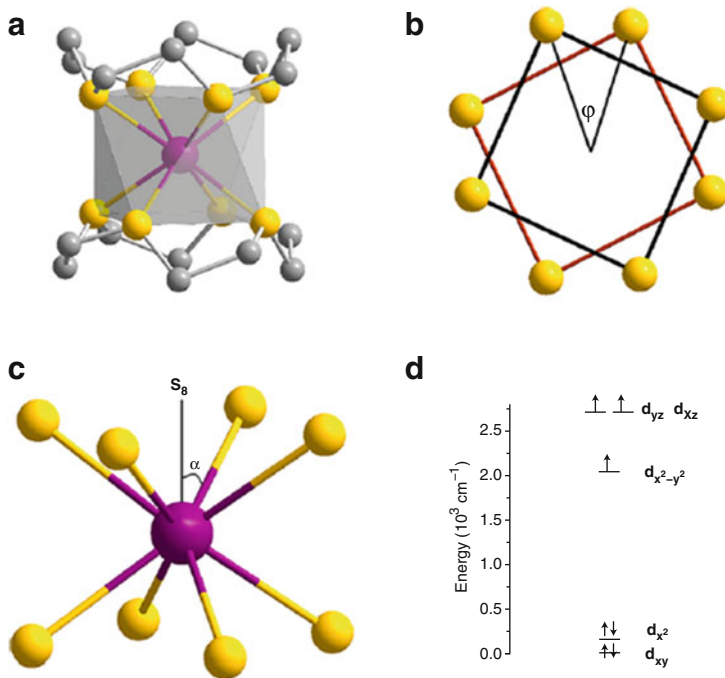
**Fig. 27** (a) EPR spectra of TAN@138 at 53.2 GHz and 4.5 K (black red trace  $D > 0$  and blue trace  $D < 0$ ). (b). Temperature dependence of  $\chi''_M$  of DCB@138, TAN@138, TOL@138, and PYR@138 under  $\pm 5.0$  G oscillating field at 672 (black), 2,043 (orange), and 10,000 Hz (green) frequencies in a dc applied static field of 1,000 G. Adapted with permission from [84] The Royal Society of Chemistry

## 8 Seven- and Eight-Coordinated Co(II) Complexes

High-coordinated Co(II) complexes are very rare. We will discuss some examples of seven- and eight-coordinated complexes in this section. All the seven-coordinated Co(II) complexes are stabilized with large positive  $D$ -values, and the relaxation mechanism is governed by multiple relaxation mechanisms (direct, Raman, QTM and rarely Orbach processes).

A representative example of a seven-coordinated Co(II) is found in the coordination polymer,  $[\text{Co}(\text{bpy})_{1.5}(\text{NO}_3)_2]$  (**140**) [88]. The Co(II) ion has a 3N,4O coordination environment in a pentagonal bipyramidal geometry. The magnetic data could be modeled by a positive  $D$ -value (+68 and  $E = 4.5$ ,  $g = 2.4$ ) which could be validated by an EPR study. Frequency-dependent ac relaxation measurements revealed a field-induced SIM behavior. It appears that incorporating a symmetrical ligand in the equatorial position and employing a weak field ligand at the axial position can lead to an increase in the positive  $D$ -value in Co(II) complexes.

In order to test if large orbital contribution to the magnetic moment can be harvested in Co(II) complexes by increasing the coordination number, a sandwich complex containing two macrocyclic 12-crown-4, (12C4) ligands was prepared [89]. The reasoning here is that, by employing a weak field ligand, the energy gap between the ground and the excited state can be fine-tuned. Thus, a large orbital angular momentum can be either harvested through first-order orbital angular momentum or through spin-orbit coupling-induced mixing of ground and excited states. In the complex,  $[\text{Co}^{\text{II}}(12\text{C}_4)_2](\text{I}_3)_2(12\text{C}_4)$  (**176**) (Fig. 28) Co(II) is sandwiched between the two crown ether ligands and exists in a distorted square antiprism geometry. The room temperature  $\chi_M T$  value for **176** is significantly higher than the expected value for a  $S = 3/2$  state signifying the non-negligible orbital

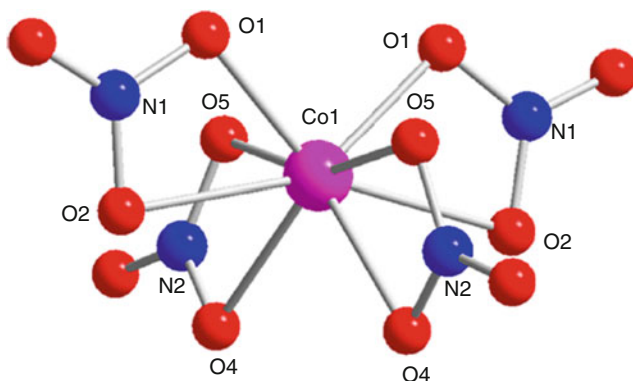


**Fig. 28** (a) Single crystal structure of **176**. (b) The dihedral angle between the two square basal planes. (c) Representation of  $\alpha$  (the measure of angle between  $\angle S8-Co-O$ ) (d) DFT computed Eigenvalue plot for **176**. Reprinted with permission from [89], Copyright (2014) The American Chemical Society

contribution to the magnetic moment. The magnetic data fit yields the parameters  $D = -38 \text{ cm}^{-1}$ ,  $E = -0.75 \text{ cm}^{-1}$ ,  $g = 2.55$ .

However, the complex does not show out-of-phase susceptibility signals in the absence of an external magnetic field, while well resolved  $\chi_M''$  signals are observed in the optimum external bias field with a small barrier height of  $17 \text{ cm}^{-1}$ . The magnitude of the latter suggests that QTM is not completely quenched even under the dc magnetic field. The SIM behavior of this complex was confirmed by the observation of a hysteresis with a blocking temperature of  $1.0 \text{ K}$ .

In the complex,  $[\text{Co}^{\text{II}}(\text{NO}_3)_4]^{2-}$  (**176**), the nitrate ligands are bound in a chelating manner to Co(II). The geometry around the metal ion was confirmed by continuous shape measurement (CShM) to be triangular dodecahedron ( $\sim D_{2d}$  symmetry). The detailed dc measurements and fitting procedure suggest that **176** is stabilized with an easy-plane anisotropy ( $D = 7.95 \text{ cm}^{-1}$ ,  $E = 1.88 \text{ cm}^{-1}$ ,  $g_x = g_y = 2.31$ , and  $g_z = 2.03$ ) (Fig. 29).



**Fig. 29** Molecular structure of **176** showing Co(II) in an eight-coordinated triangular dodecahedron geometry. Reprinted with permission from [90], Copyright (2016) The American Chemical Society

## 9 Summary and Outlook

As shown in the extensive overview above, the spin Hamiltonian parameters of monomeric Co(II) complexes can be modulated by simply modifying the ligand field. Predominantly uniaxial magnetic anisotropy values reported for two- and three-coordinate complexes of Co(II) (whose coordination sites are decorated by aliphatic amides) are based on the simulation of magnetic data. No further spectroscopic evidence or ac relaxation dynamics were reported for these complexes. By enhancing the covalency of the M-L bonds, particularly in two-coordinate Co(II) complexes, the anisotropic barrier is increased dramatically. On the other hand, the largest  $m_s$  level of a  $S = 3/2$  ground state of Co(II) can be stabilized in its  $D_{2d}$  geometry when the first coordination sphere is decorated by soft donor atoms. In addition, the second coordination sphere also has significant influence in determining not only the sign but also the magnitude of D-value. Ligands that enforce trigonal bipyramidal geometry around Co(II) ion always stabilize negative D. The latter can be enhanced further by designing the ligand in such a way that weak  $\sigma$  donor ligands are placed in the equatorial position, while strong  $\pi$  donors occupy the axial position. Irrespective of the nature of the donor atom, Co(II) complexes in an octahedral geometry generally stabilize an easy-plane anisotropy except when paramagnetic ligands are employed. In contrast to octahedral Co(II) complexes, those possessing trigonal prism geometry are found to stabilize the Ising or uniaxial anisotropy regardless of the donor atoms. Finally, Co(II) complexes possessing coordination numbers larger than six, generally, predominantly stabilize an easy-plane anisotropy.

From the above summary, it may be concluded that in the design of Co(II) SIMs, the following factors should be kept in mind.

1. Increase of Co(II)-ligand covalent character which tends to quench other relaxation process and aids in the enhancement of the anisotropy.
2. In tetrahedral Co(II) complexes, use of soft donor ligands.
3. Utilize ligands that enforce trigonal bipyramidal (five coordinate) or trigonal prism geometry (six coordinate).
4. Octahedral Co(II) complexes should possess paramagnetic ligands.

Finally, it is anticipated that future research would further focus on chiral SIMs and complexes possessing extended structures. In the latter, particularly, additional parameters, such as light, guest, etc., can be utilized as additional tweaking parameters to control the spin projections.

## References

1. Gatteschi D, Sessoli R (2003) *Angew Chem Int Ed* 42:268–297
2. Sessoli R, Gatteschi D, Caneschi A, Novak MA (1993) *Nature* 365:141
3. Kahn O, Galy J, Journaux Y, Jaud J, Morgenstern-Badarau I (1982) *J Am Chem Soc* 104:2165–2176
4. Sikorav S, Bkouche-Waksman I, Kahn O (1984) *Inorg Chem* 23:490–495
5. Kloewer F, Lan Y, Nehrkorff J, Waldmann O, Anson CE, Powell AK (2009) *Chem Eur J* 15:7413–7422
6. Milios CJ, Inglis R, Bagai R, Wernsdorfer W, Collins A, Moggach S, Parsons S, Perlepes SP, Christou G, Brechin EK (2007) *Chem Commun* 43:3476–3478
7. Milios CJ, Inglis R, Vinslava A, Bagai R, Wernsdorfer W, Parsons S, Perlepes SP, Christou G, Brechin EK (2007) *J Am Chem Soc* 129:12505–12511
8. Nemeš I, Herchel R, Machata M, Travnicek Z (2017) *New J Chem* 41:11258–11267
9. Radu I, Kravtsov VC, Ostrovsky SM, Reu OS, Kramer K, Decurtins S, Liu S-X, Klokishner SI, Baca SG (2017) *Inorg Chem* 56:2662–2676
10. Wang X-T, Wang B-W, Wang Z-M, Zhang W, Gao S (2008) *Inorg Chim Acta* 361:3895–3902
11. Castro SL, Sun Z, Grant CM, Bollinger JC, Hendrickson DN, Christou G (1998) *J Am Chem Soc* 120:2365–2375
12. Murrie M (2010) *Chem Soc Rev* 39:1986–1995
13. Ako AM, Hewitt IJ, Mereacre V, Clérac R, Wernsdorfer W, Anson CE, Powell AK (2006) *Angew Chem Int Ed* 45:4926–4929
14. Milios CJ, Vinslava A, Wood PA, Parsons S, Wernsdorfer W, Christou G, Perlepes SP, Brechin EK (2007) *J Am Chem Soc* 129:8–9
15. Freedman DE, Harman WH, Harris TD, Long GJ, Chang CJ, Long JR (2010) *J Am Chem Soc* 132:1224–1225
16. Lin C-Y, Guo J-D, Fettinger JC, Nagase S, Grandjean F, Long GJ, Chilton NF, Power PP (2013) *Inorg Chem* 52:13584–13593
17. Lin C-Y, Fettinger JC, Grandjean F, Long GJ, Power PP (2014) *Inorg Chem* 53:9400–9406
18. Yao X-N, Du J-Z, Zhang Y-Q, Leng X-B, Yang M-W, Jiang S-D, Wang Z-X, Ouyang Z-W, Deng L, Wang B-W, Gao S (2017) *J Am Chem Soc* 139:373–380
19. Eichhöfer A, Lan Y, Mereacre V, Bodenstern T, Weigend F (2014) *Inorg Chem* 53:1962–1974
20. Vaidya S, Upadhyay A, Singh SK, Gupta T, Tewary S, Langley SK, Walsh JPS, Murray KS, Rajaraman G, Shanmugam M (2015) *Chem Commun* 51:3739–3742
21. Zadrozny JM, Telser J, Long JR (2013) *Polyhedron* 64:209–217
22. Saber MR, Dunbar KR (2014) *Chem Commun* 50:12266–12269

23. Vaidya S, Singh SK, Shukla P, Ansari K, Rajaraman G, Shanmugam M (2017) *Chem Eur J* 23:9546–9559
24. Pavlov AA, Savkina SA, Belov AS, Nelyubina YV, Efimov NN, Voloshin YZ, Novikov VV (2017) *Inorg Chem* 56:6943–6951
25. Zhu Y-Y, Cui C, Zhang Y-Q, Jia J-H, Guo X, Gao C, Qian K, Jiang S-D, Wang B-W, Wang Z-M, Gao S (2013) *Chem Sci* 4:1802–1806
26. Jurca T, Farghal A, Lin P-H, Korobkov I, Murugesu M, Richeson DS (2011) *J Am Chem Soc* 133:15814–15817
27. Maganas D, Sottini S, Kyritsis P, Groenen EJJ, Neese F (2011) *Inorg Chem* 50:8741–8754
28. Vaidya S, Shukla P, Tripathi S, Rivière E, Mallah T, Rajaraman G, Shanmugam M (2018) *Inorg Chem* 57:3371–3386
29. Perfetti M (2017) *Coord Chem Rev* 348:171–186
30. Basler R, Boskovic C, Chaboussant G, Güdel HU, Murrie M, Ochsenbein ST, Sieber A (2003) *ChemPhysChem* 4:910–926
31. Baltzer P, Furrer A, Hulliger J, Stebler A (1988) *Inorg Chem* 27:1543–1548
32. Novikov VV, Pavlov AA, Belov AS, Vologzhanina AV, Savitsky A, Voloshin YZ (2014) *J Phys Chem Lett* 5:3799–3803
33. Idešicová M, Titiš J, Krzystek J, Boča R (2013) *Inorg Chem* 52:9409–9417
34. Suturina EA, Nehrkorn J, Zadrozny JM, Liu J, Atanasov M, Weyhermüller T, Maganas D, Hill S, Schnegg A, Bill E, Long JR, Neese F (2017) *Inorg Chem* 56:3102–3118
35. Deng Y-F, Wang Z, Ouyang Z-W, Yin B, Zheng Z, Zheng Y-Z (2016) *Chem Eur J* 22:14821–14825
36. Zadrozny JM, Long JR (2011) *J Am Chem Soc* 133:20732
37. Suturina EA, Maganas D, Bill E, Atanasov M, Neese F (2015) *Inorg Chem* 54:9948–9961
38. Fataftah MS, Zadrozny JM, Rogers DM, Freedman DE (2014) *Inorg Chem* 53:10716–10721
39. Tu D, Shao D, Yan H, Lu C (2016) *Chem Commun* 52:14326–14329
40. Rechkemmer Y, Breitgoff FD, van der Meer M, Atanasov M, Haki M, Orlita M, Neugebauer P, Neese F, Sarkar B, van Slageren J (2016) *Nat Commun* 7:10467
41. Vaidya S, Tewary S, Singh SK, Langley SK, Murray KS, Lan Y, Wernsdorfer W, Rajaraman G, Shanmugam M (2016) *Inorg Chem* 55:9564–9578
42. Huang W, Liu T, Wu D, Cheng J, Ouyang ZW, Duan C (2013) *Dalton Trans* 42:15326–15331
43. Zadrozny JM, Liu J, Piro NA, Chang CJ, Hill S, Long JR (2012) *Chem Commun* 48:3927–3929
44. Maganas D, Milikisyants S, Rijnbeek JMA, Sottini S, Levesanos N, Kyritsis P, Groenen EJJ (2010) *Inorg Chem* 49:595–605
45. Smolko L, Cernak J, Dusek M, Miklovic J, Titis J, Boca R (2015) *Dalton Trans* 44:17565–17571
46. Smolko L, Cernak J, Dusek M, Titis J, Boca R (2016) *New J Chem* 40:6593–6598
47. Ziegenbalg S, Hornig D, Görls H, Plass W (2016) *Inorg Chem* 55:4047–4058
48. Smolko L, Černák J, Kuchár J, Rajnák C, Titiš J, Boča R (2017) *Eur J Inorg Chem* 2017:3080–3086
49. Yang F, Zhou Q, Zhang Y, Zeng G, Li G, Shi Z, Wang B, Feng S (2013) *Chem Commun* 49:5289–5291
50. Shao D, Zhou Y, Pi Q, Shen F-X, Yang S-R, Zhang S-L, Wang X-Y (2017) *Dalton Trans* 46:9088–9096
51. Carl E, Demeshko S, Meyer F, Stalke D (2015) *Chem Eur J* 21:10109–10115
52. Boča R, Miklovič J, Titiš J (2014) *Inorg Chem* 53:2367–2369
53. García-Monforte MA, Ara I, Martín A, Menjón B, Tomás M, Alonso PJ, Arauzo AB, Martínez JJ, Rillo C (2014) *Inorg Chem* 53:12384–12395
54. Yao X-N, Yang M-W, Xiong J, Liu J-J, Gao C, Meng Y-S, Jiang S-D, Wang B-W, Gao S (2017) *Inorg Chem Front* 4:701–705
55. Brazzolotto D, Gennari M, Yu S, Pécaut J, Rouzières M, Clérac R, Orio M, Duboc C (2016) *Chem Eur J* 22:825–825
56. Doerfer LH, Bautista MT, Lippard SJ (1997) *Inorg Chem* 36:3578–3579

57. Eisenberg R, Dori Z, Gray HB, Ibers JA (1968) *Inorg Chem* 7:741–748
58. Birker PJMWL, Bour JJ, Steggerda JJ (1973) *Inorg Chem* 12:1254–1259
59. Van der Put PJ, Schilperoord AA (1974) *Inorg Chem* 13:2476–2481
60. Baker-Hawkes MJ, Billig E, Gray HB (1966) *J Am Chem Soc* 88:4870–4875
61. Bour JJ, Beurskens PT, Steggarda JJ (1972) *J Chem Soc Chem Commun* 1972:221–222
62. König E, Schnakig R, Kanellakopulos B (1975) *J Chem Phys* 62:3907–3911
63. Ruamps R, Batchelor LJ, Guillot R, Zakhia G, Barra A-L, Wernsdorfer W, Guihery N, Mallah T (2014) *Chem Sci* 5:3418–3424
64. Shao F, Cahier B, Rivière E, Guillot R, Guihéry N, Campbell VE, Mallah T (2017) *Inorg Chem* 56:1104–1111
65. Woods TJ, Ballesteros-Rivas MF, Gómez-Coca S, Ruiz E, Dunbar KR (2016) *J Am Chem Soc* 138:16407–16416
66. Mondal AK, Jover J, Ruiz E, Konar S (2017) *Chem Commun* 53:5338–5341
67. Rajnák C, Titiš J, Fuhr O, Ruben M, Boča R (2014) *Inorg Chem* 53:8200–8202
68. Shao F, Cahier B, Guihery N, Riviere E, Guillot R, Barra A-L, Lan Y, Wernsdorfer W, Campbell VE, Mallah T (2015) *Chem Commun* 51:16475–16478
69. Cahier B, Perfetti M, Zakhia G, Naoufal D, El-Khatib F, Guillot R, Rivière E, Sessoli R, Barra A-L, Guihéry N, Mallah T (2017) *Chem Eur J* 23:3648–3657
70. Mondal AK, Goswami T, Misra A, Konar S (2017) *Inorg Chem* 56:6870–6878
71. Mondal AK, Jover J, Ruiz E, Konar S (2017) *Chem Eur J* 23:12550–12558
72. El-Khatib F, Cahier B, Shao F, López-Jordà M, Guillot R, Rivière E, Hafez H, Saad Z, Girerd J-J, Guihéry N, Mallah T (2017) *Inorg Chem* 56:4601–4608
73. Habib F, Luca OR, Vieru V, Shiddiq M, Korobkov I, Gorelsky SI, Takase MK, Chibotaru LF, Hill S, Crabtree RH, Murugesu M (2013) *Angew Chem Int Ed* 52:11290–11293
74. Boča R, Dlháň LU, Linert W, Ehrenberg H, Fuess H, Haase W (1999) *Chem Phys Lett* 307:359–366
75. Rajnák C, Titiš J, Šalitraš I, Boča R, Fuhr O, Ruben M (2013) *Polyhedron* 65:122–128
76. Vallejo J, Castro I, Ruiz-García R, Cano J, Julve M, Lloret F, De Munno G, Wernsdorfer W, Pardo E (2012) *J Am Chem Soc* 134:15704–15707
77. Gómez-Coca S, Urtizberea A, Cremades E, Alonso PJ, Camón A, Ruiz E, Luis F (2014) *Nat Commun* 5:4300
78. Herchel R, Váhovská L, Potočník I, Trávníček Z (2014) *Inorg Chem* 53:5896–5898
79. Chandrasekhar V, Dey A, Mota AJ, Colacio E (2013) *Inorg Chem* 52:4554–4561
80. Shinji K, Satoru K, Motohiro N, Noboru K (2006) *Bull Chem Soc Jpn* 79:1372–1382
81. Karasawa S, Zhou G, Morikawa H, Koga N (2003) *J Am Chem Soc* 125:13676
82. Zhang Y-Z, Gomez-Coca S, Brown AJ, Saber MR, Zhang X, Dunbar KR (2016) *Chem Sci* 7:6519–6527
83. Vallejo J, Fortea-Perez FR, Pardo E, Benmansour S, Castro I, Krzystek J, Armentano D, Cano J (2016) *Chem Sci* 7:2286–2293
84. Müller A, Bhattacharyya RG, Königerahlborn E, Sharma RC, Rittner W, Neumann A, Henkel G, Krebs B (1979) *Inorg Chim Acta* 37:L493
85. Campo J, Falvello LR, Forcén-Vázquez E, Sáenz de Pipaón C, Palacio F, Tomás M (2016) *Dalton Trans* 45:16764–16768
86. Wu Y-L, Guo F-S, Yang G-P, Wang L, Jin J-C, Zhou X, Zhang W-Y, Wang Y-Y (2016) *Inorg Chem* 55:6592–6596
87. Świtlicka-Olszewska A, Palion-Gazda J, Klemens T, Machura B, Vallejo J, Cano J, Lloret F, Julve M (2016) *Dalton Trans* 45:10181–10193
88. Bartolome E, Alonso PJ, Arauzo A, Luzon J, Bartolome J, Racles C, Turta C (2012) *Dalton Trans* 41:10382–10389
89. Chen L, Wang J, Wei J-M, Wernsdorfer W, Chen X-T, Zhang Y-Q, Song Y, Xue Z-L (2014) *J Am Chem Soc* 136:12213–12216
90. Palić AV, Korchagin DV, Yureva EA, Akimov AV, Misochko WY, Aldoshin SM, Shilov GV, Talantsev AD, Morgunov RB, Tsukerblat BS (2016) *Inorg Chem* 55:9696–9706



# Cobalt(II)/(III)–Lanthanide(III) Complexes as Molecular Magnets



Atanu Dey, Shalini Tripathi, Maheswaran Shanmugam,  
Ramakirushnan Suriya Narayanan, and Vadapalli Chandrasekhar

## Contents

1	Introduction .....	78
2	Hybrid Co–4f Complexes as SMMs .....	81
2.1	Dinuclear Complexes .....	81
2.2	Trinuclear Cobalt–Lanthanide SMMs .....	84
2.3	Tetranuclear Cobalt–Lanthanide SMMs .....	85
2.4	Higher Nuclearity Cobalt–Lanthanide SMMs .....	93
3	Summary .....	97
	References .....	97

**Abstract** This chapter deals with single-molecule magnets (SMMs) obtained from heterometallic Co(II)/4f complexes. The design principles involved in building various types of heterometallic complexes are discussed along with their magnetic properties. A large group of hybrid Co(II)/4f complexes of varying nuclearity are discussed. Some examples of Co(III)/4f complexes are also presented.

**Keywords** Cluster complexes · Cobalt/lanthanide complexes · Lanthanides · Magnetism · Single molecule magnet · Slow relaxation of magnetization

---

The original version of this chapter was revised. A correction to this chapter is available at DOI [10.1007/3418\\_2019\\_33](https://doi.org/10.1007/3418_2019_33).

All the authors contributed equally to this work.

---

A. Dey and R. S. Narayanan

Tata Institute of Fundamental Research Hyderabad, Hyderabad, India

S. Tripathi and M. Shanmugam

Department of Chemistry, Indian Institute of Technology Bombay, Mumbai, Maharashtra, India

V. Chandrasekhar (✉)

Tata Institute of Fundamental Research Hyderabad, Hyderabad, India

Department of Chemistry, Indian Institute of Technology Kanpur, Kanpur, Uttar Pradesh, India

e-mail: [vc@tifrh.res.in](mailto:vc@tifrh.res.in); [vc@iitk.ac.in](mailto:vc@iitk.ac.in)

## 1 Introduction

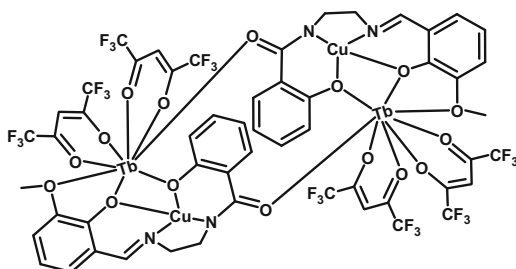
In the previous chapter while discussing the complexes containing Co(II)-based SMMs/SIMs, it was noted that the ground state  $S$  value is fixed, and the  $D$  value is the sole parameter to fine-tune the magnetic behavior. Because of factors such as (1) the small and fixed “ $S$ ” value associated with Co(II) ions, (2) quenching of orbital angular momentum due to the ligand field, (3) ligand-induced structural distortion, and (4) nuclear hyperfine interaction, faster relaxation mechanism such as QTM can become operative in homometallic Co(II) complexes [1–3]. To some extent, these factors can be overcome by employing multidentate ligand or compartmental ligand to link Co(II) along with other suitable lanthanide ions simultaneously in a heterometallic ensemble. This will be the focus of this chapter.

The first lanthanide-based SMM in 2003, a mononuclear  $[\text{Pc}_2\text{Tb}]$  complex, phthalocyanine (Pc), has attracted a great interest toward the use of lanthanide ions in SMMs [4]. Accordingly, the first heterometallic SMM, a  $\text{Cu}_2\text{Tb}_2$  complex, was reported in 2004 [5]. The heterometallic tetrameric complex was isolated by the reaction of  $\text{K}[\text{CuL}]$  and  $[\text{Tb}^{\text{III}}(\text{hfac})_3(\text{H}_2\text{O})_2]$  (**1**) where  $\text{H}_3\text{L} = 1$ -(2-hydroxybenzamido)-2-(2-hydroxy-3-methoxy-benzylideneamino)-ethane. The crystal structure of the complex with molecular formula  $[\text{Cu}^{\text{II}}\text{LTb}^{\text{III}}(\text{hfac})_2]_2$  is shown in Fig. 1. Instead of the  $[\text{CuL}]^-$  precursor, if the analogous  $[\text{NiL}]^-$  precursor  $[\text{Ni}^{\text{II}}\text{LTb}^{\text{III}}(\text{hfac})_2]_2$  (**2**) is used, where the paramagnetic Cu(II) ion was replaced with diamagnetic  $\text{Ni}^{\text{II}}$  affording an opportunity to compare the role of Cu(II) ion in **1**.

Complex **1** shows ferromagnetic interaction between the  $\text{Cu}^{\text{II}}$  and  $\text{Tb}^{\text{III}}$  ions with a positive Weiss constant ( $\theta = +14.3$  K) as originally proposed by Gatteschi and co-workers [6]. Complex **1** showed SMM behavior [ $(\tau_0) = 2.7 \times 10^{-8}$  s;  $U_{\text{eff}} = \Delta/k_{\text{B}} = 21$  K;  $T_{\text{B}} = 1.2$  K]. However, hysteresis was not observed at the measured temperatures, viz., above 2 K.

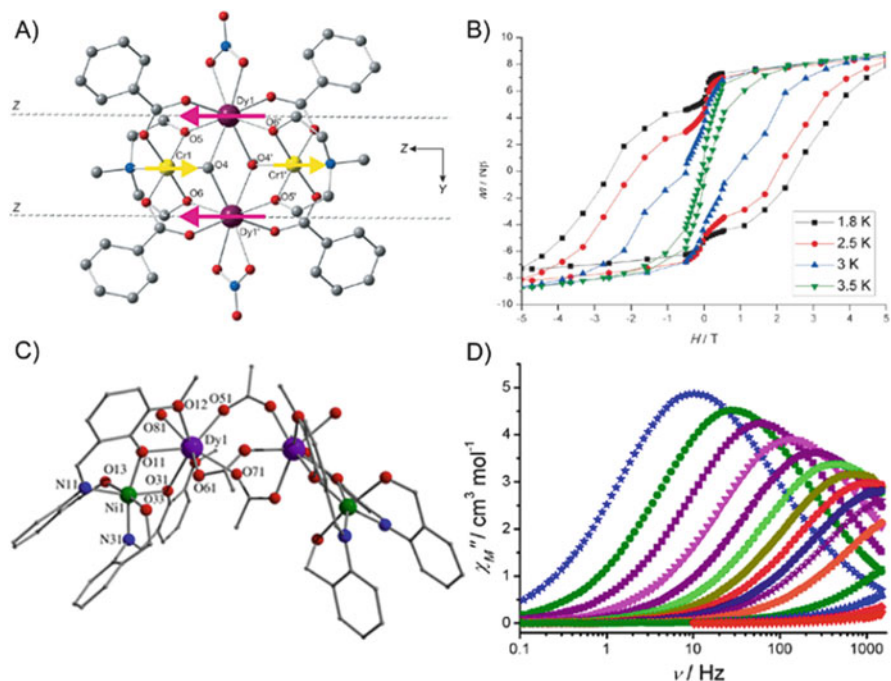
Under similar condition, complex **2** reveals a simple paramagnetic behavior that may be due to the magnetic anisotropy and/or intermolecular antiferromagnetic interaction and/or dipolar interaction. AC susceptibility measurement of **2** does not display  $\chi_M''$  signal which may be due to the fast QTM at zero magnetic field. Possibly the presence of ferromagnetic exchange interaction between Cu(II) and Tb(III) ion is likely the reason for the observed SMM behavior in **1** ( $H_{\text{DC}} = 0$ ).

**Fig. 1** Line diagram of **1**



Based on these early forays, the advantage of using 3d–4f heterometallic complexes were reasoned as: (1) relatively high spin ground state can be achieved using less number of metal ions compared to larger polynuclear 3d metal complexes, and (2) anisotropy can be harvested through the lanthanide ions by exploiting its unquenched orbital angular momentum.

Presence of QTM is a major problem in incorporating lanthanide ion although the single-ion magnetic anisotropy of these ions is generally large as compared to the 3d metal ions. Due to this fact, the blocking temperature remains well below 5 K in majority of the 3d–4f metal complexes [7]. However, this disadvantage can be minimized by enhancing the exchange interaction between 3d and 4f ions. This phenomenon was first reported by Murray and co-workers by enhancing the exchange interaction between the Cr(III) and Dy(III) ion in a heterometallic  $[\text{Cr}^{\text{III}}_2\text{Ln}^{\text{III}}_2(\text{OMe})_2(\text{mdea})_2(\text{O}_2\text{CPh})_4(\text{NO}_3)_2]$  (**3**),  $\text{Ln}^{\text{III}} = \text{Pr}, \text{Nd}, \text{Gd}, \text{Tb}, \text{Ho}, \text{and Er}$  and  $\text{mdea} = N$ -methyl diethanolamino(2–) butterfly complex where QTM is significantly reduced/quenched which facilitate in enhancing the blocking temperature [8, 9]. Due to the arrest/quenching of magnetization, opening of a hysteresis loop is generally observed unlike in transition metal clusters (Fig. 2). Similarly, heterometallic  $\text{Ni}_2\text{Dy}_2$ (**4**) complex is found to show a similar behavior, where



**Fig. 2** (a) Ball and stick presentation of **3**. (b) Magnetization vs field plot with a sweep rate of  $0.003 \text{ Ts}^{-1}$ . Adapted from *Angew. Chem. Int. Ed.* **2013**, 52, 12014 with permission from John Wiley and Sons. (c) Ball and stick presentation of **4**. (d) Frequency-dependent AC susceptibility measurements performed on polycrystalline sample of **4**. Adapted from *Chem. Eur. J.* **2014**, 20, 14235 with permission from John Wiley and Sons

QTM is found to be suppressed completely resulting in a zero-field SMM [10]. The anisotropic barrier extracted for the later complex ( $19 \text{ cm}^{-1}$ ) in zero applied DC magnetic field, and the one estimated in the presence of external magnetic field ( $18.9 \text{ cm}^{-1}$ ) is found out to be similar indicating that QTM is efficiently suppressed. In both cases ( $\text{Cr}_2\text{Dy}_2$  and  $\text{Ni}_2\text{Dy}_2$ ), quenching of QTM is attributed to the presence of enhanced exchange interaction compared to the other 3d–4f complexes reported in the literature. Further, it has been proposed that a larger  $\angle\text{Ni-O-Dy}$  angle and smaller distortion in the dihedral plane formed by Ni–O–Dy–O are the recipe for increasing the ferromagnetic exchange.

The presence of 3d ion in near vicinity of Ln(III) ion environment is not the only option, but paramagnetic bridging ligands can play a crucial role in increasing the exchange interaction. This has been elegantly proven in a series of  $\text{Ln}_2$  dimers linked through unusual  $\text{N}_2^{3-}$  radical ligand (with a blocking temperature of 14 K for the  $\text{Tb}_2$  analogue) [11, 12].

Since several 3d–4f metal complexes are known in the literature, we will restrict to Co(II)/4f SMM reported in the literature in this chapter. We will also discuss some examples of Co(III)/4f complexes. Before this a brief introduction on the nature of interaction between the 3d and 4f metal ions is in order.

To ascertain qualitatively the nature of exchange interaction between the 3d and the 4f metal ion, Andruh et al. proposed an empirical approach by considering Ni–Ln (Ln = Dy or Pr) dimeric complexes [13]. In such complexes, the total magnetic moment experimentally observed is the combination of magnetic moment contribution from individual metal ions (e.g., nickel and Ln(III) ion) along with the exchange couple state. Hence, by subtracting the individual metal ion contribution from the total magnetic moment, the masked nature of interaction will be clearly reflected by plotting the temperature-dependent  $\Delta\chi_{\text{M}}T$  value.

The empirical equation is

$$\Delta\chi_{\text{M}}T = \chi_{\text{M}}T_{\text{Ni,Dy}} - \chi_{\text{M}}T_{\text{Zn,Dy}} - \chi_{\text{M}}T_{\text{Ni,Lu}} \approx J_{\text{Ni-Dy}}$$

For example, the presence of ferromagnetic exchange interaction observed between Ni(II) and Dy(III) complexes in  $\text{Ni}_2\text{Dy}_2$  tetramer is revealed using the empirical equation shown above.

For a system with ferromagnetic interaction, the  $\Delta\chi_{\text{M}}T$  plot will raise at low temperature in positive direction, while for an antiferromagnetic interaction, the plot will plunge into negative  $\Delta\chi_{\text{M}}T$  value. The general trend noticed in case of Cu(II)–Ln or Ni(II)–Ln complexes are: (1) a ferromagnetic exchange interaction is observed if Ln(III) valence shell contains  $\geq f^7$  electrons, and (2) an antiferromagnetic coupling exists if Ln(III) valence shell electron become less than 7. This scenario is witnessed in many such complexes, which is very well exemplified [13]. We have noticed recently that a similar trend is also observed in Co(II) containing 4f complexes. Hence, targeting Co(II)–Ln(III) (where  $\text{Ln}^{\text{III}} \geq f^7$ ) is an ideal approach to reveal a new generation of SMMs. Accordingly, various Co(II)/(III)–Ln(III) SMMs reported in literature have been overviewed below.

## 2 Hybrid Co–4f Complexes as SMMs

This section deals with various examples on heterometallic Co(II)/Ln(III) and Co(III)/Ln(III) complexes. In the case of Co(III)/Ln(III) complexes, the magnetic properties are entirely due to the lanthanide ion.

Based on the above insight, several heterometallic 3d/4f complexes were investigated [7, 14–23]. The first Co/Ln SMM,  $[\text{L}_2\text{Co}^{\text{II}}\text{Gd}][\text{NO}_3]$  (**5**), was reported by Chandrasekhar and co-workers. The complex was assembled using a phosphorus-based tris-hydrazone ligand ( $\text{LH}_3$ ) and contains a linear array of metal ions [24] (Fig. 3).

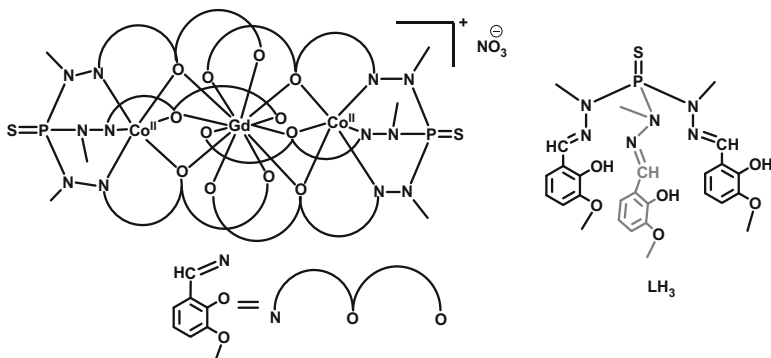
The zero-field SMM behavior of this complex was confirmed by AC susceptibility measurements (Fig. 4):  $U_{\text{eff}} = 27.2$  K and  $\tau_0 = 1.7 \times 10^{-7}$  s.

Several other structurally analogous trinuclear complexes  $\{[\text{L}_2\text{Co}^{\text{II}}\text{Ln}][\text{X}]\}$  [Ln = Eu, X = Cl; Ln = Tb, Dy and Ho, X =  $\text{NO}_3$ ] were also prepared, all of which except the  $\text{Eu}^{\text{III}}$  analogue were shown to be SMMs [25]. Table 1 summarizes the magnetic data for all of these complexes.

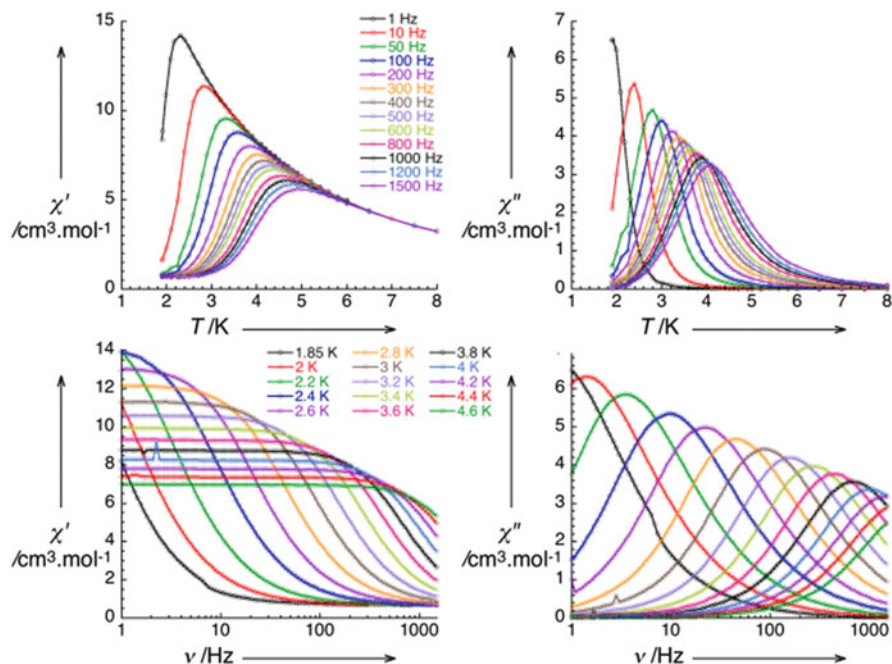
Following these first examples, there have been several studies on such heterometallic Co(II)/Ln(III) and Co(III)/Ln(III) complexes. In the subsequent sections, we will discuss these based on the nuclearity of the complexes. Only such complexes will be discussed where there has been a demonstration of SMM behavior.

### 2.1 Dinuclear Complexes

The preparation of the heterometallic complexes discussed in this and subsequent sections is dependent on the use of the so-called compartmental ligands which have specificity toward either the transition metal ion or the lanthanide metal ion.



**Fig. 3** Line diagram of **5** along with the ligand



**Fig. 4** Temperature (top) and frequency (bottom) dependence of the in-phase and out-of-phase AC susceptibility measurements under zero applied DC field. Reprinted with permission from (*Inorg Chem.* **2009**, *48*, 1148–1157), Copyright (2009) American Chemical Society

**Table 1** Magnetic data for  $[\text{L}_2\text{Co}^{\text{II}}\text{Ln}]^+$  SMMs

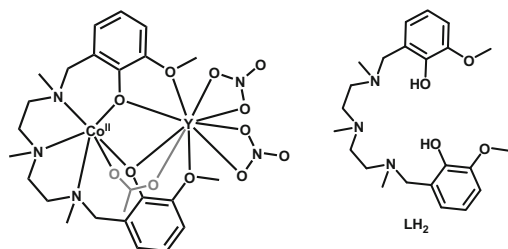
Complex	$U_{\text{eff}}$ (K), $\tau_0$ (s) at $H_{\text{DC}} = 0$	$U_{\text{eff}}$ (K), $\tau_0$ (s) at $H_{\text{DC}} \neq 0$
$[\text{L}_2\text{Co}^{\text{II}}_2\text{Gd}][\text{NO}_3]$ ( <b>5</b> )	27.2, $1.7 \times 10^{-7}$	27.4, $1.5 \times 10^{-7}$ , 1,000 Oe
$[\text{L}_2\text{Co}^{\text{II}}_2\text{Tb}][\text{NO}_3]$ ( <b>6</b> )	18.9, $5.5 \times 10^{-6}$	25.8, $3.7 \times 10^{-6}$ , 1,500 Oe
$[\text{L}_2\text{Co}^{\text{II}}_2\text{Dy}][\text{NO}_3]$ ( <b>7</b> )	14.2, $5.1 \times 10^{-6}$	–
$[\text{L}_2\text{Co}^{\text{II}}_2\text{Ho}][\text{NO}_3]$ ( <b>8</b> )	8, $13 \times 10^{-5}$	–

A cyanido-bridged complex,  $[\{\text{Dy}^{\text{III}}(3\text{-OHpy})_2(\text{H}_2\text{O})_4\}[\text{Co}^{\text{III}}(\text{CN})_6]]$  (**9**), was reported by the self-assembly reaction involving  $\text{Dy}^{\text{III}}$ –3-hydroxypyridine (3-OHpy) complexes with hexacyanidocobaltate(III). This complex, which can be considered as single-ion magnet, shows SMM behavior with a high  $U_{\text{eff}}$  of  $266 \text{ cm}^{-1}$  ( $\approx 385 \text{ K}$ ) and a  $\tau_0 = 3.2 \times 10^{-11} \text{ s}$  above 23 K at  $H_{\text{DC}} = 0 \text{ Oe}$ . Moreover, magnetization hysteresis loops are observed below 6 K with a field sweep rate of  $10 \text{ Oe s}^{-1}$  [26].

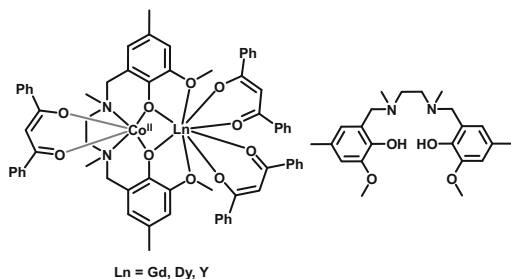
In contrast to the above, a  $\text{Co}^{\text{II}}/\text{Y}^{\text{III}}$  complex,  $[\text{Co}^{\text{II}}(\mu\text{-L})(\mu\text{-OAc})\text{Y}(\text{NO}_3)_2]$  (**10**), was prepared using a compartmental ligand  $N,N',N''$ -trimethyl- $N,N''$ -bis(2-hydroxy-3-methoxy-5-methylbenzyl)diethylenetriamine ( $\text{H}_2\text{L}$ ) [27] (Fig. 5).

Although these complexes do not show zero-field SMM behavior, AC measurements at  $H_{\text{DC}} = 1,000 \text{ Oe}$  revealed them to be SMMs. An effort was made to

**Fig. 5** Line diagram of the complex **10** along with the ligand



**Fig. 6** Line diagram of complexes **11–13** along with the ligand



modulate the structural features by varying the bridging ligand which did not result in any significant change in the magnetic properties. An interesting aspect of these complexes is that all of them have been shown to have a positive  $D$  and in spite of this they exhibit a field-induced SMM behavior, rather intriguingly [28]. Rationale for the observation of field-induced slow relaxation of magnetization with easy plane anisotropy was explained in the previous chapter.

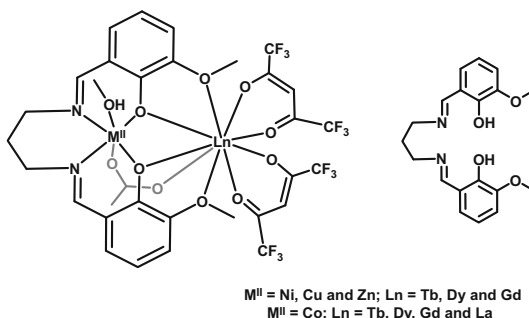
Another family of dinuclear Co–Ln complexes,  $[\text{Co}^{\text{II}}\text{Ln}^{\text{III}}(\text{L})(\text{DBM})_3]$  [ $\text{Ln} = \text{Y}$  (**11**),  $\text{Dy}$  (**12**) and  $\text{Gd}$  (**13**)], is known; the ligands used were  $N,N'$ -dimethyl- $N,N'$ -(2-hydroxy-3-methoxy-5-methyl-benzyl)ethylenediamine ( $\text{LH}_2$ ) and the anion of 1,3-diphenyl-propane-1,3-dione ( $\text{DBM}^-$ ) [29] (Fig. 6).

These complexes also reveal a positive  $D$  ( $S = 3/2$ ,  $g = 2.39$ ,  $D = 10.3 \text{ cm}^{-1}$  and  $E = 4 \times 10^{-4} \text{ cm}^{-1}$  for  $\text{Co}^{\text{II}}\text{–Y}$  analogue); the latter reveals a field-induced single-molecule magnet (SMM) behavior (Fig. 7).

$\text{M}^{\text{II}}\text{–Ln}$  binuclear complexes,  $[\text{M}^{\text{II}}(3\text{-MeOsalt})_2(\text{MeOH})(\text{OAc})\text{Ln}(\text{hfac})_2]$  ( $\text{M}^{\text{II}} = \text{Co}, \text{Ni}, \text{Cu}$  and  $\text{Zn}$ ;  $\text{Ln} = \text{Gd}^{\text{III}}, \text{Tb}^{\text{III}}, \text{Dy}^{\text{III}}, \text{La}^{\text{III}}$ ) were prepared by using  $N,N'$ -bis(3-methoxy-2-oxybenzylidene)-1,3-propanediaminato (3-MeOsalt) and hexafluoroacetylacetonato (hfac) [30]. The  $\text{M}^{\text{II}}\text{–Ln}$  magnetic interactions are ferromagnetic when  $\text{M}^{\text{II}} = (\text{Cu}^{\text{II}}, \text{Ni}^{\text{II}}, \text{and } \text{Co}^{\text{II}})$  and  $\text{Ln} = (\text{Gd}^{\text{III}}, \text{Tb}^{\text{III}}, \text{and } \text{Dy}^{\text{III}})$ . The  $D$  value was found to be positive for the  $\text{Co}^{\text{II}}/\text{La}$  analogue. These complexes however did not display zero-field SMM behavior.

Table 2 summarizes the magnetic data for some dinuclear Co(II)/Ln(III) complexes.

**Fig. 7** Line diagram of complexes **14** and **15** and the corresponding ligand



**Table 2** Magnetic properties of dinuclear [Co–Ln] SMMs

Molecular formula <sup>a</sup>	$U_{\text{eff}}$ (K), $H_{\text{DC}}$ (Oe)	$\tau_0$ (s)	Ref.
[Co <sup>II</sup> Dy(hfac) <sub>3</sub> (hfac) <sub>2</sub> (NIT-3py) <sub>2</sub> ] ( <b>16</b> )	3.61, 2000	$3.09 \times 10^{-6b}$	[31]
[Co <sup>II</sup> Y <sup>III</sup> ( $\mu$ -L)( $\mu$ -NO <sub>3</sub> )(NO <sub>3</sub> ) <sub>2</sub> ] ( <b>17</b> )	23.9	$1.5 \times 10^{-6}$	[28]
[Co <sup>II</sup> Y <sup>III</sup> ( $\mu$ -L)( $\mu$ -OAc)(NO <sub>3</sub> ) <sub>2</sub> ] ( <b>10</b> )	27.1	$4.05 \times 10^{-7}$	[27]
[Co <sup>II</sup> Tb(3-MeOsaltn)(MeOH)(OAc)(hfac) <sub>2</sub> ] ( <b>18</b> )	17, 1,000	$6.1 \times 10^{-8}$	[30]
[Ni <sup>II</sup> Tb(3-MeOsaltn)(MeOH)(OAc)(hfac) <sub>2</sub> ] ( <b>19</b> )	14.9, 1,000	$2.1 \times 10^{-7}$	[30]
[Co <sup>II</sup> Dy(HL <sup>SB</sup> )(AcO) <sub>3</sub> (H <sub>2</sub> O) <sub>3</sub> ·(AcO) ( <b>20</b> )	113, 2,000	$7.0 \times 10^{-9}$	[32]
Co <sup>III</sup> Dy <sup>I</sup> ( $\mu$ -OAc) <sub>2</sub> (NO <sub>3</sub> ) <sub>2</sub> ] ( <b>21</b> )	17.6, 1,000	$2.53 \times 10^{-6}$	[33]
	25.9, 2,000	$4.67 \times 10^{-7}$	
	29.5, 3,000	$1.14 \times 10^{-7}$	

<sup>a</sup>NIT-3py 2-(3-pyridyl)-4,4,5,5-tetramethylimidazoline-1-oxyl-3-oxide, hfac hexafluoroacetylacetonate, SB Schiff base condensation between 2-hydroxy-1,3-diaminopropane and *o*-vanillin,  $L^I H_2$  *N,N'*-ethylenebis(3-ethoxysalicylalimine),  $H_2L$  *N,N',N''*-trimethyl-*N,N,N''*-bis(2-hydroxy-3-methoxy-5-methylbenzyl)diethylenetriamine

<sup>b</sup> $\ln(\chi''/\chi') = \ln(\omega\tau_0) + \Delta_{\text{eff}}/k_B T$  [34]

## 2.2 Trinuclear Cobalt–Lanthanide SMMs

In contrast to the trinuclear complexes described above involving a phosphorus-supported ligand, another series, [Co<sup>III</sup><sub>2</sub>Dy(L)<sub>2</sub>( $\mu$ -O<sub>2</sub>CCH<sub>3</sub>)<sub>2</sub>(H<sub>2</sub>O)<sub>3</sub>](NO<sub>3</sub>) (**22**) (LH<sub>3</sub> = 2-methoxy-6-[[2-(2-hydroxyethylamino)ethylimino]-methyl]phenol), is known. This complex showed slow relaxation of magnetization at 1,000 Oe applied DC field [( $U/k_B$ ) = 88 K; ( $\tau_0$ ) =  $1.0 \times 10^{-8}$  s] [35] (Fig. 8).

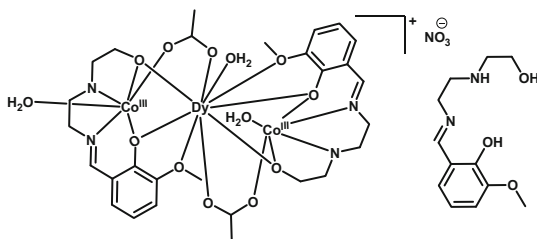
In these examples, the analogous Tb(III) complex (**23**) has a lower  $U_{\text{eff}} = 15.6$  K. It has been suggested that this may be due to the fact that while Dy(III) is a Kramers ion, the integer  $m_j$  level of Tb(III) is likely to trigger the ground state tunneling [36].

[Co<sup>II</sup>Ln<sup>III</sup>] complexes, [Ln<sup>III</sup><sub>2</sub>Co<sup>II</sup>(C<sub>7</sub>H<sub>5</sub>O<sub>2</sub>)<sub>8</sub>] [Ln = Dy (**24**) and Tb (**25**)] containing an in situ generated salicylaldehyde as the ligand, have been prepared [37] (Fig. 9).

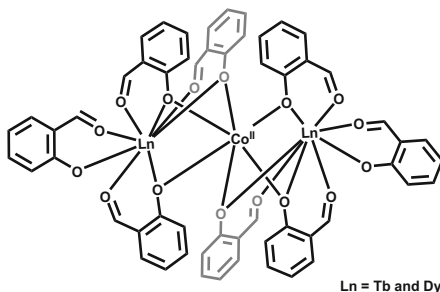
Both **24** and **25** display SMM behavior at zero DC field, although **25** does not show a clear maxima in the  $\chi''$  vs  $T$  plot. For **24**, two relaxation processes could be



**Fig. 8** Line diagram of **22** and the corresponding ligand



**Fig. 9** Line diagram of complexes **24** and **25**



delineated: relaxation at the higher temperature region (above 5 K) being suggested as being associated with the excited Kramer doublets of individual Dy<sup>III</sup> ions, while at the low temperature region (below 5 K), the weak coupling between Co<sup>II</sup> and Dy<sup>III</sup> appears to predominate [38].

Complexes containing Co(III), [Co<sup>III</sup><sub>2</sub>Dy(hmb)<sub>2</sub>(CH<sub>3</sub>O)<sub>2</sub>(OAc)<sub>3</sub>] [Ln = Dy (**26**) and Lu (**27**)], could be prepared using 2-hydroxy-3-methoxybenzylidene benzohydrazide (H<sub>2</sub>hmb) [39] (Fig. 10).

Frequency-dependent AC susceptibility measurements for **26** at 500 Oe applied DC field provide the energy barrier ( $U_{\text{eff}}$ ) = 5.5 K and  $\tau_0 = 2.7 \times 10^{-5}$  s.

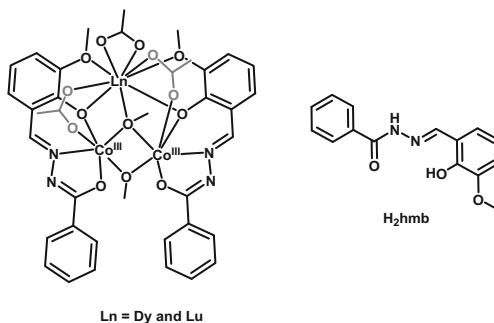
The magnetic properties of trinuclear Co(II)/Ln(III) and Co(III)/Ln(III) SMMs are summarized in Table 3.

### 2.3 Tetranuclear Cobalt–Lanthanide SMMs

A [Co<sup>II</sup><sub>2</sub>Dy<sub>2</sub>(L)<sub>4</sub>(NO<sub>3</sub>)<sub>2</sub>(THF)<sub>2</sub>] (**39**) complex having a butterfly/defect-dicubane topology was assembled using 2-[(2-hydroxy-phenylimino)-methyl]-6-methoxyphenol (H<sub>2</sub>L) [45] (Fig. 11).

Analysis of the frequency-dependent AC measurements in zero DC field revealed the presence of two thermally activated relaxation regimes [( $U_{\text{eff}}$ ) of 11.0 cm<sup>-1</sup> (15.8 K);  $\tau_0 = 7.7 \times 10^{-4}$  s in the temperature range 1.6–8 K and ( $U_{\text{eff}}$ ) of 82.1 cm<sup>-1</sup> (118.12 K);  $\tau_0 = 6.2 \times 10^{-7}$  s between 18 and 22 K]. Interestingly, this complex shows hysteresis below 3 K at a sweep rate of 235 mT s<sup>-1</sup> (Fig. 12). The coercivity of the hysteresis loops increases with decreasing temperature and increasing field

**Fig. 10** Line diagram of complexes **26** and **27** along with the ligand



**Table 3** Magnetic data of trinuclear Co(II)–Ln(III) SMMs

Molecular formula <sup>a</sup>	$U_{\text{eff}}$ (K), $H_{\text{DC}}$ (Oe)	$\tau_0$ (s)	Ref.
$[\text{Co}^{\text{II}}_2\text{Ln}(\text{Hvab})_4(\text{NO}_3)](\text{NO}_3)_2$ Ln = Sm ( <b>28</b> ), Gd ( <b>29</b> ), Tb ( <b>30</b> ) and Dy ( <b>31</b> )	No peak maxima under zero DC field		[40]
$[\text{Co}^{\text{II}}_2\text{Dy}(\text{LH}_3)_4](\text{NO}_3)_3$ ( <b>32</b> )	No peak maxima under zero DC field		[41]
$\{[\text{Co}^{\text{II}}\text{Dy}_2(\text{BPDC})_4(\text{H}_2\text{O})_6] \cdot x\text{H}_2\text{O}\}_n$ ( <b>33</b> )	$3^b, 0$	$10^{-6}$	[42]
$[\text{Co}^{\text{II}}_2\text{GdL}_2^{\text{benzi}}](\text{NO}_3)$ ( <b>34</b> )	21.3, $0^c$	$1.52 \times 10^{-7c}$	[43]
	18.9, 3,000	$2.0 \times 10^{-7}$	
$[\text{Co}^{\text{II}}_2\text{TbL}_2^{\text{benzi}}]\text{NO}_3$ ( <b>35</b> )	14.5, $0^c$	$3.0 \times 10^{-6c}$	[43]
	20.9, 3,000	$3.4 \times 10^{-6}$	
$[\text{Co}^{\text{II}}_2\text{DyL}_2^{\text{benzi}}]\text{NO}_3$ ( <b>36</b> )	$c$	$c$	[43]
$[\text{Co}^{\text{III}}_2\text{Dy}(\text{valdien})_2(\text{OCH}_3)_2(\text{chp})_2](\text{ClO}_4)$ ( <b>37</b> )	71.4, 2,000	$5.6 \times 10^{-6}$	[44]
$[\text{Co}^{\text{III}}_2\text{Tb}(\text{valdien})_2(\text{OCH}_3)_2(\text{chp})_2](\text{ClO}_4)$ ( <b>38</b> )	32.3, 2,000	$2.5 \times 10^{-10}$	[44]

<sup>a</sup> $H_2\text{vab}$  2-[(2-hydroxymethyl-phenylimino)-methyl]-6-methoxyphenol,  $LH_4$  2-(2-hydroxy-3-(hydroxymethyl)-5-methylbenzylideneamino)-2-methylpropane-1,3-diol,  $H_2\text{BPDC}$  2,2'-bipyridine-3,3'-dicarboxylic acid,  $H_2\text{valdien}$   $N1,N3$ -bis(3-methoxysalicylidene)diethylenetriamine,  $H\text{chp}$  6-chloro-2-hydroxypyridine,  $H_3L^{\text{benzi}}$   $N,N',N''$ -tris(2-hydroxy-3-methoxybenzylidene)-2-(aminomethyl)-2-methyl-1,3-propanediamine

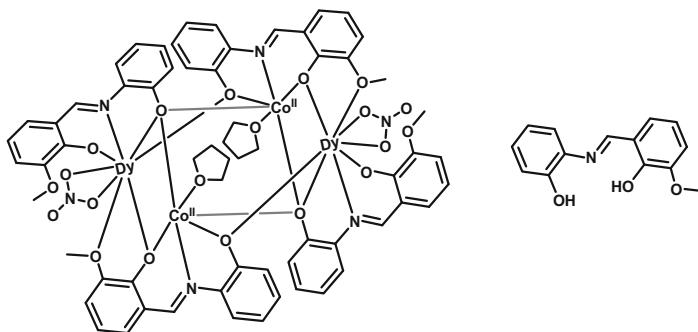
<sup>b</sup> $\ln(\chi_M''/\chi_M')$  =  $\ln(\omega\tau_0) + E_a/k_B T$

<sup>c</sup>Show hysteresis loops below 1.1 K

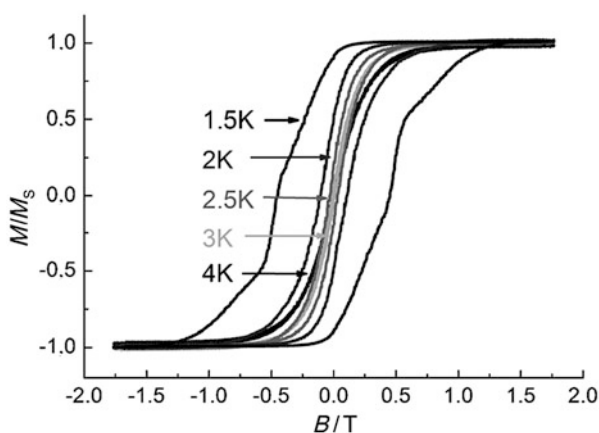
sweep rate. The loops display steplike features below 1.5 K, indicating the possibility of resonant QTM below this temperature.

Replacement of the solvent molecules coordinated with the  $\text{Co}^{2+}$  centers to form  $[\text{Co}^{\text{II}}_2\text{Dy}_2(\text{L})_4(\text{NO}_3)_2(\text{MeOH})_2]$  (**40**) and  $[\text{Co}^{\text{II}}_2\text{Dy}_2(\text{L})_4(\text{NO}_3)_2(\text{DMF})_2]$  (**41**) did not affect the compounds from being SMMs [46]. An analogous  $\text{Zn}_2\text{Dy}_2$  (**42**) complex has also been assembled. A comparison of the magnetic properties in the complexes **39–42** is given in Table 4 (Fig. 13).

A tetranuclear complex  $[\text{Co}^{\text{II}}_2\text{Dy}_2(\text{L})_4(\text{NO}_3)_2(\text{DMF})_2]$  (**43**) possessing a butterfly/defect-dicubane topology such as described above could be obtained by



**Fig. 11** Line diagram of complex **39** along with the ligand



**Fig. 12** Temperature-dependent magnetic hysteresis loops for **39** below 4 K with a sweep rate of  $235 \text{ mT s}^{-1}$ . Adapted from *Angew. Chem. Int. Ed.* **2012**, *51*, 7550–7554 with permission from John Wiley and Sons

the use of (*E*)-2-ethoxy-6-((2-hydroxyphenyl)imino)methyl)phenol ( $\text{H}_2\text{L}$ ) [47] (Fig. 14).

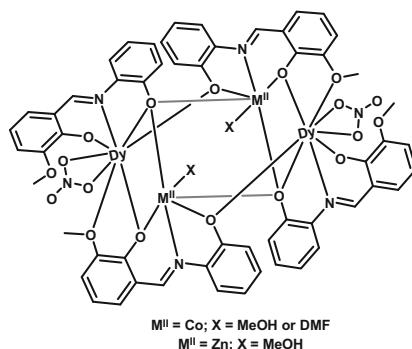
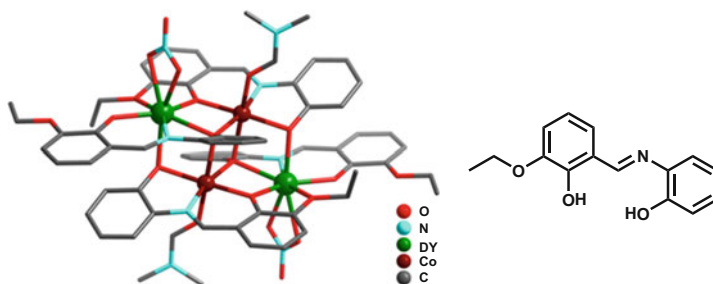
The magnetic properties of the  $[\text{Co}^{\text{II}}\text{Dy}_2]$  analogue and the analogous  $[\text{Dy}_2\text{Zn}_2(\text{L})_4(\text{NO}_3)_2(\text{CH}_3\text{OH})_2]$  (**44**) and  $[\text{Dy}_2\text{Mn}^{\text{III}}_2(\text{L})_4(\text{NO}_3)_2(\text{DMF})_2]$  (**45**) reveal that they are SMMs (Table 5).

The range of ligands that can afford tetranuclear complexes seem to be quite large. Thus, the complexes  $[\text{Co}^{\text{II}}\text{Ln}_2(\text{Hhms})_2(\text{CH}_3\text{COO})_6(\text{CH}_3\text{OH})_2(\text{H}_2\text{O})_2](\text{NO}_3)_2$  [ $\text{Ln} = \text{Dy}^{\text{III}}$  (**46**),  $\text{Gd}^{\text{III}}$  (**47**), and  $\text{Y}^{\text{III}}$  (**48**)] could be prepared by using (2-hydroxy-3-methoxybenzylidene)-semicarbazide ( $\text{H}_2\text{hms}$ ) [48] (Fig. 15).

Complex **46** shows temperature as well as frequency-dependent out-of-phase ( $\chi''$ ) signals ( $\tau_0 = 6.4 \times 10^{-6} \text{ s}$ ;  $U_{\text{eff}} = 6.7 \text{ K}$  at zero DC field;  $\tau_0 = 3.2 \times 10^{-6} \text{ s}$  and  $U_{\text{eff}} = 13.8 \text{ K}$  at  $H_{\text{DC}} = 800 \text{ Oe}$  in the range 2.0–5.5 K). Theoretical CASSCF calculation studies revealed that the Dy–Dy interactions are largely ferromagnetic

**Table 4** Comparison of energy barriers for complexes  $[\text{Co}_2\text{Dy}_2]$  (**39–41**) with the analogous  $[\text{Zn}_2\text{Dy}_2]$  (**42**)

Complexes	THF-coordinated $[\text{Co}_2\text{Dy}_2]$ ( <b>39</b> )	MeOH-coordinated $[\text{Co}_2\text{Dy}_2]$ ( <b>40</b> )	DMF-coordinated $[\text{Co}_2\text{Dy}_2]$ ( <b>41</b> )	$[\text{Zn}_2\text{Dy}_2]$ ( <b>42</b> )
Barrier of $\text{Co}^{\text{II}}-\text{Dy}^{\text{III}}$ (K)	15.8	17.9	17.5	–
Barrier of $\text{Dy}^{\text{III}}$ (K)	118.1	104.8	94.5	140.4

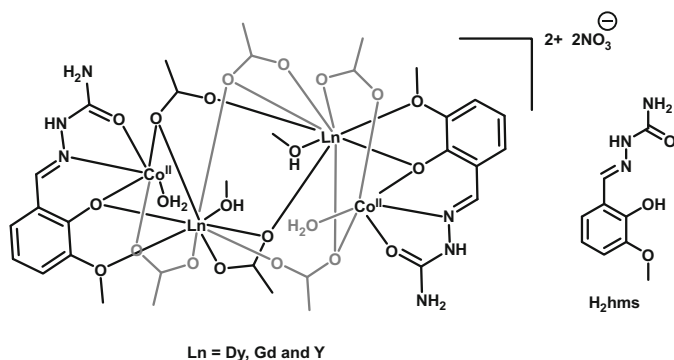
**Fig. 13** Line diagram of complexes **40** and **41****Fig. 14** Molecular structure complex **43** along with the ligand. Adapted from Ref. [47] with permission from The Royal Society of Chemistry

and dominant, while the exchange coupling ( $J_{\text{exch}}$ ) of Dy–Co in  $\{\text{Co}^{\text{II}}_2\text{Dy}^{\text{III}}_2\}$  is antiferromagnetic. Interestingly, in the analogous  $\{\text{Ni}^{\text{II}}_2\text{Dy}^{\text{III}}_2\}$  (**49**) complex, ferromagnetic exchange between  $\text{Ni}^{\text{II}}$  and  $\text{Dy}^{\text{III}}$  ions is found which is more conducive to zero-field single-molecule magnet behavior. The magnetic properties of tetranuclear complexes are summarized in Table 6.

Many tetranuclear complexes could also be assembled by the use of ethanolamine ligands. Thus, the complexes,  $[\text{Co}^{\text{III}}_2\text{Ln}^{\text{III}}_2(\text{OH})_2(\text{bdea})_2(\text{acac})_2(\text{NO}_3)_4]$  [ $\text{Ln} = \text{Tb}$  (**59**) and  $\text{Dy}$  (**60**)] and  $\text{bdeaH}_2 = n$ -butyldiethanolamine) containing two Co(III) ions, were prepared [57] (Fig. 16).

**Table 5** Comparison of the AC magnetic data for  $[\text{Co}^{\text{II}}_2\text{Dy}_2]$  with analogous  $[\text{M}^{\text{II}}_2\text{Dy}_2]$  ( $\text{M} = \text{Mn}$  and  $\text{Zn}$ )

	$\text{Dy}_2\text{Zn}_2$ (1,000 Oe) ( <b>44</b> )	$\text{Dy}_2\text{Mn}_2$ (0 Oe) ( <b>45</b> )	$\text{Dy}_2\text{Co}_2$ (0 Oe) ( <b>43</b> )	$\text{Dy}_2\text{Co}_2$ (1,000 Oe) ( <b>43</b> )
$\tau_0/\text{s}$	$2.35 \times 10^{-6}$	$1 \times 10^{-8}$	$2.67 \times 10^{-6}$	$8.77 \times 10^{-7}$
$U_{\text{eff}}/\text{K}$	115 (79.8 $\text{cm}^{-1}$ )	11 (7.6 $\text{cm}^{-1}$ )	125.1 (86.8 $\text{cm}^{-1}$ )	130 (99.4 $\text{cm}^{-1}$ )

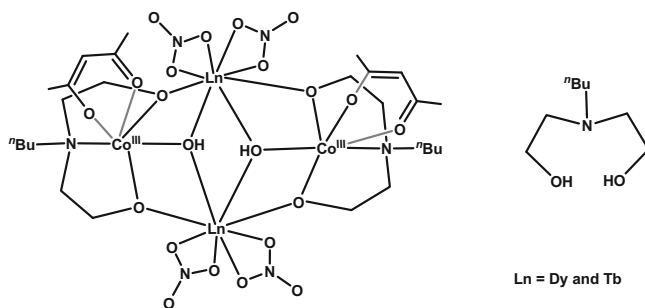
**Fig. 15** Line diagram of complexes **46–48** along with the ligand**Table 6** Magnetic properties of representative tetranuclear  $[\text{Co}_2\text{Ln}_2]$  SMMs

Molecular formula <sup>a</sup>	$U_{\text{eff}}$ (K), $H_{\text{DC}}$ (Oe)	$\tau_0$ (s)	Ref.
$[\text{Co}^{\text{II}}_2\text{Dy}_2(\text{pdmH})_4(\text{Piv})_6]$ ( <b>50</b> )	No maxima under zero DC field	–	[49]
$[\text{Co}^{\text{II}}_2\text{Gd}_2(\text{ovan})_4(\mu_3\text{-OH})_2(\text{NO}_3)_4]$ ( <b>51</b> )	Hysteresis loops observed below 0.6 K	–	[50]
$[\text{Co}^{\text{II}}_2\text{Ln}_2(\text{L}^{\text{bis-OMe}})_2(\text{PhCOO})_6(\text{MeOH})_2]$ [ $\text{Ln} = \text{Tb}$ ( <b>52</b> ) and $\text{Dy}$ ( <b>53</b> )]	No maxima under zero DC field	–	[51]
$[\text{Co}^{\text{II}}_2\text{Dy}_2(\mu_3\text{-OH})_2\text{-}(\text{O}_2\text{C}^t\text{Bu})_{10}]^+(\text{Pr}_2\text{NH}_2)_2$ ( <b>54</b> )	No maxima under zero DC field	–	[52]
$[\text{Co}^{\text{II}}_2\text{Dy}_2(\text{L}^{\text{di-Me}})_2(\text{PhCOO})_2(\text{hfac})_4]$ ( <b>55</b> )	8.8, 0 7.8, 1,000	$2.0 \times 10^{-7}$ $3.9 \times 10^{-7}$	[53]
$[\text{Co}^{\text{III}}\text{Dy}_3(\text{HBpz}_3)_6(\text{dto})_3]$ ( <b>56</b> )	52, 800	$3.6 \times 10^{-8}$	[54]
$[\text{Co}^{\text{III}}_2\text{Dy}_2(\text{L}^{\text{triamine}})_2(\text{CH}_3\text{COO})_4(\text{OH})_2(\text{H}_2\text{O})_2] \cdot (\text{ClO}_4)_2$ ( <b>57</b> )	33.8, 0	$3.73 \times 10^{-6}$	[55]
$[\text{Co}^{\text{III}}_2\text{Dy}_2(2,5\text{-pydc})_6(\text{H}_2\text{O})_4]_n$ ( <b>58</b> )	4.89, 0	$7.56 \times 10^{-8\text{b}}$	[56]

<sup>a</sup>*pdmH* 2,6-pyridinedimethanol, *pivH* pivalic acid, *HBpz*<sub>3</sub><sup>−</sup> hydrotris(pyrazolyl)borate, *dto*<sup>2−</sup> dithiooxalato dianion ligand, *ovan* ortho-vanillin, *L*<sup>bis-OMe</sup>*H*<sub>2</sub> 1,2-bis(2-hydroxy-3-methoxybenzylidene)hydrazine, *H*<sub>2</sub>*L*<sup>di-Me</sup> *N,N'*-dimethyl-*N,N'*-bis(2-hydroxy-3,5-dimethylbenzyl) ethylenediamine, *Hhfac* hexafluoroacetylacetone, *H*<sub>2</sub>*L*<sup>triamine</sup> *N*<sub>1</sub>,*N*<sub>3</sub>-bis(3-methoxysalicylidene) diethylenetriamine ligand, *2,5-pydc* 2,5-pyridine dicarboxylic acid

<sup>b</sup>SCM

Analysis of the AC susceptibility data for **60** allowed the extraction of the following parameters:  $U_{\text{eff}} = 169$  K and  $\tau_0 = 1.47 \times 10^{-7}$  s above 20 K where the relaxation is thermally activated. As the temperature is decreased, a slight curvature appears in the Arrhenius plot of  $\ln(\tau)$  vs  $1/T$  but does not become



**Fig. 16** Line diagram of complexes **59** and **60** along with the ligand

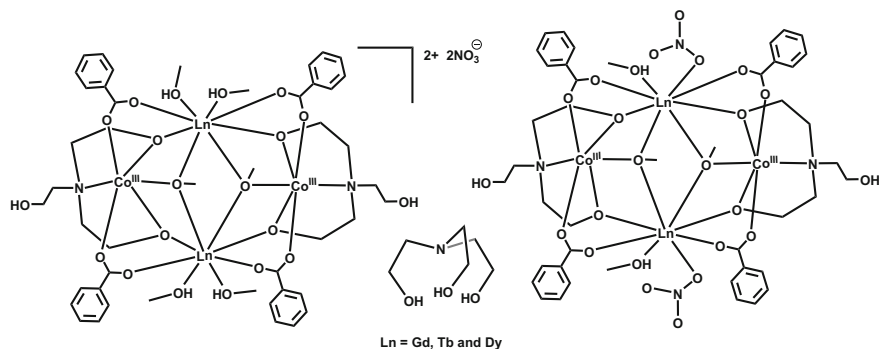
temperature independent at any point, indicating that a pure quantum regime is not observed within the timescale and temperature range of experiment. In contrast to complex **60**, **59** does not show SMM characteristics at zero DC field. However, upon application of 5,000 Oe DC field, a frequency-dependent maxima in the plot of  $\chi_M''$  vs  $T$  is seen. This phenomenon is a common feature for non-Kramers Tb<sup>III</sup>-based complexes and is due to fast zero-field quantum tunneling of the magnetization between the sublevels. The non-Kramers ion generally allows the direct mixing of opposing projections of the ground state angular momentum/spin projections by the crystal field, so that tunneling pathways become readily accessible [58–63].

Other examples of tetranuclear heterometallic complexes  $\{[Ln^{III}_2Co^{III}_2(OMe)_2(teaH)_2(O_2CPh)_4(MeOH)_4](NO_3)_2\}$  [ $Ln = Gd$  (**61**), Tb (**62**) and Dy (**63**)] were prepared using triethanolamine ( $teaH_3$ ). Interestingly two tetranuclear units containing  $[Ln^{III}_2Co^{III}_2(OMe)_2(teaH)_2(O_2CPh)_4(MeOH)_4](NO_3)_2$  and  $[Ln^{III}_2Co^{III}_2(OMe)_2(teaH)_2(O_2CPh)_4(MeOH)_2(NO_3)_2]$  are present within the same crystal [64] (Fig. 17).

AC susceptibility measurements in a zero DC field reveal the SMM behavior for the Dy<sup>III</sup> analogue with the following characteristics above 8.5 K: ( $U_{eff}$ ) of 88.8 K ( $\sim 61\text{ cm}^{-1}$ ) and  $\tau_0 = 5.64 \times 10^{-8}$  s. But below 8.5 K, the Arrhenius plot deviates slightly from linear behavior indicating the existence of QTM. However, applying field up to 1,000 Oe does not change significantly the peak maxima in the  $\chi_M''$  vs  $T$  plot, indicating that QTM is inefficient in this system.

Among other tetranuclear complexes assembled using triethanolamine as the ligand, containing two Co(III), are  $[Dy^{III}_2Co^{III}_2(OMe)_2(teaH)_2(O_2CPh)_4(MeOH)_4](NO_3)_2$  and  $[Dy^{III}_2Co^{III}_2(OMe)_2(teaH)_2(O_2CPh)_4(MeOH)_2(NO_3)_2]$  (**63**),  $[Dy^{III}_2Co^{III}_2(OMe)_2(dea)_2(O_2CPh)_4(MeOH)_4](NO_3)_2$  (**64**),  $[Dy^{III}_2Co^{III}_2(OMe)_2(mdea)_2(O_2CPh)_4(NO_3)_2]$  (**65**),  $[Dy^{III}_2Co^{III}_2(OMe)_2(bdea)_2(O_2CPh)_4(MeOH)_4](NO_3)_2$ , and  $[Dy^{III}_2Co^{III}_2(OMe)_2(bdea)_2(O_2CPh)_4(MeOH)_2(NO_3)_2]$  (**66**) ( $teaH_3$  = triethanolamine,  $deaH_2$  = diethanolamine,  $mdeaH_2$  = *N*-methyldiethanolamine, and  $bdeaH_2$  = *N*-*n*-butyldiethanolamine). The extracted magnetic parameters, from the AC measurements of these complexes, are summarized in Table 7 [65].

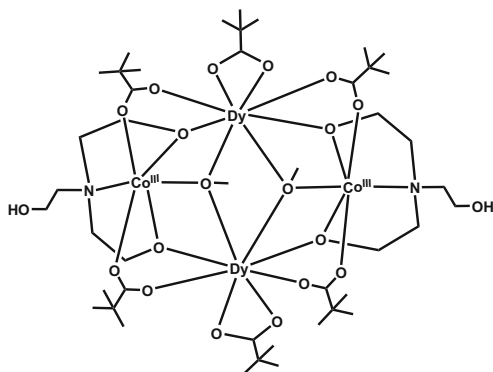
In addition to the aforementioned complexes, complex  $[Co^{III}_2Dy^{III}_2(OMe)_2(teaH)_2(Piv)_6]$  (**67**) can also be prepared using triethanolamine ligand. This complex displays SMM behavior with  $U_{eff} = 51$  K;  $\tau_0 = 6.1 \times 10^{-7}$  s and



**Fig. 17** Line diagrams of complexes **61–63** and the corresponding ligand

**Table 7** Magnetic data for **63–66**

Complex	$U_{\text{eff}}$ ( $\text{cm}^{-1}$ )	Tunneling frequency (Hz)	$\tau_{\text{QTM}}$ (s)	$\tau_0$ (s)	$\alpha$
<b>63</b>	61	<0.1	>1.5	$5.64 \times 10^{-8}$	0.29(4 K)–0.24(10.5 K)
<b>64</b>	72	1.29	0.12	$6.05 \times 10^{-8}$	0.38(1.8 K)–0.28(12 K)
<b>65</b>	55	0.79	0.20	$1.03 \times 10^{-7}$	0.42(1.8 K)–0.30(10.5 K)
<b>66</b>	80	0.34	0.48	$3.38 \times 10^{-8}$	0.26(1.8 K)–0.15(14 K)



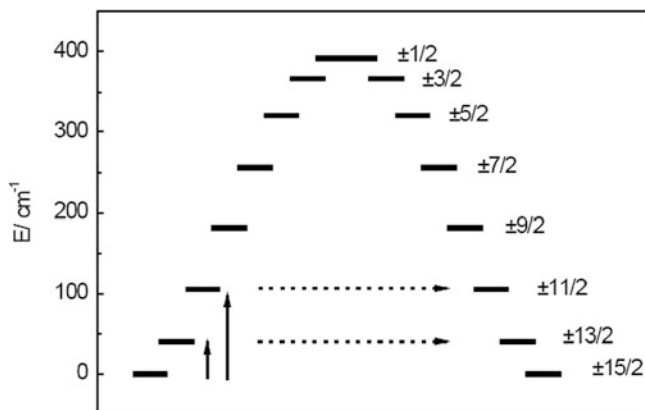
**Fig. 18** Line diagram of complex **67**

$\tau_{\text{QT}} = 7.3$  s in the range 4.5–7.5 K [ $U_{\text{eff}} = 127$  K;  $\tau_0 = 1.2 \times 10^{-9}$  s;  $C_{\text{Ram}} = 1.7 \times 10^{-3}$  in the range of 7.5–9.5 K] [66] (Fig. 18).

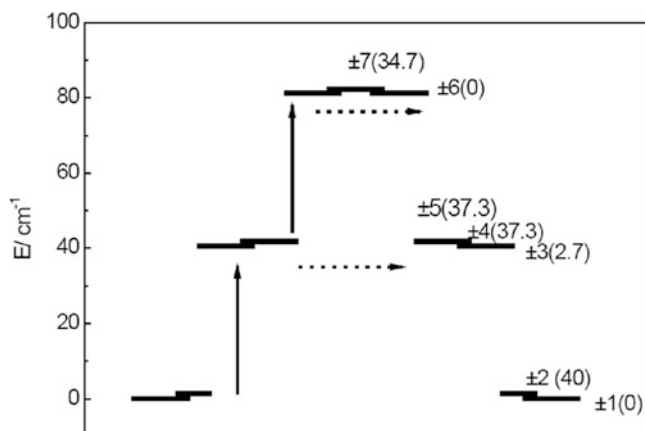
For this complex, the energy level splitting under crystal field of the  $\text{Dy}^{\text{III}}$  ground  $J = 15/2$  state was determined (Fig. 19). The thermal barrier for the fast relaxation pathways through  $m_J = \pm 13/2$  and  $m_J = \pm 11/2$  from ground state should be 39 and  $104 \text{ cm}^{-1}$ . These values compare quite well with the experimental  $U_{\text{eff}} = 35 \text{ cm}^{-1}$  (51 K) and  $88 \text{ cm}^{-1}$  (127 K) values obtained from AC data (Fig. 20).

A summary of magnetization relaxation dynamics for this  $[\text{Co}^{\text{III}}_2\text{Ln}^{\text{III}}_2]$  family (**67–70**) is shown in Table 8 [67].

*N-n*-butyldiethanolamine (bdeaH<sub>2</sub>) and *N*-methyldiethanolamine (mdeaH<sub>2</sub>) were used as ligands for preparing  $[\text{Co}_2^{\text{III}}\text{Dy}_2^{\text{III}}(\text{OMe})_2(\text{O}_2\text{CPh-2-Cl})_4(\text{bdea})_2(\text{NO}_3)_2]$



**Fig. 19** Energy level splitting under crystal field of the Dy<sup>III</sup> ground  $J = 15/2$  state, with crystal field parameters,  $B_0^2 = -2.4 \text{ cm}^{-1}$   $B_0^4 = 2.9 \times 10^{-3} \text{ cm}^{-1}$ . Arrows indicate the suggested relaxation pathways across the barrier. Adapted from Ref. [66] with permission from The Royal Society of Chemistry



**Fig. 20** Energy level splitting under crystal field of the Dy<sup>III</sup> ground  $J = 15/2$  state, with crystal field parameters,  $B_0^2 = -2.4 \text{ cm}^{-1}$   $B_0^4 = 2.9 \times 10^{-3} \text{ cm}^{-1}$  and exchange interaction  $J_{\text{exc}} = -0.046 \text{ cm}^{-1}$ . Arrows indicate the suggested relaxation pathways across the barrier. Doublets  $g_z^{\text{eff}}$  values between parentheses. Adapted from Ref. [66] with permission from The Royal Society of Chemistry

(71),  $[\text{Co}_2^{\text{III}}\text{Dy}_2^{\text{III}}(\text{OMe})_2(\text{O}_2\text{CPh-4-}^t\text{Bu})_4(\text{bdea})_2(\text{NO}_3)(\text{MeOH})_3](\text{NO}_3)$  (72),  $[\text{Co}_2^{\text{III}}\text{Co}^{\text{II}}\text{Ln}^{\text{III}}(\text{OH})(\text{O}_2\text{CPh-4-OH})(\text{bdea})_3(\text{NO}_3)_3(\text{MeOH})]$  [ $\text{Ln} = \text{Dy}$  (73),  $\text{Gd}$  (74)],  $[\text{Co}_2^{\text{III}}\text{Dy}_2^{\text{III}}(\text{OMe})(\text{OH})(\text{O}_2\text{CPh-2-CF}_3)_4(\text{bdea})_2(\text{NO}_3)_2]$  (75), and  $[\text{Co}_2^{\text{III}}\text{Dy}_2^{\text{III}}(\text{mdea})_4(\text{hfac})_3(\text{O}_2\text{CCF}_3)(\text{H}_2\text{O})]$  (76) [68]. A summary of magnetization relaxation dynamics of these complexes (71–76) is enlisted in Table 9.

Similarly a series of SMMs  $[\text{Co}^{\text{III}}_2\text{Ln}^{\text{III}}_2(\mu_3\text{-OH})_2(o\text{-tol})_4(\text{mdea})_2(\text{NO}_3)_2]$  [ $\text{Ln} = \text{Dy}$  (77),  $\text{Tb}$  (78),  $\text{Ho}$  (79)] [69],  $[\text{Dy}^{\text{III}}_2\text{Co}^{\text{III}}_2(\text{OH})_2(\text{teaH})_2(\text{acac})_6]$  (80),  $[\text{Dy}^{\text{III}}_2\text{Co}^{\text{III}}_2(\text{OH})_2(\text{bdea})_2(\text{acac})_6]$  (81), and  $[\text{Dy}^{\text{III}}_2\text{Co}^{\text{III}}_2(\text{OH})_2(\text{eeda})_2(\text{acac})_6]$  (82) ( $\text{teaH}_3 = \text{triethanolamine}$ ,  $\text{bdeaH}_2 = N\text{-}n\text{-butyldiethanolamine}$ ,  $\text{eedaH}_2 = N\text{-}$



**Table 8** Magnetization dynamics data of complexes  $[\text{Co}^{\text{III}}_2\text{Ln}^{\text{III}}_2]$  [67]

Complex	Mechanism	Parameters
$[\text{Co}^{\text{III}}_2\text{Dy}^{\text{III}}_2]$ ( <b>67</b> ) (zero DC field)	Orbach	$\tau_0 = 6.1 \times 10^{-7}$ s; $U_{\text{eff}} = 35$ cm $^{-1}$ ; $\tau_{\text{QT}} = 7.3$ s
	Orbach + Raman	$\tau_0 = 1.2 \times 10^{-9}$ s; $U_{\text{eff}} = 88$ cm $^{-1}$
$[\text{Co}^{\text{III}}_2\text{Ho}^{\text{III}}_2]$ ( <b>68</b> ) (1,500 Oe DC field)	Orbach	$\tau_0 = 6.2 \times 10^{-9}$ s; $U_{\text{eff}} = 30$ cm $^{-1}$
$[\text{Co}^{\text{III}}_2\text{Er}^{\text{III}}_2]$ ( <b>69</b> ) (3,000 Oe DC field)	Raman	$\tau_{\text{QT}}^1 = 5.1 \times 10^{-3}$ s; $C_{\text{Ram}} = 3.5 \times 10^{-2}$ s $^{-1}$ K $^{-7}$ ( $n = 7$ ); $\tau_{\text{QT}}^2 = 0.103$ s
$[\text{Co}^{\text{III}}_2\text{Yb}^{\text{III}}_2]$ ( <b>70</b> ) (3,000 Oe DC field)	Orbach	$\tau_0 = 2.1 \times 10^{-6}$ s; $U_{\text{eff}} = 23$ cm $^{-1}$ ; $\tau_{\text{QT}} = 1.3 \times 10^{-2}$ s

**Table 9** Magnetization relaxation parameters for complexes **71–76**

Complex	AC susceptibility data		
	$U_{\text{eff}}$ (applied field) (cm $^{-1}$ )	$\tau_0$ (s)	$\tau_{\text{QTM}}$ (s)
<b>71</b>	80.4 (0 Oe)	$1.8 \times 10^{-8}$	0.9
<b>72</b>	76.9 and 95.6 (0 Oe)	$3.8 \times 10^{-9}$ and $5.6 \times 10^{-8}$	0.5 and n/a
<b>73</b>	117.4 (1,500 Oe)	$3.4 \times 10^{-7}$	0.3
<b>74</b>	n/a	n/a	n/a
<b>75</b>	88.1 (0 Oe)	$1.4 \times 10^{-8}$	~1.5
<b>76</b>	22.6 (0 Oe)	$1.4 \times 10^{-6}$	0.004

ethyldiethanolamine and acacH = acetylacetonate) [70] are reported. The detailed parameters associated with their SMM behavior are summarized in Table 10 (Fig. 21).

## 2.4 Higher Nuclearity Cobalt–Lanthanide SMMs

In this section we will deal with complexes whose nuclearity is greater than 4. Only representative examples will be discussed. The magnetic data for these complexes are tabulated in Table 11. A hexanuclear complex  $[\text{Dy}_4\text{Co}^{\text{III}}_2(\text{HL}^2)_2(\mu_3\text{-OH})_2(\text{piv})_{10}(\text{OH}_2)_2]$  complex (**86**) was prepared by the use of 2-(2,3 dihydroxypropyliminomethyl)-6-methoxyphenol( $\text{H}_3\text{L}^2$ ) and pivalic acid as ligands. The molecule contains two dimeric Dy(III) sub-units on either side of a dimeric Co(III) motif. Each of the Co(III) centers along with a Dy(III) is involved in a defect cubane structural motif [83] (Fig. 22).

The field dependence of magnetization shows a rapid increase of  $M$  values at lower DC field, indicating the presence of intramolecular ferromagnetic interactions between spin carriers. The Arrhenius plot obtained from the frequency-dependent AC susceptibility measurements provides the signature of SMM with an energy gap ( $U_{\text{eff}}$ ) of 18.4 cm $^{-1}$  (26.47 K) and a pre-exponential factor  $\tau_0 = 8.7 \times 10^{-6}$  s at  $H_{\text{DC}} = 0$ . The Cole–Cole plot provides the  $\alpha$  value within the 0.19–0.13, indicating a single relaxation time is mainly involved and is independent of the temperature.

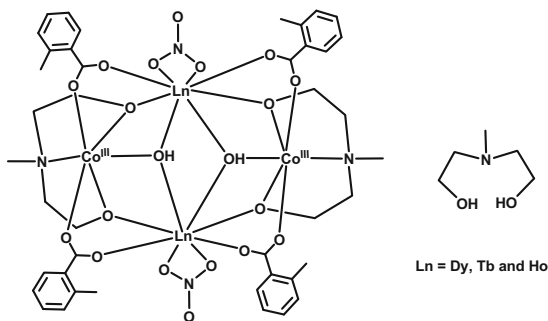
**Table 10** Magnetization relaxation parameters on heterometallic  $\{\text{Co}_2^{\text{III}}\text{Dy}_2^{\text{III}}\}$  butterfly SMMs, with the  $\text{Dy}^{\text{III}}$  ions in the body position, constructed with various ethanolamine-based ligands

Molecular formula <sup>a</sup>	$U_{\text{eff}}$ ( $\text{cm}^{-1}$ )	$\tau_{\text{QTM}}$ (s)	$\tau_0$ (s)	Ref.
$[\text{Co}_2^{\text{III}}\text{Dy}_2^{\text{III}}(\text{OH})_2(\text{acac})_2(\text{bdea})_2(\text{NO}_3)_4]$ ( <b>60</b> )	117	>1.5	$1.47 \times 10^{-7}$	[57]
$[\text{Co}_2^{\text{III}}\text{Dy}_2^{\text{III}}(\text{OMe})_2(\text{O}_2\text{CPh})_4(\text{teaH})_2(\text{MeOH})_4(\text{NO}_3)_2]$ and $[\text{Co}_2^{\text{III}}\text{Dy}_2^{\text{III}}(\text{OMe})_2(\text{O}_2\text{CPh})_4(\text{teaH})_2(\text{NO}_3)_2(\text{MeOH})_2]$ ( <b>63</b> )	61	>1.5	$5.64 \times 10^{-8}$	[64, 65]
$[\text{Co}_2^{\text{III}}\text{Dy}_2^{\text{III}}(\text{OMe})_2(\text{O}_2\text{CPh})_4(\text{dea})_2(\text{MeOH})_4(\text{NO}_3)_2]$ ( <b>64</b> )	72	0.12	$6.05 \times 10^{-8}$	[65]
$[\text{Co}_2^{\text{III}}\text{Dy}_2^{\text{III}}(\text{OMe})_2(\text{O}_2\text{CPh})_4(\text{mdea})_2(\text{NO}_3)_2]$ ( <b>65</b> )	55	0.2	$1.03 \times 10^{-7}$	[65]
$[\text{Co}_2^{\text{III}}\text{Dy}_2^{\text{III}}(\text{OMe})_2(\text{O}_2\text{CPh})_4(\text{bdea})_2(\text{MeOH})_4(\text{NO}_3)_2]$ and $[\text{Co}_2^{\text{III}}\text{Dy}_2^{\text{III}}(\text{OMe})_2(\text{O}_2\text{CPh})_4(\text{bdea})_2(\text{NO}_3)_2(\text{MeOH})_2]$ ( <b>66</b> )	80	0.48	$3.38 \times 10^{-8}$	[65]
$[\text{Co}_2^{\text{III}}\text{Dy}_2^{\text{III}}(\text{OMe})_2(\text{teaH})_2(\text{piv})_6]$ ( <b>67</b> )	35 and 88	7.3	$6.1 \times 10^{-7}$ and $1.2 \times 10^{-9}$	[66]
$[\text{Co}_2^{\text{III}}\text{Dy}_2^{\text{III}}(\text{OMe})_2(\text{O}_2\text{CPh}-2\text{-Cl})_4(\text{bdea})_2(\text{NO}_3)_2]$ ( <b>71</b> )	80	0.9	$1.8 \times 10^{-8}$	[68]
$[\text{Co}_2^{\text{III}}\text{Dy}_2^{\text{III}}(\text{OMe})_2(\text{O}_2\text{CPh}-4\text{'Bu})_4(\text{bdea})_2(\text{NO}_3)_3(\text{MeOH})_3](\text{NO}_3)]$ ( <b>72</b> )	77 and 96	0.5	$3.8 \times 10^{-9}$ and $5.6 \times 10^{-8}$	[68]
$[\text{Co}_2^{\text{III}}\text{Co}^{\text{II}}\text{Dy}_2^{\text{III}}(\text{OH})(\text{O}_2\text{CPh}-4\text{-OH})(\text{bdea})_3(\text{NO}_3)_3(\text{MeOH})]$ ( <b>73</b> )	117	0.3 (1,500 Oe)	$3.4 \times 10^{-7}$	[68]
$[\text{Co}_2^{\text{III}}\text{Dy}_2^{\text{III}}(\text{OMe})_2(\text{O}_2\text{CPh}-2\text{-CF}_3)_4(\text{bdea})_2(\text{NO}_3)_2]$ ( <b>75</b> )	88	~1.5	$1.4 \times 10^{-8}$	[68]
$[\text{Co}_2^{\text{III}}\text{Dy}_2^{\text{III}}(\text{mdea})_4(\text{hfacac})_3(\text{O}_2\text{CCF}_3)(\text{H}_2\text{O})]$ ( <b>76</b> )	23	0.004	$1.4 \times 10^{-6}$	[68]
$[\text{Co}_2^{\text{III}}\text{Dy}_2^{\text{III}}(\mu_3\text{-OH})_2(o\text{-tol})_4(\text{mdea})_2(\text{NO}_3)_2]$ ( <b>77</b> )	81.2	0.34	$9.8 \times 10^{-9}$	[69]
$[\text{Co}_2^{\text{III}}\text{Dy}_2^{\text{III}}(\text{OH})_2(\text{teaH})_2(\text{acac})_6]$ ( <b>80</b> )	49 and 31	76.5	$2.7 \times 10^{-7}$ and $3.2 \times 10^{-7}$	[70]
$[\text{Co}_2^{\text{III}}\text{Dy}_2^{\text{III}}(\text{OH})_2(\text{bdea})_2(\text{acac})_6]$ ( <b>81</b> )	19	1.4 ms	$1.0 \times 10^{-6}$	[70]
$[\text{Co}_2^{\text{III}}\text{Dy}_2^{\text{III}}(\text{OH})_2(\text{ede})_2(\text{acac})_6]$ ( <b>82</b> )	11	<sup>b</sup>	$1.3 \times 10^{-6}$	[70]
$[\text{Co}_2^{\text{III}}\text{Dy}_2^{\text{III}}(\text{OMe})_2(\text{acac})_4(\text{mdea})_2(\text{NO}_3)_2]$ ( <b>83</b> )	26	0.0025	$2.6 \times 10^{-6}$	[71]
$[\text{Co}_2^{\text{III}}\text{Dy}_2^{\text{III}}(\text{OMe})_2(\text{acac})_4(\text{teaH})_2(\text{NO}_3)_2]$ ( <b>84</b> )	19	0.00058	$8.1 \times 10^{-6}$	[71]
$[\text{Co}_2^{\text{III}}\text{Dy}_2^{\text{III}}(\text{OH})_2(\text{teaH})_2(\text{acac})_4(\text{NO}_3)_2]$ ( <b>85</b> )	20	0.00058	$7.4 \times 10^{-6}$	[71]

<sup>a</sup>*deaH*<sub>2</sub> diethanolamine, *teaH*<sub>3</sub> triethanolamine, *bdeaH*<sub>2</sub> *N-n*-butyldiethanolamine, *edeH*<sub>2</sub> *N*-ethyl-diethanolamine, *mdeaH*<sub>2</sub> *N*-methyl-diethanolamine, *o-tol* *o*-toluate, *pivH* pivalic acid, *acac* acetylacetonate, *hfacac* hexafluoroacetylacetonate

<sup>b</sup>Denotes no pure quantum tunneling relaxation regime is observed above 1.8 K

**Fig. 21** Line diagram of complexes **77–79** along with the ligand



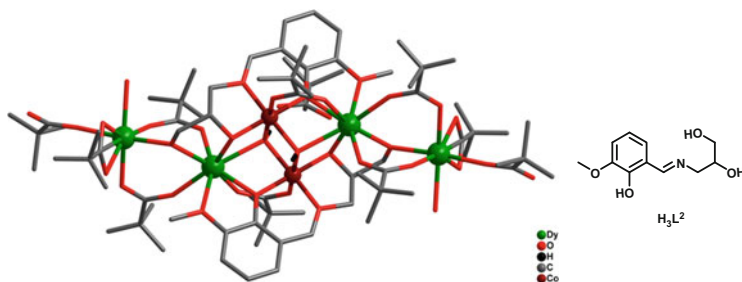
**Table 11** Magnetic properties of high nuclearity Co<sup>II</sup>/Ln<sup>III</sup> SMMs

Molecular formula <sup>a</sup>	$U_{\text{eff}}$ (K), $H_{\text{DC}}$ (Oe)	$\tau_0$ (s)	Ref.
$\{[\text{Co}^{\text{II}}_2\text{Dy}_3(\text{BPDC})_5(\text{HBPDC})(\text{H}_2\text{O})_5(\text{ClO}_4)_2 \cdot m\text{H}_2\text{O}]_n$ ( <b>90</b> )	62.89, 5,000	$6.16 \times 10^{-8}$	[72]
$\{[\text{Co}^{\text{II}}_4\text{Dy}_2(\text{L}^{\text{terpy}})_4(\text{CO}_3)_4(\text{HCOO})_2(\text{H}_2\text{O})_2] \cdot 2\text{DMF} \cdot x\text{H}_2\text{O}\}_n$ ( <b>91</b> )	7.6, 5,000	$1.9 \times 10^{-6}$	[73]
$[\text{Co}^{\text{II}}_6\text{Dy}(\text{aib})_6(\text{OH})_3(\text{NO}_3)_3(\text{CH}_3\text{OH})_5(\text{H}_2\text{O})](\text{ClO}_4)_3$ ( <b>92</b> )	No maxima under zero DC field	–	[74, 75]
$[\text{Co}^{\text{II}}_6\text{Dy}_2(\text{OH})_4(\text{chp})_6(\text{piv})_8(\text{CH}_3\text{CN})_2]$ ( <b>93</b> )	7.7, 1,000	$5.7 \times 10^{-8\text{b}}$	[76]
$[\text{Co}^{\text{II}}_4\text{Dy}_4(\text{OH})_4(\text{chp})_{10}(\text{acac})_6]$ ( <b>94</b> )	No maxima under zero DC field	–	[77]
$[\text{Co}^{\text{II}}_{11}\text{Dy}_6(\text{OH})_{14}(\text{chp})_{14}(\text{piv})_8(\text{NO}_3)_4(\text{MeCN})_4]$ ( <b>95</b> )	No maxima under zero DC field	–	[77]
$[\text{Co}^{\text{II}}_2\text{Co}^{\text{III}}_4\text{Dy}_4(\text{Htris})_8(\text{OAc})_6(\text{NO}_3)_4(\text{L}_2)(\text{NO}_3)_2]$ ( <b>96</b> )	No maxima under zero DC field	–	[78]
$[\text{Co}^{\text{II}}_3\text{Co}^{\text{III}}_2\text{Dy}_3(\mu_3\text{-OH})_5(\text{O}_2\text{C}^t\text{Bu})_{12}(\text{L}^{\text{Bu}})_2]$ ( <b>97</b> )	3.8, 2,000	$1.5 \times 10^{-6}$	[79]
$[\text{Co}^{\text{III}}_2\text{Dy}_4(\mu_3\text{-OH})_2(\text{hmp})_4(\mu\text{-N}_3)_2\text{-}(\text{piv})_8(\text{NO}_3)_2]$ ( <b>98</b> )	3.8, 600	$4.8 \times 10^{-6}$	[80]
$[\text{Co}^{\text{III}}_2\text{Dy}_4(\mu_3\text{-OH})_2(\text{salpa})_4(\text{NO}_3)_4(\text{OAc})_4(\text{H}_2\text{O})_2]$ ( <b>99</b> )	2, 0	$10^{-6\text{b}}$	[81]
$[(\text{Co}^{\text{III}}_3\text{Dy}_3(\mu_3\text{-OH})_4(\text{O}_2\text{C}^t\text{Bu})_6(\text{L}^{\text{Bu}})_3)(\text{NO}_3)_2]$ ( <b>100</b> )	17.4, 2,000	$2.5 \times 10^{-6}$	[79]
$[\text{Co}^{\text{III}}_2\text{Dy}_4(\mu_3\text{-OH})_2(\text{piv})_4(\text{hmmp})_4(\text{ae})_2] \cdot (\text{NO}_3)_2$ ( <b>101</b> )	25.2, 5,000 32.4, 8,000	$1.3 \times 10^{-6}$ $4.2 \times 10^{-7}$	[82]

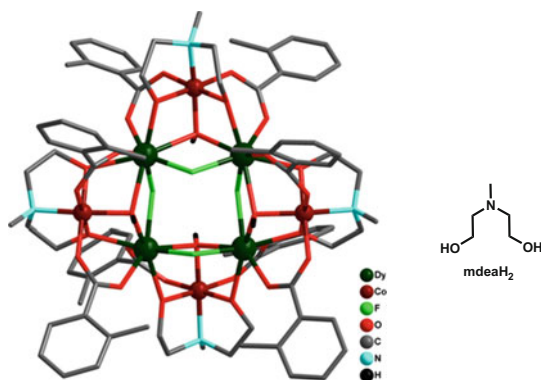
<sup>a</sup>*BPDC* 5,5'-dicarboxylate-2,2'-dipyridine anion, *Hhmp* 2-(hydroxymethyl)pyridine, *L<sup>terpy</sup>* *H* 4'-(4-Carboxyphenyl)-2,2':6',2''-terpyridine, *H<sub>3</sub>L<sup>2</sup>* 2-(2,3-dihydroxypropyliminomethyl)-6-methoxyphenol, *H<sub>2</sub>hmmp* 2-[(2-hydroxyethylimino)methyl]-6-methoxyphenol, *Hae* 2-amino ethanol, *Hpiv* pivalic acid, *H<sub>2</sub>L<sup>Bu</sup>* *n*-*N*-butyldiethanolamine, *aibH* 2-amino-isobutyric acid, *Hchp* 6-chloro-2-pyridinol, *acac<sup>-</sup>* acetylacetonate, *H<sub>3</sub>tris* *tris*-(hydroxymethyl)aminomethane

<sup>b</sup> $\ln(\chi''_{\text{M}}/\chi'_{\text{M}}) = \ln(\omega\tau_0) + E_{\text{a}}/k_{\text{B}}T$

Two octanuclear complexes,  $[\text{Co}^{\text{III}}_4\text{Dy}_4(\mu\text{-OH})_4(\mu_3\text{-OMe})_4\{\text{O}_2\text{CC}(\text{CH}_3)_3\}_4(\text{tea})_4(\text{H}_2\text{O})_4]$  (**87**) and  $[\text{Co}^{\text{III}}_4\text{Dy}^{\text{III}}_4(\mu\text{-F})_4(\mu_3\text{-OH})_4(o\text{-tol})_8(\text{mdea})_4]$  (**88**) ( $\text{tea}^{3-}$  = triply deprotonated triethanolamine;  $\text{mdea}^{2-}$  = doubly deprotonated *N*-



**Fig. 22** Molecular structure of complex **86** along with the ligand. Adapted from Ref. [83] with permission from The Royal Society of Chemistry

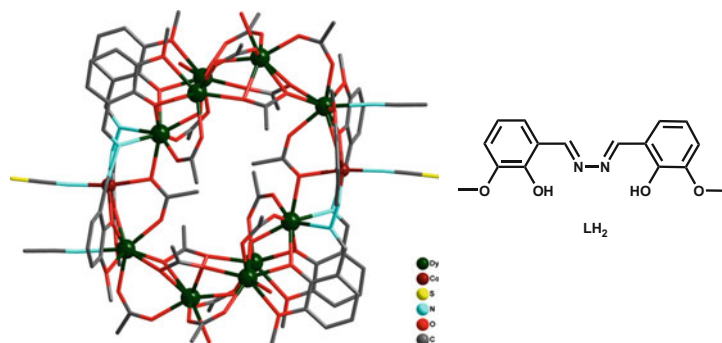


**Fig. 23** Molecular structure of complex **88** along with the ligand. Adapted from *Chem. Eur. J.* **2017**, *23*, 1654–1666 with permission from John Wiley and Sons

methyl-diethanolamine; *o*-tol = *o*-toluate), have been recently reported. The central core of the octanuclear ensemble consists of a [Dy(III)]<sub>4</sub> motif and is surrounded by four Co(III) ions. Like in the previous case, each of the Co(III) along with two Dy(III) centers is involved in a defect cubane motif [84] (Fig. 23).

Complex **87** reveals frequency-dependent “tails” in the out-of-phase susceptibility against temperature plots below 3 K at  $H_{DC} = 0$  Oe. This behavior does not improve even after application of fields up to 5,000 Oe. But for complex **88**, at  $H_{DC} = 5,000$  Oe, the corresponding energy barrier  $U_{eff} = 39$  cm<sup>-1</sup> and pre-exponential factor  $\tau_0 = 1.0 \times 10^{-6}$  s can be obtained between 8 and 10.5 K.

A dodecanuclear complex [Co<sup>II</sup><sub>2</sub>Dy<sub>10</sub>(L)<sub>4</sub>(OAc)<sub>16</sub>(SCN)<sub>2</sub>(CH<sub>3</sub>CN)<sub>2</sub>(H<sub>2</sub>O)<sub>4</sub>(OH)<sub>2</sub>( $\mu_3$ -OH)<sub>4</sub>][Co(SCN)<sub>4</sub>(H<sub>2</sub>O)<sub>2</sub>] (**89**) was assembled by using the multifunctional ligand, 1,2-bis(2-hydroxy-3-methoxybenzylidene) hydrazine (H<sub>2</sub>L). In contrast to the examples discussed above, this complex contains Co(II) [85] (Fig. 24).



**Fig. 24** Molecular structure of complex **89** along with the ligand. Adapted from Ref. [85] with permission from The Royal Society of Chemistry

The nature of the Co<sup>II</sup>–Dy and Dy–Dy interactions could not be delineated with certainty. However, the authors, based on the AC susceptibility measurements, suggest that this complex has a SMM behavior.

### 3 Summary

Co(II) is a promising 3d metal ion with first-order orbital contribution that has been investigated for its interesting magnetic properties. The combination of Co(II) and lanthanide ions in the form of heterometallic complexes leads to an interesting array of complexes where the role of the ligand seems to be extremely crucial in modulating the nuclearity and the coordination geometry. While there has been considerable progress in this field, it is anticipated that appropriate design of complexes can lead to SIMs and SMMs with even better properties. One crucial element that is missing from the studies carried out so far seems to be a strong theoretical input. Once such an understanding is in place, it becomes easier for synthetic chemists to make appropriate designs for assembling SMMs with superior properties.

### References

1. Murrie M (2010) *Chem Soc Rev* 39:1986–1995
2. Craig GA, Murrie M (2015) *Chem Soc Rev* 44:2135–2147
3. Frost JM, Harriman KLM, Murugesu M (2016) *Chem Sci* 7:2470–2491
4. Ishikawa N, Sugita M, Ishikawa T, Koshihara S-Y, Kaizu Y (2003) *J Am Chem Soc* 125:8694–8695
5. Osa S, Kido T, Matsumoto N, Re N, Pochaba A, Mrozinski J (2004) *J Am Chem Soc* 126:420–421
6. Bencini A, Benelli C, Caneschi A, Carlin RL, Dei A, Gatteschi D (1985) *J Am Chem Soc* 107:8128–8136

7. Woodruff DN, Winpenny REP, Layfield RA (2013) *Chem Rev* 113:5110–5148
8. Langley SK, Wielechowski DP, Chilton NF, Moubaraki B, Murray KS (2015) *Inorg Chem* 54:10497–10503
9. Langley SK, Wielechowski DP, Vieru V, Chilton NF, Moubaraki B, Abrahams BF, Chibotaru LF, Murray KS (2013) *Angew Chem Int Ed* 52:12014–12019
10. Ahmed N, Das C, Vaidya S, Langley SK, Murray KS, Shanmugam M (2014) *Chem Eur J* 20:14235–14239
11. Rinehart JD, Fang M, Evans WJ, Long JR (2011) *Nat Chem* 3:538
12. Rinehart JD, Fang M, Evans WJ, Long JR (2011) *J Am Chem Soc* 133:14236–14239
13. Pasatoiu TD, Sutter J-P, Madalan AM, Fellah FZC, Duhayon C, Andruh M (2011) *Inorg Chem* 50:5890–5898
14. Winpenny REP (1998) *Chem Soc Rev* 27:447–452
15. Benelli C, Gatteschi D (2002) *Chem Rev* 102:2369–2388
16. Mishra A, Wernsdorfer W, Abboud KA, Christou G (2004) *J Am Chem Soc* 126:15648–15649
17. Tanase S, Reedijk J (2006) *Coord Chem Rev* 250:2501–2510
18. Andruh M, Costes J-P, Diaz C, Gao S (2009) *Inorg Chem* 48:3342–3359
19. Sessoli R, Powell AK (2009) *Coord Chem Rev* 253:2328–2341
20. Karotsis G, Kennedy S, Teat SJ, Beavers CM, Fowler DA, Morales JJ, Evangelisti M, Dalgarno SJ, Brechin EK (2010) *J Am Chem Soc* 132:12983–12990
21. Papatriantafyllopoulou C, Wernsdorfer W, Abboud KA, Christou G (2011) *Inorg Chem* 50:421–423
22. Sharples JW, Collison D (2014) *Coord Chem Rev* 260:1–20
23. Rosado Piquer L, Sanudo EC (2015) *Dalton Trans* 44:8771–8780
24. Chandrasekhar V, Pandian BM, Azhakar R, Vittal JJ, Clérac R (2007) *Inorg Chem* 46:5140–5142
25. Chandrasekhar V, Pandian BM, Vittal JJ, Clérac R (2009) *Inorg Chem* 48:1148–1157
26. Chorazy S, Rams M, Nakabayashi K, Sieklucka B, Ohkoshi S-I (2016) *Chem Eur J* 22:7371–7375
27. Colacio E, Ruiz J, Ruiz E, Cremades E, Krzystek J, Carretta S, Cano J, Guidi T, Wernsdorfer W, Brechin EK (2013) *Angew Chem Int Ed* 52:9130–9134
28. Palacios MA, Nehrkorner J, Suturina EA, Ruiz E, Gómez-Coca S, Holldack K, Schnegg A, Krzystek J, Moreno JM, Colacio E (2017) *Chem Eur J* 23:11649–11661
29. Xie Q-W, Wu S-Q, Shi W-B, Liu C-M, Cui A-L, Kou H-Z (2014) *Dalton Trans* 43:11309–11316
30. Towatari M, Nishi K, Fujinami T, Matsumoto N, Sunatsuki Y, Kojima M, Mochida N, Ishida T, Re N, Mrozinski J (2013) *Inorg Chem* 52:6160–6178
31. Wang X, Li H, Sun J, Yang M, Li C, Li L (2017) *New J Chem* 41:2973–2979
32. Dolai M, Ali M, Titis J, Boca R (2015) *Dalton Trans* 44:13242–13249
33. Hazra S, Titis J, Valigura D, Boca R, Mohanta S (2016) *Dalton Trans* 45:7510–7520
34. Bartolomé J, Filoti G, Kuncser V, Schinteie G, Mereacre V, Anson CE, Powell AK, Prodius D, Turta C (2009) *Phys Rev B* 80:014430
35. Goura J, Brambleby J, Goddard P, Chandrasekhar V (2015) *Chem Eur J* 21:4926–4930
36. Goura J, Brambleby J, Topping CV, Goddard PA, Suriya Narayanan R, Bar AK, Chandrasekhar V (2016) *Dalton Trans* 45:9235–9249
37. Li X-L, Min F-Y, Wang C, Lin S-Y, Liu Z, Tang J (2015) *Inorg Chem* 54:4337–4344
38. Guo Y-N, Xu G-F, Wernsdorfer W, Ungur L, Guo Y, Tang J, Zhang H-J, Chibotaru LF, Powell AK (2011) *J Am Chem Soc* 133:11948–11951
39. Xue S, Ungur L, Guo Y-N, Tang J, Chibotaru LF (2014) *Inorg Chem* 53:12658–12663
40. Modak R, Sikdar Y, Thuijs AE, Christou G, Goswami S (2016) *Inorg Chem* 55:10192–10202
41. Chandrasekhar V, Das S, Dey A, Hossain S, Kundu S, Colacio E (2014) *Eur J Inorg Chem* 2014:397–406
42. Zhou J-M, Shi W, Xu N, Cheng P (2013) *Cryst Growth Des* 13:1218–1225

43. Yamaguchi T, Costes J-P, Kishima Y, Kojima M, Sunatsuki Y, Bréfuel N, Tuchagues J-P, Vendier L, Wernsdorfer W (2010) *Inorg Chem* 49:9125–9135
44. Liu C-M, Zhang D-Q, Hao X, Zhu D-B (2014) *Chem Asian J* 9:1847–1853
45. Mondal KC, Sundt A, Lan Y, Kostakis GE, Waldmann O, Ungur L, Chibotaru LF, Anson CE, Powell AK (2012) *Angew Chem Int Ed* 51:7550–7554
46. Peng Y, Mereacre V, Anson CE, Powell AK (2017) *Dalton Trans* 46:5337–5343
47. Li J, Wei R-M, Pu T-C, Cao F, Yang L, Han Y, Zhang Y-Q, Zuo J-L, Song Y (2017) *Inorg Chem Front* 4:114–122
48. Wu H, Li M, Zhang S, Ke H, Zhang Y, Zhuang G, Wang W, Wei Q, Xie G, Chen S (2017) *Inorg Chem* 56:11387–11397
49. Zhao X-Q, Lan Y, Zhao B, Cheng P, Anson CE, Powell AK (2010) *Dalton Trans* 39:4911–4917
50. Costes J-P, Vendier L, Wernsdorfer W (2011) *Dalton Trans* 40:1700–1706
51. Wu J, Zhao L, Zhang P, Zhang L, Guo M, Tang J (2015) *Dalton Trans* 44:11935–11942
52. Moreno Pineda E, Chilton NF, Tuna F, Winpenny REP, McInnes EJJ (2015) *Inorg Chem* 54:5930–5941
53. Abtab SMT, Majee MC, Maity M, Titiš J, Boča R, Chaudhury M (2014) *Inorg Chem* 53:1295–1306
54. Xu G-F, Gamez P, Tang J, Clérac R, Guo Y-N, Guo Y (2012) *Inorg Chem* 51:5693–5698
55. Zhao L, Wu J, Xue S, Tang J (2012) *Chem Asian J* 7:2419–2423
56. Huang Y-G, Wang X-T, Jiang F-L, Gao S, Wu M-Y, Gao Q, Wei W, Hong M-C (2008) *Chem Eur J* 14:10340–10347
57. Langley SK, Chilton NF, Moubaraki B, Murray KS (2013) *Chem Commun* 49:6965–6967
58. Rinehart JD, Long JR (2011) *Chem Sci* 2:2078–2085
59. Sorace L, Benelli C, Gatteschi D (2011) *Chem Soc Rev* 40:3092–3104
60. Bar AK, Pichon C, Sutter J-P (2016) *Coord Chem Rev* 308:346–380
61. Habib F, Murugesu M (2013) *Chem Soc Rev* 42:3278–3288
62. Zhang P, Guo Y-N, Tang J (2013) *Coord Chem Rev* 257:1728–1763
63. Gómez-Coca S, Aravena D, Morales R, Ruiz E (2015) *Coord Chem Rev* 289–290:379–392
64. Langley SK, Chilton NF, Ungur L, Moubaraki B, Chibotaru LF, Murray KS (2012) *Inorg Chem* 51:11873–11881
65. Langley SK, Ungur L, Chilton NF, Moubaraki B, Chibotaru LF, Murray KS (2014) *Inorg Chem* 53:4303–4315
66. Funes AV, Carrella L, Rentschler E, Albores P (2014) *Dalton Trans* 43:2361–2364
67. Funes AV, Carrella L, Rechkemmer Y, van Slageren J, Rentschler E, Albores P (2017) *Dalton Trans* 46:3400–3409
68. Langley SK, Le C, Ungur L, Moubaraki B, Abrahams BF, Chibotaru LF, Murray KS (2015) *Inorg Chem* 54:3631–3642
69. Vignesh KR, Langley SK, Murray KS, Rajaraman G (2017) *Inorg Chem* 56:2518–2532
70. Langley SK, Chilton NF, Moubaraki B, Murray KS (2015) *Inorg Chem Front* 2:867–875
71. Langley SK, Chilton NF, Moubaraki B, Murray KS (2013) *Inorg Chem* 52:7183–7192
72. Fang M, Shi P-F, Zhao B, Jiang D-X, Cheng P, Shi W (2012) *Dalton Trans* 41:6820–6826
73. Liu Y, Chen Z, Ren J, Zhao X-Q, Cheng P, Zhao B (2012) *Inorg Chem* 51:7433–7435
74. Orfanoudaki M, Tamiolakis I, Siczek M, Lis T, Armatas GS, Pergantis SA, Milios CJ (2011) *Dalton Trans* 40:4793–4796
75. Sopsis GJ, Orfanoudaki M, Zampas P, Philippidis A, Siczek M, Lis T, O'Brien JR, Milios CJ (2012) *Inorg Chem* 51:1170–1179
76. Zhao X-Q, Wang J, Bao D-X, Xiang S, Liu Y-J, Li Y-C (2017) *Dalton Trans* 46:2196–2203
77. Langley SK, Chilton NF, Moubaraki B, Murray KS (2013) *Polyhedron* 66:48–55
78. Xiang H, Lan Y, Li H-Y, Jiang L, Lu T-B, Anson CE, Powell AK (2010) *Dalton Trans* 39:4737–4739
79. Sheikh JA, Goswami S, Konar S (2014) *Dalton Trans* 43:14577–14585
80. Feuersenger J, Prodius D, Mereacre V, Clérac R, Anson CE, Powell AK (2013) *Polyhedron* 66:257–263

81. Jhan S-Y, Huang S-H, Yang C-I, Tsai H-L (2013) *Polyhedron* 66:222–227
82. Tian C-B, Yuan D-Q, Han Y-H, Li Z-H, Lin P, Du S-W (2014) *Inorg Chem Front* 1:695–704
83. Zou H-H, Sheng L-B, Liang F-P, Chen Z-L, Zhang Y-Q (2015) *Dalton Trans* 44:18544–18552
84. Vignesh KR, Langlely SK, Murray KS, Rajaraman G (2017) *Chem Eur J* 23:1654–1666
85. Zou L-F, Zhao L, Guo Y-N, Yu G-M, Guo Y, Tang J, Li Y-H (2011) *Chem Commun* 47:8659–8661



# Mannich Base Ligands as Versatile Platforms for SMMs



Enrique Colacio

*This chapter is dedicated to Prof. Jean Pierre Costes, on the occasion of his 65th birthday in recognition of his synthetic contributions to the field of 3d/4f coordination compounds.*

## Contents

1	Introduction .....	102
2	Synthesis of Ligands: Mannich Reaction .....	109
3	Homometallic 4f Complexes .....	112
3.1	Mononuclear Ln Complexes .....	112
3.2	Trinuclear Ln <sub>3</sub> Complexes .....	114
3.3	Pentanuclear Ln <sub>5</sub> Complexes .....	116
4	Heterometallic 3d-4f Complexes .....	118
4.1	Dinuclear M <sup>II</sup> Ln <sup>III</sup> Complexes .....	118
4.2	Trinuclear M <sup>II</sup> -Ln <sup>III</sup> -M <sup>II</sup> Complexes .....	130
4.3	(M <sup>II</sup> ) <sub>2</sub> (Ln <sup>III</sup> ) <sub>2</sub> Tetranuclear Complexes .....	139
4.4	(M <sup>II</sup> ) <sub>3</sub> (Ln <sup>III</sup> ) <sub>2</sub> Pentanuclear Complexes .....	144
4.5	(M <sup>II</sup> ) <sub>3</sub> (Ln <sup>III</sup> ) <sub>3</sub> Hexanuclear Complexes .....	145
4.6	(M <sup>II</sup> ) <sub>2</sub> (Ln <sup>III</sup> ) <sub>4</sub> Hexanuclear Complexes .....	147
5	Heterometallic 3d-3d' Complexes .....	149
6	Dinuclear 3d-4f Complexes as Platforms for Constructing Systems of Higher Nuclearity .....	151
6.1	Co <sup>II</sup> <sub>2</sub> Ln <sup>III</sup> <sub>2</sub> Complexes .....	151
6.2	(Ni <sup>II</sup> <sub>2</sub> Ln <sup>III</sup> <sub>2</sub> )Ru <sup>III</sup> Trimetallic Complexes .....	152
	References .....	153

**Abstract** Aminophenol Mannich base derivatives are versatile and flexible ligands for preparing a wide variety of homo- and heterometallic discrete coordination compounds, ranging from mononuclear to hexanuclear, which exhibit aesthetically pleasant structures with intricate topologies. These ligands are particularly adapted

---

E. Colacio (✉)

Department of Inorganic Chemistry, University of Granada, Granada, Spain  
e-mail: [ecolacio@ugr.es](mailto:ecolacio@ugr.es)

to obtain 3d/4f systems, where invariably the amino fragment is coordinated to the transition metal ion and the phenolate oxygen atoms bridge transition metal and lanthanide ions. Their coordination spheres are completed by donor atoms belonging either to methoxy and aldehyde groups of the Mannich base ligands or to terminal and bridging ancillary ligands. Moreover, robust 3d-4f dinuclear units can be assembled with either bridging ligands or complexes acting as bridging ligands to afford heterometallic complexes with increased nuclearity. The complexes containing one or two paramagnetic ions often exhibit appealing magnetic properties, alone or combined with other physical properties, that essentially arise from large local magnetic anisotropy and magnetic exchange coupling of the metal ions. This chapter provides an overview of recent results on single-molecule magnets (SMMs) based on aminophenol Mannich base ligands that illustrate the scope, state of the art and fruitful dynamism of this field of research.

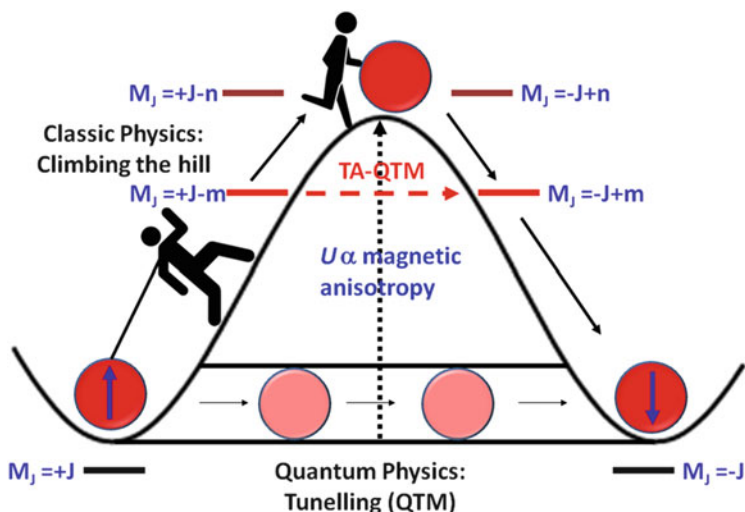
**Keywords** 3d-4f · Aminophenol · Complexes · Coordination compounds · Lanthanides · Luminescence · Magnetic properties · Mannich · Mannich ligands · Single-molecule magnets (SMMs) · Slow relaxation

## 1 Introduction

The field of Molecular Magnetism based on coordination compounds has experienced a renaissance over the past few decades impelled by the discovery of single-molecule magnets (SMMs) [1–3]. These chemically and physically intriguing nanomagnets bestride the border between classical and quantum magnetism, because they present classical properties, such as slow relaxation for magnetization reversal and magnetic hysteresis when the polarizing magnetic field is eliminated below the blocking temperature ( $T_B$  is the temperature at which magnetic hysteresis appears) [1–3] as well as quantum properties, such as macroscopic quantum tunnelling between up- and down-spin orientations (quantum tunnelling of the magnetization, QTM) and quantum phase interference between tunnelling paths [1–3]. Moreover, SMMs can function as single-domain classical magnetic nanoparticles but yet possessing some advantages over them, such as reproducibility, monodispersity, modulation of their magnetic properties by typical chemistry methods, solubility which facilitates processability (deposition and grafting on different surfaces, thin films fabrication and so forth), among others [1–5]. These exceptional properties make them suitable candidates for potential future applications, among other areas, in molecular spintronics [3, 6–17], ultra-high density magnetic information storage [18, 19], magneto-optics [20] and as qubits for quantum computing at molecular level [21–24]. The end goal of the enormous research activity in SMMs is the incorporation of these systems in nanosize devices [4, 5]. The origin of the SMM behaviour can be found in the existence of an energy barrier ( $U$ ) that prevents

magnetization reversal when the polarizing magnetic field is removed (the energy required to convert an SMM in a paramagnet), so that the molecular magnetization can be blocked either parallel or antiparallel to the magnetic field (magnetic bistability) and, as a result, slow relaxation of the magnetization appears (Fig. 1). Therefore, to observe SMM behaviour at higher temperatures, the energy barrier should be as large as possible, which would lead to a concomitant increase of  $T_B$  and relaxation times ( $\tau$ ). In the high-temperature region, the relaxation time  $\tau$  is thermally activated following the Arrhenius law with activation energy equal to  $U$ . However, at low temperature, the fast QTM relaxation across the barrier can reduce  $T_B$  and  $\tau$  to extremely small values even though  $U$  is very large [1–3]. At intermediate range of temperature (between thermally activated and QTM regimes), the so-called thermally assisted QTM (TA-QTM) occurs. This relaxation process takes place between excited states of equal  $\pm M_s$  ( $M_J$  for lanthanide ions) at both sides of the energy barrier, so that the thermal barrier is shortcut by quantum tunnelling, and  $U$  is reduced to an effective value  $U_{\text{eff}}$ .

The first reported SMMs were coordination clusters of transition metal ions [25–28], for which the activation energy barrier,  $U$ , is proportional to the product of  $|D|$  (the easy-axis magnetic anisotropy of the whole molecule which depends on the local magnetic anisotropies and their orientation) and  $S_T^2$  ( $S_T$  is the spin of the ground state) [1–3]. Therefore, a strategy to augment  $U$  would be that of increasing  $S_T$  and/or  $D$  (which should be negative to have the highest  $M_s$  value in the ground state and to observe SMM behaviour). Moreover, theoretical calculations [29, 30] have shown that  $U$  is almost independent of  $S$  and, therefore, the magnetic anisotropy is the key factor in determining the height of the energy barrier and the



**Fig. 1** Thermal energy barrier in single-molecule magnets (SMMs) and shortcuts via quantum tunnelling of the magnetization (QTM) and thermally assisted QTM (TA-QTM) relaxation mechanisms

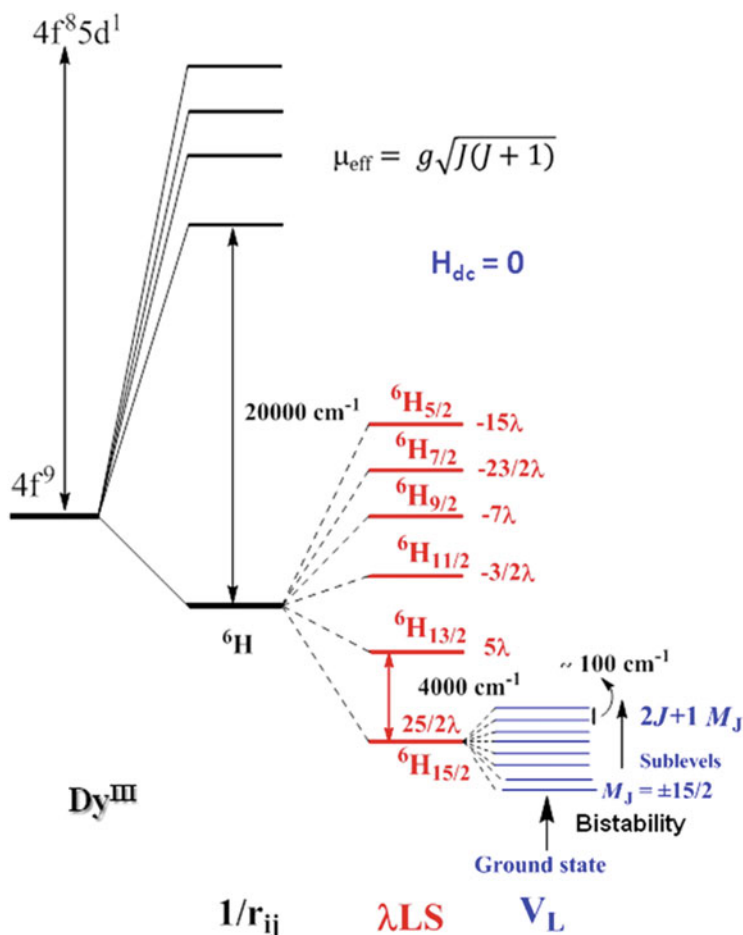
improvement of the SMM properties. In accordance with this, the best examples of transition metal coordination clusters with SMM behaviour are a  $\{\text{Mn}^{\text{III}}\}_6$  complex with  $U_{\text{eff}} = 60 \text{ cm}^{-1}$  ( $\text{Mn}^{\text{III}}$  ions present a strong second-order spin-orbit coupling and consequently large zero-field splitting [ZFS]) [31, 32] and a  $\text{Co}^{\text{II}}_2$  complex with  $U_{\text{eff}} = 62 \text{ cm}^{-1}$  ( $\text{Co}^{\text{II}}$  ions present a large first-order spin-orbit coupling and strong magnetic anisotropy) [33]. However, experimental results have shown that both parameters  $S_T$  and  $D$  are correlated, so that when  $S_T$  is very large (often observed for high-nuclearity coordination clusters),  $D$  tends to be very small (the anisotropy of the entire molecule is very hard to control in polynuclear complexes and generally low  $D$  values are observed) [34, 35], so that the enhancement of  $U$  by increasing simultaneously  $S_T$  and  $D$  is a very tricky task. In view of the above concerns, the research in this field has been focused on mononuclear metal complexes containing transition metal ions with significant first-order orbital angular momentum, such as  $\text{Co}^{\text{II}}$ ,  $\text{Fe}^{\text{II}}$  and  $\text{Fe}^{\text{I}}$ . This together with the fact that mononuclear species can present larger anisotropies than their polynuclear counterparts has stimulated the research on mononuclear SMMs, also called single-ion magnets (SIMs) [36–39]. The best example of these systems with transition metal ions is a linear  $\text{Fe}^{\text{I}}$  with large spin-orbit coupling and magnetic anisotropy, which exhibit a large  $U_{\text{eff}}$  of  $226 \text{ cm}^{-1}$  and magnetic hysteresis up to 6.5 K (in the presence of magnetic field) [40].

Another important area of research in this field is the use of lanthanide (and actinide) metal ions in designing SMMs [41–52]. This is because these metal ions exhibit strong magnetic anisotropy, which arises from the combination of large magnetic moments, strong spin-orbit coupling and crystal-field effects (Fig. 2).

The enormous amount of research along this line has afforded a large number of 3d/4f clusters [53–65] of low nuclearity and mononuclear 4f metal complexes [41–52] that exhibit slow relaxation of the magnetization and SMM behaviour. Nevertheless, it is worth mentioning that QTM under zero dc field is present in the majority of lanthanide-containing SMMs, which, as indicated elsewhere, generally reduce the height of the energy barrier and relaxation times [41–52]. This is one of the main impediments to obtain high-temperature lanthanide SMMs.

Although the 4f electrons are effectively shielded by 5s and 5p electrons, they feel the effects of the negative charges belonging to the donor atoms of the ligands. If this ligand field stabilizes the sublevels with the largest  $M_J$  values, the  $\text{Ln}^{\text{III}}$  ion exhibits easy-axis anisotropy, which favours the SMM behaviour. Of particular interest are the  $\text{Dy}^{\text{III}}$ -containing coordination compounds as the ligand field splits the ground  ${}^6\text{H}_{15/2}$  multiplet in such a way that usually the  $M_J = \pm 15/2$  is the ground Kramers doublet, which ensures large magnetic moment, bistability and easy-axis anisotropy when only the ground state is significantly populated (Fig. 2). It is worth noting that easy-axis anisotropy ( $M_J = \pm 15/2$ , ground Kramers doublet) is usually found in low-symmetry  $\text{Dy}^{3+}$  complexes. In view of the above considerations, it is not surprising that most part of the reported lanthanide-containing SMMs contain  $\text{Dy}^{\text{III}}$  ions [41–52].

For 3d/4f systems, recent experimental and theoretical studies have revealed that the height of the magnetization relaxation barrier depends on both single-ion anisotropy and 3d-4f magnetic exchange interactions [66–72]. Thus, when the 3d-4f



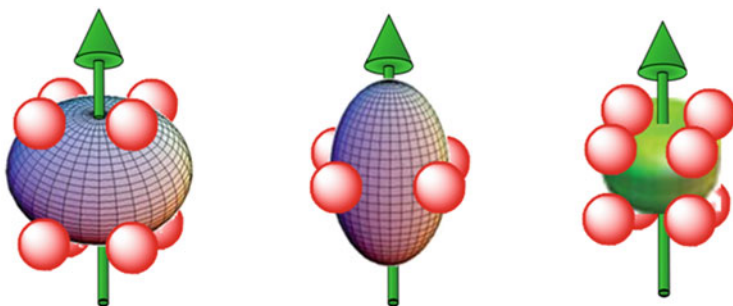
**Fig. 2** Energy levels for  $\text{Dy}^{\text{III}}$  arising from interelectronic repulsions ( $1/r_{ij}$ ), spin-orbit coupling ( $\lambda\text{LS}$ ) and crystal field ( $V_L$ ). The splitting provoked by  $V_L$  ( $\sim 100 \text{ cm}^{-1}$ ) at zero magnetic field leads to a large anisotropy (magnetic properties depending on the direction of the applied magnetic field)

magnetic exchange coupling is strong enough, the exchange-coupled levels are well separated (avoiding mixing of low-lying excited states in the ground state) and the QTM is suppressed, so that large energy barriers, hysteresis loops and relaxation times are observed. Good examples of this type of systems are butterfly-like  $\{\text{Cr}^{\text{II}}_2\text{Dy}^{\text{III}}_2\}$  complexes, for which  $U_{\text{eff}}$  values as high as  $82 \text{ cm}^{-1}$  and observable hysteresis loops up to 3.7 K have been reported [66–72]. The record of anisotropy barrier corresponds to a  $\text{Fe}^{\text{III}}\text{Dy}^{\text{III}}\text{Fe}^{\text{III}}$  complex with  $U_{\text{eff}} = 319 \text{ cm}^{-1}$  [73]. In the case of low-nuclearity lanthanide clusters  $(\text{Ln})_n$ , the same strategy for suppressing QTM as in 3d/4f SMMs should be used (strong exchange coupling between metal ions). However, the  $\text{Ln} \dots \text{Ln}$  interaction is very weak, so that, for effectively suppressing QTM, radical bridging ligands have to be used. The synergy

between strong  $\text{Ln}^{\text{III}}$ -radical magnetic exchange interaction and the large magnetic anisotropy of the  $\text{Ln}^{\text{III}}$  ion can suppress QTM relaxation pathway giving rise to SMMs exhibiting magnetic hysteresis up to 20 K [74–76].

For mononuclear lanthanide complexes, the origin of the barrier for reversal of magnetization, as indicated elsewhere, is related to the easy-axis anisotropy of the ground state. In the case of  $\text{Dy}^{3+}$ , if the axial ground Kramers doublet with  $M_J = \pm 15/2$  is pure and not mixed with low-lying excited states, QTM is suppressed and the activated relaxation behaviour occurs over a broader temperature range with the concomitant increase of  $T_B$ . This can be qualitatively justified using a simple model based on the electronic shape of the  $\text{Ln}^{\text{III}}$  ions. The free ion electron density of the ground Kramers doublet with  $M_J = \pm 15/2$  belonging to the  $\text{Dy}^{3+}$  has an oblate shape (disc shape) [75], so that an axial crystal field, where the donor atoms with the largest electron densities are located above and below the equatorial plane, minimizes the repulsive interactions between the ligands and f-electron charge clouds (Fig. 3, left) [75]. At variance, mononuclear complexes with  $\text{Ln}^{\text{III}}$  ions having a prolate electron density shape, such as  $\text{Er}^{\text{III}}$ , require an equatorial crystal field to induce an easy-axis anisotropic ground state (Fig. 3, middle). The larger is the axial magnetic anisotropy (for instance, a  $\text{Dy}^{3+}$  complex with an ideal axial symmetry and shorter  $\text{Dy}^{3+}$ -donor bond distances involving axial positions), the smaller QTM and larger  $T_B$ . This strategy for constructing an axial crystal field around the  $\text{Ln}^{3+}$  ion has led to the successful preparation of SMMs with  $U$  and  $T_B$  values as high as 1,815 K and 60 K, respectively [77–83].

It is worth mentioning at this point that the magnetic relaxation is essentially governed by QTM and spin-phonon transitions. The former can occur either within the two components of reverse magnetization of the ground doublet state or through tunnelling via excited states (TA-QTM), induced by a transversal magnetic field (externally applied or intrinsic to the compound). In Kramers complexes (half-integer spin or  $J$ ), direct QTM arises from the first-order Zeeman splitting of the

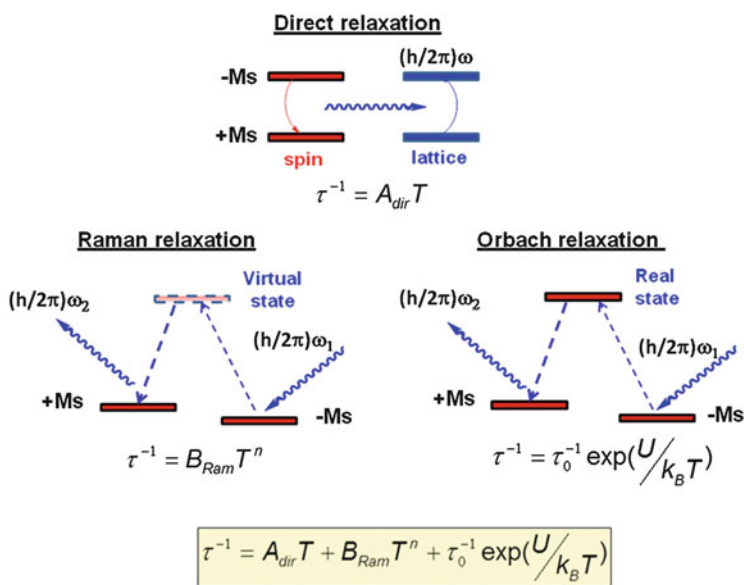


**Fig. 3** (Left) Axial crystal fields minimize the repulsion energy between the ligands (red balls) and the oblate f-electron charge cloud (grey-violet colour) leading to a ground state with high  $M_J$  value. (Middle) Equatorial crystal fields minimize the repulsion energy between the ligands (red balls) and the prolate f-electron charge cloud (grey-violet colour). (Right) Oblate (disc shape) electron density of the ground Kramers doublet with  $M_J = \pm 15/2$  belonging to the  $\text{Dy}^{3+}$  (green colour) stabilized by an axial crystal field

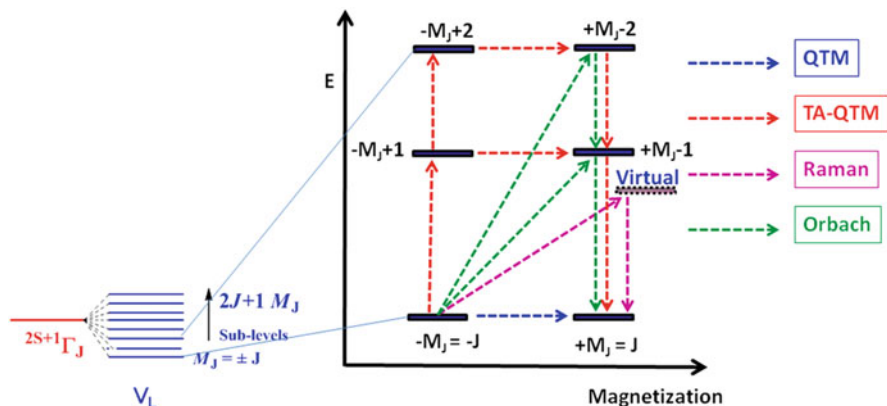
doublet state due to a transversal magnetic field, which is proportional to the matrix element of the transversal magnetic moment between the two doublet states. However, in non-Kramers complexes, the QTM is due to an intrinsic tunnelling gap at zero field. Spin–phonon transitions are, in turn, proportional to the matrix elements of transversal components of the magnetic moment and can take place via: (1) Orbach/Raman processes which account for the relaxation via the excited KDs and occur essentially due to the non-coincidence of the principal anisotropic axes, (2) TA-QTM which accounts for relaxation through the excited KDs due to their non-Ising nature and (3) direct relaxation within a doublet state whose components do not have the same energy. For Kramers ions, the direct and QTM relaxation processes in a given doublet state cannot be induced by lattice vibration phonons in strictly zero field. However, nuclear-spin interactions as well as a transversal magnetic field created by intermolecular interactions (which is proportional to the matrix element of the transversal magnetic moments between the two doublet states) split the doublet states providing relaxation channels for direct and QTM processes. It should be noted that the relaxation is defined by the shortest paths where the matrix element of the transversal magnetic moments are the largest.

The spin–phonon mechanisms are represented in Fig. 4. These relaxation pathways are given in Fig. 5 for lanthanide-containing complexes.

Some lanthanide complexes combine SMMs and luminescence properties [84–86] and therefore can be considered as bifunctional materials. The latter properties arise from f-f transitions occurring between lanthanide excited states and the ground



**Fig. 4** One-phonon (direct) and two-phonon (Raman/Orbach) relaxation processes and the temperature dependence of their relaxation times

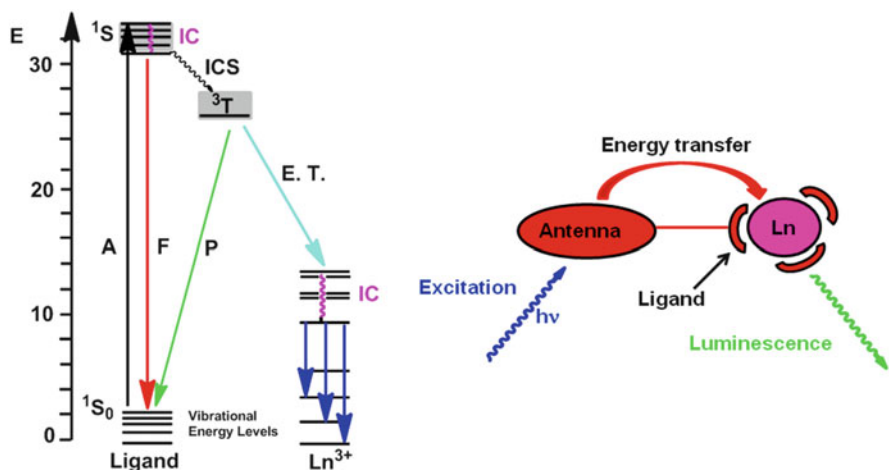


**Fig. 5** Mechanisms for magnetization reversal in lanthanides complexes with easy-axis anisotropy in the ground state

state. As the 4f orbitals of the lanthanide ions are shielded by the filled 5s25p6 subshells, they are little sensitive to the coordination environment. As a result, lanthanides exhibit 4f-4f sharp transitions covering spectral range from the near UV to the NIR region, which are typical for each Ln<sup>III</sup> ion and do not shift significantly in energy when the Ln<sup>III</sup> chemical surrounding changes [84–86]. Because f-f transitions are parity forbidden, lanthanide complexes exhibit very low absorption coefficients and long-lived (ns,  $\mu$ s or ms) emissions. The weak absorption is the principal drawback of lanthanides as their excited states cannot be efficiently populated. However, organic ligands with strongly absorbing chromophores that are able to transfer energy onto Ln<sup>III</sup> excited states can be used to circumvent that drawback [84–86]. Thus, the transferred energy to the emitting level of the lanthanide ion gives rise to intense emission bands. This process is known as sensitization of the metal-centred luminescence or antenna effect (Fig. 6). Thus, after excitation to the <sup>1</sup>S singlet ligand level, there is an intersystem crossing process to the ligand triplet state <sup>3</sup>T<sub>1</sub>. For an efficient energy transfer, the excited state of the ligand should be higher in energy than the lowest excited state of the lanthanide. It should be noted that lanthanide complexes have been applied as luminescent bioprobes in analyte sensing and tissues and cell imaging as well as monitoring drug delivery [84–86]. In particular, NIR luminescent complexes are of high interest due to their electronic and optical applications, especially for optical communications, and biological and sensor applications [84–89].

A wide variety of ligands have been employed for preparing SMMs and, among them, polydentate Schiff base ligand derivatives occupy a prominent place, particularly those bearing alkoxide and/or phenoxide moieties [90]. This is because: (1) they are easily prepared from condensation of amino and keto precursors, (2) the denticity, the number of chelating moieties, terminal and donor bridging atoms in the resulting ligand can be controlled by a rational choice of the optimal precursors, (3) the number of possible ligands is only limited by our imagination and





**Fig. 6** Simplified Jablonski energy diagram for a general  $Ln^{3+}$  chelate (left). *IC* internal conversion, *ISC* intersystem crossing, *A* ligand absorption, *F* ligand fluorescence, *P* ligand phosphorescence, *ET* energy and transfers. Antenna effect (right). An antenna ligand absorbs the excitation energy and transfers it to the  $^3T_1$  ligand level via intersystem crossing, from which it is transferred to the chelated  $Ln^{3+}$  and emitted via several transitions

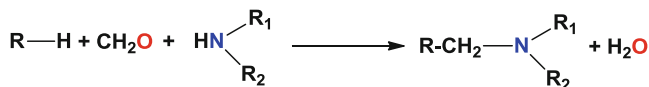
(4) they react very effectively with transition and lanthanide metal ions. Mannich base ligands have been used to a much lesser extent than the Schiff base ligand counterparts for preparing SMMs, despite the fact that the former present the same coordination features (1)–(4) as the latter and, in addition, they are more flexible (because they do not have C=N double bonds) and, in principle, can more easily accommodate metal ions. Moreover, Mannich base ligands present more synthetic versatility than Schiff base ligands because they can introduce one or two polydentate moieties per amino group in the resulting ligand, whereas in the Schiff base ligands they only incorporate one polydentate moiety per amino group.

This chapter is dedicated to present the results reported so far for SMMs prepared by assembling Mannich base ligands, transition metal and/or lanthanide metal ions and terminal and/or bridging ancillary ligands. We will restrict ourselves to aminophenol ligands that have been partly or fully synthesized through one-pot three components Mannich reaction.

## 2 Synthesis of Ligands: Mannich Reaction

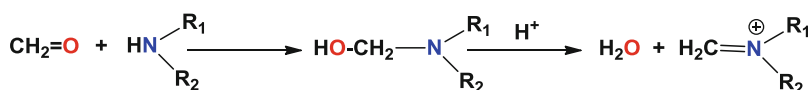
The Mannich reaction is one of the most important basic reaction types in organic chemistry and consists in a three-component condensation, in which a compound containing an active hydrogen atom reacts with formaldehyde and an NH-amine derivative. It is worth noting that secondary amines rather than primary amines are used, so that in the resulting Mannich base the N atom of the amine compound is

linked to the R substrate through a methylene group. The main characteristic of the reaction is the replacement of the active hydrogen atom by an aminomethyl or substituted aminomethyl group.

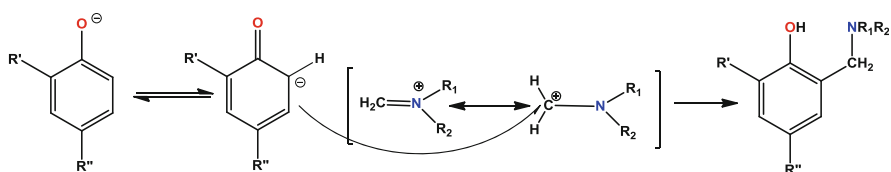


A wide variety of compounds containing an active hydrogen atom can be used as component in the Mannich reaction, such as ketones, aldehydes, acids, esters, phenols, acetylenes,  $\alpha$ -picolines, nitroalkanes, quinolines and so on. Among them, phenol, which exists almost fully as the enol form, easily undergoes electrophilic aromatic substitution to yield aminomethyl-substituted phenols. It is generally believed that the reaction takes place through the following mechanism:

1. Firstly, the condensation of paraformaldehyde with the amine affords an iminium cation with the involvement of a proton coming from the phenol component.

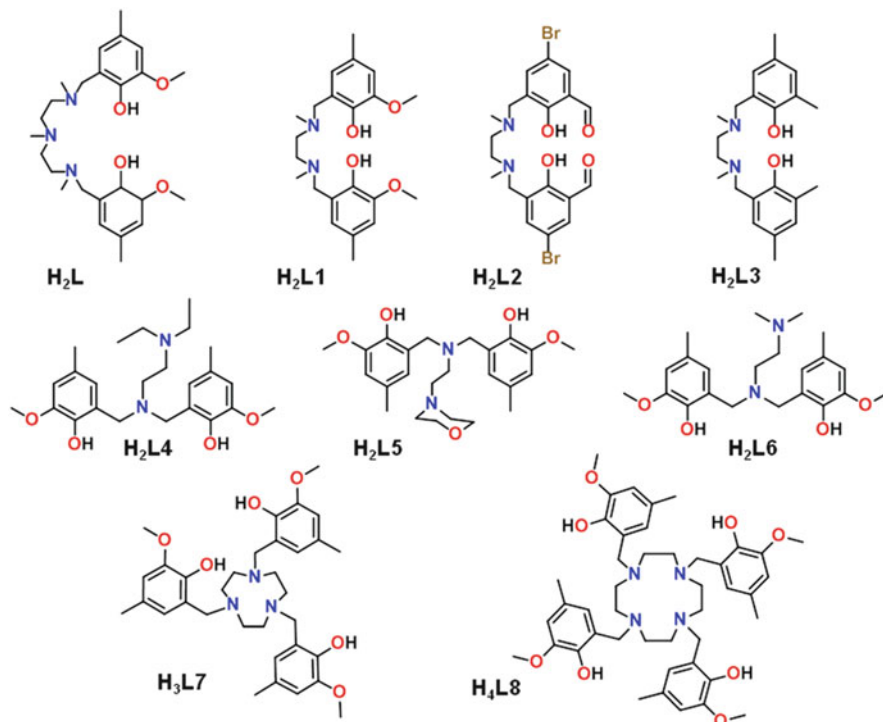


2. Secondly, the iminium cation attacks the phenolate anion to give rise to the aminomethyl-substituted phenols. In order to avoid mixture of compounds, generally one *ortho* and the *para* positions of the phenol moiety are blocked by either equal or different suitable substituents.



The polydentate Mannich base ligands synthesized employing the above reaction and used for the preparation of SMM behaviour are given in Fig. 7.

These ligands have two *cis* oxygen donor atoms coming from the phenol precursor (with the exception of H<sub>2</sub>L3) and, at least, two nitrogen atoms in the amino fragment, which have a great tendency to coordinate lanthanide ions and transition metal ions, respectively. Therefore, these ligands are particularly adapted to prepare 3d/4f heterometallic systems. The side-off compartmental ligands H<sub>2</sub>L-H<sub>2</sub>L3, H<sub>2</sub>L7 and H<sub>2</sub>L8 have two different potential coordination sites (compartments), the N<sub>x</sub>O<sub>y</sub> ( $x = 2-4$ ,  $y = 2-4$ ) inner site showing preference for transition metal ions and the O<sub>n</sub>



**Fig. 7** Mannich base ligands used for the preparation of SMM

( $n = 4-8$ ) outer open site which is able to accommodate large oxophilic lanthanide ions. This type of ligand is very appropriate to obtain a wide variety of binuclear and trinuclear 3d-4f and 3d-4f-3d complexes. For it, first the 3d metal ion is introduced in the inner site to obtain a mononuclear complex and then this metalloligand (previously isolated or formed in situ) coordinates the lanthanide ion at the outer site. Depending on the  $r = M/Ln$  molar ratio ( $M =$  transition metal,  $L_n =$  lanthanide ion) used in this latter reaction, dinuclear 3d-4f ( $r = 1$ ) and trinuclear 3d-4f-3d ( $r = 2$ ) can be, respectively, expected. In some cases, to complete the coordination sphere of the transition and lanthanide metal ions, either solvent molecules or anions (terminal or bridging) are usually coordinated to these ions. It is worth noting that robust 3d-4f dinuclear units can be assembled with either bridging ligands or complexes acting as bridging ligands to afford heterometallic complexes exhibiting increased nuclearity.

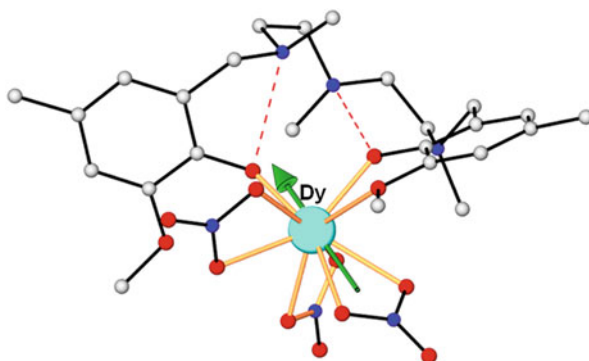
### 3 Homometallic 4f Complexes

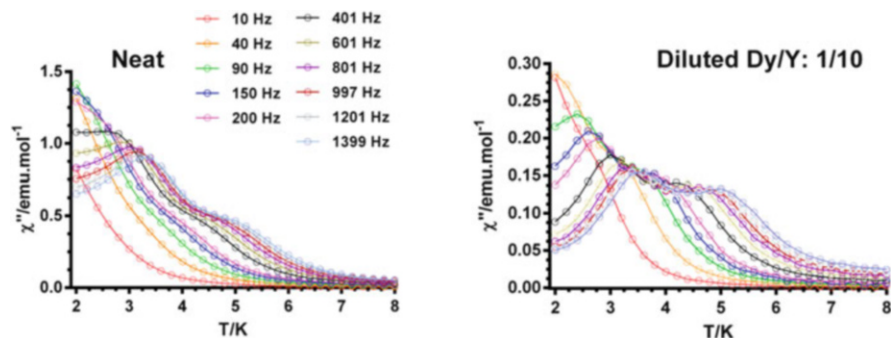
#### 3.1 Mononuclear Ln Complexes

The first genuine example of a mononuclear  $\text{Ln}^{3+}$  complex with a Mannich base ligand, of formula  $[\text{Dy}(\text{H}_2\text{L})(\text{NO}_3)_3] \cdot 2\text{CH}_3\text{OH}$ , was prepared by our group through the reaction of  $\text{H}_2\text{L}$  with  $\text{Dy}(\text{NO}_3)_3 \cdot 5\text{H}_2\text{O}$  in MeOH [91]. The structure of the compound consists of isolated  $[\text{Dy}(\text{H}_2\text{L})(\text{NO}_3)_3]$  neutral molecules and methanol crystallization molecules. Within the mononuclear unit (Fig. 8), the  $\text{Dy}^{\text{III}}$  ion exhibits a rather unsymmetrical  $\text{DyO}_9$  coordination environment which is formed by the coordination of two phenoxido and one methoxy oxygen atoms belonging to the ligand and six oxygen atoms belonging to three bidentate nitrate anions. Interestingly, the ligand remains undeprotonated and the coordination of the two phenoxido oxygen atoms to the  $\text{Dy}^{\text{III}}$  ion occurs with the simultaneous migration of the phenolic protons to the outer amine groups affording a phenolate–ammonium zwitterionic form, which is stabilized by a couple of strong hydrogen bonds involving these two groups (Fig. 8).

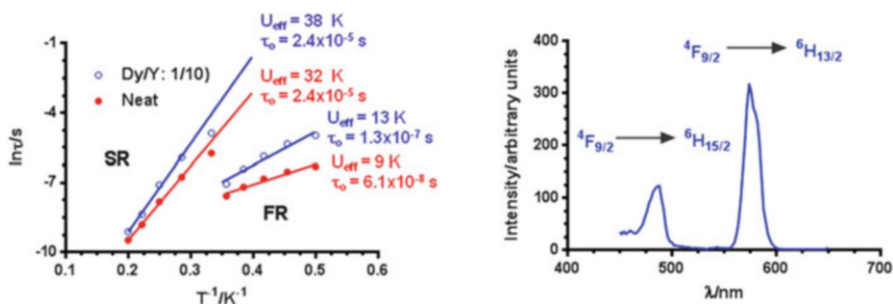
Dynamic ac magnetic susceptibility measurements showed that this complex did not show any out-of-phase  $\chi_M''$  signal, which was attributed to the presence of fast relaxation of the magnetization through QTM (promoted by transverse anisotropy, and/or dipole–dipole interactions and/or hyperfine interactions) that reduced  $U_{\text{eff}}$  to a negligible value. Theoretical ab initio CASSCF calculations showed the existence of non-negligible transverse components for the axial Kramers doublet ground state ( $g_z = 18.81$ ,  $g_x = 0.26$  and  $g_y = 0.81$ ) thus supporting the QTM at zero field. The main magnetic axis of the ground state KD lies close to the phenoxido donor atom having the greatest electron density and shortest Dy–O distance (Fig. 8), because, in such an orientation, the repulsion between this donor atom and the oblate shape electron density (which is perpendicular to the main magnetic axis) becomes minimal. When QTM was partly suppressed by applying a *dc* field of 1,000 Oe (Fig. 9), the compound showed slow relaxation of the magnetization typical of SMM behaviour below 8 K with two out-of-phase peaks. The observation of two peaks has been infrequently reported for mononuclear  $\text{Dy}^{\text{III}}$  complexes and revealed the complexity of the relaxation process in these systems.

**Fig. 8** Molecular structure of the zwitterion complex  $[\text{Dy}(\text{H}_2\text{L})(\text{NO}_3)_3] \cdot 2\text{CH}_3\text{OH}$ . Intramolecular hydrogen bonds are indicated as dotted red lines. Methanol crystallization molecules and hydrogen atoms are omitted for clarity





**Fig. 9** Temperature dependence of the out-of-phase *ac* susceptibility of the neat  $[\text{Dy}(\text{H}_2\text{L}(\text{NO}_3)_3)] \cdot 2\text{CH}_3\text{OH}$  complex (left) and the diluted  $\text{Dy}/\text{Y} = 1/10$  complex (right) under a dc magnetic field of 0.1 T



**Fig. 10** Arrhenius plot for the FR and SR processes of the neat  $[\text{Dy}(\text{H}_2\text{L}(\text{NO}_3)_3)] \cdot 2\text{CH}_3\text{OH}$  complex and the diluted  $\text{Dy}/\text{Y} = 1/10$  complex (left). Solid lines represent the best fit with the indicated parameters. Solid-state emission spectrum of  $[\text{Dy}(\text{H}_2\text{L}(\text{NO}_3)_3)] \cdot 2\text{CH}_3\text{OH}$  (right)

It should be noted that *ac* susceptibility components do not go to zero below the maxima at low temperature (Fig. 9, left), which is most likely due to ineffective suppression of QTM by the field. In light of this, the isostructural magnetic diluted complex ( $\text{Dy}/\text{Y} = 1/10$ ) was prepared to minimize the dipolar interaction between the  $\text{Dy}^{\text{III}}$  ions and so to reduce QTM. In fact, the out-of-phase signal ( $\chi''_M$ ) for the FR process at low temperature decreased in intensity (Fig. 6), thus indicating a more effective suppression of the zero-field tunnelling of the magnetization, which ultimately led to a slower relaxation of magnetization for both processes. In good accordance with these considerations, the Arrhenius analysis (Fig. 10) afforded  $U_{\text{eff}}$  values for the FR and SR processes of 9 K and 32 K, respectively, which increase in the diluted complex to 12 K and 38 K, respectively. The fact that the extracted thermal energy barrier for the SR process (38 K) was smaller than the theoretical gap between the ground and first excited Kramers doublet (105 K) was suggested to be due to possible structural changes at low temperature and/or some remaining QTM and/or limitations inherent to the ab initio quantum calculations. Finally, the compound exhibited, under excitation at the ligand absorption (270 nm),

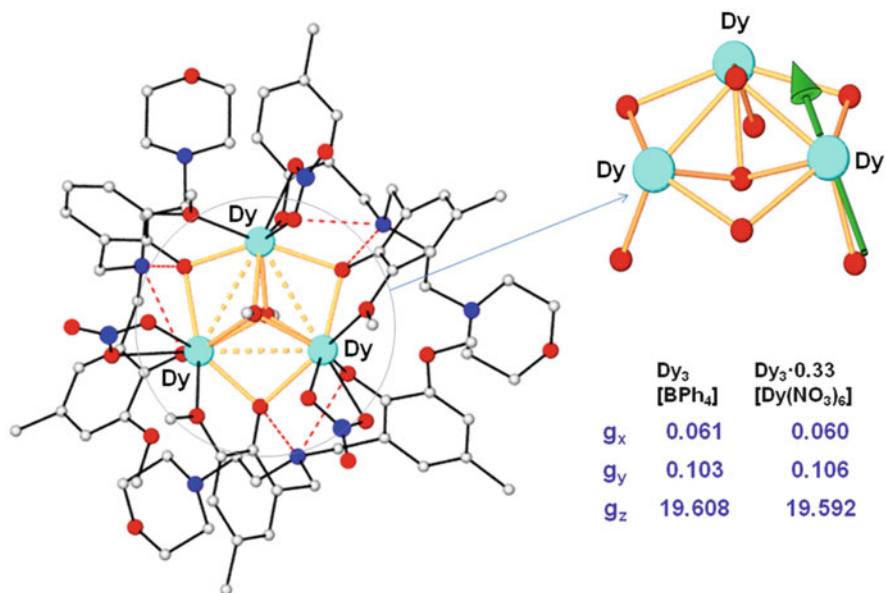
solid-state photoluminescence with the typical emission bands of the Dy<sup>III</sup> ion (Fig. 10). Therefore, this compound represented a good example of dual material combining SMM behaviour and luminescence.

### 3.2 Trinuclear Ln<sub>3</sub> Complexes

SMMs showing Dy<sub>3</sub> [92–107], Dy<sub>4</sub> [108–110] and Dy<sub>6</sub> [111, 112] cyclic structures have attracted much attention during the last decade because some of them show slow relaxation of the magnetization despite having non-magnetic ground state. Among them, Dy<sub>3</sub> triangles are the most numerous and the best studied. Experimental and theoretical studies carried out on this type of compounds demonstrated that the observed behaviour arises from non-collinearity of the planar easy anisotropy axis of the Dy<sup>III</sup> ions, leading to a toroidal alignment of the local magnetization vectors [113]. These nanomagnets called single-molecule toroids (SMTs) show spin chirality, as there exist two opposite rotations of the magnetization vectors and to convert one in the other is necessary to overcome an energy barrier. The outstanding physical properties of SMTs may open new perspectives for their potential application in quantum computing and information storage devices, as they are insensitive to homogeneous magnetic fields but interact with charge and spin currents, allowing this moment to be manipulated purely by electrical means. In view of the above considerations, much research efforts have been focused in recent years to design and prepare more examples of Dy<sub>3</sub> triangles.

The first examples of Dy<sub>3</sub> triangles with a Mannich base ligand of formulas [Dy<sub>3</sub>(μ<sub>3</sub>-OCH<sub>3</sub>)<sub>2</sub>(μ-HL)<sub>3</sub>(NO<sub>3</sub>)<sub>3</sub>][Dy(NO<sub>3</sub>)<sub>6</sub>]<sub>0.33</sub>·CH<sub>3</sub>OH·6H<sub>2</sub>O (hereafter, named Dy<sub>3</sub>·0.33[Dy(NO<sub>3</sub>)<sub>6</sub>]) and [Dy<sub>3</sub>(μ<sub>3</sub>-OCH<sub>3</sub>)<sub>2</sub>(μ-HL)<sub>3</sub>(NO<sub>3</sub>)<sub>3</sub>]BPh<sub>4</sub>·4CH<sub>3</sub>OH·H<sub>2</sub>O (hereafter, named Dy<sub>3</sub>·[BPh<sub>4</sub>]) were reported by Hänninen et al. [101] by assembling the polydentate multi-pocket aminobis(phenol) ligand 6,6'-{(2-(1-morpholy) ethylazanediyl)bis(methylene)}bis(2-methoxy-4-methylphenol) (H<sub>2</sub>L5), with Dy(NO<sub>3</sub>)<sub>3</sub>·6H<sub>2</sub>O and triethylamine in MeOH for the former and additionally adding NaBPh<sub>4</sub> for the latter.

The triangular [Dy<sub>3</sub>]<sup>+</sup> cationic units of these complexes (Fig. 11) are very similar and are made of two μ<sub>3</sub>-methoxido bridging groups that connect the Dy<sup>III</sup> ions above and below the Dy<sub>3</sub> plane and are located on the threefold axis passing through the triangle barycentre. The Dy<sub>3</sub> structure is additionally stabilized by three phenolate bridging groups belonging to the three monodeprotonated zwitterionic HL<sup>5-</sup> ligands (the amine nitrogen atoms are protonated and positively charged) that link each pair of Dy<sup>III</sup> ions, giving rise to a hexagonal bipyramidal Dy<sub>3</sub>O<sub>5</sub> bridging core. Therefore, each couple of Dy<sup>III</sup> ions is connected by double phenoxido/methoxido bridging groups. The other phenolate groups of the ligands are coordinated in a terminal mode to the corresponding Dy<sup>III</sup> ion. The remaining coordination positions of each Dy<sup>III</sup> ion are occupied by two oxygen atoms of a bidentate nitrate anion and one oxygen atom from a methoxy group affording a distorted biaugmented trigonal-prismatic DyO<sub>8</sub> coordination environment. Three strong intramolecular bifurcated hydrogen bonds are established between the amino and the phenoxide

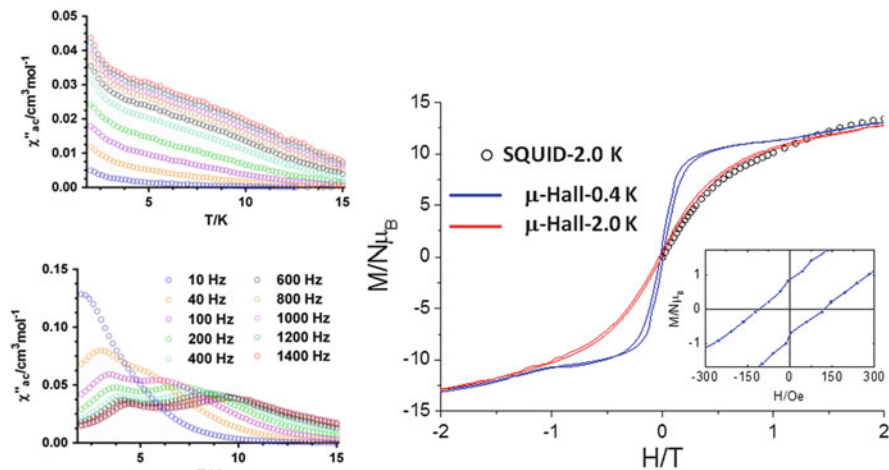


**Fig. 11** Structure of the cationic unit  $[\text{Dy}_3(\mu_3\text{-OCH}_3)_2(\mu\text{-HL})_3(\text{NO}_3)_3]^+$  (left).  $\text{Dy}_3$  unit showing only bridging and terminal phenoxido groups and orientation of the magnetic moment on one of the  $\text{Dy}^{\text{III}}$  ions (green arrow, right top). The magnetic moments of the other  $\text{Dy}^{\text{III}}$  are related by a  $C_3$ .  $g$  values for the ground KD for the indicated complexes (right bottom)

coordinated groups, which help to stabilize the conformation of the ligands and the final structure (Fig. 11).

Dc static magnetic measurements indicated that these compounds did not present the typical features of the STM systems that arise from the non-magnetic nature of the ground state, that is to say, a drop to nearly zero of the  $\chi_M T$  product at low temperature and pronounced  $S$ -shape of the  $M$  vs.  $H$  plot at low field. This behaviour was justified by the fact that, as ab initio calculations indicated, the strongly axial anisotropic axes of the ground Kramers doublet state of the  $\text{Dy}^{\text{III}}$  ions were not coplanar with the  $\text{Dy}_3$  plane but formed an angle of approximately  $70^\circ$  (as expected, the main magnetic axis of the ground state KD lies close to the oxygen atom of the terminal phenoxide, which present the greatest electron density and shortest Dy-O distance). As a result, the magnetization vectors of the ground KDs did not compensate, leading to a paramagnetic ground state and preventing this triangular molecule to behave as an SMT. Ab initio calculations also showed a weak antiferromagnetic coupling between the  $\text{Dy}^{\text{III}}$  ions ( $<0.25 \text{ cm}^{-1}$ ), with the major contribution coming from the magnetic dipolar interactions rather than from exchange coupling. Both  $\text{Dy}^{\text{III}}$  complexes exhibited under zero-field slow relaxation of the magnetization below  $\sim 15 \text{ K}$ , with broad signals in the  $\chi''_M$  vs.  $T$  plot, which was attributed to the existence of several relaxation processes, including fast relaxation of the magnetization via a QTM mechanism through the thermal energy barrier between degenerate energy levels. After partial elimination of QTM by applying a





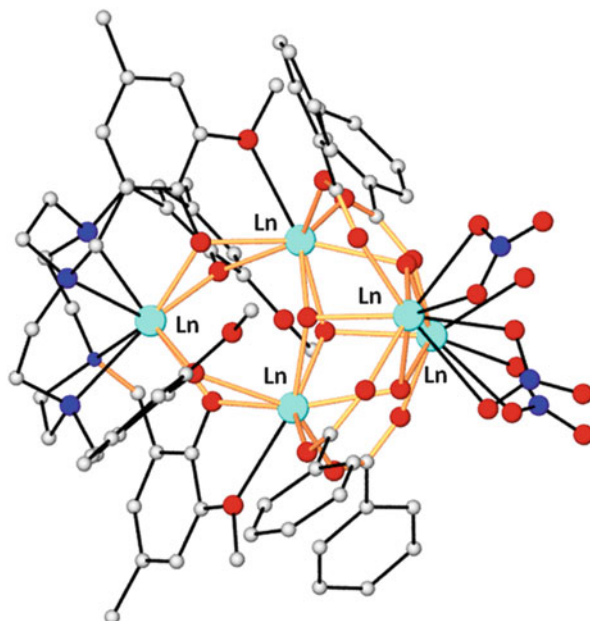
**Fig. 12** Temperature dependence of the out-of-phase  $\chi_M''$  ac signals under zero dc field (left) of 1,000 Oe (right) and hysteresis loop (inset) for  $\text{Dy}_3\text{[BPh}_4\text{]}$

small dc field of 1,000 Oe, the  $\chi_M''$  vs.  $T$  plot of the compound  $\text{Dy}_3\text{[BPh}_4\text{]}$  showed two neat peaks (another rare example of a polynuclear  $\text{Dy}^{\text{III}}$  complex where all the  $\text{Dy}^{\text{III}}$  atoms are crystallographically equivalent and, however, exhibits two relaxation two relaxation processes), whereas the  $\text{Dy}_3\cdot 0.33[\text{Dy}(\text{NO}_3)_6]$  exhibited only one peak, despite the fact that it has two different type of  $\text{Dy}^{\text{III}}$  ions (those pertaining to the  $\text{Dy}_3$  molecule and to the counteranion). The effective thermal energy barriers ( $U_{\text{eff}}$ ) extracted from the corresponding Arrhenius plots were  $U_{\text{eff}} = 34.8(2) \text{ cm}^{-1}$  with  $\tau_0 = 7.5 \times 10^{-7} \text{ s}$  for the SR process and  $U_{\text{eff}} = 19.5(2) \text{ cm}^{-1}$  with  $\tau_0 = 3.75 \times 10^{-7} \text{ s}$  for the FR process of  $\text{Dy}_3\text{[BPh}_4\text{]}$  and  $U_{\text{eff}} = 19.4(4) \text{ cm}^{-1}$  and  $\tau_0 = 4.7 \times 10^{-6} \text{ s}$ . for  $\text{Dy}_3\cdot 0.33[\text{Dy}(\text{NO}_3)_6]$  (in Fig. 12, the  $\chi_M''$  vs.  $T$  plot of the compound  $\text{Dy}_3\text{[BPh}_4\text{]}$  is given as an example). Owing to the weak magnetic interaction interactions between the  $\text{Dy}^{\text{III}}$  ions inside the  $\text{Dy}_3$  triangle, it was suggested that the observed relaxation processes arise from the levels of the individual atoms rather than from the exchange-coupled levels of the  $\text{Dy}_3$  molecule. Finally, for both compounds a narrow though noticeable loop opened as the temperature decreases from 2 K down to 0.4 K (remnant magnetization of  $\sim 1 \text{ N}\mu\text{B}$  and a coercive field of  $\sim 120 \text{ Oe}$ ), thus supporting their SMM behaviour. The hysteresis is so small because of the existence of quantum tunnelling at zero field.

### 3.3 Pentanuclear $\text{Ln}_5$ Complexes

Wu et al. [114] recently reported two  $\text{Ln}_5$  complexes of general formula  $[\text{Ln}_5(\text{H}_2\text{O})(\text{OH})_4(\text{NO}_3)_3(\text{OBz})_4(\mu_3\text{-L}8)]\cdot\text{CH}_3\text{OH}$  ( $\text{Ln}^{\text{III}} = \text{Tb}, \text{Dy}$ ), which were assembled in a





**Fig. 13** Molecular structure of  $[\text{Ln}_5(\text{H}_2\text{O})(\text{OH})_4(\text{NO}_3)_3(\text{OBz})_4(\mu_3\text{-L8})\cdot\text{CH}_3\text{OH}]$ . Hydrogen atoms and methanol crystal molecules are omitted for clarity. The bridging network is highlighted in orange colour

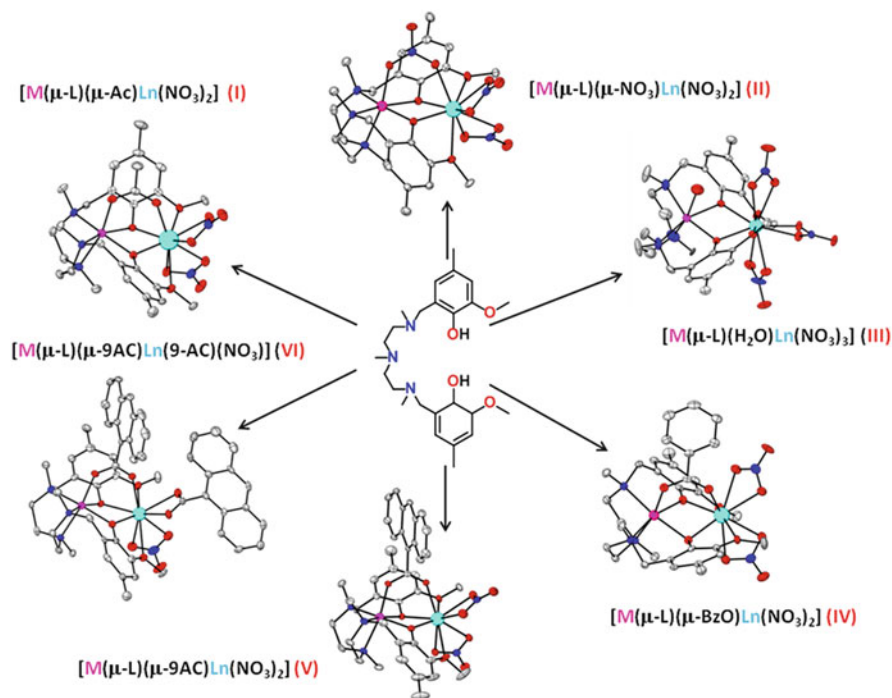
one-pot reaction between  $N,N',N'',N'''$ -tetra-(2-hydroxy-3-methoxy-5-methylbenzyl)-1,4,7,10-tetraazacyclododecane ligand ( $\text{H}_4\text{L8}$ ),  $\text{Ln}(\text{NO}_3)_3\cdot x\text{H}_2\text{O}$  and benzoic acid ( $\text{HOBz}$ ).

In the structure of these complexes (Fig. 13), one of the  $\text{Ln}^{\text{III}}$  ions occupies the inner pocket of the L8 ligand exhibiting a square prismatic  $\text{LnO}_4\text{N}_4$  coordination environment, which is formed by the coordination of the four nitrogen atoms of the amino groups and the four oxygen atoms of the phenolate groups belonging to ligand. Each pair of phenoxido oxygen atoms together with methoxy groups connects this  $\text{Ln}^{\text{III}}$  atom to another  $\text{Ln}^{\text{III}}$  ion that forms part of a tetrahydroxo-bridged cubane unit, in which each couple of  $\text{Ln}^{\text{III}}$  ions are bridged by a benzoate bridging group. The two remaining methoxy groups belonging to the ligand keep uncoordinated. Two of the  $\text{Ln}^{\text{III}}$  ions of the cubane unit exhibit bicapped trigonal-prismatic  $\text{LnO}_8$  coordination spheres, whereas the other two  $\text{Ln}^{\text{III}}$  ions display distorted  $\text{LnO}_8$  and  $\text{LnO}_9$  coordination environments. The coordination sphere of the former is completed by one water molecule and a bidentate nitrate anion, whereas two bidentate nitrate anions complete the coordination sphere of the latter. The structure is further stabilized by two strong intramolecular hydrogen bonds involving  $\mu_3\text{-OH}$  and the oxygen atoms from an uncoordinated methoxy group. Only the  $\text{Dy}^{\text{III}}$  complex shows a strong frequency dependent out-of-phase ( $\chi''_M$ )  $ac$  signal at 6 kOe, thus revealing the onset of slow relaxation of the magnetization, which is typical of SMM behaviour. However, the effective energy barrier extracted from the Arrhenius plot was shown to be very small of 4.11 K.

## 4 Heterometallic 3d-4f Complexes

### 4.1 Dinuclear $M^{II}Ln^{III}$ Complexes

The first examples of 3d-4f binuclear complexes based on Mannich base ligands exhibiting SMM behaviour were reported by our group in 2011 [115–118]. We employed the compartmental ligand  $H_2L$  ( $H_2L = N,N',N''$ -trimethyl- $N,N''$ -bis(2-hydroxy-3-methoxy-5-methylbenzyl)diethylene triamine) which possesses an  $N_3O_2$  pentadentate inner coordination compartment (formed by the three nitrogen atoms of the amine groups and two oxygen atoms from the phenol moieties) and the  $O_2O'_2$  outer site (formed from two phenolic and two methoxy oxygen atoms). Interestingly, when transition metal ions with a high tendency to adopt an octahedral geometry occupy this inner coordination site, they are forced to complete their coordination sphere with one additional donor atom, which comes from either a terminal or a bridging ligand connecting the Ln and the transition metal ions. In this latter case, triply bridged 3d-4f complexes are obtained. It should be noted that the ligand does not present active hydrogen atoms that can be involved in intermolecular hydrogen bond interactions and therefore the 3d-4f dinuclear molecules



**Fig. 14** Perspective view of the different structural types for the family of M-Ln dinuclear complexes prepared with the  $H_2L$  ligand

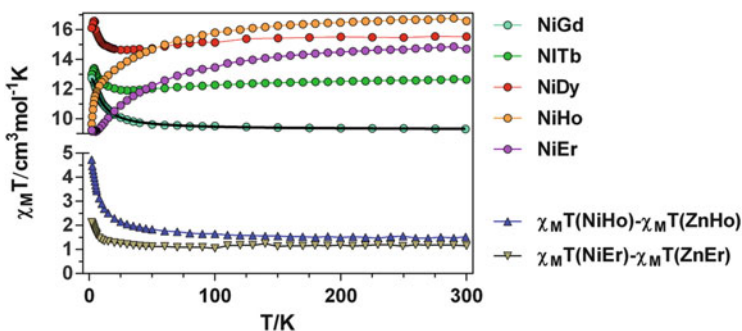
are generally well isolated in crystal lattice, which, as indicated elsewhere, favours the observation of SMM behaviour.

An extensive family of dinuclear complexes  $[M(\mu\text{-L})(\mu\text{-Ac})\text{Ln}(\text{NO}_3)_2]$  ( $M^{\text{II}} = \text{Co}, \text{Ni}, \text{Zn}$ ;  $\text{Ln}^{\text{III}} = \text{Gd}, \text{Tb}, \text{Dy}, \text{Ho}, \text{Er}, \text{and Yb}$  for  $M^{\text{II}} = \text{Zn}, \text{Ni}$ ) were prepared from the one-pot reaction of  $\text{H}_2\text{L}$  with  $M(\text{OAc})_2 \cdot n\text{H}_2\text{O}$  and subsequently with  $\text{Ln}(\text{NO}_3)_3 \cdot n\text{H}_2\text{O}$  in  $\text{MeOH}$  in 1:1:1 molar ratio (Fig. 14). The same reaction but using  $M(\text{NO}_3)_3 \cdot n\text{H}_2\text{O}$  instead of  $\text{Ni}(\text{OAc})_2 \cdot 4\text{H}_2\text{O}$  and  $\text{Ln}(\text{NO}_3)_3 \cdot 6\text{H}_2\text{O}$  led to two different M-Ln dinuclear complexes  $[M(\mu\text{-L})(\mu\text{-NO}_3)\text{Ln}(\text{NO}_3)_2] \cdot n\text{S}$  ( $M^{\text{II}} = \text{Ni}$ ,  $\text{Ln}^{\text{III}} = \text{Tb}$ ;  $M^{\text{II}} = \text{Zn}$ ,  $\text{Ln}^{\text{III}} = \text{Er}$ ;  $\text{S} = \text{MeOH}, \text{H}_2\text{O}$ ) and  $[M(\text{H}_2\text{O})(\mu\text{-L})\text{Ln}(\text{NO}_3)_3] \cdot n\text{S}$  ( $M^{\text{II}} = \text{Co}$ ,  $\text{Ln}^{\text{III}} = \text{Gd}, \text{Tb}$ ;  $M^{\text{II}} = \text{Ni}$ ,  $\text{Ln}^{\text{III}} = \text{Gd}, \text{Tb}$ ;  $M^{\text{II}} = \text{Zn}$ ,  $\text{Ln}^{\text{III}} = \text{Nd}$ ). Dinuclear complexes containing other carboxylate bridging groups such as benzoate ( $\text{BzO}^-$ ) and 9-anthracenecarboxylato ( $9\text{-AC}^-$ ) of general formula  $[M(\mu\text{-L})(\mu\text{-X})\text{Ln}(\text{NO}_3)_2]$  ( $M^{\text{II}} = \text{Ni}$ ;  $\text{Ln}^{\text{III}} = \text{Dy}$  and  $\text{X} = \text{BzO}^-$ ;  $M^{\text{II}} = \text{Zn}$ ,  $\text{Ln}^{\text{III}} = \text{Tb}, \text{Dy}, \text{Er}, \text{Yb}$  and  $\text{X} = 9\text{-AC}^-$ ) could be prepared by reacting a methanolic (or acetonitrile) solution containing  $\text{H}_2\text{L}$ ,  $\text{Ni}(\text{NO}_3)_3 \cdot 6\text{H}_2\text{O}$  and  $\text{Dy}(\text{NO}_3)_3 \cdot 6\text{H}_2\text{O}$  in 1:1:1 molar ratio with either  $\text{NaBzO}$  or a 9-anthracene carboxylic/ $\text{Et}_3\text{N}$  mixture in 1:1 molar ratio. Using the same reaction conditions as for the preparation of complexes  $[M(\mu\text{-L})(\mu\text{-Ac})\text{Ln}(\text{NO}_3)_2]$  and employing  $9\text{-AC}^-$  instead of  $\text{Ac}^-$ , powders were obtained with  $\text{Yb}^{\text{III}}$  and  $\text{Dy}^{\text{III}}$  metal ions, which after recrystallization in acetonitrile afforded the compounds of formula  $[M(\mu\text{-L})(\mu\text{-9-An})\text{Yb}(9\text{-An})(\text{NO}_3)_2] \cdot 3\text{CH}_3\text{CN}$  ( $M^{\text{II}} = \text{Ni}$ ,  $\text{Dy}^{\text{III}} = \text{Yb}$ ;  $M^{\text{II}} = \text{Zn}$ ,  $\text{Ln}^{\text{III}} = \text{Yb}$ ) having both bridging and chelating bidentate 9-anthracenecarboxylate ligands, the latter coordinated to the  $\text{Yb}^{\text{III}}$  ion. This type of complex  $[\text{Zn}(\mu\text{-L})(\mu\text{-9-An})\text{Nd}(9\text{-An})(\text{NO}_3)_2] \cdot 2\text{CH}_3\text{CN} \cdot 3\text{H}_2\text{O}$  was also obtained with  $\text{Nd}^{\text{III}}$  but using the same reaction conditions as for complexes  $[\text{Zn}(\mu\text{-L})(\mu\text{-9AC})\text{Ln}(\text{NO}_3)_2]$ . However, using methanol as solvent and  $\text{Zn}(\text{ClO}_4) \cdot 6\text{H}_2\text{O}$  instead of  $\text{Zn}(\text{NO}_3)_2 \cdot 6\text{H}_2\text{O}$ , the complex  $[\text{Zn}(\mu\text{-L})(\mu\text{-9-An})\text{Nd}(\text{CH}_3\text{OH})_2(\text{NO}_3)](\text{ClO}_4) \cdot 2\text{CH}_3\text{OH}$  could be obtained (see Fig. 14). It should be noted that Co-Ln complexes with  $\text{BzO}^-$  and  $9\text{-AC}^-$  were not prepared.

These compounds present the following common structural features:

1.  $\text{Ln}^{\text{III}}$  and  $M^{\text{II}}$  ions are triply bridged by two phenoxido groups belonging to the  $\text{L}_2^-$  ligand and one additional bidentate bridging ligand ( $\text{NO}_3^-$ ,  $\text{BzO}^-$ ,  $\text{Ac}^-$ ,  $9\text{-AC}^-$ ). Type III compounds represent an exception as they only have the two phenoxido bridging groups connecting the metal ions.
2. The transition metal ion exhibits a slightly trigonally distorted  $\text{NiN}_3\text{O}_3$  coordination environment (the five donor atoms from the ligand and the additional oxygen atoms coming from a water molecule or the anion bridging ligand), where the three nitrogen atoms from the amine groups, and consequently the three oxygen atoms, belonging to the anion bridging ligand and phenoxo-bridging groups, occupy *fac* positions.
3. The bridging anion group forces the structure to be folded with the average hinge angle of the  $M(\mu\text{-O}_2)\text{Ln}$  bridging fragment (the hinge angle,  $\beta$ , is the dihedral angle between the O-Ni-O and O-Ln-O planes in the bridging fragment) being larger for carboxylato ( $\sim 22^\circ$ ) than for nitrato ( $\sim 14^\circ$ ). When the metals ions are not connected by an anion bridging ligand, the structure is almost planar.

- The folding of the structure provoked by the coordination of the anion bridging ligand leads to a non-symmetric conformation of the  $M(\text{di-}\mu\text{-phenoxido})(\mu\text{-anion})\text{Ln}$  bridging fragment, as there are two non-equivalent  $\text{Ln-O}_{\text{phenoxido}}$  and  $\text{M-O}_{\text{phenoxido}}$  bond distances as well as two different  $\text{M-O-Ln}$  bridging angles. The difference between two non-equivalent structural parameters decreases with decreasing  $\beta$ , so that for diphenoxido-bridged planar complexes (without additional bridging anion) the bridging fragment is rather symmetric. In all cases, the  $\text{Ln-O}_{\text{phenoxido}}$  and  $\text{M-O}_{\text{phenoxido}}$  bond distances are the shortest ones. In each series of isostructural compounds, the hinge angle increases with decreasing  $\text{Ln}^{\text{III}}$  size, as expected.
- The average  $\text{Ln-O}_{\text{phenoxido}}$  bond distance for isostructural complexes, where only the lanthanide anion is changed, steadily diminishes from  $\text{Gd}^{\text{III}}$  to  $\text{Er}^{\text{III}}$  following the lanthanide contraction, with a concomitant decrease of the average  $\text{M-Ln}$  and  $\text{Ln-O}_{\text{anion}}$  bond distances.
- In all the triple-bridged complexes, the  $\text{Ln}^{\text{III}}$  ion exhibits a rather unsymmetrical  $\text{LnO}_9$  coordination sphere, consisting of the two phenoxido bridging oxygen atoms, the two methoxy oxygen atoms, one oxygen atom from the anion bridging group and four oxygen atoms belonging to two bidentate nitrate anions. For diphenoxido-bridged planar complexes (type III), the coordination of one additional bidentate nitrate ligand to the  $\text{Ln}^{\text{III}}$  ion leads to an expanded  $\text{LnO}_{10}$  coordination sphere.
- The size of the  $\text{Ln}^{\text{III}}$  ions plays a pivotal role in the adoption of a triply or doubly bridged structure in nitrate containing complexes, so that  $\text{Ln}^{\text{III}}$  ions smaller in size than  $\text{Gd}^{3+}$  always lead to nitratediphenoxido triply bridged dinuclear complexes for the  $\text{Ni}^{\text{II}}\text{Ln}^{\text{III}}$  series. However, the  $\text{Co}^{\text{II}}\text{Tb}^{\text{III}}$  ion is not able to form the nitratediphenoxido triply bridged complex, which seems to indicate that not only the size of the  $\text{Ln}^{\text{III}}$  ion plays an important role in the adoption of the triply bridged structure but also the size of the transition metal ion. In this regard, when the size of the metal ions increases, the tension of the nitrate bridging ligand becomes larger and, from definite values of the size of the metal ions, the



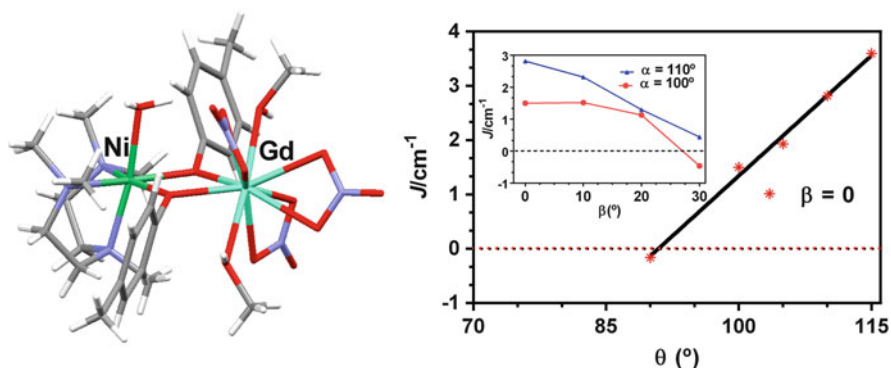
**Fig. 15** Temperature dependence of the  $\chi_M T$  product at 1,000 Oe for  $[\text{M}(\mu\text{-L})(\mu\text{-Ac})\text{Ln}(\text{NO}_3)_2]$  complexes. Black solid lines show the best fits for the NiGd complex, whereas the rest of the solid lines are a guide to the eye

formation of the nitrate bridge is unfavourable. Therefore, subtle changes in the size of the  $M^{II}$  ion on going from  $Ni^{II}$  to  $Co^{II}$  may be responsible for the presence of only a double-phenoxo bridge in the  $Co^{II}Tb^{III}$  complex.

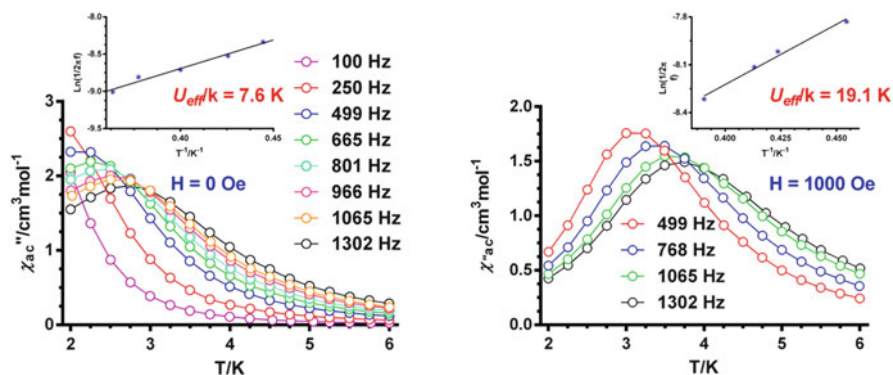
The magnetic properties of the  $[M(\mu-L)(\mu-Ac)Ln(NO_3)_2]$  complexes are given as an example in Fig. 15 in the form  $\chi_M T$  vs.  $T$  ( $\chi_M$  being the magnetic susceptibility per  $NiLn$  unit). For MDy and MTb complexes, the  $\chi_M T$  value decreases slowly with decreasing temperature until reaching a minimum at around 30 K. This behaviour is due to depopulation of the  $M_J$  sublevels of the  $Ln^{III}$  ion (and when  $M^{II} = Co$  also to the depopulation of the spin-orbit levels of this transition metal ion), which arise from the splitting of the corresponding ground term by the ligand field. Below the temperature of the minimum,  $\chi_M T$  increases to reach a maximum at very low temperature and then, in some cases, shows a sharp decrease down to 2 K. The increase in  $\chi_M T$  at low temperature is due to a ferromagnetic interaction between  $M^{II}$  and  $Ln^{III}$ , whereas the decrease of  $\chi_M T$  after the maximum is likely connected with the presence of magnetic anisotropy and/or weak antiferromagnetic interactions between the dinuclear complexes. However, in the case of MHo and MEr complexes  $\chi_M T$  decreases first slightly until  $\sim 50$  K and then sharply down to 2 K. This behaviour is mainly due to the depopulation of the  $M_J$  sublevels of the  $Ho^{III}$  and  $Er^{III}$  ion that mask the ferromagnetic interaction between  $M^{II}$  and  $Ln^{III}$ . The contribution of the crystal-field effects of the  $Ln^{III}$  ion in these complexes can be removed by subtracting from the experimental  $\chi_M T$  product for MHo and MEr those of the isostructural complexes ZnHo and ZnEr, respectively, whose magnetic behaviour depends only on the  $Ln^{III}$  ion. The resulting  $\Delta\chi_M T$  values are almost constant over the whole temperature range (see Fig. 15) and increase in the lowest-temperature region, thus supporting a ferromagnetic interaction between  $M^{II}$  and  $Ln^{III}$  ions. Therefore, the magnetic exchange interactions between  $M^{II}$  ( $M^{II} = Co, Ni$ ) and  $Ln^{III}$  ( $Ln^{III} = Gd, Tb, Dy, Ho$  and  $Er$ ), metal ions are in all cases ferromagnetic in nature. The values of the magnetic exchange coupling constant  $J_{NiGd}$  are  $+2.2$  for the planar complex  $[Ni(H_2O)(\mu-L)Gd(NO_3)_3]$  and  $+1.4 \text{ cm}^{-1}$  for the folded complex  $[Ni(\mu-L)(\mu-Ac)Gd(NO_3)_2]$ , whereas the  $J_{CoGd}$  values are found between  $+0.75 \text{ cm}^{-1}$  (planar) and  $+0.69 \text{ cm}^{-1}$  (folded). Similar  $J_{NiGd}$  values have been found for analogous binuclear complexes with compartmental Schiff base ligands [90]. It appears from the above results that the structural factors associated with the bridging fragment have less influence in determining the magnitude of the magnetic exchange interaction in Co-Ln complexes than in their Ni-Ln analogues.

Theoretical DF studies carried out on a dinuclear  $Ni^{II}-Gd^{III}$  model compound (Fig. 16, left) are in good accordance with experimental results, as they have clearly shown that the ferromagnetic magnetic interaction increases as the  $M(O)_2Gd$  bridging fragment becomes more planar and the Ni-O-Gd bridging angle increases (Fig. 16, right).

Dynamic ac magnetic susceptibility measurements performed on these  $M^{II}Ln^{III}$  ( $M^{II} = Ni, Co$ ) complexes clearly show that only the  $M^{II}Dy^{III}$  counterparts present frequency dependent in-phase ( $\chi'_M$ ) and out-of-phase ( $\chi''_M$ ) susceptibility signals and, therefore, slow relaxation of the magnetization and possible SMM behaviour. However, among  $M^{II}Dy^{III}$  complexes,  $[Ni(\mu-L)(\mu-NO_3)Dy(NO_3)_2]$  is the only one



**Fig. 16** (Left)  $[\text{Ni}(\text{PMTA})(\text{H}_2\text{O})(\mu\text{-Oph})_2\text{Gd}(\text{OCH}_3)_2(\text{NO}_3)_3]$  (PMTA = 1,1,4,7,7-pentamethyldiethylenetriamine and  $\text{Oph}^- = 4\text{-methylphenolate anion}$ ) model complex used in DF calculations. Colour code: *N* blue, *O* red, *Ni* green, *Dy* light blue and *C* grey. (Right) Variation of  $J_{\text{NiGd}}$  with the Ni-O-Gd bridging angle  $\theta$  and the hinge angle  $\beta$  (inset)



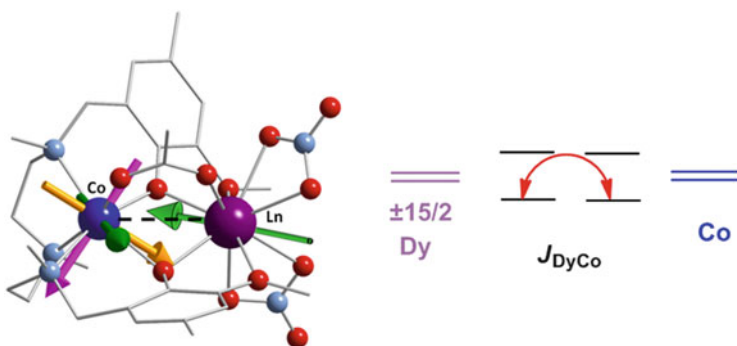
**Fig. 17** Temperature dependence of out-of-phase  $\chi''_M$  components of the ac susceptibility for complex  $[\text{Ni}(\mu\text{-L})(\mu\text{-NO}_3)\text{Dy}(\text{NO}_3)_2]$  measured under zero applied dc field (left) and 1,000 Oe (right). Solid lines are a guide to the eye. Inset: Arrhenius plot,  $\ln(2\pi f)$  vs.  $T^{-1}$

exhibiting maxima above 2 K at zero field (Fig. 17). The best fit of the temperature dependence of the relaxation times for this compound (extracted from the fitting of the frequency dependence of  $\chi''_M$  to the generalized Debye model) to the Arrhenius plot ( $\tau = \tau_0 \exp.(U_{\text{eff}}/k_B T)$ ) led to an energy barrier for magnetization reversal of 7.6 K with a pre-exponential factor  $\tau_0 = 7.2 \times 10^{-6}$  s (Fig. 17). It is well known that the application of a small magnetic field to an SMM system provokes the stabilization of negative  $M_J$  levels with respect to the positive counterparts, so that  $\pm M_J$  levels at both sides of the energy barrier become out-of-resonance and, therefore, QTM regimes and assisted QTM (TA-QTM) are partly or fully suppressed. In turn, this enhances  $U_{\text{eff}}$  and slows down the relaxation process (frequency dependent maxima in the  $\chi''_M$  vs.  $T$  plot are shifted to higher temperatures, whereas the



temperature dependent maxima in the  $\chi''_M$  vs.  $f$  plot are shifted to lower frequencies). In fact, when an external  $dc$  magnetic field of 1,000 Oe is applied, the thermally activated barrier energy of  $[\text{Ni}(\mu\text{-L})(\mu\text{-NO}_3)\text{Dy}(\text{NO}_3)_2]$  increases to a value of 19.1 K ( $\tau_0 = 7.2 \times 10^{-7}$  s). For the rest of  $\text{M}^{\text{II}}\text{Dy}^{\text{III}}$  complexes, the application of a magnetic field of 1,000 Oe leads to frequency and temperature dependent  $\chi''_M$  maxima with  $U_{\text{eff}}$  values in the range 5–10 K.

In view of the above results, it is reasonable to assume, firstly, that the combination of anisotropic ions such as  $\text{Co}^{\text{II}}$  (or  $\text{Ni}^{\text{II}}$ ) and  $\text{Ln}^{\text{III}}$  in the same compound does not guarantee SMM behaviour at zero field and, secondly, that anisotropy barrier is very small in these  $\text{M}^{\text{II}}\text{Ln}^{\text{III}}$  complexes. This fact can be due to several reasons: (1) The local anisotropies can be combined in a subtractive manner, resulting in a small anisotropy for the whole molecule. In fact, CASSCF calculations carried out on the  $[\text{Co}(\mu\text{-L})(\mu\text{-Ac})\text{Dy}(\text{NO}_3)_2]$  have showed that the ground Kramers doublet of the  $\text{Dy}^{\text{III}}$  ion is strongly axial with  $g_z = 18.9$  ( $g_x = 0.06$  and  $g_y = 0.09$ ), with the main anisotropy axis lying close to the Dy-Co direction (Fig. 18). As expected, the  $\text{Co}^{\text{II}}$  ion is much less anisotropic with  $g_z = 6.71$  along the main anisotropy axis ( $g_x = 2.02$  and  $g_y = 3.63$ ), which is directed close to the normal of the Co-Dy direction (Fig. 18, left). (2) The very weak  $J_{\text{MLn}}$  observed for these  $\text{M}^{\text{II}}\text{Ln}^{\text{III}}$  complexes ( $< 2.5 \text{ cm}^{-1}$ ) leads to a small separation between the low-lying split energy sublevels resulting from the magnetic exchange interaction between  $\text{M}^{\text{II}}$  and  $\text{Ln}^{\text{III}}$  metal ions (mixing of low-lying excited states in the ground state occurs favouring QTM), and then to small effective energy barriers for magnetization reversal (Fig. 18, right). The fact that the only compound having SMM behaviour at zero field,  $[\text{Ni}(\mu\text{-L})(\mu\text{-NO}_3)\text{Dy}(\text{NO}_3)_2]$ , is that having the stronger magnetic exchange interaction seems to support this hypothesis (3) the random transversal field for the  $\text{Ln}^{\text{III}}$  ions created by the weakly exchange-coupled paramagnetic metal ion, which favours the faster zero-field QTM process. In this respect, as indicated elsewhere, when the 3d-4f magnetic exchange coupling is strong enough, the exchange-coupled levels are well separated



**Fig. 18** (Left) Orientation of the main local anisotropic axis for  $\text{Dy}^{\text{III}}$  and  $\text{Co}^{\text{II}}$  (green arrows). (Right) Magnetic exchange coupling between the ground axial KD states of  $\text{Dy}^{\text{III}}$  and  $\text{Co}^{\text{II}}$  leading to a small thermal energy barrier

and the QTM is suppressed, so that large energy barriers, hysteresis loops and relaxation times are observed.

In the light of these considerations, it could be expected that the replacement of paramagnetic  $M^{II}$  ions in  $M^{II}Ln^{III}$  complexes by diamagnetic counterparts ( $Zn^{II}$ ,  $Cd^{II}$ ) would enhance their SMM properties. This is because the weak  $M^{II}-Ln^{III}$  interactions are removed and therefore the magnetic properties arise only from the largely anisotropic  $Ln^{III}$  ion. The goodness of this replacement strategy could be confirmed by comparing the SMM properties of triply bridged  $Zn^{II}Dy^{III}$  complexes  $[Zn(\mu-L)(\mu-X)Dy(NO_3)_2]$  ( $X = NO_3^-$ ,  $Ac^-$  and  $9-AC^-$ ) with those of the isostructural  $[M(\mu-L)(\mu-X)Dy(NO_3)_2]$  ( $M^{II} = Ni, Co$ ) counterparts. This comparison (Table 1) clearly indicates that the replacement of  $M^{II}$  ion by  $Zn^{II}$  ion in weakly exchanged  $[M(\mu-L)(\mu-X)Dy(NO_3)_2]$  complexes gives rise either to the appearance of slow relaxation of the magnetization (in the cases where the  $M^{II}$ -containing compounds do not exhibit slow relaxation of magnetization even in the presence of a small applied dc field) or to a considerable improvement of the field-induced SMM properties. Therefore, these results provide good supporting evidence that the substitution of the paramagnetic  $M^{II}$  metal ion by  $Zn^{II}$  can be an appropriate strategy to improve the SMM properties in diphenoxido-bridged 3d-4f systems.

It should be noted at this point that the crystal field around the  $Ln^{III}$  ions in these  $Zn^{II}Ln^{III}$  complexes essentially depends on the oxygen donor atoms exercising the largest electrostatic repulsion with the  $Ln^{III}$  electron density, that is to say, those possessing the shortest Dy-O distances. In the triply bridged  $Zn^{II}Ln^{III}$  complexes, the two  $Ln-O_{phenoxido}$  distances are the shortest ones and, because of the unsymmetrical nature of the  $Zn(O)_2Ln$  bridging fragment, one of them is 0.8 Å shorter than the other. In the case of  $Dy^{III}$  derivative and to reduce the repulsive interactions, the oblate surface electron density of  $Dy^{III}$  is positioned almost perpendicular to the shortest Dy-O bond and, consequently, the magnetic moment that is perpendicular to the oblate electron density (see Fig. 3) lies in the direction of the shortest Dy-O bond. Therefore, the existence of one Dy-O bond that is significantly shortest than the others can be enough to create an axial crystal field and, therefore, to lead to

**Table 1** Comparison of  $U_{eff}$  and  $\tau_0$  values for compounds  $[M(\mu-L)(\mu-X)Dy(NO_3)_2]$  ( $M^{II} = Ni, Co$ ) and  $[Zn(\mu-L)(\mu-X)Dy(NO_3)_2]$

Compound	$\chi''_M$ signal at $H = 0$ T	$U_{eff}$ (K) at $H = 0.1$ T	$\tau_0$ (s)
$[Zn(\mu-L)(\mu-OAc)Dy(NO_3)_2]$	Yes	41 (2)	$5.6 \times 10^{-7}$
$[Ni(\mu-L)(\mu-OAc)Dy(NO_3)_2]$	No	<5	–
$[Co(\mu-L)(\mu-OAc)Dy(NO_3)_2]$	No	7.6 (3)	$1.3 \times 10^{-5}$
$[Zn(\mu-L)(\mu-OAc)Er(NO_3)_2]$	No	11.7 (3)	$2.0 \times 10^{-6}$
$[Ni(\mu-L)(\mu-OAc)Er(NO_3)_2]$	No	No SMM	–
$[Co(\mu-L)(\mu-OAc)Er(NO_3)_2]$	No	No SMM	–
$[Zn(\mu-L)(\mu-9AC)Dy(NO_3)_2]$	No	32.1 (3)	$1.9 \times 10^{-7}$
$[Zn(\mu-L)(\mu-9AC)Dy(NO_3)_2]$	No	10.1 (2)	$3.4 \times 10^{-6}$
$[Zn(\mu-L)(\mu-NO_3)Yb(NO_3)_2]$	No	22 (2)	$5.3 \times 10^{-8}$
$[Ni(\mu-L)(\mu-NO_3)Yb(NO_3)_2]$	No	No SMM	–



axial anisotropy. This could be the reason why easy-axis anisotropy ( $M_J = \pm 15/2$  ground Kramers doublet) is usually found in low-symmetry  $\text{Dy}^{\text{III}}$  complexes. Nevertheless, the lack of truly axial symmetry allows the mixture of the ground and excited wave functions thus favouring QTM. In summary, the application of a  $dc$  field for quenching QTM is mandatory for this type of complexes and, moreover, because the distribution of the donor oxygen atoms around the  $\text{Dy}^{\text{III}}$  is not appropriate to create a strong axial crystal field, the thermal energy barrier is expected to be small, which agrees well with the observed results. The fact that the crystal field is not strongly axial allows that the  $\text{Er}^{\text{III}}$  with prolate electron density exhibits field-induced slow relaxation of magnetization with very small  $U_{\text{eff}}$  value. In  $\text{Yb}^{\text{III}}$  complexes, magnetization relaxation does follow the thermal energy barrier mechanism but the Raman process (see below).

The  $\text{Zn}^{\text{II}}\text{-Ln}^{\text{III}}$  complexes containing the  $\text{L}^{2-}$  bridging ligand [117], in a similar manner to their analogous Schiff base counterparts, could exhibit interesting luminescent properties. The  $\text{L}^{2-}$  Mannich ligand could act as an antenna group, sensitizing  $\text{Ln}^{\text{III}}$ -based luminescence through an intramolecular  $\text{L} \rightarrow \text{Ln}$  photoinduced energy transfer process.

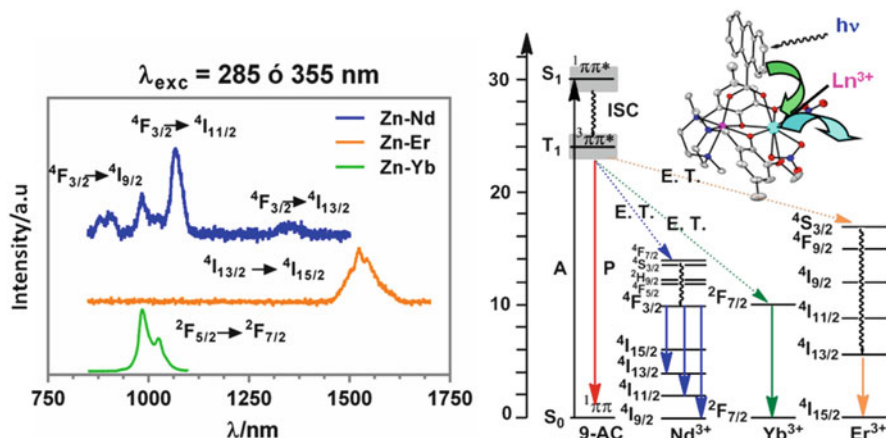
The study of the solid photophysical properties of complexes  $[\text{Zn}(\mu\text{-L})(\mu\text{-OAc})\text{Ln}^{\text{III}}(\text{NO}_3)_2]$  ( $\text{Ln}^{\text{III}} = \text{Dy}, \text{Tb}$ ) [117] clearly indicates that after excitation into the UV  $\pi\text{-}\pi^*$  absorption band of ligand  $\text{L}^{2-}$  at 290 nm characteristic  $\text{Tb}^{\text{III}}$  ( $^5\text{D}_4 \rightarrow ^7\text{F}_j$ ;  $J = 3, 4, 5, 6$ ) and  $\text{Dy}^{\text{III}}$  ( $^4\text{F}_{9/2} \rightarrow ^6\text{H}_{J/2}$ ;  $J = 15/2, 13/2$ ) emission bands appeared in the visible region, respectively. However, a significant residual ligand-centred emission is still observed which indicates that the energy transfer process is not complete. Therefore, these complexes are dual luminescent materials exhibiting emission from the ligand and lanthanide ions.

Regarding the  $\text{Zn}^{\text{II}}\text{-Ln}^{\text{III}}$  complexes ( $\text{Ln}^{\text{III}} = \text{Er}, \text{Nd}, \text{Yb}$ ) with potential emission in the NIR region, only the complex  $[\text{Zn}(\mu\text{-L})(\mu\text{-OAc})\text{Yb}(\text{NO}_3)_2]$  showed the emission characteristic of  $\text{Yb}^{\text{III}}$  ions when the compounds were excited at 290 nm, which indicates the low efficiency of ligand  $\text{L}^{2-}$  to act as antenna group for these ions. This fact is most likely due to the poor spectroscopic overlap between the ligand emission and the  $f\text{-}f$  excited states of ions  $\text{Er}^{\text{III}}$ ,  $\text{Nd}^{\text{III}}$  and  $\text{Yb}^{\text{III}}$  that could act as energy acceptors. Nevertheless, time-resolved luminescent experiments performed with an excitation wavelength of 355 nm allowed to get the emission lifetimes for these complexes, which are collected in Table 2.

To improve the NIR  $\text{Ln}^{\text{III}}$ -based emissive properties in these complexes, a better efficiency of energy transfer to the excited levels of the lanthanide ions is required,

**Table 2** Luminescence lifetimes for solid complexes of  $\text{Er}^{\text{III}}$ ,  $\text{Nd}^{\text{III}}$  and  $\text{Yb}^{\text{III}}$

Compound	$\tau$ ( $\mu\text{s}$ )	Compound	$\tau$ ( $\mu\text{s}$ )
$[\text{Zn}(\mu\text{-L})(\mu\text{-OAc})\text{Er}(\text{NO}_3)_2]$	2.08	$[\text{Zn}(\mu\text{-L})(\mu\text{-9AC})\text{Er}(\text{NO}_3)_2]$	2.77
$[\text{Zn}(\mu\text{-L})(\mu\text{-NO}_3)\text{Er}(\text{NO}_3)_2]$	2.14		
$[\text{Zn}(\mu\text{-L})(\mu\text{-OAc})\text{Yb}(\text{NO}_3)_2]$	10.3	$[\text{Zn}(\mu\text{-L})(\mu\text{-9AC})\text{Yb}(\text{NO}_3)_2]$	11.82
$[\text{Zn}(\mu\text{-L})(\mu\text{-NO}_3)\text{Yb}(\text{NO}_3)_2]$	10.0		
$[\text{Zn}(\mu\text{-L})(\text{H}_2\text{O})\text{Nd}(\text{NO}_3)_3]$	0.47	$[\text{Zn}(\mu\text{-L})(\mu\text{-9AC})\text{Nd}(\text{NO}_3)_2]$	0.80
		$[\text{Zn}(\mu\text{-L})(\mu\text{-9-An})\text{Nd}(\text{CH}_3\text{OH})_2(\text{NO}_3)]$	1.12

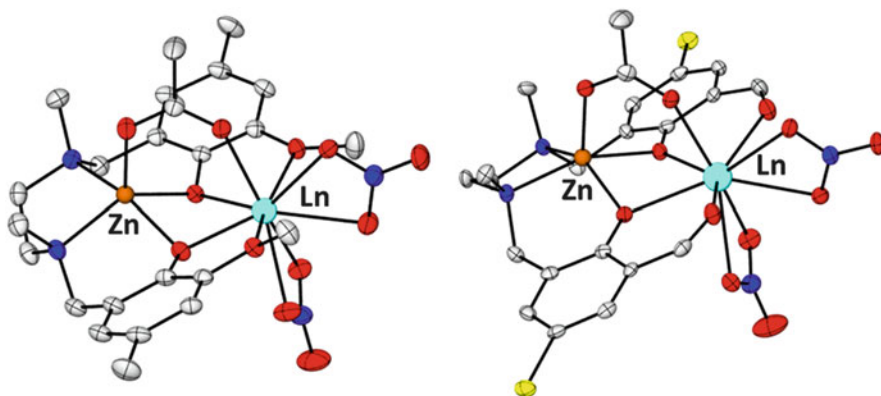


**Fig. 19** (Left) NIR sensitized emission spectra of complexes  $[\text{Zn}(\mu\text{-L})(\mu\text{-9-An})\text{Ln}(\text{NO}_3)_2] \cdot 2\text{CH}_3\text{CN}$  ( $\text{Ln}^{\text{III}} = \text{Er}$  (orange),  $\text{Yb}$  (green) and  $[\text{Zn}(\mu\text{-L})(\mu\text{-9-An})\text{Nd}(9\text{-An})(\text{NO}_3)_3] \cdot 2\text{CH}_3\text{CN} \cdot 3\text{H}_2\text{O}$  (blue) in solid state at room temperature. (Right) Jablonski diagram of these complexes

which can be accomplished by introducing a good antenna group, such as 9-anthracene carboxylate (9-An) as a bridging and/or terminal ligand. As expected, in all these cases, excitation at 355 nm resulted in the appearance of intense sensitized NIR emission from ions  $\text{Er}^{\text{III}}$ , and  $\text{Yb}^{\text{III}}$  at their characteristic wavelengths (Fig. 19).

In the light of the interesting magnetic and photophysical properties that can exhibit  $\text{Zn}^{\text{II}}\text{Ln}^{\text{III}}$  dinuclear complexes, several papers concerning this type of system containing Mannich base ligands have been recently reported. Zabala et al. [119] and Oyarzábal et al. [120] have reported in two different papers two closely related families of isostructural complexes of general formula  $[\text{Zn}(\mu\text{-L1})(\mu\text{-OAc})\text{Ln}(\text{NO}_3)_2]$  and  $[\text{Zn}(\mu\text{-L2})(\mu\text{-OAc})\text{Ln}(\text{NO}_3)_2] \cdot \text{CH}_3\text{CN}$  ( $\text{Ln}^{\text{III}} = \text{Pr}, \text{Nd}, \text{Sm}, \text{Eu}, \text{Gd}, \text{Tb}, \text{Dy}, \text{Ho}, \text{Er}, \text{Tm}, \text{Yb}$ ) with the compartmental ligands ( $N,N'$ -dimethyl- $N,N'$ -bis(2-hydroxy-3-formyl-5-bromo-benzyl)ethylenediamine ( $\text{H}_2\text{L1}$  in Fig. 7) and  $N,N'$ -dimethyl- $N,N'$ -bis(2-hydroxy-3-methoxy-5-methylbenzyl)-ethylenediamine ( $\text{H}_2\text{L2}$  in Fig. 7).

The crystal structure of these complexes (Fig. 20) is very similar to that exhibited by the analogous compounds with the  $\text{H}_2\text{L}$  ligand (type I, Fig. 14) and consists of dinuclear  $\text{Zn}^{\text{II}}\text{-Ln}^{\text{III}}$  molecules, in which the  $\text{Ln}^{\text{III}}$  and  $\text{Zn}^{\text{II}}$  ions are bridged by two phenoxido groups of either the  $\text{L1}^{2-}$  or  $\text{L2}^{2-}$  ligands and one *syn-syn* acetate group. As these ligands have the same  $\text{N}_2\text{O}_2$  inner site, the  $\text{Zn}^{\text{II}}$  ion exhibits in both types of complexes a distorted square-pyramidal  $\text{ZnN}_2\text{O}_3$  coordination environment, with the oxygen atom of the acetate bridging group occupying the axial position. The  $\text{Ln}^{\text{III}}$  ions also exhibit an  $\text{LnO}_9$  coordination sphere, which is made of the two phenoxido bridging oxygen atoms, two methoxy oxygen atoms (or two aldehyde oxygen atoms in the case of  $\text{L2}^{2-}$  ligand), one oxygen atom from the acetate bridging group and four oxygen atoms belonging to two bidentate nitrate anions. None of the complexes exhibit slow relaxation of magnetization at zero field, which points out that either



**Fig. 20** Perspective structures of  $[\text{Zn}(\mu\text{-L1})(\mu\text{-OAc})\text{Ln}(\text{NO}_3)_2]$  (left) and  $[\text{Zn}(\mu\text{-L2})(\mu\text{-OAc})\text{Ln}(\text{NO}_3)_2]$  (right). Ellipsoids represent 50% of the electron probability

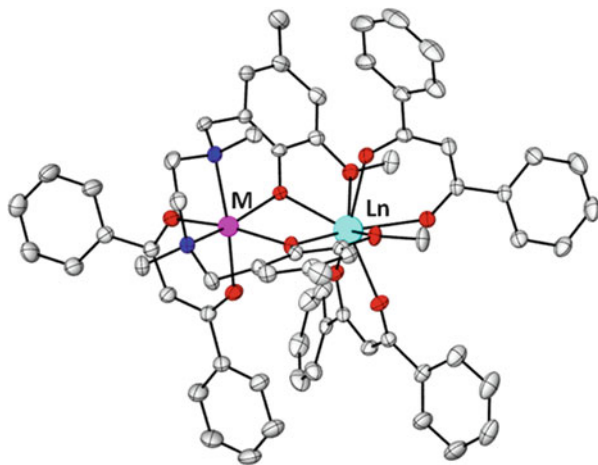
these compounds do not behave as SMMs or the QTM leads to a flipping rate that is too fast to observe the maximum in the  $\chi_M''$  vs.  $T$  plot above 2 K. However, when a small dc field is applied to partly or fully suppress QTM, the complexes  $[\text{Zn}(\mu\text{-L1})(\mu\text{-OAc})\text{Ln}(\text{NO}_3)_2]$  ( $\text{Ln}^{\text{III}} = \text{Gd}, \text{Dy}$  and  $\text{Yb}$ ) and  $[\text{Zn}(\mu\text{-L2})(\mu\text{-OAc})\text{Ln}(\text{NO}_3)_2] \cdot \text{CH}_3\text{CN}$  ( $\text{Ln}^{\text{III}} = \text{Nd}, \text{Dy}, \text{Er}$  and  $\text{Yb}$ ) exhibit a significant frequency dependence of the out-of-phase susceptibility signals and therefore field-induced slow relaxation for the reversal of the magnetization and SMM behaviour.

From the experimental relaxation times, simple/multiple relaxation mechanisms were proposed for the complexes  $[\text{Zn}(\mu\text{-L1})(\mu\text{-OAc})\text{Ln}(\text{NO}_3)_2]$  ( $\text{Ln}^{\text{III}} = \text{Gd}, \text{Dy}$  and  $\text{Yb}$ ) and  $[\text{Zn}(\mu\text{-L2})(\mu\text{-OAc})\text{Ln}(\text{NO}_3)_2] \cdot \text{CH}_3\text{CN}$  ( $\text{Ln}^{\text{III}} = \text{Nd}, \text{Dy}, \text{Er}$  and  $\text{Yb}$ ). Thus, for the  $\text{Dy}^{\text{III}}$  complexes, the relaxation takes place through thermally activated Orbach plus Raman processes with  $U_{\text{eff}}$  values of 52.6 K and 89.9 K, respectively. The Er complex relaxes via an Orbach process with  $U_{\text{eff}} = 21$  K, the Nd through a combination of Orbach plus QTM processes with a  $U_{\text{eff}} = 17.1$  K, whereas for Yb complexes the relaxation of magnetization takes place through a combination of Raman and QTM processes. Finally, for the isotropic  $\text{Gd}^{\text{III}}$  ion, a resonant phonon trapping (RTP) relaxation mechanism occurs, through a phonon-bottleneck process.

The chromophoric  $\text{L1}^{2-}$  and  $\text{L2}^{2-}$  ligands are able to act as an “antenna” group, sensitizing the characteristic luminescence in the visible region of the  $\text{Sm}^{\text{III}}, \text{Eu}^{\text{III}}, \text{Dy}^{\text{III}}$  and  $\text{Tb}^{\text{III}}$  derivatives as well as the near-infrared (NIR) luminescence of  $\text{Nd}^{\text{III}}$  (only in the case of the  $\text{L2}^{2-}$  derivative) and  $\text{Yb}^{\text{III}}$  complexes. The two  $\text{Yb}^{\text{III}}$  complexes, the  $\text{Dy}^{\text{III}}$  complex containing the  $\text{L1}^{2-}$  ligand and the  $\text{Nd}^{\text{III}}$  having the  $\text{L2}^{2-}$  ligand, present association of luminescent and field-induced SMM properties.

Using the  $\text{H}_2\text{L}_1$  ligand, Kou et al. [121] have successfully prepared a family of isostructural dinuclear complexes of general formula  $[\text{M}^{\text{II}}\text{Ln}^{\text{III}}(\text{L1})(\text{DBM})_3]$  ( $\text{M}^{\text{II}} = \text{Ni}, \text{Ln}^{\text{III}} = \text{Gd}, \text{Tb}, \text{Dy}; \text{M}^{\text{II}} = \text{Co}, \text{Ln}^{\text{III}} = \text{Gd}, \text{Dy}; \text{M}^{\text{II}} = \text{Zn}, \text{Ln}^{\text{III}} = \text{Dy}$  and  $\text{DBM} = 1,3\text{-diphenyl-propane-1,3-dione}$ ) by the one-pot self-assembly of  $\text{H}_2\text{L}_1, \text{Ln}(\text{NO}_3)_3 \cdot 6\text{H}_2\text{O}, \text{M}(\text{OAc})_2 \cdot 4\text{H}_2\text{O}, \text{HDMB}$  and  $\text{NEt}_3$  in a solution of  $\text{MeOH}/\text{MeCN}$ . The crystal structure of this family of complexes (Fig. 21) shows that  $\text{M}^{\text{II}}$  and  $\text{Ln}^{\text{III}}$

**Fig. 21** Perspective view of the structure of complexes  $[M^{II}Ln^{III}(L1)(DBM)_3]$ . Ellipsoids represent 50% of the electron probability



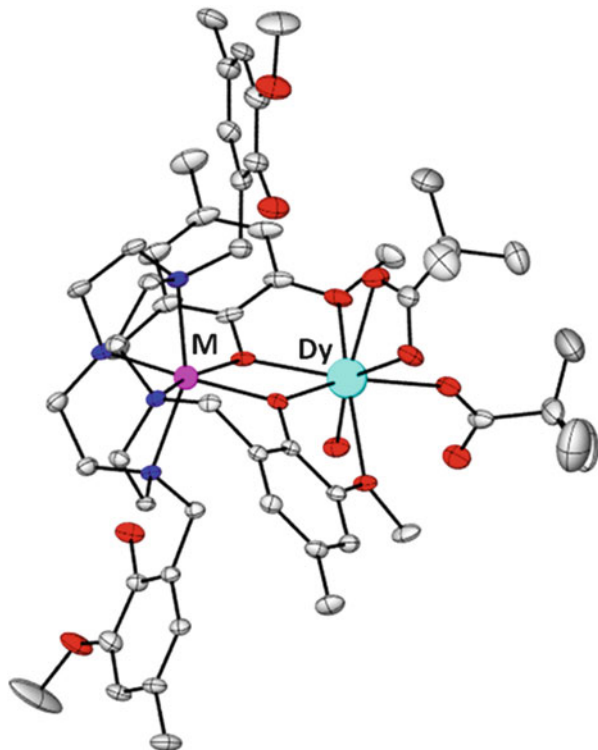
ions are only doubly bridged by the two phenoxido groups of the  $L1^{2-}$  ligand. The  $M^{II}$  ion exhibits a distorted octahedral  $MO_4N_2$  coordination environment, which is formed by the  $N_2O_2$  inner donor set of the  $L1^{2-}$  ligand and two *cis* oxygen atoms belonging to a bidentate  $DMB^-$  ancillary ligand. The  $Ln^{III}$  ion presents a distorted triangular dodecahedron  $LnO_8$  coordination sphere, which is made by four oxygen atoms from the ligand (the two phenoxido and two methoxy groups) and four oxygen atoms pertaining to two bidentate  $DMB^-$  groups.

The  $M^{II}Gd^{III}$  derivatives exhibit a ferromagnetic interaction between  $M^{II}$  and  $Gd^{III}$  ions. The magnetic exchange coupling constants were determined from magnetic susceptibility measurements using the Hamiltonian:  $\hat{H} = -J_{MGd}S_M \cdot S_{Gd}$ , affording  $J_{NiGd}$  and  $J_{CoGd}$  values of  $+2.22 \text{ cm}^{-1}$  and  $0.5 \text{ cm}^{-1}$ , respectively. These magnetic exchange parameters are similar to those found for the analogous complexes with the  $H_2L$  ligand [115–118]. The dynamic *ac* measurements reveal that among the dinuclear complexes containing paramagnetic ions only the  $[M^{II}Ln^{III}(L1)(DBM)_3]$  ( $M^{II} = Ni, Ln^{III} = Tb, Dy$ ) exhibit slow relaxation of the magnetization (but in the presence of an applied dc field) with effective thermal energy barriers ( $U_{\text{eff}}$ ) and flipping rates ( $\tau_0$ ) of 14.4 K and 11.3 K and  $6.1 \times 10^{-5} \text{ s}$  and  $3.0 \times 10^{-5} \text{ s}$ , respectively. The small values of  $U_{\text{eff}}$  are not unexpected in view of the weakness of the  $J_{NiGd}$  in these compounds.

These results reinforce the idea that the strategy of combining two exchanged anisotropic metal ions in a compound does not assure SMM behaviour even in the presence of applied magnetic field.

In this regard, Comba et al. [122] have recently reported two dinuclear complexes  $[Dy^{III}\{M^{II}(\mu-H_2L_8)\}piv_2(OH_2)]ClO_4$  ( $M^{II} = Ni, Co, H_2L_8 = 1,4,7,10$ -tetraazacyclododecane-1,4,7,10-tetrayl)-tetrakis-(methylene)-tetrakis(2-methoxy-4-methylphenol), whose theoretical CASSCF study supports this hypothesis. As usual, these complexes were prepared by one-pot reaction between the compartmental ligand  $H_2L^8$ ,  $DyCl_3 \cdot 6H_2O$ , the perchlorate salt of the corresponding transition metal ion, pivalic acid as ancillary ligand and  $NEt_3$  as base in MeOH and using

**Fig. 22** Perspective view of the structure of  $[\text{Dy}^{\text{III}}\{\text{Ni}^{\text{II}}(\text{H}_2\text{L})\}(\text{piv})_2(\text{OH}_2)]\text{ClO}_4$ . Ellipsoids represent 50% of the electron probability



a 1:1:1:2.5:4.5 molar ratio. The crystal structure of these complexes (Fig. 22) shows that the  $\text{M}^{\text{II}}$  ion occupies the  $\text{N}_4\text{O}_2$  inner site (four nitrogen atoms belonging to the macrocycle and two oxygen atoms from two 2-methoxy-4-methylphenoxido arms) exhibiting a distorted octahedral coordination environment. The phenoxido oxygen atoms are located in *cis* positions and bridge  $\text{M}^{\text{II}}$  and  $\text{Dy}^{\text{III}}$  ions. This latter ion, which is located in the  $\text{O}_4$  outer coordination site, presents a  $\text{DyO}_8$  coordination which is made by two phenoxido and two methoxy oxygen atoms from the  $\text{L}^{8-}$  ligand, one bidentate and one monodentate pivalate anions and one water molecule.

These complexes are not isostructural and there exist some differences between the  $\text{DyO}_8$  coordination sphere of both compounds. Thus, the water molecule in the  $\text{Ni}^{\text{II}}$  derivative is almost perpendicular to the Dy-Ni direction with the bidentate pivalate anion *trans* to the water molecule, whereas in the  $\text{Co}^{\text{II}}$  counterpart the water molecule is almost along the Dy-Co direction and the bidentate pivalato anion is *cis* to the water molecule.

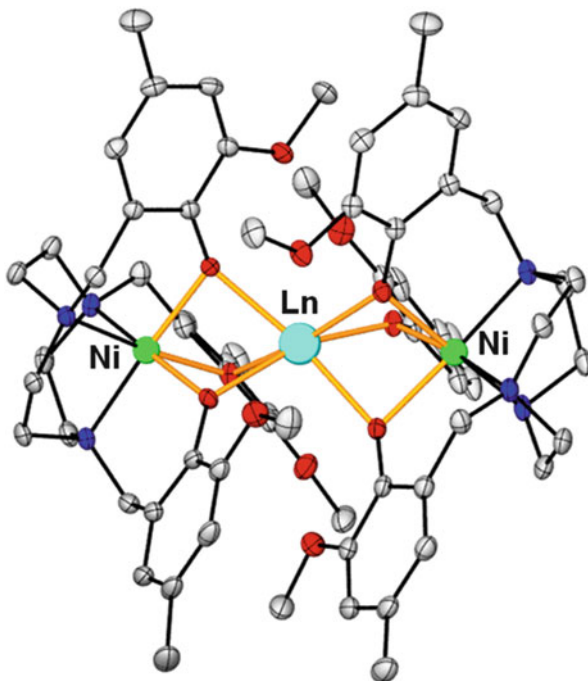
CASSCF/RASSI-SO ab initio calculations on these compounds have shown that the ground Kramers doublet of the  $\text{Ni}^{\text{II}}$  and  $\text{Co}^{\text{II}}$  counterpart is strongly axial (the ground-state wavefunction is largely dominated by the  $M_J = \pm|15/2\rangle$  function) with  $g_z = 19.75$ ,  $g_x = 0.008$  and  $g_y = 0.01$  and  $g_z = 19.65$ ,  $g_x = 0.06$  and  $g_y = 0.11$ . The smaller axiality of the  $\text{Dy}^{\text{III}}$  ground state in the  $\text{Co}^{\text{II}}$  counterpart is due to the

above indicated differences in the  $\text{DyO}_8$  coordination sphere, which give rise to slightly weak axial ligand field. As expected, the  $\text{Ni}^{\text{II}}$  is rather isotropic with  $g_z = 2.36$ ,  $g_x = 2.30$  and  $g_y = 2.31$ , whereas the  $\text{Co}^{\text{II}}$  is largely axial with  $g_z = 7.44$ ,  $g_x = 0.81$ ;  $g_y = 0.95$ . The main anisotropic axes (local magnetic axes) of  $\text{Ni}^{\text{II}}$  and  $\text{Dy}^{\text{III}}$  ions are almost collinear (deviation  $< 5^\circ$ ) whereas they are almost perpendicular in the  $\text{Co}^{\text{II}}$  counterpart. This results in a single-magnetic anisotropy axis in the  $\text{Ni}^{\text{II}}$  counterpart and in easy-plane anisotropy in the  $\text{Co}^{\text{II}}$  derivative. Therefore, SMM behaviour would be favoured in the former but not in the latter. In fact, dynamic ac measurements point out that  $\text{Ni}^{\text{II}}\text{Dy}^{\text{III}}$  complex exhibits field-induced SMM behaviour with  $U_{\text{eff}} = 19.9$  K and  $\tau_0 = 7.8 \times 10^{-7}$  s, whereas the  $\text{Co}^{\text{II}}\text{Dy}^{\text{III}}$  complex does not show any maximum in the out-of-phase ac susceptibility above 2 K even in the presence of applied field at the highest frequency of 1,500 Hz.

## 4.2 Trinuclear $M^{\text{II}}\text{-Ln}^{\text{III}}\text{-M}^{\text{II}}$ Complexes

The reaction of the tris-phenol-substituted triazacyclonane ligand  $\text{H}_3\text{L7}$  (Fig. 7) with  $\text{Ni}(\text{ClO}_4)_2 \cdot 6\text{H}_2\text{O}$  and then with  $\text{LnCl}_3 \cdot 6\text{H}_2\text{O}$  and  $\text{NEt}_3$  in 2:2:1:6 molar ratio allowed Comba et al. [123] to the preparation of the family of trinuclear complexes  $[\text{Ln}^{\text{III}}\{\text{Ni}^{\text{II}}(\text{L7})\}_2]\text{ClO}_4$  ( $\text{Ln}^{\text{III}} = \text{Y, La, Ce, Nd, Gd, Ho, Er, Tm}$  and  $\text{Lu}^{\text{III}}$ ). Within the

**Fig. 23** Perspective view of the crystal structure of  $[\text{Ln}^{\text{III}}\{\text{Ni}^{\text{II}}(\text{L7})\}_2]\text{ClO}_4$ . The perchlorate anion is omitted for clarity. The bridging fragment is highlighted in orange colour



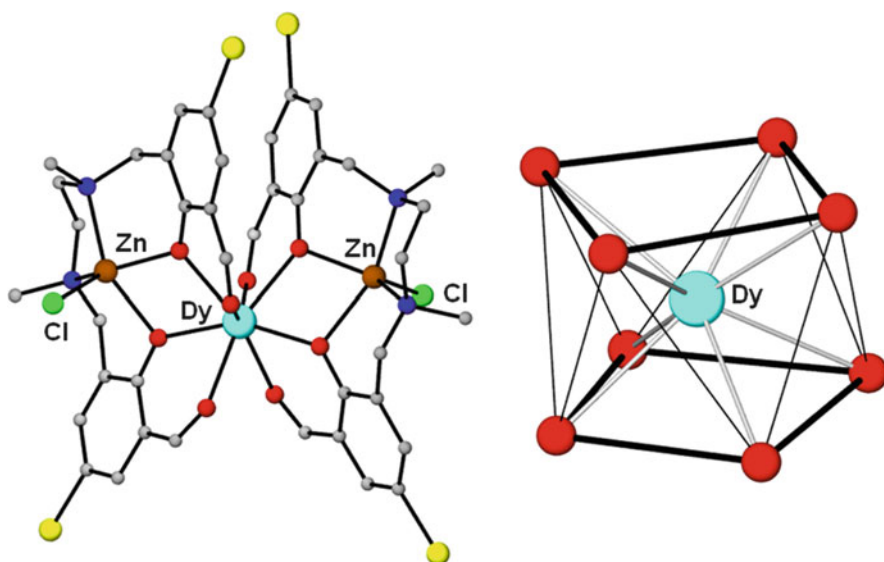
crystal structure (Fig. 23), each Ni<sup>II</sup> ion is coordinated by the three nitrogen atoms from the amine groups of the triazacyclononane and the three phenolate oxygen atoms of the three arms, giving rise to a [Ni<sup>II</sup>(L7)]<sup>-</sup> anion where the Ni<sup>II</sup> ion exhibits a distorted octahedral NiN<sub>3</sub>O<sub>6</sub> coordination environment. Two [Ni<sup>II</sup>(L7)]<sup>-</sup> units coordinate the central Ln<sup>III</sup> ion affording trinuclear Ni<sup>II</sup><sub>2</sub>Ln<sup>III</sup> cationic molecules where Ni<sup>II</sup> and Ln<sup>III</sup> ions are triply bridged by three phenolate oxygen groups (Fig. 23). The Ln<sup>III</sup> ion displays a rare LnO<sub>6</sub> coordination environment with a geometry that is intermediate between octahedral and trigonal prismatic, which is formed by the coordination of the six phenolate bridging oxygen atoms pertaining to the 2-methoxy-4-methylphenol arms. In three instances, a water molecule is coordinated to the Ln<sup>III</sup> ion (Sm<sup>III</sup> = Eu, Er, Tb) affording a monocapped trigonal-prismatic LnO<sub>7</sub> coordination sphere. NMR paramagnetic solution studies and solid-state SQUID measurements indicate that these compounds exhibit small magnetic anisotropies. This fact together with the expected small  $J_{\text{NiLn}}$  magnetic coupling for the Ni<sup>II</sup>(O<sub>phenoxide</sub>)<sub>2</sub>Ln<sup>III</sup> severely folded bridging fragment could explain why none of the Ni<sup>II</sup><sub>2</sub>Ln<sup>III</sup> complexes exhibit SMM behaviour.

By taking advantage of the simple electrostatic oblate–prolate model [67], our group [124–126] have recently designed a family of trinuclear Zn<sup>II</sup>-Dy<sup>III</sup>-Zn<sup>II</sup> complexes with the compartmental ligand H<sub>2</sub>L2 (Fig. 7). As indicated elsewhere, when the ground Kramers doublet of the Dy<sup>III</sup> ion is pure axial with  $M_J = \pm 15/2$ , its free ion electron density has an oblate disc shape, which can be better stabilized by an axial crystal field where the donor atoms with the largest electron densities are located above and below the equatorial plane, thus reducing the repulsive interactions between the ligands and f-electron charge clouds (Fig. 3). The pure axial ground state favours the SMM behaviour because the QTM, in principle, is not an operative relaxation pathway. Taking into account that in the deprotonated ligand L<sup>2-</sup> the phenoxido-oxygen donor atoms have larger negative charge than the aldehyde-oxygen donor atoms, a good approach to achieve strong easy-axis anisotropy would be that of situating the former oxygen atoms in opposite positions of the Dy<sup>III</sup> ion. This distribution of phenoxido oxygen atoms in the Dy<sup>III</sup> coordination sphere could be achieved in 3d-Dy-3d trinuclear complexes with L<sup>2-</sup> ligands bearing phenoxo-bridging groups connecting the 3d and 4f metal ions and terminal aldehyde groups coordinated to the Ln<sup>III</sup> ion. With regard to the 3d metal ion, a diamagnetic ion such as Zn<sup>II</sup> should preferably be used because theoretical and experimental studies carried out by us and others have shown that the incorporation of a diamagnetic metal ion such as Zn<sup>II</sup> in a 3d/Dy<sup>III</sup> complex enhances  $U_{\text{eff}}$  [127–130]. This observation has been suggested to be due to two factors: (1) the quenching of the Ln···Ln interactions promoted by the presence of diamagnetic Zn<sup>II</sup> ions (some kind of internal magnetic dilution) and (2) the increase of electron density on the phenoxido oxygen donor atoms connecting Zn<sup>II</sup> and Dy<sup>III</sup> ions provoked by the coordination to the Zn<sup>II</sup> ions. By exploiting these features of the Zn<sup>II</sup>/Dy<sup>III</sup> systems and following the above indicated guidelines of the simple prolate–oblate electrostatic model to achieve SMM behaviour, two pairs of phenoxido bridging oxygen atoms belonging to two [ZnL2] units were coordinated at opposite positions on Dy<sup>III</sup> coordination environment to generate the Zn<sup>II</sup>-Dy<sup>III</sup>-Zn<sup>II</sup> of general formula [ZnX



**Table 3** Formula and structural features of  $[\text{ZnX}(\mu\text{-L})\text{Dy}(\mu\text{-L})\text{XZn}]\text{Y}\cdot n\text{S}$  complexes

X	Y	S	CshM value for SAPR-8	Zn-Dy-Zn angle ( $^{\circ}$ )	Dist. upper-lower planes ( $\text{\AA}$ )	Square sides dist. ( $\text{\AA}$ )
Cl	$[\text{ZnCl}_3(\text{CH}_3\text{OH})]^-$	3MeOH	0.927	141.76	2.610	2.77
Cl	$\text{NO}_3^-$	MeOH	0.504	105.94	2.560	2.78
Cl	$\text{PF}_6^-$	–	0.547	109.48	2.565	2.78
Br	$[\text{ZnBr}_3(\text{CH}_3\text{OH})]^-$	MeOH, 2H <sub>2</sub> O	0.804	143.73	2.599	2.78
Br	$\text{NO}_3^-$	3MeOH	0.544	146.77	2.680	2.75
I	$\text{I}^-$	MeOH, 3H <sub>2</sub> O	0.458	146.25	2.613	2.74
I	$\text{NO}_3^-$	3MeOH	0.510	146.95	2.590	2.77
$\text{N}_3^-$	$\text{NO}_3^-$	MeOH, H <sub>2</sub> O	1.060	141.56	2.770	2.61



**Fig. 24** Molecular structure of  $[\text{ZnCl}(\mu\text{-L}2)\text{Dy}(\mu\text{-L}2)\text{ClZn}][\text{ZnCl}_3(\text{CH}_3\text{OH})]\cdot 3\text{CH}_3\text{OH}$ . Hydrogen atoms, the  $[\text{ZnCl}_3(\text{CH}_3\text{OH})]^-$  counteranion and methanol molecules have been omitted for the sake of clarity (left). Square-antiprism  $\text{DyO}_8$  coordination sphere (right)

$(\mu\text{-L})\text{Dy}(\mu\text{-L})\text{XZn}]\text{Y}\cdot n\text{S}$ , where X is the coligand ( $X = \text{Cl}, \text{Br}, \text{I}$  and  $\text{N}_3$ ), Y is the counteranion and S are the crystallization solvent molecules. The specific formula and some selected structural parameters of these complexes are gathered in Table 3.

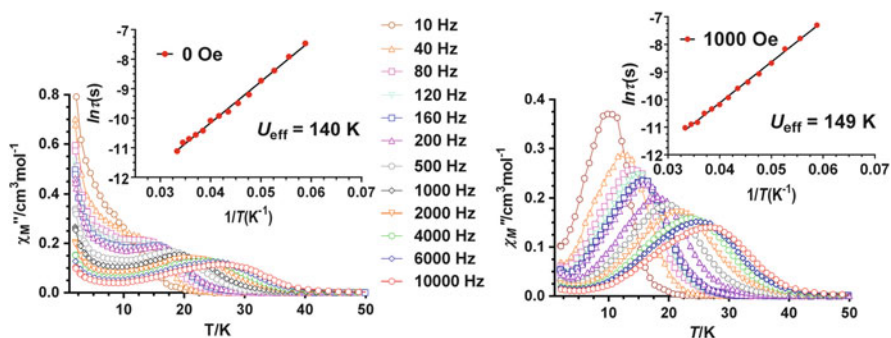
The structures of these complexes essentially differ in the coligands connected to Zn(II) ions, the counteranions and crystal solvent molecules. The structure of the trinuclear cationic units  $[\text{ZnX}(\mu\text{-L}2)\text{Dy}(\mu\text{-L}2)\text{XZn}]^+$  is very similar between them, and in Fig. 24 is given as an example that of the complex  $[\text{ZnCl}(\mu\text{-L}2)\text{Dy}(\mu\text{-L}2)$



$\text{ClZn}][\text{ZnCl}_3(\text{CH}_3\text{OH})]\cdot 3\text{CH}_3\text{OH}$  [124]. Within the trinuclear  $[\text{ZnCl}(\mu\text{-L})\text{Dy}(\mu\text{-L})\text{ClZn}]^+$  unit of this compound, two  $[\text{ZnCl}(\text{L}_2)]^-$  entities are coordinated at opposite sides of the central  $\text{Dy}^{\text{III}}$  ion in a bent manner through the oxygen atoms of the phenoxido bridging groups and the neutral aldehyde oxygen atoms, which agrees with that expected with the envisaged synthetic strategy. The  $\text{DyO}_8$  coordination sphere exhibits compressed square-antiprism geometry, whereas the  $\text{Zn}^{\text{II}}$  ions exhibit a distorted square-pyramidal  $\text{ZnO}_2\text{N}_2\text{Cl}$  coordination environment. The  $\text{Zn}^{\text{III}}\text{-Dy}^{\text{III}}\text{-Zn}^{\text{III}}$  bent angles, the average distance between the upper and lower planes containing the four oxygen atoms (two phenoxo and two aldehyde) and the average shape measures for the square-antiprismatic  $\text{DyO}_8$  are given in Table 3.

Dynamic *ac* magnetic susceptibility measurements indicate that under zero-external *dc* field all the compounds exhibit a strong frequency dependence of the out-of-phase susceptibility ( $\chi''_M$ ) signals below approximately 40 K, which clearly indicates the occurrence of slow relaxation of the magnetization and SMM behaviour. The  $\chi''_M$  component does not go to zero below the maxima at low temperature, which is due to the existence of fast relaxation of the magnetization via a QTM mechanism (Fig. 25 shows the data for the compound  $[\text{ZnCl}(\mu\text{-L}_2)\text{Dy}(\mu\text{-L}_2)\text{ClZn}][\text{ZnCl}_3(\text{CH}_3\text{OH})]\cdot 3\text{CH}_3\text{OH}$  as an example). The temperature dependence of the relaxation times ( $\tau$ ) for these compounds, extracted from the fitting of the frequency-dependent out-of-phase susceptibility data at each temperature to the generalized Debye, was fitted to the Arrhenius equation affording effective energy barriers ( $U_{\text{eff}}$ ) gathered in Table 3. As expected, after the application of a small external *dc* field for partly or fully suppressing QTM, the tails below 10 K almost vanished and the high-temperature peaks remained at similar temperatures (Fig. 25). In fact, in general, the  $U_{\text{eff}}$  values were only slight higher and the  $\tau_0$  values only slightly lower than those found at zero *dc* field (Table 4).

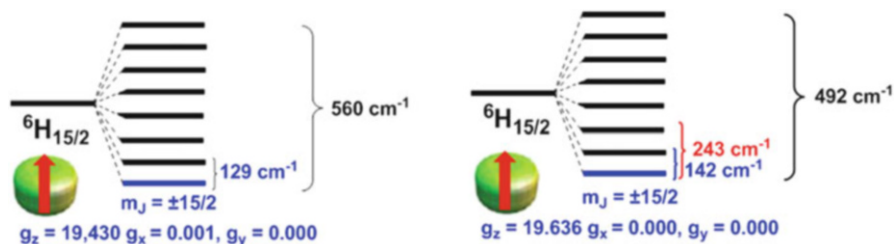
The effective energy barriers ( $U_{\text{eff}}$ ) for these complexes at zero field were found to be in the 144–170 K range (Table 4), with the exception of compound  $[\text{ZnCl}(\mu\text{-L})$



**Fig. 25** Temperature dependence of out-of-phase  $\chi''_M$  components of the *ac* susceptibility for complex  $[\text{ZnCl}(\mu\text{-L}_2)\text{Dy}(\mu\text{-L}_2)\text{ClZn}][\text{ZnCl}_3(\text{CH}_3\text{OH})]\cdot 3\text{CH}_3\text{OH}$  measured under zero applied *dc* field (left) and 1,000 Oe (right). Solid lines are a guide to the eye. Inset: Arrhenius plot,  $\ln \tau$  vs.  $T^{-1}$

**Table 4**  $U_{\text{eff}}$  and  $\tau_0$  values for complexes of  $[\text{ZnX}(\mu\text{-L})\text{Dy}(\mu\text{-L})\text{XZn}]\text{Y}$ 

X	Y	$U_{\text{eff}}$ (K) at $H = 0$ Oe	$\tau_0$ (s) at $H = 0$ Oe	$U_{\text{eff}}$ (K) at $H = 1,000$ Oe	$\tau_0$ (s) at $H = 1,000$ Oe
Cl	$[\text{ZnCl}_3(\text{CH}_3\text{OH})]^-$	140	$1.4 \times 10^{-7}$	149	$1.07 \times 10^{-7}$
Cl	$\text{NO}_3^-$	170	$4.3 \times 10^{-7}$	178	$4.14 \times 10^{-8}$
Cl	$\text{PF}_6^-$	258	$5.0 \times 10^{-10}$	319	$5.7 \times 10^{-11}$
Br	$[\text{ZnBr}_3(\text{CH}_3\text{OH})]^-$	164	$6.1 \times 10^{-8}$	165	$4.8 \times 10^{-8}$
Br	$\text{NO}_3^-$	150	$6.2 \times 10^{-8}$	154	$4.9 \times 10^{-8}$
I	$\text{I}^-$	144	$1.0 \times 10^{-7}$	147	$9.0 \times 10^{-8}$
I	$\text{NO}_3^-$	156	$4.3 \times 10^{-8}$	163	$4.4 \times 10^{-8}$
$\text{N}_3^-$	$\text{NO}_3^-$	159	$3.1 \times 10^{-8}$	167	$2.4 \times 10^{-8}$

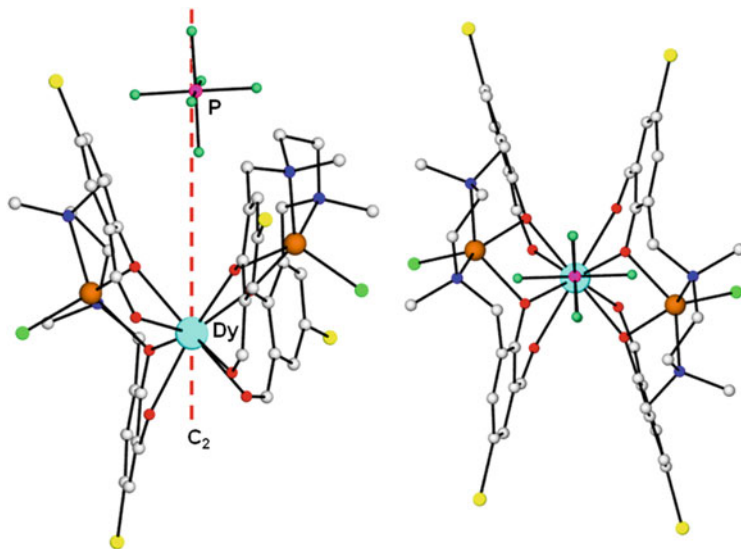


**Fig. 26** Energy interval for the splitting of the  ${}^6\text{H}_{15/2}$  spin-orbit term by ligand field effects, for  $[\text{ZnCl}(\mu\text{-L}2)\text{Dy}(\mu\text{-L}2)\text{ClZn}][\text{ZnCl}_3(\text{CH}_3\text{OH})]\cdot 3\text{CH}_3\text{OH}$  (left) and  $[\text{ZnCl}(\mu\text{-L})\text{Dy}(\mu\text{-L})\text{ClZn}]\text{PF}_6$  (right). The  $g$  factors for the ground Kramer's doublet (KD1) and the energy gap between the ground and first excited doublet are indicated in blue colour

$\text{Dy}(\mu\text{-L})\text{ClZn}]\text{PF}_6$ , which exhibited a larger  $U_{\text{eff}}$  value of 258 K. Electronic calculations based on the CASSCF+RASSI/SINGLE-ANISO [131] method using MOLCAS 7.8 code [132–136] were performed on the complexes  $[\text{ZnCl}(\mu\text{-L}2)\text{Dy}(\mu\text{-L}2)\text{ClZn}][\text{ZnCl}_3(\text{CH}_3\text{OH})]\cdot 3\text{CH}_3\text{OH}$  and  $[\text{ZnCl}(\mu\text{-L})\text{Dy}(\mu\text{-L})\text{ClZn}]\text{PF}_6$  [125] with the following aims: (1) to support the presence of axial anisotropy in the ground state, which would be responsible of the SMM behaviour, (2) for deep insight in the mechanism of the slow magnetic relaxation properties and (3) to rationalize the difference in  $U_{\text{eff}}$  between these two complexes.

The ab initio results for  $\text{ZnCl}(\mu\text{-L}2)\text{Dy}(\mu\text{-L}2)\text{ClZn}][\text{ZnCl}_3(\text{CH}_3\text{OH})]\cdot 3\text{CH}_3\text{OH}$  and  $[\text{ZnCl}(\mu\text{-L})\text{Dy}(\mu\text{-L})\text{ClZn}]\text{PF}_6$  indicate that:

1. The ground Kramer's doublet (KD1) is almost pure  $M_J = \pm 15/2$  with effective  $g_z$  and  $g_{x,y}$  values approaching to 20 and zero, respectively, for both complexes (Fig. 26). Therefore, KD1 is an almost ideal Ising state which favours the slow relaxation of the magnetization and the SMM behaviour, in accordance with the zero-field SMM properties observed for these complexes.
2. The energy spectrum of the eight Kramer's doublets (KDs) spans up to 560 and 492  $\text{cm}^{-1}$  and the energy gap between the ground and first excited is 129 and



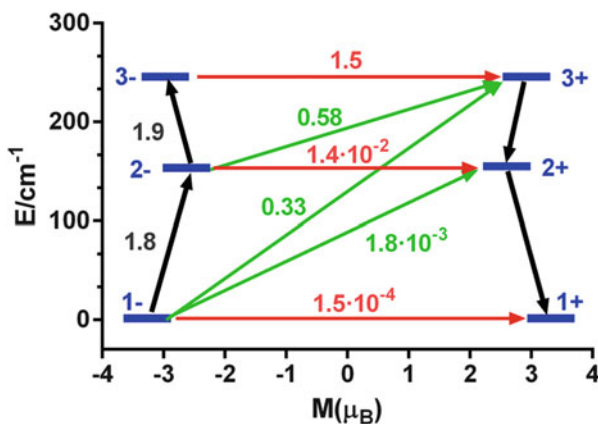
**Fig. 27** Two perspective views of the complex  $[\text{ZnCl}(\mu\text{-L})\text{Dy}(\mu\text{-L})\text{ClZn}]\text{PF}_6$  showing the location of the  $C_2$  axis

$144\text{ cm}^{-1}$ , for  $[\text{ZnCl}(\mu\text{-L2})\text{Dy}(\mu\text{-L2})\text{ClZn}][\text{ZnCl}_3(\text{CH}_3\text{OH})]\cdot 3\text{CH}_3\text{OH}$  and  $[\text{ZnCl}(\mu\text{-L})\text{Dy}(\mu\text{-L})\text{ClZn}]\text{PF}_6$ , respectively.

- As expected, from the simple oblate–prolate electrostatic repulsive model [67], the main magnetic axis of the ground state KD1 lies close to the two phenoxide donor atoms with greater electron density and shorter Dy–O distances (Fig. 30, left). Moreover, the orientation of the anisotropic axis on the  $\text{Dy}^{\text{III}}$  ion calculated using a simple electrostatic approach compares rather well with that obtained by ab initio methods. This fact highlights the suitability of an axially repulsive coordination environment for achieving SMM properties in  $\text{Dy}^{\text{III}}$  compounds, as qualitatively predicted by the oblate–prolate model. A good supporting evidence of this hypothesis was the absence of a significant energy barrier for magnetization reversal even at  $H_{\text{dc}} = 1,000\text{ Oe}$  for the compound  $[\text{ZnCl}(\mu\text{-L2})\text{Er}(\mu\text{-L2})\text{ClZn}][\text{ZnCl}_3(\text{CH}_3\text{OH})]\cdot 3\text{CH}_3\text{OH}$  (isostructural to the  $\text{Dy}^{\text{III}}$  counterpart), which should be due to the lack of easy-axis anisotropy. This can be easily understood by taking into account that  $\text{Er}^{\text{III}}$  has a prolate electron density distribution and therefore would lead to an easy-plane anisotropy stabilizing a ground state with a low  $M_J$  value, which would explain the absence of SMM behaviour [67].
- The extracted effective energy barrier at zero  $dc$  field for the complex  $[\text{ZnCl}(\mu\text{-L2})\text{Dy}(\mu\text{-L2})\text{ClZn}][\text{ZnCl}_3(\text{CH}_3\text{OH})]\cdot 3\text{CH}_3\text{OH}$  is relatively close to the energy gap between the ground and first excited KDs doublets ( $97.2$  vs.  $129\text{ cm}^{-1}$ ), which seems to indicate that the relaxation of the magnetization takes place through Orbach/Raman mechanism via the first excited doublet (KD2). The fact that the extracted  $U_{\text{eff}}$  is lower than predicted by electronic structure calculations could be justified by the existence of fast QTM relaxation. However, for the

complex  $[\text{ZnCl}(\mu\text{-L})\text{Dy}(\mu\text{-L})\text{ClZn}]\text{PF}_6$ , the extracted  $U_{\text{eff}}$  is  $40\text{ cm}^{-1}$  larger than the energy gap between the ground and first excited KDs and therefore the relaxation of the magnetization cannot take place via the first excited state. However, the relaxation could occur through the second excited KD, which is located  $243.3\text{ cm}^{-1}$  above the ground KD1. If so, the extracted  $U_{\text{eff}}$  would be lower than predicted by electronic structure calculations, which, as indicated above, could be explained by the existence of fast QTM relaxation. In fact, the value of energy barrier extracted from the *ac* measurements under an applied *dc* field of 1 kOe ( $U_{\text{eff}} = 222\text{ cm}^{-1}$ ), when the QTM relaxation is almost quenched, is close to the energy of the second excited state (Fig. 26). The reason why the relaxation does not proceed via the first excited state can be found in the collinearity of the main anisotropy axes of the ground and first easy-axis excited states (the angle is  $2.4^\circ$ ), which is due to the presence of a  $C_2$  axis around the  $\text{Dy}^{\text{III}}$  ion (Fig. 27) [127, 137, 138]. This is one of the few cases where this type of symmetry-driven relaxation mechanism has been observed [127, 137, 138] and the first case where it is due to a structural change promoted by the replacement of the counteranion. In  $[\text{ZnCl}(\mu\text{-L}2)\text{Dy}(\mu\text{-L}2)\text{ClZn}][\text{ZnCl}_3(\text{CH}_3\text{OH})]\cdot 3\text{CH}_3\text{OH}$ , however, the lack of symmetry axis leads to the non-collinearity of the main anisotropy axes of the ground and first easy-axis excited states and, therefore, the relaxation via KD2 is not blocked.

5. The computed transition magnetic moment matrix elements between the connecting pairs of opposite magnetization (Fig. 28) supported the magnetization relaxation mechanism in the complex  $[\text{ZnCl}(\mu\text{-L})\text{Dy}(\mu\text{-L})\text{ClZn}]\text{PF}_6$ . In this regard, QTM was expected to be very weak, because of the low magnitude of

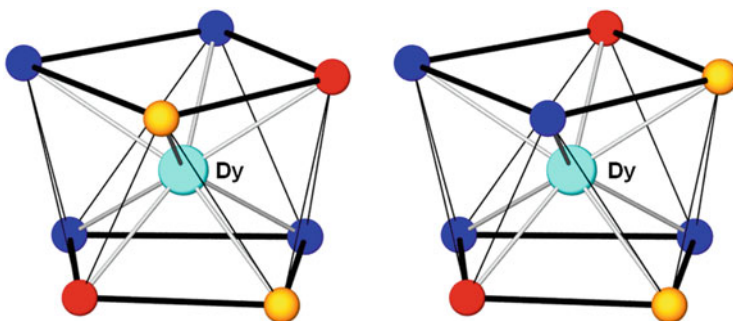


**Fig. 28** Lowest three Kramer's doublets (KD) and ab initio computed relaxation mechanism in  $[\text{ZnCl}(\mu\text{-L})\text{Dy}(\mu\text{-L})\text{ClZn}]\text{PF}_6$ . The thick blue lines indicate the Kramer's doublets as a function of their magnetic moment along the main anisotropy axis. The red lines correspond to ground state QTM and TA-QM via the first and second excited KDs. The black and green lines indicate spin-phonon transition (Orbach/Raman) processes. The values indicated close to the arrows indicate the matrix elements of the transition magnetic moments

the transition magnetic moment element between the ground state KDs ( $\sim 10^{-4} \mu_B$ ) and this was suggested to be the reason why this complex exhibited SMM behaviour at zero field. The same argument was used to justify the absence of thermally assisted quantum tunnelling of magnetization (TA-QTM) through the first excited state. However, the TA-QTM mechanism via the second excited KD ( $\pm 3$  states) was expected to be dominant as it exhibited the largest value of the transition magnetic moment element ( $1.5 \mu_B$ ).

As expected for the collinearity of the main anisotropy axes of the ground and first excited KDs, the off-diagonal term connecting these KDs (related with the Orbach process) was very small ( $\sim 10^{-3} \mu_B$ ). Nevertheless, the Orbach process was shown to be operative via the second excited state as the transversal magnetic moments showed moderate values ( $0.33$  and  $0.58 \mu_B$ ). Therefore, the relaxation of the magnetization occurred through the second excited state via Orbach/TA-QTM processes.

For the rest of  $[\text{ZnX}(\mu\text{-L})\text{Dy}(\mu\text{-L})\text{XZn}]\text{Y}$  complexes indicated in Table 4, the strong axial crystal field, created by the donor atoms with the shortest Dy-O distances (atoms with larger charge density) located above and below the equatorial plane (where the neutral aldehyde oxygen atoms are found), favours the adoption of an  $M_J = \pm 15/2$  Kramers doublet ground state, leading to easy-axis anisotropy and SIM behaviour with a high-energy barrier. Nevertheless, the small but significant differences in the  $U_{\text{eff}}$  values for these compounds remained to be undisclosed. At first glance, the analysis of the magneto-structural data for these compounds did not reveal any significant correlation between the magnitude of  $U_{\text{eff}}$  and structural parameters such as the distortion of the  $\text{DyO}_8$  coordination polyhedron from the square-antiprism geometry, the Zn-Dy-Zn angle (Table 3), the anionic coligand coordinated to the  $\text{Zn}^{\text{II}}$  ions and the differences between the average  $\text{Dy-O}_{\text{phenoxido}}$  distances. However, a close examination of the disposition of the oxygen atoms (the charge distribution) around the  $\text{Dy}^{\text{III}}$  ion suggested an explanation to the

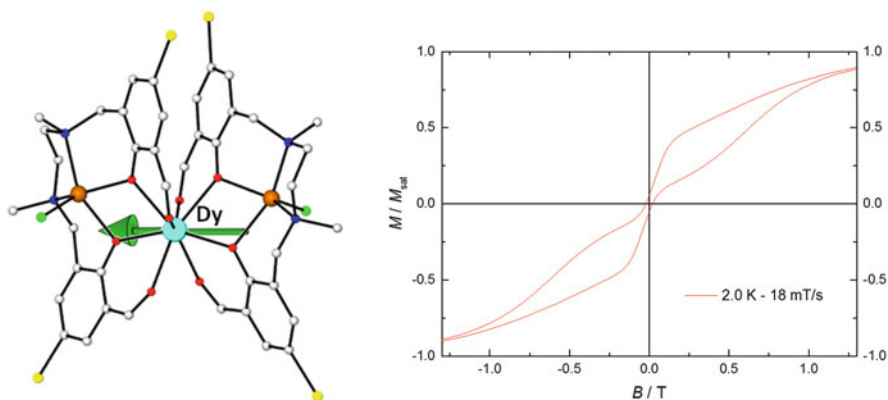


**Fig. 29** The two distributions of the oxygen atoms in the  $\text{DyO}_8$  coordination polyhedron for the complexes  $[\text{ZnCl}(\mu\text{-L})\text{Dy}(\mu\text{-L})\text{ClZn}]\text{NO}_3 \cdot \text{CH}_3\text{OH}$  (left) and  $[\text{ZnCl}(\mu\text{-L2})\text{Dy}(\mu\text{-L2})\text{ClZn}][\text{ZnCl}_3(\text{CH}_3\text{OH})]$  (right). Red and orange balls represent the shortest and longest phenoxido oxygen atoms. Blue balls correspond to the aldehyde oxygen atoms

variation of the  $U_{\text{eff}}$  values. As can be seen in Fig. 29, the oxygen atoms are distributed in two general manners in the square-antiprismatic  $\text{DyO}_8$  coordination polyhedron. Thus, if the same oxygen disposition in the lower plane is adopted for all the complexes, the two phenoxido oxygen atoms of the upper plane can exhibit two dispositions: (1) a rotation of  $45^\circ$  with regard to the same couple in the lower plane as in the case compound  $[\text{ZnCl}(\mu\text{-L})\text{Dy}(\mu\text{-L})\text{ClZn}]\text{NO}_3\cdot\text{CH}_3\text{OH}$  (Fig. 29, left) and (2) a rotation of  $135^\circ$  for the rest of complexes, including the complex  $[\text{ZnCl}(\mu\text{-L2})\text{Dy}(\mu\text{-L2})\text{ClZn}][\text{ZnCl}_3(\text{CH}_3\text{OH})]$  (Fig. 29, right). Interestingly, complexes with the first  $\text{DyO}_8$  distribution show the highest  $U_{\text{eff}}$  values, whereas complexes with the second oxygen disposition show intermediate or the lowest values of  $U_{\text{eff}}$  (Table 4).

In fact, the direction of the anisotropy axis for complex  $[\text{ZnCl}(\mu\text{-L})\text{Dy}(\mu\text{-L})\text{ClZn}]\text{NO}_3\cdot\text{CH}_3\text{OH}$  was shown to clearly deviate from those for the remaining compounds. It should be noted that complex  $[\text{ZnCl}(\mu\text{-L})\text{Dy}(\mu\text{-L})\text{ClZn}]\text{PF}_6$  also exhibits the first oxygen disposition around  $\text{Dy}^{\text{III}}$  ion and the calculated energy gap between the ground and first excited state is  $142\text{ cm}^{-1}$ , whereas the compound  $[\text{ZnCl}(\mu\text{-L})\text{Dy}(\mu\text{-L})\text{ClZn}]\text{NO}_3\cdot\text{CH}_3\text{OH}$ , that displays the second disposition, has an energy gap of  $129\text{ cm}^{-1}$ . Therefore, the experimental results support the theoretical predictions. In view of the above considerations, authors concluded [126] that the differences between the  $U_{\text{eff}}$  observed for this family of  $\text{Zn}^{\text{II}}\text{Dy}^{\text{III}}\text{Zn}^{\text{II}}$  trinuclear complexes are mainly due to the disposition of the oxygen atoms with the shortest Dy-O distances on the  $\text{DyO}_8$  coordination sphere, which is in turn affected by the coligands and counteranions that are present in these complexes. Compound  $[\text{ZnCl}(\mu\text{-L})\text{Dy}(\mu\text{-L})\text{ClZn}]\text{PF}_6$  is an excellent example of this effect, as the change of the counteranion increase twice  $U_{\text{eff}}$ .

All these complexes displayed at 2 K butterfly shaped hysteresis loops, thus confirming their SMM properties (Fig. 30, right). The large step observed near zero



**Fig. 30** Direction of the magnetic moment of the ground state indicated as a green arrow (left) and magnetic hysteresis loops for within  $-1.5 < H/T < 1.5$  at 2 K and a sweep rate of 18 mT/s for the complex  $[\text{ZnCl}(\mu\text{-L2})\text{Dy}(\mu\text{-L2})\text{ClZn}][\text{ZnCl}_3(\text{CH}_3\text{OH})] 3\text{CH}_3\text{OH}$

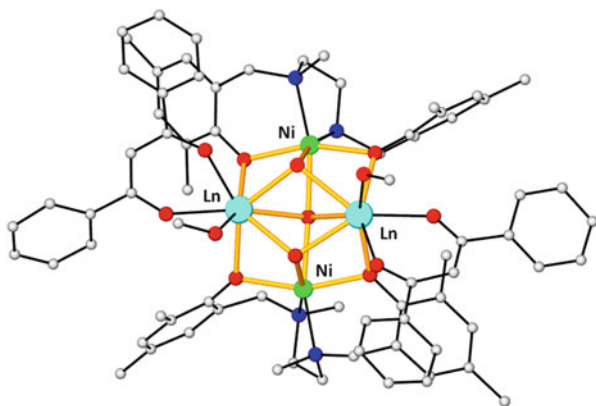
field (Fig. 30, the hysteresis plot for  $[\text{ZnCl}(\mu\text{-L2})\text{Dy}(\mu\text{-L2})\text{ClZn}][\text{ZnCl}_3(\text{CH}_3\text{OH})]$  is given as an example) is consistent with the QTM generally found for 4f containing complexes and with the tail that this family of compounds exhibits at low temperature in the  $\chi_M''$  vs.  $T$  plot.

The ongoing results for  $[\text{ZnX}(\mu\text{-L})\text{Dy}(\mu\text{-L})\text{XZn}]\text{Y}$  complexes represent a clear example of how the simple model based on the prolate–oblate electron density distribution of the  $\text{Ln}^{\text{III}}$  ions can be used to rationally design, from the magnetic point of view, mononuclear lanthanide-based complexes with strong easy-axis anisotropy and slow relaxation of the magnetization (SMM behaviour).

### 4.3 $(\text{M}^{\text{II}})_2(\text{Ln}^{\text{III}})_2$ Tetranuclear Complexes

A new family of tetranuclear  $\text{M}^{\text{II}}_2\text{Ln}^{\text{III}}_2$  heterometallic complexes of general formula  $[\text{M}^{\text{II}}_2\text{Ln}^{\text{III}}_2(\text{L3})_2(\mu_3\text{-OH})_2(\mu_4\text{-OH})(\text{dbm})_2(\text{MeOH})_2]\text{X}\cdot n\text{H}_2\text{O}\cdot m\text{MeOH}$  ( $\text{M}^{\text{II}} = \text{Ni}$ ,  $\text{Ln}^{\text{III}} = \text{Dy}$ ,  $\text{Tb}$ ,  $\text{Gd}$ ,  $\text{X} = \text{NO}_3^-$ ,  $\text{Ln}^{\text{III}} = \text{La}$ ,  $\text{X} = \text{ClO}_4^-$ ,  $\text{M}^{\text{II}} = \text{Zn}$ ,  $\text{Ln}^{\text{III}} = \text{Dy}$ ,  $\text{X} = \text{NO}_3^-$ ;  $\text{H}_2\text{L3} = N,N'$ -dimethyl $N,N'$ -bis(2-hydroxy-3,5-dimethylbenzyl) ethylenediamine,  $\text{Hdbm} = \text{dibenzoylmethane}$ ) were reported by Chaudhury et al. [139]. These complexes were prepared in a simple one-pot reaction by using the “metal complex as ligand” strategy, from the reaction between the metalloligand  $[\text{M}^{\text{II}}(\text{HL})(\text{dbm})]$ ,  $\text{LnX}_3\cdot 6\text{H}_2\text{O}$  ( $\text{X} = \text{NO}_3^-$  and  $\text{ClO}_4^-$ ) and  $[\text{N}(\text{Bu})_4]\text{OH}$  in 1:1:2 molar ratio in methanol. Within the tetranuclear cationic unit  $[\text{M}^{\text{II}}_2\text{Ln}^{\text{III}}_2(\text{L3})_2(\mu_3\text{-OH})_2(\mu_4\text{-OH})(\text{dbm})_2(\text{MeOH})_2]^+$ , Fig. 31, metal atoms are connected by two  $\mu_3\text{-OH}^-$  groups (bridging two  $\text{Ln}^{\text{III}}$  and one  $\text{Ni}^{\text{II}}$  ions), one  $\mu_4\text{-OH}^-$  group (bridging two  $\text{Ln}^{\text{III}}$  and two  $\text{Ni}^{\text{II}}$  ions) and four  $\mu$ -phenoxido oxygen atoms from two deprotonated  $\text{L3}^{2-}$  ligands (bridging one  $\text{Ln}^{\text{III}}$  and one  $\text{Ni}^{\text{II}}$  ions). The  $\text{M}^{\text{II}}$  ions exhibit  $\text{N}_2\text{O}_4$  distorted octahedral coordination environments, which are formed by the two nitrogen atoms from the  $\text{L3}^{2-}$  ligand, two oxygen atoms belonging to phenoxido bridging groups and two oxygen coming from the

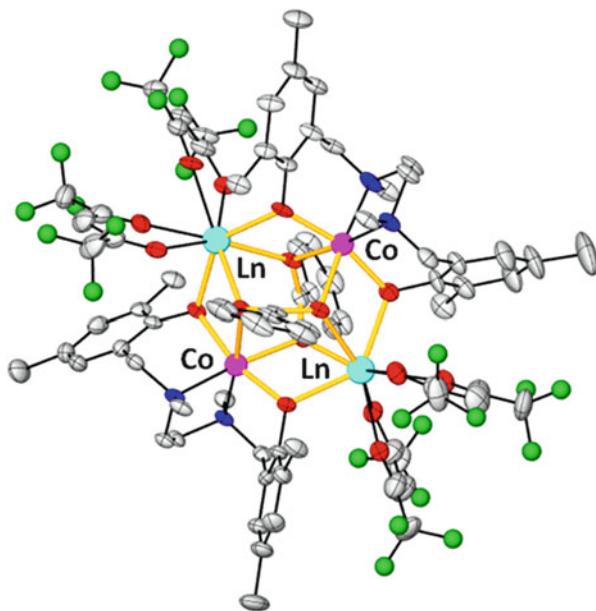
**Fig. 31** Molecular structure of  $[\text{Ni}^{\text{II}}_2\text{Ln}^{\text{III}}_2(\text{L3})_2(\mu_3\text{-OH})_2(\mu_4\text{-OH})(\text{dbm})_2(\text{MeOH})_2]\text{X}$  complexes. Anions are omitted for clarity. The bridging fragment is highlighted in orange colour





$\mu_3\text{-OH}^-$  and  $\mu_4\text{-OH}^-$  bridging groups. The  $\text{Ln}^{\text{III}}$  ions present a distorted dodecahedral  $\text{LnO}_8$  coordination sphere, which is made of the oxygen atoms belonging to the two  $\mu_3\text{-OH}^-$  and the  $\mu_4\text{-OH}^-$  groups, two phenoxido bridging groups of two different  $\text{L}_3^{2-}$  ligands, one  $\text{dmb}^-$  bidentate anion and one methanol molecule. Magnetic measurements indicate that metal ions are antiferromagnetically coupled in these complexes with  $J_{\text{NiNi}}$ ,  $J_{\text{NiGd}}$  and  $J_{\text{GdGd}}$  coupling constants for the  $\text{Ni}_2\text{Gd}_2$  derivative of  $-50\text{ cm}^{-1}$ ,  $-4.65\text{ cm}^{-1}$  and  $-0.02\text{ cm}^{-1}$ , respectively. None of these complexes show frequency dependent maxima above 2 K under zero applied magnetic field. The absence of SMM could be justified, as indicated elsewhere, due to the weak antiferromagnetic coupling between  $\text{Ni}^{\text{II}}$  and  $\text{Ln}^{\text{III}}$  ions, which allows mixing of the low-lying excited states in the ground state thus favouring fast QTM and quenching slow relaxation of magnetization. Moreover, the distribution of oxygen atoms around the  $\text{Ln}^{\text{III}}$  ions is not appropriate to afford a strong crystal field. This is the main reason why the  $\text{Zn}^{\text{II}}_2\text{Dy}^{\text{III}}_2$  complex does not exhibit SMM behaviour.

Chaudhury et al. [140] have also recently reported a family of isostructural tetranuclear heterometallic complexes  $[\text{M}^{\text{II}}_2(\text{L}3)_2(\text{PhCOO})_2\text{Ln}^{\text{III}}_2(\text{hfac})_4]$  ( $\text{M}^{\text{II}} = \text{Co}$ ,  $\text{Ln}^{\text{III}} = \text{Gd}, \text{Tb}, \text{Dy}, \text{La}$ ;  $\text{M}^{\text{II}} = \text{Zn}$ ,  $\text{Ln}^{\text{III}} = \text{Dy}$ ;  $\text{H}_2\text{L}3 = N,N'$ -dimethyl- $N,N'$ -bis(2-hydroxy-3,5-dimethylbenzyl)ethylenediamine,  $\text{Hhfac} =$  hexafluoroacetylacetonate and  $\text{PhCOO}$  is the benzoate anion), which were successfully prepared by self-assembly of the preformed  $[\text{Co}^{\text{II}}(\text{H}_2\text{L})(\text{PhCOO})_2]$  and  $[\text{Ln}^{\text{III}}(\text{hfac})_3(\text{H}_2\text{O})_2]$  building blocks. The structure of these complexes (Fig. 32) shows that metal ions are connected



**Fig. 32** Molecular structure of  $[\text{Co}^{\text{II}}_2(\text{L}3)_2(\text{PhCOO})_2\text{Ln}^{\text{III}}_2(\text{hfac})_4]$  complexes. The bridging fragment is highlighted in orange colour

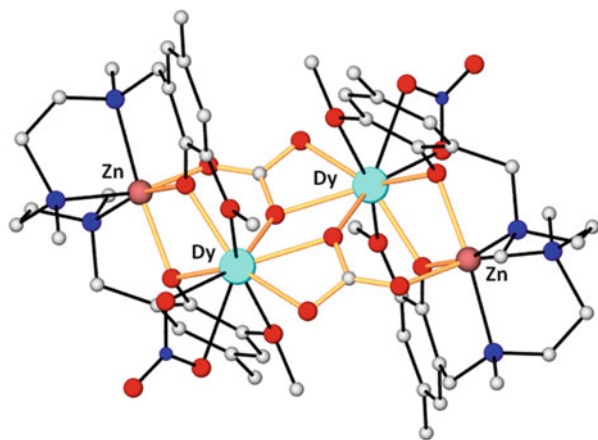


by four phenoxido groups belonging to two different  $L3^{2-}$  ligands and two benzoato ligands acting in a rare  $\mu_4\text{-}\eta^2\text{:}\eta^2$  mode, giving rise to alternate disposition of  $\text{Ln}^{\text{III}}$  and  $\text{M}^{\text{II}}$  ions with rhombus-like shape, in which each  $\text{M}^{\text{II}}\text{Ln}^{\text{III}}$  pair is doubly bridged by two oxygen atoms, one belonging to a phenoxido group and the other one coming from a benzoate group. Benzoate ligands are mutually perpendicular and located above and below the metal ion plane.  $\text{M}^{\text{II}}$  ions exhibit an  $\text{MN}_2\text{O}_4$  coordination sphere, which is formed by the coordination of two nitrogen atoms from the ligand, two phenoxido oxygen atoms in *trans* positions and two benzoate oxygen atoms in *cis* position. The lanthanide ion displays an  $\text{LnO}_8$  coordination sphere, which is made of two oxygen atoms belonging to phenoxido groups, two oxygen atoms pertaining to two different benzoate anions and four oxygen atoms coming from two bidentate hexafluoroacetylacetonato ancillary ligands.

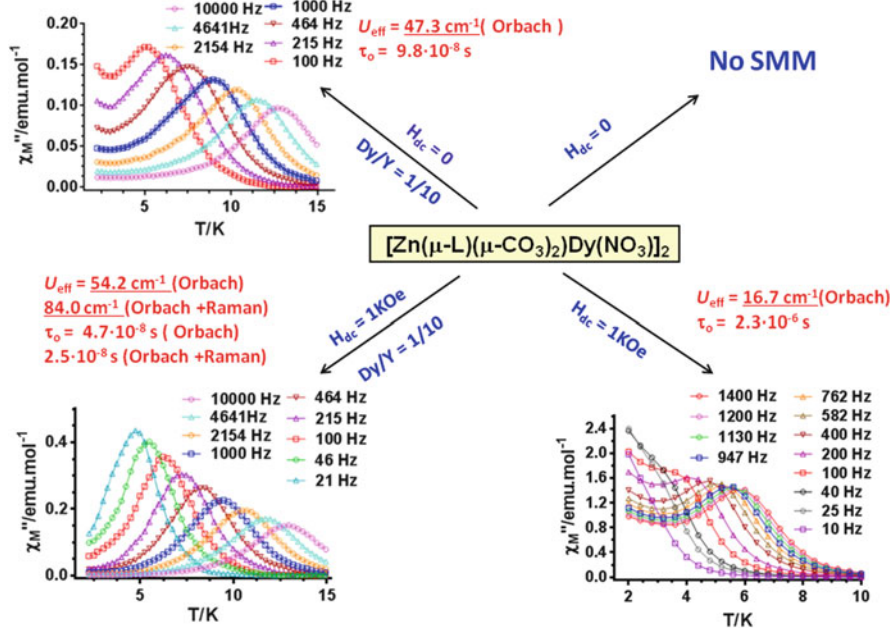
Magnetic *dc* measurements indicated the existence of an antiferromagnetic coupling between metal ions in these heterometallic complexes. Dynamic *ac* measurements showed that only  $[\text{Co}^{\text{II}}_2\text{Dy}^{\text{III}}_2]$  and  $[\text{Zn}^{\text{II}}_2\text{Dy}^{\text{III}}_2]$  compounds exhibited slow relaxation of the magnetization at zero field. However, the former compounds do not show any maximum in frequency dependence out-of-phase *ac* signals at different temperatures, whereas the latter exhibits maxima in the 5–9 K. In accordance with this different behaviour, the  $[\text{Zn}^{\text{II}}_2\text{Dy}^{\text{III}}_2]$  has a thermal energy barrier  $U_{\text{eff}}/k_{\text{B}} = 47.9$  K ( $\tau_0 = 2.75 \times 10^{-7}$  s), whereas in the complex  $[\text{Co}^{\text{II}}_2\text{Dy}^{\text{III}}_2]$  presents a smaller value of  $U_{\text{eff}}/k_{\text{B}} = 8.8$  K ( $\tau_0 = 2.0 \times 10^{-7}$  s). The SMM behaviour observed for  $[\text{Zn}^{\text{II}}_2\text{Dy}^{\text{III}}_2]$ , which is essentially single ion in origin, should be due to an appropriate distribution of the oxygen donor atoms in the  $\text{DyO}_8$  coordination sphere to afford an axial ligand field. The reduction of the barrier to spin reversal and a faster magnetic relaxation in  $[\text{Co}^{\text{II}}_2\text{Dy}^{\text{III}}_2]$  is not unexpected taking into account the weakness of the  $\text{Ln}^{\text{III}}\text{-Co}^{\text{II}}$  magnetic interaction.

Two tetranuclear complexes of general formulas  $\{(\mu_3\text{-CO}_3)_2[\text{Zn}(\mu\text{-L})\text{Dy}(\text{NO}_3)_2]\}_2 \cdot 4\text{CH}_3\text{OH}$  and  $\{(\mu_3\text{-CO}_3)_2[\text{Zn}(\mu\text{-L})\text{Yb}(\text{H}_2\text{O})_2]\}_2 (\text{NO}_3)_2 \cdot 4\text{CH}_3\text{OH} \cdot 2\text{H}_2\text{O}$  (hereafter, namely  $\text{Zn}^{\text{II}}_2\text{Dy}^{\text{III}}_2$  and  $\text{Zn}^{\text{II}}_2\text{Yb}^{\text{III}}_2$ , respectively, were prepared in our

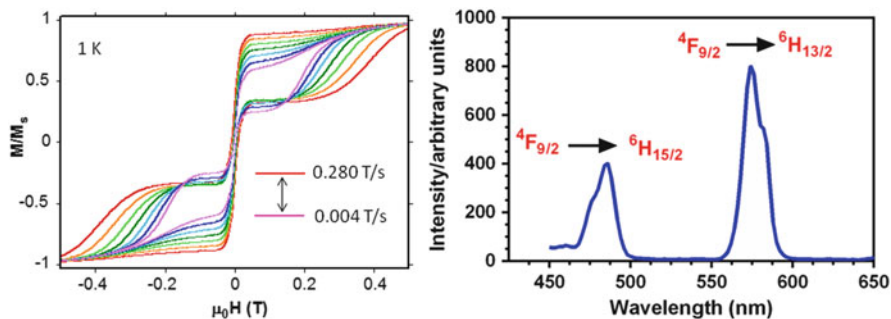
**Fig. 33** Molecular structure of  $[\text{Zn}(\mu\text{-L})(\mu\text{-CO}_3)_2]\text{Dy}(\text{NO}_3)_2 \cdot 2\text{CH}_3\text{OH}$ . Hydrogen atoms and methanol crystallization molecules are omitted for clarity. The bridging fragment is highlighted in orange colour



group [141] from the reaction of  $\text{H}_2\text{L}$  with  $\text{Zn}(\text{NO}_3)_2 \cdot 6\text{H}_2\text{O}$  and subsequently with  $\text{Ln}(\text{NO}_3)_3 \cdot 5\text{H}_2\text{O}$  ( $\text{Ln}^{\text{III}} = \text{Dy}$  and  $\text{Yb}$ ) and triethylamine in  $\text{MeOH}$  using a 1:1:1:1 molar ratio. The  $\text{Zn}^{\text{II}}_2\text{Dy}^{\text{III}}_2$  complex has a centrosymmetric tetranuclear structure (see Fig. 33), consisting of two diphenoxido-bridged  $[\text{Zn}(\mu\text{-L})\text{Dy}(\text{NO}_3)]$  dinuclear units (similar to those described in Sect. 4.1) connected by two tetradentate carbonato bridging ligands acting with a  $\mu_3\text{-}\kappa^2\text{-O, O}' : \kappa\text{-O}' : \kappa\text{-O}''$  coordination mode. The carbonato ligand is generated from the fixation of atmospheric  $\text{CO}_2$  in basic medium. The chelating part of the carbonato ligand is coordinated to the  $\text{Dy}^{3+}$  ion of a dinuclear entity, whereas the remaining oxygen atom is coordinated to the  $\text{Zn}^{\text{II}}$  ion of the centrosymmetrically related dinuclear unit, giving rise to a rhomboidal  $\text{Dy}(\text{O})_2\text{Dy}$  bridging unit with a  $\text{Dy-O-Dy}$  bridging angle of  $115.72^\circ$  and two different  $\text{Dy-O}$  distances of 2.360 and 2.419 Å. The  $\text{Zn}^{\text{II}}$  ions exhibit a slightly trigonally distorted  $\text{ZnN}_3\text{O}_3$  coordination polyhedron (three nitrogen atoms from the amine groups and three oxygen atoms belonging to the carbonato and phenoxido bridging groups), whereas the  $\text{Dy}^{\text{III}}$  ion displays a rather non-symmetrical  $\text{DyO}_9$  coordination (formed by the two phenoxido bridging oxygen atoms, the two methoxy oxygen atoms, three oxygen atoms from the carbonato bridging groups and two oxygen atoms belonging to a bidentate nitrate anion).



**Fig. 34** Temperature dependence of out-of-phase  $\chi''_M$  components of the ac susceptibility for complex  $[\text{Zn}(\mu\text{-L})(\mu\text{-CO}_3)_2]\text{Dy}(\text{NO}_3)_2$  measured under zero applied dc field (top) and 1,000 Oe (bottom) on the net (right) and diluted (left) versions. Solid lines are a guide to the eye.  $U_{\text{eff}}$  and  $\tau_0$  values are given in red colour



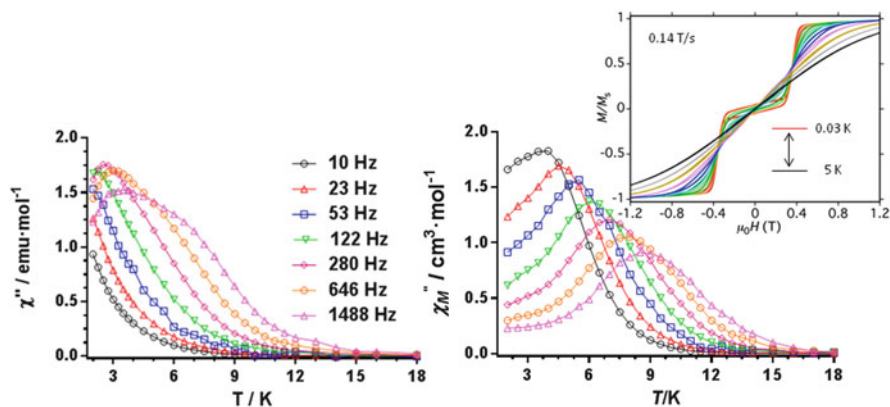
**Fig. 35** Normalized magnetizations ( $M/M_s$ ) vs. applied dc field sweeps at the indicated sweep rates and temperature for the diluted complex derived from  $[\text{Zn}(\mu\text{-L})(\mu\text{-CO}_3)_2\text{Dy}(\text{NO}_3)_2] \cdot 2\text{CH}_3\text{OH}$  (left). Solid emission spectrum of the neat complex (right)

The structure  $\text{Zn}^{\text{II}}\text{Yb}^{\text{III}}_2$  is very similar to that of  $\text{Zn}^{\text{II}}\text{Dy}^{\text{III}}_2$  but has a water molecule coordinated to the  $\text{Yb}^{\text{III}}$  ion instead of a bidentate nitrate ion (Fig. 33). This change is probably due to the significant size reduction on going from  $\text{Dy}^{\text{III}}$  to  $\text{Yb}^{\text{III}}$  as a consequence of the lanthanide contraction, thus favouring the adoption of an eight-coordinated  $\text{YbO}_8$  coordination polyhedron instead of a nine-coordinated one.

The  $\text{Zn}^{\text{II}}\text{Dy}^{\text{III}}_2$  complex did not exhibit slow relaxation of the magnetization at zero field due to fast QTM relaxation processes. However, in the presence of a small external dc field, the QTM was partly suppressed and the compound exhibited SMM behaviour (Fig. 34). Interestingly, the diluted complex crystallized using a 1:10 Dy/Y ratio showed an almost complete quenching of the QTM and SMM behaviour is observed at zero field with almost three times higher thermal energy barrier (Fig. 34), indicating that QTM essentially occurs by intermolecular dipolar interactions. This is one of the few examples of  $\text{Dy}^{3+}$  complexes where the SMM behaviour is activated by dilution.

The magnetization study of the diluted complex at low temperatures using a micro-SQUID device confirmed the SMM behaviour (Fig. 35, left) and clearly showed that the slow relaxation of the magnetization is due to the single-ion relaxation of the  $\text{Dy}^{3+}$ . After dilution and in the presence of an applied magnetic field, when the QTM is eliminated, the thermal energy barrier increases again but the experimental relaxation times still deviate from the Orbach linear law due to a Raman relaxation (Fig. 34). Finally, the luminescence spectrum of  $[\text{Zn}(\mu\text{-L})(\mu\text{-CO}_3)_2\text{Dy}(\text{NO}_3)_2] \cdot 2\text{CH}_3\text{OH}$  (Fig. 35, right) suggests that the ligand is suitable for the sensitization of yellow luminescence of  $\text{Dy}^{3+}$ . Therefore, this complex can be considered as a bifunctional material exhibiting both SMM behaviour and luminescence properties.

The  $\text{Zn}^{\text{II}}\text{Yb}^{\text{III}}_2$  complex exhibits field-induced SMM behaviour, the relaxation of the magnetization on the  $\text{Yb}^{\text{III}}$  centres taking place through a Raman-like process rather than through an activated Orbach process. Moreover, it shows luminescence in the NIR region and therefore can be considered as dual magneto-luminescence materials combining NIR emission and field-induced SMM behaviour.



**Fig. 36** Perspective view of the structure of  $[\text{Ln}_2(\text{ML})_3(\mu_3\text{O})_3\text{H}]^+$  cationic unit. The perchlorate anion and water crystallization molecules are omitted for clarity. The bridging fragment is highlighted in orange colour

#### 4.4 $(\text{M}^{\text{II}})_3(\text{Ln}^{\text{III}})_2$ Pentanuclear Complexes

Also, Chaudhury et al. [142], using the hexadentate aminobis(phenol)-based ligand, *N,N*-bis(2-hydroxy-3-methoxy-5-methylbenzyl)-*N',N'*-diethylethylenediamine ( $\text{H}_2\text{L4}$ ), have recently reported a new family of isostructural pentanuclear complexes having the general formula  $[\text{Ln}_2(\text{ML})_3(\mu_3\text{-O})_3\text{H}](\text{ClO}_4)_x \cdot x\text{H}_2\text{O}$  ( $\text{M}^{\text{II}} = \text{Cu}$ ,  $\text{Ln}^{\text{III}} = \text{Nd}$ ,  $\text{Gd}$ ,  $\text{Tb}$ ;  $\text{M}^{\text{II}} = \text{Zn}, \text{Ni}$ ,  $\text{Ln}^{\text{III}} = \text{Nd}$ ). These complexes were prepared by one-pot self-assembly reaction between  $\text{M}^{\text{II}}(\text{ClO}_4)_2$ ,  $\text{H}_2\text{L4}$ ,  $\text{Ln}^{\text{III}}(\text{ClO}_4)_3$  and  $\text{NEt}_3$  in 2:1:1:2 molar ratio in methanol. The structure of the cationic unit of these complexes (Fig. 36) consists of three  $[\text{M}^{\text{II}}\text{L}]$  units linked through two phenoxido oxygen atoms to two  $\text{Ln}^{\text{III}}$  ions. In addition, three  $\mu_3$ -oxido bridging ligands connect the two  $\text{Ln}^{\text{III}}$  and each of the  $\text{M}^{\text{II}}$  ions, giving rise to a  $[\text{M}^{\text{II}}_3\text{Ln}^{\text{III}}_2]$  core with trigonal bipyramidal geometry where the  $\text{Ln}^{\text{III}}$  occupies the apical positions. It should be noted that the  $\text{H}^+$  ions are located at the threefold axis passing through the two  $\text{Ln}^{\text{III}}$  ions.  $\text{M}^{\text{II}}$  ions exhibit a distorted square-pyramidal  $\text{MN}_2\text{O}_3$  coordination sphere, which is made of the two nitrogen atoms of the  $\text{L4}^{2-}$  ligand and three oxygen atoms coming from two phenoxido and one  $\mu_3$ -oxido groups. The lanthanide ions present a distorted monocapped square-antiprismatic  $\text{LnO}_9$  coordination geometry, which is formed by the oxygen atoms belonging to three phenoxide, three  $\mu_3$ -oxido and three methoxy groups.

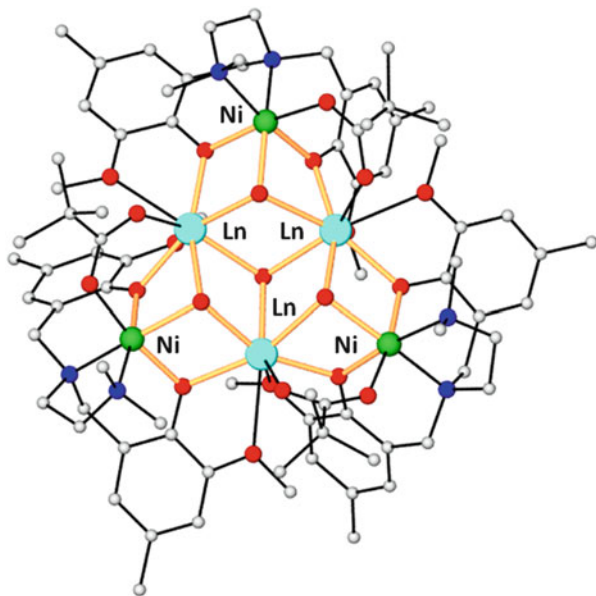
Magnetic dc measurements revealed very weak ferromagnetic  $\text{Cu}^{\text{II}} \cdots \text{Gd}^{\text{III}}$  ( $J = 0.57 \text{ cm}^{-1}$ ) and  $\text{Gd}^{\text{III}} \cdots \text{Gd}^{\text{III}}$  ( $J = 0.14 \text{ cm}^{-1}$ ) magnetic exchange interactions. None of these compounds exhibit slow relaxation of the magnetization at zero field, which is likely due to the weak coupling observed between the metal ions.

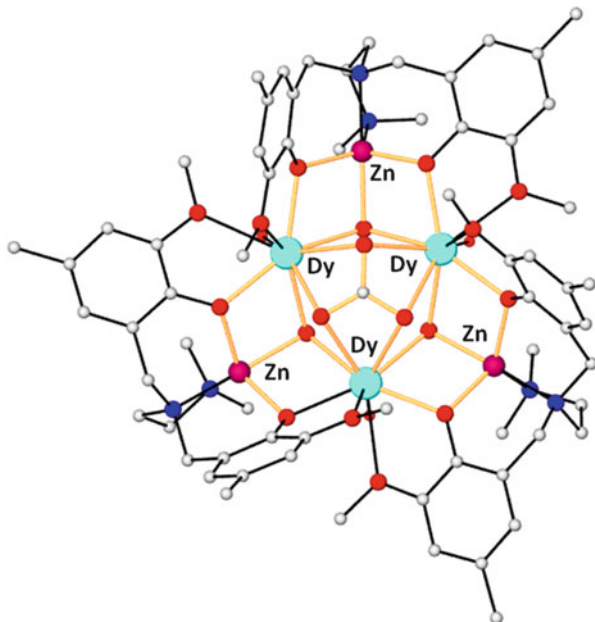
#### 4.5 $(M^{II})_3(Ln^{III})_3$ Hexanuclear Complexes

Chandrasekhar et al. [143] have reported a family of heterometallic hexanuclear  $Ni^{II}_3Ln^{III}_3$  complexes of general composition  $[Ni_3Ln_3(\mu_3-O)(\mu_3-OH)_3(L6)_3(\mu-OOCCMe_3)_3] \cdot ClO_4 \cdot xS$  ( $Ln^{III} = Dy, Tb, Gd, Ho$  and  $Er$ ;  $S = H_2O$  and/or  $CH_2Cl_2$  and/or  $CH_3OH$ ), which were synthesized by the one-pot reaction between the polydentate multi-pocket ligand 6,6'-{(2-(dimethylamino)ethylazanediy)bis(methylene)}bis(2-methoxy-4-methylphenol) ( $H_2L6$ ),  $Ni(ClO_4)_2 \cdot 6H_2O$ ,  $Ln(NO_3)_3 \cdot nH_2O$ ,  $NEt_3$  and pivalic acid. Within the  $[Ni_3Ln_3(\mu_3-O)(\mu_3-OH)_3(L6)_3(\mu-OOCCMe_3)_3]^+$  cationic unit,  $Ni^{II}$  and  $Ln^{III}$  ions are connected by phenoxido bridging groups, a  $\mu_3-OH$  group links an  $Ni^{II}$  and two  $Ln^{III}$  ions and a  $\mu_3-O$  joins the three  $Ln^{III}$  ions. Additionally, three pivalate anions link in an alternate manner  $Ni^{II}$  and  $Ln^{III}$  ions, which results in a double triangular topology of the metal ions with the  $C_3$  axis passing through the  $\mu_3-O$  oxide group (Fig. 37).  $Ni$  ions present a distorted octahedral  $NiN_2O_4$  coordination sphere, which is made of two amine nitrogen atoms and two phenoxide oxygen atoms belonging to the  $L6^{2-}$  ligand, the  $\mu_3-OH$  oxygen atom and one oxygen atoms coming from a pivalate bridging anion. The distorted trigonal-dodecahedron  $LnO_8$  coordination sphere is formed by the coordination of two phenoxide and two methoxy oxygen atoms belonging to two different  $L6^{2-}$  ligands, two  $\mu_3-OH$  oxygen atoms, the  $\mu_3-O$  oxide oxygen atoms and one oxygen atom pertaining to pivalate bridging ligands.

Magnetic dc measurements revealed very weak  $Ni^{II} \dots Gd^{III}$  ferromagnetic coupling ( $J = 0.57 \text{ cm}^{-1}$ ) and  $Gd^{III} \dots Gd^{III}$  antiferromagnetic interactions ( $J = -0.18 \text{ cm}^{-1}$ ). None of these compounds exhibit slow relaxation of the

**Fig. 37** Molecular structure of the cationic unit  $[Ni_3Ln_3(\mu_3-O)(\mu_3-OH)_3(L6)_3(\mu-OOCCMe_3)_3]^+$ . The perchlorate anion and solvent molecules are omitted for clarity. The bridging fragment is highlighted in orange colour





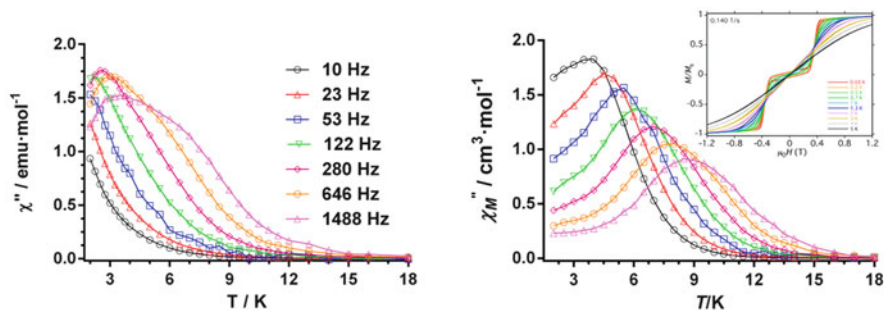
**Fig. 38** Molecular structure of  $[\text{Zn}_3\text{Dy}_3(\mu_6\text{-CO}_3)(\mu_3\text{-OH})_3(\text{L})_3(\text{H}_2\text{O})_3]\cdot 3\text{ClO}_4\cdot\text{NO}_3$ . Perchlorate and nitrate anions and hydrogen atoms are omitted for clarity. The bridging fragment is highlighted in orange colour

magnetization at zero field, which is likely due to the weak coupling observed between the metal ions. Only the  $\text{Ni}^{\text{II}}_3\text{Dy}^{\text{III}}_3$  derivative exhibits a very weak slow relaxation of the magnetization under a magnetic field of 0.3 T with a  $U_{\text{eff}} < 10$  K).

The reaction of the same Mannich base ligand,  $\text{H}_2\text{L6}$  with  $\text{Zn}(\text{ClO}_4)_2\cdot 6\text{H}_2\text{O}$ ,  $\text{Ln}(\text{NO}_3)_3\cdot n\text{H}_2\text{O}$  and  $\text{Et}_3\text{N}$  in methanol at room temperature allowed the Chandrasekhar's group [107] to prepare the first examples of hexanuclear  $\text{Zn}^{\text{II}}_3\text{Ln}^{\text{III}}_3$  complexes of general formula  $[\text{Zn}_3\text{Ln}_3(\mu_6\text{-CO}_3)(\mu_3\text{-OH})_3(\text{L})_3(\text{H}_2\text{O})_3]\cdot 3\text{ClO}_4\cdot\text{NO}_3$  ( $\text{Ln}^{\text{III}} = \text{Dy, Tb}$ ). The cationic unit of these complexes (Fig. 38) possesses a unique double triangular topology, in which the phenoxido oxygen atoms from the ligand and a  $\mu_3\text{-OH}$  group doubly bridge each pair of  $\text{Zn}^{\text{II}}$  and  $\text{Dy}^{\text{III}}$  metal ions, whereas each pair of  $\text{Dy}^{\text{III}}$  ions are doubly bridged by the  $\mu_3\text{-OH}$  group and an oxygen atom belonging to a  $\mu_6\text{-carbonato}$  anion. This latter anion is, as usual, generated in situ from atmospheric  $\text{CO}_2$  fixation in basic medium and it exhibits a unique coordination mode.

The  $\text{Zn}^{\text{II}}$  centres exhibit a distorted trigonal bipyramidal  $\text{ZnN}_2\text{O}_3$  coordination sphere whereas the  $\text{Dy}^{\text{III}}$  centre displays a distorted monocapped square-antiprismatic  $\text{DyO}_9$  coordination sphere. The  $\mu_6\text{-CO}_3$  ligand lies above the  $\text{Dy}_3$  plane and cap the three Dy centres, while the  $\mu_3\text{-OH}$  ligands lay below this plane. The  $\text{Dy}^{\text{III}}$  complex exhibited slow relaxation of the magnetization and SMM





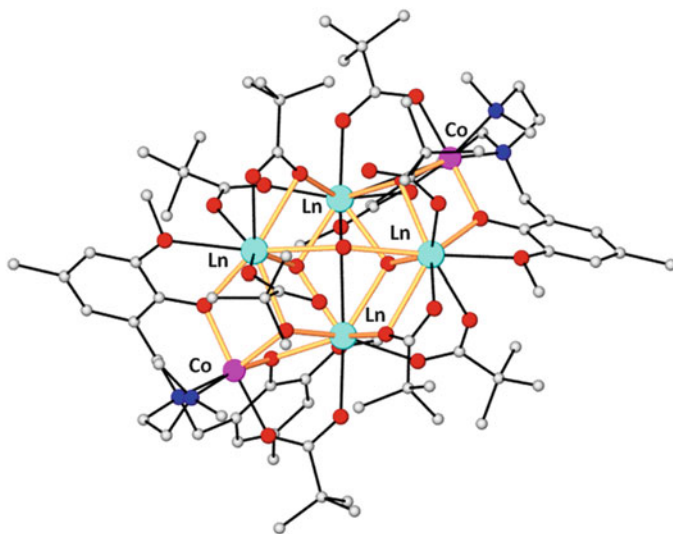
**Fig. 39** Temperature dependence of the out-of-phase  $\chi_M''$  *ac* signals under zero dc field (left) and 1 kOe (right) for  $[\text{Zn}_3\text{Dy}_3(\mu_6\text{-CO}_3)(\mu_3\text{-OH})_3(\text{L})_3(\text{H}_2\text{O})_3]\cdot 3\text{ClO}_4\cdot\text{NO}_3$ . Solid lines are guides for the eye. Inset: magnetization ( $M$ ) vs. field hysteresis loops for a single crystal of  $[\text{Zn}_3\text{Dy}_3(\mu_6\text{-CO}_3)(\mu_3\text{-OH})_3(\text{L})_3(\text{H}_2\text{O})_3]\cdot 3\text{ClO}_4\cdot\text{NO}_3$  at a sweep rate of 0.14 T/s in the 0.03–5 K temperature range. The  $M$  is normalized to its saturation value  $M_s$  at 1.4 T

behaviour at zero field (Fig. 39), while the relaxation of the magnetization in the  $\text{Tb}^{\text{III}}$  counterpart above 2 K, even in the presence of an applied field, was shown to be much faster than the maximum available frequency. Temperature and field dependence of the relaxation times suggested that the magnetic relaxation takes place through a combination of QTM, direct and Raman relaxation processes, the Raman process being dominant above 3 K.

Micro-SQUID measurements indicated that the  $\text{Dy}^{3+}$  complex shows both temperature and field sweep-rate dependent hysteresis loops below 3 K, which unequivocally confirmed its SMM behaviour (Fig. 39, inset). This hysteresis showed an S-shape, which is typical of antiferromagnetically coupled Ising systems, and a large coercive field at zero field upon cooling pointing out a very slow zero-field relaxation. Moreover, the hysteresis showed a broad strongly field sweep-rate dependent step at around  $\pm 0.35$  T corresponding to avoiding level crossings. Ab initio calculations indicate the almost pure axial anisotropy of the ground Kramers doublet and that the local axial magnetic moments are almost coplanar and tangential to the  $\text{Ln}^{3+}$  ions defining an equatorial triangle, and therefore  $[\text{Zn}_3\text{Dy}_3(\mu_6\text{-CO}_3)(\mu_3\text{-OH})_3(\text{L})_3(\text{H}_2\text{O})_3]\cdot 3(\text{ClO}_4)\cdot\text{NO}_3$  can be considered SMTs with almost zero total magnetic moment in the ground state. Both dipole and antiferromagnetic exchange interactions stabilize the “chiral” doublet ground state in the coupled systems. The absence of SMM behaviour in the  $\text{Tb}^{\text{III}}$  counterpart was justified by the splitting of the degeneracy of the ground state of the exchange-coupled system at zero field, which favours the fast QTM.

#### 4.6 $(\text{M}^{\text{II}})_2(\text{Ln}^{\text{III}})_4$ Hexanuclear Complexes

Also, Chandresekhar et al. [144], using the same ligand as in the previous  $\text{Ni}^{\text{II}}_3\text{Ln}^{\text{II}}_3$  complexes, 6,6'-{(2-(dimethylamino) ethylazanediyl)bis(methylene)}bis

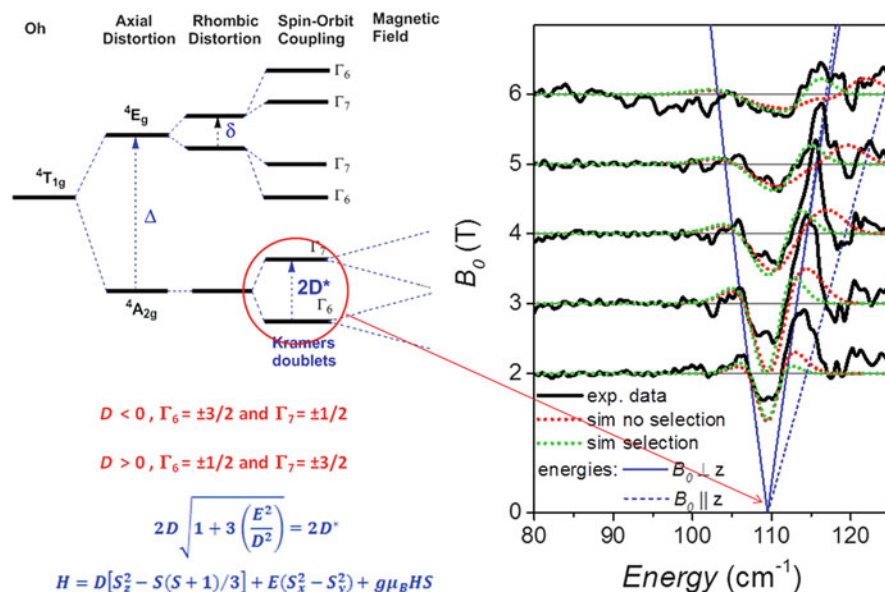


**Fig. 40** Molecular structure of complexes  $[\text{Co}^{\text{II}}_2\text{Ln}_4(\mu_3\text{-OH})_4(\text{L})_2(\text{piv})_8(\mu\text{-OH}_2)]$ . The bridging fragment is highlighted in orange colour

(2-methoxy-4-methylphenol) ( $\text{H}_2\text{L6}$ ), have achieved the preparation of a family of hexanuclear complexes  $[\text{Co}^{\text{II}}_2\text{Ln}_4(\mu_3\text{-OH})_4(\text{L})_2(\text{piv})_8(\mu\text{-OH}_2)] \cdot x\text{S}$  ( $\text{Ln}^{\text{III}} = \text{Gd}, \text{Tb}$  and  $\text{Dy}$ ;  $\text{S} = \text{H}_2\text{O}$  and/or  $\text{CH}_2\text{Cl}_2$  and/or  $\text{CH}_3\text{OH}$ ) by reacting  $\text{H}_2\text{L6}$  with  $\text{Co}(\text{ClO}_4)_2 \cdot 6\text{H}_2\text{O}$ ,  $\text{Ln}(\text{NO}_3)_3 \cdot x\text{H}_2\text{O}$ ,  $\text{NEt}_3$  and pivalic acid in a 2:3:3:8:4 stoichiometric ratio. The structure of these hexanuclear  $\text{Co}^{\text{II}}_2\text{Ln}^{\text{III}}_4$  complexes (Fig. 40) can be considered as formed by two defective cubane  $\text{Co}^{\text{II}}\text{Ln}^{\text{III}}_2$  units linked together through two  $\mu_3\text{-OH}$  groups, two pivalato ligands and one water molecule, all of them bridging lanthanide ions. Moreover, within each  $\text{Co}^{\text{II}}\text{Ln}^{\text{III}}_2$  unit,  $\text{Co}^{\text{II}}$  and  $\text{Ln}^{\text{III}}$  ions are bridged by two phenoxide groups and one  $\mu_3\text{-OH}$  group as well as a *syn,syn* pivalato bridging group. The  $\text{Co}^{\text{II}}$  presents a distorted octahedral  $\text{CoN}_2\text{O}_4$  coordination environment, whereas there are two different types of lanthanide ions with distorted trigonal-dodecahedron  $\text{DyO}_8$  and monocapped square-antiprism  $\text{DyO}_9$  coordination spheres.

Alternating current ac measurements indicate that none of the hexanuclear  $\text{Co}^{\text{II}}_2\text{Ln}^{\text{III}}_4$  complexes exhibit maxima in the temperature dependence of the out-of-phase ac signals at different frequencies above 2 K, even in the presence of an applied magnetic field to suppress QTM. This fact, as usual, could be the result of very weak magnetic coupling between the metal ions.





**Fig. 41** Qualitative energy level diagram for a distorted octahedral Co<sup>II</sup> complex (left). FD-FT THz-EPR of [Co( $\mu$ -L)( $\mu$ -9AC)Y(NO<sub>3</sub>)<sub>2</sub>] (right)

## 5 Heterometallic 3d-3d' Complexes

Our research group have successfully prepared a series of Co<sup>II</sup>Y<sup>III</sup> complexes of general formula [Co( $\mu$ -L)( $\mu$ -X)Y(NO<sub>3</sub>)<sub>2</sub>] ( $X$  = acetate, nitrate, benzoate or 9-anthracenecarboxylato bridging ligands), which exhibit the same structures as the dinuclear M<sup>II</sup>Ln<sup>III</sup> complexes I, II, IV and V given in Sect. 4.1 and Fig. 14 [145, 146]. As Y<sup>III</sup> is a diamagnetic ion, they can be considered, from the magnetic point of view, as mononuclear Co<sup>II</sup> complexes. Interestingly, these complexes exhibited field-induced mononuclear SMM behaviour either in their bulk or magnetic diluted versions. The change of the ancillary bridging group connecting Co<sup>II</sup> and Y<sup>III</sup> ions was shown not only to induce small differences in the trigonally distorted CoN<sub>3</sub>O<sub>3</sub> coordination sphere that adjust the magnetic anisotropy but also to modify the packing and intermolecular exchange and dipolar interactions, which ultimately affect the dynamics of magnetization relaxation.

In these complexes, the combined action of the octahedral field and axial and rhombic distortions leads to a <sup>4</sup>A<sub>2</sub> ground term for the Co<sup>II</sup> ion (Fig. 41), which is additionally split by second-order spin-orbit coupling leading to two Kramers doublets ( $\Gamma_6$  and  $\Gamma_7$ ), so that the energy gap between them can be considered as a ZFS within the quartet state. Therefore, magnetic and spectroscopic properties were interpreted by using the following Hamiltonian:  $H = D[S_z^2 - S(S+1)/3] + E(S_x^2 - S_y^2) + g\mu_B HS$ , where  $D$  and  $E$  are the axial and transverse magnetic anisotropies, respectively. If  $E = 0$ , then  $2D$  symbolizes

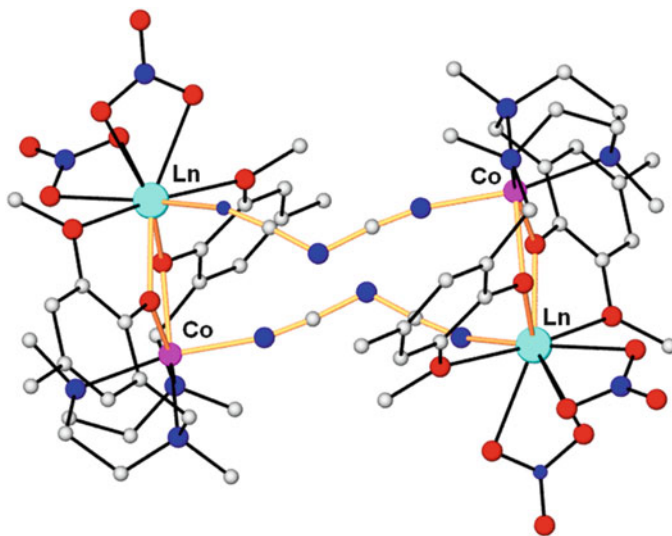
**Table 5** Shape measures of the  $\text{CoN}_3\text{O}_3$  coordination sphere, energy gap between the low-lying KDs and effective energy barrier for the neat and diluted complexes

Compound	Shape (OC-6)	$2D^*/\text{cm}^{-1}$	$U_{\text{eff}}/\text{cm}^{-1}$ (neat)	$U_{\text{eff}}/\text{cm}^{-1}$ (diluted)
$[\text{Co}(\mu\text{-L})(\mu\text{-OAc})\text{Y}(\text{NO}_3)_2]$	2.80	+95.2	15.7	18.8
$[\text{Co}(\mu\text{-L})(\mu\text{-NO}_3)\text{Y}(\text{NO}_3)_2]$	2.10	+100.1	16.6	19.1
$[\text{Co}(\mu\text{-L})(\mu\text{-9AC})\text{Y}(\text{NO}_3)_2]$	1.70	+109.4	–	24.2
$[\text{Co}(\mu\text{-L})(\mu\text{-OBz})\text{Y}(\text{NO}_3)_2]$	1.60	+127.7	–	23.1

the energy gap between  $\pm 1/2$  and  $\pm 3/2$  Kramers doublets (KD) arising from second-order SOC of the quartet ground state.

The collective results of dc magnetic measurements, HFEPR, ab initio theoretical calculations indicated that these complexes possess large and positive anisotropy ( $D$  values  $\sim +50 \text{ cm}^{-1}$ ). Moreover, direct measurements of the energy gap between the low-lying KD doublets by using inelastic neutron scattering for  $[\text{Co}(\mu\text{-L})(\mu\text{-OAc})\text{Y}(\text{NO}_3)_2]$  [143] and FD-FT THz-EPR spectroscopies for this and the complex  $[\text{Co}(\mu\text{-L})(\mu\text{-9Ac})\text{Y}(\text{NO}_3)_2]$  [143] supported the magnitude of  $D$  values (Fig. 38). These studies allowed drawing the following conclusion: If direct techniques cannot be used for extracting the magnitude of the energy gap between the two low-lying KD doublets because of their limited access, then a combination of magnetic, HFEPR and theoretical calculations would be mandatory to achieve reliable values of  $D$  and  $E$ . Interestingly, it was shown that  $D$  values decrease with increasing the distortion of the  $\text{Co}^{\text{II}}$  coordination sphere from octahedral to trigonal prismatic along the  $\text{OC6} \leftrightarrow \text{TPR6}$  deformation pathway (see Table 5).

The compounds with nitrate and acetate as ancillary bridging ligands exhibited field-induced SIM behaviour, whereas those with benzoate and 9-anthracenecarboxylate had to be magnetically diluted ( $\text{Zn/Co} = 1/10$ ) to exhibit such a behaviour. In all these mononuclear SMMs, the Raman relaxation process was shown to be dominant above 3 K. The slow magnetic relaxation properties of these complexes were rationalized by taking into consideration the nature of the intermolecular interactions (exchange and dipolar) as well as the shielding effect exerted by the triamine fragment of the ligand on the  $\text{Co}^{\text{II}} \cdots \text{Co}^{\text{II}}$  dipolar interactions. It was concluded that the existence/absence of large intermolecular interactions seems to switch off/on the field-induced SIM behaviour. In view of this, it is always best to use, if possible, magnetic diluted complexes to eventually remove intermolecular interactions. In doing so, fast QTM would be suppressed, at least partially, and “hidden SIM” could emerge. Finally, as expected for a dominant Raman mechanism, there is not any clear correlation between the anisotropy and the  $U_{\text{eff}}$  values (extracted from the Arrhenius plot) for these complexes.



**Fig. 42** Perspective view of the molecular structure of  $[\text{Co}(\mu\text{-L})(\mu\text{-N}(\text{CN})_2)\text{Ln}(\text{NO}_3)_2]_2$ . Methanol crystallization molecules and hydrogen atoms are omitted for clarity. The bridging network is highlighted in orange colour

## 6 Dinuclear 3d-4f Complexes as Platforms for Constructing Systems of Higher Nuclearity

Binuclear  $[\text{M}(\mu\text{-L})(\text{S})(\mu\text{-NLn}(\text{NO}_3)_3)]$  ( $\text{S} = \text{H}_2\text{O}$  and  $\text{MeOH}$ ) can be used as building blocks to be deliberately assembled with bringing ligands (either simple anions or complexes acting “as ligands”) to generate homo- and heteronuclear complexes with higher nuclearity, respectively. In the dinuclear complexes, ligands that are weakly coordinated to the  $\text{M}^{\text{II}}$  and  $\text{Ln}^{\text{III}}$  metal ions can be replaced by bridging ligands.

### 6.1 $\text{Co}^{\text{II}}\text{Ln}^{\text{III}}_2$ Complexes

Following this strategy, our research group was able to prepare tetranuclear  $\text{Co}^{\text{II}}_2\text{Ln}^{\text{III}}_2$  complexes of general formula  $[\text{Co}_2(\mu\text{-L})_2(\mu\text{-N}(\text{CN})_2)_2\text{Ln}_2(\text{NO}_3)_6]$  ( $\text{Ln}^{\text{III}} = \text{Gd}, \text{Tb}, \text{Dy}, \text{Ho}, \text{Er}$ ) by assembling  $\text{Co}^{\text{II}}\text{Ln}^{\text{III}}$  dinuclear units, formed in situ by reacting a methanolic solution containing  $\text{H}_2\text{L}$ ,  $\text{Co}(\text{NO}_3)_3 \cdot 6\text{H}_2\text{O}$  and  $\text{Dy}(\text{NO}_3)_3 \cdot 6\text{H}_2\text{O}$  1:1:1, with the equimolecular amount of  $\text{NaN}(\text{CN})_2$  in the same solvent [118]. These complexes are isostructural and their structure consists of centrosymmetric tetranuclear molecules  $[\text{Co}(\mu\text{-L})(\mu\text{-N}(\text{CN})_2)\text{Ln}(\text{NO}_3)_2]_2$ , in which  $\text{Co}^{\text{II}}$  and  $\text{Ln}^{\text{III}}$  ions are connected by two 1,5-dicyanamide bridging ligands in a “head to tail” arrangement

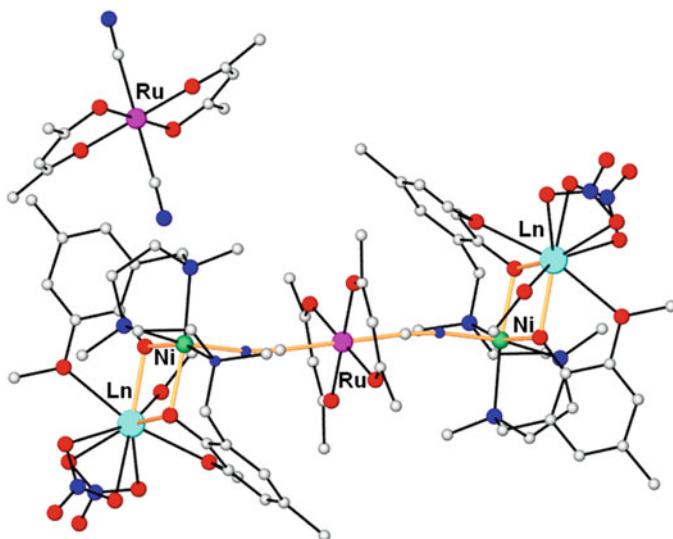
(Fig. 42). The  $\text{Co}^{\text{II}}$  ions exhibit distorted octahedral  $\text{CoN}_4\text{O}_2$  coordination spheres whereas the lanthanide displays an  $\text{LnO}_8\text{N}$  coordination environment.

These complexes exhibit, as their dinuclear precursors, ferromagnetic interactions between the  $\text{Co}^{\text{II}}$  and  $\text{Ln}^{\text{III}}$  ions through the bis(diphenoxido) bridging groups ( $J = +0.75 \text{ cm}^{-1}$ ) and a very weak antiferromagnetic coupling between these metal ions through the dicyanamide bridging ligands ( $j = -0.02 \text{ cm}^{-1}$ ), which is not unexpected as dicyanamide is a poor mediator for the magnetic exchange interaction.

None of these tetranuclear  $\text{Co}_2\text{Ln}_2$  compounds exhibit slow relaxation of the magnetization, even under an external *dc* field, which may be related to the existence of very weak Co-Ln antiferromagnetic interactions between each pair of centrosymmetrically related dinuclear Co-Ln units. These interactions generate small separations of the low-lying split sublevels, which lead to a very small energy barrier for the flipping of the magnetization and favour QTM.

## 6.2 $(\text{Ni}^{\text{II}}_2\text{Ln}^{\text{III}}_2)\text{Ru}^{\text{III}}$ Trimetallic Complexes

In order to obtain metal complexes with enhanced magnetic anisotropy and magnetic moment in the ground state, our group assembled  $[\text{Ni}(\mu\text{-L})\text{Ln}(\text{NO}_3)_3]^+$  cationic units (formed in situ from the reaction of  $\text{H}_2\text{L}$  with  $\text{Ni}(\text{NO}_3)_2 \cdot 6\text{H}_2\text{O}$  and subsequently with  $\text{Ln}(\text{NO}_3)_3 \cdot n\text{H}_2\text{O}$  in MeOH and using a 1:1:1 molar ratio) and the



**Fig. 43** Molecular structure of  $[\{\mu\text{-Ru}(\text{acac})_2(\text{CN})_2\}\{\text{Ni}(\mu\text{-L})\text{Ln}(\text{CH}_3\text{OH})(\text{NO}_3)_2\}_2][\text{Ru}(\text{acac})_2(\text{CN})_2] \cdot 4\text{CH}_3\text{OH}$ . Methanol crystallization molecules and hydrogen atoms are omitted for clarity. The bridging network is highlighted in orange colour

$\text{Ph}_4\text{P}^+$  salt of the anisotropic *trans*- $[\text{Ru}^{\text{III}}(\text{acac})_2(\text{CN})_2]^-$  cyanometallato anion in 1:1 molar ratio, affording discrete trimetallic  $(\text{Ln}^{\text{III}}\text{Ni}^{\text{II}})\text{Ru}^{\text{III}}$  species of general formula  $[\{\mu\text{-Ru}(\text{acac})_2(\text{CN})_2\}\{\text{Ni}(\mu\text{-L})\text{Ln}(\text{CH}_3\text{OH})(\text{NO}_3)_2\}_2] [\text{Ru}(\text{acac})_2(\text{CN})_2]\cdot 4\text{CH}_3\text{OH}$  ( $\text{Ln}^{\text{III}} = \text{Gd}$  and  $\text{Dy}$ ) [147].

These compounds are isostructural and its structure consists of *S*-shaped centrosymmetric pentanuclear  $[\{\mu\text{-Ru}(\text{acac})_2(\text{CN})_2\}\{\text{Ni}(\mu\text{-L})\text{Gd}(\text{NO}_3)_3\}_2]^+$  cations, centrosymmetric *trans*- $[\text{Ru}(\text{acac})_2(\text{CN})_2]^-$  anions and four methanol molecules of crystallization (Fig. 43), linked together by hydrogen bonds. Inside each pentanuclear  $[(\text{NiGd})_2\text{Ru}]^+$  cationic unit, two dinuclear cationic fragments  $[\text{Ni}(\mu\text{-L})\text{Ln}(\text{CH}_3\text{OH})(\text{NO}_3)_2]^+$ , in which the  $\text{Ln}^{\text{III}}$  and  $\text{Ni}^{\text{II}}$  ions are bridged by two phenoxido groups of the  $\text{L}^{2-}$  ligand, are connected at the available coordination position of the  $\text{Ni}^{\text{II}}$  ions by the linear *trans*- $[\text{Ru}(\text{acac})_2(\text{CN})_2]^-$  metalloligand. The  $\text{Ni}^{\text{II}}$  and  $\text{Ru}^{\text{III}}$  ions display distorted octahedral  $\text{NiN}_4\text{O}_2$  and  $\text{RuC}_2\text{O}_4$  coordination polyhedra, respectively, whereas the  $\text{Ln}^{\text{III}}$  ion exhibits an  $\text{LnO}_9$  coordination sphere.

The new pentanuclear  $[(\text{LnNi})_2\text{Ru}]^+$  complexes ( $\text{Ln}^{\text{III}} = \text{Gd}$  and  $\text{Dy}$ ) exhibit ferromagnetic interactions between the  $\text{Ni}^{2+}$  and  $\text{Ln}^{3+}$  as well as between the  $\text{Ni}^{2+}$  and  $\text{Ru}^{3+}$  ions, leading, in the case of the  $\text{Gd}^{\text{III}}$  derivative, to an  $S = 19/2$  ground spin state ( $J_{\text{GdNi}} = +1.86 \text{ cm}^{-1}$ ,  $J_{\text{RuNi}} = +3.02 \text{ cm}^{-1}$ ). The  $\text{Dy}^{\text{III}}$  counterpart seems to exhibit slow relaxation of the magnetization but without reaching any maximum in the temperature dependence of the out-of-phase susceptibility above 2 K. These results show once again that the introduction of several anisotropic ions, such as  $\text{Ni}^{\text{II}}$ ,  $\text{Dy}^{\text{III}}$  and  $\text{Ru}^{\text{III}}$ , does not guarantee a larger uniaxial anisotropy, as the local anisotropies can be combined in a subtractive manner. This together with the very weak  $J_{\text{NiLn}}$  and  $J_{\text{NiRu}}$  coupling constants could promote smaller values of the energy barrier.

**Acknowledgements** I would like to express my most sincere gratitude and deep appreciation to all my collaborators, colleagues and students. Their names appear in the reference list. I am also very grateful to Ministerio de Economía y Competitividad (MINECO) of Spain for Project CTQ2014-56312-P and *EU Feder Fund*, the Junta de Andalucía (FQM-195 and the Project of excellence P11-FQM-7756) and the University of Granada for financial support.

## References

1. Gatteschi D, Sessoli R, Villain J (2006) *Molecular nanomagnets*. Oxford University Press, Oxford
2. Bartolomé J, Luis F, Fernández JF (2014) *Molecular magnets: physics and applications*. Springer-Verlag, Berlin, Heidelberg
3. Gao S (2015) *Molecular nanomagnets and related phenomena*. Structure and bonding, vol 164. Springer-Verlag, Berlin, Heidelberg
4. Cornia A, Mannini M (2015) *Single-molecule magnets on surfaces*. Structure and bonding, vol 164. Springer-Verlag, Berlin, Heidelberg, pp 293–330

5. Moreno Pineda E, Komeda T, Katoh K, Yamashita M, Ruben M (2016) Surface confinement of TbPc2-SMMs: structural, electronic and magnetic properties. *Dalton Trans* 45:18417–18433
6. Bogani L, Wernsdorfer W (2008) Molecular spintronics using single-molecule magnets. *Nat Mater* 7:179–186
7. Prezioso M, Riminucci A, Graziosi P, Bergenti I, Rakshit R, Cecchini R, Vianelli A, Borgatti F, Haag N, Willis M, Drew AJ, Gillin WP, Dediu VA (2013) A single-device universal logic gate based on a magnetically enhanced memristor. *Adv Mater* 25:534–538
8. Vincent R, Klyatskaya S, Ruben M, Wernsdorfer W, Balestro F (2012) Electronic read-out of a single nuclear spin using a molecular spin transistor. *Nature* 488:357–360
9. Ganzhorn M, Klyatskaya S, Ruben M, Wernsdorfer W (2013) Strong spin–phonon coupling between a single-molecule magnet and a carbon nanotube nanoelectromechanical system. *Nat Nanotechnol* 8:165–169
10. Jenkins M, Hümmer T, Martínez-Pérez MJ, García-Ripoll J, Zueco D, Luis F (2013) Coupling single-molecule magnets to quantum circuits. *New J Phys* 15:095007
11. Mannini M, Pineider F, Danieli C, Totti F, Sorace L, Sainctavit P, Arrio MA, Otero E, Joly L, Cezar JC, Cornia A, Sessoli R (2010) Quantum tunnelling of the magnetization in a monolayer of oriented single-molecule magnets. *Nature* 468:417–421
12. Thiele S, Balestro F, Ballou R, Klyatskaya S, Ruben M, Wernsdorfer W (2014) Electrically driven nuclear spin resonance in single-molecule magnets. *Science* 344:1135–1138
13. Sanvito S (2011) Molecular spintronics. *Chem Soc Rev* 40:3336–3355
14. Katoh K, Isshiki H, Komeda T, Yamashita M (2012) Molecular spintronics based on single-molecule magnets composed of multiple-decker phthalocyaninato terbium(III) complex. *Chem Asian J* 7:1154–1169
15. Jiang SD, Goß K, Cervetti C, Bogani L (2012) An introduction to molecular spintronics. *Sci China Chem* 55:867–882
16. Lumetti S, Candini A, Godfrin C, Balestro F, Wernsdorfer W, Klyatskaya S, Ruben M, Affronte M (2016) Single-molecule devices with graphene electrodes. *Dalton Trans* 45:16570–16574
17. Cornia A, Seneor P (2017) Spintronics: the molecular way. *Nat Mater* 16:505–506
18. Rocha AR, García-Suárez VM, Bailey SW, Lambert CJ, Ferrerand J, Sanvito S (2005) Towards molecular spintronics. *Nat Mater* 4:335–339
19. Affronte M (2009) Molecular nanomagnets for information technologies. *J Mater Chem* 19:1731–1737
20. Sessoli R, Boulon ME, Caneschi A, Mannini M, Poggini L, Wilhelm F, Rogalev A (2015) Strong magneto-chiral dichroism in a paramagnetic molecular helix observed by hard X-rays. *Nat Phys* 11:69–74
21. Leuenberger MN, Loss D (2001) Quantum computing in molecular magnets. *Nature* 410:789–793
22. Ardavan A, Rival O, Morton JJJ, Blundell SJ, Tyryshkin AM, Timco GA, Winpenny RPA (2007) Will spin-relaxation times in molecular magnets permit quantum information processing? *Phys Rev Lett* 98:057201
23. Stamp PCE, Gaita-Ariño A (2009) Spin-based quantum computers made by chemistry: hows and whys. *J Mater Chem* 19:1718–1730
24. Martínez-Pérez MJ, Cardona-Serra S, Schlegel C, Moro F, Alonso PJ, Prima-García H, Clemente-Juan JM, Evangelisti M, Gaita-Ariño A, Sesé J, Van Slageren J, Coronado E, Luis F (2012) Gd-based single-ion magnets with tunable magnetic anisotropy: molecular design of spin qubits. *Phys Rev Lett* 108:247213
25. Aromí G, Brechin GEK (2006) Synthesis of 3d metallic single-molecule magnets. *Structure and bonding*, vol 122, pp 1–67
26. Bagai R, Christou G (2009) The Drosophila of single-molecule magnetism. *Chem Soc Rev* 38:1011
27. Brechin EK (ed) (2010) “Molecular Magnets”, themed issue. *Dalton Trans*

28. Murrie M (2010) Cobalt (II) single-molecule magnets. *Chem Soc Rev* 39:1986–1995
29. Neese F, Pantazis DA (2011) What is not required to make a single molecule magnet. *Faraday Discuss* 148:229–238
30. Waldmann O (2007) A criterion for the anisotropy barrier in single-molecule magnets. *Inorg Chem* 46:10035–10037
31. Milios CJ, Vinslava A, Wernsdorfer W, Moggach S, Parsons S, Perlepes SP, Christou G, Brechin EK (2007) A record anisotropy barrier for a single-molecule magnet. *J Am Chem Soc* 129:2754–2755
32. Inglis R, Taylor SM, Jones LF, Papaefstathiou GS, Perlepes SP, Datta S, Hill S, Wernsdorfer W, Brechin EK (2009) *Dalton Trans*:9157–9168
33. Yoshihara D, Karasawa S, Koga N (2008) Cyclic single-molecule magnet in heterospin system. *J Am Chem Soc* 130:10460–10461
34. Tasiopoulos AJ, Vinslava A, Wernsdorfer W, Abboud KA, Christou G (2004) Giant single-molecule magnets: a {Mn<sub>8</sub>} torus and its supramolecular nanotubes. *Angew Chem Int Ed* 43:2117–2121
35. Ako AM, Hewitt IJ, Mereacre V, Clerac R, Wernsdorfer W, Anson CE, Powell AK (2006) A ferromagnetically coupled Mn<sub>19</sub> aggregate with a record  $S = 83/2$  ground spin state. *Angew Chem Int Ed* 45:4926–4929
36. Frost JM, Harriman KLM, Murugesu M (2016) The rise of 3-d single-ion magnets in molecular magnetism: towards materials from molecules? *Chem Sci* 7:2470–2491
37. Bar AK, Pichon C, Sutter J-P (2016) Magnetic anisotropy in two- to eight-coordinated transition–metal complexes: recent developments in molecular magnetism. *Coord Chem Rev* 308:346–380
38. Craig GA, Murrie M (2015) 3d single-ion magnets. *Chem Soc Rev* 44:2135–2147
39. Gómez-Coca S, Aravena D, Morales R, Ruiz E (2015) Large magnetic anisotropy in mono-nuclear metal complexes. *Coord Chem Rev* 289–290:379–392
40. Zadrozny JM, Xiao DJ, Atanasov M, Long GJ, Grandjean F, Neese F, Long JR (2013) Magnetic blocking in a linear iron(I) complex. *Nat Chem* 5:577–581
41. Layfield RA, Murugesu M (eds) (2015) Lanthanides and actinides in molecular magnetism. Wiley-VCH, Weinheim
42. Rinehart JD, Long JR (2011) Exploiting single-ion anisotropy in the design of f-element single-molecule magnets. *Chem Sci* 2:2078–2085
43. Guo YN, Xu GF, Guo Y, Tang J (2011) *Dalton Trans* 40:9953–9963
44. Sorace L, Benelli C, Gatteschi D (2011) Lanthanides in molecular magnetism: old tools in a new field. *Chem Soc Rev* 40:3092–3104
45. Luzon J, Sessoli R (2012) *Dalton Trans* 41:13556–13567
46. Clemente-Juan JM, Coronado E, Gaita-Ariño A (2012) Magnetic polyoxometalates: from molecular magnetism to molecular spintronics and quantum computing. *Chem Soc Rev* 41:7464–7478
47. Woodruff DN, Winpenny REP, Layfield RA (2013) Lanthanide single-molecule magnets. *Chem Rev* 113:5110–5148
48. Zhang P, Guo Y, Tang J (2013) Recent advances in dysprosium-based single molecule magnets: structural overview and synthetic strategies. *Coord Chem Rev* 257:1728–1763
49. Habib F, Murugesu M (2013) Lessons learned from dinuclear lanthanide nano-magnets. *Chem Soc Rev* 42:3278–3288
50. Layfield RA (2014) Organometallic single-molecule magnets. *Organometallics* 33:1084–1099
51. Harriman KLM, Murugesu M (2016) An organolanthanide building block approach to single-molecule magnets. *Acc Chem Res* 49:1158–1167
52. Wang BW, Gao S (2012) In: Atwood DA (ed) *The rare earth elements, fundamental and applications*. Wiley, Hoboken, pp 153–160
53. Winpenny REP (1998) The structures and magnetic properties of complexes containing 3d- and 4f-metals. *Chem Soc Rev* 27:447–452
54. Sakamoto M, Manseki K, Okawa H (2001) d–f Heteronuclear complexes: synthesis, structures and physicochemical aspects. *Coord Chem Rev* 219:379–414

55. Huang Y-G, Jiang F-L, Hong M-C (2009) Magnetic lanthanide–transition-metal organic–inorganic hybrid materials: from discrete clusters to extended frameworks. *Coord Chem Rev* 253:2814–2834
56. Benelli C, Gatteschi D (2002) Magnetism of lanthanides in molecular materials with transition-metal ions and organic radicals. *Chem Rev* 102:2369–2388
57. Sessoli R, Powell AK (2009) Strategies towards single molecule magnets based on lanthanide ions. *Coord Chem Rev* 253:2328–2341
58. Andruh M, Costes JP, Diaz C, Gao S (2009) 3d–4f combined chemistry: synthetic strategies and magnetic properties. *Inorg Chem* 48:3342–3359
59. Brechin EK (ed) (2010) “Molecular magnets” themed issue. *Dalton Trans* 39:4653–5040
60. Sharples JW, Collison D (2014) The coordination chemistry and magnetism of some 3d–4f and 4f amino-polyalcohol compounds. *Coord Chem Rev* 260:1–20
61. Zheng Y-Z, Zhou G-J, Zheng Z, Winpenny REP (2014) *Chem Soc Rev* 43:1462–1475
62. Rosado L, Sañudo EC (2015) Heterometallic 3d–4f single-molecule magnets. *Dalton Trans* 44:8771–8780
63. Chow CY, Trivedi ER, Pecoraro V, Zaleski CM (2015) Heterometallic mixed 3d–4f metallacrowns: structural versatility, luminescence, and molecular magnetism, comments. *Inorg Chem* 35:214–253
64. Liu K, Shi W, Cheng P (2015) Toward heterometallic single-molecule magnets: synthetic strategy, structures and properties of 3d–4f discrete complexes. *Coord Chem Rev* 289–290:74–122
65. Polyzou CD, Efthymiou CG, Escuer A, Cunha-Silva L, Papatriantafyllopoulou C, Perlepes SP (2013) In search of 3d/4f-metal single-molecule magnets: nickel(II)/lanthanide(III) coordination clusters. *Pure Appl Chem* 85:315–327
66. Vignesh KR, Langley SK, Murray KS, Rajaraman G (2017) Quenching the quantum tunneling of magnetization in heterometallic octanuclear  $\{\text{TM}^{\text{III}}_4\text{Dy}^{\text{III}}_4\}$  (TM = Co and Cr) single-molecule magnets by modification of the bridging ligands and enhancing the magnetic exchange coupling. *Chem Eur J* 23:1654–1666
67. Langley SK, Wielechowski DP, Moubaraki B, Murray KS (2016) Enhancing the magnetic blocking temperature and magnetic coercivity of  $\{\text{Cr}^{\text{III}}_2\text{Ln}^{\text{III}}_2\}$  single-molecule magnets via bridging ligand modification. *Chem Commun* 52:10976–10979
68. Gupta T, Beg MF, Rajaraman G (2016) Role of single-ion anisotropy and magnetic exchange interactions in suppressing zero-field tunnelling in  $\{3d\text{--}4f\}$  single molecule magnets. *Inorg Chem* 55:11201–11215
69. Singh SK, Beg MF, Rajaraman G (2016) Role of magnetic exchange interactions in the magnetization relaxation of  $\{3d\text{--}4f\}$  single-molecule magnets: a theoretical perspective. *Chem Eur J* 22:672–680
70. Li X-L, Min F-Y, Wang C, Lin S-Y, Liu Z, Tang J (2015) Utilizing 3d–4f magnetic interaction to slow the magnetic relaxation of heterometallic complexes. *Inorg Chem* 54:4337–4344
71. Langley SK, Le C, Ungur L, Moubaraki B, Abrahams BF, Chibotaru LF, Murray KS (2014) Heterometallic 3d–4f single-molecule magnets: ligand and metal ion influences on the magnetic relaxation. *Inorg Chem* 53:8970–8978
72. Langley SK, Wielechowski DP, Vieru V, Chilton NF, Moubaraki B, Abrahams BF, Chibotaru LF, Murray KS (2013) A  $\{\text{Cr}^{\text{III}}_2\text{Dy}^{\text{III}}_2\}$  single-molecule magnet: enhancing the blocking temperature through 3d magnetic exchange. *Angew Chem Int Ed* 52:12014–12019
73. Liu J-L, Wu J-Y, Chen Y-C, Mereacre V, Powell AK, Ungur L, Chibotaru LF, Chen X-M, Tong M-L (2014) A heterometallic  $\text{Fe}^{\text{II}}\text{--Dy}^{\text{III}}$  single-molecule magnet with a record anisotropy barrier. *Angew Chem Int Ed* 53:12966–12970
74. Rinehart JD, Fang M, Evans WJ, Long JR (2011) Strong exchange and magnetic blocking in  $\text{N}_2^{3-}$ -radical-bridged lanthanide complexes. *Nat Chem* 3:538–542
75. Rinehart JD, Fang M, Evans WJ, Long JR (2011) A  $\text{N}_2^{3-}$ -radical-bridged terbium complex exhibiting magnetic hysteresis at 14 K. *J Am Chem Soc* 133:14236–14239



76. Demir S, Gonzalez MI, Darago L, Evans WJ, Long JR (2017) Giant coercivity and high magnetic blocking temperatures for  $N_2^{3-}$  radical-bridged lanthanide complexes upon ligand dissociation. *Nat Commun* 8:2144. <https://doi.org/10.1038/s41467-017-01553-w>
77. Ding YS, Chilton NF, Winpenny RE, Zheng YZ (2016) On approaching the limit of molecular magnetic anisotropy: a near-perfect pentagonal bipyramidal dysprosium(III) single-molecule magnet. *Angew Chem Int Ed Engl* 55:16071–16074
78. Chen Y, Liu J, Ungur L, Liu J, Li Q, Wang L, Ni Z, Chibotaru LF, Chen X, Tong ML (2016) Symmetry-supported magnetic blocking at 20 K in pentagonal bipyramidal Dy(III) single-ion magnets. *J Am Chem Soc* 138:2829–2837
79. Gupta SK, Rajeshkumar T, Rajaraman G, Murugavel R (2016) An air-stable Dy(III) single-ion magnet with high anisotropy barrier and blocking temperature. *Chem Sci* 7:5181–5191
80. Liu J, Chen Y, Jia J, Liu J, Vieru V, Ungur L, Chibotaru LF, Lan Y, Wernsdorfer W, Gao S, Chen X, Tong M (2016) A stable pentagonal bipyramidal Dy(III) single-ion magnet with a record magnetization reversal barrier over 1,000 K. *J Am Chem Soc* 138:5441–5450
81. Zhong ZQ, Mansikkamäki A, Ungur L, Jia JH, Chibotaru LF, Han JB, Wernsdorfer W, Chen XM, Tong ML (2017) Dynamic magnetic and optical insight into a high performance pentagonal bipyramidal  $Dy^{III}$  single-ion magnet. *Chem Eur J* 23:1–9
82. Goodwin CAP, Ortu F, Reta D, Chilton NF, Mills DP (2017) Molecular magnetic hysteresis at 60 K in dysprosocenium. *Nature* 548:439–442
83. Guo S, Day BM, Chen Y-C, Tong M-L, Mansikkamäki A, Layfield RA (2017) A dysprosium metallocene single-molecule magnet functioning at the axial limit. *Angew Chem Int Ed* 56:11445–11449
84. Bünzli J-CG (2014) Lanthanide coordination chemistry: from old concepts to coordination polymers. *J Coord Chem* 67:3706–3733
85. Bünzli J-CG (2010) Lanthanide luminescence for biomedical analyses and imaging. *Chem Rev* 11:2729–2755
86. Eliseeva SV, Bünzli JC (2010) Lanthanide luminescence for functional materials and bio-sciences. *Chem Soc Rev* 39:189–227
87. Faulkner S, Pope SJA, Burton-Pye BP (2005) Lanthanide complexes for luminescence imaging applications. *Appl Spectrosc Rev* 40:1
88. Liu S (2004) The role of coordination chemistry in the development of target specific radiopharmaceuticals. *Chem Soc Rev* 33:445
89. Amoroso AJ, Pope SJ (2015) Using lanthanide ions in molecular bioimaging. *Chem Soc Rev* 44:4723–4742
90. Andruh M (2015) The exceptionally rich coordination chemistry generated by Schiff-base ligands derived from o-vanillin. *Dalton Trans* 44:16633–16653
91. Ruiz J, Mota AJ, Rodríguez-Diéguez A, Titos S, Herrera JM, Ruiz E, Cremades E, Costes JP, Colacio E (2012) Field and dilution effects on the slow relaxation of a luminescent  $DyO_9$  low-symmetry single-ion magnet. *Chem Commun* 48:7916–7918
92. Tang J, Hewitt I, Madhu NT, Chastanet G, Wernsdorfer W, Anson CE, Benelli C, Sessoli R, Powell AK (2006) Dysprosium triangles showing single-molecule magnet behavior of thermally excited spin states. *Angew Chem Int Ed* 45:1729–1733
93. Luzon J, Bernot K, Hewitt I, Anson CE, Powell AK, Sessoli R (2008) Spin chirality in a molecular dysprosium triangle: the archetype of the noncollinear ising model. *Phys Rev Lett* 100:247205–247204
94. Chibotaru LF, Ungur L, Soncini A (2008) The origin of nonmagnetic kramers doublets in the ground state of dysprosium triangles: evidence for a toroidal magnetic moment. *Angew Chem Int Ed* 47:4126–4129
95. Hewitt IJ, Tang J, Madhu NT, Anson CE, Lan Y, Luzon J, Etienne M, Sessoli R, Powell AK (2010) Coupling  $Dy_3$  triangles enhances their slow magnetic relaxation. *Angew Chem Int Ed* 49:6352–6356
96. Chibotaru LF, Ungur L, Soncini A (2012) Coupling  $Dy_3$  triangles to maximize the toroidal moment. *Angew Chem Int Ed* 51:12767–12771

97. Wang Y, Shi W, Li H, Song Y, Fang L, Lan Y, Powell AK, Wernsdorfer W, Ungur L, Chibotaru L, Shen M, Cheng P (2012) A single-molecule magnet assembly exhibiting a dielectric transition at 470 K. *Chem Sci* 3:3366–3370
98. Lin S, Zhao L, Guo Y, Zhang P, Guo Y, Tang J (2012) Two new Dy<sup>3</sup> triangles with trinuclear circular helicates and their single-molecule magnet behavior. *Inorg Chem* 51:10522–10528
99. Lin S, Guo Y, Guo Y, Zhao L, Zhang P, Ke H, Tang J (2012) Macrocyclic ligand encapsulating dysprosium triangles: axial ligands perturbed magnetic dynamics. *Chem Commun* 48:6924–6926
100. Xue S, Chen X, Zhao L, Guo Y, Tang J (2012) Two bulky-decorated triangular dysprosium aggregates conserving vortex-spin structure. *Inorg Chem* 51:13264–13270
101. Hänninen MM, Mota AJ, Aravena D, Ruiz E, Sillanpää R, Camón A, Evangelisti M, Colacio E (2014) Two C<sub>3</sub>-symmetric Dy<sup>3</sup> complexes with triple di- $\mu$ -methoxy- $\mu$ -phenoxy bridges, magnetic ground state, and single-molecule magnetic behavior. *Chem Eur J* 20:8410–8420
102. Grindell R, Vieru R, Pugh T, Chibotaru LF, Layfield RA (2016) Magnetic frustration in a hexaazatrinaphthylene-bridged trimetallic dysprosium single-molecule magnet. *Dalton Trans* 45:16556–16560
103. Díaz-Ortega IF, Herrera JM, Gupta T, Rajaraman G, Nojiri H, Colacio E (2017) Design of a family of Ln<sub>3</sub> triangles with the HAT ligand (1,4,5,8,9,12-hexaazatriphenylene): single-molecule magnetism. *Inorg Chem* 15:5594–5610
104. Novitchi G, Pilet G, Ungur L, Moshchalkov VV, Wernsdorfer W, Chibotaru LF, Luneau D, Powell AK (2012) Heterometallic Cu<sup>II</sup>/Dy<sup>III</sup> 1D chiral polymers: chirogenesis and exchange coupling of toroidal moments in trinuclear Dy<sub>3</sub> single molecule magnets. *Chem Sci* 3:1169–1176
105. Zhang L, Zhang P, Zhao L, Wu J, Guo M, Tang J (2016) Single-molecule magnet behavior in an octanuclear dysprosium(III) aggregate inherited from helical triangular Dy<sub>3</sub> SMM-building blocks. *Dalton Trans* 45:10556–10562
106. Gysler M, Hallak FE, Ungur L, Marx R, Hakl M, Neugebauer P, Rechkemmer Y, Lan Y, Sheikin I, Orlita M, Anson CE, Powell AK, Sessoli R, Chibotaru LF, Van Slageren J (2016) Multitechnique investigation of Dy<sub>3</sub> – implications for coupled lanthanide clusters. *Chem Sci* 7:4347–4354
107. Goura J, Colacio E, Herrera JM, Suturina EA, Kuprov I, Lan Y, Wernsdorfer W, Chandrasekhar V (2017) Heterometallic Zn<sub>3</sub> Ln<sub>3</sub> ensembles containing ( $\mu_6$ -CO<sub>3</sub>) ligand and triangular disposition of Ln<sup>3+</sup> ions: analysis of single-molecule toric (SMT) and single-molecule magnet (SMM) behavior. *Chemistry* 23:16621–16636
108. Das C, Vaidya S, Gupta T, Frost JM, Righi M, Brechin EK, Affronte M, Rajaraman G, Shanmugam M (2015) Single-molecule magnetism, enhanced magnetocaloric effect, and toroidal magnetic moments in a family of Ln<sub>4</sub> squares. *Chem Eur J* 21:15639–15650
109. Guo P, Liu J, Zhang Z, Ungur L, Chibotaru LF, Leng J, Guo F, Tong M (2012) The first {Dy<sub>4</sub>} single-molecule magnet with a toroidal magnetic moment in the ground state. *Inorg Chem* 51:1233–1235
110. Biswas SD, Gupta T, Singh SK, Pissas M, Rajaraman G, Chandrasekhar V (2016) Observation of slow relaxation and single-molecule toroidal behavior in a family of butterfly-shaped Ln<sub>4</sub> complexes. *Chem Eur J* 22:18532–18550
111. Li X, Wu J, Tang J, Le Guennic B, Shi W, Cheng P (2016) A planar triangular Dy<sub>3</sub> + Dy<sub>3</sub> single-molecule magnet with a toroidal magnetic moment. *Chem Commun* 52:9570–9573
112. Ungur L, Langley SK, Hooper TN, Moubaraki B, Brechin EK, Murray KS, Chibotaru LF (2012) Net toroidal magnetic moment in the ground state of a {Dy<sub>6</sub>}-triethanolamine ring. *J Am Chem Soc* 134:18554–18557
113. Ungur L, Lin S, Tang J, Chibotaru LF (2014) Single-molecule toroics in Ising-type lanthanide molecular clusters. *Chem Soc Rev* 43:6894–6905
114. Wang G, Weia Y, Wu K (2016) Goblet-shaped pentanuclear lanthanide clusters assembled with a cyclen derivative ligand exhibiting slow magnetic relaxation. *Dalton Trans* 45:12734–12738

115. Colacio E, Ruiz-Sanchez J, White FJ, Brechin EK (2011) Strategy for the rational design of asymmetric triply bridged dinuclear 3d-4f single-molecule magnets. *Inorg Chem* 50:7268
116. Colacio E, Ruiz J, Mota AJ, Palacios MA, Cremades E, Ruiz E, White FJ, Brechin EK (2012) Family of carboxylate- and nitrate-diphenoxo triply bridged dinuclear  $\text{Ni}^{\text{II}}\text{Ln}^{\text{III}}$  complexes ( $\text{Ln} = \text{Eu}, \text{Gd}, \text{Tb}, \text{Ho}, \text{Er}, \text{Y}$ ): synthesis, experimental and theoretical magneto-structural studies, and single-molecule magnet behavior. *Inorg Chem* 51:5857–5868
117. Palacios MA, Titos-Padilla S, Ruiz J, Herrera JM, Pope SJ, Brechin EK, Colacio E (2014) Bifunctional  $\text{Zn}(\text{II})\text{Ln}(\text{III})$  dinuclear complexes combining field induced SMM behavior and luminescence: enhanced NIR lanthanide emission by 9-anthracene carboxylate bridging ligands. *Inorg Chem* 53:1465–1474
118. Colacio E, Ruiz J, Mota AJ, Palacios MA, Ruiz E, Cremades E, Hänninen MM, Sillanpää R, Brechin EK (2012)  $\text{Co}^{\text{II}}\text{Ln}^{\text{III}}$  dinuclear complexes ( $\text{Ln}^{\text{III}} = \text{Gd}, \text{Tb}, \text{Dy}, \text{Ho}$  and  $\text{Er}$ ) as platforms for 1,5-dicyanamide-bridged tetranuclear  $\text{Co}^{\text{II}}_2\text{Ln}^{\text{III}}_2$  complexes: a magneto-structural and theoretical study. *C R Chim* 15:878–888
119. Zabala-Lekuona A, Cepeda J, Oyarzabal I, Rodríguez-Diéguez A, García JA, Seco JM, Colacio E (2017) Rational design of triple-bridged dinuclear  $\text{Zn}^{\text{II}}\text{Ln}^{\text{III}}$ -based complexes: a structural, magnetic and luminescence study. *CrystEngComm* 19:256–264
120. Oyarzabal I, Artetxe B, Rodríguez-Diéguez A, García JA, Seco JM, Colacio E (2016) A family of acetato-diphenoxo triply bridged dimetallic  $\text{Zn}^{\text{II}}\text{Ln}^{\text{III}}$  complexes: SMM behavior and luminescent properties. *Dalton Trans* 45:9712
121. Xie Q-W, Wu S-Q, Shi W-B, Liu C-M, Cui AL, Kou H-Z (2014) Heterodinuclear  $\text{M}^{\text{II}}-\text{Ln}^{\text{III}}$  single molecule magnets constructed from exchange-coupled single ion magnets. *Dalton Trans* 43:11309–11316
122. Bender M, Comba P, Demeshko S, Großhauser M, Müller D, Wadepohl H (2015) Theoretically predicted and experimentally observed relaxation pathways of two heterodinuclear 3d-4f complexes. *Z Anorg Allg Chem* 641(12–13):2291–2299
123. Comba P, Enders M, Großhauser M, Hiller M, Müller D, Wadepohl H (2017) Solution and solid state structures and magnetism of a series of linear trinuclear compounds with a hexacoordinate  $\text{Ln}^{\text{III}}$  and two terminal  $\text{Ni}^{\text{II}}$  centers. *Dalton Trans* 46:138–149
124. Oyarzabal I, Ruiz J, Seco JM, Evangelisti M, Camón A, Ruiz E, Aravena D, Colacio E (2014) Rational electrostatic design of easy-axis magnetic anisotropy in a  $\text{Zn}^{\text{II}}\text{-Dy}^{\text{III}}\text{-Zn}^{\text{II}}$  single-molecule magnet with a high energy barrier. *Chem Eur J* 20:14262–14269
125. Oyarzabal I, Ruiz J, Ruiz E, Aravena D, Seco JM, Colacio E (2015) Increasing the effective energy barrier promoted by the change of a counteranion in a  $\text{Zn-Dy-Zn}$  SMM: slow relaxation via the second excited state. *Chem Commun* 51:12353–12356
126. Oyarzabal I, Rodríguez-Diéguez A, Barquín M, Seco JM, Colacio E (2017) The effect of the disposition of coordinated oxygen atoms on the magnitude of the energy barrier for magnetization reversal in a family of linear trinuclear  $\text{Zn-Dy-Zn}$  complexes with a square-antiprism  $\text{DyO}_8$  coordination sphere. *Dalton Trans* 46:4278–4286
127. Upadhyay A, Singh SK, Das C, Mondol R, Langley SK, Murray KS, Rajaraman G, Shanmugam M (2014) Enhancing the effective energy barrier of a  $\text{Dy}(\text{III})$  SMM using a bridged diamagnetic  $\text{Zn}(\text{II})$  ion. *Chem Commun* 50:8838–8841
128. Liu J-L, Chen Y-C, Zheng Y-Z, Lin W-Q, Ungur L, Wernsdorfer W, Chibotaru LF, Tong M-L (2013) Switching the anisotropy barrier of a single-ion magnet by symmetry change from quasi- $\text{D}_{5h}$  to quasi-Oh. *Chem Sci* 4:3310–3316
129. Titos-Padilla S, Ruiz J, Herrera JM, Brechin EK, Wernsdorfer W, Lloret F, Colacio E (2013) Dilution-triggered SMM behavior under zero field in a luminescent  $\text{Zn}_2\text{Dy}_2$  tetranuclear complex incorporating carbonato-bridging ligands derived from atmospheric  $\text{CO}_2$  fixation. *Inorg Chem* 52:9620–9626
130. Watanabe A, Yamashita A, Nakano M, Yamamura T, Kajiura T (2011) Multi-path magnetic relaxation of mono-dysprosium(III) single-molecule magnet with extremely high barrier. *Chem Eur J* 17:7428–7432
131. Ungur L, Chibotaru LF (2015) Computational modeling of magnetic properties of lanthanide compounds. In: Layfield RA, Murugesu M (eds) *Lanthanides and actinides in molecular magnetism*. Wiley-VCH, Weinheim, pp 153–184

132. Aquilante F, Autschbach J, Carlson RK, Chibotaru LF, Delcey MG, De Vico L, Fdez Galván I, Ferré N, Frutos LM, Gagliardi L, Garavelli M, Giussani A, Hoyer CE, Li Manni G, Lischka H, Ma D, Malmqvist PÅ, Müller T, Nenov A, Olivucci M, Pedersen TB, Peng D, Plasser F, Pritchard B, Reiher M, Rivalta I, Schapiro I, Segarra-Martí J, Stenrup M, Truhlar DG, Ungur L, Valentini A, Vancoillie S, Veryazov V, Vysotskiy VP, Weingart O, Zapata F, Lindh R (2016) Molcas 8: new capabilities for multiconfigurational quantum chemical calculations across the periodic table. *J Comput Chem* 37:506–541
133. Aquilante F, De Vico L, Ferre N, Ghigo G, Malmqvist PA, Neogrady P, Pedersen TB, Pitonak M, Reiher M, Roos BO, Serrano-Andres L, Urban M, Veryazov V, Lindh R (2010) MOLCAS 7: the next generation. *J Comput Chem* 31:224–247
134. Duncan JA (2009) MOLCAS 7.2. *J Am Chem Soc* 131:2416–2416
135. Veryazov V, Widmark PO, Serrano-Andres L, Lindh R, Roos BO (2004) 2MOLCAS as a development platform for quantum chemistry software. *Int J Quantum Chem* 100:626–635
136. Karlstrom G, Lindh R, Malmqvist PA, Roos BO, Ryde U, Veryazov V, Widmark PO, Cossi M, Schimmelpfennig B, Neogrady P, Seijo L (2003) MOLCAS: a program package for computational chemistry. *Comput Mater Sci* 28:222–239
137. Guo Y-N, Ungur L, Granroth GE, Powell AK, Wu C, Nagler SE, Tang J, Chibotaru LF, Cui D (2014) An NCN-pincer ligand dysprosium single-ion magnet showing magnetic relaxation via the second excited state. *Sci Rep* 4:5471
138. Singh SK, Gupta T, Shanmugam M, Rajaraman G (2014) Unprecedented magnetic relaxation via the fourth excited state in low-coordinate lanthanide single-ion magnets: a theoretical perspective. *Chem Commun* 50:15513–15516
139. Abtab SMT, Maity M, Bhattacharya K, Carolina Sañudo E, Chaudhury M (2012) Syntheses, structures, and magnetic properties of a family of tetranuclear hydroxido-bridged  $\text{Ni}^{\text{II}}_2\text{Ln}^{\text{III}}_2$  (Ln = La, Gd, Tb, and Dy) complexes: display of slow magnetic relaxation by the zinc(II) – dysprosium(III) analogue. *Inorg Chem* 51:10211–10221
140. Abtab SMT, Majee MC, Maity M, Titiš J, Boča R, Chaudhury M (2014) Tetranuclear heterometal  $[\text{Co}^{\text{II}}_2\text{Ln}^{\text{III}}_2]$  (Ln = Gd, Tb, Dy, Ho, La) complexes involving carboxylato bridges in a rare  $\mu_4 - \eta_2:\eta_2$  mode: synthesis, crystal structures, and magnetic properties. *Inorg Chem* 53:1295–1306
141. Ruiz J, Lorusso G, Evangelisti M, Brechin EK, Pope SJ, Colacio E (2014) Closely-related Zn(II) $2\text{Ln}(\text{III})_2$  complexes (Ln(III) = Gd, Yb) with either magnetic refrigerant or luminescent single-molecule magnet properties. *Inorg Chem* 53:3586–3594
142. Maity M, Majee MC, Kundu S, Samanta SK, Carolina Sañudo E, Ghosh S, Chaudhury M (2015) Pentanuclear 3d–4f heterometal complexes of  $\text{M}^{\text{II}}_3\text{Ln}^{\text{III}}_2$  (M = Ni, Cu, Zn and Ln = Nd, Gd, Tb) combinations: syntheses, structures, magnetism, and photoluminescence properties. *Inorg Chem* 54:9715–9726
143. Goura J, Rogez G, Rivière E, Chandrasekhar V (2014) Hexanuclear, heterometallic,  $\text{Ni}_3\text{Ln}_3$  complexes possessing O-capped homo- and heterometallic structural subunits: SMM behavior of the dysprosium analogue. *Inorg Chem* 53:7815–7823
144. Goura J, Chakraborty A, Walsh JPS, Tuna F, Chandrasekhar V (2015) Hexanuclear 3d–4f neutral  $\text{Co}^{\text{II}}_2\text{Ln}^{\text{III}}_4$  clusters: synthesis, structure, and magnetism. *Cryst Growth Des* 15:3157–3165
145. Colacio E, Ruiz J, Ruiz E, Cremades E, Krzystek J, Carretta S, Cano J, Guidi T, Wernsdorfer W, Brechin EK (2013) Slow magnetic relaxation in a Co(II)–Y(III) single-ion magnet with positive axial zero-field splitting. *Angew Chem Int Ed* 52:9130–9134
146. Palacios MA, Nehrkorn J, Suturina E, Ruiz E, Gómez-Coca S, Holldack K, Schnegg A, Krzystek J, Moreno JM, Colacio E (2017) Analysis of magnetic anisotropy and the role of magnetic dilution in triggering single-molecule magnet (SMM) behavior in a family of  $\text{Co}^{\text{II}}\text{Y}^{\text{III}}$  dinuclear complexes with easy-plane anisotropy. *Chemistry* 23:11649–11661

147. Palacios MA, Mota AJ, Ruiz J, Hänninen MM, Sillanpää R, Colacio E (2012) Diphenoxo-bridged  $\text{Ni}^{\text{II}}\text{Ln}^{\text{III}}$  dinuclear complexes as platforms for heterotrimetallic  $(\text{Ln}^{\text{III}}\text{Ni}^{\text{II}})_2\text{Ru}^{\text{III}}$  systems with a high-magnetic-moment ground state: synthesis, structure, and magnetic properties. *Inorg Chem* 51:7010–7012

# Tetrathiafulvalene-Based Magnets of Lanthanides



Olivier Cador and Fabrice Pointillart

## Contents

1	Introduction .....	164
2	Preamble .....	165
3	Mononuclear TTF-Dy(III) SMMs: The N <sub>2</sub> O <sub>6</sub> Saga .....	166
4	A Journey in TTF-Ln SMMs .....	173
4.1	Nitrogen-Based Donor-Acceptor Type Dyads .....	173
5	Oxygen-Based TTF-Based Ligands .....	176
6	Polynuclear TTF-Dy(III) SMMs .....	179
7	Conclusions .....	184
	References .....	185

**Abstract** Tetrathiafulvalene (TTF)-based ligands and lanthanide ions have been intensively used for their electronic conductivity and optical properties, respectively. Their combination leads to a new class of coordination compounds that are able to display single-molecule magnet (SMM) behavior. Magnetic bistability resulting of such behavior could find potential applications in high-density data storage and quantum computing. In this chapter, a library of TTF-based magnets containing lanthanide ions is presented. Among this series, the influence of the coordination sphere and intra- and intermolecular interactions such as exchange, dipolar, supra-molecular, and hyperfine interactions is probed through molecular engineering, magnetic dilutions, and isotopic enrichment.

**Keywords** Ab initio calculations · Coordination sphere · Hyperfine interaction · Lanthanide · Single-molecule magnets · Tetrathiafulvalene

---

O. Cador (✉) and F. Pointillart  
Institut des Sciences Chimiques de Rennes, UMR 6226 CNRS-Université de Rennes 1, Rennes,  
Cedex, France  
e-mail: [olivier.cador@univ-rennes1.fr](mailto:olivier.cador@univ-rennes1.fr)

## 1 Introduction

Magnets have been discovered about four millennia ago in ancient Greece. Nowadays, in 2015, permanent magnets market is valued to 15 billion € and is expected to grow according to the demands for medical and industrial devices. In this market, the segment occupied by the badly named rare-earth<sup>1</sup>-based magnets continues to expand owing to superior properties (such as saturation magnetization).

In the 1990s, a new class of magnets emerged in the scientific community with the discovery of the single-molecule magnets (SMMs) [1]. In these magnets, the magnetic memory is stored by the magnetic moment of a single molecule constituted of 12 manganese ions. This scientific finding reduced the size of a storage unit (byte) to nanometer. At the same time, the storage capacity of hard disks based on molecules would increase drastically. The drawback is the operating temperature range, below liquid helium ( $-269^{\circ}\text{C}$ ). In the last three decades, the quest for better SMMs never really stopped. In 2003, Ishikawa et al. [2] discovered that a single lanthanide ion ( $\text{Ln} = \text{Tb}^{\text{III}}$ ) embedded in a double-decker complex behaved as a SMM. To date, the lanthanide series is the most productive SMMs line in Mendeleev's periodic table with a recent tremendous record of closure of the magnetic hysteresis loop at 60 K [3, 4], close to liquid nitrogen.

Tetrathiafulvalene (TTF) and its analogues are well known in the field of molecular materials to produce organic metals, semiconductors, and superconductors [5, 6]. The functionalization of the electron donor TTF core by an acceptor moiety contributed to the development of functional materials such as switches, sensors, photovoltaic cells, and nonlinear optical systems [7–9]. It was then logical to adapt the acceptor moiety to coordinate transition metals for (1) elaboration of multifunctional materials with both paramagnetism and electrical conductivity [10, 11] and (2) the synthesis of polynuclear transition metal complexes exhibiting SMM properties embedded in a conducting material [12–16]. One must admit that all tentative proposals were not very successful except Oshio's work [17] which shows SMM behavior but without conductivity.

The first TTF-Ln system was reported by Faulkner et al. [18] with the assembly in solution of tetrathiafulvalene carboxylic acid and ytterbium. In 2003 [19], the first structurally characterized TTF-Ln system in the solid state was reported. There was no chemical bond between the lanthanide ion and the TTF moiety, so the chemical approach is the so-called through space. We have published almost 10 years ago the first isolated TTF-Ln coordination complex [20] based on the spin-only Gd(III) ion, which, of course, does not behave as a SMM. Since 2009, several groups [21–24], including us [25], have paid much attention to TTF-Ln systems with the objectives to combine conductivity (electrical transport), magnetism (magnetic memory), and luminescence (light emitter) in a single chemical object. In this frame, the TTF moiety turns out to be a powerful sensitizer of the NIR luminescence of

---

<sup>1</sup>Most of the rare earths are not rare: cerium is more abundant than copper on earth, and thulium (the most rare) is more abundant than silver.

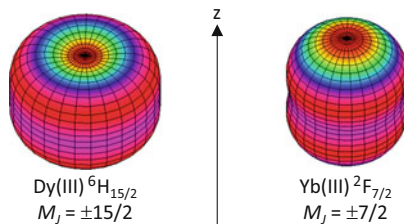
lanthanides [26]. Nevertheless and despite colossal efforts of the scientific community, electrical conductivity has never been observed in TTF-Ln systems. One could say that the necessary oxidation (partial) of the TTF moiety to promote electronic transport does not preserve the chemical integrity of the complex (dissociation) except when both TTF core and coordinating moiety are not fused [27]. Despite several attempts, there is no SMM based on TTF and strongly anisotropic 3-D transition metals such as Co(II) and Ni(II) [12, 13, 28, 29]. But TTF performed in the field of SMMs with plethora of mononuclear and polynuclear complexes which possess a magnetic memory in the absence and, in less extent, in the presence of an external constant magnetic field. Since highly anisotropic magnetic moments are necessary, Dy(III) and Tb(III) are the ideal candidates [30–37]. These two ions represent almost 99% of reported Ln-based SMMs [38] with a preponderant role played by Dy(III)-based systems.

## 2 Preamble

Naturally, researchers have at first focused their attention on the synthesis of mononuclear TTF-Dy complexes. Like most of the time, the first attempt was not very successful [39]. The reaction of two equivalents of tetrathiafulvalene-amido-2-pyridine-*N*-oxide with  $[\text{Dy}(\text{hfac})_3] \cdot 2\text{H}_2\text{O}$  ( $\text{hfac}^-$ : 1,1,1,5,5,5-hexafluoroacetylacetonate anion) precursor produced mononuclear species in which Dy(III) is surrounded by eight oxygen atoms: two from pyridine-*N*-oxide moieties and six from three bidentates  $\text{hfac}^-$ . This fully oxygenated environment adopts a coordination polyhedron close to square antiprism (SAP)  $D_{4d}$  with  $\text{CShM} = 0.528$  [40]. The material does not show any out-of-phase component of the AC susceptibility in zero external dc field down to 2 K below oscillating field frequencies of 1 kHz. In other words, it is not a magnet. Probably, the charge distribution around the Dy(III) center does not match the axiality required by the simple but chemically implementable precepts exposed by Rinehart et al. [41]. Performant magnets are obtained when the largest  $M_J$  states are stabilized for a given multiplet ground state ( $M_J = \pm 15/2$  for Dy(III)). The analysis of the electron density distribution provides a simple tool to anticipate what might be the ground state in a given environment [42]. The charge density distribution of the Ising component (the largest  $M_J$  values) of the multiplet ground state of the oblate Dy(III) is represented on Fig. 1. The electrons are principally located in a plane ( $xy$ ), so the disposition of negatively charged ligands in the  $z$  direction will stabilize this Kramers state. It is the opposite for the prolate Yb(III) for which the negative charges must lie in the  $xy$  plane. This textbook analysis guided the synthesis of the most efficient SMM reported so far [3, 4]. Additionally, advanced quantum calculations have demonstrated that such approach might provide high-temperature SMMs (if chemically accessible) [43, 44].



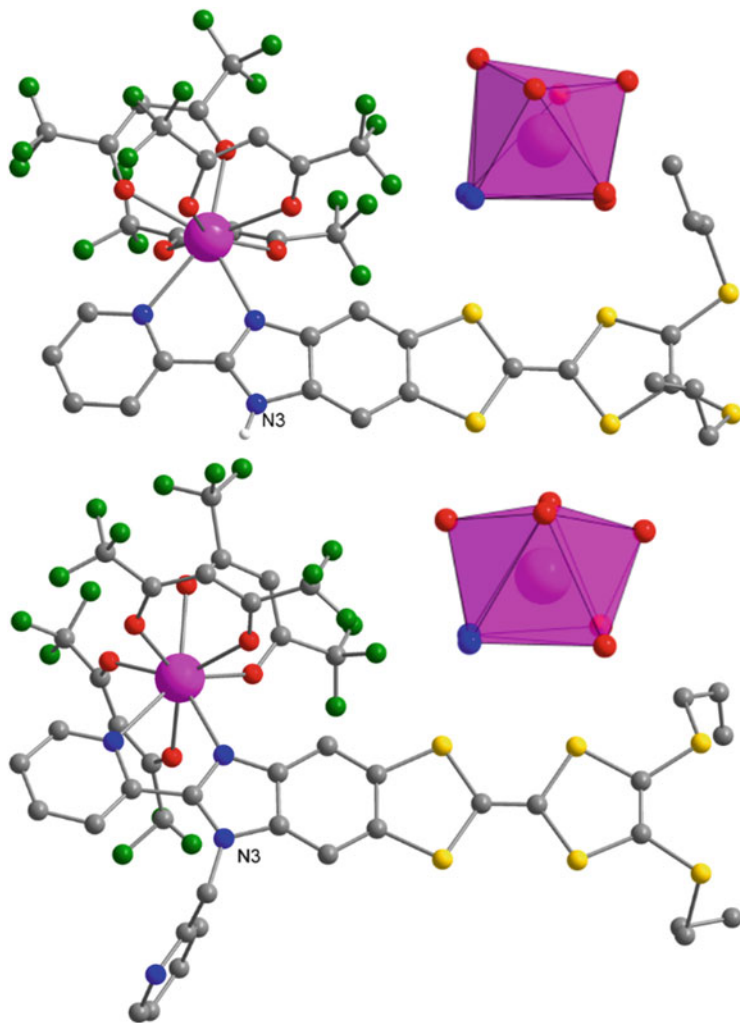
**Fig. 1** Angular dependences of the total  $4f$  charge density for largest  $M_J$  states of the multiplet ground state for Dy(III) and Yb(III)



### 3 Mononuclear TTF-Dy(III) SMMs: The $N_2O_6$ Saga

We have sought, at first, for neutral complexes to crystallize with bidentate TTF-based ligands in order to (1) stabilize the complexes and (2) minimize the degrees of freedom of the coordination sphere. The use of three negatively charged acetylacetonate ( $-1$ ) ancillary ligands counterbalances the charge  $+3$  of the lanthanide ions and insures complex neutrality. To complete the coordination sphere, TTF-based ligands with nitrogen-coordinating sites have been designed to desymmetrize the ligand field (preamble). The first two complexes synthesized with this approach are  $[Dy(hfac)_3L^1]$  and  $[Dy(hfac)_3L^2]$  (with  $L^1 = 2\text{-}\{4,5\text{-}[4,5\text{-bis}(\text{propylthio})\text{-tetrathiafulvalenyl}]\text{-1H-benzimidazol-2-yl}\}$ pyridine and  $L^2 = 2\text{-}\{1\text{-methylpyridyl-4,5-}[4,5\text{-bis}(\text{propylthio})\text{tetra-thiafulvalenyl}]\text{-1H-benzimidazol-2-yl}\}$ pyridine) [45] (Fig. 2). Except the obvious chemical difference at N3 (alkylation), the analysis of the crystallographic structure revealed the presence of intermolecular hydrogen bond at N3 site in  $[Dy(hfac)_3L^1]$ . Such intermolecular connection does not exist in  $[Dy(hfac)_3L^2]$ , and it has a dramatic consequence on the coordination polyhedra. Indeed, the polyhedron is strongly distorted in  $[Dy(hfac)_3L^1]$  with respect to the one in  $[Dy(hfac)_3L^2]$  (Fig. 2). As a consequence, the magnetic properties of these two, apparently similar, complexes differ. In zero external dc field,  $[Dy(hfac)_3L^2]$  behaves as a SMM with the apparition of a frequency-dependent out-of-phase component of the ac susceptibility. Such signal is absent for  $[Dy(hfac)_3L^1]$  which is not a SMM, as far as the crystalline condensed phase is concerned. The hydrogen-bonding network plays a crucial role in the modification of this behavior. Magnetic measurements in solution reveal the true nature of the complexes. Of course, one must be sure that the complexes are stable in solution. They both behave the same, as molecular magnets. This proves two important characteristics: (1) the behavior of SMM can be preserved in solution. This is an important issue since one may say that the observed behavior is truly of molecular origin and then the molecular magnet can be manipulated. (2) The destruction of the intermolecular network by dissolution restores the molecular property. The absence of SMM behavior in crystalline condensed phase must be taken carefully, and the impact of the crystal packing must be analyzed prior any hasty conclusion.

The ground multiplet ground state  ${}^6H_{15/2}$  of Dy(III) splits under the effect of crystal field in several sublevel characterized by pure  $M_J$  levels or a mixture of  $M_J$  levels depending on the symmetry of the ligand field. In this frame, the effective  $1/2$



**Fig. 2** Representation of the complexes  $[\text{Dy}(\text{hfac})_3\text{L}^1]$  (top) and  $[\text{Dy}(\text{hfac})_3\text{L}^2]$  (bottom) with the alkylated nitrogen atom N3. Coordination polyhedra are also represented

is often used to describe these Kramers sublevels. Then, the Kramers ground state possesses an effective spin  $1/2$  with an effective  $\mathbf{g}$ -tensor in the reference frame of the complex. It is not difficult to show that for the two Ising components  $M_J = \pm 15/2$  of the  ${}^6\text{H}_{15/2}$  multiplet the  $\mathbf{g}$ -tensor is characterized by  $g_x = g_y = 0$  and  $g_z = 20$  with  $z$  the axis of projection. Experimentally, the orientation and the amplitude of the  $\mathbf{g}$ -tensor are available under certain conditions: the complex must crystallize in the triclinic system with only one Dy(III) crystallographic site. Measurements of the magnetization on an oriented single crystal in three perpendicular planes as a function of the angle ( $\theta$ ) between the magnetic field ( $H$ ) with the axes of the single

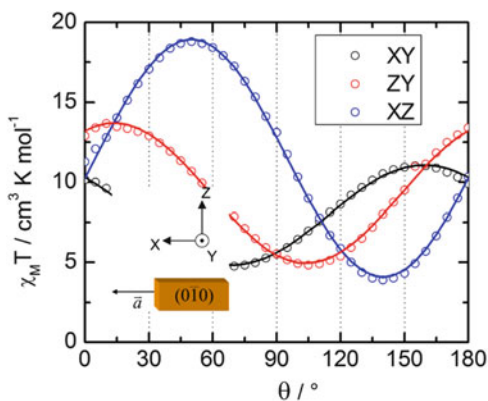
crystal allow the determination without ambiguity of the  $\mathbf{g}$ -tensor. The magnetic susceptibility in a plane can be fitted with the following equation:

$$\chi_M T = \frac{MT}{H} = \chi_{\alpha\alpha} T \cos^2 \theta + \chi_{\beta\beta} T \sin^2 \theta + 2\chi_{\alpha\beta} T \sin \theta \cos \theta$$

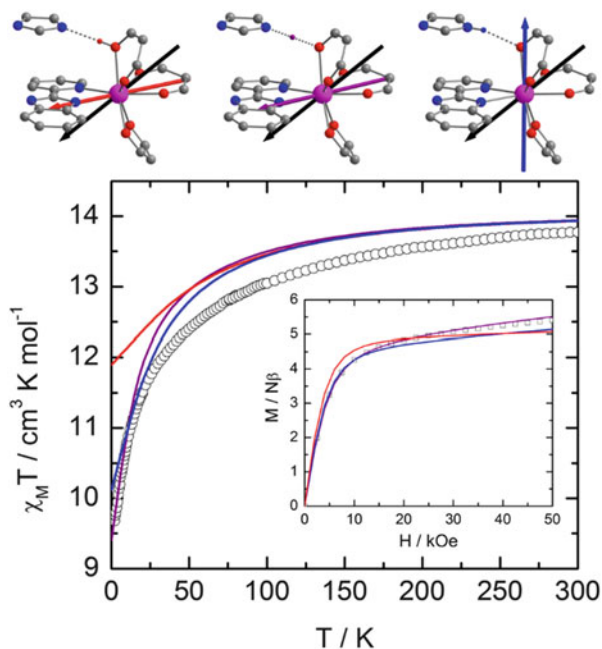
where  $\alpha$  and  $\beta$  are the directions  $X$ ,  $Y$ , and  $Z$  of the crystal reference frame in a circular permutation (Fig. 3) and  $\chi_M$  and  $T$  are, respectively, the molar magnetic susceptibility and the temperature expressed in Kelvin.

In the effective spin-1/2 frame, the principal values of  $\mathbf{g}$ -tensor are  $g_z = 14.22$ ,  $g_y = 3.96$ , and  $g_x = 9.43$ . These values are far away from those expected for a purely axial system and explain why  $[\text{Dy}(\text{hfac})_3\text{L}^1]$  is not a SMM in the condensed crystalline phase. The orientation of the  $g_z$  is represented on Fig. 4 with a black arrow. In the present case, in order to simulate physical properties such as magnetism, the neighboring molecules need to be explicitly integrated. The calculated orientation of the most magnetic axis is also represented on Fig. 4. Clearly, calculations with N–H bond fail to reproduce the orientation of the magnetic poles as well as the standards  $\chi_M T$  vs.  $T$  and  $M$  vs.  $H$  plots (Fig. 4 top right,  $M$  the magnetization expressed in Bohr magneton per mole) [46]. One can notice however that in this chemical configuration, the magnetic moment of a Dy(III) ion resides in a direction passing through the most negatively charged direction (two  $\text{hfac}^-$  anions) and perpendicular to the plane defined with the less electronegative nitrogen atoms from imidazole and pyridine moieties, in agreement with basic electrostatic considerations. The hydrogen atom must be positioned between two heteroatoms: the nitrogen N3 of imidazole of one complex and one oxygen atom of one  $\text{hfac}^-$  moiety of a neighboring complex. In other words, in the crystal, the N–H bond disappeared with a hydrogen atom, in average, localized at an intermediate position between the two atoms. Nevertheless, the calculated orientation is still at  $30^\circ$  of the experimental one and that dynamical effects should also probably be included to properly account for the experience.

**Fig. 3** Angular dependence of  $\chi_M T$  measured at 2 K for  $[\text{Dy}(\text{hfac})_3\text{L}^1]$  with a 1 kOe magnetic field in three perpendicular planes ( $XY$ ,  $ZY$ , and  $XZ$ ). In inset a schematic representation of a single crystal of  $[\text{Dy}(\text{hfac})_3\text{L}^1]$  with crystallographic axes in the frame of the single crystal



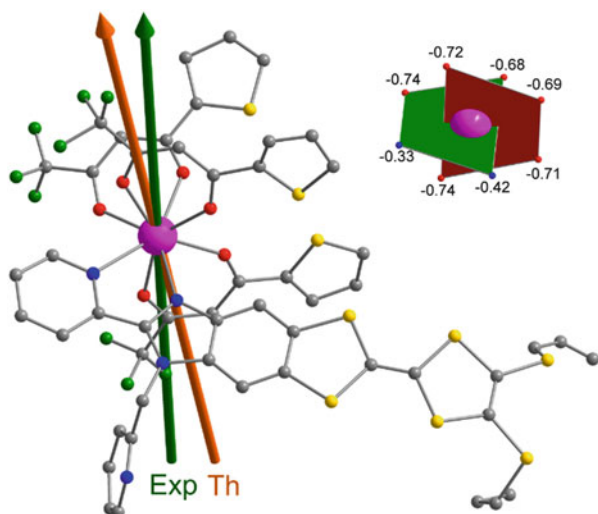
**Fig. 4** (Top) orientations of the experimental  $z$  magnetic axis represented in black for  $[\text{Dy}(\text{hfac})_3\text{L}^1]$  with the calculated orientation for different positions of the hydrogen atom (O–H in red, N–H in blue, and middle in purple). (Bottom) thermal variations of the experimental (white symbols) and calculated (full-colored lines)  $\chi_M T$  within the inset of the experimental and calculated field variation of the magnetization at 2 K



At this stage  $\text{L}^2$  seems to be a good starting point, but the use of  $\text{hfac}^-$  produces a SMM with relatively low efficiency. Indeed, the energy necessary to reverse the magnetic moment is less than 20 K (the barrier) and a temperature-independent relaxation process (quantum tunneling of the magnetization) of the order of 100  $\mu\text{s}$ . In order to improve the SMM in keeping this topology, one possibility is to play with the ancillary ligand. Thiophene groups are less electroattractive than  $\text{CF}_3$ , and then the substitution of one  $\text{CF}_3$  by one thiophene should increase the negative charges on coordinated oxygen atoms.

The magnetic properties of  $[\text{Dy}(\text{tta})_3\text{L}^2]$  ( $\text{tta}^-$ : 2-thenoyltrifluoroacetate) have been studied in the crystalline condensed phase and in frozen solution [47]. Qualitatively, the magnetism corresponds to  $[\text{Dy}(\text{hfac})_3\text{L}^2]$ : it is a SMM in solid state and in solution. Quantitatively, the energy barrier has been multiplied by a factor two and validates our approach. Ab initio calculations showed that the negative charges carried by oxygen atoms are larger, in amplitude, than for  $[\text{Dy}(\text{hfac})_3\text{L}^2]$  ( $-0.71$  vs.  $-0.68$  in average) according to electrostatic considerations [46, 47]. Interestingly, SHAPE analyses [40] on  $[\text{Dy}(\text{tta})_3\text{L}^2]$  and  $[\text{Dy}(\text{hfac})_3\text{L}^2]$  reveal nearly the same distortions. In both structures, Dy(III) resides in SAP environment with  $\text{CShM} = 0.538$  and  $0.597$ , respectively. Angular-resolved magnetometry measurements show that the anisotropy axis (the easy magnetization axis) is parallel to the most negatively charged direction (Fig. 5). This experimental finding is supported by ab initio calculations with a gap between the calculated and the experimental easy axis of only  $7.6^\circ$ . Furthermore, the calculated  $g_z$  (19.5) is very close to the Ising limit. The examination of the temperature dependence of the relaxation time of the

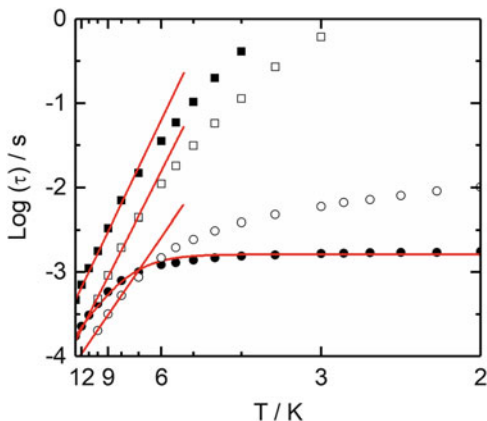
**Fig. 5** Representation of the molecule  $[\text{Dy}(\text{tta})_3\text{L}^2]$  avec and the calculated (orange) and experimental (green) magnetic axes. Insert: scheme of the coordination sphere of Dy (III) ion with the calculated charges of the coordinated atoms



magnetic moment reveals the presence of a thermally activated regime at a high temperature, while the system enters a thermally independent regime below 6 K (Fig. 6). It can be reproduced with a combination of the Orbach [48] (over the barrier) and tunneling (through the barrier) processes:  $\tau^{-1} = \tau_0^{-1} \exp(\Delta/T) + \tau_{\text{TI}}^{-1}$  with  $\Delta=42$  K,  $\tau_0 = 8 \times 10^{-6}$  s, and  $\tau_{\text{TI}} = 1.62 \times 10^{-3}$  s. Dy(III) is a Kramers ion, and the magnetic moment should not be able to tunnel through the barrier: the two Ising components cannot be mixed by modulation of the crystal field. The application of a moderate external dc field (1 kOe) destroys this relaxation path, and the system falls in a pure thermally activated regime with nearly the same activation energy. Additional perturbations must affect the Kramers ground state in zero external dc field to allow the system to oscillate between the “up” and “down” states. In the condensed crystalline state, the molecules are closely packed, and interactions of dipolar origin may propagate through space. This is especially true when someone deals with heavy lanthanides which possess the largest magnetic moments of the periodic table. Transverse component of this internal field can mix the Kramers doublets and facilitate the tunneling. The dilution of the complex in a diamagnetic medium (at low concentration) minimizes this internal field and is supposed to suppress the tunneling. However, one can see on Fig. 6 that dissolution in dichloromethane is not enough: leveling of the relaxation time still persists at low temperature. Compared to the application of an external dc field of 1 kOe, which completely lifts the degeneracy of the ground state and destroys the tunneling effect (Fig. 6), in solution, the relaxation time remains rapid (about 100 times faster). The consequence is that, even in solution, the hysteresis loop remains closed in zero field while it is opened up in field (butterfly-shaped hysteresis) at any temperatures above 500 mK [47].

Then, if the closure of the hysteresis loop at the origin does not arise from intermolecular considerations, it might come from inside the complex. Dysprosium

**Fig. 6** Log-scale representation of the thermal variation of the relaxation time of  $[\text{Dy}(\text{tta})_3\text{L}^2]$  in solid state (full symbols) and in solution (empty symbols), in zero external dc field (circles) and under 1 kOe external dc field (squares). Solid red lines correspond to the best fitted curves with a modified Arrhenius law at zero field and a Arrhenius law in field

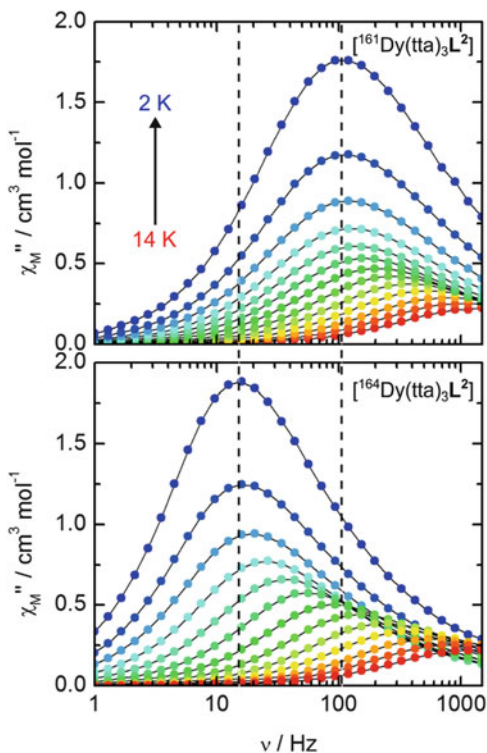


is one of the elements in the periodic which consists of different and stable isotopes ( $^{161}\text{Dy}$ ,  $^{162}\text{Dy}$ ,  $^{163}\text{Dy}$ , and  $^{164}\text{Dy}$ ) in quasi-equivalent natural abundance. Two of them, with an even mass number, possess a nuclear spin ( $I = 0$ ), and the two others have a nuclear spin  $I = 5/2$ . We have then decided to study the influence of this nuclear spin on the relaxation of the electronic magnetic moment [49] coupled with magnetic dilution. Hyperfine interactions and dilution are known to affect the relaxation of the magnetic moments [50–52]. Clearly, metal-centered isotopic enrichment modifies the relaxation rate in the quantum regime (Fig. 7).

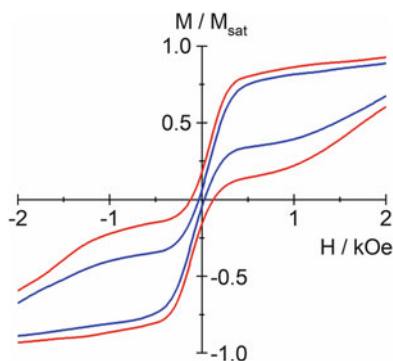
Below 6 K when the system enters in the quantum regime, the relaxation time of the magnetic moment is ten times slower for the isotopically enriched complex  $[\text{Dy}(\text{tta})_3\text{L}^2]$  ( $I = 0$ ) than for the isotopically enriched complex  $[\text{Dy}(\text{tta})_3\text{L}^2]$  ( $I = 5/2$ ). This is true in zero external dc field in the condensed crystalline phase but also when the enriched complex is diluted in a diamagnetic isomorphous crystalline matrix ( $[\text{Dy}_{0.04}\text{Y}_{0.96}(\text{tta})_3\text{L}^2] \cdot \text{C}_6\text{H}_{14}$  vs.  $[\text{Dy}_{0.03}\text{Y}_{0.97}(\text{tta})_3\text{L}^2] \cdot \text{C}_6\text{H}_{14}$ ). The dramatic difference is that the dilution in a diamagnetic medium of these isotopically enriched complexes slows the relaxation enough to observe the opening of the hysteresis loop at the origin for the  $^{164}\text{Dy}$  derivative and not for the  $^{161}\text{Dy}$  derivative. At this stage we proved that isotopes chemistry drives some electronic properties. Nevertheless, one must keep in mind that the hysteresis (the memory) in the absence of an external stimulus shows up only when the molecules are far away from each other. Thus, the deposition of juxtaposed SMMs on surfaces can lead to unexpected results because they will behave, in a certain manner, collectively and not individually (Fig. 8).

In addition, we recently investigated the magnetism of the last two stable enriched complexes  $[\text{Dy}(\text{tta})_3\text{L}^2]$  and  $[\text{Dy}(\text{tta})_3\text{L}^2]$  [53].  $[\text{Dy}(\text{tta})_3\text{L}^2]$  is the copy paste of  $[\text{Dy}(\text{tta})_3\text{L}^2]$  because the nuclear spin of Dy(III) is zero in both cases. The nuclear spins of  $^{163}\text{Dy}$  and  $^{161}\text{Dy}$  are indeed equal ( $I = 5/2$ ), but the hyperfine coupling constant  $A_{\text{HF}}$  differs [54, 55] and then the relaxation rate affected. This is perceptible in condensed crystalline phase with  $[\text{Dy}(\text{tta})_3\text{L}^2]$

**Fig. 7** Frequency dependences of  $\chi_M''$  of  $[^{164}\text{Dy}(\text{tta})_3\text{L}^2]$  and  $[^{161}\text{Dy}(\text{tta})_3\text{L}^2]$  in zero field in the temperature range 2–14 K



**Fig. 8** Normalized magnetic hysteresis loops measured at 460 mK for  $[^{164}\text{Dy}_{0.04}\text{Y}_{0.96}(\text{tta})_3\text{L}^2] \cdot \text{C}_6\text{H}_{14}$  (red line) and  $[^{161}\text{Dy}_{0.03}\text{Y}_{0.97}(\text{tta})_3\text{L}^2] \cdot \text{C}_6\text{H}_{14}$  (blue line)



slightly faster than  $[^{161}\text{Dy}(\text{tta})_3\text{L}^2]$ , but at this stage, the relaxation is essentially driven by intermolecular interactions. Once diluted,  $[^{161}\text{Dy}_{0.05}\text{Y}_{0.95}(\text{tta})_3\text{L}^2] \cdot \text{C}_6\text{H}_{14}$  is about ten times slower than  $[^{163}\text{Dy}_{0.05}\text{Y}_{0.95}(\text{tta})_3\text{L}^2] \cdot \text{C}_6\text{H}_{14}$ . Sign and/or amplitude of the hyperfine coupling seem to play also a fundamental role on the relaxation in quantum regime.



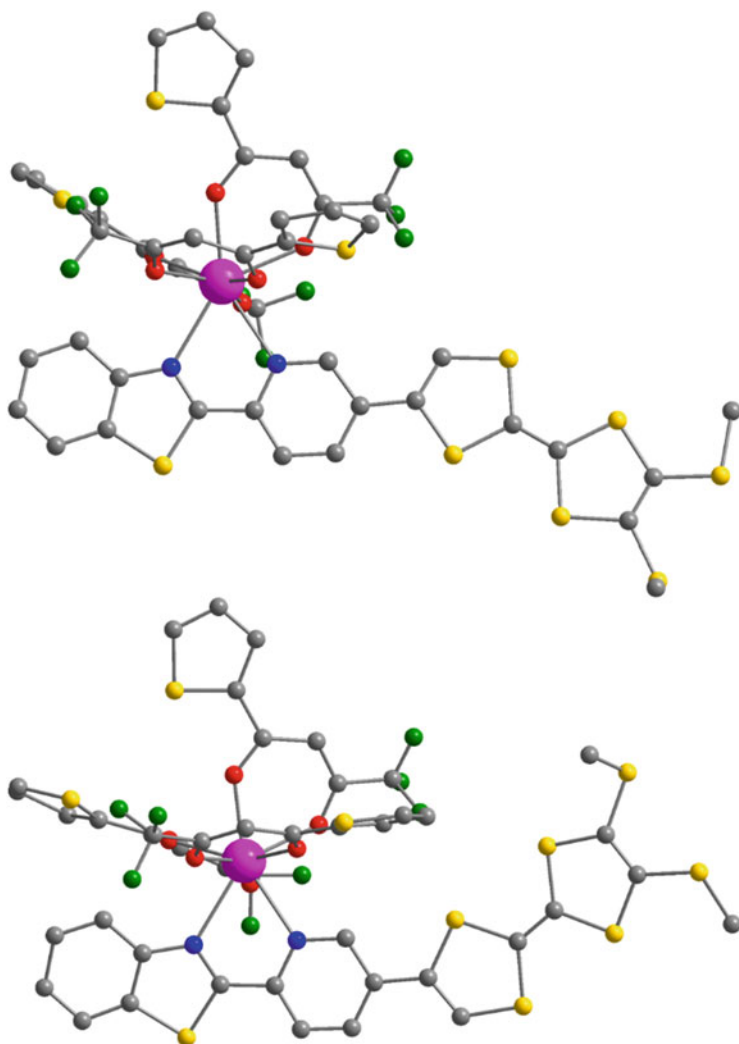
## 4 A Journey in TTF-Ln SMMs

There are additional TTF-Dy(III) [N<sub>2</sub>O<sub>6</sub>] mononuclear complexes which behave as SMMs in the literature. Also, higher coordination number, typically N<sub>3</sub>O<sub>6</sub>, has been envisaged with less success. Environment such as O<sub>8</sub> for which the charge distribution is more symmetric has also been investigated. Some of these complexes are *stricto sensu* (chemically) mononuclear complexes, but some of them are polynuclear complexes but in which the distances between metallic centers are so large that we can consider they are mononuclear from a magnetic point of view. In other words, there are no interactions between those centers. Such complexes might be described as an assembly of mononuclear SMMs.

### 4.1 Nitrogen-Based Donor-Acceptor Type Dyads

The first example we want to introduce is based on a similar TTF ligand with a benzothiazole group. The ligand **L**<sup>3</sup> (**L**<sup>3</sup> = 4-[6-(1,3-benzothiazol-2-yl)pyridin-3-yl]-4',5'-bis(methyl-thio)tetrathiafulvene) is similar to **L**<sup>1</sup> with however no possible intermolecular hydrogen bond [56]. Such benzothiazole group might also be of interest to realize photoswitchable conductors and photoelectric conversion materials [57]. Reaction of **L**<sup>3</sup> with [Ln(tta)<sub>3</sub>]·2H<sub>2</sub>O gives [Ln(tta)<sub>3</sub>**L**<sup>3</sup>] complex which crystallize in the P-1 triclinic space group for light elements and in the P2<sub>1</sub>/a monoclinic space group for heavy elements. For intermediate Dy(III), the two polymorphs can be obtained. Like in the previous section, Dy(III) ion is in a N<sub>2</sub>O<sub>6</sub> environment (Fig. 9) with a square antiprismatic idealized coordination polyhedron. The complexes behave as SMMs with slightly different energy barriers (57 K vs. 42 K). The coordination polyhedron is slightly more distorted in the triclinic phase than in the monoclinic one with however the highest energy barrier. One should then conclude that there is no direct correlation between symmetry and activation energy. Additional factors, which are not that clear and yet to be identified, influence the energy splitting diagram. Quantum chemistry calculations qualitatively reproduce this experimental fact: the first excited state is located higher in energy in the monoclinic phase than in the triclinic. These barriers are also similar to the one found for [Dy(tta)<sub>3</sub>**L**<sup>2</sup>] (due the similarities between the two environments). Here again, the calculated and the experimental orientation of the easy magnetic axis are in very good agreement with less than 10° of mismatch and an orientation in the most negatively charged direction. The dilution+enrichment protocol has been applied to both polymorphs, but only nuclear spin-free isotopes were employed to slow down the relaxation as much as we could. The same receipts give the same results: the hysteresis loops open in zero field for the enriched and diluted complexes.

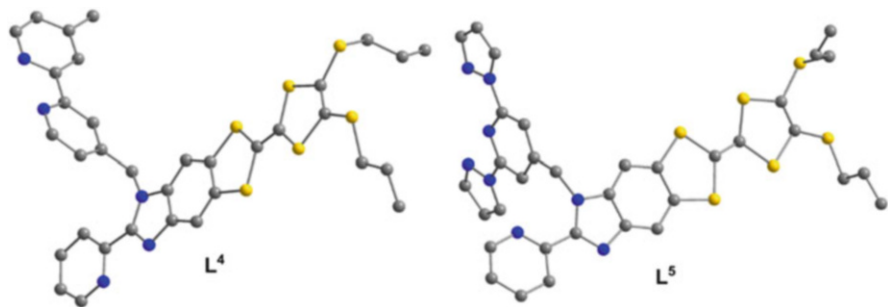




**Fig. 9** Representation of the complex  $[\text{Dy}(\text{tta})_3\text{L}^3]$  in the triclinic (top) and monoclinic (bottom) forms

All the TTF-based ligand envisaged so far could be coordinated only by one metal center, so we imagined and designed new TTF-based ligand to incorporate, in a bridging ligand, different coordination sites. The ideas behind were to (1) select different metals in incorporating different chelating sites (e.g., tris-) and (2) to accommodate the same metal in different environments to tune its magnetic properties (Fig. 10) [58].

When reacted with  $[\text{Dy}(\text{hfac})_3] \cdot 2\text{H}_2\text{O}$ ,  $\text{L}^4$  coordinates from both bischelating sites to form  $[\text{Dy}_2(\text{hfac})_6\text{L}^4]$  neutral complex. Each Dy(III) ion is surrounded by six



**Fig. 10** Representations of  $L^4$  and  $L^5$  ligands

oxygen and two nitrogen atoms and lies in almost the same  $N_2O_6$   $D_{4d}$  environment and is separated by more than  $10 \text{ \AA}$  [58]. From a magnetic point of view, these two sites should behave the same, and this is what is observed. Both behave as SMMs in zero external dc field, and the extended Debye analysis [59] reveals only one relaxation process. Seventy percent of the magnetic moments relax at the same frequency. The relaxation is however too fast in zero field to be quantitatively analyzed. In applying an external field to suppress the thermally independent regime, only one relaxation time that includes both sites is identified. At the optimum field, i.e., the external field for which the relaxation is the slowest (800 Oe), the thermal variation of the relaxation time does not follow the Arrhenius law expected for the Orbach process [60] but can be easily reproduced with a Raman process ( $\tau = CT^n$ ,  $C = 4.8 \times 10^{-3}$ , and  $n = 6.26$ ). This tends to prove that the relaxation does not occur through the first excited state, at least, as long as the in-field relaxation is concerned.

The reaction of  $[Dy(hfac)_3] \cdot 2H_2O$  with  $L^5$  leads to dinuclear species ( $[Dy_2(hfac)_6L^5]$ ) with two different coordination polyhedra [61],  $N_2O_6$  ( $CShM_{SAPR-8}$  ( $D_{4d}$ ) = 0.435) and  $N_3O_6$  ( $CShM_{TCTPR-9}$  ( $D_{3h}$ ) = 0.586). The  $N_2O_6$  sites behave in a standard way (SMM in zero external field), while the nonacoordinated site does not show any out-of-phase signal in zero external field. The application of a moderate external dc field slows down the relaxation with the emergence of two identifiable processes that can be safely attributed to the two different sites. An extended Debye model featuring two relaxation times has been employed to treat the ac data. Interestingly, the analyses reveal the ratio of the magnetic susceptibility which relaxes at the two relaxation time to be close to 50:50 in agreement with the chemical structure. Furthermore, the energy barrier for the octacoordinated site is in good agreement with its mononuclear equivalent [45]. From a chemical point of view, it was interesting to look for site selectivity with regard to different  $Dy(\beta\text{-diketonate})_3$  precursors. A 1:1 ratio of  $[Dy(hfac)_3] \cdot 2H_2O$  and  $[Dy(tta)_3] \cdot 2H_2O$  was reacted with  $L^5$ , and it forms dinuclear species

[Dy<sub>2</sub>(hfac)<sub>3</sub>(tta)<sub>3</sub>L<sup>5</sup>]. The crystal structure of the complex reveals ligand exchange, with the N<sub>2</sub>O<sub>6</sub> site made of two tta<sup>-</sup> and one hfac<sup>-</sup> ligands and the N<sub>3</sub>O<sub>6</sub> site made of one tta<sup>-</sup> and two hfac<sup>-</sup> ligands. We think this ligand exchange occurs as a consequence of a subtle balance between the size of the metallic precursors and the coordination which leads to a minimum steric hindrance. The magnetic behaviors of these two metallic sites are qualitatively identical to [Dy<sub>2</sub>(hfac)<sub>6</sub>L<sup>5</sup>] with the N<sub>2</sub>O<sub>6</sub> site being a SMM in zero field while the N<sub>3</sub>O<sub>6</sub> site being a SMM only in field [61].

At this stage, it appears that N<sub>2</sub>O<sub>6</sub> coordination polyhedron around Dy(III) systematically produces SMMs in zero field. Liu et al. [62] developed a TTF-fused donor-acceptor system based on dipyrido[3,2-*a*:2',3'-*c*]phenazine (dppz) which can be reacted with Dy(β-diketonate)<sub>3</sub> precursors ([Dy(hfac)<sub>3</sub>]·2H<sub>2</sub>O and [Dy(tta)<sub>3</sub>]·2H<sub>2</sub>O) [63]. Two mononuclear units are obtained with Dy(III) in the standard N<sub>2</sub>O<sub>6</sub> SAP coordination polyhedron made of three β-diketonate ligands and one dipyridyl moiety (CShM<sub>SAPR-8</sub> (D<sub>4d</sub>) = 0.724 for the hfac<sup>-</sup> derivative and CShM<sub>SAPR-8</sub> (D<sub>4d</sub>) = 0.507 for the tta<sup>-</sup> derivative) from the ligand L<sup>6</sup> (L<sup>6</sup> = TTF-fused dipyrido[3,2-*a*:2',3'-*c*]phenazine). Both compounds behave as SMM in zero field, but they are “faster,” and they relax at higher frequencies, than previous N<sub>2</sub>O<sub>6</sub> systems with however the tta<sup>-</sup> derivative slower than the hfac<sup>-</sup>. Typically, at 2 K, the maximum on the χ<sub>M</sub>'' vs. ν curves shows up at 700 Hz for [Dy(tta)<sub>3</sub>L<sup>6</sup>], while it is located above 1,500 Hz for [Dy(hfac)<sub>3</sub>L<sup>6</sup>]. To compare, for [Dy(hfac)<sub>3</sub>L<sup>2</sup>], the maximum was at 970 Hz and at 56 Hz for [Dy(tta)<sub>3</sub>L<sup>2</sup>] in the same sample environment. Such comparison, if natural, is however dangerous since in the low-temperature regime, where thermally independent processes take over all the others, the relaxation in the condensed crystalline phase is governed by the combination of magnetic intermolecular interactions (of dipolar origin) and hyperfine coupling. One can say that this N<sub>2</sub>O<sub>6</sub> topology (three bischelating oxygenate ligand and one bischelating nitrogenated ligand) provides efficient magnets that qualitatively behave the same and quantitatively almost the same. The difference resides in the electron withdrawing or donating ability of the chemical groups on the β-diketonate ligands.

## 5 Oxygen-Based TTF-Based Ligands

The strong oxophilic characters of lanthanide authorize the synthesis of fully oxygenated coordination polyhedron around metal centers. However, such environment does not, a priori, create the expected dissymmetry of charges to produce SMMs in the specific case of Dy(III) at least as far as O<sub>8</sub> environments are concerned. The reaction of [Dy(hfac)<sub>3</sub>]·2H<sub>2</sub>O with 4,4',7,7'-tetra-*tert*-butyl-2,2'-bi-1,3-benzodithiole-5,5',6,6'-tetrone ligand [64] (L<sup>7</sup>) forms a dinuclear complex [Dy<sub>2</sub>(hfac)<sub>6</sub>(H<sub>2</sub>O)<sub>2</sub>L<sup>7</sup>] [65]. In this complex, two Dy(III) ions, related by an inversion center, in O<sub>9</sub> coordination polyhedron, are linked by an acceptor-donor-acceptor triad (Fig. 11). Eight of the nine are coming from bischelating ligands (three hfac<sup>-</sup> and one quinone), and the last one is coming from a water molecule. The intramolecular

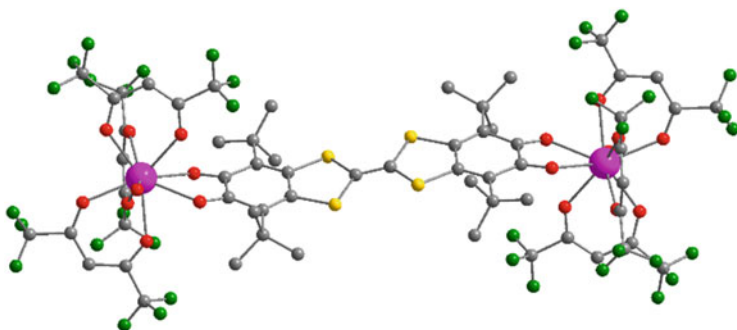


Fig. 11 View of the dinuclear compound  $[\text{Dy}_2(\text{hfac})_6(\text{H}_2\text{O})_2\text{L}^7]$

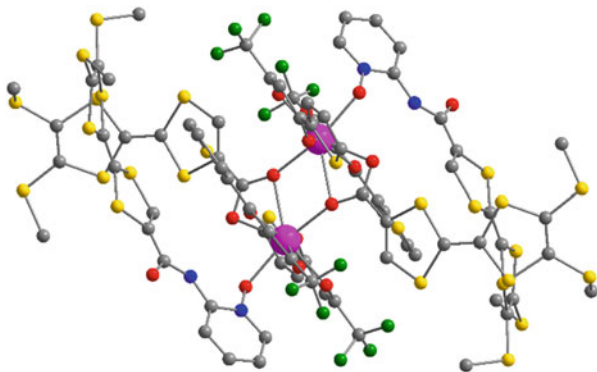
Dy-Dy distance is close to 17.5 Å, so there is no superexchange interaction between the two metals.

In this environment, Dy behaves as a SMM in zero external field. Interestingly, the equivalent complex obtained from the reaction of  $\text{L}^7$  with  $[\text{Dy}(\text{tta})_3] \cdot 2\text{H}_2\text{O}$  does not produce SMM. The steric hindrance of  $\text{tta}^-$  avoids water molecule to coordinate Dy(III), and therefore in this dinuclear complex, the coordination polyhedron is only made of eight oxygen atoms which is probably less suitable to promote axial anisotropy. This simple analysis is counterbalanced by other investigations [66] which clearly demonstrate that  $\text{O}_8$  environment could perfectly produce SMMs with Dy(III) ions. Probably, the primary approach which consists of considering only the point charge model might be oversimplified. Some authors pointed out with a deeper analysis that dipole and quadrupole moments in the electrostatic potential expansion play a significant role on the magnetic anisotropy [67, 68].

To conclude this section, we would like to briefly discuss one peculiar system. Two different TTF-based ligands are used to produce a dinuclear Yb(III)-based complex  $[\text{Yb}(\text{tta})_2\text{L}^8\text{L}^9]_2$  [69]. The redox active ligand 4,5-bis(thiomethyl)-4'-carboxylic tetrathiafulvalene ( $\text{L}^8$ ) is bridging two Yb(III) ions through  $\mu_2(\eta_1, \eta_2)$  oxygen atoms, and 4,5-bis(thiomethyl)-4'-ortho-pyridyl-N-oxide-carbamoyl-tetrathiafulvalene ( $\text{L}^9$ ) is terminal (Fig. 12). The coordination sphere around each Yb(III) is made of eight oxygen atoms, and the two ions are separated by only 3.89 Å.

The static magnetic properties reveal what could be analyzed as a sign of ferromagnetic interactions between the two  $^2\text{F}_{7/2}$  multiplet ground states. Indeed, on cooling from room temperature,  $\chi_{\text{M}}T$  decreases continuously in agreement with the thermal depopulation of  $M_J$  states, passes through a broad minimum at 9 K, and then slightly increases on cooling further down to the lowest temperature. We have attempted to fit the  $\chi_{\text{M}}T$  vs.  $T$  plot taking into account the crystal field effects by the extended Stevens operators technique [48] and the interaction between magnetic moments. The Hamiltonian to consider is the following:

**Fig. 12** View of the dinuclear compound  $[\text{Yb}(\text{tta})_2\text{L}^8\text{L}^9]_2$

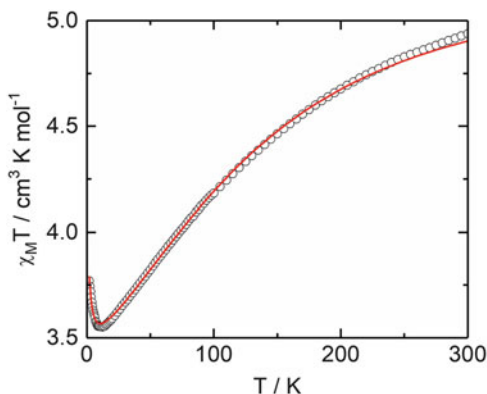


$$\begin{aligned} \widehat{H} = & \sum_{i=1}^2 (B_2^0 \widehat{O}_2^0 i + B_2^2 \widehat{O}_2^2 i + B_4^0 \widehat{O}_4^0 i + B_4^2 \widehat{O}_4^2 i + B_4^4 \widehat{O}_4^4 i + B_6^0 \widehat{O}_6^0 i + B_6^2 \widehat{O}_6^2 i + B_6^4 \widehat{O}_6^4 i + B_6^6 \widehat{O}_6^6 i) \\ & + \beta (g_J \widehat{J}_1 + g_J \widehat{J}_2) \cdot \vec{H} - J \widehat{J}_1 \cdot \widehat{J}_2 \end{aligned} \quad (1)$$

The first line corresponds to the crystal field effect at the two lanthanide sites with  $\widehat{O}_k^q$  the operator equivalents which can be expressed as polynomials of the total angular momentum matrices ( $\widehat{J}^2$ ,  $\widehat{J}_z$ ,  $\widehat{J}_+$ , and  $\widehat{J}_-$ ) associated with the  ${}^2F_{7/2}$  multiplet ground state. The second line corresponds to the Zeeman effects on  $\widehat{J}_i$  which are coupled through  $J$ . A homemade program has been developed to fit the magnetic data. Surprisingly a fairly good agreement (Fig. 13) is obtained without any interaction ( $J = 0 \text{ cm}^{-1}$ ), so one can consider this dimer as two isolated Yb(III) centers. The wave function analysis reveals that the Kramers ground state is the pure  $M_J = \pm 7/2$  component, separated only by  $2.6 \text{ cm}^{-1}$  from the first excited state  $M_J = \pm 1/2$ . The stabilization of the largest  $M_J$  component can be viewed in the frame of point charge model. The carboxylate group acts as a tweezer which projects the  $-1$  charge in a plane containing two hfac<sup>-</sup> ligands (Fig. 12). Then, ligand charges are condensed in a plane around this prolate ion (Fig. 1) and stabilize the largest  $M_J$  doublet state.

As a consequence of this Ising-type anisotropy, the complex behaves as a SMM with however a small energy barrier ( $\sim 21 \text{ K}$ ) determined from the temperature dependence of the relaxation time. This value can be compared with estimated gap between the ground and the first excited states (see above,  $\sim 4 \text{ K}$ ) from DC magnetic measurements. To support this interpretation, luminescence provides a unique tool to probe energy levels. The low-temperature ( $77 \text{ K}$ ) excitation of the sample at  $20,000 \text{ cm}^{-1}$  sensitizes the  ${}^2F_{5/2} \rightarrow {}^2F_{7/2}$  transitions in the range of  $10,400\text{--}9,400 \text{ cm}^{-1}$ . The excitation corresponds to LLCT (ligand-to-ligand charge transfer) and highlights the role of antenna played by the redox-active TTF ligands. We must mention that Dy(III) luminescence cannot be probed with TTF-based ligand since the emission lines fall in the absorption bands of the ligands. The

**Fig. 13** Temperature dependences of  $\chi_M T$  (open circles) with the best fitted curve (red line)



emission profile can be deconvoluted in four transitions (9,703, 9,936, 10,197, and 10,213  $\text{cm}^{-1}$ ). The gap between the two most energetic transitions (23 K) gives the exact gap between the Kramers doublet ground state and the first excited state. It is almost in perfect agreement with magnetism.

## 6 Polynuclear TTF-Dy(III) SMMs

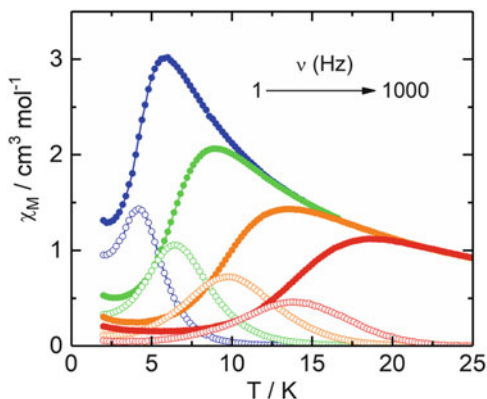
One question emerges from the previous paragraph. Does the nonexistence of interactions between Yb(III) in Yb derivative  $[\text{Yb}(\text{tta})_2\text{L}^8\text{L}^9]_2$  can be generalized to other lanthanide? The synthesis of  $[\text{Dy}(\text{tta})_2\text{L}^8\text{L}^9]_2$ , isostructural of Yb derivative, provides an answer [70]. On cooling,  $\chi_M T$  vs.  $T$  plot passes through a broad minimum at 16 K that cannot be reproduced without taking into account interactions. The best fits are obtained with a ferromagnetic interaction  $J = 2.98 \times 10^{-3} \text{ cm}^{-1}$ . This interaction is very weak with respect to the energy engaged in crystal field splitting (hundreds of wave numbers). In this frame the Kramers ground state for each Dy(III) ion corresponds to more than 99% of the  $M_J = \pm 15/2$ . In this effective spin-1/2 model, one expects  $g = 20$  in one direction and 0 in a perpendicular plane. Then, the coupling of dipolar origin between the two magnetic moment can be easily calculated from the Hamiltonian  $\hat{H} = -J_{dd}\hat{\sigma}_1 \cdot \hat{\sigma}_2$  where  $\hat{\sigma}_i$  are the operators associated with the effective 1/2 and  $J_{dd} = -(\mu_0 g^2 \beta^2 / 4\pi \hbar c r^3)(1 - 3\cos^2 \theta) \text{ cm}^{-1}$  ( $r$  is the distance between the metal centers, and  $\theta$  is the angle between the anisotropy axis and the  $r$  vector). Such interaction can be ferro- or antiferromagnetic depending on  $\theta$ . The amplitude can also be rather large at short distances, with  $r = 4 \text{ \AA}$   $J_{dd}$  varies from  $-2$  to  $+5 \text{ cm}^{-1}$ , to compare with  $J = 0.67 \text{ cm}^{-1}$  estimated from DC measurements in the same spin-1/2 model ( $2.98 \times 10^{-3} \times 15 \times 15$ ). Transferred to Yb(III) system, the interaction of dipolar origin is more than six times stronger in the very hypothetical case of identical  $\theta$ . Taking into account the interaction between the two Ising centers, we can describe the ground state with two components:  $|\uparrow\uparrow\rangle$  and

$|\downarrow\downarrow\rangle$  separated by  $J/2$  ( $0.335\text{ cm}^{-1}$ ) from the excited state described by  $|\uparrow\downarrow\rangle$  and  $|\downarrow\uparrow\rangle$ . The complex is a SMM. However, the thermal variation of the relaxation time at low temperature is very different from what we are used to observe on mononuclear complexes. Indeed, there is no leveling of the relaxation time on cooling in zero external dc field down to 2 K:  $\tau$  increases continuously on cooling. This is certainly the consequence of the thermal population of the four levels. Remarkably, within an external DC field,  $\tau$  does not greatly vary. This is a consequence of the condensation of the four states on few tenths of wave numbers.

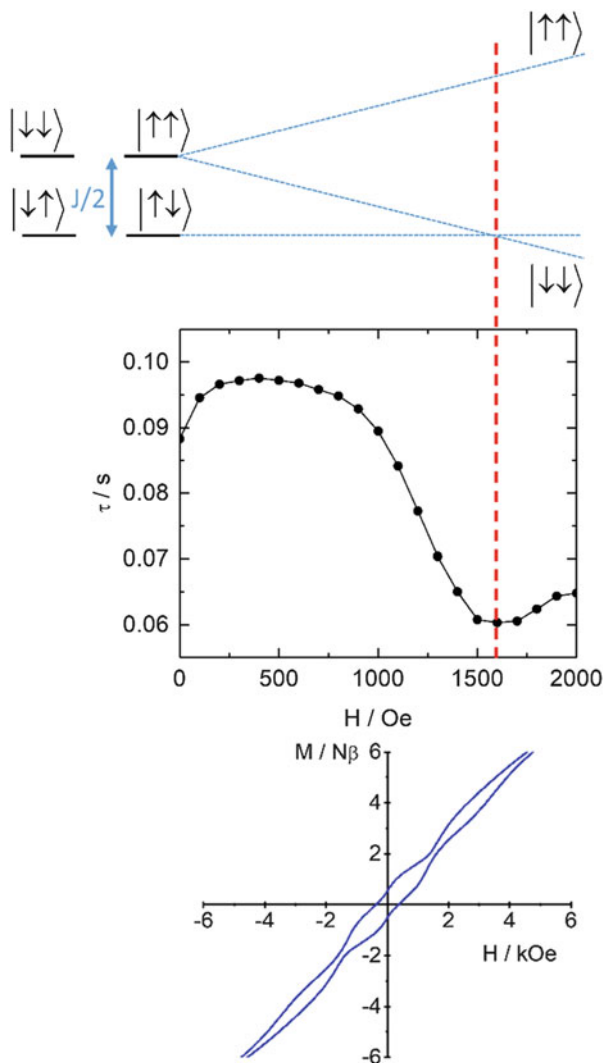
The implication of magnetic interactions on slow relaxation dynamics in dimers is confirmed by other investigations on TTF-based Dy(III) dinuclear complexes. The reaction of tetrathiafulvalene-3-pyridine-N-oxide ligand ( $\mathbf{L}^{10}$ ) with  $[\text{Dy}(\text{tta})_3]\cdot 2\text{H}_2\text{O}$  gives the centrosymmetric complex  $[\text{Dy}(\text{tta})_3\mathbf{L}^{10}]_2$  [39]. The  $\chi_M T$  vs.  $T$  plot shows strong antiferromagnetic interactions between  ${}^6\text{H}_{15/2}$  multiplets. In the effective spin-1/2 model, the interaction is estimated at  $-2.3\text{ cm}^{-1}$  with a  $g$  value (19.2) close to the Ising limit (20). The nonmagnetic ground state is then described by  $|\uparrow\downarrow\rangle$  and  $|\downarrow\uparrow\rangle$ , with the first excited state ( $|\uparrow\uparrow\rangle$  and  $|\downarrow\downarrow\rangle$ ) at  $1.3\text{ cm}^{-1}$ . Despite the nonmagnetic nature of the ground state,  $[\text{Dy}(\text{tta})_3\mathbf{L}^{10}]_2$  behaves as a SMM (Fig. 14). The thermal variation of the relaxation time  $\tau$  does not follow a simple mathematical law since various energy levels are involved at temperatures as low as 2 K. The application of an external dc field corroborates the interpretations based on dc measurements. The field behavior of  $\tau$  does reflect the low-level energy diagram.

At low field and temperatures below 8 K,  $\tau$  decreases with the field (Fig. 15) with a clear dip at 1.6 kOe. At such temperatures, the first magnetically active ( $|\uparrow\uparrow\rangle$  and  $|\downarrow\downarrow\rangle$ ) excited states are thermally populated. It must be pointed out that the transition between these two states necessitates to flip simultaneously both magnetic moments, so the transition probability is very small and the relaxation time long. On increasing the magnetic field, there is a crossing between levels (Fig. 15), and, at the intersection, transition between two states involves “only” to flip one magnetic moment, and the relaxation time shortens. The minimum of  $\tau$  should occur at a field which can be related to the interaction between Dy(III). With  $J = -2.3\text{ cm}^{-1}$ , the crossing should occur at 1.3 kOe which relatively close to the measured value. This in-field behavior

**Fig. 14** Temperature dependences of  $\chi_M'$  and  $\chi_M''$  measured at 1 Hz (black), 10 Hz (light gray), 100 Hz (mid gray), and 1,000 Hz (dark gray) for  $[\text{Dy}(\text{tta})_3\mathbf{L}^{10}]_2$  in the absence of an external dc field. Full symbols correspond to  $\chi_M'$  and empty symbols to  $\chi_M''$



**Fig. 15** (Top) field dependence of the relaxation time  $\tau$  at 5 K with the magnetic field evolution of the energy levels in an Ising pattern for  $[\text{Dy}(\text{tta})_3\text{L}^{10}]_2$ . (Bottom) hysteresis loop for  $[\text{Dy}(\text{tta})_3\text{L}^{10}]_2$  measured at 1.5 K at a sweep rate of  $66 \text{ Oe s}^{-1}$



has also a consequence on the magnetic hysteresis. At 1.5 K, the magnetic hysteresis loop measured at  $66 \text{ Oe s}^{-1}$  differs significantly from those of mononuclear species (Fig. 15) [71]. The butterfly transforms into a double butterfly. The neck at 1.3 kOe traduces the acceleration of the relaxation at crossing field. In addition, the loop is opened at the origin. One may say that this nonmagnetic object possesses a magnetic memory anyway.

$[\text{Dy}(\text{hfac})_2(\text{SO}_3\text{CF}_3)\text{L}^{11*+}]_2$  is another example of dinuclear TTF-Ln-based complexes [27] with 4,5-bis(3-pyridyl-N-oxidemethylthio)-4',5'-methylthio-tetrathiafulvalene ligand ( $\text{L}^{11}$ ). This complex has some common points with  $[\text{Dy}(\text{tta})_3\text{L}^{10}]_2$ : the coordination polyhedron is made of eight oxygen atoms, and

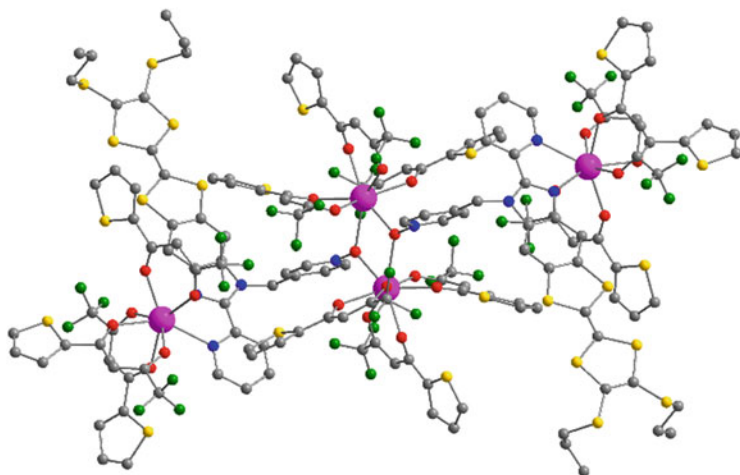


pyridine *N*-oxide bridges two Dy(III) ions. However, in this system, one monoanionic  $\beta$ -diketonate moiety has been substituted by one monoanionic sulfonate. One oxygen atom from pyridine *N*-oxide group completes the coordination sphere. The ligand  $\mathbf{L}^{11}$  has been oxidized during galvanostatic. The TTF core is almost planar in agreement with its radical cationic form  $\mathbf{L}^{11+\cdot}$ . Two non-coordinated sulfonate anions balance the positive charge of the complex. In the crystal lattice, the TTF cores are dimerized with short intermolecular S...S contacts ( $\sim 3.35$  Å), and then the radicals are magnetically inactive (strongly antiferromagnetically coupled). This is confirmed by the very weak EPR signal centered at  $g \sim 2.007$  measured at 77 K. The electrical resistivity measured at room temperature on single crystals corresponds to an insulator. The analysis of the static magnetic properties reveals a weak antiferromagnetic coupling ( $J = -3 \times 10^{-3}$  cm<sup>-1</sup> according to Eq. 1) and a Kramers ground state mainly constituted of  $M_J = \pm 13/2$ . The  $\chi_M''$  vs.  $\nu$  curves at zero field does not pass through the characteristic maximum at low temperature, so even if it is clear that  $[\text{Dy}(\text{hfac})_2(\text{SO}_3\text{CF}_3)\mathbf{L}^{11+\cdot}]_2$  behaves as a SMM, it is less efficient than the previous example probably because the environment around the lanthanide is chemically different.

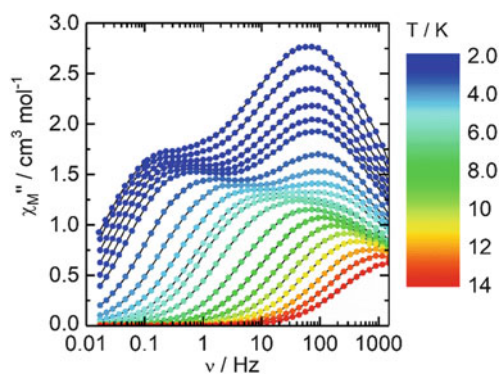
The last two examples we would like to tackle are polynuclear complexes which feature more than two metal centers. The rational design of a lanthanide-based complex featuring different lanthanide motifs can be safely envisaged in combining  $[\text{Dy}(\text{tta})_3\mathbf{L}^{10}]_2$  and  $[\text{Dy}(\text{tta})_3\mathbf{L}^2]$ . To do so a TTF-based ligand has been designed to feature a bridging site of pyridine *N*-oxide type and a bischelating nitrogen-based site [72]. The ligand 2-{1-methylpyridine-*N*-oxide-4,5-[4,5-bis(pro-pylthio)tetrathiafulvalenyl]-1H-benzimidazol-2-yl}pyridine ( $\mathbf{L}^{12}$ ) was then treated with two equivalents of  $[\text{Dy}(\text{tta})_3] \cdot 2\text{H}_2\text{O}$  to give the complex  $[\text{Dy}_4(\text{tta})_{12}(\mathbf{L}^{12})_2]$  (Fig. 16). In the complex, the reader will recognize one moiety similar to  $[\text{Dy}(\text{tta})_3\mathbf{L}^{10}]_2$  and two moieties similar to  $[\text{Dy}(\text{tta})_3\mathbf{L}^2]$ . The distance between these moieties (metal-metal) is above 10 Å, so there is no direct interaction between these three distinct SMMs. The magnetism of this object should coincide with the superposition of two different SMMs.

In zero external field, the  $\chi_M''$  vs.  $\nu$  curves at various temperatures between 2 and 11 K clearly show two well-separated relaxations which can be confronted to the measurements on the isolated species. The presence of a slow and a fast process at low and high frequencies, respectively, matches almost perfectly with the isolated species. The low-frequency side corresponds to the dinuclear part and the high frequency to the mononuclear. It is also possible to analyze quantitatively the thermal and the in-field behaviors with a combination of two extended Debye models. At this stage our synthetic approach allowed us to conceive a complex which contains two different SMMs which act differently in the temperature and time scales. This rational design is very promising to elaborate multifunctional complexes (Fig. 17).

The last example we would like to comment concerns the polymeric species.  $[\text{Yb}(\text{hfac})_3] \cdot 2\text{H}_2\text{O}$  was reacted with the disodium salt of  $\mathbf{L}^{13}$  with  $\mathbf{H}_2\mathbf{L}^{13} = 4,5$ -bis(carboxylic)-4',5'-methylthiotetrathiafulvene in dimethylformamide (DMF) to produce  $\{[\text{Yb}\mathbf{L}^{13}(\text{H}_2\text{O})_3(\text{DMF})] \cdot (\mathbf{HL}^{13}) \cdot (\text{H}_2\text{O})\}_n$  [73]. The monodimensional



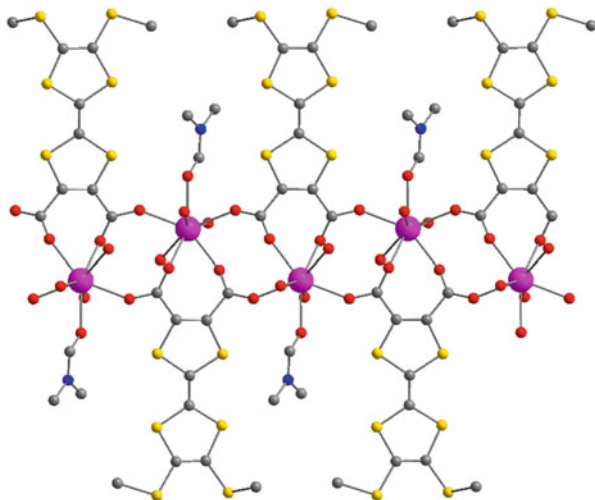
**Fig. 16** Single-crystal X-ray structure of the tetranuclear complex  $[\text{Dy}_4(\text{tta})_{12}(\mathbf{L}^{12})_2]$



**Fig. 17** Temperature and frequency dependence of the out-of-phase component of the ac susceptibility  $[\text{Dy}_4(\text{tta})_{12}\mathbf{L}^{12}_2]$  measured in zero external dc field

polymer consists of chain of Yb(III) bridged by carboxylate anions in a  $\mu_2(\eta_1, \eta_1)$  mode (Fig. 18). Coordination compounds of lanthanide ions with TTF-based ligands are not so common and are essentially 0D. This is the first example of coordination polymer of lanthanide with TTF-based ligand. The coordination polyhedron is made of eight oxygen atoms in a  $D_{4d}$  environment ( $\text{CShM}_{\text{SAPR-8}} = 0.454$ ). Our efforts to produce the dysprosium derivative were unsuccessful. It must be mentioned that no  $\text{hfac}^-$  anions are present in the structure and that the polymer cannot be obtained from nitrate or halogenate salts of Yb(III). The system crystallizes in the triclinic space group  $P\bar{1}$  with one Yb(III) site, so the  $g$ -tensor can be extracted from single-crystal rotating magnetometry. In the effective spin-1/25 model,  $g_x = 3.24$ ,  $g_y = 1.53$ , and  $g_z = 4.25$ . These values are far away from the Ising limit for which

**Fig. 18** Representation of the one-dimensional structure. The counterion ( $\text{HL}^{13-}$ ) has not been represented



$g_x = g_y = 0$  and  $g_z = 8.00$ . As a result, the polymer does not behave as a SMM in zero external dc field. Only when an external dc field is applied that  $\chi_M''$  shows up.  $g_z$  orientation almost coincides with the fourfold axis of the square antiprism. We tentatively tried to reproduce the static magnetic properties using the ab initio CASSCF/PT2/SI-SO approach. Unfortunately, all tentative efforts failed to properly reproduce the magnetic susceptibility and magnetization curves. This underlines the difficulties already observed in the literature to efficiently model both the wave function and the energy of the low-lying multiplets of Yb(III) complexes.

## 7 Conclusions

In this chapter we wish to have convinced the reader that TTF-based ligands can be employed to produce SMMs. We have focused the first part of this chapter on strategies to enhance the magnetic performance of Dy-based SMM in a  $\text{N}_2\text{O}_6$  environment. A simple molecular engineering consisting in the modulation of the electron withdrawing strength of the  $\beta$ -diketonate ancillary ligand highlighted the importance of the electron charge density carried by the first neighboring atom to control the energy crystal splitting and well isolate the ground multiplet state. The canceling of the intermolecular (hydrogen bond and dipolar) interactions, thanks to magnetic dilutions and spin-free isotopic enrichment, showed their efficiency to decrease the quantum tunneling of the magnetization and therefore optimize the magnetic properties of the SMM. Then the influence of the nature of the coordination sphere was studied by the analysis of mononuclear SMM library in which the Dy(III) is in  $\text{N}_2\text{O}_6$ ,  $\text{N}_3\text{O}_6$ ,  $\text{O}_8$ , and  $\text{O}_9$  environments. When the Dy(III) is placed in a  $\text{N}_2\text{O}_6$  environment, the Ising character of the magnetic anisotropy is enhanced compared to

the  $N_3O_6$  environment. In a general manner, SMM behavior is detected when the negative charge is localized along an axis and in a plan, respectively, for the Dy(III) and Yb(III) ions [41]. In a second part, we have increased the nuclearity of the complexes. The role of the intramolecular magnetic interactions on the slow magnetic relaxation has been demonstrated.

Finally it is worth to notice that a large panel of theoretical and experimental tools is available and can be used to reach a high level of understanding of the lanthanide SMM magnetic properties, i.e., experimental measurements of the angular dependence of the magnetization, correlation between magnetism and experimental luminescence, crystal-field determination by Stevens method, and *ab initio* calculations.

## References

1. Sessoli R, Gatteschi D, Caneschi A, Novak MA (1993) Magnetic bistability in a metal-ion cluster. *Nature* 365:141–143
2. Ishikawa N, Sugita M, Ishikawa T, Koshihara S, Kaizu Y (2003) Lanthanide double-decker complexes functioning as magnets at the single-molecular level. *J Am Chem Soc* 125:8694–8695
3. Guo F-S, Day BM, Chen Y-C, Tong M-L, Mansikkamäki A, Layfield RA (2017) A dysprosium metallocene single-molecule magnet functioning at the axial limit. *Angew Chem Int Ed* 56:11445–11449
4. Goodwin CAP, Ortu F, Reta D, Chilton NF, Mills DP (2017) Molecular magnetic hysteresis at 60 kelvin in dysprosocenium. *Nature* 548:439–442
5. Kobayashi H, Kobayashi A, Cassoux P (2000) BETS as a source of molecular magnetic superconductors (BETS = bis(ethylenedithio)tetraselenafulvalene). *Chem Soc Rev* 29:325–333
6. Coronado E, Galán-Mascarós JR, Gómez-García CJ, Laukhin V (2000) Coexistence of ferromagnetism and metallic conductivity in a molecule-based layered compound. *Nature* 408:447–449
7. Yamada J, Sugimoto T (2004) TTF chemistry: fundamentals and applications of tetrathiafulvalene. Kodansha, Tokyo, Springer, Berlin
8. Bendikov M, Wudl F, Perepichka DF (2004) Tetrathiafulvalenes, oligoacenes, and their buckminsterfullerene derivatives: the brick and mortar of organic electronics. *Chem Rev* 104:4891–4946
9. Gorgues A, Hudhomme P, Sallé M (2004) Highly functionalized tetrathiafulvalenes: riding along the synthetic trail from electrophilic alkynes. *Chem Rev* 104:5151–5184
10. Lorcy D, Bellec N, Fourmigué M, Avarvari N (2009) Tetrathiafulvalene-based group XV ligands: Synthesis, coordination chemistry and radical cation salts. *Coord Chem Rev* 253:1398–1438
11. Pointillart F, Golhen S, Cador O, Ouahab L (2013) Paramagnetic 3d coordination complexes involving redox-active tetrathiafulvalene derivatives: an efficient approach to elaborate multi-properties materials. *Dalton Trans* 42:1949–1960
12. Gavrilenko KS, Gal YL, Cador O, Golhen S, Ouahab L (2007) First trinuclear paramagnetic transition metal complexes with redox active ligands derived from TTF:  $Co_2M(PhCOO)_6(TTF-CHCH-py)_2 \cdot 2CH_3CN$ ,  $M = Co^{II}, Mn^{II}$ . *Chem Commun* 280–282
13. Benbellat N, Gavrilenko KS, Le Gal Y, Cador O, Golhen S, Gouasmia A, Fabre J-M, Ouahab L (2006) Co(II)–Co(II) paddlewheel complex with a redox-active ligand derived from TTF. *Inorg Chem* 45:10440–10442

14. Kolotilov SV, Cador O, Pointillart F, Golhen S, Le Gal Y, Gavrilenko KS, Ouahab L (2010) A new approach towards ferromagnetic conducting materials based on TTF-containing polynuclear complexes. *J Mater Chem* 20:9505–9514
15. Liu S-X, Ambrus C, Dolder S, Neels A, Decurtins S (2006) A dinuclear Ni(II) complex with two types of intramolecular magnetic couplings: Ni(II)–Ni(II) and Ni(II)–TTF<sup>•+</sup>. *Inorg Chem* 45:9622–9624
16. Cui L, Geng Y-F, Leong CF, Ma Q, D'Alessandro DM, Deng K, Zeng Q-D, Zuo J-L (2016) Synthesis, properties and surface self-assembly of a pentanuclear cluster based on the new  $\pi$ -conjugated TTF-triazole ligand. *Sci Rep* 6:srep25544
17. Mitsumoto K, Nishikawa H, Newton GN, Oshio H (2012) Encapsulation controlled single molecule magnetism in tetrathiafulvalene-capped cyanide-bridged cubes. *Dalton Trans* 41:13601–13608
18. Faulkner S, Burton-Pye BP, Khan T, Martin LR, Wray SD, Skabara PJ (2002) Interaction between tetrathiafulvalene carboxylic acid and ytterbium DO3A: solution state self-assembly of a ternary complex which is luminescent in the near IR. *Chem Commun* 1668–1669
19. Cui H, Otsuka T, Kobayashi A, Takeda N, Ishikawa M, Misaki Y, Kobayashi H (2003) Structural, electrical, and magnetic properties of a series of molecular conductors based on BDT-TTP and lanthanoid nitrate complex anions (BDT-TTP = 2,5-bis(1,3-dithiol-2-ylidene)-1,3,4,6-tetrathiapentalene). *Inorg Chem* 42:6114–6122
20. Pointillart F, Le Gal Y, Golhen S, Cador O, Ouahab L (2009) 4f Gadolinium(III) complex involving tetrathiafulvalene-amido-2-pyrimidine-1-oxide as a ligand. *Inorg Chem* 48:4631–4633
21. Gao F, Cui L, Liu W, Hu L, Zhong Y-W, Li Y-Z, Zuo J-L (2013) Seven-coordinate lanthanide sandwich-type complexes with a tetrathiafulvalene-fused Schiff base ligand. *Inorg Chem* 52:11164–11172
22. Gao F, Zhang X-M, Cui L, Deng K, Zeng Q-D, Zuo J-L (2014) Tetrathiafulvalene-supported triple-decker phthalocyaninato dysprosium(III) complex: synthesis, properties and surface assembly. *Sci Rep* 4:srep05928
23. Ran Y-F, Steinmann M, Sigrist M, Liu S-X, Hauser J, Decurtins S (2012) Tetrathiafulvalene-based lanthanide coordination complexes: synthesis, crystal structure, optical and electrochemical characterization. *Comptes Rendus Chim* 15:838–844
24. Ueki S, Nogami T, Ishida T, Tamura M (2006) ET and TTF salts with lanthanide complex ions showing frequency-dependent ac magnetic susceptibility. *Mol Cryst Liq Cryst* 455:129–134
25. Pointillart F, le Guennic B, Cador O, Maury O, Ouahab L (2015) Lanthanide ion and tetrathiafulvalene-based ligand as a “magic” couple toward luminescence, single molecule magnets, and magnetostructural correlations. *Acc Chem Res* 48:2834–2842
26. D'Aleo A, Pointillart F, Ouahab L, Andraud C, Maury O (2012) Charge transfer excited states sensitization of lanthanide emitting from the visible to the near-infra-red. *Coord Chem Rev* 256:1604–1620
27. Pointillart F, Guennic BL, Golhen S, Cador O, Ouahab L (2013) Slow magnetic relaxation in radical cation tetrathiafulvalene-based lanthanide(III) dinuclear complexes. *Chem Commun* 49:11632–11634
28. Uzelmeier CE, Smucker BW, Reinheimer EW, Shatruk M, O'Neal AW, Fourmigué M, Dunbar KR (2006) A series of complexes of the phosphorus-based TTF ligand o-P2 with the metal ions Fe<sup>II</sup>, Co<sup>II</sup>, Ni<sup>II</sup>, Pd<sup>II</sup>, Pt<sup>II</sup>, and Ag<sup>I</sup>. *Dalton Trans* 5259–5268
29. Xiong J, Li G-N, Sun L, Li Y-Z, Zuo J-L, You X-Z (2011) Mono- and dinuclear Co/Ni complexes bearing redox-active tetrathiafulvaleneacetylacetonate ligands – syntheses, crystal structures, and properties. *Eur J Inorg Chem* 5173–5181
30. Guo YN, Xu GF, Gamez P, Zhao L, Lin SY, Deng R, Tang J, Zhang HJ (2010) Two-step relaxation in a linear tetranuclear dysprosium (III) aggregate showing single-molecule magnet behavior. *J Am Chem Soc* 132:8538–8539

31. Guo YN, Xu GF, Wernsdorfer W, Ungur L, Guo Y, Tang J, Zhang HJ, Chibotaru LF, Powell AK (2011) Strong axiality and Ising exchange interaction suppress zero-field tunneling of magnetization of an asymmetric Dy<sub>2</sub> single-molecule magnet. *J Am Chem Soc* 133:11948–11951
32. Lin S-Y, Wernsdorfer W, Ungur L, Powell AK, Guo Y-N, Tang J, Zhao L, Chibotaru LF, Zhang H-J (2012) Coupling Dy<sub>3</sub> triangles to maximize the toroidal moment. *Angew Chem Int Ed* 51:12767–12771
33. Guo Y-N, Ungur L, Granroth GE, Powell AK, Wu C, Nagler SE, Tang J, Chibotaru LF, Cui D (2014) An NCN-pincer ligand dysprosium single-ion magnet showing magnetic relaxation *via* the second excited state. *Sci Rep* 4:5471
34. Layfield RA (2014) Organometallic single-molecule magnets. *Organometallics* 33:1084–1099
35. Guo Y-N, Xu G-F, Guo Y, Tang J (2011) Relaxation dynamics of dysprosium(III) single molecule magnets. *Dalton Trans* 40:9953–9963
36. Zhang P, Zhang L, Tang J (2015) Lanthanide single molecule magnets: progress and perspective. *Dalton Trans* 44:3923–3929
37. Ungur L, Lin S-Y, Tang J, Chibotaru LF (2014) Single-molecule toroids in Ising-type lanthanide molecular clusters. *Chem Soc Rev* 43:6894–6905
38. Pointillart F, Cador O, Le Guennic B, Ouahab L (2017) Uncommon lanthanide ions in purely 4f single molecule magnets. *Coord Chem Rev* 346:150–175
39. Pointillart F, Le Gal Y, Golhen S, Cador O, Ouahab L (2011) Single-molecule magnet behaviour in a tetrathiafulvalene-based electroactive antiferromagnetically coupled dinuclear dysprosium(III) complex. *Chem Eur J* 17:10397–10404
40. Llunell M, casanova D, Cicera J, Bofill JM, Alemany P, Alvarez S (2013) SHAPE (version 2.1)
41. Rinehart JD, Long JR (2011) Exploiting single-ion anisotropy in the design of f-element single-molecule magnets. *Chem Sci* 2:2078–2085
42. Sievers J (1982) Asphericity of 4f-shells in their Hund's rule ground states. *Z Für Phys B Condens Matter* 45:289–296
43. Ungur L, Chibotaru LF (2011) Magnetic anisotropy in the excited states of low symmetry lanthanide complexes. *Phys Chem Chem Phys* 13:20086–20090
44. Ungur L, Chibotaru LF (2016) Strategies toward high-temperature lanthanide-based single-molecule magnets. *Inorg Chem* 55:10043–10056
45. Cosquer G, Pointillart F, Golhen S, Cador O, Ouahab L (2013) Slow magnetic relaxation in condensed versus dispersed dysprosium(III) mononuclear complexes. *Chem Eur J* 19:7895–7903
46. Jung J, Cador O, Bernot K, Pointillart F, Luzon J, Le Guennic B (2014) Influence of the supramolecular architecture on the magnetic properties of a DyIII single-molecule magnet: an ab initio investigation. *Beilstein J Nanotechnol* 5:2267–2274
47. da Cunha TT, Jung J, Boulon M-E et al (2013) Magnetic poles determinations and robustness of memory effect upon solubilization in a DyIII-based single ion magnet. *J Am Chem Soc* 135:16332–16335
48. Orbach R (1961) Spin-lattice relaxation in rare-earth salts. *Proc R Soc Lond A* 264:458–484
49. Pointillart F, Bernot K, Golhen S, Le Guennic B, Guizouan T, Ouahab L, Cador O (2015) Magnetic memory in an isotopically enriched and magnetically isolated mononuclear dysprosium complex. *Angew Chem Int Ed* 54:1504–1507
50. Gatteschi D, Sessoli R (2003) Quantum tunneling of magnetization and related phenomena in molecular materials. *Angew Chem Int Ed* 42:268–297
51. Ishikawa N, Sugita M, Wernsdorfer W (2005) Nuclear spin driven quantum tunneling of magnetization in a new lanthanide single-molecule magnet: bis(phthalocyaninato)holmium anion. *J Am Chem Soc* 127:3650–3651
52. Ishikawa N, Sugita M, Wernsdorfer W (2005) Quantum tunneling of magnetization in lanthanide single-molecule magnets: bis(phthalocyaninato)terbium and bis(phthalocyaninato)dysprosium anions. *Angew Chem Int Ed* 44:2931–2935

53. Flores Gonzales J, Pointillart F, Ouahab L, Cador O. Hyperfine coupling and slow magnetic relaxation in isotopically enriched Dy(III) mononuclear single-molecule magnets. Submitted
54. Ebenhöf W, Ehlers VJ, Ferch J (1967) Hyperfine-structure measurements on Dy<sup>161</sup> and Dy<sup>163</sup>. *Z Für Phys* 200:84–92
55. Childs WJ (1970) Hyperfine structure of <sup>5</sup>I<sub>8,7</sub> atomic states of Dy<sup>161,163</sup> and the ground-state nuclear moments. *Phys Rev A* 2:1692–1701
56. Kishi Y, Pointillart F, Lefevre B, Riobé F, Guennic BL, Golhen S, Cador O, Maury O, Fujiwara H, Ouahab L (2017) Isotopically enriched polymorphs of dysprosium single molecule magnets. *Chem Commun* 53:3575–3578
57. Fujiwara H, Yokota S, Hayashi S, Takemoto S, Matsuzaka H (2010) Development of photofunctional materials using TTF derivatives containing a 1,3-benzothiazole ring. *Phys B Condens Matter* 405:S15–S18
58. Speed S, Feng M, Garcia GF et al (2017) Lanthanide complexes involving multichelating TTF-based ligands. *Inorg Chem Front* 4:604–617
59. Cole KS, Cole RH (1941) Dispersion and absorption in dielectrics I. Alternating current characteristics. *J Chem Phys* 9:341–351
60. Abragam A, Bleaney B (2012) Electron paramagnetic resonance of transition ions. Reprint edn. Oxford University Press, Oxford
61. Feng M, Pointillart F, Lefevre B, Dorcet V, Golhen S, Cador O, Ouahab L (2015) Multiple single-molecule magnet behaviors in dysprosium dinuclear complexes involving a multiple functionalized tetrathiafulvalene-based ligand. *Inorg Chem* 54:4021–4028
62. Jia C, Liu S-X, Tanner C, Leiggener C, Neels A, Sanguinet L, Levillain E, Leutwyler S, Hauser A, Decurtins S (2007) An experimental and computational study on intramolecular charge transfer: a tetrathiafulvalene-fused dipyrrophenazine molecule. *Chem Eur J* 13:3804–3812
63. Pointillart F, Jung J, Berraud-Pache R et al (2015) Luminescence and single-molecule magnet behavior in lanthanide complexes involving a tetrathiafulvalene-fused dipyrrophenazine ligand. *Inorg Chem* 54:5384–5397
64. Kuropatov V, Klementieva S, Fukin G, Mitin A, Ketkov S, Budnikova Y, Cherkasov V, Abakumov G (2010) Novel method for the synthesis of functionalized tetrathiafulvalenes, an acceptor–donor–acceptor molecule comprising of two o-quinone moieties linked by a TTF bridge. *Tetrahedron* 66:7605–7611
65. Pointillart F, Klementieva S, Kuropatov V, Gal YL, Golhen S, Cador O, Cherkasov V, Ouahab L (2012) A single molecule magnet behaviour in a D<sub>3h</sub> symmetry Dy(III) complex involving a quinone–tetrathiafulvalene–quinone bridge. *Chem Commun* 48:714–716
66. Soussi K, Jung J, Pointillart F, Guennic BL, Lefevre B, Golhen S, Cador O, Guyot Y, Maury O, Ouahab L (2015) Magnetic and photo-physical investigations into Dy(III) and Yb(III) complexes involving tetrathiafulvalene ligand. *Inorg Chem Front* 2:1105–1117
67. Huang G, Fernandez-Garcia G, Badiane I et al. Magnetic slow relaxation in a metal organic framework made of chains of ferromagnetically coupled single-molecule magnets. *Chem Eur J*. doi: <https://doi.org/10.1002/chem.201800095>
68. Zhang P, Jung J, Zhang L, Tang J, Le Guennic B (2016) Elucidating the magnetic anisotropy and relaxation dynamics of low-coordinate lanthanide compounds. *Inorg Chem* 55:1905–1911
69. Pointillart F, Guennic BL, Golhen S, Cador O, Maury O, Ouahab L (2013) A redox-active luminescent ytterbium based single molecule magnet. *Chem Commun* 49:615–617
70. Pointillart F, Golhen S, Cador O, Ouahab L Slow magnetic relaxation in a redox-active tetrathiafulvalene-based ferromagnetic dysprosium complex. *Eur J Inorg Chem* 2014, 2014:4558–4563
71. Pointillart F, Le Guennic B, Maury O, Golhen S, Cador O, Ouahab L (2013) Lanthanide dinuclear complexes involving tetrathiafulvalene-3-pyridine-N-oxide ligand: semiconductor radical salt, magnetic, and photophysical studies. *Inorg Chem* 52:1398–1408

72. Pointillart F, Guizouarn T, Lefeuvre B, Golhen S, Cador O, Ouahab L (2015) Rational design of a lanthanide-based complex featuring different single-molecule magnets. *Chem Eur J* 21:16929–16934
73. Belio Castro A, Jung J, Golhen S, Le Guennic B, Ouahab L, Cador O, Pointillart F (2016) Slow magnetic relaxation in unprecedented mono-dimensional coordination polymer of ytterbium involving tetrathiafulvalene-dicarboxylate linker. *Magnetochemistry* 2:26



# Geometry and Magnetism of Lanthanide Compounds



Zhenhua Zhu and Jinkui Tang

## Contents

1	Lanthanide Coordination Chemistry in Single Molecule Magnets .....	192
1.1	Introduction to the Lanthanides .....	192
1.2	The Crystal Field and Molecular Symmetry .....	193
1.3	The Coordination Numbers and Geometry in Lanthanide Single Molecule Magnets ..	195
2	Geometry-Dependent Magnetic Behaviors in Lanthanide Single Molecule Magnets .....	213
2.1	Constitutional (Structural) Isomerism Effect .....	215
2.2	Ligand Influences .....	217
2.3	Anion Inducing .....	219
2.4	Predominant Bonds in Lanthanide Single Molecule Magnets .....	220
3	Conclusions and Prospects .....	222
	References .....	222

**Abstract** Lanthanide single molecule magnets (Ln-SMMs) were still been considered as the exceptionally promising candidates in high-density data storage and quantum calculation although the single atom magnets with smaller size have been discovered. Recent developments that the intrinsic magnetic properties of Ln-SMMs can be preserved when deposited on the surface of substrates greatly inspired us to make more efforts in facilitating the above practical applications. It is well-known that the single molecule magnet (SMM) behavior is strongly dependent on the coordination environments experienced by the lanthanide ions. Here, we focus on the representative Ln-SMMs with different coordination geometries from the view of coordination numbers, discuss the methods of modulating ligand fields, highlight the importance of constructing predominant bonds, and explain the relationship between the geometry, crystal field, and molecular magnetisms.

---

Z. Zhu and J. Tang (✉)

State Key Laboratory of Rare Earth Resource Utilization, Changchun Institute of Applied Chemistry, Chinese Academy of Sciences, Changchun, P. R. China  
e-mail: [tang@ciac.ac.cn](mailto:tang@ciac.ac.cn)

**Keywords** Coordination geometry · Coordination number · Lanthanide single molecule magnets (Ln-SMMs) · Ligand field · Predominant bond · Slow magnetic relaxation

## 1 Lanthanide Coordination Chemistry in Single Molecule Magnets

### 1.1 Introduction to the Lanthanides

Lanthanide chemistry started from 1794, when an “earth”(oxide) was obtained successfully from a black mineral. Lanthanide ions, whose normal valence is 3+, have the electronic configuration  $[\text{Xe}]4f^n$  with the 4f subshell gradually filled from 0 to 14 electrons. It is the well-known that the separation of lanthanide ions is an extremely difficult undertaking due to the popular phenomenon, “lanthanide contraction,” referring to the shrinkage of the ionic radii, which causes a pronounced similarity of lanthanide ions to each other [1]. The lanthanides exhibit lots of characteristics that can differentiate them from the d-block metals and from the perspective of molecular magnetisms; the most important feature is that the 4f orbitals cannot participate directly in bonding due to the shielding effect of outer 5d and 6s electrons, in conjunction with the slight penetrating of 4f orbitals to the xenon core. So, the bonding between lanthanide ions and ligands depends primarily on the electronegativity of coordination atoms; that is to say, the bonding is intrinsically electrostatic [2–5]. The little interaction between the 4f orbitals and ligand orbitals means that the crystal effects can be regarded as a perturbation on free lanthanide ions, leading to the inability of forming  $\pi$  bonds. Consequently, the coordination geometries are determined by ligand steric factors instead of crystal field effects. Unlike the lanthanide ions, the transition metals exhibit strong interaction with ligands typically evident by the  $\text{M}=\text{O}$  or  $\text{M}\equiv\text{N}$  multiple bonds and the spectral shifts of the order of  $1,000\text{ cm}^{-1}$  between different transition metal compounds, however, which are only  $10\text{--}20\text{ cm}^{-1}$  in the lanthanide spectra [6]. As we know, the magnitude of the magnetic anisotropy is dependent on the quenching extent of the orbital moment as the spin is isotropic, namely, which is closely related to the electrostatic crystal field interactions. Therefore, lanthanide ions show the larger spin–orbit couplings due to the smaller crystal field interactions, resulting in the higher magnetic anisotropy compared to the d-block metal ions. From the discovery of lanthanide-based single molecule magnets (Ln-SMMs) [7], the lanthanide ions have been considered as excellent candidates in designing high-temperature single molecule magnets (SMMs).

A general comparison between lanthanide ions and transition metal ions excluding the magnetic properties mentioned above is given in Table 1.

**Table 1** Comparison of 4f-3d metal ions

	4f ions	3d ions
Stable oxidation states	Usually +3	Variable
Ionic radii (Å)	1.06–0.85	0.75–0.6
Coordination numbers	Commonly 8–12	Usually 4–6
Typical coordination polyhedra	Trigonal prism Square antiprism Dodecahedron	Square planar Tetrahedron Octahedron
Bonding strength	Ligand bonds in order of electronegativity	Determined by orbital interaction
Bonding direction	Little preference in bond directions	Strong direction bonding
Crystal field effects	Weak	Strong
Electronic spectra of ions	Sharp lines	Broad lines

## 1.2 The Crystal Field and Molecular Symmetry

As for lanthanide ions, although the spin–orbit couplings are much more stronger than crystal field effects, once placed in a coordination environment with nonspherical symmetry, the electrostatic field of the ligands can also lift the degeneration of the  $^{2S+1}L_J$  multiplets like magnetic fields, resulting in  $2J + 1$  sublevels called Stark sublevels, and further play a significant role in creating a highly anisotropic ground state [8, 9]. Hence, the effects of the ligands on lanthanide ions are equivalent to electrostatic potential acting on the  $4f^n$  electrons. There are two types of formalisms describing the electrostatic potential produced by the ligands [9, 10], one is *Stevens Formalism* proved to be very powerful for molecular magnetism studies, in which the electrostatic potential is expressed by the Stevens operator equivalents expanded by angular momentum operators, little different from standard operators but producing the same results. The other is *Wybourne Formalism* employing irreducible tensor operators turned out to be useful in optical studies, for which *Stevens Formalism* is not well-suited. Accordingly, the ligand field potential can be expressed as the following equation:

$$U_{CF} = \widehat{H}_{CF} = \underbrace{\sum_{k=2,4,6} \rho^k \sum_{q=-k}^k A_k^q \langle r^k \rangle \widehat{O}_k^q}_{\text{Stevens Formalism}} = \underbrace{\sum_{k=0}^{\infty} \left[ B_0^k C_0^k(i) + \sum_{q=1}^k B_q^k \left( C_{-q}^k(i) + (-1)^q C_q^k(i) \right) + i B_q^k \left( C_{-q}^k(i) - (-1)^q C_q^k(i) \right) \right]}_{\text{Wybourne Formalism}}$$

where  $A_k^q \langle r^k \rangle$  or  $B_q^k$  and  $B_q^k$  are called the crystal field parameters, it is noted that the number of parameters to be included in above equation is determined by the point symmetry of the lanthanide center;  $\widehat{O}_k^q$  is the operator equivalent of the crystal field potential and  $C_q^k(i)$  is called the tensor operator, related to the spherical harmonics;  $\rho^k$  is a number, different for the different  $f^n$  configurations and  $k$  values. The operators with even terms ( $k = 0, 2, 4, 6$ ) are responsible for the crystal field splitting, while

with odd ones ( $k = 1, 3, 5, 7$ ) are responsible for the intensity of the induced electric dipole transitions in optical spectroscopy, so the latter can be neglected as they do not affect magnetic properties for Ln-SMMs.

In fact, the crystal field parameters based on either the Stevens or *Wybourne formalism* can be used because they are related to each other. Furthermore, the *Wybourne formalism* is becoming increasingly applied to the field of molecular magnetism in recent years, since it can provide the direct comparisons with data obtained by optical spectroscopy, which now is considered as the most accurate technique in exploring the relaxation mechanism and the energy pattern for Ln-SMMs. In this chapter, we will adopt the *Wybourne formalism* to describe the crystal field parameters, which are greatly dependent on the molecular symmetry of Ln-SMMs. In general, the lower the symmetry of coordination environments, the larger the number of parameters will be, and if the symmetry is low enough, the number of the independent parameters is too high, up to 27 and some of them are the imaginary components of operators ( $q < 0$  terms). The 27 parameters usually were used to describe the crystal field in detail by the “classical” calculation models such as electrostatic point-charge and phenomenological crystal field (CF) models but through which the results are not precise due to the over-parameterization and they will also cause some difficulties in ab initio methods owing to the large number of parameters, which maybe the most reliable tool for decent descriptions of the crystal field of Ln-SMMs [11]. In practice, most Ln-SMMs possess a low-symmetry coordination environment and to avoid the problem of over-parameterization, it is a common strategy to approximate the real symmetry of the system to a higher one so that only  $q > 0$  terms will be considered. On the contrary, when lanthanide ions are placed in a high symmetry ligand field, the better magnetic properties will be obtained, which have been proved by lots of experimental data and theoretical calculations. To some extent, the high symmetry coordination environment experienced by lanthanide ions means that the strong axiality (the magnetism along one axis, namely principal axis  $Z$ , is greatly distinguished from the other two axes, called transversal axes  $X, Y$ ) of spin-orbit multiplets of Ln-SMMs is achieved. In purely symmetric geometries including  $D_{4d}$ ,  $C_{5h}$ ,  $D_{5h}$ ,  $D_{6d}$ ,  $C_n$ ,  $C_{nv}$ , and  $C_{nh}$ , only the parameters with  $q = 0$  are different from 0; that is to say, the axiality of ligand fields is perfect with  $g_x = g_y = 0$ . Table 2 lists the representative high-performance Ln-SMMs, which all have a strong axial ligand field.

It is well-known that the diatomic complex,  $[\text{DyO}]^+$ , have a perfect axial symmetry with the best quantum numbers  $M_J$ , which means that all the Kramers doublets (KD) are characterized by definite projections  $M$  of the total angular momentum  $J$  on the axis  $Z$ , leading to magnetic relaxation passing through the highest excited state with an effective energy barrier ( $U_{\text{eff}}$ ) exceeding 3,000 K [20]. It is clear that if Ln-SMMs belong to the above axial symmetry group, the perfect axial doublets will be obtained; however, this situation is quite rare due to the changeable coordination models of lanthanide ions, so the actual situation often encountered is that most Ln-SMMs have a low symmetric ligand environment. In this case, another pronounced strategy in constructing high-performance Ln-SMMs has to be mentioned

**Table 2** The representative high-performance Ln-SMMs with a highly symmetric geometry

Compounds	Symmetry	$U_{\text{eff}}/\text{K}$	Year	Ref.
[Tb(Pc)(Pc')]	$D_{4d}$	938	2013	[12]
[Dy(Lz) <sub>2</sub> (o-vanilin) <sub>2</sub> ]-NO <sub>3</sub>	$D_{4d}$	615	2016	[13]
[Dy <sup>III</sup> (OPCy <sub>3</sub> ) <sub>2</sub> (H <sub>2</sub> O) <sub>5</sub> ] <sup>3+</sup>	$D_{5h}$	543	2016	[14]
[Dy <sup>III</sup> (OP <sup>t</sup> Bu(NH <sup>t</sup> Pr) <sub>2</sub> ) <sub>2</sub> (H <sub>2</sub> O) <sub>5</sub> ] <sup>3+</sup>	$D_{5h}$	735	2016	[15]
[Dy <sup>III</sup> (bbpen)Br]	$D_{5h}$	1,025	2016	[16]
[Dy <sup>III</sup> (O <sup>t</sup> Bu) <sub>2</sub> (py) <sub>5</sub> ] <sup>+</sup>	$D_{5h}$	1,815	2016	[17]
[(Cp <sup>III</sup> ) <sub>2</sub> Dy] <sup>+</sup>	<b>Metallocene</b>	1,837	2017	[18, 19]

Pc' = Pc-[O-(C<sub>6</sub>H<sub>4</sub>)-*p*-<sup>t</sup>Bu]<sub>g</sub>; Lz = 6-pyridin-2-yl-[1,3,5]triazine-2,4-diamine; Cp<sup>III</sup> = 1,2,4-tri(tert-butyl)cyclopentadienide;

H<sub>2</sub>bbpen = *N,N'*-bis(2-hydroxybenzyl)-*N,N'*-bis(2-methylpyridyl)ethylenediamine)

**Table 3** The representative high-performance Ln-SMMs with predominant bonds

Compounds	Center	Average lengths of predominant bond (Å)	Average lengths of all other bonds (Å)	$U_{\text{eff}}/\text{K}$	Year	Ref.
DyNCN	Dy	2.393	2.571	335	2014	[22]
C=Dy=C	Dy	2.432	2.474	810	2016	[23]
DyN <sub>5</sub> -O <sup>t</sup> Bu	Dy	2.112	2.561	1,815	2016	[17]
Zn-Dy-Zn	Dy	2.208	2.393	439	2013	[24]
Zn <sub>2</sub> -Dy-Zn <sub>2</sub>	Dy	2.324	2.675	430	2016	[25]
Dy <sub>4</sub> K <sub>2</sub>	Dy1	2.072	2.353	696	2013	[26]
	Dy2	2.071	2.368			
	Dy3	2.099	2.377			
	Dy4	2.114	2.371			

here and will be highlighted in the next section. If the lanthanide ions interact much stronger with one or two ligand atoms than the rest, the axial components of CF passing through that atom are the strongest and the main magnetic axis of the ground KD state is also dominantly oriented by that atom. According to the CF theory, the strength of the interaction between the central ion and the ligand atom greatly depends on the length of the bond between them [21]. This shortest chemical bond can be named by *predominant bond* in the field of Ln-SMMs. Therefore, it is a noteworthy and promising method in designing high-performance Ln-SMMs by constructing the predominant bond. Table 3 presents some representative high-performance Ln-SMMs with one or two predominant bonds.

### 1.3 The Coordination Numbers and Geometry in Lanthanide Single Molecule Magnets

About 50 years ago, very little was known about lanthanide compounds. Initially, inspired by the transition metal compounds, it is usually supposed that the lanthanide ions also accommodate six ligands in their coordination sphere like 3d ions, now has

been proved to be wrong [27]. In fact lanthanide ions showed a wider variety of coordination number than 3d ions due to the bigger ion radii and the “special” 4f orbitals. Up to now, all kinds of lanthanide compounds with the coordination number from 2 to 12 have been reported by the researchers in various fields based on coordination chemistry. In a word, the coordination number adopted by lanthanide ions is determined by how many ligands can be packed around the central metal ion and generally speaking, the situation that the coordination sphere is saturated will appear via two ways, one is called First-Order effects, the other is called Second-Order effects [28]. The former circumstance refers to small ligands like water, methanol, or halogen etc., the coordination number is dependent on the repulsion among the donor atoms directly contacting with lanthanide ions, while the latter is targeted at certain “bulky” ligands like bis(trimethylsilyl)amido [ $-\text{N}(\text{SiMe}_3)_2$ ], and the isolobal alkyl [ $-\text{CH}(\text{SiMe}_3)_2$ ], etc., the lanthanide ions can only bond with few donor atoms owing to the bulk of the rest of the ligand shielding the metal from other would-be ligands, generating lanthanide complexes with low coordination numbers. As was pointed out above, the magnetic properties of Ln-SMMs strongly depend on the symmetry of ligand field, and in general different coordination numbers of lanthanide ions bring about different geometries of ligand fields, leading to different magnetic properties of Ln-SMMs. So, we shall review Ln-SMMs from the perspective of coordination number and geometry, according to the order of first low coordination Ln-SMMs below 6 after those with higher coordination number from 7 to 9 (Table 4).

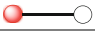
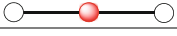

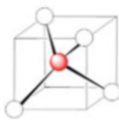
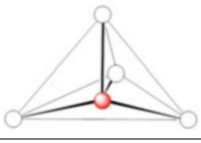
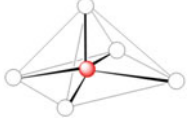
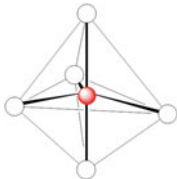

### 1.3.1 Coordination Numbers 1 and 2

It is an unlikely coordination number for lanthanide ions that only a single donor bond with the central metal leaving the metal highly exposed, unless in the gas phase under high dilution conditions, where metal–ligand encounters are limited, like diatom molecule [ $\text{Dy}^{2+}\text{O}^{2-}$ ] discovered in 1986 [29]. Nonetheless, we should have confidence in the synthesis of two coordination Ln-SMMs and a near-linear bis(amide) complex [ ${}^i\text{Pr}_3\text{Si}$ ] $_2\text{N-Sm-N}(\text{Si}^i\text{Pr}_3)_2$ ] with an N–Sm–N angle of  $175.52^\circ$  (Fig. 1) has been reported by Winpenny group [30], which provide a blueprint for a high-temperature Ln-SMMs, encouraging the researchers in this field to make more efforts to synthesize two-coordinated  $\text{Dy}^{3+}$ -SMMs by using the “bulky” ligands.

### 1.3.2 Coordination Number 3


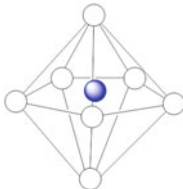
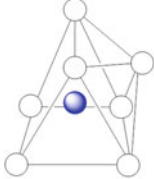
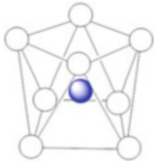
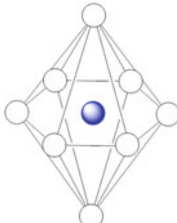
The first three-coordinate Ln-SMMs with an equatorially coordinated triangle geometry,  $\text{Ln}[\text{N}(\text{SiMe}_3)_2]_3$  (Ln = Dy, Er), were reported by our group in 2014 [31]. Alternating current (ac) susceptibility measurements provided an indication that the  $\text{Er}[\text{N}(\text{SiMe}_3)_2]_3$  is a typical SMM with well-resolved out-of-phase ( $\chi''$ ) ac susceptibility maxima varying with frequency (Fig. 2), while the  $\text{Dy}[\text{N}(\text{SiMe}_3)_2]_3$  does not exhibit any out-of-phase ac signals under zero applied direct current (dc) field, which

**Table 4** Common geometries for Ln-SMMs with coordination number from 3 to 9

Coordination number	Shape	Symmetry	Common geometries for lanthanide compounds
<i>Low coordination numbers</i>			
1	Linear	$C_{\infty v}$	
2	Linear	$D_{\infty h}$	
3	Trigonal planar	$D_{3h}$	
4	Tetrahedral	$T_d$	
	Trigonal pyramidal	$C_{3v}$	
5	Square pyramidal	$C_{4v}$	
	Trigonal bipyramidal	$D_{3h}$	
6	Octahedral	$O_h$	

(continued)

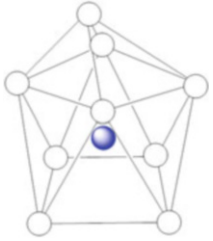
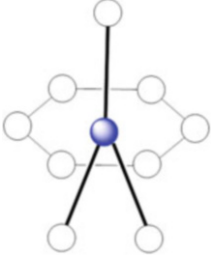
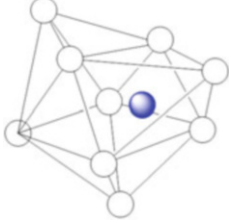
**Table 4** (continued)

Coordination number	Shape	Symmetry	Common geometries for lanthanide compounds
	Trigonal prismatic	$D_{3h}$	
<i>High coordination numbers</i>			
7	Pentagonal bipyramid	$D_{5h}$	
	Capped trigonal prism	$C_{2v}$	
8	Square antiprism	$D_{4d}$	
	Hexagonal bipyramid	$D_{6h}$	

(continued)



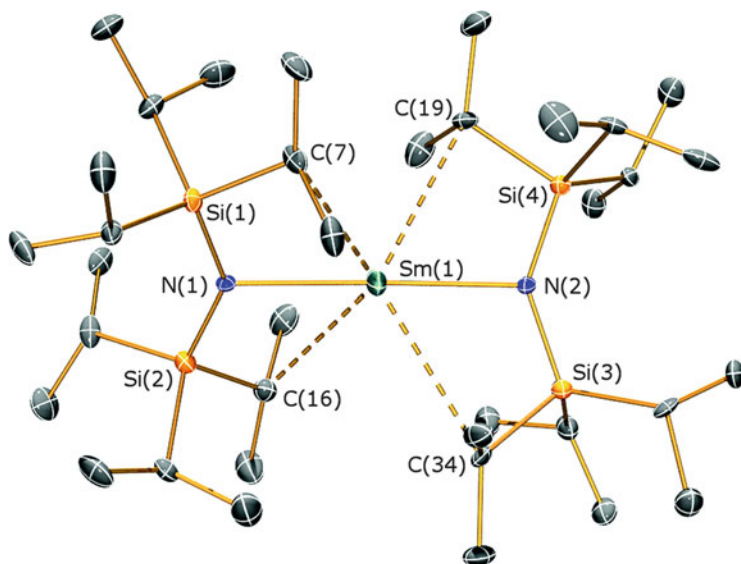
**Table 4** (continued)

Coordination number	Shape	Symmetry	Common geometries for lanthanide compounds
9	Capped square antiprism	$C_{4v}$	
	Hula-hoop	$C_{2v}$	
	Tricapped trigonal prism	$D_{3h}$	

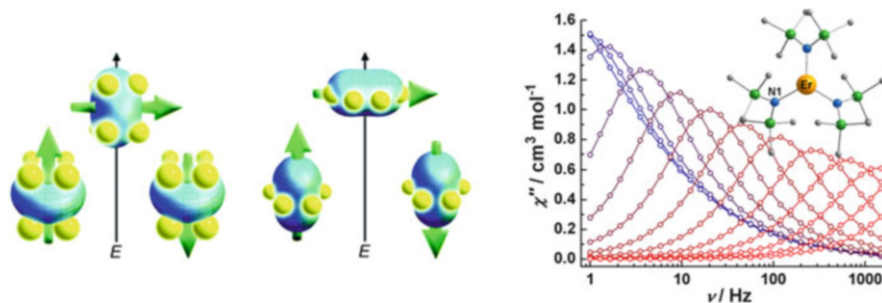
strongly corroborate the simple model put forward by Long groups which can direct the design of Ln-SMMs [32]. Now, the model was often employed to predict the impact of geometry of ligand field on magnetic anisotropy of lanthanide ions with two shapes of 4f electron densities, one is oblate like  $Dy^{3+}$  ions enjoying axial ligand fields, the other is prolate like  $Er^{3+}$  ions suitable to equatorial ligand fields.

### 1.3.3 Coordination Number 4

The  $Er[N(SiMe_3)_2]_3$  was synthesized by the ligand  $NaN(SiMe_3)_2$  reacting with anhydrous  $ErCl_3$  in THF, and when the ligand was replaced by  $\{Li(THF)(\mu-N(SiMe_3)_2)\}_2$  or  $LiN(SiMe_3)_2$ , a four-coordinate lanthanide compound was obtained.



**Fig. 1** Molecular structure of  $[\text{Pr}_3\text{Si})_2\text{N-Sm-N}(\text{Si}^i\text{Pr}_3)_2]$ . Reprinted with permissions from [30]. Copyright 2015 The Royal Society of Chemistry



**Fig. 2** Depictions of low- and high-energy configurations of the f-orbital electron density with respect to the crystal field environment for a 4f ion of oblate and prolate electron density (left). Reprinted with permissions from [32]. Copyright 2011 The Royal Society of Chemistry. Molecular structure and temperature dependence of  $\chi''$  (right). Reprinted with permissions from [31]. Copyright 2014 American Chemical Society

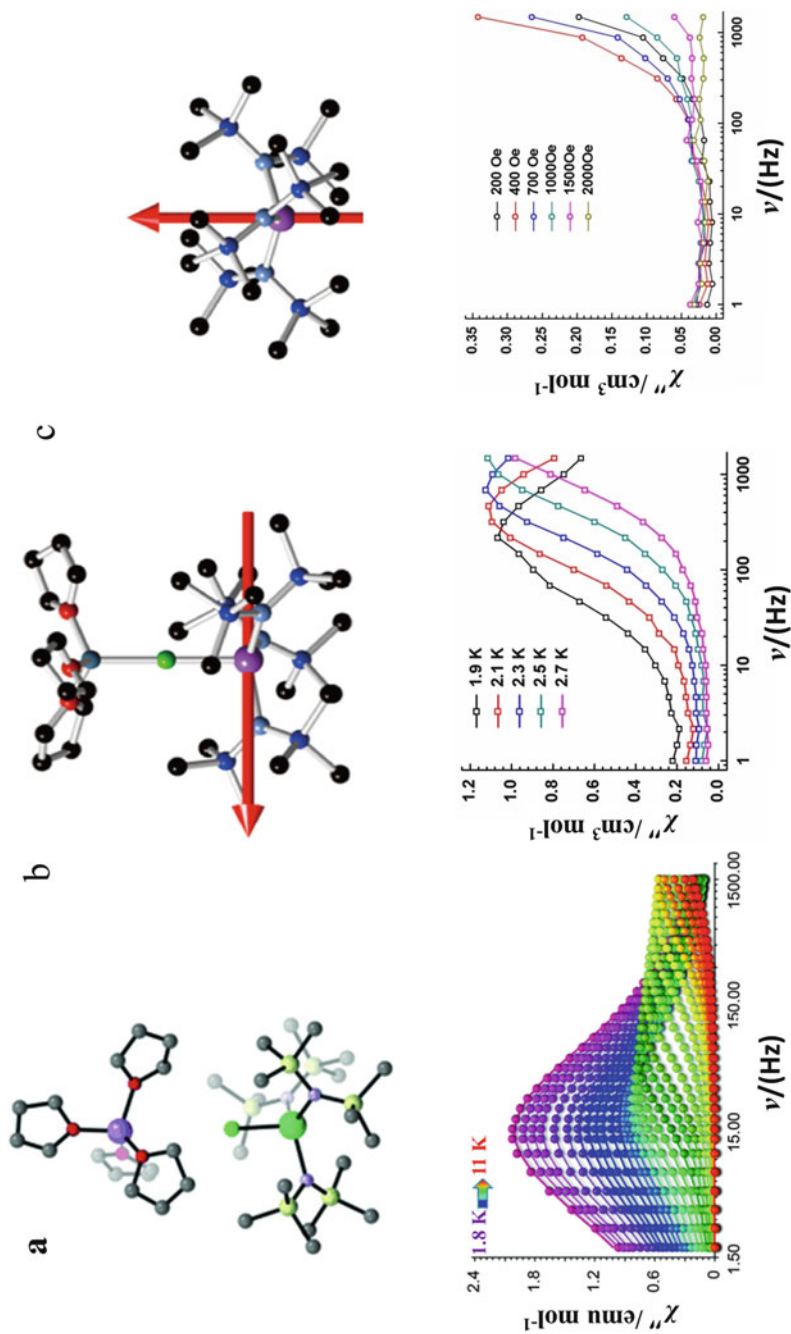
In 2015, Dunbar et al. reported four-coordinate Ln-SMMs,  $[\text{Li}(\text{THF})_4][\text{Er}\{\text{N}(\text{SiMe}_3)_2\}_3\text{Cl}]\cdot 2\text{THF}$  with a trigonal pyramidal geometry and ac susceptibility measurements, clearly exhibited the slow magnetic relaxation behavior under a zero applied dc magnetic field in the temperature range of 1.8–11 K, demonstrating the typical SMM characteristic [33]. Compared to  $\text{Er}[\text{N}(\text{SiMe}_3)_2]_3$  with an effective energy barrier of 122 K, the  $[\text{Li}(\text{THF})_4][\text{Er}\{\text{N}(\text{SiMe}_3)_2\}_3\text{Cl}]\cdot 2\text{THF}$  have a smaller energy barrier, 63 K. The author pointed out that the presence of the axial chloride ligand should account for

the smaller energy barrier owing to the moderate destruction to equatorial-type ligand field. Lately, in 2016, our group reported a series of four-coordinate Ln-SMMs,  $\text{Ln}[\text{N}(\text{SiMe}_3)_2]_3\text{CLi}(\text{THF})_3$  ( $\text{Ln} = \text{Dy}, \text{Er}$ ) using the ligand  $\text{LiN}(\text{SiMe}_3)_2$ , with a little difference in structure to the first one, the  $[\text{Li}(\text{THF})_3]^+$  cation is connected to the  $\text{Cl}^-$  [34]. Interestingly,  $\text{Dy}[\text{N}(\text{SiMe}_3)_2]_3\text{CLi}(\text{THF})_3$  exhibited a significantly different SMM behavior featuring the small out-of-phase ac signals in the absence of dc applied field compared to  $\text{Dy}[\text{N}(\text{SiMe}_3)_2]_3$  which did not show any ac signals. Ab initio calculations in conjunction with the electrostatic potential mapping approach confirmed that distinguished magnetic properties between them can be assigned to the different symmetry of the whole molecule rather than the presence of  $\text{CLi}(\text{THF})_3$  moiety (Fig. 3).

### 1.3.4 Coordination Number 5

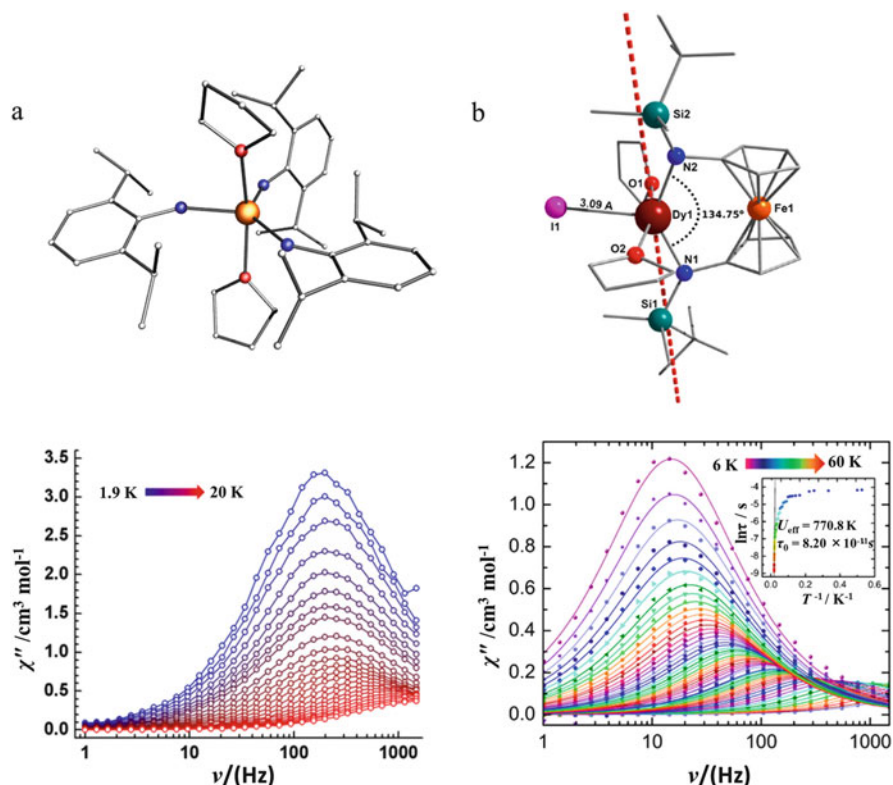
The amended valence shell electron pair repulsion (VSEPR) model predicts two forms of five-coordination, one is square-based pyramid geometry (or, simply, square pyramid) and the other is trigonal bipyramid geometry (Table 4), which both have been clearly identified by the transition metal chemistry. However, this is also a rare coordination number for lanthanide ions and up to now, to our knowledge, only two examples of mononuclear Ln-SMMs with trigonal bipyramid geometry and none of square pyramidal mononuclear Ln-SMMs have been reported. It is reasonable to suppose that the  $\text{LnL}_3$  can adopt two neutral ligands on the axial positions; in this case, the trigonal bipyramidal compounds will be achieved. In 2014, a five-coordinate Ln-SMM,  $[\text{Dy}(\text{NHPh}^i\text{Pr}_2)_3(\text{THF})_2]$  with two THF molecules above and below equatorial plane, was reported by our group [31]. Ac susceptibility measurements reveal a clear zero-field SMM behavior although the fast tunneling relaxation was observed at low temperature, while the three-coordinate compound,  $\text{Dy}[\text{N}(\text{SiMe}_3)_2]_3$ , just exhibited very poor SMM behavior due to the planar magnetic anisotropy of this complex (Fig. 4), which imply that sometimes low-symmetry ligand fields maybe are advantage for  $\text{Dy}^{3+}$ -SMMs. In 2017, another  $\text{Dy}^{3+}$ -SMMs also possessing a trigonal bipyramid geometry, the  $(\text{NN}^{\text{TBS}})\text{DyI}(\text{THF})_2$  ( $\text{NN}^{\text{TBS}} = \text{fc}$  ( $\text{NHSi}^i\text{BuMe}_2$ ),  $\text{fc} = 1,1'$  ferrocenediyl) with a large energy barrier of 771 K and magnetic blocking temperature of 14 K, was reported by Murugesu group [35]. The equatorial sphere of the compound is occupied by two molecules of THF and an iodide, as the same time, the axial position is completed by two nitrogen atoms deriving from the  $\text{NN}^{\text{TBS}}$  ligand with an angle of  $137.7^\circ$ , producing strong interactions between the N atoms of the  $\text{NN}^{\text{TBS}}$  ligand and the  $\text{Dy}^{3+}$  ion in the axial positions due to the shorter distance of Dy-N bond (Fig. 4). Ab initio calculations were performed in order to explore the root reason that governs the magnetization blocking barrier and expectedly, it is the axial ligands that elicit the significant magnetic axiality. Moreover, when the transverse ligands, THF and iodide, are removed completely, a near threefold improvement on the  $U_{\text{eff}}$  can be fulfilled, up to 2,289 K.

In addition to the abovementioned, herein an interesting SMM,  $\text{Dy}@\text{SiO}_2$  with isolated Dy(III) sites distributed at the surface of silica nanoparticles exhibiting



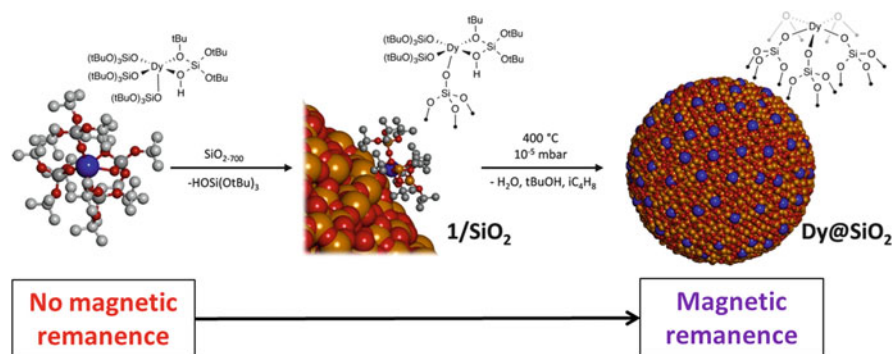
**Fig. 3** (a) Molecular structure (*top*) and imaginary component of the ac magnetic susceptibility data plotted versus frequency of [Li(THF)<sub>4</sub>][Er(N(SiMe<sub>2</sub>)<sub>3</sub>Cl)<sub>2</sub>THF] (*bottom*). Reprinted with permissions from [33]. Copyright 2015 WILEY-VCH. (b) Molecular structure (*top*) and frequency-dependent

← **Fig. 3** (continued) of  $\chi''$  of ac susceptibility at different temperatures under a 600 Oe dc field (*bottom*) for  $\text{Dy}[\text{N}(\text{SiMe}_3)_2]_3\text{Cl}_4(\text{THF})_3$ . The red arrow represents the orientation of the calculated  $g_z$  direction associated with the ground KD. Reprinted with permissions from [34]. Copyright 2016 American Chemical Society.  
(c) Molecular structure (*top*) and frequency dependence at 1.9 K of the out-of-phase ac susceptibility component at different dc fields for  $\text{Dy}[\text{N}(\text{SiMe}_3)_2]_3$ . The red arrow represents the orientation of the calculated  $g_z$  direction associated with the ground KD



**Fig. 4** (a) Molecular structure (*top*) and frequency-dependent of  $\chi''$  (*bottom*) for  $[\text{Dy}(\text{NHPh}^i\text{Pr}_2)_3(\text{THF})_2]$ . Reprinted with permissions from [31]. Copyright 2014 American Chemical Society. (b) Molecular structure (*top*) and frequency-dependent of  $\chi''$  (*bottom*) for  $(\text{NN}^{\text{TBS}})\text{DyI}(\text{THF})_2$ . Dashed lines represent the magnetic axis in the ground, first excited, and second excited KD states. Inset: Relaxation time of the magnetization,  $\ln(\tau)$  vs  $T^{-1}$ . Reprinted with permissions from [35]. Copyright 2017 American Chemical Society

magnetic remanence and displaying a hysteresis loop at cryogenic temperatures, was reported by Copéret group in 2017 [36]. This special SMM was synthesized by two steps: (1) a five-coordinate  $\text{Dy}^{3+}$  molecular precursor,  $\text{Dy}[\text{OSi}(\text{O}^t\text{Bu})_3]_3[\kappa^2\text{-HOSi}(\text{O}^t\text{Bu})_3]$  which does not show any magnetic memory, was grafted on  $\text{SiO}_2$  generating  $1/\text{SiO}_2$ ; (2) the  $1/\text{SiO}_2$  was treated at  $400^\circ\text{C}$  under high vacuum affording the fully inorganic material  $\text{Dy}@/\text{SiO}_2$  as a white solid (Fig. 5). The extended X-ray absorption fine structure (EXAFS) results show that the “bare”  $\text{Dy}^{3+}$  in  $\text{Dy}@/\text{SiO}_2$  is also bound to five oxygen atoms. All organic fragments including the ligand of the  $\text{Dy}^{3+}$  molecular precursor are removed leaving the surface as the sole ligand; that is to say, the coordination environment of  $\text{Dy}^{3+}$  has been changed in spite of the coordination number unchanged, which should account for the different magnetic properties between the precursor and  $\text{Dy}@/\text{SiO}_2$ .



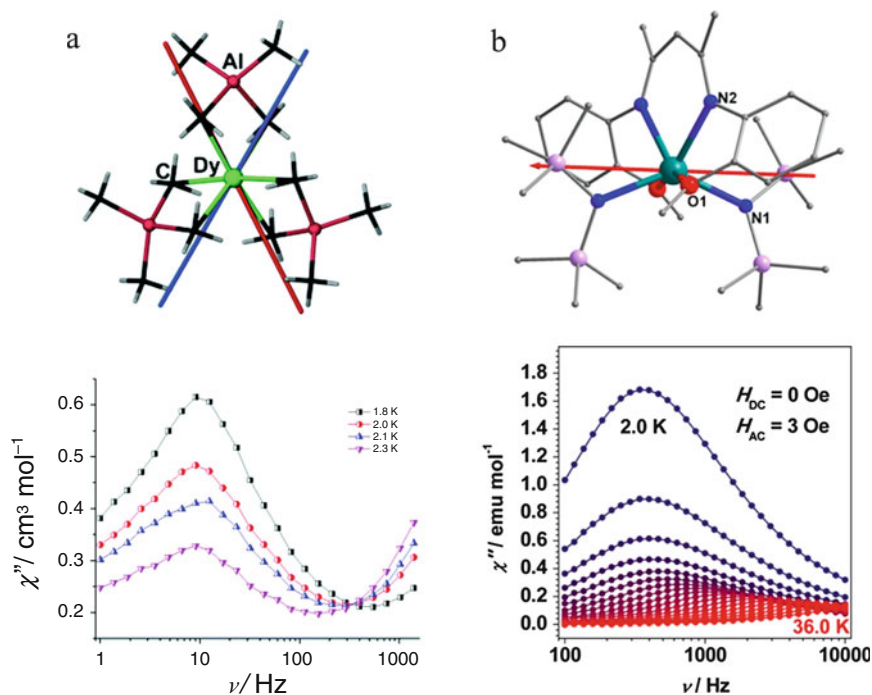
**Fig. 5** The strategy for immobilization of  $\text{Dy}^{3+}$  ions on metal oxide surfaces, based on a grafting step and a thermolytic step. Reprinted with permissions from [36]. Copyright 2017 American Chemical Society

### 1.3.5 Coordination Number 6

According to VSEPR model, there are two limiting geometries for six-coordination, the octahedral geometry and trigonal prismatic, the former is the most common coordination type by far for the transition metal ions, which has been widely employed in supramolecular chemistry such as the design of the molecular knot [37, 38] and the synthesis of metal–organic capsule [39, 40], while the latter is not so popular as the former due to the six donor atoms in this shape with the closer contact than in the octahedral geometry, resulting in the more unstable architecture. As for Ln-SMMs, there are few examples with six-coordination geometry in that most of them hardly exhibit SMM behavior under a zero dc field [24, 41, 42]. Taking the compound  $[\text{Dy}(\text{AlMe}_4)_3]$  with a slightly distorted octahedral geometry as an example, which was reported by Layfield group in 2014 [42] (Fig. 6). Dynamic magnetic susceptibility measurements on this compound reveal fast relaxation of the magnetization through quantum tunneling that was explained by ab initio calculations, whose results show that the ground KD is axial but displays significant transverse anisotropies and the first excited state is lacking uniaxiality with the principle axes orientated at an angle of  $38.7^\circ$  to the ground-state axes.

In 2017, another six-coordinate Ln-SMM,  $[(\text{L}^{\text{CO}})\text{Dy}(\text{N}^*)_2]$  ( $\text{L}^{\text{COH}} = \{\text{N}-(2\text{-MeO})\text{-C}_6\text{H}_5\}$ ) $\text{N} = \text{C}(\text{Me})\text{CH} = \text{C}(\text{Me})\text{N}(\text{H})\{\text{N}'-(2\text{-MeO})\text{C}_6\text{H}_5\}$ ),  $\text{HN}^* = \text{HN}(\text{SiMe}_3)_2$ ) with relatively rare reported trigonal prismatic geometry, was reported by Gao group in 2017 [43]. Magnetic analysis reveals that it is a typical SMM with an energy barrier of 190 K, evident by a strong frequency dependence of out-of-phase ac susceptibilities in the absence of an applied dc field (Fig. 6). To investigate the magnetic anisotropy in detail, ab initio calculations were performed and the results indicated that the magnetic easy axis was oriented along the direction of  $([\text{N}^*]^-)\text{N}-\text{N}([\text{N}^*]^-)$  with a small angle of  $5.9^\circ$  due to the shorter bond length of  $\text{Dy}-\text{N}([\text{N}^*]^-)$  and the significant negative charges locating on two  $[\text{N}^*]^-$  ligands, both of them leading to an axial ligand field.



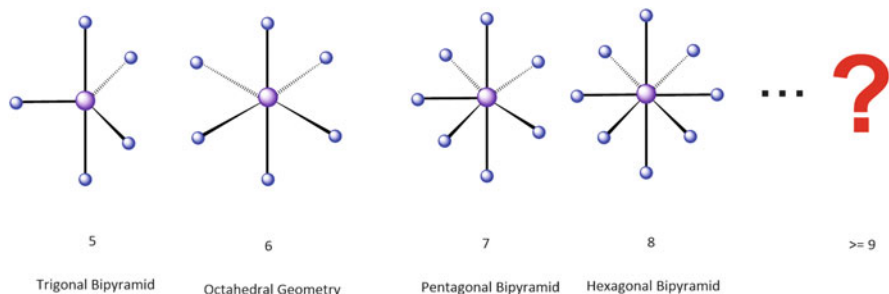


**Fig. 6** (a) Molecular structure (*top*) and frequency-dependent of  $\chi''$  (*bottom*) under a 1,000 Oe dc field for  $[\text{Dy}(\text{AlMe}_4)_3]$ . The blue line and red line represent the orientation of the magnetic moments of the ground and the first excited state, respectively. Reprinted with permissions from [42]. Copyright 2015 The Royal Society of Chemistry. (b) Molecular structure (*top*) and frequency-dependent of  $\chi''$  (*bottom*) for  $[(\text{L}^{\text{CO}})\text{Dy}(\text{N}^*)_2]$ . The red arrow represents the magnetic easy-axis orientation. Reprinted with permissions from [43]. Copyright 2017 American Chemical Society

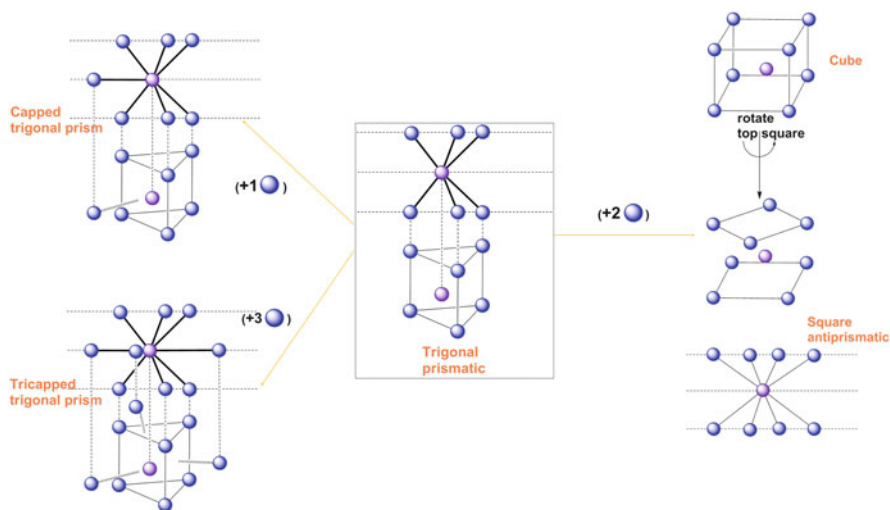
When the coordination number continues to be expanded beyond six-coordinate, there will be more options of geometry for lanthanide compounds, but if we view the shape of trigonal bipyramid (five-coordinate) geometry and octahedral (six-coordinate) geometry carefully, it is easy to find that they are associated with each other, by an increase in the number of groups around an equatorial plane while the number of groups on the axial sites remains unchanged. Following this tendency, one seven-coordinate shape, in which lanthanide ions are surrounded by five groups around the plane, was achieved called pentagonal bipyramid geometry which has been proved to be able to offer a very powerful axial ligand field for Ln-SMMs and in the same way, the hexagonal bipyramid geometry can also be obtained (Fig. 7).

However, as more and more ligands are placed into the plane around the lanthanide ions, the steric factors will be more important clearly. If the central metal is large enough or the steric hindrance of the ligand is very small or the distance between the metal and the ligand is considerably long, the heptagonal bipyramid geometry for nine-coordinate or octagonal bipyramid for ten-coordinate will be possible and by analogy in the same way for higher coordination number. In general, there is another





**Fig. 7** Selective geometries in the same form with coordination number from 5 to 8



**Fig. 8** Methods of converting the six-coordinate trigonal prismatic shape into various seven-, eight-, and nine-coordinate shapes

approach to the increase of coordination number that seems to be more popular than the above discussed by expanding the layers (or planes) of donors around a lanthanide ion [28], which is best explained by the following illustrations starting from the six-coordinate trigonal prismatic geometry (Fig. 8).

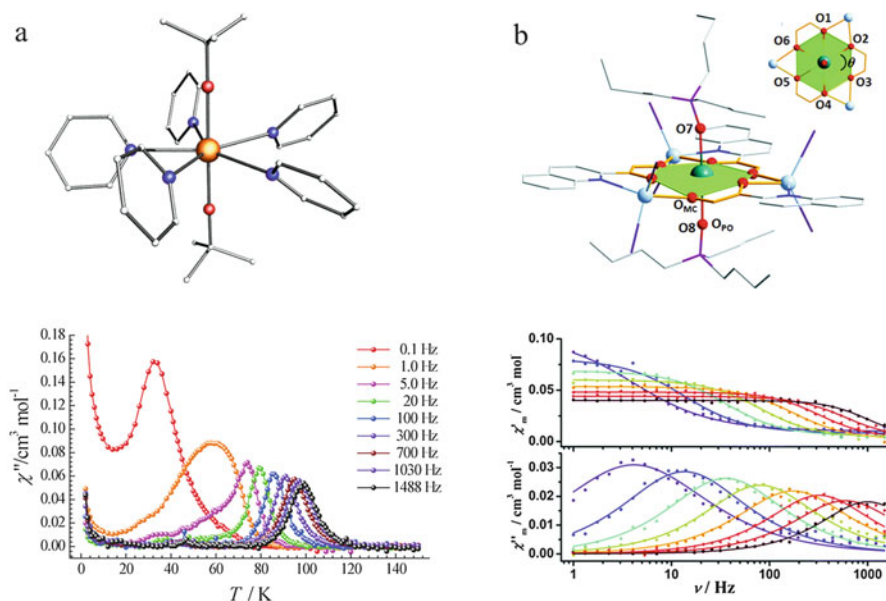
### 1.3.6 Coordination Number 7–9

*First approach* seen in Fig. 7.

Recently, the Ln-SMMs possessing pentagonal bipyramid coordination geometry are very popular in this field as they broke not only the energy barrier record of 938 K created by a double sandwich SMM with the square antiprism

(SAP) geometry [12] but also the blocking temperature record of 14 K, achieved in the  $N_2^{3-}$ -bridged  $Tb_2$  SMM with a very large magnetic coupling between spin centers [44]. In 2016, Tong group firstly reported two  $Dy^{III}$ -SMMs both with pentagonal bipyramid geometry, one is  $[Dy^{III}(OPCy_3)_2(H_2O)_5] Br_3 \cdot 2(Cy_3PO) \cdot 2H_2O \cdot 2EtOH$  with a large blocking temperature of 20 K at the average sweep rate of 200 Oe/s [14], and the other is  $[Dy^{III}(bbpen)Br]$  with a relatively high-energy barrier of 1,025 K [16]. The reason why both exhibit pronounced SMM behaviors is that the axial ligand field is much more stronger than equatorial components featuring the shorter axial bond length or more powerful negatively charged axial ligands or their combinations, which provide a new design strategy for high-performance Ln-SMMs and more importantly, it is probable a more excellent Ln-SMM will be obtained if a further step toward continuously strengthening the axial and weakening the equatorial ligand field is taken. Following this design criterion, a remarkable Ln-SMM,  $[Dy^{III}(O^tBu)_2(py)_5][BPh_4]$ , with a massive magnetic anisotropy exhibiting a very large energy barrier to spin reversal of 1,815 K was reported by Zheng group in 2017 [17]. The compound also has a pentagonal bipyramidal coordination geometry and the axial sites are occupied by anionic O-donors from more electron-donated *tert*-butoxide ligands with shorter Dy-O bond lengths of 2.110 and 2.114 Å indicating a very strong interaction between them, meanwhile the central metal ion was surrounded by five neutral N-donors from pyridine molecule with obviously much longer Dy-N bond lengths exceeding 2.5 Å; besides, the bond angles are close to a perfect situation including the O-Dy-O angle of 178.91°, close to 180° and O-Dy-N angles of 87.41–92.52° approaching to 90° (Fig. 9). Therefore, it is the strong axial ligand field and the highly symmetrical environment that determined the remarkable magnetic properties for this compound together. Although the peaks of out-of-phase ac signals of the compound were observed above 100 K already reaching the scope of application of liquid nitrogen, however the zero-field quantum tunneling of the magnetization (QTM) was still severely evident by the magnetic hysteresis curves, which will hamper the potential applications in information storage.

If we continue to add one donor to the equatorial plane based on the pentagonal bipyramid geometry, how will this affect the magnetic properties of Ln-SMMs? However, eight-coordinate Ln-SMMs with the hexagonal bipyramid geometry have not been reported as it is difficult to arrange six donors in the same plane in addition to linear axial coordination until a metallacrown generally made up by organic ligands and transition metal ions, 15-MC-5, joint with a suitable axial ligand, tributylphosphine oxide, were employed together to successfully construct two light lanthanide complexes  $[LnCd_3(Hquinha)_3(n-Bu_3PO)_2I_3] \cdot EtOH \cdot 2H_2O$  ( $H_2quinha =$  quinaldichydroxamic acid; Ln = Ce, Nd,) both with the hexagonal bipyramid geometry reported by Tong group in 2016 [45]. It is noted that according to the CF theory, there is a non-axial CF term  $B_6^0$  existing in  $D_{6h}$  symmetry, and so the off-axial mixing will appear for heavy lanthanide compounds with the maximum  $\Delta m_J$  more than 6. Ac susceptibility measurements reveal that the two compounds are both field-induced SMMs featuring no out-of-signals observed under a zero dc field due to the fast QTM but clear peaks of the signals appearing upon applying an optimized dc field (Fig. 9). Furthermore, the study

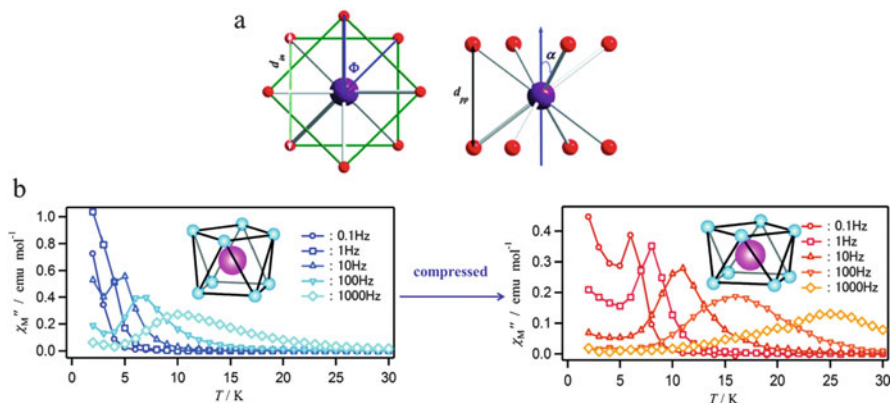


**Fig. 9** (a) Molecular structure (*top*) and temperature-dependent of  $\chi''$  (*bottom*) under a zero dc field for  $[\text{Dy}^{\text{III}}(\text{O}^t\text{Bu})_2(\text{py})_5][\text{BPh}_4]$ . Reprinted with permissions from [17]. Copyright 2016 WILEY-VCH. (b) Molecular structure (*top*) and frequency-dependent of  $\chi''$  (*bottom*) for  $[\text{CeCd}_3(\text{Hquinha})_3(\text{n-Bu}_3\text{PO})_2\text{I}_3]_3 \cdot \text{EtOH} \cdot 2\text{H}_2\text{O}$  under a 1,500 Oe dc field. Reprinted with permissions from [45]. Copyright 2016 The Royal Society of Chemistry

of the relaxation mechanism indicated that the relaxation process for these two compounds was dominated by Raman process rather than Orbach process, which account for the small energy barrier and large pre-exponential factor. Nonetheless, the discovery of Ln-SMMs with the hexagonal bipyramid geometry provided us a strategy to achieve higher axial symmetries.

*Second approach* seen in Fig. 8.

For eight-coordinate lanthanide compounds, the most common coordination geometries are triangular dodecahedron and SAP. It is well-known that the first Ln-SMM possessed a SAP geometry with close to  $D_{4d}$  symmetry [7], where the lanthanide ion was coordinated by eight pyrrole nitrogen atoms from two phthalocyanine ligands parallel to each other. In addition, there are other almost equally important species including LnPOM and Dy- $\beta$ -diketones series which are also in SAP coordination environments [46, 47]. As for ideal SAP geometry, the two most important parameters put forward by Dante Gatteschi,  $\Phi$  and  $\alpha$ , are  $45^\circ$  and  $54.74^\circ$ , respectively, the former defined by the torsion angle between upper and lower squares and the latter referring to the angle between the tetragonal axis and coordination chemical bonds (Fig. 10). If  $\alpha > 54.74^\circ$ , the SAP is compressed and conversely called elongated. In 2008, the cationic complex  $[\{\text{Pc}(\text{OEt})_8\}_2\text{Dy}]^+$  ( $\text{SbCl}_6$ ) $^-$  was prepared successfully by two-electron oxidation of the anionic complex  $[\{\text{Pc}(\text{OEt})_8\}_2\text{Dy}]^-(\text{n-Bu}_4\text{N})^+$ , reported by Ishikawa group [49]. Ac

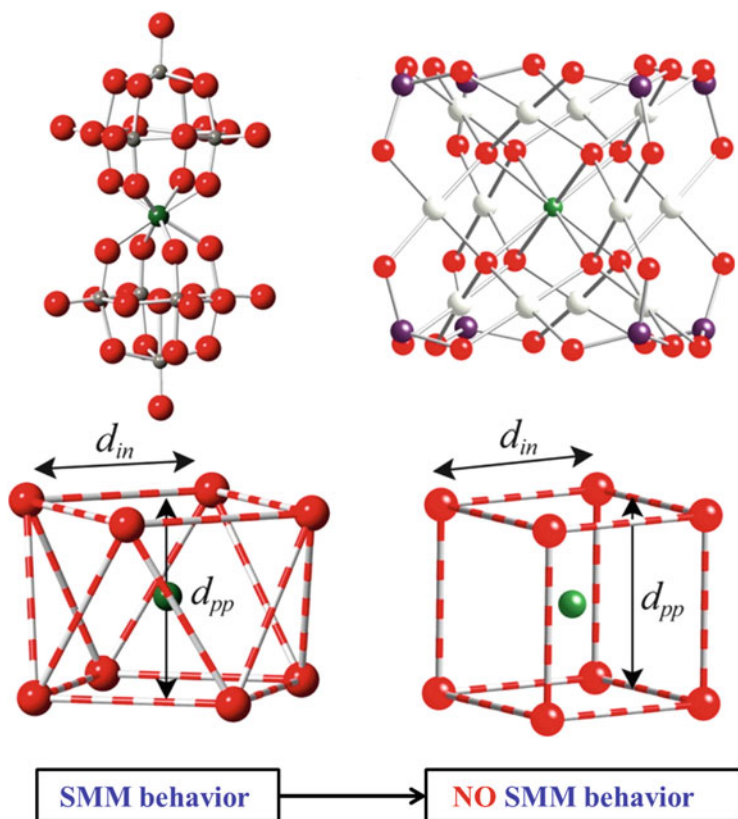


**Fig. 10** (a) Details of the relevant structural parameters in a SAP. *Left* (view along the  $S_8$  axis):  $d_{pi}$ , the shorter L–L distance in the  $L_4$  square and  $\Phi$ , the skew angle, the torsion angle between upper and lower squares. *Right* (lateral view, perpendicular to the  $S_8$  axis which is represented by the blue arrow):  $d_{pp}$ , the distance between the two parallel  $L_4$  squares and  $\alpha$ , the angle between the tetragonal axis and coordination chemical bonds. Reprinted with permissions from [48]. Copyright 2011 The Royal Society of Chemistry. (b) Temperature-dependent of  $\chi''$  under a zero dc field for the anionic complex  $[\{Pc(OEt)_8\}_2Dy]^- (n-Bu_4N)^+$  (*left*) and the cationic complex  $[\{Pc(OEt)_8\}_2Dy]^+ (SbCl_6)^-$  (*right*). Reprinted with permissions from [49]. Copyright 2008 American Chemical Society

susceptibility measurements showed that the peak of out-of-phase ac signals of 1,000 Hz for the cationic compound was observed at about 25 K which is 15 K higher than that of the anionic complex, indicating the significant increase of the barrier energy for the cationic compound. In fact, the effective energy barrier of  $[\{Pc(OEt)_8\}_2Dy]^+$  increases about twice as large as that of  $[\{Pc(OEt)_8\}_2Dy]^-$  due to the geometric changes caused by the oxidation process. In the case of bis(phthalocyaninato) lanthanide compounds, when the anionic complex is oxidized, the electrons in the highest occupied molecular orbital are removed first resulting in a shorter Pc–Pc distance  $d_{pp}$ , which has been confirmed by the density functional theory (DFT) calculation [50]; that is to say, the SAP coordination polyhedral was compressed longitudinally (the increase of  $\alpha$ ) owing to the oxidation, leading to the increasing of energy gap between the lowest and second lowest sublevels in the ground multiplet due to a more stronger interaction between the single lanthanide ion electron density and the crystal field environment.

In contrast, the distortion of  $\Phi$  will make a more important effect on the magnetic properties of Ln-SMMs due to the change of symmetry, for example, from  $45^\circ$  in the  $D_{4d}$  symmetry to  $0^\circ$  in the  $O_h$  symmetry. As is well-known, in terms of crystal field parameters, only  $q = 0$  term containing  $B_2^0 B_4^0 B_6^0$  must be considered for ideal  $D_{4d}$  symmetry indicating a perfect axial ligand field, so if the lanthanide ions are placed in this ligand field, the wavefunctions will be described by pure  $\pm M_J$  values without mixing. In the case of tetrahedron, octahedron, or cube environments which all possess the  $O_h$  symmetry, the  $q = \pm 4$  terms also must be included in a fixed ratio with the  $q = 0$  term implying that the transverse components are introduced. It

should be remembered that the parameters  $B_4^0$  and  $B_6^0$  are invariant with respect to  $\Phi$ ; on the contrary, the  $q \neq 0$  terms will be changed under rotation of the reference system [48]. Taking the cube symmetry as an example, this system can be defined only by two parameters,  $B_4^0$  and  $B_6^0$  due to  $B_2^0 = 0$  and  $B_4^4/B_4^0 = 5$ ,  $B_6^4/B_4^0 = -21$ . So, we can find the reason why this geometry is not suitable for Ln-SMMs from the view of CF parameters [51]: (1) the key parameter  $B_2^0$  which determines the gap between the ground doublets and the excited states is zero, and (2) the presence of the parameters  $B_4^4$  and  $B_6^4$  will lead to an extensive mixing of wavefunctions. Fortunately, LnPOM compounds can provide proper examples to prove the impact of the distortion of  $\Phi$  on the magnetic anisotropy. In 2008, the first LnPOM compound exhibiting SMM behavior under a zero dc field,  $[\text{ErW}_{10}\text{O}_{36}]^{9-}$ , was reported by Coronado group [46]. X-ray structure analysis showed that the  $\text{Er}^{\text{III}}$  is sandwiched by two anionic  $[\text{W}_5\text{O}_{18}]^{6-}$  moieties exhibiting the SAP geometry and each moiety is twisted  $44.2^\circ$  with respect to the other, very close to  $45^\circ$  (Fig. 11). Low-temperature

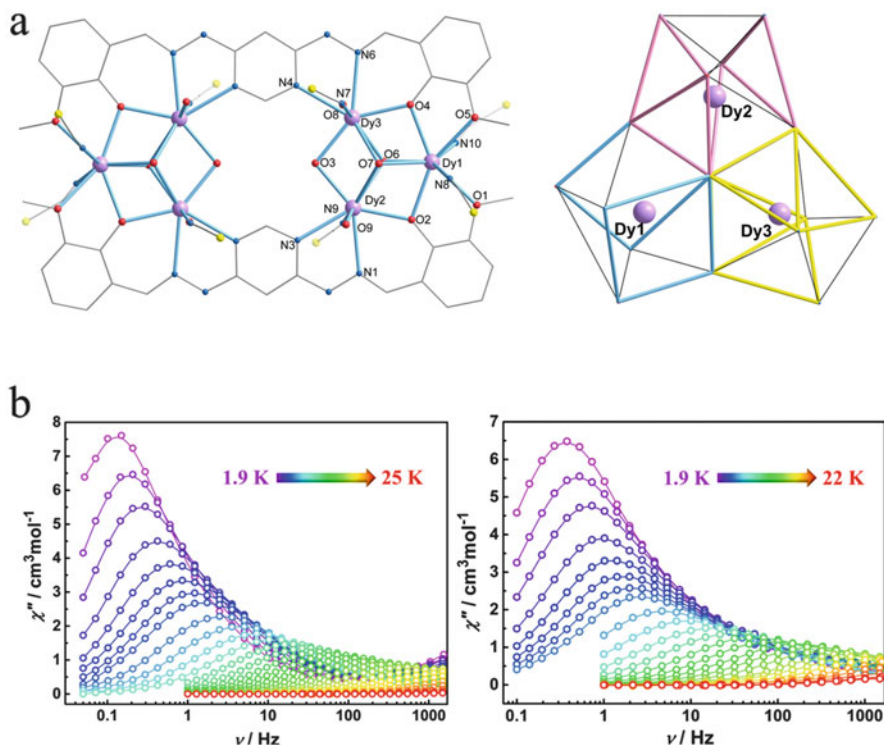


**Fig. 11** Schematic structures of two different POM complexes with interesting coordination symmetry (*top*) and their coordination polyhedral (*bottom*), (a) for  $[\text{ErW}_{10}\text{O}_{36}]^{9-}$  and (b) for  $[\text{ErPd}^{\text{II}}_{12}(\text{As}^{\text{V}}\text{Ph})_8\text{O}_{32}]^{5-}$ . Reprinted with permissions from [52]. Copyright 2012 American Chemical Society

ac magnetic susceptibility measurements revealed the typical SMM behavior featuring the frequency dependence of the  $\chi''$  peaks with the energy barrier of 55.2 K. Taking a detailed analysis on the structure, it can be found that the interplanar distance,  $d_{pp} = 2.47 \text{ \AA}$ , is smaller than the average O–O distance within the oxygen-based square planes,  $d_{pi} = 2.85 \text{ \AA}$ , clearly indicating an axial compression of the SAP. The theoretical calculations demonstrated that the compound preserved a 99.96% purity of the ground-state doublet corresponding to the highest  $M_J = \pm 15/2$  separated from the first excited state  $M_J = \pm 13/2$  by 81.7 K close to the energy barrier determined experimentally, which explained the SMM behavior observed in this compound [52]. However, when the  $\text{Er}^{\text{III}}$  was placed in a cube environment with the  $O_h$  symmetry, taking the compound  $[\text{ErPd}^{\text{II}}_{12}(\text{As}^{\text{V}}\text{Ph})_8\text{O}_{32}]^{5-}$  as an example reported by Kortz group in 2010 [53], the slow relaxation of magnetization of the compound vanished. Calculations performed on the compound revealed that the ground-state doublet was mixed extensively by the most important contributions  $M_J = \pm 1/2$ , followed by the  $\mp 1/2$ ,  $\mp 3/2$ , and  $\pm 5/2$ , leading to a fast QTM. Meanwhile, the ground state was mainly described by the smallest  $M_J$  value ( $\pm 1/2$ ) which explain why this compound does not show SMM behavior like the  $[\text{ErW}_{10}\text{O}_{36}]^{9-}$ .

In addition, another common eight-coordinate environment is triangular dodecahedron presenting  $D_{2d}$  symmetry, closely related to  $S_4$ . The most important example for this geometry was found in the salts  $\text{Er}_x\text{Ca}_{1-x}\text{WO}_4$  and  $\text{LiHo}_x\text{Y}_{1-x}\text{F}_4$ . Taking the latter as an example, theoretical calculations showed that it is the presence of non-negligible extradiagonal parameters  $B_4^4$  and  $B_6^4$  that lead to the mixture of  $M_J$  evident by the calculated splitting diagram, similarly to cube environments. In 2015, our group reported a  $\text{Dy}_6$  cluster, herein abbreviated as  $\text{Dy}_6\text{-SCN}$ , featuring a fascinating  $\text{Dy}_3 + \text{Dy}_3$  structure (Fig. 12) [54]. Structural analysis shows that the two  $\text{Dy}_3$  units are identically connected by a multidentate Schiff-base ligand. Within the triangle, all of the  $\text{Dy}^{\text{III}}$  are eight-coordinate but with different coordination geometries:  $\text{Dy}1$  has a slightly distorted SAP geometry whereas  $\text{Dy}2$  and  $\text{Dy}3$  possess the distorted dodecahedral geometry. Interestingly, the ac susceptibility measurements exhibited the possible occurrence of two relaxation processes with the first peak observed at lower frequencies and a tail of the second peak appearing at higher frequencies. Compared to the analogical complex  $\text{Dy}_6\text{-NO}_3$  with the distorted monocapped square-antiprismatic geometries for  $\text{Dy}2$  and  $\text{Dy}3$ , which show a single relaxation process at the same conditions, it can be concluded that the different magnetic properties derive from the different coordination environments, but why does the triangular dodecahedron geometry seem to be better for magnetic properties than monocapped square-antiprismatic geometry in this system? Inspired by the calculations carried on  $\text{LiHo}_x\text{Y}_{1-x}\text{F}_4$ , it can be speculated that although the parameters  $B_4^4$  and  $B_6^4$  indeed lead to the mixture of  $M_J$ , there is no occurrence of QTM within the ground-state doublets due to the poor overlap of the two wavefunctions which usually was employed to describe the KD states. Therefore, the spin relaxation will take place by tunneling within the first excited-state doublets for  $\text{Dy}2$  and  $\text{Dy}4$  in  $\text{Dy}_6\text{-SCN}$  making some contributions to the energy barrier.

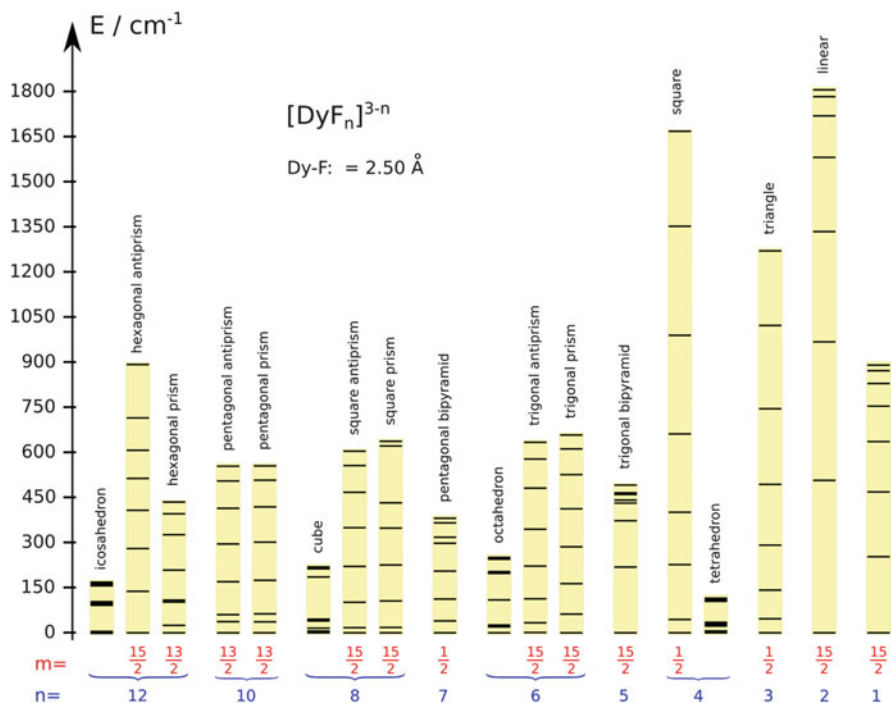




**Fig. 12** (a) Molecular structure (*left*) and coordination polyhedra observed in Dy<sub>6</sub>-SCN (*right*). (b) Frequency-dependent of  $\chi''$  under a zero dc field for Dy<sub>6</sub>-SCN (*left*) and Dy<sub>6</sub>-NO<sub>3</sub> (*right*). Reprinted with permissions from [54]. Copyright 2015 The Royal Society of Chemistry

## 2 Geometry-Dependent Magnetic Behaviors in Lanthanide Single Molecule Magnets

Through discussion in the first section, it can be concluded that in most cases distinct coordination geometries of lanthanide ions will result in different magnetic properties for Ln-SMMs. In order to evaluate the general dependence of CF parameters on the geometry and symmetry of the coordination environments, the hypothetical complexes [DyF<sub>n</sub>]<sup>3-n</sup>, where the dysprosium ion is three-valent and the distance of Dy-F was fixed at 2.5 Å, were employed to calculate the CF spectrum for various complexes with different coordination numbers and geometries [21]. It is noted specially that the predominant bond was excluded in the calculation process as all Dy-F bonds are equal in length and strength for each complex, so the calculation results will focus more on the effect of the symmetry on the magnetic properties.



**Fig. 13** Structure of CF doublets of the ground-state  $J = 15/2$  manifold of hypothetical  $[\text{DyF}_n]^{3-n}$  complexes, calculated ab initio for various coordination geometries at an arbitrary fixed Dy-F distance (2.50 Å). Reprinted with permissions from [21]. Copyright 2016 American Chemical Society

From the CF spectrum seen in Fig. 13, the following conclusions can be drawn:

1. The combination of low coordination numbers and uniaxial symmetry will lead to the largest CF splitting.
2. The spherical-symmetry electrostatic potential distribution of the ligand will result in the smallest CF splitting. So, the complexes which possess cubic (including cube, octahedron, and tetrahedron) and icosahedral coordination geometry did not show any SMM behavior in principle.
3. The complexes which possess axial coordination geometry including two bipyramids, monopyrmaid as well as prism, etc. exhibited typical SMM behavior owing to the presence of strong anisotropic KD states in these environments. Moreover, the axiality and the extent of CF splitting depend on the ratio between the transverse magnetic anisotropy deriving from equatorial CF contributions and the axial magnetic anisotropy caused by axial ligand fields. The smaller the ratio, the stronger the axiality will be and if the ratio is zero, the perfect axial ligand field can be obtained like in F-Dy-F and Dy-F complexes only with two and one coordination number, respectively.

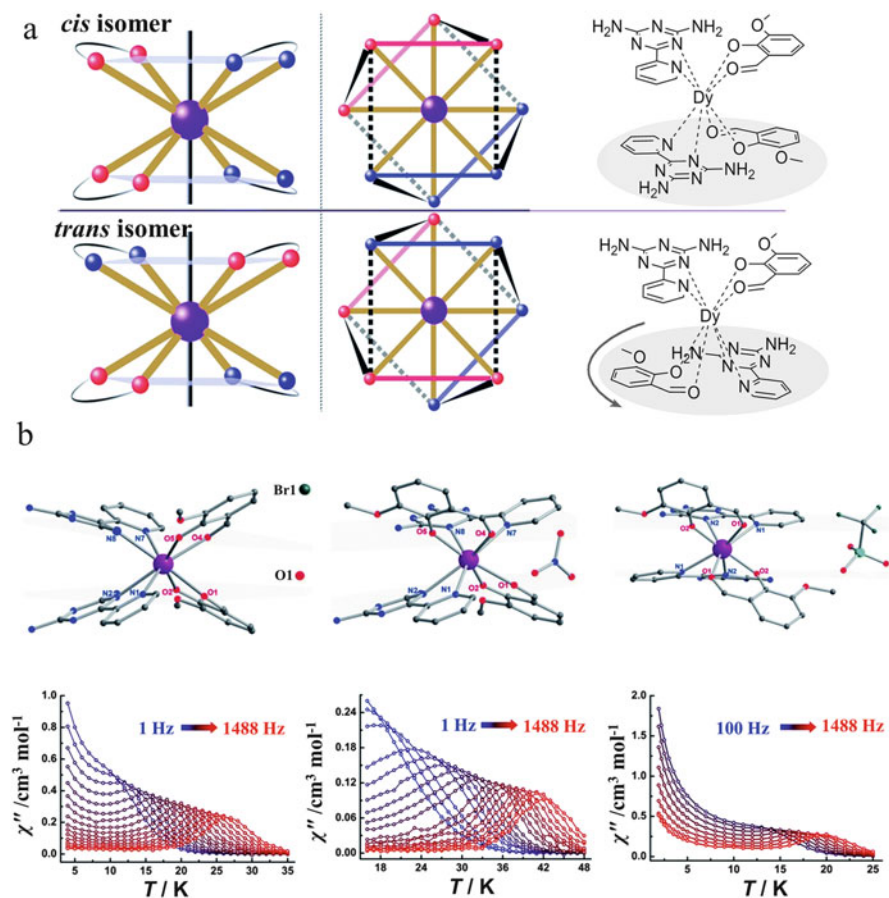


4. One should note that even though the environments of trigonal and pentagonal bipyramid geometry can possess doublets of perfect axiality, the QTM still appears between the doublets if the order of the main rotational axes in such complexes is lower than 8, which has been proved by the complex  $[\text{Dy}^{\text{III}}(\text{O}^t\text{Bu})_2(\text{py})_5][\text{BPh}_4]$ , whose energy barrier is up to 1,815 K whereas the blocking temperature is only 14 K. In 2017, a dysprosium metallocene SMM,  $[(\text{Cp}^{\text{III}})_2\text{Dy}]^+$  ( $\text{Cp}^{\text{III}} = 1,2,4\text{-tri(tert-butyl)cyclopentadienide}$ ), was reported by Layfield group and Mills group [18, 19] not only with a record energy barrier of 1,837 K but also a record blocking temperature up to 60 K due to a higher symmetry environment for this compound. So, the symmetry of the molecule also needs to be considered carefully in the design of high-temperature Ln-SMMs.

In this section, we will focus on the methods of regulating magnetic dynamics of Ln-SMMs by varying the ligand field. It is noteworthy that when the ligand field was changed, the geometry maybe also be altered but perhaps unchanged just with fine-tunings.

## 2.1 Constitutional (Structural) Isomerism Effect

In 2016, our group reported a series of mononuclear dysprosium complexes with the formula of  $[\text{DyLz}_2(\text{o-vanilin})_2]\cdot\text{X}\cdot\text{solvent}$  ( $\text{Lz} = 6\text{-pyridin-2-yl-[1,3,5]triazine-2,4-diamine}$ ;  $\text{X} = \text{Br}^-, \text{NO}_3^-, \text{CF}_3\text{SO}_3^-$ ) and all complexes have the SAP geometry with an approximate  $D_{4d}$  symmetry here abbreviated as 8-Dy-Br, 8-Dy- $\text{NO}_3$ , and 8-Dy- $\text{CF}_3\text{SO}_3$ , respectively [13]. In these three complexes, the  $\text{Dy}^{\text{III}}$  was coordinated by four nitrogen atoms and four oxygen atoms coming from the two Lz ligands and the two o-vanilin ligands, respectively (Fig. 14). Compared to 8-Dy-Br and 8-Dy- $\text{CF}_3\text{SO}_3$ , the complex 8-Dy- $\text{NO}_3$  has a longitudinally elongated coordination environment due to the insertion of the  $\text{NO}_3^-$  between the two coordination planes, while in the two former complexes, the counter-anions,  $\text{Br}^-$  and  $\text{CF}_3\text{SO}_3^-$ , reside outside these planes leading to a longitudinally contracted circumstance. Meanwhile, the complex 8-Dy- $\text{CF}_3\text{SO}_3$  was further compressed compared to 8-Dy-Br due to the stronger  $\pi$ -stacking interactions. A closer look at the structural features reveals that the complexes 8-Dy-Br and 8-Dy- $\text{CF}_3\text{SO}_3$  both have the *cis* configuration due to the two Lz ligands being in the *cis* position relative to each other and as a comparison, the complex 8-Dy- $\text{NO}_3$  possesses a *trans* configuration, which is most likely induced by the change of counter-anions. Ab initio calculations were performed on the above complexes suggesting that all complexes have a perfectly axial ground state with zero transversal components and the magnetic relaxation goes more or less through the same state. In fact, obviously different magnetic properties were observed by ac susceptibility measurements with the peaks of out-of-phase magnetic susceptibility signals appearing under 1,488 Hz at 27 K (8-Dy-Br), 42 K (8-Dy- $\text{NO}_3$ ), and 20 K (8-Dy- $\text{CF}_3\text{SO}_3$ ) under a zero dc field, respectively, indicating the almost same



**Fig. 14** (a) Schematic drawing of the complexes (*right*) and absolute configurations with top views (*middle*) for the *cis* (*top*) and *trans* (*bottom*) configurations. (b) Molecular structure and temperature-dependent of  $\chi''$  under a zero dc field for 8-Dy-Br (*left*), 8-Dy-NO<sub>3</sub> (*middle*), and 8-Dy-CF<sub>3</sub>SO<sub>3</sub> (*right*). Reprinted with permissions from [13]. Copyright 2016 The Royal Society of Chemistry

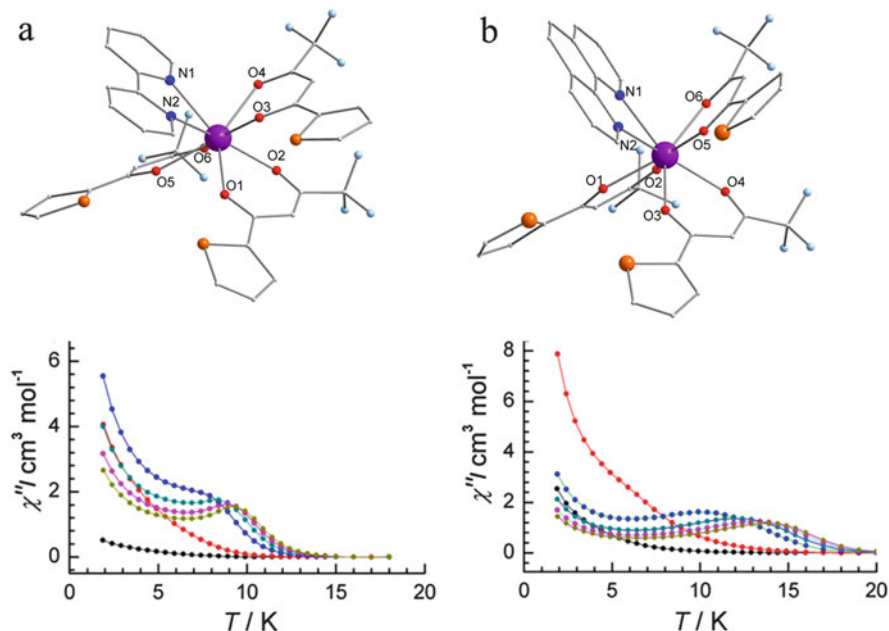
properties for 8-Dy-Br and 8-Dy-CF<sub>3</sub>SO<sub>3</sub> but an extraordinarily remarkable SMM behavior for 8-Dy-NO<sub>3</sub> with the highest energy barrier of 615 K among them, which might be ascribed to the rotation of the coordinating plane of the SAP geometry.

In summary, it is the different counter-anions that result in the different structural features which determine the different magnetic properties. Undoubtedly, this work provide a new way, the *cis-trans* isomerism, to modulate the geometries of Ln-SMMs so as to facilitate spin reversal climbing up to higher energy levels.

## 2.2 Ligand Influences

Obviously, each ligand is unique owing to its shape, size as well as coordination model. It is well-known that the lanthanide ions have the bigger ionic radii compared to the transition metal ions leading to the higher coordination numbers and more coordination geometries. So, it is easy to come up with the method of modulating coordination environments of Ln-SMMs by changing the ligands.

In 2011, our group reported two mononuclear Dy<sup>III</sup>-SMMs synthesized through the substitution of coordinated water molecules of [Dy(TTA)<sub>3</sub>(H<sub>2</sub>O)<sub>2</sub>] (TTA = 4,4,4-trifluoro-1-(2-thienyl)-1,3-butanedionate) by using 2,2-bipyridine (bpy) and 1,10-phenanthroline (phen) capping ligands [55]. Structural analyses revealed that each Dy<sup>III</sup> ion is coordinated by six oxygen atoms and two nitrogen atoms coming from three TTA anions and above capping ligands, respectively, forming an O<sub>6</sub>N<sub>2</sub> coordination environment corresponding to the SAP geometry (Fig. 15), so there are two key parameters that need to be jointly considered: the skew angle  $\Phi$  and the magic angle  $\alpha$ . These two compounds are slightly longitudinally compressed due to the  $\alpha$  parameters of 57.2° for Dy(TTA)<sub>3</sub>(bpy) and 56.4° for Dy(TTA)<sub>3</sub>(phen), respectively, both larger than 54.74°. Meanwhile, compared to the compound Dy(TTA)<sub>3</sub>(phen) with the  $\Phi$  value of 42.1°, the compound Dy(TTA)<sub>3</sub>(bpy) seems to deviate more from an

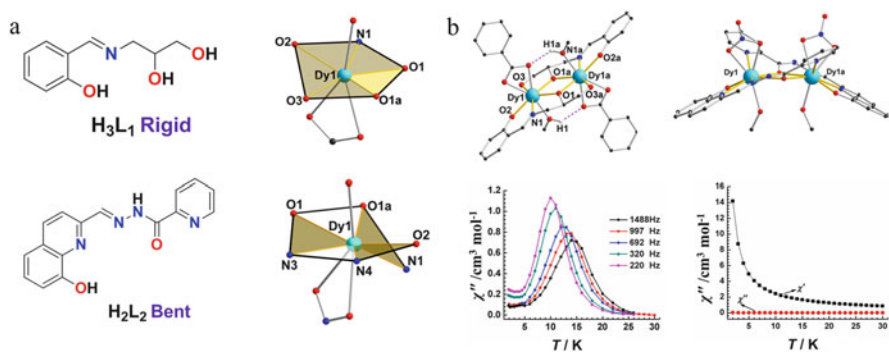


**Fig. 15** (a) Molecular structure (*top*) and temperature-dependent of  $\chi''$  under a zero dc field (*bottom*) for Dy(TTA)<sub>3</sub>(bpy). (b) Molecular structure (*top*) and temperature-dependent of  $\chi''$  under a zero dc field (*bottom*) for Dy(TTA)<sub>3</sub>(phen). Reprinted with permissions from [55]. Copyright 2011 WILEY-VCH

ideal SAP geometry owing to the smaller  $\Phi$  value of  $39.7^\circ$ . Although the two complexes have the same coordination geometry, the small difference in skew angles strongly affected the dynamics behavior of the system evident by the ten times faster QTM rates found in  $\text{Dy}(\text{TTA})_3(\text{bpy})$  than that in  $\text{Dy}(\text{TTA})_3(\text{phen})$  due to the larger deviation from the ideal SAP geometry for the former. Besides, another more intuitive distinction can be observed from the variable-temperature magnetic susceptibility data, but it is worth noticing that the diluted samples exhibited almost equal energy barrier of 96 K for  $\text{Dy}(\text{TTA})_3(\text{bpy})$  and 102 K for  $\text{Dy}(\text{TTA})_3(\text{phen})$  inherently reflecting the nearly same distributions of low-lying states for these two complexes due to the similar values of  $\alpha$ . Compared to the parameter  $\alpha$ , the variation of  $\Phi$  maybe play a more important effect on the dynamic magnetic properties of Ln-SMMs.

In principle, the different QTM rates seen in these two complexes are due to the employment of different capping ligands, resulting in a subtle but crucial structural difference in respective coordination environments and further affecting the dynamic magnetic behavior.

In 2013, two dinuclear dysprosium compounds,  $[\text{Dy}_2(\text{HL}_1)_2(\text{PhCOO})_2(\text{CH}_3\text{OH})_2]$  and  $[\text{Dy}_2(\text{L}_2)_2(\text{NO}_3)_2 \cdot (\text{CH}_3\text{OH})_2] \cdot 2\text{CH}_3\text{OH} \cdot 4\text{H}_2\text{O}$ , abbreviated as  $\text{Dy}_2\text{-L}_1$  and  $\text{Dy}_2\text{-L}_2$ , were assembled exhibiting the distinct coordination geometry for lanthanide ions due to the employment of two ligands with different coordination models, the former displaying the hula hoop-like geometry and the latter showing the broken hula hoop-like geometry, reported by our group [56]. Ac susceptibility measurements showed that the compound  $\text{Dy}_2\text{-L}_1$  is a typical SMM with the peak of out-of-phase signals of magnetic susceptibility appearing at 15 K for 1,488 Hz due to the axial ligand field in combination with the strong ferromagnetic interactions. As for the compound  $\text{Dy}_2\text{-L}_2$ , no SMM behavior was observed under a zero dc field mainly resulting from the broken coordination geometry which introduces a significant transverse anisotropy terms leading to the fast QTM (Fig. 16).



**Fig. 16** (a) Schematic diagram of ligands (left) and the coordination geometry for the central lanthanide ions in  $\text{Dy}_2\text{-L}_1$  (top right) and  $\text{Dy}_2\text{-L}_2$  (bottom right). (b) Molecular structure and temperature-dependent of  $\chi''$  under a zero dc field for  $\text{Dy}_2\text{-L}_1$  (left)  $\text{Dy}_2\text{-L}_2$  (right). Reprinted with permissions from [56]. Copyright 2013 American Chemical Society

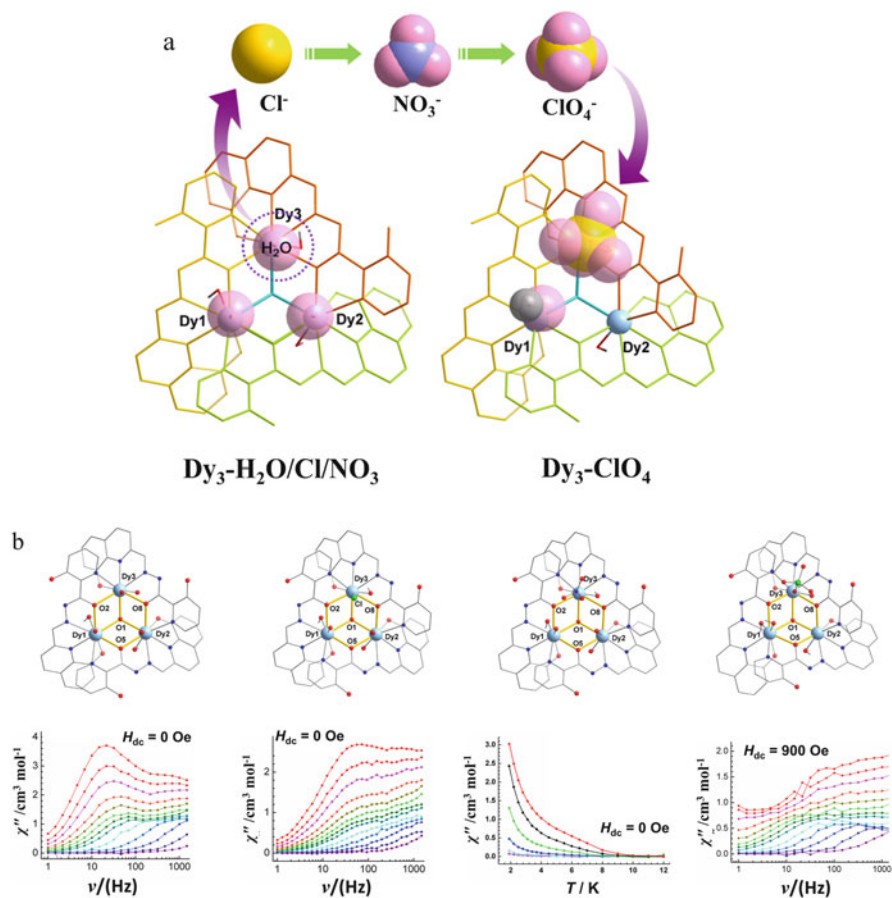
The reason why the hula hoop-like geometry in the compound  $\text{Dy}_2\text{-L}_2$  was broken is the bent nature of  $\text{H}_2\text{L}_2$  ligand, while the  $\text{H}_3\text{L}_1$  ligand is rigid with the two coordination pockets arranged linearly.

### 2.3 Anion Inducing

It is well-known that the templating effect of different anions has been widely investigated in coordination-driven self-assembly as the anions can not only play an important role in balancing the charge of the system but also induce the formation of various architectures with different coordination geometries and sizes [57–59]. Similarly, the anion-inducing effects can also be used in the field of Ln-SMMs based on coordination chemistry like supramolecular self-assembly.

In 2015, a family of four  $\text{Dy}_3$  triangular circular helicates, herein abbreviated as  $\text{Dy}_3\text{-H}_2\text{O}$ ,  $\text{Dy}_3\text{-Cl}$ ,  $\text{Dy}_3\text{-NO}_3$ , and  $\text{Dy}_3\text{-ClO}_4$ , were synthesized by using the different dysprosium (III) salts with the aim of investigating the effect of anion size on the local coordination geometry [60]. Structural analyses suggested that the four compounds are essentially isomorphous all with a similar triangular core structure and the critical difference is distinct terminal coordination anions at the Dy3 site, namely  $\text{H}_2\text{O}$ ,  $\text{Cl}^-$ ,  $\text{NO}_3^-$ , and  $\text{ClO}_4^-$ , respectively, showing a trend of increasing size (Fig. 17). Through the continuous shape measures (CShM) method using SHAPE software, we can find that the compounds  $\text{Dy}_3\text{-H}_2\text{O}$  and  $\text{Dy}_3\text{-Cl}$  exhibit a similar coordination environment with a nine-coordinated monocapped square-antiprismatic geometry for all of the  $\text{Dy}^{\text{III}}$  sites. However, as for the compounds  $\text{Dy}_3\text{-NO}_3$  and  $\text{Dy}_3\text{-ClO}_4$ , the CShM value at the Dy3 site was changed significantly as the result of the larger  $\text{NO}_3^-$  and  $\text{ClO}_4^-$  anions coordinated to Dy3 ion making a prominent effect on the coordination environments. Remarkably, the coordination environments for the Dy1 and Dy2 sites in all complexes are completed by two solvent molecules ( $\text{H}_2\text{O}$  and  $\text{CH}_3\text{OH}$ ) except the Dy2 site in  $\text{Dy}_3\text{-ClO}_4$  which is eight-coordinated with only one solvent molecule due to the presence of the bulky  $\text{ClO}_4^-$  anion. So, the compounds  $\text{Dy}_3\text{-NO}_3$  and  $\text{Dy}_3\text{-ClO}_4$  exhibited completely different coordination environments at all three Dy sites from those in compounds  $\text{Dy}_3\text{-H}_2\text{O}$  and  $\text{Dy}_3\text{-Cl}$ . The dynamic magnetic properties of these four compounds were investigated under a zero dc field by using ac susceptibility measurements and the results indicated that the compounds  $\text{Dy}_3\text{-H}_2\text{O}$  and  $\text{Dy}_3\text{-Cl}$  show a similar SMM behavior with broad frequency-dependent peaks demonstrating the presence of two-step relaxation process due to the different spin centers in these systems. Conversely and expectedly, the compounds  $\text{Dy}_3\text{-NO}_3$  and  $\text{Dy}_3\text{-ClO}_4$  only display the strong frequency-dependent out-of-phase signals but no peaks were observed below 10 K suggesting the onset of slow relaxation of the magnetization and the presence of fast QTM.

In summary, it is the different sizes of terminal ligands ( $\text{H}_2\text{O}$ ,  $\text{Cl}^-$ ,  $\text{NO}_3^-$ , and  $\text{ClO}_4^-$ ) around the Dy3 site in these three compounds that lead to the subtle differences in their local environments and further affect the dynamics of magnetic relaxation proving that the anion-induced effect is a promising method in the fine-tuning of the magnetic properties of Ln-SMMs.



**Fig. 17** (a) Crystal structures of the four compounds with the terminal ligand around Dy centers represented by space-filling models. (b) Molecular structure and frequency/temperature-dependent of  $\chi''$  for Dy<sub>3</sub>-H<sub>2</sub>O, Dy<sub>3</sub>-Cl, Dy<sub>3</sub>-NO<sub>3</sub> (0 Oe dc field), and Dy<sub>3</sub>-ClO<sub>4</sub> (900 Oe dc field), respectively (from left to right). Reprinted with permissions from [60]. Copyright 2015 American Chemical Society

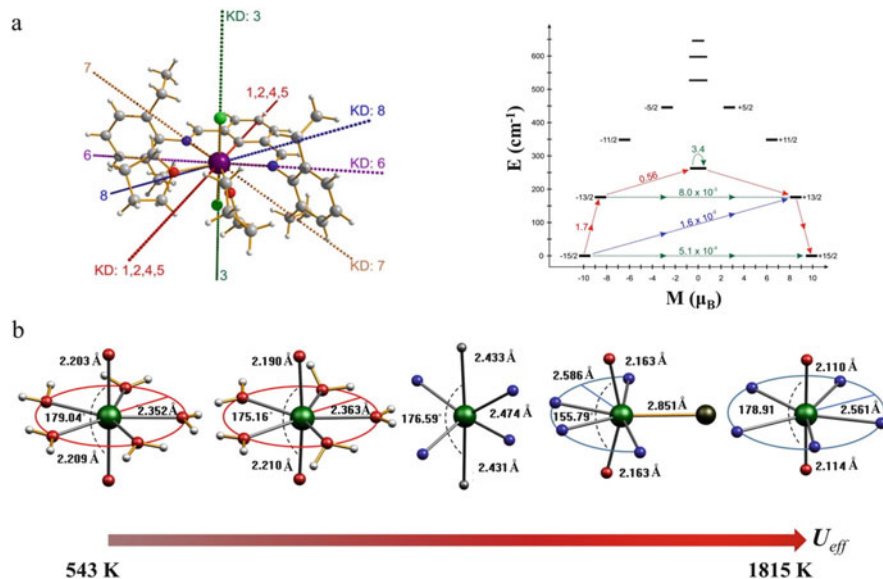
## 2.4 Predominant Bonds in Lanthanide Single Molecule Magnets

We have seen in the previous sections that the large CF splitting and axially of the KD doublets for Ln-SMMs will be obtained in low-coordinated environments best with the coordination number of one or two. However, it is really difficult to construct lanthanide compounds with one, two, or even three chemical bonds due to the large ionic radii and various coordination models of lanthanide ions. Moreover, the instability of the compound in the air further increases the difficulty of synthesis. At the same time, the current situation is that most of the lanthanide compounds are in a low-symmetry environment with coordination number from 8 to 12. Fortunately, in



the compound  $\text{Dy}(\text{L})\text{Cl}_2(\text{THF})_2$  ( $\text{LiL} = (2,6\text{-bis}(\text{E})\text{-}((2,6\text{-diethylphenyl})\text{imino})\text{methylphenyl})\text{lithium}$ ), herein abbreviated as DyNCN, a new relaxation mechanism, the magnetic relaxation passing through the second excited KD, was firstly discovered by our group in 2012 [22, 61]. Ab initio calculations indicated that the main anisotropy axes in the ground and first excited KDs are co-parallelly passing through the Dy-C chemical bond which provide the strongest interaction to the center metal ion due to the shortest distance of this bond, in combination with the strongest ligand field deriving from carbanion (Fig. 18). The shortest chemical bond in Ln-SMMs like the Dy-C bond in DyNCN is called predominant bond. Inspired by this, if we can construct one predominant bond or two with an approximate angle of  $180^\circ$  in common lanthanide compounds, a very strong axial ligand field can also be obtained and the orientation of magnetic anisotropy of the lanthanide ions will be dominated by this bond, so the effective coordination numbers of the compound depend on the number of the closest bonding atoms.

It is noted that the presence of the predominant bond does not change the geometry and symmetry of the coordination environments for Ln-SMMs but can provide a relatively powerful axial ligand field and the strategy of constructing the predominant bond has been proved and widely used in designing high-performance Ln-SMMs.



**Fig. 18** (a) The anisotropy axes in eight lowest KDs at the  $\text{Dy}^{\text{III}}$  site of DyNCN (*left*). Magnetization blocking barrier of the DyNCN, the arrows represent the averaged matrix element of the transversal magnetic moment connecting the corresponding states and red arrows show the most probable path for the magnetic relaxation at high temperatures (*right*). Reprinted with permissions from [22]. Copyright 2014 The Author(s). (b) A simple structural correlation of axiality and coordination environment of the compounds  $[\text{Dy}^{\text{III}}(\text{OPCy}_3)_2(\text{H}_2\text{O})_5]^{3+}$ ,  $[\text{Dy}^{\text{III}}(\text{OP}^t\text{Bu}(\text{NH}^i\text{Pr})_2)_2(\text{H}_2\text{O})_5]^{3+}$ ,  $[\text{Dy}^{\text{III}}(\text{BIPM})_2]$ ,  $[\text{Dy}^{\text{III}}(\text{bbpen})\text{Br}]$ , and  $[\text{Dy}^{\text{III}}(\text{O}^i\text{Bu})_2(\text{py})_3]^{+}$ , respectively, (*from left to right*) in respect to their magnetic behavior. Reprinted with permissions from [62]. Copyright 2017 ELSEVIER

In recent years, some pseudo-linear Ln-SMMs with the  $O_h$  or  $D_{5h}$  symmetry have been reported featuring the same core structure of linear L-Ln-L, where L is the closest bonding atom. There are some common structural characteristics in these complexes: (1) the axial sites of the compounds are occupied by two negatively charged ligands forming the predominant bonds while the equatorial sites are occupied by much weaker ligand donors forming the much longer chemical bonds, and (2) there is a bending angle in the core structure of linear L-Ln-L. Magnetic properties measurements indicated that all these compounds have a high-energy barrier from 543 to 1,815 K [62] (Fig. 18) which encouraged us to make more efforts to construct the strictly linear two-coordinate L-Ln-L compounds.

### 3 Conclusions and Prospects

In this chapter, we focus on the effects of geometry of the coordination environments on the magnetic behaviors for Ln-SMMs mainly including the representative Ln-SMMs with different geometries and coordination numbers from 3 to 8 and the significant methods in modulating the ligand fields clearly explaining the relationships between the geometry, crystal field, and molecular magnetisms. Considering that most of lanthanide compounds are in low-symmetry coordination environments with the number of CF parameters of 27, it is necessary to take measures to improve the coordination geometry of Ln-SMMs so that the non-axial CF terms can be completely removed. When the lanthanide ions are placed in the  $D_{4d}$ - and  $D_{5h}$ -symmetry coordination environments, all CF parameters will vanish except the  $q = 0$  term indicating the presence of a strong axial ligand field, which have been verified by experimental reports and theoretical calculations. In practice, it is really difficult to control the coordination environments of lanthanide ions into the highly symmetric geometries, so the construction of the predominant bond was introduced in detail.

In addition, the methods of tuning ligand fields for Ln-SMMs such as *cis-trans* isomerism effect, anion-inducing effect, etc. were introduced briefly emphasizing the great dependence of SMM behavior on the ligand field which both has pros and cons, prompting us to be careful with the coordination geometry especially when the Ln-SMMs were deposited on the native or prefunctionalized surfaces and entrapped in cages.

It is worth noting that the interaction between the lanthanide ions and ligand donors is not very strong even if the predominant bond is present, so if the double chemical bonds like Ln = N can be constructed successfully, a much stronger interaction with much shorter distance between them will be achieved, which was believed to further enhance the axiality of the ligand field.

### References

1. Cotton S (2006) Introduction to the lanthanides. Lanthanide and actinide chemistry. Wiley, Chichester, pp 1–7. <https://doi.org/10.1002/0470010088.ch1>



- Woodruff DN, Winpenny REP, Layfield RA (2013) Lanthanide single-molecule magnets. *Chem Rev* 113(7):5110–5148. <https://doi.org/10.1021/cr400018q>
- Zhang P, Guo Y-N, Tang J (2013) Recent advances in dysprosium-based single molecule magnets: structural overview and synthetic strategies. *Coord Chem Rev* 257(11):1728–1763. <https://doi.org/10.1016/j.ccr.2013.01.012>
- Liddle ST, van Slageren J (2015) Improving f-element single molecule magnets. *Chem Soc Rev* 44(19):6655–6669. <https://doi.org/10.1039/C5CS00222B>
- Tang J, Zhang P (2015) Lanthanide single-ion molecular magnets. *Lanthanide single molecule magnets*. Springer, Berlin, Heidelberg. [https://doi.org/10.1007/978-3-662-46999-6\\_2](https://doi.org/10.1007/978-3-662-46999-6_2)
- Karraker DG (1970) Coordination of trivalent lanthanide ions. *J Chem Educ* 47(6):424. <https://doi.org/10.1021/ed047p424>
- Ishikawa N, Sugita M, Ishikawa T, S-y K, Kaizu Y (2003) Lanthanide double-decker complexes functioning as magnets at the single-molecular level. *J Am Chem Soc* 125(29):8694–8695. <https://doi.org/10.1021/ja029629n>
- Perfetti M, Pointillart F, Cador O, Sorace L, Ouahab L (2017) Luminescent molecular magnets. *Molecular magnetic materials*. Wiley, Weinheim, pp 345–368. <https://doi.org/10.1002/9783527694228.ch14>
- Jiang S-D, Wang B-W, Gao S (2015) Advances in lanthanide single-ion magnets. In: Gao S (ed) *Molecular nanomagnets and related phenomena*. Springer, Berlin, Heidelberg, pp 111–141. [https://doi.org/10.1007/430\\_2014\\_153](https://doi.org/10.1007/430_2014_153)
- Sorace L, Gatteschi D (2015) Electronic structure and magnetic properties of lanthanide molecular complexes. *Lanthanides and actinides in molecular magnetism*. Wiley, Weinheim, pp 1–26. <https://doi.org/10.1002/9783527673476.ch1>
- Ungur L, Chibotaru LF (2017) Ab initio crystal field for lanthanides. *Chem Eur J* 23(15):3708–3718. <https://doi.org/10.1002/chem.201605102>
- Ganivet CR, Ballesteros B, de la Torre G, Clemente-Juan JM, Coronado E, Torres T (2013) Influence of peripheral substitution on the magnetic behavior of single-ion magnets based on homo- and heteroleptic Tb<sup>III</sup> bis(phthalocyaninate). *Chem Eur J* 19(4):1457–1465. <https://doi.org/10.1002/chem.201202600>
- Wu J, Jung J, Zhang P, Zhang H, Tang J, Le Guennic B (2016) Cis-trans isomerism modulates the magnetic relaxation of dysprosium single-molecule magnets. *Chem Sci* 7(6):3632–3639. <https://doi.org/10.1039/C5SC04510J>
- Chen Y-C, Liu J-L, Ungur L, Liu J, Li Q-W, Wang L-F, Ni Z-P, Chibotaru LF, Chen X-M, Tong M-L (2016) Symmetry-supported magnetic blocking at 20 K in pentagonal bipyramidal Dy(III) single-ion magnets. *J Am Chem Soc* 138(8):2829–2837. <https://doi.org/10.1021/jacs.5b13584>
- Gupta SK, Rajeshkumar T, Rajaraman G, Murugavel R (2016) An air-stable Dy(III) single-ion magnet with high anisotropy barrier and blocking temperature. *Chem Sci* 7(8):5181–5191. <https://doi.org/10.1039/C6SC00279J>
- Liu J, Chen Y-C, Liu J-L, Vieru V, Ungur L, Jia J-H, Chibotaru LF, Lan Y, Wernsdorfer W, Gao S, Chen X-M, Tong M-L (2016) A stable pentagonal bipyramidal Dy(III) single-ion magnet with a record magnetization reversal barrier over 1000 K. *J Am Chem Soc* 138(16):5441–5450. <https://doi.org/10.1021/jacs.6b02638>
- Ding Y-S, Chilton NF, Winpenny REP, Zheng Y-Z (2016) On approaching the limit of molecular magnetic anisotropy: a near-perfect pentagonal bipyramidal dysprosium(III) single-molecule magnet. *Angew Chem Int Ed* 55(52):16071–16074. <https://doi.org/10.1002/anie.201609685>
- Guo F-S, Day BM, Chen Y-C, Tong M-L, Mansikkamäki A, Layfield RA (2017) A dysprosium metallocene single-molecule magnet functioning at the axial limit. *Angew Chem Int Ed* 56(38):11445–11449. <https://doi.org/10.1002/anie.201705426>
- Goodwin CAP, Ortu F, Reta D, Chilton NF, Mills DP (2017) Molecular magnetic hysteresis at 60 kelvin in dysprosocenium. *Nature* 548:439–442. <https://doi.org/10.1038/nature23447>

20. Ungur L, Chibotaru LF (2011) Magnetic anisotropy in the excited states of low symmetry lanthanide complexes. *Phys Chem Chem Phys* 13(45):20086–20090. <https://doi.org/10.1039/C1CP22689D>
21. Ungur L, Chibotaru LF (2016) Strategies toward high-temperature lanthanide-based single-molecule magnets. *Inorg Chem* 55(20):10043–10056. <https://doi.org/10.1021/acs.inorgchem.6b01353>
22. Guo Y-N, Ungur L, Granroth GE, Powell AK, Wu C, Nagler SE, Tang J, Chibotaru LF, Cui D (2014) An NCN-pincer ligand dysprosium single-ion magnet showing magnetic relaxation via the second excited state. *Sci Rep* 4:5471. <https://doi.org/10.1038/srep05471>
23. Gregson M, Chilton NF, Ariciu A-M, Tuna F, Crowe IF, Lewis W, Blake AJ, Collison D, McInnes EJJ, Winpenny REP, Liddle ST (2016) A monometallic lanthanide bis(methanediide) single molecule magnet with a large energy barrier and complex spin relaxation behaviour. *Chem Sci* 7(1):155–165. <https://doi.org/10.1039/C5SC03111G>
24. Liu J-L, Chen Y-C, Zheng Y-Z, Lin W-Q, Ungur L, Wernsdorfer W, Chibotaru LF, Tong M-L (2013) Switching the anisotropy barrier of a single-ion magnet by symmetry change from quasi-D5h to quasi-Oh. *Chem Sci* 4(8):3310–3316. <https://doi.org/10.1039/C3SC50843A>
25. Sun W-B, Yan P-F, Jiang S-D, Wang B-W, Zhang Y-Q, Li H-F, Chen P, Wang Z-M, Gao S (2016) High symmetry or low symmetry, that is the question – high performance Dy(III) single-ion magnets by electrostatic potential design. *Chem Sci* 7(1):684–691. <https://doi.org/10.1039/C5SC02986D>
26. Blagg RJ, Ungur L, Tuna F, Speak J, Comar P, Collison D, Wernsdorfer W, McInnes EJJ, Chibotaru LF, Winpenny REP (2013) Magnetic relaxation pathways in lanthanide single-molecule magnets. *Nat Chem* 5(8):673–678. <https://doi.org/10.1038/nchem.1707>
27. Cotton S (2006) Coordination chemistry of the lanthanides. *Lanthanide and actinide chemistry*. Wiley, Chichester, pp 35–60. <https://doi.org/10.1002/0470010088.ch4>
28. Lawrance GA (2009) Shape. *Introduction to coordination chemistry*. Wiley, Chichester, pp 83–124. <https://doi.org/10.1002/9780470687123.ch4>
29. Linton C, Gaudet DM, Schall H (1986) Laser spectroscopy of dysprosium monoxide: observation and analysis of several low-lying electronic states. *J Mol Spectrosc* 115(1):58–73. [https://doi.org/10.1016/0022-2852\(86\)90275-4](https://doi.org/10.1016/0022-2852(86)90275-4)
30. Chilton NF, Goodwin CAP, Mills DP, Winpenny REP (2015) The first near-linear bis(amide) f-block complex: a blueprint for a high temperature single molecule magnet. *Chem Commun* 51(1):101–103. <https://doi.org/10.1039/C4CC08312A>
31. Zhang P, Zhang L, Wang C, Xue S, Lin S-Y, Tang J (2014) Equatorially coordinated lanthanide single ion magnets. *J Am Chem Soc* 136(12):4484–4487. <https://doi.org/10.1021/ja500793x>
32. Rinehart JD, Long JR (2011) Exploiting single-ion anisotropy in the design of f-element single-molecule magnets. *Chem Sci* 2(11):2078–2085. <https://doi.org/10.1039/C1SC00513H>
33. Brown AJ, Pinkowicz D, Saber MR, Dunbar KR (2015) A trigonal-pyramidal erbium(III) single-molecule magnet. *Angew Chem Int Ed* 54(20):5864–5868. <https://doi.org/10.1002/anie.201411190>
34. Zhang P, Jung J, Zhang L, Tang J, Le Guennic B (2016) Elucidating the magnetic anisotropy and relaxation dynamics of low-coordinate lanthanide compounds. *Inorg Chem* 55(4):1905–1911. <https://doi.org/10.1021/acs.inorgchem.5b02792>
35. Harriman KLM, Brosmer JL, Ungur L, Diaconescu PL, Murugesu M (2017) Pursuit of record breaking energy barriers: a study of magnetic axiality in diamide ligated Dy(III) single-molecule magnets. *J Am Chem Soc* 139(4):1420–1423. <https://doi.org/10.1021/jacs.6b12374>
36. Allouche F, Lapadula G, Siddiqi G, Lukens WW, Maury O, Le Guennic B, Pointillart F, Dreiser J, Mougél V, Cador O, Copéret C (2017) Magnetic memory from site isolated Dy(III) on silica materials. *ACS Cent Sci* 3(3):244–249. <https://doi.org/10.1021/acscentsci.7b00035>
37. Zhang G, Gil-Ramirez G, Markevicius A, Browne C, Vitorica-Yrezabal IJ, Leigh DA (2015) Lanthanide template synthesis of trefoil knots of single handedness. *J Am Chem Soc* 137(32):10437–10442. <https://doi.org/10.1021/jacs.5b07069>

38. Danon JJ, Krüger A, Leigh DA, Lemonnier J-F, Stephens AJ, Vitorica-Yrezabal IJ, Woltering SL (2017) Braiding a molecular knot with eight crossings. *Science* 355(6321):159–162. <https://doi.org/10.1126/science.aal1619>
39. Bolliger JL, Belenguier AM, Nitschke JR (2013) Enantiopure water-soluble [Fe4L6] cages: host–guest chemistry and catalytic activity. *Angew Chem Int Ed* 52(31):7958–7962. <https://doi.org/10.1002/anie.201302136>
40. Percástegui EG, Mosquera J, Nitschke JR (2017) Anion exchange renders hydrophobic capsules and cargoes water-soluble. *Angew Chem Int Ed* 56(31):9136–9140. <https://doi.org/10.1002/anie.201705093>
41. Meihaus KR, Rinehart JD, Long JR (2011) Dilution-induced slow magnetic relaxation and anomalous hysteresis in trigonal prismatic dysprosium(III) and uranium(III) complexes. *Inorg Chem* 50(17):8484–8489. <https://doi.org/10.1021/ic201078r>
42. König SN, Chilton NF, Maichle-Mossmar C, Pineda EM, Pugh T, Anwander R, Layfield RA (2014) Fast magnetic relaxation in an octahedral dysprosium tetramethyl-aluminate complex. *Dalton Trans* 43(8):3035–3038. <https://doi.org/10.1039/C3DT52337C>
43. Liu S-S, Meng Y-S, Zhang Y-Q, Meng Z-S, Lang K, Zhu Z-L, Shang C-F, Wang B-W, Gao S (2017) A six-coordinate dysprosium single-ion magnet with trigonal-prismatic geometry. *Inorg Chem* 56(13):7320–7323. <https://doi.org/10.1021/acs.inorgchem.7b00952>
44. Rinehart JD, Fang M, Evans WJ, Long JR (2011) A  $N_2^{3-}$  radical-bridged terbium complex exhibiting magnetic hysteresis at 14 K. *J Am Chem Soc* 133(36):14236–14239. <https://doi.org/10.1021/ja206286h>
45. Li Q-W, Wan R-C, Chen Y-C, Liu J-L, Wang L-F, Jia J-H, Chilton NF, Tong M (2016) Unprecedented hexagonal bipyramidal single-ion magnets based on metallacrowns. *Chem Commun*. <https://doi.org/10.1039/C6CC06924J>
46. Aldamen MA, Clemente-Juan JM, Coronado E, Martí-Gastaldo C, Gaita-Ariño A (2008) Mononuclear lanthanide single-molecule magnets based on polyoxometalates. *J Am Chem Soc* 130(28):8874–8875. <https://doi.org/10.1021/ja801659m>
47. Jiang S-D, Wang B-W, Su G, Wang Z-M, Gao S (2010) A mononuclear dysprosium complex featuring single-molecule-magnet behavior. *Angew Chem Int Ed* 49(41):7448–7451. <https://doi.org/10.1002/anie.201004027>
48. Sorace L, Benelli C, Gatteschi D (2011) Lanthanides in molecular magnetism: old tools in a new field. *Chem Soc Rev* 40(6):3092–3104. <https://doi.org/10.1039/C0CS00185F>
49. Ishikawa N, Mizuno Y, Takamatsu S, Ishikawa T, S-y K (2008) Effects of chemically induced contraction of a coordination polyhedron on the dynamical magnetism of bis(phthalocyaninato) dysprosium, a single-4f-ionic single-molecule magnet with a Kramers ground state. *Inorg Chem* 47(22):10217–10219. <https://doi.org/10.1021/ic8014892>
50. Takamatsu S, Ishikawa N (2007) A theoretical study of a drastic structural change of bis(phthalocyaninato)lanthanide by ligand oxidation: towards control of ligand field strength and magnetism of single-lanthanide-ionic single molecule magnet. *Polyhedron* 26(9):1859–1862. <https://doi.org/10.1016/j.poly.2006.09.020>
51. Clemente-Juan JM, Coronado E, Gaita-Ariño A (2015) Mononuclear lanthanide complexes: use of the crystal field theory to design single-ion magnets and spin qubits. *Lanthanides and actinides in molecular magnetism*. Wiley, Weinheim, pp 27–60. <https://doi.org/10.1002/9783527673476.ch2>
52. Baldoví JJ, Cardona-Serra S, Clemente-Juan JM, Coronado E, Gaita-Ariño A, Palií A (2012) Rational design of single-ion magnets and spin qubits based on mononuclear lanthanoid complexes. *Inorg Chem* 51(22):12565–12574. <https://doi.org/10.1021/ic302068c>
53. Barsukova M, Izarova NV, Biboum RN, Keita B, Nadjo L, Ramachandran V, Dalal NS, Antonova NS, Carbó JJ, Poblet JM, Kortz U (2010) Polyoxopalladates encapsulating yttrium and lanthanide ions,  $[X^{III}Pd^{II}_{12}(AsPh)_8O_{32}]^{5-}$  (X=Y, Pr, Nd, Sm, Eu, Gd, Tb, Dy, Ho, Er, Tm, Yb, Lu). *Chem Eur J* 16(30):9076–9085. <https://doi.org/10.1002/chem.201000631>
54. Li X-L, Li H, Chen D-M, Wang C, Wu J, Tang J, Shi W, Cheng P (2015) Planar  $Dy_3 + Dy_3$  clusters: design, structure and axial ligand perturbed magnetic dynamics. *Dalton Trans* 44(47):20316–20320. <https://doi.org/10.1039/C5DT03931B>

55. Bi Y, Guo Y-N, Zhao L, Guo Y, Lin S-Y, Jiang S-D, Tang J, Wang B-W, Gao S (2011) Capping ligand perturbed slow magnetic relaxation in dysprosium single-ion magnets. *Chem Eur J* 17(44):12476–12481. <https://doi.org/10.1002/chem.201101838>
56. Zhang P, Zhang L, Lin S-Y, Xue S, Tang J (2013) Modulating magnetic dynamics of Dy<sub>2</sub> system through the coordination geometry and magnetic interaction. *Inorg Chem* 52(8):4587–4592. <https://doi.org/10.1021/ic400150f>
57. Riddell IA, Hristova YR, Clegg JK, Wood CS, Breiner B, Nitschke JR (2013) Five discrete multinuclear metal-organic assemblies from one ligand: deciphering the effects of different templates. *J Am Chem Soc* 135(7):2723–2733. <https://doi.org/10.1021/ja311285b>
58. Wei R-J, Tao J, Huang R-B, Zheng L-S (2013) Anion-dependent spin crossover and coordination assembly based on [Fe(tpa)]<sup>2+</sup> [tpa = tris(2-pyridylmethyl)amine] and [N(CN)<sub>2</sub>]<sup>-</sup>: square, zigzag, dimeric, and [4+1]-cocrystallized complexes. *Eur J Inorg Chem* 2013(5–6):916–926. <https://doi.org/10.1002/ejic.201200541>
59. Cook TR, Stang PJ (2015) Recent developments in the preparation and chemistry of metacycles and metallacages via coordination. *Chem Rev* 115(15):7001–7045. <https://doi.org/10.1021/cr5005666>
60. Zhang L, Zhang P, Zhao L, Wu J, Guo M, Tang J (2015) Anions influence the relaxation dynamics of mono-μ<sub>3</sub>-OH-capped triangular dysprosium aggregates. *Inorg Chem* 54(11):5571–5578. <https://doi.org/10.1021/acs.inorgchem.5b00702>
61. Guo Y-N (2012) Relaxation dynamics of dysprosium(III) single molecule magnets. PhD thesis, Changchun Institute of Applied Chemistry, Chinese Academy of Science
62. McAdams SG, Ariciu A-M, Kostopoulos AK, Walsh JPS, Tuna F (2017) Molecular single-ion magnets based on lanthanides and actinides: design considerations and new advances in the context of quantum technologies. *Coord Chem Rev* 346:216–239. <https://doi.org/10.1016/j.ccr.2017.03.015>

# Single-Ion Anisotropy: An Insight to Complicated Magnetic Molecules



Shang-Da Jiang, Bing-Wu Wang, and Song Gao

## Contents

1	Introduction .....	228
2	Theoretical Approach .....	229
2.1	The Spin Hamiltonian for Transition Ions .....	229
2.2	The Crystal Field Hamiltonian for Lanthanides .....	230
2.3	The Aspheric Electron Cloud for Lanthanide Ions .....	231
2.4	The Ab Initio Approach .....	232
3	Experimental Approach .....	232
3.1	Determination of the Magnetic Anisotropy Axes .....	233
3.2	Determination of the Electronic Fine Structure .....	235
4	Strategies in Construction SIMs .....	236
4.1	Symmetry .....	237
4.2	Orbital Hybridization .....	238
4.3	Charges Location .....	239
5	Single-Ion Anisotropy in Complicated Systems .....	240
5.1	Dinuclear Systems .....	241
5.2	Axial Cluster .....	242
5.3	Magnetic Chain .....	243
6	Conclusion Remarks .....	245
	References .....	246

**Abstract** Molecular magnetism has been developed by chemists for a few decades. The research focus shifted from magnetic frameworks and clusters to mononuclear molecules from the beginning of this century due to the poor understanding of single-ion anisotropy. In the past decades, huge triumphs on the mononuclear researches have been achieved, while we feel that it is the moment to move to more complicated molecules with the present knowledge. Based on the overview of the theoretical models for the molecular magnetism, some unconventional characterization methods to investigate the magnetic anisotropy are introduced. We

---

S.-D. Jiang, B.-W. Wang, and S. Gao (✉)

Beijing National Laboratory of Molecular Science, College of Chemistry and Molecular Engineering, Peking University, Beijing, P. R. China

e-mail: [gaosong@pku.edu.cn](mailto:gaosong@pku.edu.cn)

discussed the strategies to control the magnetic anisotropy of spin carriers as a hint to understand the magnetic clusters' behavior. More importantly, the researches on the complicated magnetic molecules based on the information of the single-ion anisotropy are summarized. To the end, a few conclusions are provided, as well as the perspectives for the further researches in molecular magnetism with respect to chemistry.

**Keywords** Magnetic coupling · Molecular engineering · Molecular magnetism · Single-ion anisotropy · Single-molecule magnet

## 1 Introduction

Chemists started to involve in the area of magnetism since the quantum mechanics is very well developed so as to explain the origination of the magnetism, and a new direction named molecular magnetism is founded by inorganic and physical chemists by constructing molecule-based magnets with organic ligands and metal ion as spin carriers [1]. In the beginning of the 1990s, chemists found that the magnetic bistability can be achieved in superparamagnetic systems which are uniformly distributed in molecular level [2]. These molecules are able to maintain their magnetic moments below the blocking temperature in the scale of individual molecule because of their strong easy-axis anisotropy, and these sort of molecules are later on literally named as single-molecule magnets (SMMs) [3]. The discovery of SMMs offers the opportunity of molecular information storage overcoming the problems predicted by Moore's Law, as well as quantum computing which is believed as the computer of the next generation [4]. Since the magnetic properties of SMMs are represented by those individual molecules, a new area of molecular spintronics is proposed and developed [5, 6].

Scientists immediately realized that in order to enhance the magnetic bistability of SMMs, the overall magnetic easy-axis anisotropy and the molecular ground spin state are of crucial importance, which are determined by the single-ion anisotropy and the magnetic coupling as well as the symmetry with respect to each other spin carriers [7]. However, the single-ion anisotropy, especially which possesses unneglectable spin-orbit coupling, is very challenging to control and predict [8]. Consequently, chemists turned to investigate the SMMs with only one spin carrier which is normally a *d*- or *f*-block metal ion [9, 10], and these mononuclear SMMs are nowadays denoted as single-ion magnets (SIMs) [11, 12]. This seems to be a vast success: chemists have rationalized the strategies to design a transition or rare-earth ion of strong Ising-type anisotropy [13, 14]; the slow relaxation energy barrier between the bistable states is gradually increased to nearly 2,000 K [15] and hysteresis blocking temperature to around 60 K [16–19], greatly exceeding the observations in most of the cluster-based SMMs [20].

Nevertheless, we feel that going back to the more complicated molecular systems with the present knowledge is necessary at this moment. It was because the chemists understood the single-ion anisotropy so few when dealing with the multinuclear

molecules that we moved to the present hot topic. As this goal has been somehow approached, it is essential to again confront the previous complexities. On the other hand, the difficulties encountered in SIMs such as fast tunneling due to the small spin could be very well exceeded by synergistic effect, which therefore requests the introduction of appropriate magnetic coupling and rationalized organization of magnetic anisotropy from each ion.

The present perspective intends to overview the researches on single-ion magnets, including a brief introduction of the theoretical systems, some unconventional experimental approaches, and the rationalized strategies in construction  $3d$ - and  $4f$ -block SIMs. More importantly, we illustrate the methods in the research on complicated systems with the information of single-ion anisotropy where a few examples are provided. The comments as well as some perspectives of the next step in this direction are discussed at last.

## 2 Theoretical Approach

In contrast to the SMM clusters, where the magnetic coupling generally exists, the overall magnetic anisotropy of SIMs originates solely from single ion. The magnetic properties of the spin carriers can be severely different according to their unpaired electron shell category, i.e., lanthanide ions, due to the inner shell localized  $4f$  electrons [21, 22], distinguish from transition ions, whose  $d$ -orbital electrons are exposed directly to the crystal field and the orbital momentum are largely quenched. Besides, a stronger relativistic effect happens for heavier elements and consequently the spin-orbit coupling of lanthanide is much stronger than that of transition metal ions. The orbit momentum of  $3d$ -block ions is treated as perturbation, and the spin is a well-defined quantum number there; however, neither spin nor orbit momentum is an observable quantity, while the total angular quantum number  $J$  is generally accepted in describing the magnetic properties of lanthanide ions. The  $f^n$  configuration of trivalent lanthanide ions is characterized by  $^{2S+1}L_J$  terms, and the relative energy diagram between these terms follows Hund's rules [23].

### 2.1 The Spin Hamiltonian for Transition Ions

The magnetic properties of  $3d$ -block SMMs are generally described by spin Hamiltonian, which is an effective Hamiltonian approach by mapping the low-energy part of the spectrum to a linear combination of spin operators. A typical spin Hamiltonian can be expressed by

$$\hat{H} = \sum_i \left[ \hat{H}_{\text{Zeeman}}(i) + \hat{H}_{\text{ZFS}}(i) \right] + \sum_i \sum_{j>i} \hat{H}_{\text{coupling}}(i, j),$$

where the first summation bracket denotes the Zeeman and zero field splitting (ZFS) effect, respectively, for each spin carrier  $i$  and the second one denotes the magnetic coupling between the spin carriers. The hyperfine interaction and nuclear Zeeman effects are small perturbation to the system which is therefore neglected. There is only one spin carrier in SIMs, and the electron-electron interaction vanishes thereby.

The single-ion anisotropy is described in the first summation bracket by both Zeeman effect and ZFS. The  $\tilde{\mathbf{g}}$  tensor in the Zeeman term can in part contribute to the single-ion anisotropy with the existence of magnetic field, while its contribution is slight since the eigenvalues of the  $\tilde{\mathbf{g}}$  tensor merely faintly deviate from spin-only value of 2 due to the largely quenched orbit momentum. However, for the ions with only one unpaired  $3d$  electron ( $S = 1/2$ ), such as  $\text{Cu}^{2+}$  and  $\text{Ti}^{3+}$ , the ZFS does not exist, and  $\tilde{\mathbf{g}}$  tensor anisotropy works as the only contribution to the single-ion anisotropy in a magnetic field.

The  $(2S + 1)$  spin multiplets of spin state  $S$  can be split by the ZFS effect when  $S > 1/2$ ; this is normally the major contribution of the single-ion anisotropy. The ZFS tensor is not merely limited to second rank with only  $D$  and  $E$  term, but higher  $k$ th rank splittings are applicable to the spin multiplet  $S$  when  $2S \geq k$  [24]. The most popular expressions of various higher-rank splitting terms are named after K. W. H. Stevens as Stevens operators [25], whose detailed expression can be found elsewhere [26]. The molecular symmetry determines a few Stevens operators responsible for the ZFS of the system [27].

The electron-electron interaction does not exist in single-ion Hamiltonian, while it can dominate the magnetic properties in spin clusters. The general magnetic coupling Hamiltonian is expressed as

$$\hat{H}_{\text{MC}} = \hat{S}_i^T \tilde{\mathbf{J}} \hat{S}_j,$$

where  $\tilde{\mathbf{J}}$  is a second rank tensor describing the magnetic coupling between two spin carriers including the magnetic dipolar interactions. The second rank  $\tilde{\mathbf{J}}$  tensor can be decomposed into its irreducible tensor components as isotropic (0th rank, a scalar), antisymmetric (1st rank, a vector), and asymmetric (2nd rank, a traceless symmetric matrix) tensors [28]. The latter two are also noted as anisotropic exchange interactions and can contribute to the overall magnetic anisotropy. This has been proved to be an efficient approach to construct the SMMs with spin carriers with orbital-degenerate ground state with unquenched orbital momentum, normally the  $4d$ -,  $5d$ -, and even lanthanide ions [29–31].

## 2.2 The Crystal Field Hamiltonian for Lanthanides

Due to the large residual orbital momentum and strong spin-orbit coupling, the effective spin Hamiltonian cannot be applied to lanthanide ions directly, while a crystal field Hamiltonian approach is necessary. In the crystal field Hamiltonian, the operators are not spin operators described above, but Racah operators in spherical



harmonic function form. To calculate the matrix element, the Wigner-Eckart theorem is required, and the Russel-Saunders multiplet mixing is normally considered. In the case of heavy lanthanides, the excited multiplets lie thousands of wave number higher and the multiplet mixing contributes less than 1% to the ground one. Therefore, it is popular and reasonable to consider only the ground Russel-Saunders term splitting to describe the magnetic properties of the heavy lanthanide ions as an approximation. In this case, according to the Racah relations [32–34], the irreducible tensor operators can be simplified as momentum operators, or more specifically as spin operators, which could largely reduce the complexity in the matrix element calculation for lanthanide ions. This simplified crystal field Hamiltonian is noted as Stevens notation. The present perspective is not going to deduce the crystal field Hamiltonian formalism, which can be found elsewhere [27].

It is worth noting that even though the Stevens notation is very similar to the effective spin Hamiltonian for transition ions, there are some fundamental differences between these two. The higher-rank terms in transition ions' case are perturbation in the ZFS and are normally orders of smaller than the  $D$  term, while it is not necessarily the case for lanthanide ions. The values of the crystal field parameters highly depend on the way of choosing the coordination frame.

Just as the case in transition ions, the understanding of the magnetic properties of rare-earth ions relies on a proper model and a set of well-determined Hamiltonian parameters. Schilder and Lueken have developed a CONDON program to fit the crystal field parameters based on magnetic susceptibility data [35, 36]. The CONDON employs Racah operators affording that the calculation is based on the Hilbert space generated by all the possible microstates. This code is also possible to fit a few sorts of dinuclear coupling systems. However, the over-fitting or multi-solutions can happen for low symmetric lanthanide systems. An alternative approach is to investigate the crystal field parameters based on the molecular structures, which can largely reduce the fitting parameters as some intuitionistic distance and charge values. This is an effective point-charge method developed by Coronado, Gaita-Ariño, and their coworkers to calculate the ground multiplet splittings [37, 38]. The charges of the first coordinating sphere are reasonably considered to deviate from the nucleus. The absolute charge value and the deviation distance are to be fitted into the magnetic susceptibility data, so as to obtain the crystal field parameters.

### ***2.3 The Aspheric Electron Cloud for Lanthanide Ions***

The electron cloud of a free ion is isotropic and spherical, while a crystal field can remove the degeneracy of the multiplets when spin-orbit coupling exists, which is the source of magnetic anisotropy. This can be viewed from the shape of electron cloud, which is expected to be aspheric and can even be calculated by multipolemoment expansion in lanthanide ions [39]. This is a simple ratiocination of crystal field theory and becomes very simple when the microstate is pure. In the

first-order approximation, a quadrupole moment is considered, and the Ising limit state of ground-state multiplets for lanthanide ions is attributed into two types as axial elongated and compressed [40]. Based on this simple idea, Rinehart and Long proposed to rational design the lanthanide-based SIMs by placing the negative-charge positions so as to stabilize the Ising state of the lanthanide ions [14].

Chilton and his coworkers, based on the work of Sievers, proposed to predict the orientations of the quantized axis of  $\text{Dy}^{\text{III}}$  ion with  $2^k$ -multipolemoment expansion up to  $k = 6$ , which is proved to be successful and much more efficient than the quantum chemistry calculation approach [41]. Jiang and Qin have improved this method by considering the negative-charge displacement and extend the application to all the lanthanide ions and their various microstates [42]. These quantized axis orientation prediction methods would be very useful in understanding the magnetic properties of multinuclear molecules.

## 2.4 *The Ab Initio Approach*

The ab initio approach is of course one of the most important but the most expensive theoretical methods in understanding the magnetic properties. There are various successful examples in calculating the electronic fine structure, the magnetic principal axes, and even the magnetic coupling properties. Recently, it is very popular to employ MOLCAS package which considers the relativistic effects by post-Hartree-Fock approach [43]. It is able to, after the ab initio calculation, map the lower-lying energy diagrams to the crystal field Hamiltonian to provide the parameters as a reference for the experimental investigation [44]. More interestingly, the POLY\_ANISO program encoded in MOLCAS can also, based on the calculated single-ion energy diagram, fit the magnetic susceptibility data to obtain the magnetic coupling constants [45].

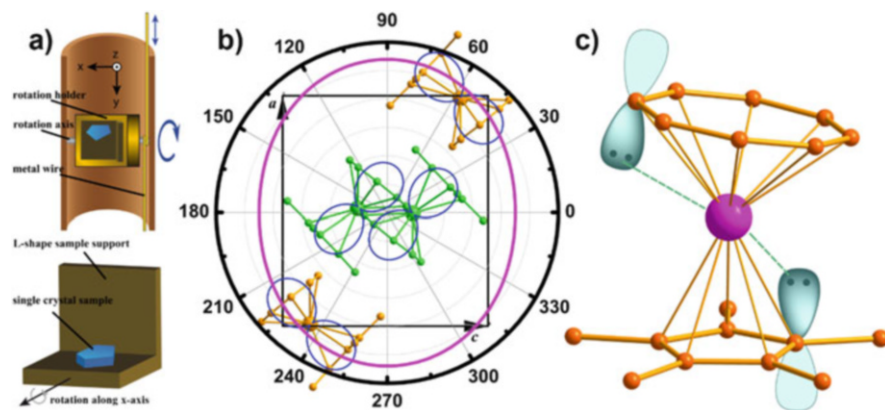
## 3 Experimental Approach

The magnetic properties of molecular magnetism are generally characterized by magnetometer with direct or alternative current magnetic field. However, some unconventional methods are employed recently to provide some useful single-ion anisotropy information directly concerning the single-ion anisotropy. In this part we introduce some of these techniques.

### 3.1 Determination of the Magnetic Anisotropy Axes

It is always difficult to identify the magnetic principal axes directly from the structure. For transition metal ions, a slight deviation from the standard coordination polyhedron will lead to a vast variation on the electronic structure and can even change the magnetic anisotropy type. For the lanthanide ions, the prediction of magnetic principal axes is not straightforward due to the low symmetry. The aforementioned prediction method according to aspheric electron cloud is based on the assumption that the ground microstate is nearly pure. Therefore the experimental determination of the molecular magnetic principal axes is of fundamental importance in understanding the magnetic anisotropy.

The angular-resolved magnetometry method has recently been generally applied for this purpose. This method measures the magnetization as a function of the rotation angle with respect to three orthogonal axes to determine the crystal magnetic susceptibility tensor. The rotator is figured in Fig. 1a, and the detailed introduction of this method was discussed elsewhere [23, 46]. The eigenvectors of this second rank tensor denote the magnetic principal axes. However, there are a few limitations for this angular-resolved magnetometry. Firstly, it is necessary that there is only one anisotropic spin carrier in the unit cell, since the magnetometer measures the overall magnetic properties rather than a specific molecule. While more restrictedly, the measurement is based on the magnetic susceptibility tensor of the molecule that is identical to the one of the crystal, which is not always the case if the spin carrier does not locate on the highest symmetry position of the unit cell. Once the molecule



**Fig. 1** (a) The sketch map of the angular-resolved magnetometry and the L-shaped sample support. The measurement can be performed along three orthogonal directions so as to extract the magnetic susceptibility tensor with respect to the experimental frame. (b) The explanation of the two sets of molecules (green and gold) in the double-decker erbium unit cell. The blue and pink curves indicate the simulated molecular and crystal magnetization as a function of the rotation angle around  $b$  axis, respectively. (c) The displaced charges from the carbon atom nuclei contribute a stronger electronic repulsion near the equator plane, explaining the easy-axial anisotropy of the erbium ion

locates on a trivial position, the susceptibility tensors for other symmetrically related molecules can be calculated by symmetric operations. While the summation of the molecular tensors leads to vanishing of some elements of the crystal susceptibility tensor, ensuring that symmetric axes of the crystal being the magnetic principal axes. This can be understood by the Neumann's principle, stating that the symmetry elements of any physical properties of a crystal must include the symmetry elements of the point group of the crystal. There is, however, one example of single-crystal measurement out of this limitation on the double-decker erbium molecule crystallized in  $P_{nma}$  space group [47]. The measurement there was always a summation of two differently oriented molecule families, and it is not possible to associate unambiguously each contribution to one particular family (Fig. 1b). This example actually illustrates the restriction above.

In addition to the angular-resolved magnetometry method, it is worth noting that many single-crystal rotation methods in a magnetic field are possible to provide the magnetic principal axes of the crystal, as long as the molecular susceptibility tensor is identical to the crystal one. The cantilever torque magnetometry is one of the leading approaches among the techniques determining the sample anisotropy. The featuring advantage of cantilever torque method is its extreme sensitivity to magnetic anisotropy. There has been very successful application of this method on the investigation of the magnetic anisotropy on thin layers (around 100 nm) composed of anisotropic molecules [48]. Further investigation of this method on coordination molecular crystals is mostly reported by Sessoli's group. The detailed experimental and theoretical introduction of the cantilever torque magnetometry can be found elsewhere [49].

An alternation is to employ the diffraction method. The polarized neutron diffraction is able to go beyond the symmetric limitation, providing the magnetization density map in the unit cell at the atomic scale. By measuring the flipping ration of the Bragg reflections, one can determine the local spin carrier magnetic susceptibility tensor, so as to view the orientation and magnitude of the magnetic moments [50]. One of the recent research on a Co monomer molecule crystallized in Pca21 space group has successfully applied this technique [51]. The molecular magnetic susceptibility tensor can be determined in a rather good accuracy. The crystal susceptibility tensor is obtained by molecular tensor summation, which coincides precisely with the magnetometry approach. The polarized neutron diffraction can provide extremely accurate orientation of the magnetic principal axes with respect to the crystal symmetry as the direction is determined from the orientation matrix. The case for the magnetometry is lack of accuracy in the orientation, since the crystal is normally placed in the experimental coordination frame manually, which could lead to the misalignment of 1–2° at least. It is worth noting that the diffraction method has, however, lack of accuracy in magnetic moment amplitude. This is because the measurement on the diffractometer is under low-field limitation in order to keep the linear response of the magnetization to the magnetic field, and the magnetic moment at low field determined from neutron diffraction has a large uncertainty.

A third approach is to determine the electron density distribution of the paramagnetic centers in the very high precision up to  $(\sin\theta/\lambda)_{\max} > 1.1 \text{ \AA}^{-1}$  [52]. It has been

applied to a wide series of molecules in viewing the bond nature for organic and coordination molecules [53, 54]. The research in this field has offered vast information of the metal-to-ligand and metal-to-metal bonding. As the orbital momentum of the first-row transition ions are largely quenched and the ligand atoms can interact directly with the  $d$  orbitals, the anisotropy of the metal ions can hardly be observed directly from its electronic density. While on the contrary, the  $4f$ -shells of rare-earth ions are hidden in the  $5d$  and  $6s$  orbitals, and an ionic-bond-like coordinating interaction between the lanthanide ions and the ligands generally exists, it would be a possibility, at low temperature, to view the  $4f$ -shell electron density shapes of various lanthanides in their relative ground states of the fine electronic structures. This can be interpreted from the previous discussion that by removing the manyfold degeneration due to crystal field effect, the  $4f$ -shell is aspheric, while the other  $s$ ,  $p$ ,  $d$  orbitals are close shell and isotropic [39]. For those lanthanides of Ising limit contained molecules, the electron clouds are of axial anisotropy, whose axes coincide with the magnetic easy axes. One can therefore determine the single-ion anisotropy from this electron density distribution determination. However, it can be imagined that to view the  $4f$ -shell anisotropy is of vast difficulties. The anisotropic atomic thermal vibration could formally diminish the intrinsic electronic asphericity. The measurement at very low temperature, at around 10 K or even lower, to suppress the atomic vibration is necessary. Moreover, as lanthanide ions are heavier than first-row transition ions, the diffraction from the isotropic electrons has a much larger contribution to the overall signal. This would make the direct observation of the  $4f$ -shell anisotropy even more difficult. We expect the crystallographic scientists would commit into this direction.

### 3.2 Determination of the Electronic Fine Structure

The way to view the electronic structure is normally approached by spectroscopic methods. The fine electronic structure of transition metal ions is generally determined by high-field and high-frequency electron paramagnetic resonance (HFEPR) [55–58], and the spin Hamiltonian parameters can be determined thereby. The slight variation on the transverse anisotropy parameters can influence the quantum tunneling of magnetization behavior largely [59, 60]. Besides the conventional EPR methods, a few magnetization-detected EPR measurement implementations are available [61]. This is based on the small change of magnetization when the transition happens. The detection can be based on the micro-SQUID [62], the Hall-bar sensor [63], and even torque magnetometry [64]. The advantage of the magnetization-detected EPR is its high sensitivity. The micro-SQUID-detected EPR can view the magnetic moment of  $10^3$  spins [65].

The HFEPR is limited by the excitation microwave frequency and the magnetic field. A system with energy splitting larger than  $20\text{ cm}^{-1}$  (600 GHz) will be very difficult to view in HFEPR. The frequency-domain magnetic-resonance spectroscopic (FDMRS) method therefore turns out to be very useful [66]. A dozen of

backward-wave oscillators can cover the frequency range from 1 to  $50\text{ cm}^{-1}$ . The Fourier transform far-infrared spectrometer can cover the range from 20 up to a few hundred wave numbers. Combining these spectrometers with a superconducting magnet equipped with optical windows, one can set up an FDMR spectrometer, which can measure the transitions in the relative frequency range, and the magnetic transitions can be distinguished by applying the magnetic field. With the FDMRS, it is possible to directly observe the very large ZFS in transition ions. A recent research on a tetrahedral  $\text{Ni}^{\text{II}}$  is reported to possess the ZFS of  $45\text{ cm}^{-1}$ , and this is directly measured, rather than by fitting magnetization data, via the FDMRS in magnetic field [67]. Normal HFEPR shows silent signal in this molecule. Interestingly, the anisotropic type of the Ni can also be determined by this method. The temperature dependence of the two magnetic transitions shows different dependence in different types of anisotropy. The direct observation of very large ZFS in transition ions is also reported in other Ni and Co molecules [66, 68, 69]. One can even see some transitions of lanthanide-containing molecules between the low-lying microstates [70], while it is difficult to see the whole spectrum range in FDMRS, which is normally accessed by high-resolution luminescence spectroscopy.

The luminescence with high resolution can be a powerful tool to scan to full crystal field splitting of lanthanide ions [46, 71]. The fine structure of the emission line is attributed to the crystal field splitting of the ground multiplets when the hot band relaxes faster at low temperature [72]. By fitting the fine structure of the emission line with a few Gaussian lines, one is able to see the whole crystal field splitting diagram of the ground multiplet. There is still substantial space to explore with respect to these methods. The present article focuses on the electronic fine structure only, but the energy levels' response to the magnetic field remains to be an open question, which could shine lights on the state components and provide the magnetic anisotropic properties of the molecule.

The last approach discussed here in viewing the electronic structure is not a spectroscopic method but by fitting the magnetic response to the temperature to obtain the crystal field parameters. It has been discussed previously that the CONDON and SIMPRE codes are developed to fit the magnetic susceptibility data as a function of temperature to obtain the crystal field parameters. Sessoli and her coworkers have developed a method to fit the single-crystal torque magnetometry data to the crystal field Hamiltonian to obtain the relative parameters [73, 74]. This method opens a new access to the energy diagram. As a fitting approach, the over fitting problem is not avoidable when many parameters exist to determine. Therefore, the molecules of the higher symmetry with less crystal field Hamiltonian terms are preferable.

## 4 Strategies in Construction SIMs

There have been a few examples in constructing transition ion-based SIMs and plenty of SIMs with lanthanide ions. The difficulties in building  $3d$  ion-based SIM are that the orbital momentum of the spin carriers has been largely quenched and the

spin-orbit coupling is therefore a perturbation as a role in the magnetic anisotropy. While in the contrary, the heavy lanthanide ions behave much larger residual orbital momentum and magnetic anisotropy. Herein we will discuss several examples to summarize the strategies in controlling magnetic anisotropy of various metal ions.

## 4.1 Symmetry

The first of all consideration is the symmetry. Symmetry dictates interaction and determines energy splitting. In a specific model geometry, such as triangular pyramid ( $C_{3v}$ ), octahedral ( $O_h$ ), or trigonal prism ( $D_{3d}$ ), the five degenerated  $d$  orbitals are split due to the crystal field effects affording a new degeneracy, which, very frequently, can be further removed by the Jahn-Teller distortion. The non-degeneracy of the  $d$  orbitals leads to the quench of the orbital momentum of the ground state, while the large ZFS originates from excited states without spin-orbit contributions lying close to the ground state.

It is not a trial task to calculate the ZFS tensor elements so as to conclude the magnetic anisotropy type and magnitude based on the simple symmetry analysis. However, recently, Ruiz and his coworkers have analyzed the whole first-row transition series members based on the molecular orbitals of  $Fe^{II}(NH_3)_x$  in 31 sorts of optimized coordination symmetries with respect to coordination number  $x$  from 2 to 8 [13]. Even though Ruiz's approach has simplified largely the model, it is still rather complicated for some of the electron configurations. For instance, the octahedral  $Mn^{III}$  can be either easy-axial or easy-plane anisotropy in different distortions. This would lead to the difficulties in rational design of the SIMs; however, some predictions can still be made according to this model.

The  $d^6$  configuration in most of the geometry and their distortion form is able to behave the large negative  $D$  value offering an easy-axial anisotropy. The magnetic anisotropy of  $Fe^{II}$  with  $d^6$  configuration in trigonal pyramid symmetry ( $C_{3v}$ ) has been very well discussed by Ruiz [75], Coronado [76], and Neese's group [77] and confirming the validity of the present model. Contrary to  $d^6$ , the  $d^2/d^7$  and  $d^3/d^8$  configuration has a higher probability in behaving an easy-plane anisotropy. For instance, the tetrahedron  $Co^{II}$  can behave either positive [78] or negative [10]  $D$  value in large magnitude; one can therefore find both cases in literatures. We have reported a  $Co^{II}Co^{III}_3$  tetranuclear compound with only one spin carriers  $Co^{II}$  whose local symmetry can be approximated to  $D_3$  [79]. It is proved to behave SMM behaviors, which coincide with the "trigonal prism-6" model.

In contrast to the transition ions, the crystal field effect for lanthanide ions is much smaller than the spin-orbit coupling and therefore cannot vary the energy of the multiplet. The removal of the many-fold degeneration is determined by the crystal field as previously discussed in the crystal field Hamiltonian part. It is interesting to note that the lucid selection of the local symmetry can make the control of the lanthanide ions anisotropy rationally. For instance, the crystal field of several symmetries can always offer eigenfunctions in pure. The terms in the crystal field



Hamiltonian for the symmetry of  $D_{5h}$ ,  $D_{\infty h}$ ,  $D_{4d}$ ,  $D_{6d}$ ,  $C_{\infty v}$ , and  $S_8$  consist of only axial ones, always affording pure states.

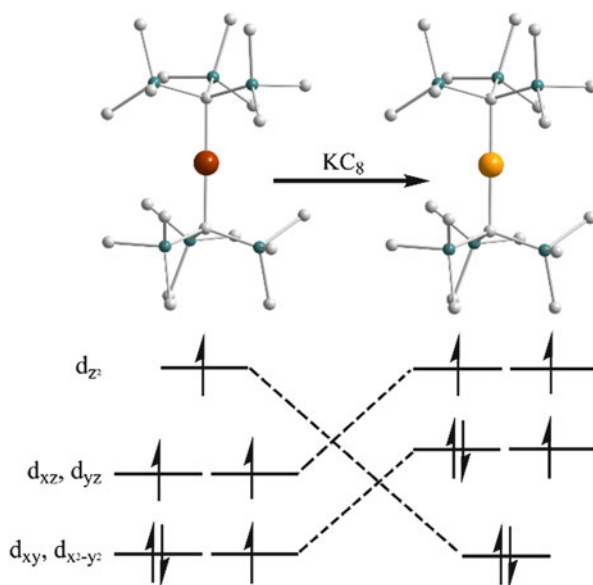
## 4.2 Orbital Hybridization

Long's group has reported a series of two-coordinated linear Fe molecules behaving very large relaxation energy barriers [80]. Due to the largely unquenched orbital momentum, the fitting of the magnetization data to the spin Hamiltonian failed. It is very interesting to notice that the coordinating  $\sigma$ -bond is participated by metal centered both  $3d_{z^2}$  and  $4s$  orbitals, affording a  $4s-3d$  mixing [81]. This sort of hybridization is able to largely stabilize the energy of  $3d_{z^2}$ , converting it from strong antibonding to weak one.

Phenomenally, one can imagine that the crystal field is attenuated by reducing the valance of the iron, so that the static electronic interaction is weaker. Long and his coworkers have reported a linear-shaped Fe(I) complex, where the  $3d_{z^2}$  orbital is further stabilized to even lower energy than  $d_{x^2-y^2}/d_{xy}$  and  $d_{xz}/d_{yz}$ , owing to the hybridization of  $3d_{z^2}$  and  $4s$  (Fig. 2) [80]. Furthermore, due to the very weak crystal field effect, an almost unquenched orbital momentum is established. Taking the advantage of Kramers system, the tunneling splitting is theoretically avoided. The magnetic hysteresis can be observed above 5 K with a slow relaxation energy barrier over 300 K.

It is necessary to note that the outstanding behavior of this complex relies not only on the linear coordination mode. Theoretical calculation implies that once the

**Fig. 2** The structure of the linear-shaped two-coordinated Fe molecules and the electronic configuration of their  $d$  orbitals. The existence of  $3d-4s$  hybridization largely stabilizes the  $d_{z^2}$  orbital (the location of each orbital is plotted for indication, not precisely representing their relative energies). By reducing the  $Fe^{II}$  to  $Fe^I$ , the  $d_{z^2}$  is further stabilized to even the lowest energy among the five  $d$  orbitals. The orbital momentum of the molecule is thus largely sustained





coordination atom is substituted from  $sp^3$  carbon into any other hybridization type ( $sp^2$  or  $sp$ ), a strong  $\sigma$ - $\pi$  mixing occurs. Dalal and his coworker has reported another linear-shaped Fe(I) complex with carbene as coordination ligand, whereas the magnetic hysteresis is absent and the relaxation energy barrier is reduced to 10% of Long's one [82]. The major reason of this is due to the coordinating carbon that is of  $sp^2$  type and  $\sigma$ - $\pi$  mixing destructives on the axiality of the Fe ion.

Contrary to lanthanides, the  $3d$  orbitals of transition metal ions are valence orbitals, and the orbital angular momentum can be readily quenched by ligand fields. Thus, the second-order SOC, stemming from excited states mixing with the ground states through the spin-orbit operator, plays the major role in the magnetic anisotropy of transition metal complexes in most cases. Nevertheless, low coordination number, e.g., linear two-coordinate complexes, could preserve the first-order orbital angular momentum and significantly improve the magnetic anisotropy. In contrast to many SMMs, in which the metal-ligand interactions are quite ionic or single-bond in character, Gao and coworkers studied three two-coordinate cobalt imido complexes in the form of (NHC)CoNAr, which feature  $Co = N$  double bonds. Among them, one compound shows slow relaxation of magnetization at temperatures up to 50 K, and features the record effective relaxation barrier of  $363\text{ cm}^{-1}$  known for transition-metal SMMs to date. Theoretical studies disclosed that the fine performance of these cobalt imido SMMs stems from the intrinsic uniaxial anisotropy of the metal ion  $[CoN]^+$  that resembles a lanthanide ion with a  $|M_J| = \pm 7/2 >$  ground Kramers doublet, proving the effectiveness of the present strategy in improving the magnetic anisotropy of transition-metal SMMs [83].

### 4.3 Charges Location

As described previously, the electron cloud of the ground-state rare earth is not spherical with the presence of crystal field. In order to reduce the electronic static repulsion, a lucid organization of the coordination atoms with negative charges around the rare-earth ions would be able to stabilize their Ising states [14]. For instance, the electron cloud of  $Tb^{3+}/Dy^{3+}$  ions in their Ising state is axially pressed as a pancake; therefore, the wise location of the negative charges to stabilize this state is around the two poles of a virtual axis, which could turn out to be very close to the quantized axis or magnetic easy axis of the  $Tb^{3+}/Dy^{3+}$  ion.

There have been plenty of examples with  $Dy^{3+}$  ion confirming this strategy, and the efforts from Sessoli [72], Boulon [84], and Jiang [23] provide solid evidence of the easy axis orientation by the angular-resolved magnetometry measurement. Jiang and Wang have reported the sole example of the  $Tb^{3+}$  containing SMM with well-determined magnetic easy axis [85]. Even though it is a tetranuclear complex with a pair of  $Tb^{3+}$  and  $Cu^{2+}$  dimers, the major anisotropy of the molecule is contributed by the  $Tb^{3+}$  ions related by a pseudo-inversion center, offering the possibility of determination of the magnetic principal axes. The experimental and theoretical

magnetic easy axis orients along the direction of the negative charges of azide, phenolic oxygen atoms, proving the validity of the above strategy.

The electron cloud of  $\text{Er}^{3+}$  and  $\text{Tm}^{3+}$  ions, of axial-elongated type in the Ising state, is contrary to the previous two. This has led to some doubts in understanding the charge locations [86]. Some very well-established SMMs containing  $\text{Er}^{3+}$  ion feature sandwiched structures with aromatic rings [12, 87–90], seeming that the negative charges are along the pseudo-axial direction. However, the crystal field analysis by Coronado and his coworkers provides that the on-nuclei negative charges can never reproduce the magnetic susceptibility, while a charge displacement is necessary [91]. Jiang and Qin have built up the potential energy map of the interaction between  $\text{Er}^{3+}$  ion and the aromatic ligands, concluding that the offset of the charge and nuclei plays an important role in stabilizing the prolate-shaped Ising state (Fig. 1c) [42]. Both experimental and theoretical investigations elucidating the magnetic easy axis are approximately normal to the aromatic rings indeed. A recent work from Gao's group confirms the validity of  $\text{Tm}^{3+}$  model [92]. The negative charges from the aromatic ring are displaced from the carbon nuclei to the equator plane of the electron cloud of  $\text{Tm}^{3+}$  ion, so as to stabilize the Ising state of axial-elongated type.

Gao and coworkers used a low-coordinate strategy to control the single-ion anisotropy of lanthanide compounds. A series of phenol-supported rare-earth complexes  $[(\text{ArO})\text{Ln}(\text{OAr}')]$  ( $\text{Ln} = \text{Tb}, \text{Dy}, \text{Ho}, \text{Er}, \text{Tm}$ ) were synthesized by one-step reaction. Despite the opposite  $4f$  electron distribution of the dysprosium and erbium ion in their Ising limit ground states, both the dysprosium and erbium analogs exhibited single-ion magnet behavior in this facial structure. It is an interesting phenomenon, showing the “Janus” character of the  $\text{ArOH}$  ligand and the promising prospect of the real two-coordinate lanthanide complexes [93].

## 5 Single-Ion Anisotropy in Complicated Systems

The original idea to investigate the SIMs is to provide an access to understand the magnetic behavior of complicated systems with more spin carriers. The syntheses and researches on mononuclear molecules featuring similar structural unit of clusters or coordination polymers are a typical molecular engineering approach to understand the complicated magnetic behavior caused by the differently oriented magnetic easy axes and the interaction between them. However, this sort of researches are limited majorly because the rational design and synthesis of specific coordination molecules are still a challenge for inorganic chemists. Luckily, theorists have contributed very powerful tools to access to the mononuclear behavior in the coordination clusters. The quantum chemistry calculation can provide rather accurate information about the magnetic easy axis orientation and its wavefunction combination [44]. Some further semiempirical approach can offer the magnetic interaction information [45]. Nevertheless, the chemists should always make efforts from experimental

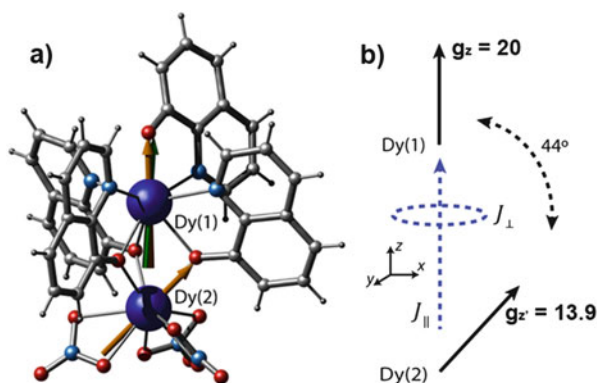
approaches to investigate the complicated systems, since the first principle methods are limited to large clusters due to its calculation accuracy and capacity.

In this part we will show a few examples to illustrate the importance of the single-ion anisotropy information in understanding the overall magnetic behavior.

## 5.1 Dinuclear Systems

A molecule with only two magnetic anisotropy centers is the simplest system in molecular clusters. However, it turns out to be already complicated enough for experimentalists to investigate. Winpenny and his coworkers have reported a molecule containing two dysprosium ions [94]. In addition to the low symmetry of the crystal symmetry, there are two symmetrically independent  $\text{Dy}^{3+}$  within one molecule. It is therefore impossible to identify the magnetic principal axes from magnetic measurement. However, the *ab initio* methods provide abundant information about the single-ion anisotropy. Both the two  $\text{Dy}^{3+}$  ions show strong Ising-type anisotropy, and one of them almost reaches its Ising limit state.

The most exciting result in this research is the direct measurement of the anisotropic interaction based on the above single-ion anisotropy information. The EPR measurement revealed different spectra on pure and magnetic site diluted samples, indicating the existence of the magnetic coupling between the spin carriers. By assuming the two  $\text{Dy}^{3+}$  ions as effective spin 1/2 with  $g_{\text{eff}} = 20$  and 14, the anisotropic interaction constants less than  $2 \text{ cm}^{-1}$  can be precisely determined (Fig. 3). It is a big challenge to obtain such small interaction constants by fitting the magnetic data. One has to note that the success of this determination highly relies on the previous quantum chemistry calculation providing the single-ion anisotropy.



**Fig. 3** (a) The molecule structure of the  $\text{Dy}_2$  molecule. The golden arrows indicate the magnetic easy axes of the dysprosium ions according to the *ab initio* calculation. (b) The schematic plot of the respective magnetic anisotropy of the molecule. The easy axes of the two ions within the molecule make an angle of  $44^\circ$ , responsible for the anisotropic exchange coupling

The quantum calculation in this example is proved to be powerful but with a limited accuracy. The calculated crystal field splitting information was evaluated by the magnetic resonance spectrometer. The experimental determined two crystal field transitions that are 1.6 times higher than the theoretical ones. This could be possibly attributed to the calculation capacity. It is therefore necessary to bear in mind the importance of accessing the single-ion anisotropy from experimental approach.

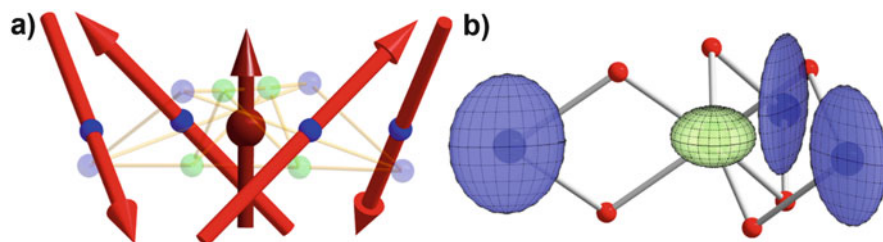
The magnetic anisotropy information of spin carriers which are not symmetrically related can also be determined from polarized neutron experiment. Very similar to the  $\text{Dy}_2$  example, a dinuclear  $\text{Co}^{2+}$  molecule was reported by Gillon and her coworkers [51]. The PND provides clear single-ion magnetic susceptibility tensor information on both cobalt ions, which coincides with the molecular tensor determined by the magnetic measurement on a single crystal. A surprising result is that one of the eigenvalues of the susceptibility tensor for both  $\text{Co}^{2+}$  ions is negative, distinct from the classical paramagnetic behavior. This observation is attributed to the existence of strong antiferromagnetic interaction between the two spin carriers, since one of the spins is along the magnetic field and the strong magnetic interaction forces the other one to align against the field direction. Additionally, the non-collinear magnetic principal axes of the two spin centers result in an asymmetric interaction, which is also confirmed by both the PND and the magnetic susceptibility measurement previously.

## 5.2 Axial Cluster

A higher symmetry can largely reduce the Hamiltonian parameters, therefore offering the possibility to understand large clusters. In the field of the molecular magnetism, the axial symmetry is often the strategy to constrain the uniaxial anisotropy, while there are not many examples in discussing the role of the single-ion anisotropy in constructing the overall magnetic behavior. Herein we provide two examples in this sort of research.

The  $\text{Mn}_{12}$  is the first-observed SMM and the most well-investigated one. The original  $\text{Mn}_{12}$ 's axial symmetry is destroyed by the disordered acetic acid molecules which interact with the  $\text{Mn}_{12}$  molecule via hydrogen bond [95]. Substituting the aside methyl groups by bulky tert-butyl, an ideal fourfold symmetry  $\text{Mn}_{12}$  can be obtained [96]. Gatteschi and his coworkers have measured the HFEP with the magnetic field scanning in the hard plane [97]. The transition fields are found to oscillate as a function of the rotation angle with a periodicity of  $90^\circ$ . This is not surprising in an ideal fourfold symmetry. This observation is actually the direct evidence of the transverse anisotropy in the hard plane. Within the giant spin model, the anisotropy parameters up to sixth rank are reported with very high precision.

The power of these results is revealed by the multi-spin model. As the Hilbert space dimension is expected to be  $10^8$  with a full consideration of the electron spins, far beyond the computer capacity, a simplified model by coupling 8 manganese ions as one anisotropic spin carrier is employed, affording a dimension of 3,125 matrix to



**Fig. 4** The investigation of the magnetic anisotropy origination for  $\text{Mn}_{12}$  (a) and  $\text{Fe}_3\text{Cr}$  (b). (a) The red arrows indicate the direction of the Jahn-Teller as well as the easy axis direction of the  $\text{Mn}^{\text{III}}$  ions. The rest of the spin carriers are denoted in transparent and treated as a total spin of 2 expressed in dark red, behaving an overall easy-axial anisotropy. The side  $\text{Mn}^{\text{III}}$  ions are responsible for the transverse anisotropy in the fourfold molecule. (b) The elliptical spheres in blue denote the  $\text{Fe}^{\text{III}}$  ions behaving easy-plane anisotropy, and the green one is that of hard axial  $\text{Cr}^{\text{III}}$  ion (see the text). This orientation of the easy-plane anisotropy ions making an Ising-type molecule

diagonalize. The single-ion anisotropy of four the side  $\text{Mn}^{3+}$  ions is provided by the angular overlap model, whose easy axes are along the Jahn-Teller elongated axes.

This multi-spin Hamiltonian can very well reproduce the above fourfold oscillation pattern, illustrating the validity of the model. As these side  $\text{Mn}^{3+}$  ions are the only source of fourfold anisotropy, one can conclude that the Jahn-Teller distortion is responsible for the transverse anisotropy of  $\text{Mn}_{12}$  (Fig. 4a). It is further confirmed by the influence on the tunneling splitting by varying the angle between the fourfold molecular axis and the easy axis of the distorted  $\text{Mn}^{3+}$ . This conclusion closes the question of the origination of the transverse anisotropy of axial  $\text{Mn}_{12}$ .

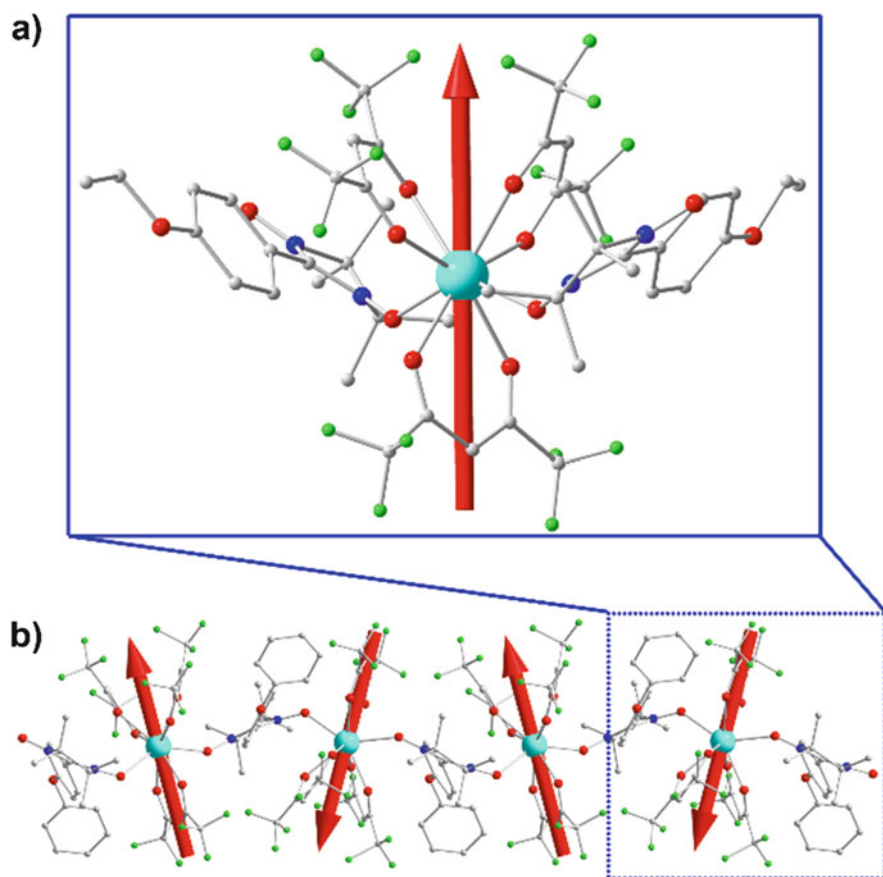
Very similar to this research, a molecule  $\text{Fe}_3\text{Cr}$  of ideal threefold symmetry is investigated by Sorace and his coworkers [98]. The measurement was performed on a single crystal by the W-band EPR. The transition field as a function of rotation angle in the hard plane was found to feature sixfold pattern, owing to an additional inversion symmetry of the magnetic field. Again, the multi-spin Hamiltonian approach was applied with the light of the previously determined single-ion anisotropy [99]. It is interesting to notice that both types of spin carriers are of hard axial type, while the overall molecular anisotropy is easy axial (Fig. 4b). The multi-spin Hamiltonian simulation concludes that the non-collinear orientation of the  $\text{Fe}^{3+}$  ZFS tensor leads to the molecular easy-axial anisotropy. The orientation mode features that the easy planes of the  $\text{Fe}^{3+}$  ions almost parallel to the threefold axis and intersect to each other on the molecular symmetry axis.

### 5.3 Magnetic Chain

Gatteschi's group has reported a series of single-chain magnets with rare-earth ions and organic radical as spin carriers [100, 101]. The slow magnetic relaxation behavior of the magnetic chain can be explained by Glauber's theory, which requests

the spin carriers are of Ising type. It can be easily interpreted that the  $\text{Dy}^{3+}$  ions in the chain are of strong easy-axial anisotropy, whereas the question lies in where each easy axis orients. This is a critical information that determines how the spin couples to each other. In cooperation with the ab initio calculation, the magnetization measurement along and normal to the chain reveals that the weak ferromagnetic interaction is characterized within the one-dimensional topologic structure [102]. The strong uniaxial anisotropic  $\text{Dy}^{3+}$  ions interact with the radical and the next-to-nearest rare-earth center via Heisenberg exchange interaction featuring spin-canted antiferromagnetic arrangement (Fig. 5b).

A later work from this group has successfully synthesized a monomer unit of this chain with only one  $\text{Dy}^{3+}$  center and two radicals [103]. The monomer crystallized in a triclinic space group offering the possibility of determining the magnetic easy axis experimentally. As the radicals are isotropic, the molecular anisotropy is expressed



**Fig. 5** The magnetic anisotropy direction of the dysprosium magnetic chain (b) and its unit (a). The monomer anisotropy is determined by angular-resolved magnetometry and confirmed by the ab initio calculation. This experiment explains the spin canting behavior in the magnetic chain

only by the  $\text{Dy}^{3+}$  ion. The angular-resolved magnetometry measurement shows that the  $\text{Dy}^{3+}$  ion is of strong Ising type as expected by the *ab initio* result. More importantly, the magnetic easy axis of the  $\text{Dy}^{3+}$  center is well-established experimentally (Fig. 5a). It is very close to the pseudo-twofold symmetry axis which is also confirmed by the quantum chemistry calculation. This result offers the solid evidence that the aforementioned magnetic chain is indeed spin canting caused by the strong uniaxial anisotropy of  $\text{Dy}^{3+}$  center. It is worth remarking that this work is a typical example that a complicated system is very well viewed from its unit's magnetic behavior. Different from the previous examples, there is no explanation that heavily relies on the *ab initio* calculation, which finally turns out to be just a supporting to the experimental results.

## 6 Conclusion Remarks

This perspective has majorly overviewed the theoretical and experimental considerations in constructing the single-ion magnets and their role in understanding as well as designing more complicated chemical systems. In the past 23 years, the chemists have made large achievements in the molecular magnetism. Specialists from material and physical field have successfully put magnetic molecules onto surface or nanotubes to construct molecular-based devices for further application. The molecular spintronics is developing rapidly, while it is very much limited on only a few well-established magnetic molecules. This requests the chemists to make further exploit in syntheses and characterizations of new molecules.

The tendency has shifted from large molecules to small ones. One of the major driving forces is that small ones could be simpler to investigate and control. However, at this moment, when we have quite plenty of knowledges about how to implement magnets with single ion, it would be the right time to again go back to some rational designed complicated systems of more spin carriers, since the proper synergistic effect could enhance the overall magnetic anisotropy much more efficient than only focusing on mononuclear itself. By manipulating the orientation of the single-ion anisotropy, the magnetic easy axes can parallelly construct the molecular structure and the ferromagnetic coupling or dipole interaction would be able to slow down the spin-lattice relaxation time and increase the energy barrier. Moreover, the molecule-based model of some interesting physical phenomena can also be constructed by this sort of engineering, including the spin ice [104], spin liquid [105], and spin chirality [106] et al. Many of these systems are based on the well-defined Ising-type anisotropy and their relative topology. It is therefore of heavy demand to construct the molecule-based clusters as well as frameworks with special topology of magnetic anisotropy from molecular engineering approach. This would increase the variety of the structures in chemistry aspect so as to investigate the physical phenomena diversely, which is actually the chemists' fundamental responsibility in the development of molecular magnetism.



The second remark herein is the necessity of employing more unconventional characterization methods in addition to the traditional magnetic measurement. As were reviewed in this perspective, the angular-resolved magnetometry, the PND, the HFEPR and related FDMRS, the high-resolution luminescence spectroscopy, the torque magnetometry, and plenty of other advanced characterization methods not discussed here can always offer direct evidence of energy levels, magnetic coupling, and anisotropy-type information. The combination of these methods would lead to solidier conclusions than pure ab initio calculations.

Molecular magnets, the molecules with well-defined electronic fine structures, have been very well investigated about their magnetic anisotropy, energy levels, or their interactions. These researches are based on quantum mechanics conclusions but more similar to the classical properties in molecular size. The quantum computation requests the quantum coherent properties in these molecules [4, 107], while most of the molecular magnetism research is far away from that. Winpenny and Ardavan [108–111], van Slageren [112, 113], Du [114], Takahashi [115, 116], Coronado [117, 118], Freedman [119], and more groups have made excellent achievements in manipulating the quantum coherent state of molecular magnetism. Remarkably, van Slageren and Takahashi have made the success in single-molecule magnets, and Ardavan together with Winpenny has made the coherent interaction between two molecular magnets [120, 121]. The quantum computation is always mentioned in the publications as one of the promising applications of molecular magnetism, while the related quantum coherent engineering is lack of investigation from chemistry point of view. The physicists have provided clear approaches to increase the quantum coherent time, such as decrease the dipolar and hyperfine interaction [122]. There is a large space for chemists making efforts to improve the long-lasting quantum phase [123–125], as was done in improving the relaxation energy barriers in SMMs.

In conclusion, there has been a huge success in the field of molecular magnetism. While there still left a long way ahead for chemists to exploit so as to push them to final application, the combination of tools from various fields is necessary to view the future of this direction.

**Acknowledgment** We thank the National Science Foundation of China and the National Basic Research Program of China for support.

## References

1. Kahn O (1993) Molecular magnetism. VCH Publishers, New York, Weinheim
2. Sessoli R, Gatteschi D, Caneschi A, Novak MA (1993) Magnetic bistability in a metal-ion cluster. *Nature* 365(6442):141–143
3. Eppley HJ, Aubin SMJ, Wemple MW, Adams DM, Tsai HL, Grillo VA, Castro SL, Sun ZM, Foltling K, Huffman JC, Hendrickson DN, Christou G (1997) Single-molecule magnets: characterization of complexes exhibiting out-of-phase AC susceptibility signals. *Mol Cryst Liq Cryst Sci Technol* 305:167–179



4. Leuenberger MN, Loss D (2001) Quantum computing in molecular magnets. *Nature* 410(6830):789–793
5. Bogani L, Wernsdorfer W (2008) Molecular spintronics using single-molecule magnets. *Nat Mater* 7(3):179–186
6. Jiang SD, Goss K, Cervetti C, Bogani L (2012) An introduction to molecular spintronics. *Sci China Chem* 55(6):867–882
7. Aromi G, Brechin EK (2006) Synthesis of 3d metallic single-molecule magnets. *Struct Bond* 122:1–67
8. Gatteschi D, Sorace L (2001) Hints for the control of magnetic anisotropy in molecular materials. *J Solid State Chem* 159(2):253–261
9. Ishikawa N, Sugita M, Ishikawa T, Koshihara S, Kaizu Y (2003) Lanthanide double-decker complexes functioning as magnets at the single-molecular level. *J Am Chem Soc* 125(29):8694–8695
10. Zadrozny JM, Long JR (2011) Slow magnetic relaxation at zero field in the tetrahedral complex [Co(SPh)(4)](2-). *J Am Chem Soc* 133(51):20732–20734
11. Jiang SD, Wang BW, Su G, Wang ZM, Gao S (2010) A mononuclear dysprosium complex featuring single-molecule-magnet behavior. *Angew Chem Int Ed* 49(41):7448–7451
12. Jiang SD, Wang BW, Sun HL, Wang ZM, Gao S (2011) An organometallic single-ion magnet. *J Am Chem Soc* 133(13):4730–4733
13. Gomez-Coca S, Cremades E, Aliaga-Alcalde N, Ruiz E (2013) Mononuclear single-molecule magnets: tailoring the magnetic anisotropy of first-row transition-metal complexes. *J Am Chem Soc* 135(18):7010–7018
14. Rinehart JD, Long JR (2011) Exploiting single-ion anisotropy in the design of f-element single-molecule magnets. *Chem Sci* 2(11):2078–2085
15. Ding YS, Chilton NF, Winpenny REP, Zheng YZ (2016) On approaching the limit of molecular magnetic anisotropy: a near-perfect pentagonal bipyramidal dysprosium(III) single-molecule magnet. *Angew Chem Int Ed* 55(52):16071–16074
16. Guo FS, Day BM, Chen YC, Tong ML, Mansikkamaki A, Layfield RA (2017) A dysprosium metallocene single-molecule magnet functioning at the axial limit. *Angew Chem Int Ed* 56(38):11445–11449
17. Goodwin CAP, Ortu F, Reta D, Chilton NF, Mills DP (2017) Molecular magnetic hysteresis at 60 kelvin in dysprosocenium. *Nature* 548(7668):439–442
18. Ganivet CR, Ballesteros B, de la Torre G, Clemente-Juan JM, Coronado E, Torres T (2013) Influence of peripheral substitution on the magnetic behavior of single-ion magnets based on homo- and heteroleptic TbIII bis(phthalocyaninate). *Chem Eur J* 19(4):1457–1465
19. Rinehart JD, Fang M, Evans WJ, Long JR (2011) Strong exchange and magnetic blocking in N-2(3-)-radical-bridged lanthanide complexes. *Nat Chem* 3(7):538–542
20. Milios CJ, Vinslava A, Wernsdorfer W, Moggach S, Parsons S, Perlepes SP, Christou G, Brechin EK (2007) A record anisotropy barrier for a single-molecule magnet. *J Am Chem Soc* 129(10):2754–2755
21. Benelli C, Gatteschi D (2002) Magnetism of lanthanides in molecular materials with transition-metal ions and organic radicals. *Chem Rev* 102(6):2369–2387
22. Sorace L, Benelli C, Gatteschi D (2011) Lanthanides in molecular magnetism: old tools in a new field. *Chem Soc Rev* 40(6):3092–3104
23. Qian K, Baldovi JJ, Jiang S-D, Gaita-Arino A, Zhang Y-Q, Overgaard J, Wang B-W, Coronado E, Gao S (2015) Does the thermal evolution of molecular structures critically affect the magnetic anisotropy? *Chem Sci* 6(8):4587–4593
24. Abragam A, Bleaney B (2012) *Electron paramagnetic resonance of transition ions*. Oxford University Press, Oxford
25. Stevens KWH (1952) Matrix elements and operator equivalents connected with the magnetic properties of rare earth ions. *Proc Phys Soc Lond A* 65(387):209–215
26. Rudowicz C, Chung CY (2004) The generalization of the extended Stevens operators to higher ranks and spins, and a systematic review of the tables of the tensor operators and their matrix elements. *J Phys Condens Mat* 16(32):5825–5847

27. Görrler-Walrand C, Binnemans K (1996) Rationalization of crystal-field parametrization. In: Gschneidner Jr KA, Le Roy E (eds) Handbook on the physics and chemistry of rare earths, vol 23. Elsevier, Amsterdam, pp 121–283
28. Bencini A, Gatteschi D (2012) EPR of exchange coupled systems. Dover, Illinois
29. Mironov VS, Chibotaru LF, Ceulemans A (2003) Mechanism of a strongly anisotropic Mo-III-CN-Mn-II spin-spin coupling in molecular magnets based on the [Mo(CN)(7)](4-) heptacyanometalate: a new strategy for single-molecule magnets with high blocking temperatures. *J Am Chem Soc* 125(32):9750–9760
30. Qian K, Huang XC, Zhou C, You XZ, Wang XY, Dunbar KR (2013) A single-molecule magnet based on heptacyanomolybdate with the highest energy barrier for a cyanide compound. *J Am Chem Soc* 135(36):13302–13305
31. Magee SA, Sproules S, Barra AL, Timco GA, Chilton NF, Collison D, Winpenny REP, McInnes EJL (2014) Large zero-field splittings of the ground spin state arising from antisymmetric exchange effects in heterometallic triangles. *Angew Chem Int Ed* 53(21):5310–5313
32. Racah G (1942) Theory of complex spectra I. *Phys Rev* 61(3/4):186–197
33. Racah G (1942) Theory of complex spectra. II. *Phys Rev* 62(9/10):438–462
34. Racah G (1943) Theory of complex spectra. III. *Phys Rev* 63(9/10):367–382
35. Schilder H, Lueken H (2004) Computerized magnetic studies on d, f, d-d, f-f, and d-S, f-S systems under varying ligand and magnetic fields. *J Magn Magn Mater* 281(1):17–26
36. van Leusen J, Speldrich M, Schilder H, Kogerler P (2015) Comprehensive insight into molecular magnetism via CONDON: full vs. effective models. *Coord Chem Rev* 289:137–148
37. Baldovi JJ, Borrás-Almenar JJ, Clemente-Juan JM, Coronado E, Gaita-Arino A (2012) Modeling the properties of lanthanoid single-ion magnets using an effective point-charge approach. *Dalton Trans* 41(44):13705–13710
38. Baldovi JJ, Cardona-Serra S, Clemente-Juan JM, Coronado E, Gaita-Arino A, Palić A (2013) SIMPRE: a software package to calculate crystal field parameters, energy levels, and magnetic properties on mononuclear lanthanoid complexes based on charge distributions. *J Comput Chem* 34(22):1961–1967
39. Sievers J (1982) Asphericity of 4f-shells in their Hund rule ground-states. *Z Phys B Condens Matter* 45(4):289–296
40. Skomski, R., Simple models of magnetism. Oxford University Press: Oxford, New York, 2008
41. Chilton NF, Collison D, McInnes EJL, Winpenny REP, Soncini A (2013) An electrostatic model for the determination of magnetic anisotropy in dysprosium complexes. *Nat Commun* 4:3551
42. Jiang S-D, Qin S-X (2015) Prediction of the quantized axis of rare-earth ions: the electrostatic model with displaced point charges. *Inorg Chem Front* 2(7):613–619
43. Aquilante F, De Vico L, Ferre N, Ghigo G, Malmqvist PA, Neogrady P, Pedersen TB, Pitonak M, Reiher M, Roos BO, Serrano-Andres L, Urban M, Veryazov V, Lindh R (2010) Software news and update MOLCAS 7: the next generation. *J Comput Chem* 31(1):224–247
44. Chibotaru LF, Ungur L (2012) Ab initio calculation of anisotropic magnetic properties of complexes. I. Unique definition of pseudospin Hamiltonians and their derivation. *J Chem Phys* 137(6):064112
45. Chibotaru LF, Ungur L, Aronica C, Elmoll H, Pilet G, Luneau D (2008) Structure, magnetism, and theoretical study of a mixed-valence (Co<sub>3</sub>Co<sub>4</sub>III)-Co-II heptanuclear wheel: lack of SMM behavior despite negative magnetic anisotropy. *J Am Chem Soc* 130(37):12445–12455
46. Luzon J, Sessoli R (2012) Lanthanides in molecular magnetism: so fascinating, so challenging. *Dalton Trans* 41(44):13556–13567
47. Boulon ME, Cucinotta G, Liu SS, Jiang SD, Ungur L, Chibotaru LF, Gao S, Sessoli R (2013) Angular-resolved magnetometry beyond triclinic crystals: out-of-equilibrium studies of Cp\*ErCOT single-molecule magnet. *Chem Eur J* 19(41):13726–13731
48. Perfetti M, Serri M, Poggini L, Mannini M, Rovai D, Sainctavit P, Heutz S, Sessoli R (2016) Molecular order in buried layers of TbPc<sub>2</sub> single-molecule magnets detected by torque magnetometry. *Adv Mater* 28(32):6946–6951

49. Perfetti M (2017) Cantilever torque magnetometry on coordination compounds: from theory to experiments. *Coord Chem Rev* 348:171–186
50. Gukasov A, Brown PJ (2002) Determination of atomic site susceptibility tensors from polarized neutron diffraction data. *J Phys Condens Matter* 14(38):8831–8839
51. Ridier K, Gillon B, Gukasov A, Chaboussant G, Cousson A, Luneau D, Borta A, Jacquot J-F, Checa R, Chiba Y, Sakiyama H, Mikuriya M (2015) Polarized neutron diffraction as a tool for mapping molecular magnetic anisotropy: local susceptibility tensors in CoII complexes. *Chem Eur J*. <https://doi.org/10.1002/chem.201503400>
52. Jorgensen MRV, Hathwar VR, Bindzus N, Wahlberg N, Chen YS, Overgaard J, Iversen BB (2014) Contemporary X-ray electron-density studies using synchrotron radiation. *IUCrJ* 1:267–280
53. Koritsanzky TS, Coppens P (2001) Chemical applications of X-ray charge-density analysis. *Chem Rev* 101(6):1583–1627
54. Stalke D (2011) Meaningful structural descriptors from charge density. *Chem-Eur J* 17(34):9264–9278
55. Barra AL, Brunel LC, Gatteschi D, Pardi L, Sessoli R (1998) High-frequency EPR spectroscopy of large metal ion clusters: from zero field splitting to quantum tunneling of the magnetization. *Acc Chem Res* 31(8):460–466
56. Hagen WR (1999) High-frequency EPR of transition ion complexes and metalloproteins. *Coord Chem Rev* 192:209–229
57. Gatteschi D, Barra AL, Caneschi A, Cornia A, Sessoli R, Sorace L (2006) EPR of molecular nanomagnets. *Coord Chem Rev* 250(11–12):1514–1529
58. Krzystek J, Ozarowski A, Telser J (2006) Multi-frequency, high-field EPR as a powerful tool to accurately determine zero-field splitting in high-spin transition metal coordination complexes. *Coord Chem Rev* 250(17–18):2308–2324
59. del Barco E, Kent AD, Hill S, North JM, Dalal NS, Rumberger EM, Hendrickson DN, Chakov N, Christou G (2005) Magnetic quantum tunneling in the single-molecule magnet Mn-12-acetate. *J Low Temp Phys* 140(1–2):119–174
60. Hill S, Datta S, Liu J, Inglis R, Milios CJ, Feng PL, Henderson JJ, del Barco E, Brechin EK, Hendrickson DN (2010) Magnetic quantum tunneling: insights from simple molecule-based magnets. *Dalton Trans* 39(20):4693–4707
61. van Slageren J (2012) New directions in electron paramagnetic resonance spectroscopy on molecular nanomagnets. In: Drescher M, Jeschke G (eds) *EPR spectroscopy*, vol 321. Springer, Berlin, Heidelberg, pp 199–234
62. Wernsdorfer W, Muller A, Maily D, Barbara B (2004) Resonant photon absorption in the low-spin molecule V-15. *Europhys Lett* 66(6):861–867
63. Bal M, Friedman JR, Suzuki Y, Rumberger EM, Hendrickson DN, Avraham N, Myasoedov Y, Shtrikman H, Zeldov E (2005) Non-equilibrium magnetization dynamics in the Fe-8 single-molecule magnet induced by high-intensity microwave radiation. *Europhys Lett* 71(1):110–116
64. El Hallak F, van Slageren J, Dressel M (2010) Torque detected broad band electron spin resonance. *Rev Sci Instrum* 81(9):095105
65. Jamet M, Wernsdorfer W, Thirion C, Maily D, Dupuis V, Melinon P, Perez A (2001) Magnetic anisotropy of a single cobalt nanocluster. *Phys Rev Lett* 86(20):4676–4679
66. van Slageren J, Vongtragoon S, Gorshunov B, Mukhin AA, Karl N, Krzystek J, Telser J, Muller A, Sangregorio C, Gatteschi D, Dressel M (2003) Frequency-domain magnetic resonance spectroscopy of molecular magnetic materials. *Phys Chem Chem Phys* 5(18):3837–3843
67. Jiang SD, Maganas D, Levesanos N, Ferentinos E, Haas S, Thirunavukkuarasu K, Krzystek J, Dressel M, Bogani L, Neese F, Kyritsis P (2015) Direct observation of very large zero-field splitting in a tetrahedral (NiSe4)-Se-II coordination complex. *J Am Chem Soc* 137(40):12923–12928
68. Rogez G, Rebilly JN, Barra AL, Sorace L, Blondin G, Kirchner N, Duran M, van Slageren J, Parsons S, Ricard L, Marvilliers A, Mallah T (2005) Very large ising-type magnetic anisotropy in a mononuclear Ni-II complex. *Angew Chem Int Ed* 44(12):1876–1879

69. Ray K, Begum A, Weyhermuller T, Piligkos S, van Slageren J, Neese F, Wieghardt K (2005) The electronic structure of the isoelectronic, square-planar complexes [Fe-II(L)(2)](2-) and [Co-III(L-Bu)(2)](-) (L2- and (L-Bu)(2-) = benzene-1,2-dithiolates): an experimental and density functional theoretical study. *J Am Chem Soc* 127(12):4403–4415
70. Marx R, Moro F, Dorfel M, Ungur L, Waters M, Jiang SD, Orlita M, Taylor J, Frey W, Chibotaru LF, van Slageren J (2014) Spectroscopic determination of crystal field splittings in lanthanide double deckers. *Chem Sci* 5(8):3287–3293
71. Yi XH, Bernot K, Le Corre V, Calvez G, Pointillart F, Cador O, Le Guennic B, Jung J, Maury O, Placide V, Guyot Y, Roisnel T, Daiguebonne C, Guillou O (2014) Unraveling the crystal structure of lanthanide-murexide complexes: use of an ancient complexometry indicator as a near-infrared-emitting single-ion magnet. *Chem Eur J* 20(6):1569–1576
72. Cucinotta G, Perfetti M, Luzon J, Etienne M, Car PE, Caneschi A, Calvez G, Bernot K, Sessoli R (2012) Magnetic anisotropy in a dysprosium/DOTA single-molecule magnet: beyond simple magneto-structural correlations. *Angew Chem Int Ed* 51(7):1606–1610
73. Perfetti M, Cucinotta G, Boulon ME, El Hallak F, Gao S, Sessoli R (2014) Angular-resolved magnetometry beyond triclinic crystals part II: torque magnetometry of Cp\*ErCOT single-molecule magnets. *Chem Eur J* 20(43):14051–14056
74. Perfetti M, Lucaccini E, Sorace L, Costes JP, Sessoli R (2015) Determination of magnetic anisotropy in the LnTRENALS complexes (Ln = Tb, Dy, Er) by torque magnetometry. *Inorg Chem* 54(7):3090–3092
75. Cremades E, Ruiz E (2011) Mononuclear Fe-II single-molecule magnets: a theoretical approach. *Inorg Chem* 50(9):4016–4020
76. Palić AV, Clemente-Juan JM, Coronado E, Klokishner SI, Ostrovsky SM, Reu OS (2010) Role of orbital degeneracy in the single molecule magnet behavior of a mononuclear high-spin Fe(II) complex. *Inorg Chem* 49(17):8073–8077
77. Atanasov M, Ganyushin D, Pantazis DA, Sivalingham K, Neese F (2011) Detailed Ab initio first-principles study of the magnetic anisotropy in a family of trigonal pyramidal Iron (II) pyrrolide complexes. *Inorg Chem* 50(16):7460–7477
78. Zdrozny JM, Liu JJ, Piro NA, Chang CJ, Hill S, Long JR (2012) Slow magnetic relaxation in a pseudotetrahedral cobalt(II) complex with easy-plane anisotropy. *Chem Commun* 48(33):3927–3929
79. Zhu YY, Cui C, Zhang YQ, Jia JH, Guo X, Gao C, Qian K, Jiang SD, Wang BW, Wang ZM, Gao S (2013) Zero-field slow magnetic relaxation from single Co(II) ion: a transition metal single-molecule magnet with high anisotropy barrier. *Chem Sci* 4(4):1802–1806
80. Zdrozny JM, Atanasov M, Bryan AM, Lin CY, Rekker BD, Power PP, Neese F, Long JR (2013) Slow magnetization dynamics in a series of two-coordinate iron(II) complexes. *Chem Sci* 4(1):125–138
81. Atanasov M, Zdrozny JM, Long JR, Neese F (2013) A theoretical analysis of chemical bonding, vibronic coupling, and magnetic anisotropy in linear iron(II) complexes with single-molecule magnet behavior. *Chem Sci* 4(1):139–156
82. Samuel PP, Mondal KC, Sk NA, Roesky HW, Carl E, Neufeld R, Stalke D, Demeshko S, Meyer F, Ungur L, Chibotaru LF, Christian J, Ramachandran V, van Tol J, Dalal NS (2014) Electronic structure and slow magnetic relaxation of low-coordinate cyclic Alkyl(amino) carbene stabilized Iron(I) complexes. *J Am Chem Soc* 136(34):11964–11971
83. Yao XN, Du JZ, Zhang YQ, Leng XB, Yang MW, Jiang SD, Wang ZX, Ouyang ZW, Deng L, Wang BW, Gao S (2017) Two-coordinate Co(II) imido complexes as outstanding single molecule magnets. *J Am Chem Soc* 139(1):373–380
84. da Cunha TT, Jung J, Boulon ME, Campo G, Pointillart F, Pereira CLM, Le Guennic B, Cador O, Bernot K, Pineider F, Golhen S, Ouahab L (2013) Magnetic poles determinations and robustness of memory effect upon solubilization in a Dy-III-based single ion magnet. *J Am Chem Soc* 135(44):16332–16335
85. Huang XC, Vieru V, Chibotaru LF, Wernsdorfer W, Jiang SD, Wang XY (2015) Determination of magnetic anisotropy in a multinuclear Tb-III-based single-molecule magnet. *Chem Commun* 51(52):10373–10376

86. Ren M, Zheng L-M (2015) Lanthanide-based single molecule magnets. *Acta Chim Sin* 73(11):1091–1113
87. Meihaus KR, Long JR (2013) Magnetic blocking at 10 K and a dipolar-mediated avalanche in salts of the Bis(eta(8)-cyclooctatetraenide) complex [Er(COT)(2)](-). *J Am Chem Soc* 135(47):17952–17957
88. Le Roy JJ, Jeletic M, Gorelsky SI, Korobkov I, Ungur L, Chibotaru LF, Murugesu M (2013) An organometallic building block approach to produce a multidecker 4f single-molecule magnet. *J Am Chem Soc* 135(9):3502–3510
89. Jeletic M, Lin PH, Le Roy JJ, Korobkov I, Gorelsky SI, Murugesu M (2011) An organometallic sandwich lanthanide single-ion magnet with an unusual multiple relaxation mechanism. *J Am Chem Soc* 133(48):19286–19289
90. Le Roy JJ, Ungur L, Korobkov I, Chibotaru LF, Murugesu M (2014) Coupling strategies to enhance single-molecule magnet properties of erbium-cyclooctatetraenyl complexes. *J Am Chem Soc* 136(22):8003–8010
91. Baldovi JJ, Clemente-Juan JM, Coronado E, Gaita-Arino A (2014) Molecular anisotropy analysis of single-ion magnets using an effective electrostatic model. *Inorg Chem* 53(20):11323–11327
92. Wang B-W, Meng Y, Qiao Y, Zhang Y, Jiang S, Meng Z, Wang Z, Gao S (2016) Can non-Kramers TmIII mononuclear molecules be SMMs? *Chem Eur J* 22(14):4704–4708
93. Meng YS, Xu L, Xiong J, Yuan Q, Liu T, Wang BW, Gao S (2018) Low-coordinate single-ion magnets by intercalation of lanthanides into a phenol matrix. *Angew Chem Int Ed* 57(17):4673–4676
94. Pineda EM, Chilton NF, Marx R, Dorfel M, Sells DO, Neugebauer P, Jiang SD, Collison D, van Slageren J, McInnes EJJ, Winpenny REP (2014) Direct measurement of dysprosium(III) ... dysprosium(III) interactions in a single-molecule magnet. *Nat Commun* 5:5243
95. Cornia A, Sessoli R, Sorace L, Gatteschi D, Barra AL, Daiguebonne C (2002) Origin of second-order transverse magnetic anisotropy in Mn-12-acetate. *Phys Rev Lett* 89(25):257201
96. Wernsdorfer W, Murugesu M, Christou G (2006) Resonant tunneling in truly axial symmetry Mn-12 single-molecule magnets: sharp crossover between thermally assisted and pure quantum tunneling. *Phys Rev Lett* 96(5):057208
97. Barra AL, Caneschi A, Cornia A, Gatteschi D, Gorini L, Heiniger LP, Sessoli R, Sorace L (2007) The origin of transverse anisotropy in axially symmetric single molecule magnets. *J Am Chem Soc* 129(35):10754–10762
98. Sorace L, Boulon ME, Totaro P, Cornia A, Fernandes-Soares J, Sessoli R (2013) Origin and spectroscopic determination of trigonal anisotropy in a heteronuclear single-molecule magnet. *Phys Rev B* 88(10):104407
99. Tancini E, Rodriguez-Douton MJ, Sorace L, Barra AL, Sessoli R, Cornia A (2010) Slow magnetic relaxation from hard-axis metal ions in tetranuclear single-molecule magnets. *Chem Eur J* 16(34):10482–10493
100. Bogani L, Sangregorio C, Sessoli R, Gatteschi D (2005) Molecular engineering for single-chain-magnet behavior in a one-dimensional dysprosium-nitronyl nitroxide compound. *Angew Chem Int Ed* 44(36):5817–5821
101. Bernot K, Bogani L, Caneschi A, Gatteschi D, Sessoli R (2006) A family of rare-earth-based single chain magnets: playing with anisotropy. *J Am Chem Soc* 128(24):7947–7956
102. Bernot K, Luzon J, Caneschi A, Gatteschi D, Sessoli R, Bogani L, Vindigni A, Rettori A, Pini MG (2009) Spin canting in a Dy-based single-chain magnet with dominant next-nearest-neighbor antiferromagnetic interactions. *Phys Rev B* 79(13):134419
103. Bernot K, Luzon J, Bogani L, Etienne M, Sangregorio C, Shanmugam M, Caneschi A, Sessoli R, Gatteschi D (2009) Magnetic anisotropy of dysprosium(III) in a low-symmetry environment: a theoretical and experimental investigation. *J Am Chem Soc* 131(15):5573–5579
104. Bramwell ST, Gingras MJP (2001) Spin ice state in frustrated magnetic pyrochlore materials. *Science* 294(5546):1495–1501
105. Balents L (2010) Spin liquids in frustrated magnets. *Nature* 464(7286):199–208

106. Luzon J, Bernot K, Hewitt IJ, Anson CE, Powell AK, Sessoli R (2008) Spin chirality in a molecular dysprosium triangle: the archetype of the noncollinear Ising model. *Phys Rev Lett* 100(24):247205
107. Ahn J, Weinacht TC, Bucksbaum PH (2000) Information storage and retrieval through quantum phase. *Science* 287(5452):463–465
108. Moro F, Kaminski D, Tuna F, Whitehead GFS, Timco GA, Collison D, Winpenny REP, Ardavan A, McInnes EJJ (2014) Coherent electron spin manipulation in a dilute oriented ensemble of molecular nanomagnets: pulsed EPR on doped single crystals. *Chem Commun* 50(1):91–93
109. Ardavan A, Rival O, Morton JJJ, Blundell SJ, Tyryshkin AM, Timco GA, Winpenny REP (2007) Will spin-relaxation times in molecular magnets permit quantum information processing? *Phys Rev Lett* 98(5):057201
110. Bellini V, Lorusso G, Candini A, Wernsdorfer W, Faust TB, Timco GA, Winpenny REP, Affronte M (2011) Propagation of spin information at the supramolecular scale through heteroaromatic linkers. *Phys Rev Lett* 106(22):227205
111. Wedge CJ, Timco GA, Spielberg ET, George RE, Tuna F, Rigby S, McInnes EJJ, Winpenny REP, Blundell SJ, Ardavan A (2012) Chemical engineering of molecular qubits. *Phys Rev Lett* 108(10):107204
112. Bader K, Dengler D, Lenz S, Endeward B, Jiang SD, Neugebauer P, van Slageren J (2014) Room temperature quantum coherence in a potential molecular qubit. *Nat Commun* 5:5304
113. Schlegel C, van Slageren J, Manoli M, Brechin EK, Dressel M (2008) Direct observation of quantum coherence in single-molecule magnets. *Phys Rev Lett* 101(14):147203
114. Yang JH, Wang Y, Wang ZX, Rong X, Duan CK, Su JH, Du JF (2012) Observing quantum oscillation of ground states in single molecular magnet. *Phys Rev Lett* 108(23):230501
115. Takahashi S, Tupitsyn IS, van Tol J, Beedle CC, Hendrickson DN, Stamp PCE (2011) Decoherence in crystals of quantum molecular magnets. *Nature* 476(7358):76–79
116. Takahashi S, van Tol J, Beedle CC, Hendrickson DN, Brunel LC, Sherwin MS (2009) Coherent manipulation and decoherence of  $S = 10$  single-molecule magnets. *Phys Rev Lett* 102(8):087603
117. Baldovi JJ, Cardona-Serra S, Clemente-Juan JM, Coronado E, Gaita-Arino A, Prima-Garcia H (2013) Coherent manipulation of spin qubits based on polyoxometalates: the case of the single ion magnet [GdW<sub>30</sub>P<sub>5</sub>O<sub>110</sub>](14-). *Chem Commun* 49(79):8922–8924
118. Martinez-Perez MJ, Cardona-Serra S, Schlegel C, Moro F, Alonso PJ, Prima-Garcia H, Clemente-Juan JM, Evangelisti M, Gaita-Arino A, Sese J, van Slageren J, Coronado E, Luis F (2012) Gd-based single-ion magnets with tunable magnetic anisotropy: molecular design of spin qubits. *Phys Rev Lett* 108(24):247213
119. Zadrozny JM, Niklas J, Poluektov OG, Freedman DE (2014) Multiple quantum coherences from hyperfine transitions in a vanadium(IV) complex. *J Am Chem Soc* 136(45):15841–15844
120. Timco GA, Faust TB, Tuna F, Winpenny REP (2011) Linking heterometallic rings for quantum information processing and amusement. *Chem Soc Rev* 40(6):3067–3075
121. Ardavan A, Bowen AM, Fernandez A, Fielding AJ, Kaminski D, Moro F, Murny CA, Wise MD, Ruggi A, McInnes EJJ, Severin K, Timco GA, Timmel CR, Tuna F, Whitehead GFS, Winpenny REP (2015) Engineering coherent interactions in molecular nanomagnet dimers. *NPJ Quantum Inf* 1:15012
122. Wernsdorfer W (2007) A long-lasting phase. *Nat Mater* 6(3):174–176
123. Moreno-Pineda E, Damjanovic M, Fuhr O, Wernsdorfer W, Ruben M (2017) Nuclear spin isomers: engineering a Et<sub>4</sub>N[DyPc<sub>2</sub>] spin qubit. *Angew Chem Int Ed* 56(33):9915–9919
124. Pointillart F, Bernot K, Golhen S, Le Guennic B, Guizouarn T, Ouahab L, Cador O (2015) Magnetic memory in an isotopically enriched and magnetically isolated mononuclear dysprosium complex. *Angew Chem Int Ed* 54(5):1504–1507
125. Chen YC, Liu JL, Wernsdorfer W, Liu D, Chibotaru LF, Chen XM, Tong ML (2017) Hyperfine-interaction-driven suppression of quantum tunneling at zero field in a holmium (III) single-ion magnet. *Angew Chem Int Ed* 56(18):4996–5000

# Lanthanide Organometallics as Single-Molecule Magnets



María José Heras Ojea, Lewis C. H. Maddock, and Richard A. Layfield

## Contents

1	Introduction .....	254
2	Lanthanide SMMs with $\eta^5$ -Cyclopentadienyl Ligands .....	258
2.1	Cationic Dysprosium Metallocene SMMs .....	259
2.2	Metallocene SMMs with Competing Equatorial Ligands .....	263
2.3	Radical-Bridged Lanthanide Metallocene SMMs .....	266
3	Lanthanide SMMs with $\eta^6$ -Arene and $\eta^7$ -Cycloheptatrienyl Ligands .....	268
3.1	Arene-Ligated Lanthanide SMMs .....	268
3.2	Cycloheptatrienyl-Ligated SMMs .....	271
4	Lanthanide SMMs with $\eta^8$ -Cyclo-octatetraenyl Ligands .....	272
4.1	SMMs Based on [CpLn(COT)] and [Ln(COT) <sub>2</sub> ] <sup>-</sup> Units .....	272
4.2	COT-Ligated SMMs with Heteroaromatic Ligands .....	275
5	Conclusions .....	278
	References .....	279

**Abstract** Innovative synthetic chemistry has underpinned many important advances in molecular magnetism, particularly so with the development of single-molecule magnets (SMMs). Recently, the organometallic approach to SMMs has provided a series of eye-catching materials based on certain lanthanides that have re-energised a mature field of magnetism research. This chapter summarises the main highlights and shows that three lanthanides – terbium, dysprosium and erbium – and two ligands, cyclopentadienyl and cyclo-octatetraenyl, have played pivotal roles. The chapter considers the lanthanides in terms of conceptually simple models of 4f electronic structure and spin–orbit coupling and their relationship with the popular oblate and prolate depictions of electron density. For organisational purposes, the chapter is loosely divided by ligand hapticity, beginning with a review of  $\eta^5$ -cyclopentadienyl compounds of dysprosium, from the discovery of the first

organometallic SMM in 2010 to a series of cationic dysprosium metallocenes and radical-bridged SMMs that currently define the state of the art. Ingenious combinations of the  $\eta^8$ -cyclo-octatetraenyl ligand with erbium, and the SMM properties of the ensuing compounds, are described. Less widely used organometallic ligands such as  $\eta^6$ -arene and  $\eta^7$ -cycloheptatrienyl are also considered, as are heteroaromatic ligands in which a carbon atom is replaced by an isolobal fragment based on, e.g., boron or phosphorus.

Organometallic chemistry has provided a valuable approach to the design of lanthanide SMMs that complements the impressive achievements made with Werner-type coordination chemistry. Important challenges remain to be surmounted, and the main message is that if SMMs are to achieve their potential in the arena of device technology then there is a clear need for more research into this fascinating family of magnetic materials.

**Keywords** Cyclo-octatetraenyl · Cyclopentadienyl · Dysprosium · Erbium · Sandwich complexes · Single-molecule magnet · Terbium

## 1 Introduction

Single-molecule magnets (SMMs) are coordination compounds that retain magnetisation in the absence of a magnetic field. A bewildering variety of such compounds has been described in the last 25 years, including examples based on transition metals, lanthanides and actinides [1–7]. The fascination with SMMs stems from the fact that bulk samples of structurally well-defined molecules – often containing only a single metal ion – display magnetic hysteresis reminiscent of traditional atom-based inorganic materials, such as rare-earth magnets. The hysteresis properties of SMMs have therefore inspired proposals for applications in molecule-based memory devices, and, as the wider field of molecular nanomagnetism has evolved, SMMs have also strongly influenced the evolution of closely aligned, emerging disciplines such as molecular spintronics [8].

Some SMMs perform better than others. If these materials are to offer realistic opportunities for developing new forms of technology based on electron spin, new systems that function at practically useful temperatures are essential. The problem is that the SMM phenomenon is strongly temperature-dependent, with the demagnetisation process being subject to a thermal energy barrier that is typically surmountable even at liquid-helium temperatures. The challenge of increasing the temperature at which SMMs function is therefore one that must be met. Here, the molecular nature of SMMs is an advantage because insightful synthetic chemistry allows the electronic structure of a compound to be modified in well-defined ways. Ligand design is a critical part of the strategy, with two complementary approaches both enabling progress in different ways, i.e. classical Werner-type coordination chemistry and nonclassical organometallic chemistry. This chapter focuses on key discoveries in the organometallic approach to lanthanide SMMs and shows how

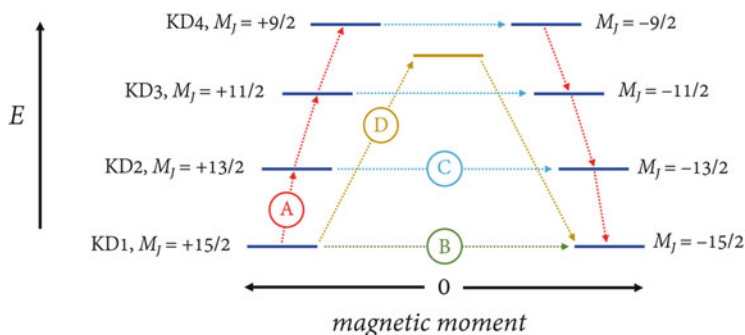


carbon-based ligands can be used to establish design principles that relate the electronic structure and magnetism of organo-lanthanide compounds to their often unique molecular structures [9–11].

Synthetic routes to f-block organometallics have been established over a period spanning several decades, but they have only recently been applied in the context of single-molecule magnetism [12]. Since the bonding in lanthanide compounds is electrostatic, common organometallic ligands tend to be anionic, the most popular being cyclopentadienyl and cyclo-octatetraenyl, i.e.  $[\text{Cp}]^-$  and  $[\text{COT}]^{2-}$ . In the context of SMMs, not every lanthanide produces the desired properties: dysprosium dominates, terbium and erbium are popular, and the other lanthanides are usually not effective. The reason for the popularity of these three metals can be understood by considering their ground state term symbols, i.e.  ${}^7\text{F}_6$  for  $\text{Tb}^{3+}$  ( $4\text{f}^8$ ),  ${}^6\text{H}_{15/2}$  for  $\text{Dy}^{3+}$  ( $4\text{f}^9$ ) and  ${}^4\text{I}_{15/2}$  for  $\text{Er}^{3+}$  ( $4\text{f}^{11}$ ). The large  $J$ -values that define the ground terms imply strong spin-orbit coupling, leading to large magnetic moments for compounds of these lanthanides. The angular dependence of the 4f orbitals confer terbium, dysprosium and erbium with very strong magnetic anisotropy, meaning that certain orientations of the magnetic moment are more stable than others, which is of fundamental importance in single-molecule magnetism. In the case of terbium and dysprosium, the anisotropic f-electron densities are said to take on an oblate spheroidal shape, meaning that the electron density extends further into the  $xy$ -plane than in the  $z$ -direction [13]. For erbium the electron density is prolate spheroidal and extends further in the  $z$ -direction than in the  $xy$ -plane. The aim of the coordination chemist is to enhance the anisotropy by establishing a strong crystal field along the  $z$ -axis for terbium and dysprosium, whereas for erbium the aim is to establish a strong crystal field in the  $xy$ -plane.

A lanthanide defined by a spin-orbit-coupled ground state produces  $2J + 1$  crystal field states, denoted by  $M_J$ . In the absence of a crystal field, the  $M_J$  states are degenerate, but in a crystal field, the degeneracy is lifted in a manner that reflects the symmetry of the coordination environment [13–15]. Dysprosium is a Kramers ion, hence the  $M_J$  states occur as a series of eight so-called Kramers doublets (KDs), and in an axial crystal field consisting of two point-charge ligands on the  $z$ -axis, the maximum value of  $M_J$  defines the magnetic ground state, i.e.  $M_J = \pm 15/2$  for  $\text{Dy}^{3+}$ . In a perfectly axial crystal field, the first excited KD is defined by the second largest  $M_J$  value of  $\pm 13/2$ ; the second excited KD is defined by the third largest  $M_J$  value of  $\pm 11/2$  and so on up to the eighth and highest KD with  $M_J = \pm 1/2$  (Scheme 1).

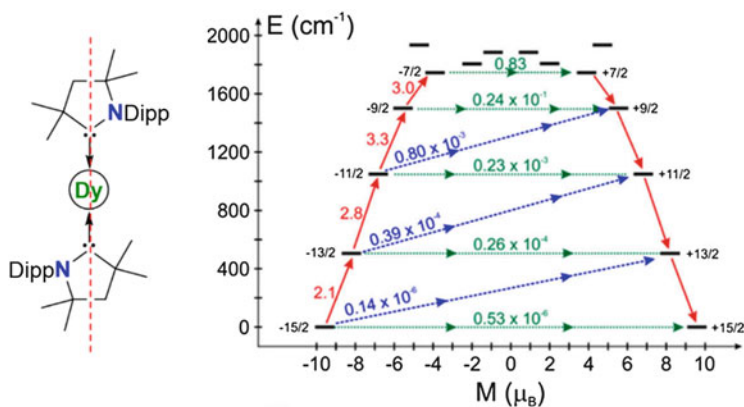
Magnetic anisotropy results in one component of the ground KD being occupied in preference to the other; hence the molecule is magnetised. When the SMM undergoes magnetic relaxation, the other component of the ground KD becomes populated, an equilibrium is established, the molecule becomes a simple paramagnet, and the magnetic memory is wiped. The mechanism by which the equilibrium is reached can consist of multiple steps, the physics of which has been described in detailed reviews and monographs [1–7, 9–12]; hence only a summary is provided here. From the point of view of SMM performance at high temperatures, the preferred relaxation route involves the absorption of phonons from the lattice, which allows the system to relax through consecutive states defined by, e.g., positive  $M_J$  up



**Scheme 1** The four lowest-energy Kramer doublets of the eight Kramer doublets arising from the  ${}^6\text{H}_{15/2}$  ground term of  $\text{Dy}^{3+}$  in an axial crystal field. The dashed lines indicate possible relaxation processes. (A) Red arrows, Orbach relaxation via real excited states. (B) Green arrow, ground state QTM. (C) Blue arrows, thermally assisted QTM. (D) Raman relaxation via a virtual excited state

to the highest KD and then down the series of states defined by negative  $M_J$  (or vice versa). Dominant relaxation through this so-called Orbach route gives rise to the characteristic thermal energy barrier ( $U_{\text{eff}}$ , also called the anisotropy barrier) of the molecule. To date, there are no examples of dysprosium SMMs that relax via the eighth KD; rather, under-barrier shortcuts reduce the amount of energy required for the SMM to relax, effectively reducing the temperature at which it functions. For example, the most efficient way for an SMM to relax is to tunnel through the energy barrier from one component of the ground KD to the other, in a temperature-independent process known as quantum tunnelling of the magnetisation (QTM). Alternatively, it is possible for Orbach processes to occur up to one of the excited KDs and then for the system to tunnel through the energy barrier before relaxing, known as thermally assisted QTM. Alternatively, Raman processes, in which the magnetisation relaxes via fleeting or virtual excited states, also play an important role in some SMMs.

It is an accurate reflection of the complex physics of SMMs that more than one relaxation processes can occur in the same molecule, often simultaneously. In terms of the relationship between the relaxation mechanism and the molecular structure, deviations from perfectly axial symmetry allow mixing of the  $M_J$  wave functions, which increases the probability of relaxation via an under-barrier tunnelling process. Hence, for dysprosium SMMs, the core of any molecular design strategy is to have a strong axial crystal field. To illustrate the approach, we can consider the calculated magnetic properties of the hypothetical linear two-coordinate dysprosium complex  $[\text{Dy}(\text{CAAC})_2]^{3+}$  (**1**) in which the metal is ligated by two cyclic alkyl amino carbene (CAAC) ligands, as described in a recent theoretical study [16]. In the energy spectrum of **1** (Fig. 1), the most probable relaxation route consists of a series of excitations from the ground KD with  $M_J = +15/2$  up to the fourth excited KD, followed by thermally assisted QTM and then relaxation to the ground KD with opposite  $M_J$  projection of  $-15/2$ . The anisotropy barrier  $U_{\text{eff}}$  is defined by the energy of the highest KD reached by the system during the relaxation process. In the case of **1**, the barrier is calculated to be approximately  $1,750\text{ cm}^{-1}$ , which is, currently,

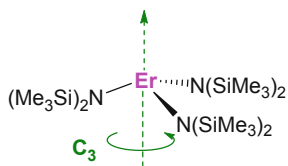


**Fig. 1** Left: structure of hypothetical  $[\text{Dy}(\text{CAAC})_2]^{3+}$  (**1**) (Dipp = 2,6-diisopropylphenyl). Right: the energies of the eight Kramer doublets arising from the  ${}^6\text{H}_{15/2}$  multiplet of **1** as a function of magnetic moment, imposing a C–Dy–C angle of  $180^\circ$ . Red arrows represent the most probable relaxation route; green arrows represent QTM processes; blue arrows represent other Orbach and Raman processes. The numbers associated with each arrow are the average transition dipole moments. Adapted from Ref. [16] with the permission of the American Chemical Society

markedly higher than the barrier determined for any experimental system. The relaxation process illustrated for strictly axial **1** provides an illustration of the relaxation in real systems with strongly axial crystal fields, which also do not reach the highest possible KD. However, in real systems, the geometry will deviate from strictly axial, but according to theoretical studies, the impact of bending the X–Dy–X angle on the magnitude of  $U_{\text{eff}}$  may not be very significant [16, 17]. Conveniently, therefore, to observe a large anisotropy barrier in an experimental dysprosium SMM does not require strict axial symmetry.

An additional reason why dysprosium is the most popular lanthanide in studies of SMMs is that the Kramer nature of  $\text{Dy}^{3+}$  ensures a bistable magnetic ground state regardless of the geometry. For terbium, which also has oblate electron density, the non-Kramer nature of  $\text{Tb}^{3+}$  necessitates strict axial symmetry for magnetic bistability; hence control over the properties of terbium SMMs is harder to achieve. Selected examples of organo-terbium SMMs will be discussed in the following sections. The design strategy applied to erbium SMMs is complementary to dysprosium: because  $\text{Er}^{3+}$  has prolate electron density, a strong equatorial crystal field is required to establish a magnetic ground state defined by  $M_J = \pm 15/2$ , although because erbium is a Kramer ion the geometry does not need to have strict axial symmetry. Note that an equatorial crystal field and an axially symmetrical coordination environment are not mutually exclusive because the symmetry axis can, of course, be perpendicular to the coordination plane, as found in  $\text{C}_{3v}$ -symmetric  $[\text{Er}\{\text{N}(\text{SiMe}_3)_2\}_3]$  (**2**) (Fig. 2) [18].

Several key examples of organo-erbium SMMs that highlight the general design principles are discussed at length in the following sections.

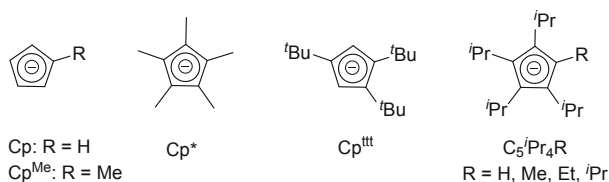


**Fig. 2** Structure of **2** illustrating the equatorial coordination geometry with axial  $C_3$  symmetry

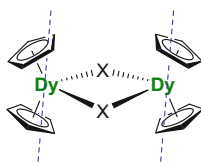
## 2 Lanthanide SMMs with $\eta^5$ -Cyclopentadienyl Ligands

Of the many types of ligand used in organo-lanthanide SMMs, none have been more prolific than cyclopentadienyl (Cp) [11, 19–22]. As the following highlight examples illustrate, Cp-ligated dysprosium compounds account for SMMs with some of the most impressive performance parameters, including the highest anisotropy barriers and magnetic blocking temperatures reported to date. The focus of this section is to set the scene in terms of a magneto-structural correlation in which the crystal field properties of cyclopentadienyl ligands are designed to complement the oblate spheroidal electron density of dysprosium. Where appropriate, additional consideration will be given to SMMs based on terbium and erbium. Although Cp-ligated SMMs abound, relatively few different Cp ligands have been used in the context of SMM design: important examples are shown in Fig. 3, and this section will emphasise the most important recent developments.

To understand why Cp has been so successful in targeting high-performance dysprosium SMMs, the compact size and monoanionic nature of the ligand are important considerations: two such ligands engage in strong electrostatic interactions with  $Dy^{3+}$  cations, resulting in the  $[Cp_2Dy]^+$  metallocene building block, with each ligand coordinating in an  $\eta^5$ -manner. The geometry of the metallocene unit is invariably bent, as measured through the Cp–Dy–Cp angle, i.e. with respect to the centroid positions of the Cp ligands. Typically, the Dy–C distances to one Cp vary appreciably across a range of approximately 0.1 Å, resulting in a tilting of the ligand with respect to the metal-centroid axis. However, regardless of this asymmetry, the metal still experiences a strong axial crystal field, as defined by the Cp ligands. Considered in the context of dysprosium SMMs, an axial crystal field does not require the metal to occupy an environment with strict axial point symmetry; hence pseudosymmetric environments are often conducive to SMM behaviour. In the absence of substantial steric bulk, the large radii of dysprosium and other lanthanides



**Fig. 3** Commonly used cyclopentadienyl ligands in lanthanide SMMs



**Fig. 4** Schematic representation of the easy axes of magnetisation in the ground Kramers doublets of the  $\text{Dy}^{3+}$  ions in  $[\text{Cp}_2\text{Dy}(\mu\text{-X})]_n$  (**3** with  $n = 2$ )

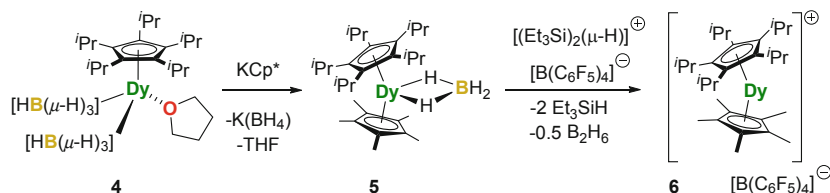
typically result in one or more additional ligands, X, coordinating to the metal, which are regarded as occupying equatorial positions. Depending on the nature of the X ligand, the resulting molecular structure of  $[\text{Cp}_2\text{DyX}]_n$  can either be monometallic ( $n = 1$ ) with a seven-coordinate metal ( $\eta^5\text{-Cp}$  is regarded as occupying three coordination sites) or polymetallic with an eight-coordinate metal and  $\mu$ -bridging X ligands, with dimers and trimers being most common ( $n = 2, 3$ ) [9]. Several studies have found that the equatorial X ligands compete with the axial Cp ligands and diminish the SMM properties to an extent that varies with the nature of the donor atom, although in the majority of cases the Cp ligands dominate the crystal field [11].

The simple design principles described above are based partly on chemical intuition but also on the results of theoretical studies of selected systems. Computational studies of the electronic structure of  $[\text{Cp}_2\text{DyX}]_n$  (**3**) SMMs have consistently shown that the strong axial crystal field stabilises the Kramers doublet with  $M_J = \pm 15/2$  as the magnetic ground state [22]. The easy axis of magnetisation in this ground KD is typically oriented towards (and often passing through) the cyclopentadienyl rings, as illustrated in a model system in Fig. 4.

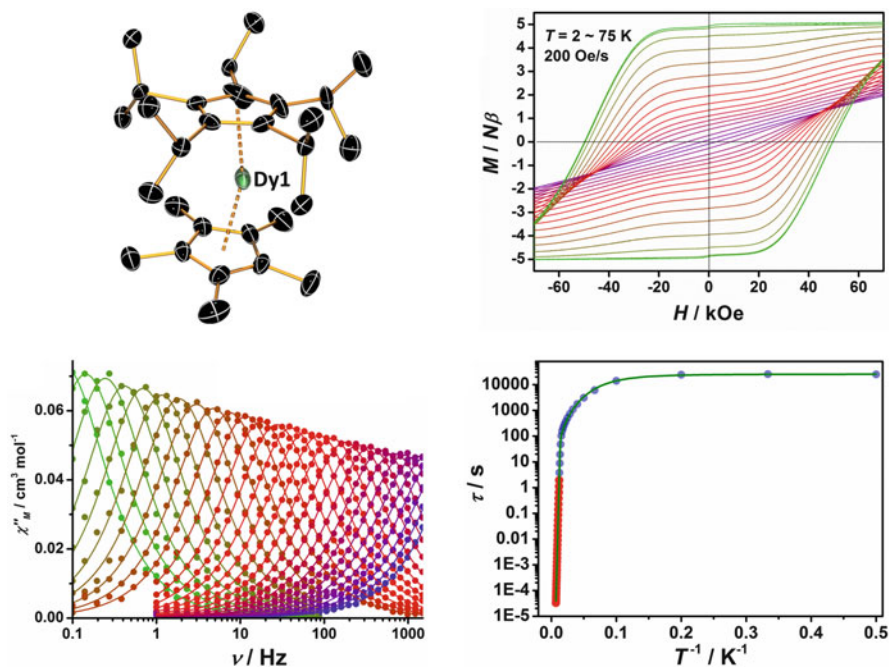
The equatorial X ligands introduce non-negligible transverse components to the crystal field, which can lead to mixing of the wave functions that describe the higher-lying KDs, leading to under-barrier relaxation processes and, ultimately, greatly reduced anisotropy barriers relative to systems with negligible equatorial crystal fields. Furthermore, the equatorial X ligands in  $[\text{Cp}_2\text{DyX}]_n$  SMMs are invariably responsible for precipitous drops in magnetisation around zero field in the magnetic hysteresis measurements. Specific examples of such SMMs are described below; however the main conclusion arising from the detailed experimental and theoretical studies on metallocene SMMs is that a metallocene building block of the type  $[\text{Cp}_2\text{Dy}]^+$ , without any equatorial ligands, should give rise to very strong axial magnetic anisotropy, large anisotropy barriers and magnetic hysteresis properties that feature remanence and coercivity [11, 22].

## 2.1 Cationic Dysprosium Metallocene SMMs

The design principles described above are illustrated by  $[(\eta^5\text{-Cp}^*)\text{Dy}(\eta^5\text{-C}_5^i\text{Pr}_5)][\text{B}(\text{C}_6\text{F}_5)_4]$  (**[6]** $[\text{B}(\text{C}_6\text{F}_5)_4]$ ), which was synthesised from the precursor  $[(\eta^5\text{-Cp}^*)\text{Dy}(\eta^5\text{-C}_5^i\text{Pr}_5)(\text{BH}_4)]$  (**5**) according to Scheme 2 [23].



**Scheme 2** Synthesis of  $[6][\text{B}(\text{C}_6\text{F}_5)_4]$

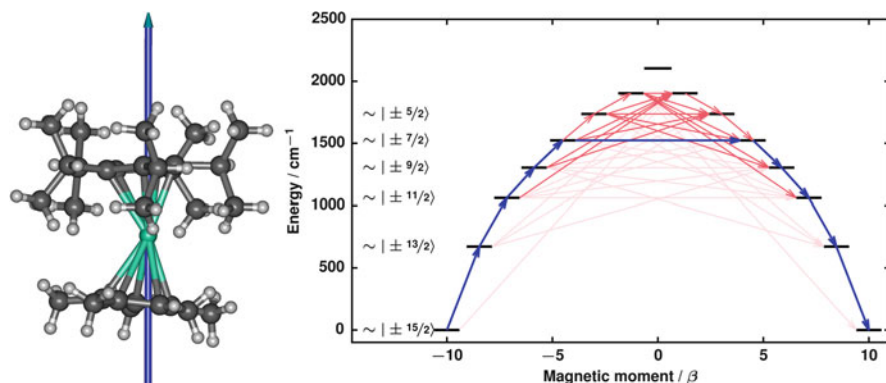


**Fig. 5** Top left: molecular structure **6**. Top right:  $M(H)$  hysteresis at 2–75 K and a scan rate of 200 Oe  $\text{s}^{-1}$ . Bottom left: frequency dependence of  $\chi''$  in zero DC field. Bottom right: temperature dependence of the relaxation time. Adapted from Ref. [23] with the permission of the American Association for the Advancement of Science

The molecular structure of the cation **6** (Fig. 5) consists of a  $\text{Dy}^{3+}$  centre sandwiched between two cyclopentadienyl ligands, with Dy–Cp distances of 2.296(1) and 2.284(1) Å and a Cp–Dy–Cp angle of 162.507(1)°. The  $\chi''(\nu)$  isotherms for  $[6][\text{B}(\text{C}_6\text{F}_5)_4]$  show peaks up to 130 K, and the resulting temperature dependence of the relaxation time ( $\tau$ ) reveals three different regimes, i.e. a linear dependence of  $\tau$  on temperatures between 55 and 138 K, which can be assigned to Orbach relaxation, a temperature-independent process below 10 K associated with QTM and a curvature between 10 and 55 K that may be caused by Raman processes (Fig. 5). A fit of the data gave  $U_{\text{eff}} = 1,540(11) \text{ cm}^{-1}$  with  $\tau_0 = 4.2(6) \times 10^{-12} \text{ s}$ , and a Raman

coefficient of  $C = 3.1(1) \times 10^{-8} \text{ s}^{-1} \text{ K}^{-n}$  was determined with a Raman exponent of  $n = 3$ . The unusually low Raman exponent is thought to be related to the vibrational properties of the Cp ligands. The rate of QTM was found to be  $\tau_{\text{QTM}} = 2.5(2) \times 10^4 \text{ s}$ , which is extremely slow. Magnetisation ( $M$ ) versus field ( $H$ ) hysteresis measurements were performed on  $[\mathbf{6}][\text{B}(\text{C}_6\text{F}_5)_4]$  using a scan rate of  $200 \text{ Oe s}^{-1}$ , with the resulting loops remaining open up to 85 K, leading to a coercive field of  $H_c = 210 \text{ Oe}$  at this temperature (Fig. 5). Further isothermal  $M(H)$  experiments were undertaken at 77 K varying the field scan rate from 700 to  $25 \text{ Oe s}^{-1}$ , the outcome of which was to approximately halve the coercive field with the decrease in scan rate, i.e. 5,802 Oe at  $700 \text{ Oe s}^{-1}$  to 191 Oe at  $25 \text{ Oe s}^{-1}$ . At 80 K and  $25 \text{ Oe s}^{-1}$ , a coercive field of 63 Oe was determined, which represents the first example of an SMM to show hysteresis above the boiling point of liquid nitrogen. The field-cooled/zero-field cooled (FC-ZFC) magnetic susceptibility measurements on  $[\mathbf{6}][\text{B}(\text{C}_6\text{F}_5)_4]$  diverge at 78 K when using a scan rate of  $2 \text{ K min}^{-1}$ .

Ab initio theoretical studies on the cation  $\mathbf{6}$  provided deeper insight into the electronic structure by illustrating the easy axes of magnetisation in the eight KDs arising from the  $J = 15/2$  multiplet of  $\text{Dy}^{3+}$  [23]. The magnetic axes in the first seven KDs are projected towards the centres of the two Cp ligands, with the maximum deviation of  $5.3^\circ$  highlighting the axiality of the system (Fig. 6). The calculated  $g$ -tensor of the ground state is perfectly axial (i.e.  $g_z = 20$ ,  $g_x = g_y = 0$ ), which is consistent with the absence of QTM at zero field in the hysteresis measurements. The transverse components of the  $g$ -tensors only become significant in the higher excited doublets, and relaxation is likely to occur via the fifth KD, which was calculated to lie at  $1,524 \text{ cm}^{-1}$  above the ground KD, in excellent agreement with the experimental anisotropy barrier of  $1,540(11) \text{ cm}^{-1}$ . The possible influence of ligand vibrations on the magnetic relaxation in  $\mathbf{6}$  was also evaluated by density functional theory (DFT). The Orbach process is thought to be initiated by an out-of-plane vibration of



**Fig. 6** Left: calculated easy axis of magnetisation in the ground Kramers doublet for  $\mathbf{6}$ . Right: relaxation pathways for  $\mathbf{6}$ , where blue arrows show the most probable relaxation and red arrows show transitions between states with less probable but non-negligible matrix elements; darker shading indicates a higher transition probability. Adapted from Ref. [23] with the permission of the American Association for the Advancement of Science



the Cp\* ligand. The hypothesis is based on the similar energy values calculated for the gap between ground KD and first excited KD ( $672\text{ cm}^{-1}$ ) and the frequencies of the pertinent vibrational modes ( $632.9$  and  $640.5\text{ cm}^{-1}$ ). Since the out-of-plane vibrations of the Cp\* are coupled to the methyl vibrational modes, a replacement of the substituents by substituents containing heavier atoms may further improve the SMM properties. For comparative purposes, the impact of the negligible equatorial crystal field in **6** is highlighted by the SMM properties of the precursor compound **5**, which shows fast magnetic relaxation in zero DC field dominated by QTM, with a miniscule anisotropy barrier of  $7\text{ cm}^{-1}$  and waist-restricted hysteresis loops only up to 2 K.

The properties of the related SMM  $[(\text{Cp}^{\text{tr}})_2\text{Dy}][\text{B}(\text{C}_6\text{F}_5)_4]$  (**8**) $[\text{B}(\text{C}_6\text{F}_5)_4]$ , Cp<sup>tr</sup> = 1,2,4-tri-*tert*-butylcyclopentadienyl) include an impressive anisotropy barrier of  $1,277\text{ cm}^{-1}$  (or  $1,223\text{ cm}^{-1}$ ) and a blocking temperature of 60 K, as determined from hysteresis measurements (scan rate of  $39\text{ Oe s}^{-1}$ ) and from the FC–ZFC susceptibility measurements [24–26]. The 100-s blocking temperature of **8** is 53 K. Ab initio theoretical studies performed on **8** established that the easy axis of magnetisation in the ground KD is oriented towards the centres of the Cp ligands, consistent with **7** and with the magneto-structural correlation in Fig. 4. The magnetic axes of the next six KDs in **8** are essentially colinear with the ground state axis, with a maximum deviation of only  $5.6^\circ$ . The splitting of the  $^6\text{H}_{15/2}$  multiplet also reveals that each doublet is defined by a single  $M_J$  value and that mixing between states is negligible, resulting in an almost perfectly axial crystal field. However, the presence of very small transverse components seemingly precludes magnetic relaxation via the eighth and highest KD. Additional DFT calculations on **8** carried out in a separate study proposed that local molecular vibrations control the Orbach mechanism, with the calculated transition rates between electronic states suggesting that the C–H vibrations in the Cp ligands initiate the relaxation.

A related series of homoleptic dysprosium metallocene SMMs with different bulky substituents on cyclopentadienyl ligands provided further insight into how sensitive the SMM properties are to subtle changes in molecular structure. Thus,  $[(\text{C}_5^i\text{Pr}_4\text{R})_2\text{Dy}][\text{B}(\text{C}_6\text{F}_5)_4]$ , where R = H (**9**), Me (**10**), Et (**11**) and *i*Pr (**12**), show strong frequency-dependent, out-of-phase AC susceptibility signals in zero DC field, with magnetic blocking temperatures of 17, 62, 59 and 56 K, respectively, based on the temperatures at which the relaxation time is 100 s (Table 1) [27]. As the R

**Table 1** Selected geometric parameters and magnetic properties for **8–13**

	<b>8</b>	<b>9</b>	<b>10</b>	<b>11</b>	<b>12</b>	<b>13</b>
Cp–Dy–Cp ( $^\circ$ )	162.507	152.7	147.2	156.6	161.1	162.1
Cp–Dy ( $\text{\AA}$ )	2.296(1) 2.284(1)	2.316(3)	2.29(1)	2.298(5)	2.302(6)	2.340(7)
$U_{\text{eff}}$ ( $\text{cm}^{-1}$ ) <sup>a</sup>	1,540	1,277	1,285	1,468	1,380	1,334
$T_{\text{B}}$ (K) <sup>b</sup>	80	60	32	72	66	66

<sup>a</sup>Determined in zero applied DC field

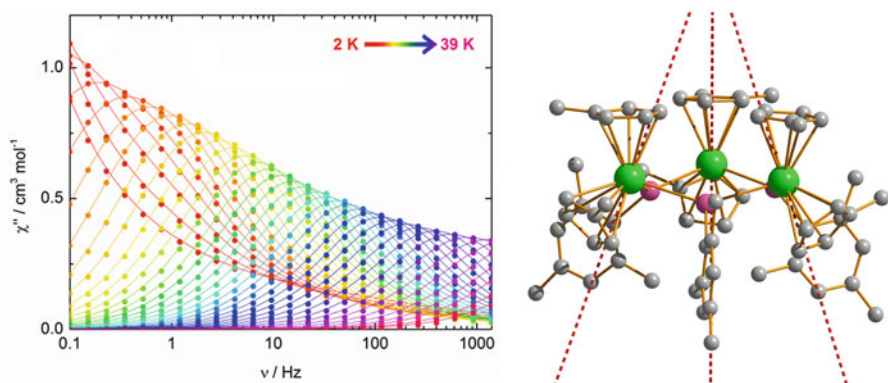
<sup>b</sup>Defined as the maximum hysteresis temperature



substituent on the  $[\text{C}_5^i\text{Pr}_4\text{R}]^-$  ligands gradually increases in size, the Cp–Dy–Cp angle becomes wider, creating a more axial coordination environment. However, greater axiality alone does not result in an increase in the anisotropy barrier and the blocking temperature because the longer Dy–C distances that occur in the presence of greater steric bulk seemingly reduce the strength of the axial crystal field, which explains why the performance parameters of **8** surpass those of **9–13**.

## 2.2 Metallocene SMMs with Competing Equatorial Ligands

The recent studies of cationic dysprosium metallocene SMMs highlight the need to strike a careful balance between steric and electronic effects in order to obtain large  $U_{\text{eff}}$  and  $T_{\text{B}}$  values. The cations **8–13** mark the culmination of several years of detailed preliminary work in which the properties of  $[\text{Cp}_2\text{DyX}]_n$  SMMs were established with numerous different equatorial X ligands, including the pnictogen-ligated compounds  $[(\text{Cp}^{\text{Mec}})_2\text{Dy}\{\mu\text{-E(H)Mes}\}]_3$  with E = P (**14**), As (**15**) or Sb (**16**) and  $[\text{Li}(\text{THF})_4]_2[\{(\text{Cp}^{\text{Mec}})_2\text{Dy}(\mu\text{-EMes})\}_3\text{Li}]$  with E = P (**17**), As (**18**) [28–30]. Indeed, the SMM properties of **14–18** allowed the first systematic investigation into the impact of varying the equatorial donor atom as different members of the same p-block group. The metallocene building blocks in compounds **14–16** have very similar geometric parameters, which result in approximate  $\text{C}_{2v}$  site symmetry at dysprosium. On moving through the phosphide-, arsenide- and stibinide-ligated compounds, the dysprosium–pnictogen bond lengths increase in the order 2.920(6)–2.946(6) Å to 2.984(2)–3.012(2) Å to 3.118(2)–3.195(2) Å, respectively. Compounds **14–16** all show well-defined maxima in the  $\chi''(\nu)$  data, which results in a gradual increase in the anisotropy barrier from 210  $\text{cm}^{-1}$  to 256  $\text{cm}^{-1}$  to 345  $\text{cm}^{-1}$ , respectively (Fig. 7).

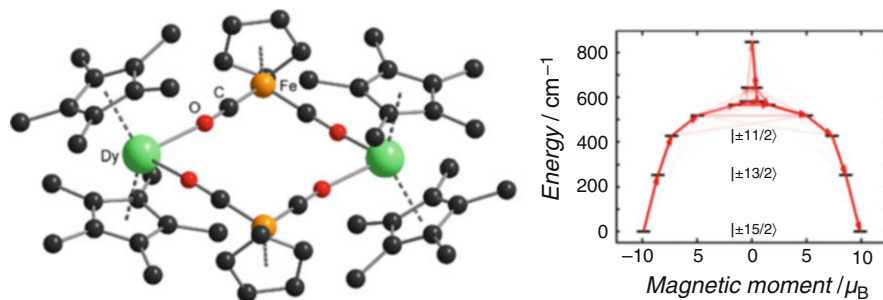


**Fig. 7** Left: frequency dependence of  $\chi''$  in zero DC field for **15**. Right: molecular structure and calculated easy axes of magnetisation in the ground Kramers doublets for the  $\text{Dy}^{3+}$  centres in **15** (Dy, green; As, purple; C, grey). Adapted from Ref. [29] with the permission of the Royal Society of Chemistry

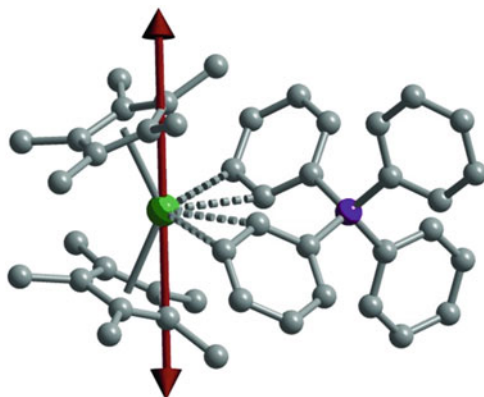
The detrimental influence of magnetic exchange interactions in **14** and **15** became apparent from the magnetic dilution studies in the isostructural yttrium compounds ( $\text{Dy}/\text{Y} = 1:19$ ), which resulted in larger anisotropy barriers of  $256$  and  $301 \text{ cm}^{-1}$ , respectively. A key outcome of the theoretical investigations of **14–18** was that slow magnetic relaxation properties arise from magnetic axiality of the  $\{\text{Cp}_2\text{Dy}\}^+$  building block, with the easy axis of magnetisation in the ground KD being oriented towards the cyclopentadienyl ligands, as found in **8** and **9**. The pnictogen ligands therefore reside in equatorial coordination sites, the effect of which is to mix the wave function corresponding to the various  $M_J$  states in the high-energy KDs and therefore reduce the thermal barrier height. It can therefore be argued that the different anisotropy barriers determined for **14–16** are a consequence of the lengthening of the dysprosium–pnictogen bonds, which gradually weakens the equatorial component of the crystal field.

In a further extension of the magneto-structural correlation shown in Fig. 4, weak-field isocarbonyl ligands were used as the equatorial bridging ligands in  $[(\text{Cp}^*)_2\text{Dy}(\mu\text{-Fp})]_2$  (**19**,  $\text{Fp} = \text{CpFe}(\text{CO})_2$ ). The molecular structure of **19** consists of two  $\{\text{Cp}^*_2\text{Dy}\}$  units bridged via the Fp metallo-ligands, leading to a diamond-shaped  $\{\text{Ln}(\text{OC})_2\text{Fe}\}_2$  core (Fig. 8) [22]. The SMM properties in zero DC field were established by AC magnetic susceptibility experiments, along with the magnetic hysteresis loops, which remain open up to  $6.2 \text{ K}$  at zero field using a scan rate of  $20 \text{ Oe s}^{-1}$ . Modelling the temperature dependence of the relaxation time produced a large anisotropy barrier of  $662 \text{ cm}^{-1}$ , corresponding to dominant relaxation via Orbach processes, with contributions from Raman and QTM processes at low temperatures. The results of ab initio calculations on **19** are consistent with previous theoretical studies on dysprosium metallocene SMMs, revealing that the ground Kramers doublet is essentially of pure  $M_J = \pm 15/2$  character and that the easy axis of magnetisation is oriented towards the  $\text{Cp}^*$  ligands. The first three excited states are also well-defined, with nearly pure  $M_J = \pm 13/2$ ,  $\pm 11/2$  and  $\pm 9/2$  character, resulting in magnetisation reversal occurring via the fourth, fifth or sixth excited KDs (Fig. 8).

Other studies of dysprosium metallocene SMMs are consistent with the magneto-structural correlation shown in Fig. 4. For instance,  $[\text{Cp}^*_2\text{Ln}(\mu\text{-Ph}_2\text{BPh}_2)]$  ( $\text{Ln} = \text{Tb}$



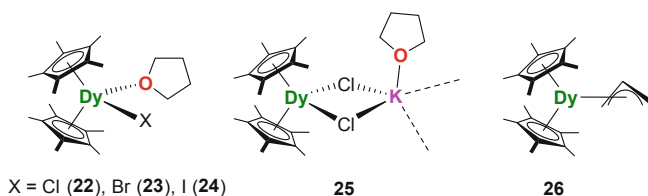
**Fig. 8** Left: molecular structure of  $[(\text{Cp}^*)_2\text{Dy}(\mu\text{-Fp})]_2$  (**19**). Right: relaxation pathways for **19**, where the red arrows show transitions between states; darker shading indicates a higher transition probability. Adapted from Ref. [22] with the permission of Wiley-VCH



**Fig. 9** Molecular structure of **21** showing the orientation of the main magnetic axis in the ground Kramers doublet (Dy, green; B, purple; C, grey). Reproduced from Ref. [21] with the permission of Wiley-VCH

**20** or Dy **21**) highlights some of the qualitative similarities in the electronic structure of the non-Kramers ion  $Tb^{3+}$  and Kramers  $Dy^{3+}$  and how it impacts on the slow magnetic relaxation [31]. The cation- $\pi$  interactions between  $[BPh_4]^-$  and  $Ln^{3+}$  in **20** and **21** result in weak equatorial fields, which results in the main magnetic axis in the ground KD of **21** being aligned with the two  $Cp^*$  ligands (Fig. 9). An analysis of the temperature dependence of the relaxation times on magnetically pure and dilute samples of **20** and **21** ( $Ln/Y = 1:3$  and  $1:4$ , respectively) revealed that QTM and Raman processes are significant in the former, whereas in the latter, the relaxation is dominated by a thermal pathway, leading to anisotropy barriers of 216 and  $331\text{ cm}^{-1}$ , respectively, with  $\tau_0 = 8 \times 10^{-10}\text{ s}$  and  $\tau_0 = 1 \times 10^{-9}\text{ s}$  in zero applied DC field. The magnetic hysteresis measurements on **20** with scan rates of  $20\text{ Oe s}^{-1}$  showed slight opening of the loops at 1.8 K, whereas with **21** the loops are waist-restricted up to 5.8 K, although in both cases the drop in magnetisation around zero field results in very low remanent magnetisation. Slight enhancements in the hysteresis were observed for the diluted analogues of **20** and **21**, indicating that intermolecular dipole-dipole interactions play a role in the relaxation of the non-dilute samples.

The homologous series of dysprosium metallocenes  $[Cp^*_2DyCl(THF)]$  (**22**),  $[Cp^*_2DyBr(THF)]$  (**23**),  $[Cp^*_2DyI(THF)]$  (**24**) and  $[Cp^*_2Dy(\mu-Cl)_2K]_n$  (**25**) all show slow magnetic relaxation in zero applied DC field, whereas  $[Cp^*_2Dy(\eta^3\text{-allyl})]$  (**26**) shows field-induced slow relaxation in an applied DC field of 4 kOe (Scheme 3) [32]. The anisotropy barriers for **22–24** increase in the order 112, 163 and  $419\text{ cm}^{-1}$ , respectively, with the associated QTM times determined to be 0.28, 1.4 and 6.7 ms. Since the molecular structures of **22–24** are very similar, the differences in their SMM properties were interpreted in terms of the longer Dy-X bonds generating weaker equatorial crystal fields and, hence, more dominant axial crystal field, which is consistent with observations on the pnictogen-ligated compounds **14–16**. The relaxation in the low-barrier SMMs **22** and **23** was calculated to

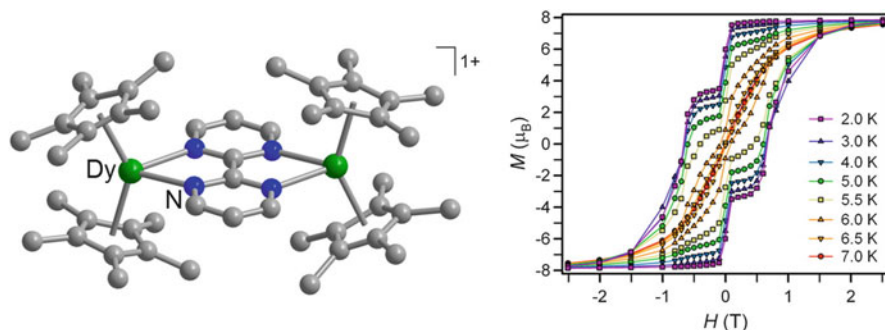


**Scheme 3** Structures of **22–26**

proceed via the first excited KD, whereas in **24** the second excited KD is the dominant relaxation pathway. The barrier of  $379\text{ cm}^{-1}$  determined for the doubly chloride-bridged coordination polymer **25** is much larger than that of **22**, as is the QTM time of 70 ms, the explanation of which invokes the more symmetrical dysprosium coordination environments and, presumably, the fact that the Dy–Cl distances are approximately  $0.06\text{ \AA}$  longer in **25**. As with **24**, the relaxation in **25** should proceed via the second excited KD. The lack of slow relaxation in zero DC field for **26** was ascribed to the ability of the anionic  $\eta^3$ -allyl ligand to compete effectively with the axial crystal field established by the Cp\* ligand, with a theoretical analysis revealing that QTM in the ground KD is more significant than in other members of the series.

### 2.3 Radical-Bridged Lanthanide Metallocene SMMs

Although most dysprosium metallocene SMMs show appreciable anisotropy barriers, the majority are also plagued by magnetic hysteresis with efficient QTM near zero DC field, leading to weak remnant magnetisation and very little coercivity [1–7]. However, a highly effective strategy has been developed in which radical ligands are used to bridge between the lanthanide centres in polymetallic compounds, which can mitigate the effects of QTM and lead to exceptionally large coercivity [33–36]. The first such compounds were the terbium and dysprosium amido complexes  $[\text{K}(18\text{-crown-6})(\text{THF})_2][\text{Ln}_2\{\text{N}(\text{SiMe}_3)_2\}_4(\text{THF})_2(\mu\text{:}\eta^2\text{:}\eta^2\text{-N}_2)]$  with Ln = Tb ( $[\text{K}(18\text{-crown-6})(\text{THF})_2][\textbf{27}]$ ) and Dy ( $[\text{K}(18\text{-crown-6})(\text{THF})_2][\textbf{28}]$ ), in which the  $\text{Ln}^{3+}$  ions are bridged by the  $S = 1/2$  radical  $[\text{N}_2]^{3-}$  [37, 38]. In contrast to all previous examples, the magnetic hysteresis in **27** and **28** retains coercivity up to the blocking temperatures of 14 and 8.3 K, respectively. The related SMM  $[(\text{Cp}^*_2\text{Dy})_2(\mu\text{-bpym})][\text{BPh}_4]$  (**29**) [ $\text{BPh}_4$ ] consists of two metallocene units connected by the  $S = 1/2$  radical anion of bipyrimidyl (bpym) (Fig. 10). The static magnetic susceptibility of the isotropic gadolinium analogue  $[(\text{Cp}^*_2\text{Gd})_2(\mu\text{-bpym})][\text{BPh}_4]$  (**30**) [ $\text{BPh}_4$ ] revealed an  $S = 13/2$  ground state with very strong antiferromagnetic coupling between the metal and the bipyrimidyl radical, with an exchange coupling constant of  $J = -10\text{ cm}^{-1}$  ( $-2J$  formalism). Exchange coupling of comparable strength is thought to occur in **29** [39].

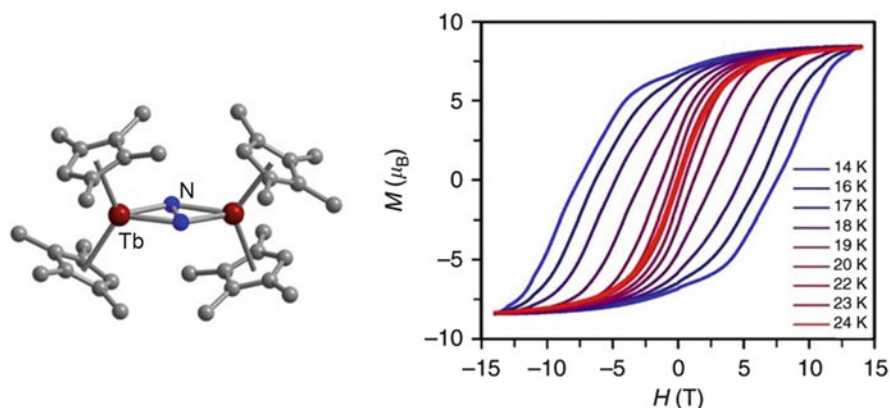


**Fig. 10** Left: structure of  $[(\text{Cp}^*_2\text{Dy})_2(\mu\text{-bpym})]^-$  (**29**). The arrows indicate the antiferromagnetic coupling between the  $\text{Dy}^{3+}$  centres and the radical bridge. Hydrogen atoms omitted for clarity. Right: hysteresis loops in the temperature range 2–17 K using scan rate of  $30 \text{ Oe s}^{-1}$  and (inset) temperature dependence of the relaxation time in zero DC field. Adapted from Ref. [39] with the permission of the American Chemical Society

The spin density of the radical bridging ligand in **29** essentially acts as an internal magnetic field, which lifts the degeneracy of the two components of each KD, therefore reducing the probability of QTM. This effect, referred to as an exchange bias, was confirmed in **29** by studying the relaxation times, which are strongly temperature-dependent across the full range for which data are available (Fig. 10). Although the anisotropy barrier and blocking temperature of  $88 \text{ cm}^{-1}$  and  $6.5 \text{ K}$  (scan rate of  $20 \text{ Oe s}^{-1}$ ), respectively, are moderate, the open hysteresis loops observed in the temperature range 2–6.5 K contrast in appearance to the closed loops typically observed in SMMs, with a coercive field of  $0.6 \text{ T}$  recorded at  $3 \text{ K}$ .

The dilanthanide complexes  $[\text{K}(2.2.2\text{-crypt})(\text{THF})][\{(\text{C}_5\text{Me}_4\text{H})_2\text{Ln}(\text{THF})\}_2(\mu\text{-N}_2)]$  with  $\text{Ln} = \text{Gd}$  (**31**),  $\text{Tb}$  (**32**) and  $\text{Dy}$  (**33**) were synthesised by the one-electron reduction of  $[\{(\text{C}_5\text{Me}_4\text{H})_2\text{Ln}(\text{THF})\}_2(\mu\text{-N}_2)]$  with  $\text{KC}_8$  [40]. Subsequent redissolution of **31–33** in 2-methyl-THF led to dissociation of the THF ligands to give  $[\text{K}(2.2.2\text{-crypt})][\{(\text{C}_5\text{Me}_4\text{H})_2\text{Ln}\}_2(\mu\text{-N}_2)]$  with  $\text{Ln} = \text{Gd}$  (**34**),  $\text{Tb}$  (**35**) and  $\text{Dy}$  (**36**), which feature more symmetrical coordination environments (Fig. 11). The structures of **31–33** and **34–36** are quite similar with the two lanthanide ions each complexed by two  $\eta^5\text{-C}_5\text{Me}_4\text{H}$  ligands and a bridging  $[\text{N}_2]^{3-}$  radical ligand; however, removing the THF ligands increases the  $\text{Ln}(\text{N}_2)\text{Ln}$  dihedral angles, e.g. from  $173.45(16)^\circ$  in **32** to  $178.5(2)^\circ$  in **35**, which is thought to be important for the exchange interactions and, hence, for the SMM properties. The temperature dependence of  $\chi_M T$  showed that the lanthanide ions are antiferromagnetically coupled to the radical ligand, and modelling of the data for **31** yielded a gadolinium–radical exchange coupling constant of  $J = -20 \text{ cm}^{-1}$  ( $-2J$  formalism), which is of comparable magnitude to the coupling in the diterbium compounds **32** and **35**, i.e.  $-20.2$  and  $-23.1 \text{ cm}^{-1}$ , respectively. In contrast, the exchange coupling in **33** and **36** is much weaker ( $J \approx -7 \text{ cm}^{-1}$ ).

Compounds **32**, **33**, **35** and **36** display peaks in the frequency dependence of the out-of-phase AC magnetic susceptibility, with anisotropy barriers of  $242$ ,  $110$ ,  $276$  and  $108.1 \text{ cm}^{-1}$ , respectively. The lower barriers displayed by **33** and **36** are



**Fig. 11** Left: structure of  $[(C_5Me_4H)_2Ln]_2(\mu-N_2)^-$  (**35**). Hydrogen atoms omitted for clarity. Right: variable-field magnetisation data and FC–ZFC plot (inset). Adapted from Ref. [40] with the permission of Nature Publishing Group

apparently a consequence of the weaker dysprosium–radical exchange coupling. It is noticeable that the impact of removing the THF ligand on the anisotropy barrier is not very significant for any of these compounds on the timescale of the AC susceptibility measurements. The SMM properties were further established by the observation of hysteresis loops in the variable-field magnetisation measurements for **32**, **35** and **36**, whereas **33** did not produce any open hysteresis loops. The most striking result is the coercive field of 7.9 T for **35** at 10 K, which is the largest yet recorded for any molecule-based magnet (Fig. 11).

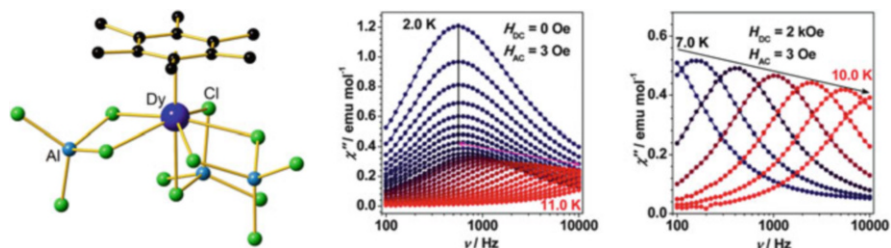
Compounds **32**, **33**, **35** and **36** further demonstrate that using radical bridging ligands in polymetallic lanthanide SMMs is an effective approach to suppressing QTM processes and, therefore, for improving the SMM properties. It is instructive to compare the properties of radical-bridged SMMs with those of the cationic dysprosium metallocenes **8–13**; whereas the radical ligands clearly play an important role in the hysteresis properties, the anisotropy barriers determined for, e.g., **32** and **35** are modest. Since the magnetic axiality ultimately derives from the  $\{Cp_2Dy\}^+$  building block, the local symmetry of the lanthanide coordination environment remains a significant factor even in the presence of a radical ligand.

### 3 Lanthanide SMMs with $\eta^6$ -Arene and $\eta^7$ -Cycloheptatrienyl Ligands

#### 3.1 Arene-Ligated Lanthanide SMMs

Arene-ligated lanthanide SMMs are rare, presumably because the charge-neutral nature of the ring results in weak bonding to lanthanides and in the formation of



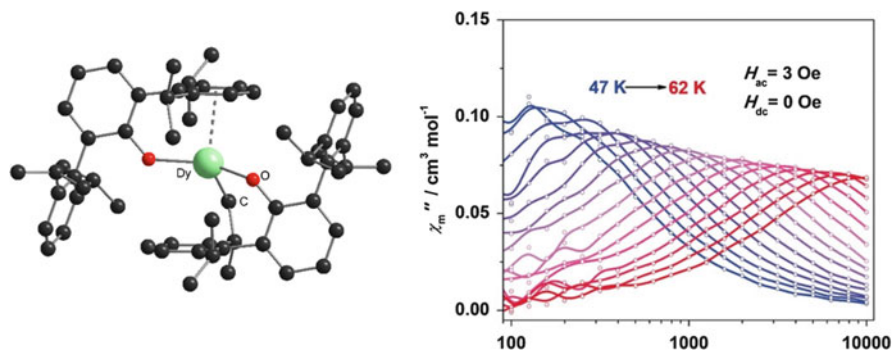


**Fig. 12** Left: molecular structure of **37**. Centre: frequency dependence of  $\chi''$  in zero DC field. Right: frequency dependence of  $\chi''$  in a 2 kOe applied DC field. Adapted from Ref. [41] with the permission of the Royal Society of Chemistry

much weaker crystal fields than those found in cyclopentadienyl-ligated lanthanide SMMs. Despite this, several arene-ligated lanthanide SMMs are known, the majority being half-sandwich complexes with additional anionic ligands. The anisotropy barriers in arene-ligated SMMs are typically in the region of  $100\text{ cm}^{-1}$ , and the magnetic hysteresis loops are usually waist-restricted, leading to blocking temperatures in the liquid-helium regime. The first arene-ligated SMMs were the isostructural half-sandwich complexes  $[(\eta^6\text{-C}_6\text{Me}_6)\text{Dy}(\text{AlCl}_4)_3]$  (**37**),  $[(\eta^6\text{-C}_6\text{H}_5\text{Me})\text{Dy}(\text{AlCl}_4)_3]$  (**38**) and  $[(\eta^6\text{-C}_6\text{H}_5\text{Me})\text{Dy}(\text{AlBr}_4)_3]$  (**39**), in which the tetrahaloaluminate ligands  $\kappa^2$ -coordinate to the metal via two halogen atoms (Fig. 12) [41, 42].

The symmetry of the coordination environments in **37–39** was described as distorted pentagonal bipyramidal by virtue of five equatorial halide ligands, an axial halide ligand and the centroid of the arene ligand. The average Dy–X distances in **37–39** are 2.801, 2.789 and 2.957 Å, respectively, and the Dy–arene centroid distances are 2.471, 2.476 and 2.503 Å, respectively. The metal–arene distances are therefore considerably longer than the analogous distances in Cp-ligated SMMs, suggesting that the crystal field provided by the arene ligands is indeed very weak and that the SMM properties should be poorer.

The AC magnetic susceptibility measurements on **37** reveal SMM behaviour in zero applied DC field, with the dominant relaxation involving an Orbach process via the first excited KD, but also with appreciable QTM at lower temperatures [41]. The ab initio calculated energy gap of  $80\text{ cm}^{-1}$  agrees well with the experimental anisotropy barrier of  $70\text{ cm}^{-1}$  (with  $\tau_0 = 5.1 \times 10^{-10}\text{ s}$ ) extracted from the AC susceptibility data in zero DC field. The barrier rises to  $89\text{ cm}^{-1}$  in an applied DC field of 2 kOe. In addition, ab initio calculations showed that the easy axis of magnetisation coincides with the Cl–Dy–arene axis. Replacing the hexamethylbenzene ligand in **37** by the less bulky toluene ligand in **38** and **39** leads to a slight enhancement of the SMM properties, with the anisotropy barriers increasing by several wave numbers [42]. The enhancement in the SMM performance is thought to be related to the degree of distortion of the local symmetry around the Dy<sup>3+</sup> ions, with deviations from ideal D<sub>5h</sub> symmetry reducing the anisotropy barriers.

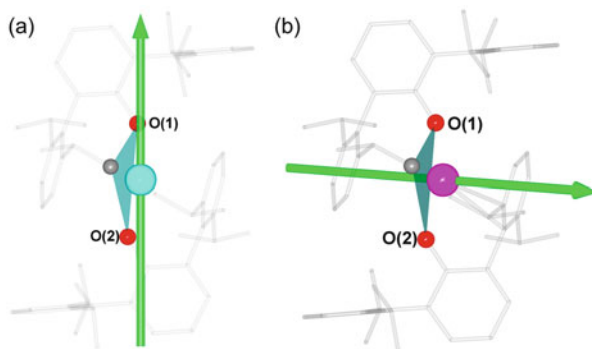


**Fig. 13** Left: molecular structure of **40**. Right: frequency dependence of  $\chi''$  in zero DC field. Adapted from Ref. [43] with the permission of Wiley-VCH

Serendipitous formation of  $\eta^6$ -arene ligands was observed in the reaction of  $[\text{Dy}(\text{CH}_2\text{SiMe}_3)_3(\text{THF})_2]$  with the bulky phenol ArOH, in which Ar = *bis*-2,6-(2,6-diisopropylphenyl)phenyl [43]. The intended outcome of the reaction was presumably phenol deprotonation and formation of the three-coordinate compound  $[(\text{ArO})_2\text{Ln}(\text{CH}_2\text{SiMe}_3)]$ . However, a methyl group on one of the phenol pro-ligands was also deprotonated, resulting in formation of a tethered phenoxy-alkyl ligand, with the second equivalent of pro-ligand being singly deprotonated and coordinating to the metal as a tethered phenoxy-arene ligand. The result is  $[(\text{ArO})\text{Ln}(\text{OAr}')]$  (Ln = Dy **40**, Er **41**, Fig. 13), which consists of a pseudo-four-coordinate dysprosium centre, with the two phenoxide ligands producing an O–Dy–O angle of  $144.7^\circ$ .

Compound **40** and the isostructural erbium analogue **41** display slow magnetic relaxation in zero DC field. However, the QTM is strong in **41**, and an applied field of 1 kOe was used to resolve the peaks in the frequency dependence of the out-of-phase susceptibility. The magnetic hysteresis (scan rate of  $1.7 \text{ Oe s}^{-1}$ ) and the ZFC–FC susceptibility measurements on **40** produced a blocking temperature of about 6 K. Modelling the zero-field AC susceptibility data suggested that thermal relaxation occurs through an Orbach process with  $U_{\text{eff}} = 668 \text{ cm}^{-1}$  and  $\tau_0 = 8.2 \times 10^{-12} \text{ s}$ , in addition to QTM and Raman processes occurring at lower temperatures. Coordination of the benzylic carbon to dysprosium in **40** introduces transverse components into the crystal field that prevent slow relaxation through higher excited KDs. A similar analysis of **41** yielded a much smaller anisotropy barrier of  $60 \text{ cm}^{-1}$  and  $\tau_0 = 1.7 \times 10^{-8} \text{ s}$ . Notably, **40** and **41** both show magnetic relaxation despite their 4f electron densities adopting different angular dependences, i.e. oblate and prolate, respectively. Ab initio calculations on **40** led to the proposal that coordination of the formally anionic oxygen atoms to dysprosium forces the easy axis of magnetisation in the ground KD to be aligned with the O–Dy–O connectivity. In contrast, the easy axis in the ground KD of **41** is oriented towards the arene centroid and the benzylic carbon donor atom, i.e. almost perpendicular to the O–Er–O direction (Fig. 14).

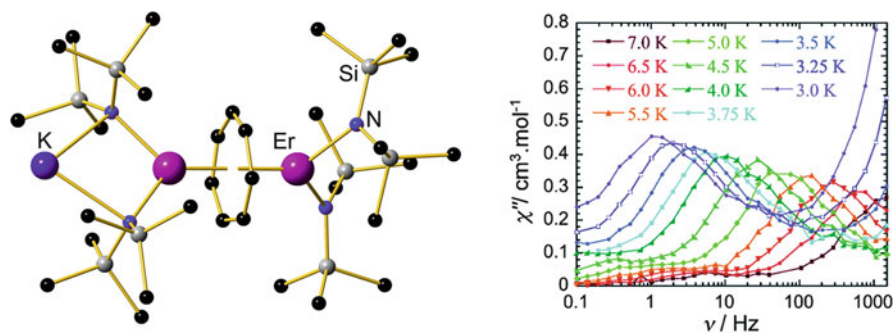




**Fig. 14** Calculated easy axes of magnetisation in the ground Kramers doublet of **40** (left) and **41** (right). Reproduced from Ref. [43] with the permission of Wiley-VCH

### 3.2 Cycloheptatrienyl-Ligated SMMs

To date, only three SMMs containing cycloheptatrienyl ligands are known, i.e. the bimetallic compounds  $[\text{KLn}_2(\eta^7\text{-C}_7\text{H}_7)\{\text{N}(\text{SiMe}_3)_2\}_4]$  ( $\text{Ln} = \text{Dy}$  **42**,  $\text{Er}$  **43**) and the THF-solvated  $[\text{K}(\text{THF})_2\text{Er}_2(\eta^7\text{-C}_7\text{H}_7)\{\text{N}(\text{SiMe}_3)_2\}_4]$  (**44**). These inverse sandwich complexes were synthesised by reacting  $\text{KC}_7\text{H}_9$  with  $[\text{Ln}\{\text{N}(\text{SiMe}_3)_2\}_3]$ , the effect of which is to doubly deprotonate the seven-membered ring to generate the  $10\text{-}\pi$ -aromatic cycloheptatrienyl trianion [44]. The structures of compounds **42–44** consist of two  $\text{Ln}^{3+}$  cations  $\mu$ -bridged by an  $\eta^7\text{-C}_7\text{H}_7$  ligand, with the potassium cation being complexed by two amido nitrogen atoms. In **42** and **43** the potassium cation exhibits a long contact to a neighbouring molecule, resulting in a linear coordination polymer (Fig. 15). Each of **42–44** was found to exhibit field-induced SMM behaviour, with the AC susceptibility in zero DC field showing significant QTM. In an optimised DC field of 2 kOe, compound **42** shows peaks in the frequency



**Fig. 15** Left: molecular structure of **43**. Right: frequency dependence of  $\chi''$  in an 800 Oe applied DC field. Adapted from Ref. [44] with the permission of the Royal Society of Chemistry

dependence of the out-of-phase susceptibility below 4 K. The position of the peaks did not shift to higher frequency with increasing temperature, suggesting that the magnetisation relaxes via QTM, which could be single ion in origin or possibly due to intramolecular interactions. As a result, an anisotropy barrier could not be extracted. In contrast, slow relaxation of the magnetisation was observed for **43** in an applied DC field of 800 Oe, which allowed an anisotropy barrier of  $40 \text{ cm}^{-1}$  and  $\tau_0 = 2.9 \times 10^{-8} \text{ s}$  to be determined.

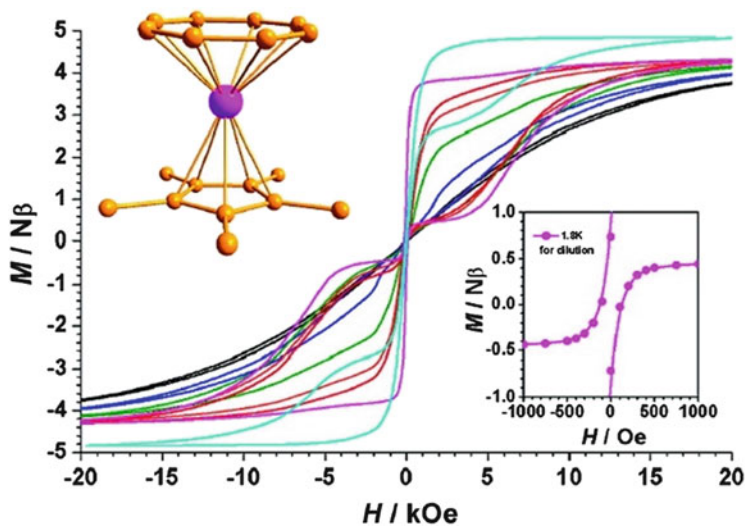
The contrasting properties of **42** and **43** imply that the crystal field arising from the  $[\text{C}_7\text{H}_7]^{3-}$  ligand may be better suited to the prolate electron density of  $\text{Er}^{3+}$  ions than to the oblate electron density of  $\text{Dy}^{3+}$ . This notion implies that cycloheptatrienyl ligands provide an equatorial crystal field in manner reminiscent of the cyclo-octatetraenyl ligand,  $[\text{COT}]^{2-}$  (see Sect. 4). For **44**, two independent relaxation processes below 4 K were observed, and although the two processes could be resolved using optimum DC fields of 1 and 2 kOe, it was not possible to extract anisotropy barriers. Ab initio calculations identified that the main magnetic axis in the ground KD of the dysprosium compound **42** coincides with the  $\text{DyN}_2$  plane, whereas for **43** and **44** the axes are almost perpendicular to the  $\text{ErN}_2$  planes.

## 4 Lanthanide SMMs with $\eta^8$ -Cyclo-octatetraenyl Ligands

### 4.1 SMMs Based on $[\text{CpLn}(\text{COT})]$ and $[\text{Ln}(\text{COT})_2]^-$ Units

After the cyclopentadienyl ligand, the most popular organometallic ligand used in the development of lanthanide SMMs is dianionic,  $10\pi$ -electron cyclo-octatetraenyl,  $[\text{COT}]^{2-}$ . As with Cp, the COT ligand and its substituted derivatives have been known in f-block chemistry for many years; hence the synthetic routes to lanthanide SMMs draw on a substantial body of important prior art [45]. Experimental studies of the magnetic properties of lanthanide–COT complexes coupled with insight from theoretical calculations have revealed COT ligands to be particularly well suited to the electronic structure of  $\text{Er}^{3+}$  for SMM applications. The large effective diameter of COT is thought to create an equatorial crystal field, with the  $\pi$ -electron cloud extending into the equatorial plane around the prolate-shaped electron density of erbium. The effect of the erbium–COT interaction is to stabilise  $M_J = \pm 15/2$  as the magnetic ground state and to increase the energy gap between the ground and first excited KD, typically defined by  $M_J = \pm 13/2$ . In contrast, the oblate electron density of  $\text{Dy}^{3+}$  does not complement the COT equatorial crystal field, with the  $M_J = \pm 15/2$  state often significantly destabilised relative to the analogous situation in dysprosium–cyclopentadienyl SMMs.

These design principles were first illustrated with  $[(\text{Cp}^*)\text{Er}(\text{COT})]$  (**45**), in which the  $\text{Er}^{3+}$  cation is sandwiched between the two ligands but lies much closer to the COT ligand ( $\text{Er}–\text{COT} = 1.662 \text{ \AA}$ ) than to the  $\text{Cp}^*$  ligand ( $\text{Er}–\text{Cp} = 2.271 \text{ \AA}$ ) (Fig. 16) [46, 47]. The coexistence of two structural conformations of **45**, corresponding to different orientations of the COT ligand, leads to two independent

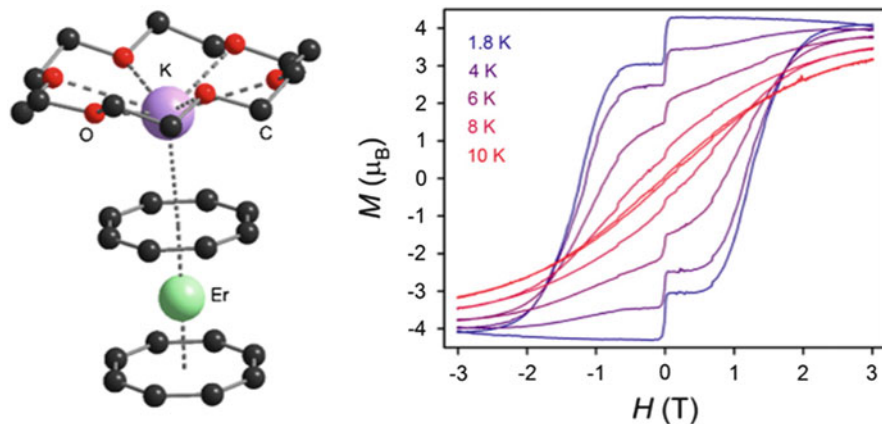


**Fig. 16** Molecular structure of **45** (Er, pink; C, orange) and magnetic hysteresis loops recorded in the temperature range 0.5 K (turquoise trace) to 5.0 K (black trace) using a scan rate of  $9 \text{ Oe s}^{-1}$ . Inset: hysteresis loop for a magnetically dilute sample of **45** at 1.8 K. Reproduced from Ref. [46] with the permission of the American Chemical Society

thermally activated relaxation processes, with  $U_{\text{eff}} = 224 \text{ cm}^{-1}$  and  $\tau_0 = 8.17 \times 10^{-11} \text{ s}$  and  $U_{\text{eff}} = 137 \text{ cm}^{-1}$  and  $\tau_0 = 3.13 \times 10^{-9} \text{ s}$ , respectively. Butterfly-shaped magnetisation hysteresis loops were observed below 5 K with a scan rate of  $9 \text{ Oe s}^{-1}$ .

Since the  $\text{Cp}^*$  ligand in **45** contributes an axial crystal field, its replacement by a second COT ligand to give the homoleptic sandwich complex  $[\text{Er}(\text{COT})_2]^-$  should enhance the SMM properties, an idea that was realised with the contact ion pair  $[\text{K}(18\text{-crown-6})(\mu\text{-}\eta^8\text{-}\eta^8\text{-COT})\text{Er}(\eta^8\text{-COT})]$  (**46**) [48, 49]. In **46**, the  $\text{Er}^{3+}$  ion is sandwiched between two almost coplanar  $\eta^8\text{-COT}$  ligands, with the COT ligand that bridges to the potassium being disordered over two sites, resulting in the formation of staggered and eclipsed conformations (Fig. 17). Under zero DC field, the frequency dependence of the out-of-phase magnetic susceptibility displayed a single peak in each isotherm at temperatures between 15 and 27 K. The relaxation is dominated by an Orbach process, and fitting the temperature dependence of the relaxation time yielded  $U_{\text{eff}} = 147 \text{ cm}^{-1}$  and  $\tau_0 = 8.3(6) \times 10^{-8} \text{ s}$ . A blocking temperature of 10.1 K was determined for **46** based upon extrapolation of the relaxation time data to low temperatures and on the variable-field magnetisation measurements up to 30 kOe, which show waist-restricted hysteresis loops between 1.8 and 10 K. However, the coercivity is small, even at low temperatures, and thus at 10 K the loop is closed. At 1.8 K a coercive field of 7 kOe was measured. A separate study of **46** reported very similar findings, with a blocking temperature of 11 K [49].

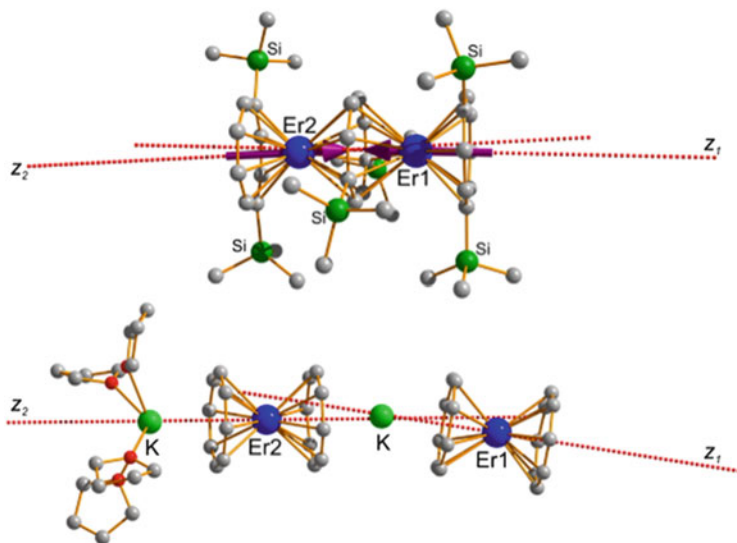
The DC relaxation time measurements at 1.8 K on **46** revealed a dramatic drop in the magnetisation upon removal of the magnetic field, which was attributed to a



**Fig. 17** Left: molecular structure of **46**. Right: hysteresis loops for the magnetically dilute analogue with an Er/Y dilution level of 1:85, in the temperature range 1.8–10 K using scan rate of  $7.8 \text{ Oe s}^{-1}$ . Adapted from Ref. [48] with the permission of the American Chemical Society

magnetic avalanche effect, i.e. a spin–lattice interaction in which the thermal energy generated by spin relaxation triggers a cascade of spin relaxation in neighbouring molecules [48]. To investigate the origin of the avalanche effect, the ion-separated complex  $[\text{K}(18\text{-crown-6})(\text{THF})_2][\text{Er}(\text{COT})_2]$  ( $[\text{K}(18\text{-crown-6})(\text{THF})_2][\mathbf{47}]$ ) was synthesised. The main structural difference between **46** and **47** is that the disorder in the COT ligand is removed on formation of **47**. The static and dynamic magnetic properties of both compounds are almost identical, which implies that differences in the coordination environments do not have a substantial bearing on the magnetic relaxation. Magnetically dilute samples of **47** in a matrix of the isostructural yttrium compound (Er:Y = 1:19, **47a**; 1:84, **47b**) displayed similar magnetic properties to **46** and **47** [48]. However, the variable-field magnetisation data for the diluted samples showed a more gradual loss of magnetisation at zero field relative to the non-dilute material, corresponding to a suppression of the magnetic avalanche effect, which implies that intermolecular dipolar exchange interactions do not impact significantly on the magnetic relaxation. Ab initio calculations on **47** revealed that the main magnetic axis in the ground and first excited KDs are essentially colinear and highly axial in nature, with negligible transverse components of the crystal field, suggesting that relaxation can only occur via the first excited KD.

In an attempt to enhance the SMM properties, the multi-decker complexes  $[\text{Er}_2(\text{COT}'')_3]$  (**48**) ( $\text{COT}'' = 1,4\text{-bis}(\text{trimethylsilyl})\text{cyclo-octatetraenyl}$ ) and  $[\text{K}_2(\text{THF})_4\text{Er}_2(\text{COT})_4]$  (**49**) were synthesised [50]. In **48**, a central  $\mu:\eta^8:\eta^8\text{-COT}''$  ligand bridges the erbium centres, which are separated by  $4.11 \text{ \AA}$  and capped by an  $\eta^8\text{-COT}''$  ligand. The three  $\text{COT}''$  rings are almost perfectly parallel and the Er–COT–Er angle is  $175.65^\circ$ . Compound **49** contains two  $\{\text{Er}(\text{COT})_2\}^-$  units bridged by potassium, with the second potassium capping one of the  $\eta^8\text{-COT}$  ligands (Fig. 18). The DC magnetic susceptibility data for **48** revealed a non-negligible

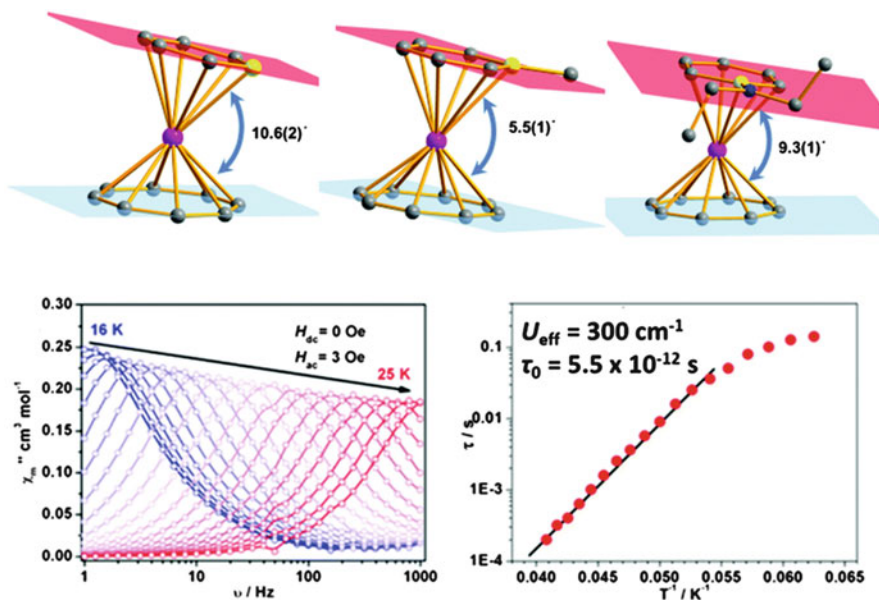


**Fig. 18** Molecular structures of **48** and **49** with the calculated easy axes of magnetisation in the ground Kramers doublets. Reproduced from Ref. [50] with the permission of the American Chemical Society

antiferromagnetic interaction between the erbium atoms, whereas in **49** the erbium centres only very weakly coupled. The magnetic hysteresis measurements on **48** and **49** produced blocking temperatures of 12 K. Furthermore, in a dilute frozen solution of **48**, hysteresis could be observed up to 14 K. The improved blocking temperatures of **48** and **49** relative to those determined for the monometallic compounds **46** and **47** occur for different reasons: in the case of **48**, the short Er–Er distance and the associated exchange interaction play a role in the enhanced properties; in **49**, where the exchange is negligible, the molecular geometry of the two  $\{\text{Er}(\text{COT})_2\}$  units is thought to be better suited to magnetic blocking.

## 4.2 COT-Ligated SMMs with Heteroaromatic Ligands

The incorporation of heteroatoms into the carbocyclic framework of lanthanide sandwich complexes potentially represents an important strategy for tuning the magnetic properties, with the different energies of the molecular vibrations being able to influence the Orbach relaxation processes. The use of boratabenzene ligands of the type  $[\eta^6\text{-C}_5\text{H}_5\text{BR}]^-$  in molecular magnetism is very rare; however these  $6\pi$ -aromatic anions are reminiscent of more common ligands such as cyclopentadienyl and cyclo-octatetraenyl and, hence, their role in promoting SMM properties is of interest. Boratabenzenes are electron-deficient relative to



**Fig. 19** Upper: molecular structures of **51a–51c** depicting the dihedral angles formed by the mean planes of the two ligands (Er, pink; B, yellow; C, grey). Lower: frequency dependence of  $\chi''$  for **51b** in zero DC field and the temperature dependence of the relaxation time. Adapted from Ref. [51] with the permission of the Royal Society of Chemistry

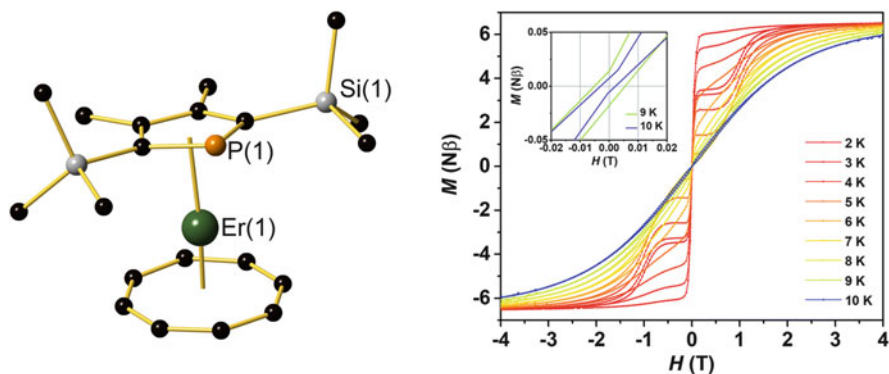
cyclopentadienyl, and the  $\text{BC}_5$  rings have a larger effective diameter; hence they can provide different crystal field properties. Although no homoleptic boratabenzene-ligated SMMs are known, the heteroleptic compounds  $[(\eta^6\text{-C}_5\text{H}_5\text{BR})\text{Ln}(\eta^8\text{-COT})]$  with Ln = Dy and R = H (**50a**), Me (**50b**) or  $\text{NEt}_2$  (**50c**) or Ln = Er and R = H (**51a**), Me (**51b**) or  $\text{NEt}_2$  (**51c**) have been studied in detail [51]. Whilst **50a–50c** only show field-induced slow relaxation with anisotropy barriers ranging from 20 to 30  $\text{cm}^{-1}$ , compounds **51a–51c** displayed slow relaxation in zero DC field, with open hysteresis loops up to 8 K (Fig. 19). In all three erbium compounds, the metal is closer to the COT centroid than to the boratabenzene centroid, with average Er centroid distances of 1.6763 and 2.252 Å for **51a–51c**, respectively. Also, ring slippage of the boratabenzene occurs in **51a–51c**, with the  $\text{Er}^{3+}$  ion being positioned closer to the *para* carbon in all three compounds; the deviation is most pronounced in **51c** as a result of the strong  $\pi$ -interaction between boron and  $\text{NEt}_2$ .

The sharp decreases in  $\chi_{\text{M}}T(T)$  at low temperatures for **51a–51c** indicated magnetic blocking, and the AC susceptibility measurements produced anisotropy barriers of 258 and 300  $\text{cm}^{-1}$ , for **51a** and **51b**, respectively, with  $\tau_0$  values of  $5.3 \times 10^{-12}$  and  $5.5 \times 10^{-12}$  s. Open hysteresis loops were also measured up to 8 and 6 K for **51a** and **51b**, respectively. For **51c**, relaxation via QTM is more prominent, and, thus, a lower anisotropy barrier of 175  $\text{cm}^{-1}$  was determined, and magnetic hysteresis loops were only observed up to 2 K. The poorer SMM behaviour



of **51c** was attributed to a structural distortion in which the boron atom deviates further from the boratabenzene plane (0.097 Å) than in **51a** and **51b** (0.028 and 0.059 Å, respectively), which is a consequence of the strong B–N  $\pi$ -interaction, a notion supported by *ab initio* calculations. Measurements on a magnetically dilute analogue of **51c** revealed a slightly improved energy of barrier of 239 cm<sup>-1</sup> but only a minor improvement in the hysteresis, which was observed up to 3 K. These results were taken to mean that intermolecular dipole–dipole interactions are not significant in **51c** and that differences in magnetic behaviour are mainly a result of the different molecular structures of the three boratabenzene complexes. The increased anisotropy barriers and blocking temperatures of **51a** and **51b** relative to those of [(Cp\*)Er(COT)] (**45**) were attributed to the poorer electron-donating character of boratabenzene ligands, which leads to a weaker axial crystal field that is also unsuited to the prolate electron density of Er<sup>3+</sup>. The local geometry of the boratabenzene ligands in **51a** and **51b** also allow closer approach of the COT ligand than in **45**, which ultimately increases the strength of the equatorial crystal field.

In a related isolobal study, using the phosphacyclopentadienyl ligand 3,4-dimethyl-2,5-bis(trimethylsilyl)phospholyl (Dsp) allows access to a series of sandwich complexes with the general composition [( $\eta^5$ -Dsp)Ln( $\eta^8$ -COT)], with the derivatives containing Dy (**52**), Er (**53**) (Fig. 20) and Tm (**54**) showing slow relaxation of the magnetisation [52]. Compounds **52** and **54** are field-induced SMMs with anisotropy barriers of 40 and 76 cm<sup>-1</sup>, respectively; however **53** has an impressive anisotropy barrier of 249 cm<sup>-1</sup> in zero DC field. The blocking temperature determined from the hysteresis measurements is 9 K. The SMM behaviour of [(Dsp)Er(COT)] (**53**) is a slight improvement over **45**, which is thought to be related to weaker coordination of the Dsp ligand, which allows the Er<sup>3+</sup> ion to reside closer to the centre of the COT ligand, which can therefore exert a stronger equatorial ligand field. The magneto-structural correlation arising from observations on **45–53** is that shorter Er–COT distances lead to larger anisotropy barriers, an observation which is consistent with recent findings on a series of erbium–COT half sandwich complexes [53, 54].



**Fig. 20** Molecular structure of **53** and magnetic hysteresis curves recorded using scan rate of 200 Oe s<sup>-1</sup>. Adapted from Ref. [52] with the permission of the Royal Society of Chemistry

## 5 Conclusions

Following the discovery of slow magnetic relaxation in compounds containing dysprosium metallocene and erbium–COT structural units, lanthanide organometallic chemistry has become one of the most valuable strategies for designing new types of single-molecule magnet. Organometallic chemistry has made significant fundamental contributions to our understanding of the relationship between the electronic structure of the lanthanides and how it can be influenced in targeted, well-defined ways with specific types of ligand that were previously regarded as unconventional in the context of molecular magnetism. From the earliest organo-lanthanide SMMs, with properties such as modest anisotropy barriers and magnetic hysteresis in the liquid-helium temperature regime, the science has evolved to deliver materials that define the current state of the art, including the landmark of hysteresis above the boiling point of liquid nitrogen. As this chapter has highlighted, progress with organometallic SMMs has been enabled by successful collaborations across traditional discipline boundaries, where synthetic organometallic chemists have applied their methods to target materials with unusual physics and magnetochemists have turned their hands to synthetic organometallic chemistry as a test bed for theoretical models of magnetism. Through their collaborations with organometallic chemists, experimental and theoretical physicists and materials scientists have enabled many important advances in our knowledge and understanding of SMMs.

After almost a decade of organo-lanthanide SMMs, the field remains vibrant and primed for further discoveries. Important challenges remain, some of which are elaborated here. Firstly, *improved* hysteresis above liquid-nitrogen temperatures is a key target and must include systems with strong coercive fields and magnetic remanence. The recent discovery of cationic dysprosium metallocene SMMs provides some encouragement for realistically achieving this target. Secondly, studying the properties of organometallic SMMs in environments other than polycrystalline forms is essential, i.e. surface deposition and manipulation of properties at the level of single molecules are important for the wider development of the field. Thirdly, although perhaps less importantly, air sensitivity is occasionally cited as a drawback of organo-lanthanide SMMs, with the stability of these materials often relying on kinetic factors such as bulky ligand substituents. The design of SMMs that might tolerate ambient conditions should, therefore, be considered. However, air sensitivity does not preclude the long-term applications of organometallic SMMs: the fate of a molecule when deposited on a surface does not necessarily depend on the ‘type’ of chemistry. Furthermore, if a transformative organometallic SMM is discovered, the methods of device construction may adapt accordingly. Motivation for continuing the development of organo-lanthanide SMMs comes in different forms, including the pursuit of record-breaking properties, the desire for technological applications and, most importantly, the quest for greater fundamental understanding. Whatever the driving force, lanthanide organometallic chemistry will play an important role in advancing the frontiers in SMM research for years to come.



**Acknowledgements** The authors thank the Royal Society Newton Fund, the European Research Council (Consolidator Grant RadMag), the EPSRC and the University of Sussex for financial support.

## References

1. Liu JL, Chen YC, Tong ML (2018). *Chem Soc Rev* 47:2431
2. Feng M, Tong ML (2018). *Chem A Eur J* 24:7574
3. Gupta SK, Murugavel R (2018). *Chem Commun* 54:3685
4. Lu J, Guo M, Tang J (2017). *Chem Asian J* 12:2772
5. Pointillart F, Cadour O, Le Guennic B, Ouahab L (2017). *Coord Chem Rev* 346:150
6. Frost JM, Harriman KLM, Murugesu M (2016). *Chem Sci* 7:2470
7. Woodruff DN, Winpenny REP, Layfield RA (2013). *Chem Rev* 113:5110
8. Cornia A, Seneor P (2017). *Nat Mater* 16:505
9. Layfield RA (2014). *Organometallics* 33:1084
10. Harriman KLM, Murugesu M (2016). *Acc Chem Res* 49:1158
11. Day BM, Guo F-S, Layfield RA (2018). *Acc Chem Res* 51:1880
12. Layfield RA, McDouall JJW, Sulway SA, Tuna F, Collison D, Winpenny REP (2010). *Chem A Eur J* 16:4442
13. Rinehart JD, Long JR (2011). *Chem Sci* 2:2078
14. Benelli C, Gatteschi D (2015) Introduction to molecular magnetism: from transition metals to lanthanides. Wiley-VCH, Weinheim
15. Gatteschi D, Sessoli R, Villain J (2011) Molecular nanomagnets. Oxford University Press, Oxford
16. Ungur L, Chibotaru LF (2016). *Inorg Chem* 55:10043
17. Chilton NF (2015). *Inorg Chem* 54:2097
18. Zhang P, Zhang L, Wang C, Xue S, Lin SY, Tang J (2014). *J Am Chem Soc* 136:4484
19. Tuna F, Smith CA, Bodensteiner M, Ungur L, Chibotaru LF, McInnes EJJ, Winpenny REP, Collison D, Layfield RA (2012). *Angew Chem Int Ed* 51:6976
20. Burns CP, Wilkins BO, Dickie CM, Latendresse TP, Vernier L, Vignesh KR, Bhuvanesh NS, Nippe M (2017). *Chem Commun* 53:8419
21. Burns CP, Yang X, Wofford JD, Bhuvanesh NS, Hall MB, Nippe M (2018). *Angew Chem Int Ed* 57:8144
22. Pugh T, Chilton NF, Layfield RA (2016). *Angew Chem Int Ed* 55:11082
23. Guo FS, Day BM, Chen YC, Tong ML, Mansikkamäki A, Layfield RA (2018). *Science* 362:1400
24. Guo FS, Day BM, Chen YC, Tong ML, Mansikkamäki A, Layfield RA (2017). *Angew Chem Int Ed* 56:11445
25. Goodwin CAP, Ortu F, Reta D, Chilton NF, Mills DP (2017). *Nature* 548:439
26. Goodwin CAP, Reta D, Ortu F, Chilton NF, Mills DP (2017). *J Am Chem Soc* 139:18714
27. McClain KR, Gould CA, Chakarawet K, Teat SJ, Groshens TJ, Long JR, Harvey BG (2018). *Chem Sci* 9:8492
28. Pugh T, Tuna F, Ungur L, Collison D, McInnes EJJ, Chibotaru LF, Layfield RA (2015). *Nat Commun* 6:7492
29. Pugh T, Vieru V, Chibotaru LF, Layfield RA (2016). *Chem Sci* 7:2128
30. Pugh T, Chilton NF, Layfield RA (2017). *Chem Sci* 8:2073
31. Demir S, Zadrozny JM, Long JR (2014). *Chem A Eur J* 20:9524
32. Meng YS, Zhang YQ, Wang ZM, Wang BW, Gao S (2016). *Chem A Eur J* 22:12724
33. Demir S, Nippe M, Gonzalez MI, Long JR (2014). *Chem Sci* 5:4702
34. Guo F-S, Layfield RA (2017). *Chem Commun* 53:3130

35. Gould CA, Darago LE, Gonzalez MI, Demir S, Long JR (2017). *Angew Chem Int Ed* 56:10103
36. Demir S, Jeon IR, Long JR, Harris TD (2015). *Coord Chem Rev* 289:149
37. Rinehart JD, Fang M, Evans WJ, Long JR (2011). *Nat Chem* 3:538
38. Rinehart JD, Fang M, Evans WJ, Long JR (2011). *J Am Chem Soc* 133:14236
39. Demir S, Zadrozny JM, Nippe M, Long JR (2012). *J Am Chem Soc* 134:18546
40. Demir S, Gonzalez MI, Darago LE, Evans WJ, Long JR (2017). *Nat Commun* 8:2144
41. Liu S-S, Ziller JW, Zhang Y-QQ, Wang B-WW, Evans WJ, Gao S (2014). *Chem Commun* 50:11418
42. Liu S-S, Yan B, Meng Z-S, Gao C, Wang BW, Gao S (2017). *Inorg Chem Commun* 86:312
43. Meng YS, Xu L, Xiong J, Yuan Q, Liu T, Wang BW, Gao S (2018). *Angew Chem Int Ed* 57:4673
44. Harriman KLM, Le Roy JJ, Ungur L, Holmberg RJ, Korobkov I, Murugesu M (2016). *Chem Sci* 8:231
45. Rausch J, Apostolidis C, Walter O, Lorenz V, Hrib CG, Hilfert L, Kühling M, Busse S, Edelmann FT (2015). *New J Chem* 39:7656
46. Da Jiang S-D, Wang B-WW, Sun H-L, Wang Z-MM, Gao S (2011). *J Am Chem Soc* 133:4730
47. Da Jiang S-D, Liu S-S, Zhou L-N, Wang B-W, Wang Z-M, Gao S (2012). *Inorg Chem* 51:3079
48. Meihaus KR, Long JR (2013). *J Am Chem Soc* 135:17952
49. Ungur L, Leroy JJ, Korobkov I, Murugesu M, Chibotaru LF (2014). *Angew Chem Int Ed* 53:4413
50. Le Roy JJ, Ungur L, Korobkov I, Chibotaru LF, Murugesu M (2014). *J Am Chem Soc* 136:8003
51. Meng Y-S, Wang C-H, Zhang Y-Q, Leng X-B, Wang B-W, Chen Y-F, Gao S (2016). *Inorg Chem Front* 3:828
52. Chen S-M, Xiong J, Zhang Y-Q, Yuan Q, Wang B-W, Gao S (2018). *Chem Sci* 9:7540
53. Hilgar JD, Flores BS, Rinehart JD (2017). *Chem Commun* 53:7322
54. Hilgar JD, Bernbeck MG, Flores BS, Rinehart JD (2018). *Chem Sci* 9:7204

# Role of Ab Initio Calculations in the Design and Development of Lanthanide Based Single Molecule Magnets



Tulika Gupta, Mukesh Kumar Singh, and Gopalan Rajaraman

## Contents

1	Introduction .....	282
1.1	Theoretical Depiction of Crystal Field Splitting .....	283
2	Modelling Magnetic Anisotropy of Lanthanide Single-Ion Magnets Using Ab Initio Calculations .....	287
3	Ab Initio Calculations on Lanthanide Based Magnets .....	291
3.1	Illustrative Examples of Dy <sup>III</sup> Single-Ion Magnets Studied Using Ab Initio Calculations .....	293
3.2	Model Complexes Predicted Using Ab Initio Calculations .....	324
3.3	Review on Er <sup>III</sup> Containing Single-Ion Magnets .....	330
3.4	Review on Unconventional Ln <sup>III</sup> Containing Single-Ion Magnets .....	339
4	Conclusions .....	345
4.1	Future Outlook .....	348
	References .....	350

**Abstract** In this book chapter, we have reviewed recent trends in employing ab initio calculations based on complete active space self-consistent field (CASSCF)/restricted active space spin interaction with spin–orbit coupling (RASSI-SO) procedure to interpret, rationalize and predict suitable lanthanide based molecular magnets. We begin with the general introduction on the methods used followed by various pragmatic instances where ab initio calculations have been employed to understand the magnetic anisotropy in lanthanide based single-ion magnets (SIMs). While a detailed section is dedicated to the mononuclear Dy<sup>III</sup> SIMs, we have also covered other lanthanide SIMs briefly. Particularly, we have classified various SIMs based on the observed crystal-field splitting between ground and first excited states and this likely to shed light on the most important issue of suitable geometries that could yield high blocking temperature SIMs.

---

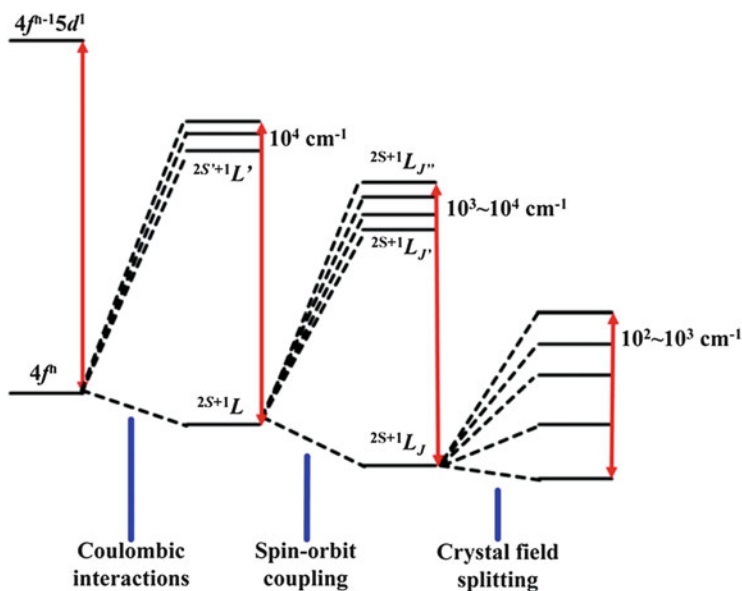
T. Gupta, M. K. Singh, and G. Rajaraman (✉)  
Department of Chemistry, IIT Bombay, Mumbai, India  
e-mail: [rajaraman@chem.iitb.ac.in](mailto:rajaraman@chem.iitb.ac.in)

**Keywords** Ab initio calculations · CASSCF/RASSI-SO approach · Dy<sup>III</sup> SIMs · Lanthanides · Mechanism of relaxation · Single-ion magnet (SIM)

## 1 Introduction

Since the first invention of single molecule magnet (SMM) in 1993, various realms have been researched ranging from zero-dimensional polymeric metal clusters to metal–radical SMMs, 1D single chain magnets (SCMs) and single-ion magnets (SIMs), etc. [1–11] While tremendous progress on synthesis of polynuclear metal clusters/SCMs/metal–radical systems has been achieved, structures are often not predictable and so is the magnetic characteristic. SIMs enact as remedy in this regard due to their facile synthesis and simplified structures compared to the complexities that lie in polynuclear SMMs [12]. Magnetic properties of SIMs are linked to the adjacent crystal field generated by the coordinated ligands [13]. This cumulatively invokes improved understanding between structural and magnetic properties in SIMs and entails the pivotal role of ligand field in the design and development of novel SIMs. For SIMs, the coordination number, local point group symmetry as well as crystal field strength need to be manoeuvred simultaneously to achieve larger energy barrier for magnetization reversal ( $U_{\text{eff}}$ ). In SIMs, interaction between magnetic ion and surrounding ligand field is the origin of magnetic anisotropy. Compared to 3d and 5f congeners, 4f (Lanthanide, Ln<sup>III</sup>) based SIMs are more successful in achieving attractive magnetization blocking temperatures [14–17]. This is due to weaker lanthanide–ligand interactions and large unquenched orbital angular momentum, rendering strong spin–orbit coupling (SOC), leading to a large inherent magnetic anisotropy. Complexes with more than one 4f magnetic ions evoke weaker 4f–4f exchange rendering faster quantum tunnelling of magnetization (QTM) leading to a drastic reduction in the desired magnetization blockade. This is one of the major problems in the area of SMM where scientists are indulged in improving energy barrier and the blocking temperature. Recent breakthroughs in Ln<sup>III</sup>-SIMs, exhibiting improved energy barrier [18–20] and blocking temperature up to 60 K appeared [21, 22] to some extent relieve the ongoing contention and now focus is to enhance blocking temperature beyond liquid nitrogen temperatures.

Accounting these facts, we would confine our discussions to Ln<sup>III</sup>-based SIMs in this chapter. We will begin our discussion with the theoretical depiction of crystal field splitting and various avenues available to compute these parameters for Ln-based molecules. This will be followed up by brief discussion on the ab initio CASSCF/CASPT2 methodologies that are widely employed for the computation of spin Hamiltonian parameters of Ln<sup>III</sup> SIMs. This will be followed by discussion on various Ln<sup>III</sup> SIMs reported in the literature. While a detailed section has been devoted to Dy<sup>III</sup> ion based SIMs, for other lanthanide ions a succinct section is presented followed by conclusions and future outlook.



**Fig. 1** Schematic diagram of the plausible energy level splitting for lanthanide ions in logarithmic energy scale. Reprinted with permission from Meng et al. [23] Copyright ©1997 American Chemical Society

### 1.1 Theoretical Depiction of Crystal Field Splitting

Considering the strong SOC in lanthanides, patterns of  $^{2S+1}L_J$  multiplets can be deduced by accounting strong inter-electron repulsion (coulombic) followed by the SOC. Weaker ligand field effect (compared to 3d congeners) subsequently promotes splitting of the  $^{2S+1}L_J$  multiplets (see Fig. 1) [23]. As the ligand field splitting is dependent on the coordination environment, it dictates in the  $\text{Ln}^{\text{III}}$ -SIMs/SMMs, the nature of magnetic anisotropy and its relaxation process [24]. It is a well-established fact that, in order to gain insights into the magnetic characteristics in  $\text{Ln}^{\text{III}}$ -SIMs/SMMs and develop magneto-structural correlation, we need to estimate the corresponding crystal field parameters [25]. This solely relies on the 27 crystal field parameters corresponding to the symmetry of central lanthanide ions. The crystal field can be denoted as follows [26]:

$$\hat{H} = \sum_{i,k,q} B_k^q O_k^q(\theta_i, \varphi_i) \quad (1)$$

where  $O_k^q(\theta_i, \varphi_i)$  delineates Stevens operator which relies on angular coordinates  $(\theta_i, \varphi_i)$  as expressed within the given coordinate system,  $B_k^q$  depicts crystal field parameters for the ranks = 2, 4, 6,  $i$  indicates the number of electrons and  $q$  ranges from  $-k$  to  $+k$ . Although efforts have been made to estimate these parameters using experimental techniques, as there are numerous possibilities, a single experimental/spectroscopic technique alone is not suffice to obtain the full depiction of crystal

field splitting and directions of local anisotropy axes precisely. This rejuvenates the need to implicate versatile theoretical models [27, 28] to illustrate crystal field splitting in Ln<sup>III</sup>-SIMs/SMMs and with time it has proven to be extremely useful both for understanding the anisotropy and also to design molecules possessing attractive magnetic properties.

### 1.1.1 Ab Initio Description of Crystal Field Splitting

As explained earlier, various experimental obstacles necessitate the estimation of crystal field parameters from first principles to facilitate targeted synthesis of lanthanide compounds to avoid serendipitous assembly. In this context, ab initio methodologies embedded within MOLCAS [29–35] suite have been proven to be viable in the depiction of wave functions, energies as well as Zeeman interactions in terms of the pseudospin operators of the low-lying multiplets [36]. These calculations for lanthanide elements were pioneered by Chibotaru and co-workers and remain ubiquitous for the rationalization of the magnetic properties of lanthanides [37]. Within the used approach, relativistic effects have been considered based on Douglas–Kroll–Hess (DKH) Hamiltonian [38, 39]. In the first step of this computational process, scalar relativistic effects are considered for the generation of basis sets. In the next step, spin-free eigenstates are generated with active space formed by the lanthanide 4f orbitals embedded within CASSCF (complete active space self-consistent field) approach of MOLCAS module. This is followed by restricted active space (RAS) [35] calculation accounting spin–spin and spin–orbit coupling (RASSI-SO) employing the previous steps resultant eigenfunctions as input states. Here, the SOC is illustrated within the atomic mean field integral (AMFI) approximation [40]. This leads to the generation of spin–orbit eigenfunctions as linear combinations of aforestated spin-free functions. At the final step, specifically selected precise eigenfunctions are projected onto pseudospin operator  $\tilde{S}$ . The aforementioned ab initio approach postulates crystal field splitting of the ground atomic J-multiplet of lanthanide ions (multiplet specific crystal field Hamiltonian) [26, 28]. For accurate determination of crystal field parameters ( $B_k^q$ ), highly beneficial irreducible tensor operator (ITO) technique has been employed (within SINGLE\_ANISO module of MOLCAS). The advantage of this approach is well established and can be expressed in terms of crystal field states  $|J_M\rangle$  [26]. This induces acquirement of crystal field parameters for specific coordination frame/quantization axis [26]. The key feature of this approach lies in unique way of deducing crystal field parameters without the utilization of fitting procedure as employed in other methods. Therefore, the spin–orbit energy multiplets obtained from the previous RASSI-SO step will be subsequently used to derive crystal field parameters [37, 41]. For the deduction of principal g-tensor values of Kramers doublet, pseudospin  $\tilde{S} = \frac{1}{2}$  formalism has been utilized. Hence, the ab initio calculations render accurate illustration of the energy multiplets and corresponding energies. Although these calculations are expensive, their robustness made them persuasive towards rational design of 4f – based SIMs/SMMs.

### 1.1.2 Electrostatic Definition for Crystal Field Splitting Based on True Electronic Charge Distribution

Despite the versatility of the ab initio calculations, these calculations are often computationally demanding and possibly cannot be used for screening large number of molecules. To overcome these shortcomings, other qualitative methodologies to obtain CF parameters are proposed. In this regard, the electrostatic effects of the ligands coordinated to lanthanide on the ground state have been considered. This electrostatic model (true electronic charge based) has been developed counting on the aspherical lanthanide 4f electron density distribution for the free ions following Hund's rule and  $|\pm M_J\rangle$  energy state configuration [42–44], positions and charges of the adjacent coordinated ligands. Minimization of electrostatic energy for the estimation of ground state magnetic anisotropy axis forms the basis of this methodology. The charge of the coordinated atoms of the ligands dictates the electrostatic potential realized by the central metal ion. This induces evaluation of electrostatic field generated by ligand charges within minimal valence bond (VB) model [42] and promotes construction of crystal field potential from fractional formal charges as embedded within the aforementioned model (exclusion of neutral atoms). After the deduction of ligand charges based on charge partitioning, electrostatic potential can be estimated from the well-known crystal field theory. This instigates estimation of the  $|\pm M_J\rangle$  multiplet energy as a function of ion orientation. Therefore, VB model coupled with electrostatic energy minimization generates specific orientation of principal anisotropy axis and preferential alignment of the crystal field quantization axis for a specific geometry. The issues pertain to addressing neutral ligands and failing to address systems where the ground state  $|\pm M_J\rangle$  strongly mixes with excited states restricting the prevalence of this model towards precise deduction of magnetic anisotropy/crystal field parameters; yet, as these methods are computationally robust, this has been often used to screen large number of molecules possessing interesting magnetic characteristics.

### 1.1.3 Electrostatic Description for Crystal Field Splitting Based on Effective Point-Charge Distribution

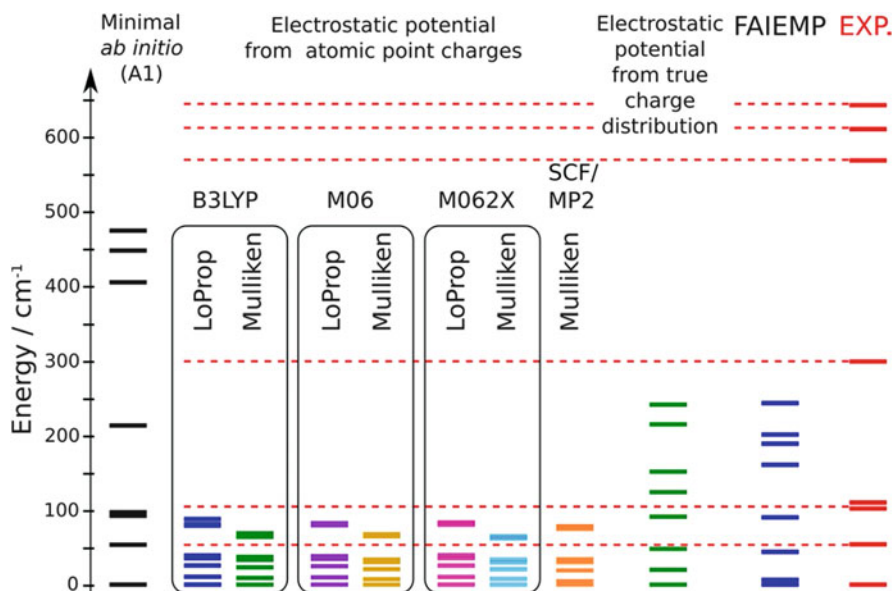
This model is based on the estimation of effective crystal field Hamiltonian, which considers classical effective point-charge electrostatic (PCE) model around the central magnetic ion [24, 45–51]. This model parameterizes ligand field effect around the central  $\text{Ln}^{\text{III}}$  ion by positioning point charges (LoProp, Mulliken) at the pertinent metal surrounding ligand atom positions. Further improvements to this model were implemented by placing effective charges amidst the chemical bonds, different donor atoms, by incorporating ab initio computed charges/parameters. Using this point-charge model, splitting of lanthanide  $|\pm M_J\rangle$  sublevels has been nicely illustrated. In this approach, effective charge, effective radial distance along the bond between metal and coordinated ligand atom, effective displacement perpendicular to that bond and a few other parameters are taken into consideration.

These are free fitting parameters acquired from high-resolution spectroscopic data for the corresponding lanthanide systems.

The accuracy of these models depends on how good these models are in replicating the experimental data? The electrostatic anisotropy axis (orientation of the principal magnetization based on electrostatic model of true charges) [42] lies in close proximity to the *ab initio* calculated and experimentally determined anisotropy axis (wherever applicable). But, this model is not valid when: (1) a system possesses ground state which strongly mixes with the excited states and (2) a system does not take into consideration the uncharged ligands. The PCE model nicely explains the experimental SMM/SIM characteristics through estimation of crystal field parameters and eigenvector contributions of the low-lying energy multiplets [49]. This model is known to closely replicate the energies of the first excited energy levels against experiment. However, higher energy levels as predicted by this model deviate from experimental data by <15% and also fourth range extra-diagonal crystal field parameters come into play [48]. Lack of accurate determination of symmetry axis within the molecule diverts the expected direction of principal magnetization direction. But, the bottleneck of this model underlies in the estimation of varieties of transferable robust parameters for broad range of ligands. In the literature, most of the single-crystal magnetometry measured crystal field splitting direction were compared with respect to that obtained from *ab initio* calculations accentuating its prevalence over other models. The divergence between *ab initio* calculations and experimental data has generally been found to be  $\sim 10\text{--}20\text{ cm}^{-1}$ / $\sim 30\%$ . The deviation ascribes to the fact that the calculations are undertaken on non-optimized geometries and at  $\sim 100\text{ K}$ . However, the magnetic and spectroscopic measurements are usually performed at comparatively much lower temperatures. Incorporation of dynamic correlation (CASPT2) or enhancement of active space (RASSCF) in conjunction with electrostatic Madelung potential of the crystal attenuates the demarcation between the experimental and *ab initio* calculated energies [26]. Accounting all these explanations, *ab initio* calculations seem to be promising in deducing crystal field splitting energy levels of the lanthanide complexes (see Fig. 2). Recent years have witnessed substantial progress in the *ab initio* calculations owing to precision and pace towards novel synthetic design of SIMs/SMMs. Efficient intuitive potential continues to keep them in the limelight and they continue to play pivotal role towards experimental synthesis of SIMs/SMMs beyond serendipity.

Utilizing *ab initio* calculations for the deduction of exchange spectrum and exchange parameters in polynuclear lanthanide complexes remains elusive compared to the estimation of crystal field splitting in mononuclear SIMs. Polymeric complexes are dealt in two steps: (a) fragmentation of the polymeric structure into mononuclear fragments and rigorous *ab initio* calculations on each monomeric fragment. This is followed by (b) effective evaluation of the magnetic exchange interaction between the monomeric fragments [28]. The magnetic coupling between the magnetic sites is accounted within the Lines model [52] where dipole–dipole coupling is considered exactly. The Lines model evokes derivation of anisotropic magnetic coupling between the spin moments of the magnetic centres in the absence of SOC by a single parameter. Incorporation of isotropic Heisenberg model with





**Fig. 2** Comparisons of the crystal field spectrum in Er-trensal complexes as obtained from various electrostatic models and *ab initio* calculations. Reprinted from Ungur and Chibotaru [26] with permission from John Wiley and Sons

effective parameter implicating true spins of the two magnetic sites has been carried out. This is followed by composition of the matrix based on the products from the localized lowest energy levels of the two magnetic sites obtained from fragmented *ab initio* calculations. The resultant exchange matrix outlines the exchange interaction in three limiting instances: (1) one anisotropic and one isotropic magnetic centre (Ising + Heisenberg = Ising exchange), (2) two anisotropic magnetic centres (Ising exchange) and (3) two isotropic magnetic centres (Heisenberg exchange). The Lines model depicts the magnetic coupling accurately in first case mentioned above (between the anisotropic and the isotropic ions). In remaining instances, Lines model enacts as a reasonable approximation and implementation of these methodologies in POLY\_ANISO routine by Chibotaru and co-workers enables one to carry out such simulations for {3d-4f} systems [37, 53].

## 2 Modelling Magnetic Anisotropy of Lanthanide Single-Ion Magnets Using *Ab Initio* Calculations

Due to the multi-configurational nature of the ground as well as low-lying excited states of the lanthanide ions, *ab initio* CASSCF approach is indispensable for the description of the lanthanide electronic and magnetic properties. Selection of orbitals in CASSCF approach is undertaken by partitioning the molecular orbitals (MO) into:

inactive (doubly occupied), active and virtual (empty) orbitals. The inactive and virtual orbitals remain doubly occupied and empty, respectively, in all possible configurations utilized to construct CASSCF wave function. The rest of the electrons occupy correlated orbitals and that is considered as active space. The CASSCF wave function can be considered as linear combination of all plausible configurations (Slater determinants, SDs) which are formed by the partitioning scheme. The CASSCF active orbitals are supposedly some of the highest occupied and lowest unoccupied orbitals generated from restricted Hartree–Fock (RHF) calculations. Within the active MOs, full configuration interaction (CI) calculations are carried out and all configurational state functions (CSF) must be included within the CASSCF optimization. Coefficients of the SDs (CI coefficients) and the MO consideration rendered minimization of energy. Within active space, only limited/specific numbers of SD configurations are constructed by allowing electronic excitation to higher energy orbitals. Therefore, the CASSCF wave function can be variationally optimized through optimization of CI coefficients in the CI expansion and the MOs, as mentioned earlier. The type of orbitals to be incorporated into the active space of CASSCF approach is dependent upon the nature of computational problem we intend to address. The viability of CASSCF approach in resolving lanthanide problems lies in its ability to depict systems possessing near-degeneracy and close-lying excited states. This make this method ubiquitous for the delineation of magnetic anisotropy and the associated crystal field parameters of lanthanide complexes. CASSCF wave function accounts only for the static electronic correlation and meagre number of electrons spreading the frontier MOs are correlated between them. In order to consider dynamic electron correlation, perturbative CASPT2 approach consideration is indispensable which renders better description of the magnetic properties (as stated in Sect. 1.1.3). Although CASSCF remains the omnipresent electronic structure method to study the multi-configurational systems, computational cost enhances proportionally with the number of active orbitals and active electrons. This poses a challenge to the method as often larger reference space is required to address complex chemical problems. If excitations from/to the orbitals beyond the chosen CAS reference space are envisioned, alternative approach can be adapted to enhance the size of the reference space. This secondary space is known as ‘RAS’ and excitation limits to one or two electrons only. In this RASSCF methodology, active MOs are partitioned into three sections: RAS1, RAS2 and RAS3 containing restrictions on the number of allowed excitations (occupations). The RAS1 and RAS3 space belongs to doubly occupied and empty MOs of the HF reference determinants, respectively. Limited number of excitations from RAS1 is allowed while identical excitation is allowed from RAS1/RAS2 to RAS3. RAS2 is reminiscent of the active space depicted earlier in the CASSCF approach where all plausible electronic arrangements within the orbitals are allowed. Henceforth, although all plausible electronic configurations within CAS space are permitted, only specific number of RAS configurations exists. So, RASSCF renders reasonable solutions for degenerate systems both in ground and excited states. Notably, in general calculations, we only consider RAS2 active space putting no holes/electrons/orbitals in RAS1/RAS3 space. However, enhancement of the active space by

the utility of RAS1/RAS3 space has pronounced effect in providing better depiction of the electronic and magnetic properties (as stated in Sect. 1.1.3). All these key features are inscribed within MOLCAS suite. MOLCAS suite also enables estimation of the molecular properties harnessing formulas of expectation values or finite perturbation theory utilizing the RASSI (restricted active space spin interaction) programme. RASSI evaluates interaction between various CASSCF/RASSCF wave functions based on orbitals that are non-orthonormal. RASSI is generally used to evaluate transition dipole moments in spectroscopy and to acquire eigenstates of relativistic Hamiltonian with the incorporation of spin-orbit (SO) interaction. During the study of lanthanide properties, precision of SO coupling treatment is a crucial feature to comply with their pertinent vital relativistic effects. Within the RASSI-SO approach, as implemented in MOLCAS package, SOC is considered non-perturbatively within the mean-field theory. It is noteworthy to mention here that RASSI-SO treats all wave functions as ‘frozen’, i.e. CASSCF/RASSCF wave functions do not alter during the computations. In the end, these consequential ground as well as excited spin-orbit multiplets are harnessed to perform non-perturbative computation of: (a) effective spin (pseudospin) Hamiltonian, (b) static field and temperature dependence magnetic features and (c) pseudospin Hamiltonians for Zeeman interaction (g tensors) using the SINGLE\_ANISO routine of MOLCAS.

Another important aspect that needs to be considered for lanthanides is the relativistic effects. The scalar relativistic effects are treated within the basis set consideration of atomic natural orbitals (ANOs) embedded with relativistic correction. The ANOs are obtained from the average density matrix of the ground and lowest excited states of the element and the element in an electric field. The ANO-RCC (RCC invokes relativistic and (semi-)core correlation) basis sets for the whole periodic table were formed utilizing average density matrix acquired from CI computation on ground as well as excited states of the ions inside the electric field (describing polarizability of the elements). These basis sets were constructed for relativistic one- or two-component calculations which include scalar relativistic effect via second order DKH Hamiltonian. For heavier elements, incorporation of correlation from semi-core electrons becomes extremely imperative. For lanthanides, 5s and 5p semi-core electrons are added in the correlation treatment entailing their inclusion even when the basis sets are being used. The remaining core electrons are delineated through minimal basis set and are abstained from the correlation treatment to evade larger basis set superposition errors. Hence, the standard ANO-RCC basis set library as embedded within MOLCAS routine is optimized for use with DKH transformation of one-electron integrals. Meticulous literature perusal on the ab initio calculations of lanthanide systems suggest that in all instances ANO-RCC basis sets as embedded within MOLCAS package were employed. However, the range of basis sets employed for the involved elements varied from ANO-RCC-VQZP  $\rightarrow$  ANO-RCC-VTZP  $\rightarrow$  ANO-RCC-VDZP  $\rightarrow$  ANO-RCC-VDZ. At this level, the accuracy or choice of basis set for these types of anisotropy calculations remains elusive. However, from survey, we can postulate that: (a) increase of basis set (from double to triple to quadruple) on lanthanide ions always leads an enhancement in energy gap between ground and first

excited states as well as higher energy multiplets [13, 54] though reverse trend is also noted in some cases [55], (b) modification from ANO-RCC-VTZP  $\rightarrow$  ANO-RCC-VDZP reveals  $\sim 10\text{--}15\text{ cm}^{-1}$  increment in barrier height estimated, (c) however, change from ANO-RCC-VQZP  $\rightarrow$  ANO-RCC-VTZP poses hardly any effect on the barrier value or anisotropy nature, (d) in all these variations of ANO-RCC-VQZP  $\rightarrow$  ANO-RCC-VTZP  $\rightarrow$  ANO-RCC-VDZP, the  $g_{zz}$  values remain uniform throughout, (e) however, prominent change in barrier value/anisotropy behaviour was detected for basis set changes between ANO-RCC-VTZP  $\rightarrow$  ANO-RCC-VTZ and ANO-RCC-VDZP  $\rightarrow$  ANO-RCC-VDZ, i.e. addition of polarization functions in the basis sets found to induce pronounced impact and (f) in order to consider impact of neighbouring molecules, point charges were located at each atomic position of the crystal which does not exert prominent effect on anisotropy [54, 56]. The information required to perform computation on individual lanthanide ions are described in Table 1.

Cholesky decomposition of the two-electron integrals with a threshold of  $10^{-8}$  is generally employed to avoid large usage of hard disk and reduce computational

**Table 1** Illustrative table describing the electronic configuration of the individual  $\text{Ln}^{\text{III}}$  ions along with the expected  $g_{zz}$  value of the largest  $|M_J\rangle$  level and possible multiplets that could be adapted for: (1) CASSCF calculations and (2) RASSI-SO step

Ions	Number of 4f electrons ( $4f^N$ )	Ground state term symbol	Expected $g_{zz}$ for the highest $ \pm M_J\rangle$	Active space CAS ( $n, m$ )	Plausible CASSCF configurations	Multiplets mixed in the RASSI step
$\text{Ce}^{\text{III}}$	$4f^1$	$^2F_{5/2}$	4.5	CAS (1, 7)	7 doublets	7 doublets
$\text{Nd}^{\text{II}}$	$4f^3$	$^4I_{9/2}$	6.55	CAS (3, 7)	35 quartets and 112 doublets	35 quartets and 112 doublets
$\text{Tb}^{\text{III}}$	$4f^8$	$^7F_6$	18	CAS (8, 7)	7 septets, 140 quintets and 195 triplets	7 septets, 105 quintets and 112 triplets
$\text{Dy}^{\text{III}}$	$4f^9$	$^6H_{15/2}$	20	CAS (9, 7)	21 sextets, 224 quartets and 158 doublets <sup>a</sup>	21 sextets, 128 quartets and 130 doublets
$\text{Ho}^{\text{III}}$	$4f^{10}$	$^5I_8$	20	CAS (10, 7)	35 quintets, 210 triplets and 196 singlets	30 quintets, 99 triplets and 31 singlets
$\text{Er}^{\text{III}}$	$4f^{11}$	$^4I_{15/2}$	18	CAS (11, 7)	35 quartets and 112 doublets	35 quartets and 112 doublets
$\text{Tm}^{\text{III}}$	$4f^{12}$	$^3H_6$	14	CAS (12, 7)	21 triplets and 28 singlets	21 triplets and 28 singlets
$\text{Yb}^{\text{III}}$	$4f^{13}$	$^2F_{7/2}$	8	CAS (13, 7)	7 doublets	7 doublets

Here,  $n$  electrons are distributed in all plausible pathways in  $m$  orbitals

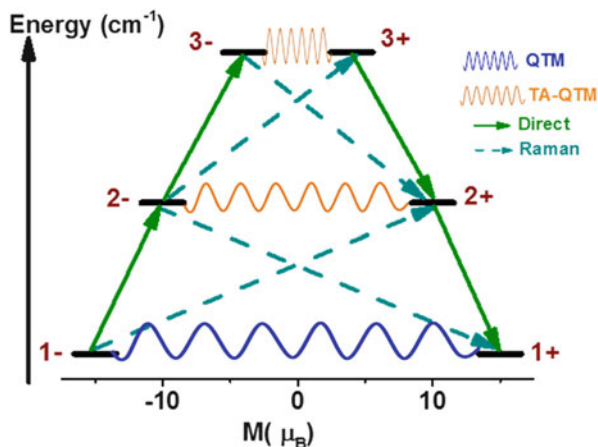
<sup>a</sup>Sometimes 21 sextets in CASSCF and RASSI-SO step would suffice the desired anisotropy behaviour in  $\text{Dy}^{\text{III}}$

demand. The molecular orbitals (MOs) were optimized in state-averaged CASSCF calculations, where the active space was defined by the nine 4f electrons in the seven 4f orbitals of Dy<sup>III</sup> (see Table 1). Considering the SOC, for the Dy<sup>III</sup> site, the CASSCF calculation is executed at ground state ( $S = \frac{5}{2}$ ) with all of the 21 configurations, the first excited state ( $S = \frac{3}{2}$ ) with all of the 224 configurations and the second excited state ( $S = \frac{1}{2}$ ) with the 158 configurations independently for each spin state. After the CASSCF calculation, the RASSI-SO calculations of RAS state interaction are undertaken. In this step, 21 configurations for the ground state; 128 configurations for the  $S = \frac{3}{2}$  state and 130 configurations for the state  $S = \frac{1}{2}$  states were mixed by SOC corresponding to an energy cut-off of  $\sim 50,000 \text{ cm}^{-1}$ . However, only consideration of 21 sextets in CASSCF and RASSI-SO step for Dy<sup>III</sup> has proven to be apt towards the determination of pertinent anisotropy [57]. For the Er<sup>III</sup> centre, both the CASSCF and RAS calculations are executed at the ground state with all of the 35 configurations, and the doublet states with all of the 112 configurations. In a similar manner, for other Tb<sup>III</sup>, Ho<sup>III</sup>, Nd<sup>III</sup>, Tm<sup>III</sup>, Yb<sup>III</sup> and Ce<sup>III</sup> lanthanide ions specific numbers of configurations were harnessed in the CASSCF step which was followed by admixing of certain configurations in RASSI-SO approach as shown in Table 1.

### 3 Ab Initio Calculations on Lanthanide Based Magnets

Before we delve into the detailed compilation of the ab initio calculations on several experimental crystallographic geometries, it is important to stress on the prerequisites and suitable geometries for SIM characteristics. In transition metal based SMMs, the barrier height for reorientation of magnetization is known to be correlated to the  $10Dq$  (for integer spin systems) with  $D$  representing axial zero-field splitting and  $S$  represents the ground state  $S$  value. In lanthanides, the anisotropy is correlated to the splitting of the lowest spin-orbit states by the crystal field terms. For example, in Dy<sup>III</sup> SIMs, the splitting of  ${}^6H_{15/2}$  by the crystal field determines the barrier height. This can be correlated to the familiar  $DS^2$  equation of transition metals SMMs, where crystal field that plays the role of  $D$  and  $S$  is represented by the corresponding  $|\pm M_J\rangle$  levels. Naturally, to have a higher barrier height, a strong crystal field in particular direction and a large  $|\pm M_J\rangle$  level as the ground state are desired. In lanthanides, stabilization of the highest  $|\pm M_J\rangle$  level and minimal mixing of the corresponding ground multiplet wave function with the excited states are crucial to obtain larger energy barrier for magnetization reversal ( $U_{\text{eff}}/U_{\text{cal}}$ ; in  $\text{cm}^{-1}$ ).

As the nature of the anisotropy in lanthanides is correlated to the nature of electron density at the ground  $|\pm M_J\rangle$  level, the lanthanide ions are qualitatively divided into oblate and prolate type ions [43]. Depending on the type of ions, preferably axial and equatorial crystal fields are required to stabilize maximum angular momentum projection in oblate (Ce<sup>III</sup>, Pr<sup>III</sup>, Nd<sup>III</sup>, Tb<sup>III</sup>, Dy<sup>III</sup> and Ho<sup>III</sup>) and prolate (Pm<sup>III</sup>, Sm<sup>III</sup>, Er<sup>III</sup>, Tm<sup>III</sup> and Yb<sup>III</sup>) ions, respectively. Meticulous



**Fig. 3** Schematic representation of the energy multiplets ( $\pm n$ ) pertinent to the crystal field components of the ground atomic  $J$  multiplet. The two energy states of specific doublet boast opposing values of magnetization such as  $|+M_J\rangle$  and  $| -M_J\rangle$ , respectively. There are four kinds of relaxation pathways as indicated by the respective texts representing each arrows and curved arrows. Ideally, relaxation should be promoted by the direct (green arrows) process subject to the quenching of other relaxation mechanisms

literature perusal accentuates that compounds with point groups  $C_{\infty v}$ ,  $D_{\infty h}$ ,  $S_8$ ,  $D_{4d}$ ,  $D_{5h}$  and  $D_{6d}$  are most suited to achieve improved SIM/SMM behaviour [17, 58, 59]. Computed crystal field parameter  $B_2^0$  (see Eq. 1) determines the nature of  $\text{Ln}^{\text{III}}$  centre and its corresponding sign (negative preferred) governs the magnitude of  $U_{\text{eff}}/U_{\text{cal}}$  values [49]. Complexes with suppressed QTM (as for  $\pm 1$  as indicated in Fig. 3) [24–26, 28, 60] within the ground multiplets of reverse magnetization (for Kramers ion and for non-Kramers ions lower value of tunnel splitting;  $\Delta_{\text{tun}}$ ) are favourable for SIM/SMMs. Besides, the ground multiplet should be strongly axial with oppressed transversal components ( $g_{zz} \gg g_{xx}/g_{yy}$ ), reasserting the need for higher ligand field symmetry around the central  $\text{Ln}^{\text{III}}$  metal ion to induce larger barrier. Thermally assisted QTM (TA-QTM; between  $\pm 2$  and  $\pm 3$  as represented by Fig. 3) within the higher energy levels of reversed magnetization also should ideally remain quenched. This should be accompanied by stronger spin–phonon relaxation pathways (Orbach, Raman and direct; between  $\pm 1$  and  $\pm 2$  or  $\pm 2$  and  $\pm 3$  states) via the higher energy multiplets to promote relaxation and procurement of larger barrier. Through ab initio calculations, one can attempt to estimate the transversal magnetic moment of the electronic transition matrix element corresponding to the various relaxation pathways, i.e. QTM, TA-QTM, Raman, Orbach, etc. [60, 61] One can also obtain the  $g_{xx}/g_{yy}/g_{zz}$  values pertaining to the energy levels to determine the axially/non-axiality of the complexes. Besides, the resultant crystal field parameters as acquired from the output of the ab initio calculations render determination of the preferred relaxation pathways and nature of the complexes. All aforesaid avenues

will be taken into account in the following pragmatic discussion on calculation of magnetic anisotropy in lanthanide complexes.

We would like to note here that often the ab initio calculations yield barrier heights which are larger than the ones estimated from experiments. To distinguish these two parameters, here we are using the terminology  $U_{\text{cal}}$  for theoretically estimated effective energy barrier and  $U_{\text{eff}}$  for the values obtained from experiments. While the accuracy of the chosen methodology can be improved (incorporation of dynamic correlation, expansion of reference space, larger basis sets, etc.), still the differences are often larger. This difference between  $U_{\text{cal}}$  and  $U_{\text{eff}}$  values can be attributed to one of the following reasons: (1) while probability for QTM can be computed, this relaxation pathway is not taken in consideration while estimating  $U_{\text{cal}}$  values; (2) intermolecular interactions often play a critical role in the relaxation mechanism. Since the dipolar coupling between the metal ions is rather strong in lanthanides, this can facilitate further relaxation and this effect is not captured in the calculated  $U_{\text{cal}}$  values; (3) hyperfine coupling of metal ions and the coordinated ligands facilitate tunnelling process and this effect is completely neglected in the  $U_{\text{cal}}$  estimates and (4) other relaxation processes such as spin–lattice, multi-phonon excitations, etc. are possible while this has not been accounted in the estimate of  $U_{\text{cal}}$  values.

### 3.1 *Illustrative Examples of Dy<sup>III</sup> Single-Ion Magnets Studied Using Ab Initio Calculations*

Since the invention of Ln<sup>III</sup>-based SIM/SMM, Dy<sup>III</sup> (<sup>6</sup>H<sub>15/2</sub>) complexes remain pervasive and this can be accrued onto their: (a) large total spin–orbit angular momentum quantum number,  $J/M_J$ , (b) stronger magnetic anisotropy compared to other lanthanides, (c) strongest magnetic moment and (d) odd number of 4f electrons assuring the presence of magnetic bistability and Kramers nature of ground multiplets. The Dy<sup>III</sup> ion is an oblate type ion with equatorially expanded electron density and axial crystal field is imperative to stabilize the highest angular momentum projection. Stabilization of the largest  $M_J$  level as the ground state and the crystal field splitting of the  $M_J$  levels are the most desired characteristics of lanthanide based SMMs. Here, we intend to cover various Dy<sup>III</sup> SIMs based on their ground state  $|\pm M_J\rangle$  levels and the computed crystal field splitting. This will help the research groups to choose the best ligand field suitable for Dy<sup>III</sup> ion to develop new generation SMMs. Thus, here we classify the Dy<sup>III</sup> SIMs/SMMs into six different categories: (1) category **A** deals with complexes having ground state other than  $\frac{15}{2}$  ( $|\pm M_J \neq \frac{15}{2}\rangle$ ), (2) category **B** deals with Dy<sup>III</sup> SMMs possessing  $|\pm M_J = \frac{15}{2}\rangle$  ground state but with significant QTM contributions leading to a field-induced SIM (f-SIM) behaviour, (3) category **C** deals with Dy<sup>III</sup> SIMs possessing  $|\pm M_J = \frac{15}{2}\rangle$  ground state with weak crystal field splitting (first excited state lying at within  $\sim 50 \text{ cm}^{-1}$ ) exhibiting zero-field SMM characteristics, (4) category **D** deals with

Dy<sup>III</sup> SIMs possessing  $|\pm M_J = \frac{15}{2}\rangle$  ground state with moderate crystal field splitting (first excited state lying within  $\sim 100\text{ cm}^{-1}$ ) exhibiting zero-field SMM characteristics, (5) category **E** deals with Dy<sup>III</sup> SIMs possessing  $|\pm M_J = \frac{15}{2}\rangle$  ground state with strong crystal field splitting (first excited state lying at  $> 100\text{ cm}^{-1}$ ) exhibiting zero-field SMM characteristics and (6) category **F** deals with Dy<sup>III</sup> SIMs with easy plane/hard axis anisotropy behaviour. To avoid repetition of molecular formulas and other details, we have listed all the molecular formula of all the complexes described in this chapter in a tabular form (see Table 2). Individual section deals with list of molecules belonging to their categories and this will be followed by non-Dy<sup>III</sup> SIMs. In the conclusions section, we have cross compared the geometries and the computed barrier height to assess and understand how different geometries and ligand donor strength yield superior SIMs for Dy<sup>III</sup>/Er<sup>III</sup> and Tb<sup>III</sup> ions. This will be followed by the future outlook describing the future directions that the ab initio calculations likely to focus in years to come.

### 3.1.1 Ab Initio Studies on Category A Complexes: Dy<sup>III</sup> Complexes Having Ground State Other than $|\pm M_J = \frac{15}{2}\rangle$ ( $|\pm M_J \neq \frac{15}{2}\rangle$ )

Although the largest  $|\pm M_J\rangle$  ( $\pm = \frac{15}{2}$  in this instance) stabilization is the most preferred ground state for the Dy<sup>III</sup> ions, there are a few examples in the literature where complexes with concomitant non- $|\pm M_J = \frac{15}{2}\rangle$  ground energy level exhibit SIMs/SMMs behaviour. CASSCF+RASSI-SO+SINGLE\_ANISO calculations performed on complex **1** (see Table 2 for molecular formula) suggest the ground state wave function to be  $|\pm M_J = \frac{13}{2}\rangle$  state [62]. This was further corroborated by the computed  $g_{zz}$  value of 16.9 corresponding to the  $|\pm M_J = \frac{13}{2}\rangle$  energy level in conjunction with prominent transverse anisotropy components, i.e.  $g_{xx} = 0.4$  and  $g_{yy} = 0.3$  (see Fig. 4a and Table 3). Magnetic measurements indicate an f-SIM behaviour for **1** with  $U_{\text{eff}}$  value estimated to be  $23.63\text{ cm}^{-1}$ . Ab initio calculations, however, yield the effective barrier ( $U_{\text{cal}}$ ) of  $84.7\text{ cm}^{-1}$  (with respect to first excited Kramers doublet; KD) [62]. Complex **1** has ten-coordinate Dy<sup>III</sup> centre with four nitrogen donors and six oxygen donor atoms (see Fig. 4a and Table 3), and the weaker coordination by the nitrogen donors leads to the stabilization of  $|\pm M_J = \frac{13}{2}\rangle$  state. From the combined experimental and theoretical studies, it becomes clear that for the Dy<sup>III</sup> ion, placing the crystal field above and below the XY plane along the computed  $g_{zz}$  axis likely yields the largest  $M_J$  value as ground state and improved SMM characteristics [62].

Complex  $[\text{Dy}(\text{COT})_2]^-$  (**2**) (see Fig. 4b and Tables 2 and 3) is a zero-field SIM and is found to possess  $|\pm M_J = \frac{9}{2}\rangle$  ground state with nominal contributions from other  $|\pm M_J\rangle$  projections. This was supported by pronounced QTM within ground multiplet as revealed by pertinent transversal magnetic moment of  $0.04\ \mu_{\text{B}}$ . Computed main  $g$ -anisotropic factors, i.e.  $g_{xx} = g_{yy} = 1.6 \times 10^{-1}$  and  $g_{zz} = 12.64$  favoured the nature of aforementioned ground state wave function (see Table 3). The non-axiality of first excited KD in combination with non-collinear anisotropy axis



**Table 2** Molecular formula of all the studied complexes

	Structure
<b>1</b>	[Dy (L)]; (L = <i>N,N'</i> -bis(amine-2-yl)methylene-1,8-diamino-3,6-dioxaoctane)
<b>2</b>	[Dy(COT) <sub>2</sub> ] <sup>-</sup> ; ({COT} = Cyclooctatetraene)
<b>3</b>	[DyPc <sub>2</sub> ] <sup>-</sup> ; (Pc = Phthalocyanine)
<b>4</b>	[Dy(FTA) <sub>3</sub> L]; {FTA = 2-furyl-trifluoro-acetate, L = (S,S)-2,2'-Bis(4-benzyl-2-oxazoline)}
<b>5</b>	[Dy(12C4)(H <sub>2</sub> O) <sub>5</sub> ] (ClO <sub>4</sub> ) <sub>3</sub> .H <sub>2</sub> O; ({12C4} = 12-crown-4)
<b>6</b>	[Dy(H <sub>2</sub> L)(NO <sub>3</sub> ) <sub>3</sub> ]; {H <sub>2</sub> L = <i>N,N',N''</i> -trimethyl- <i>N,N''</i> -bis(2-hydroxy-3-methoxy-5-methylbenzyl)}
<b>7</b>	[Dy(paaH*) <sub>2</sub> (NO <sub>3</sub> ) <sub>2</sub> (MeOH)][NO <sub>3</sub> ]; (paaH* = The neutral zwitterionic <i>N</i> -(2-Pyridyl)-ketoacetamide)
<b>8</b>	[Dy(H <sub>2</sub> DABPH) <sub>2</sub> ](NO <sub>3</sub> ) <sub>3</sub> ; (H <sub>2</sub> DABPH = 2,6-diacetylpyridinebis(benzoic acid hydrazone))
<b>9</b>	[Dy(H <sub>2</sub> DABPH)(HDABPH)](NO <sub>3</sub> ) <sub>2</sub>
<b>10</b>	[Na{Dy(DOTA)(H <sub>2</sub> O)}]; (DOTA = 1,4,7,10-tetraazacyclo-dodecane-1,4,7,10-tetraaceticacid)
<b>11</b>	[Dy(9Accm) <sub>2</sub> -(NO <sub>3</sub> )(dmf) <sub>2</sub> ]; (Accm = 1,7-di-9-anthracene-1,6-heptadiene-3,5-dione)
<b>12</b>	[Dy(NTA) <sub>3</sub> L]; (L = (1R,2R)-1,2-diphenylethane-1,2-diamine, NTA = Nitriiotriacetic acid)
<b>13</b>	[K(DME) <sub>2</sub> ][Dy(tmtaa) <sub>2</sub> ]; (H <sub>2</sub> tmtaa = acrocyclic 6,8,15,17-tetramethyl-dibenzotetraaza [14]annulene)
<b>14</b>	[K(DME)(18-crown-6)][Dy(tmtaa) <sub>2</sub> ]
<b>15</b>	[Dy(TTA) <sub>3</sub> (L <sub>3</sub> )]; (TTA = 2-thenoyltrifluoroacetate; L <sub>3</sub> = 4,5-pinenebipyridine)
<b>16</b>	[Dy(H <sub>2</sub> BPz <sup>Me<sub>2</sub></sup> ) <sub>3</sub> ]
<b>17</b>	[Zn <sub>3</sub> Dy(L <sup>Pr</sup> )(NO <sub>3</sub> ) <sub>3</sub> (MeOH) <sub>3</sub> ].4H <sub>2</sub> O; specific macrocycle (L <sup>Pr</sup> ) <sup>6-</sup> was prepared by reaction between 1,4-diformyl-2,3-dihydroxybenzene and 1,3-diaminopropane at room temperature in methanol
<b>18</b>	[R,R-ZnLDy(μ-OAc)(NO <sub>3</sub> ) <sub>2</sub> ]; (H <sub>2</sub> L = phenol,2,2'[2,2-diphenyl-1,2-ethanediy]bis[(E)-nitrilomethylidyne]-bis(6-methoxy))
<b>18a</b>	[S,S-ZnLDy(μ-OAc)(NO <sub>3</sub> ) <sub>2</sub> ]; (H <sub>2</sub> L = phenol,2,2'[2,2-diphenyl-1,2-ethanediy]bis[(E)-nitrilomethylidyne]-bis(6-methoxy))
<b>19</b>	[DyCo <sub>2</sub> (hmb) <sub>2</sub> (CH <sub>3</sub> O) <sub>2</sub> (OAc) <sub>3</sub> ]; (H <sub>2</sub> hmb = 2-hydroxy-3-methoxybenzylidene benzohydrazide)
<b>20</b>	[ZnDy(NO <sub>3</sub> ) <sub>2</sub> (L) <sub>2</sub> (CH <sub>3</sub> CO <sub>2</sub> )]; (HL = 2-methoxy-6-[(E)-phenyliminomethyl]phenol)
<b>20a</b>	[Dy(HL) <sub>2</sub> (NO <sub>3</sub> ) <sub>3</sub> ]; (HL = 2-methoxy-6-[(E)-phenyliminomethyl]phenol)
<b>21</b>	[Dy(H <sub>3</sub> L) <sub>2</sub> ](NO <sub>3</sub> ); (H <sub>4</sub> L = 2,2'-{[(2-aminoethyl)imino]bis[2,1-ethanediy]-nitriloethylidyne}bis-2-hydroxy-benzoic acid)
<b>22</b>	[Dy(hfac) <sub>3</sub> (L)] .0.5C <sub>6</sub> H <sub>14</sub> ; (L = 3-(2-pyridyl)-4-aza[6]-helicene(racemic))
<b>23</b>	[Dy(15C5)(H <sub>2</sub> O) <sub>4</sub> ](ClO <sub>4</sub> ) <sub>3</sub> . (15C5); ({15C5} = 15-crown-5)
<b>24</b>	[Dy(COT'') <sub>2</sub> Li(THF)(DME)]; {(COT'') = 1,4-bis(trimethylsilyl)cyclooctatetraenyl dianion}
<b>25</b>	[Dy(COT'') <sub>2</sub> ] <sup>-</sup>
<b>26</b>	[Dy(dpq)(acac) <sub>3</sub> ]
<b>27</b>	[Dy(dppz)(acac) <sub>3</sub> ]
<b>28</b>	[Dy(acac) <sub>3</sub> (H <sub>2</sub> O) <sub>2</sub> ]
<b>29a</b>	[Dy(phen)(acac) <sub>3</sub> ]

(continued)

Table 2 (continued)

	Structure
29b	[Dy(TTA) <sub>3</sub> (2,2'-bipyridine)]; (TTA = 4,4,4-trifluoro-1-(2-thienyl)-1,3-butanedionate)
30	[Dy(TTA) <sub>3</sub> (1,10-phenanthroline)];
31a	[Dy(hfac) <sub>3</sub> (L)]·C <sub>6</sub> H <sub>14</sub> ; {hfac <sup>-</sup> = 1,1,1,5,5,5-hexafluoroacetylacetonate}
31b	[Dy(tta) <sub>3</sub> (L)]·C <sub>6</sub> H <sub>14</sub> ; {tta <sup>-</sup> = 2-thenoyltrifluoroacetate}
32	[DyL]; (L = <i>N,N'</i> -bis(imine-2-yl)methylene-1,8-diamino-3,6-dioxaoctane)
33	[Dy(hfac) <sub>3</sub> (L)]; (L = 3-(2-pyridyl)-4-aza[6]-helicene (enantiomerically pure))
34	[Dy(tta) <sub>3</sub> (L)]; (tta <sup>-</sup> = 2-thenoyltrifluoroacetate, L = 2-{1-methylpyridyl-4,5-[4,5-bis(propylthio)tetrathiafulvalenyl]-1H-benzimidazol-2-yl}pyridine)
35	[ZnCl(μ-L)Dy(μ-L)ClZn]; (H <sub>2</sub> L = <i>N,N'</i> -dimethyl- <i>N,N'</i> -bis(2-hydroxy-3-formyl-5-bromobenzy)ethylenediamine)
36	[{LZn(H <sub>2</sub> O)} <sub>2</sub> Dy(H <sub>2</sub> O)] <sup>3+</sup> ; (L <sup>2-</sup> = di-deprotonated form of the N <sub>2</sub> O <sub>2</sub> compartmental <i>N,N'</i> -2,2-dimethylpropylenedi(3-methoxysalicylideneiminato))
37	[Dy(paaH*) <sub>2</sub> (H <sub>2</sub> O) <sub>4</sub> ][Cl] <sub>3</sub> ; (paaH* = <i>N</i> -(2-Pyridyl)-ketoacetamide)
38	[DyLCl <sub>2</sub> (THF) <sub>2</sub> (DyNCN)]; (L = 2,6-(2,6-C <sub>6</sub> H <sub>3</sub> R <sub>2</sub> N=CH) <sub>2</sub> -C <sub>6</sub> H <sub>3</sub> )
39	[Ln(BIPM <sup>TM</sup> ) <sub>2</sub> ][K(18C6)(THF) <sub>2</sub> ]; ({18C6} = 18-crown-6)
40	[(Zn <sub>2</sub> (L <sup>1</sup> ) <sub>2</sub> DyCl <sub>3</sub> ); (H <sub>2</sub> L <sup>1</sup> = <i>N,N'</i> -bis(3-methoxysalicylidene)phenylene-1,2-diamine)
41	[Zn <sub>2</sub> (L <sup>1</sup> ) <sub>2</sub> Dy(MeOH)Br <sub>3</sub> ]; (H <sub>2</sub> L <sup>1</sup> = <i>N,N'</i> -bis(3-methoxysalicylidene)phenylene-1,2-diamine)
42	[Zn <sub>2</sub> (L <sup>1</sup> ) <sub>2</sub> Dy(H <sub>2</sub> O)Br <sub>2</sub> ]; (H <sub>2</sub> L <sup>1</sup> = <i>N,N'</i> -bis(3-methoxysalicylidene)phenylene-1,2-diamine)
43	[Zn <sub>2</sub> (L <sup>2</sup> ) <sub>2</sub> DyCl <sub>3</sub> ]; (H <sub>2</sub> L <sup>2</sup> = <i>N,N'</i> -bis(3-methoxysalicylidene)-1,2-diaminocyclohexane:)
44	Li(DME) <sub>3</sub> [Dy(DAD) <sub>2</sub> ]; (DAD = ene-diamido[2,6-iPr <sub>2</sub> C <sub>6</sub> H <sub>3</sub> N-CH=CH-NC <sub>6</sub> H <sub>3</sub> iPr <sub>2</sub> -2,6] <sup>2-</sup> )
45	[Dy <sup>III</sup> (NHPhIPr <sub>2</sub> ) <sub>3</sub> (THF) <sub>2</sub> ]
46	[Dy(Bc <sup>Me</sup> ) <sub>3</sub> ]; (Bc <sup>Me-</sup> = dihydrobis(methylimidazolyl)borate)
47	[Dy(LH) <sub>3</sub> ]; (LH <sup>-</sup> = 2-hydroxy- <i>N'</i> -[(E)-(2-hydroxy-3-methoxyphenyl) methylidene] benzohydrazide)
48	[{LZn(Br)} <sub>2</sub> Dy(H <sub>2</sub> O)] <sup>+</sup> ; (L <sup>2-</sup> = di-deprotonated form of the N <sub>2</sub> O <sub>2</sub> compartmental <i>N,N'</i> -2,2-dimethylpropylenedi(3-methoxysalicylideneiminato))
49	[{LZn(Cl)} <sub>2</sub> Dy(H <sub>2</sub> O)] <sup>+</sup> ; (L <sup>2-</sup> = di-deprotonated form of the N <sub>2</sub> O <sub>2</sub> compartmental <i>N,N'</i> -2,2-dimethylpropylenedi(3-methoxysalicylideneiminato))
50	[LZnBrDy(ovan)(NO <sub>3</sub> )(H <sub>2</sub> O)]; (L <sup>2-</sup> = di-deprotonated form of the N <sub>2</sub> O <sub>2</sub> compartmental <i>N,N'</i> -2,2-dimethylpropylenedi(3-methoxysalicylideneiminato))
51	[LZnClDy(thd) <sub>2</sub> ]; (thd = 2,2,6,6-tetramethyl-3,5-heptanedionato ligand)
52	[(LZnBr) <sub>2</sub> Dy (MeOH) <sub>2</sub> ] <sup>+</sup> ; L = dideprotonated forms of the 2-{(E)-[(3-[(2E,3E)-3-(hydroxyimino)-butan-2-ylidene]amino)-2,2-dimethylpropyl]imino]methyl}-6-methoxyphenol
53	[(Cp <sup>III</sup> ) <sub>2</sub> Dy][B(C <sub>6</sub> F <sub>5</sub> ) <sub>4</sub> ]; (Cp <sup>III</sup> = 1,2,4-tri(tertbutyl)cyclopentadienide)
54	[Dy(Cp <sup>III</sup> ) <sub>2</sub> ][B(C <sub>6</sub> F <sub>5</sub> ) <sub>4</sub> ]; (Cp <sup>III</sup> = {C <sub>5</sub> H <sub>2</sub> <sup>t</sup> Bu <sub>3</sub> -1,2,4} and <sup>t</sup> Bu = C(CH <sub>3</sub> ) <sub>3</sub> )
55	[Dy(tta) <sub>3</sub> (L)] (polymorph-t); (L = 4-[6-(1,3-benzothiazol-2-yl)pyridin-3-yl]-4' <sup>5'</sup> -bis(methylthio)tetrathiafulvene)
55'	[Dy(tta) <sub>3</sub> (L)] (polymorph-m); (L = 4-[6-(1,3-benzothiazol-2-yl)pyridin-3-yl]-4' <sup>5'</sup> -bis(methylthio)tetrathiafulvene)
56	[Dy(Cy <sub>3</sub> PO) <sub>2</sub> (H <sub>2</sub> O) <sub>5</sub> Cl] <sub>3</sub> ; (Cy <sub>3</sub> PO = tricyclohexyl phosphine oxide)
57	[Dy(Cy <sub>3</sub> PO) <sub>2</sub> (H <sub>2</sub> O) <sub>5</sub> Br] <sub>3</sub> ; (Cy <sub>3</sub> PO = tricyclohexyl phosphine oxide)
58	[Dy(bbpen)Cl]; (H <sub>2</sub> bbpen = <i>N,N'</i> -bis(2-hydroxybenzyl)- <i>N,N'</i> -bis(2-methylpyridyl) ethylenediamine)

(continued)

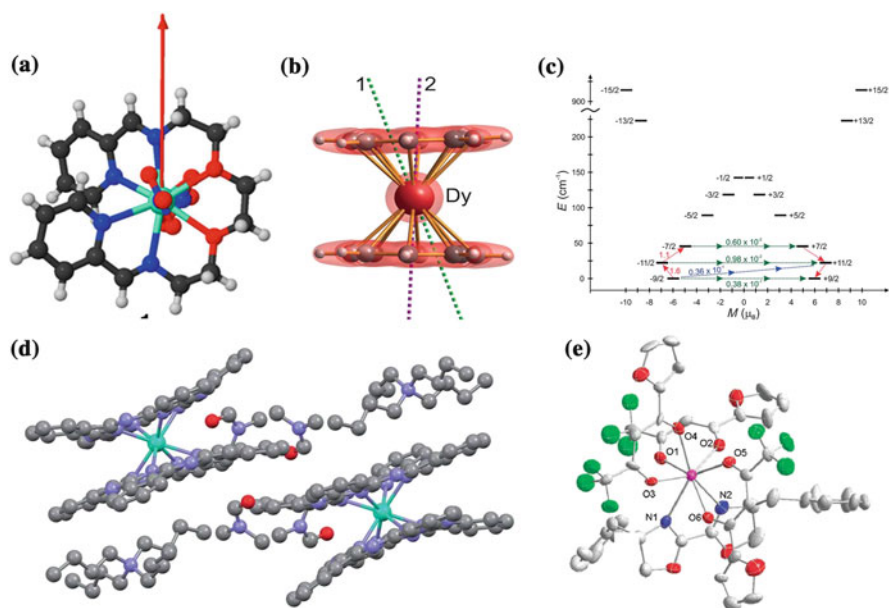
**Table 2** (continued)

	Structure
59	[Dy(bbpen)Br]; (H <sub>2</sub> bbpen = <i>N,N'</i> -bis(2-hydroxybenzyl)- <i>N,N'</i> -bis(2-methylpyridyl) ethylenediamine)
60	[Zn <sub>2</sub> DyL <sub>2</sub> (MeOH)] <sup>+</sup> ; (L = 2,2',2''-((nitritotris(ethane-2,1-diy))tris(azanediy))tris(methylene)tris-(4-bromophenol))
61	[Dy(O <sup>t</sup> Bu) <sub>2</sub> (py) <sub>5</sub> ][BPh <sub>4</sub> ]
62	[L <sub>2</sub> Dy(H <sub>2</sub> O) <sub>5</sub> ][I <sub>3</sub> ]; (L = <sup>t</sup> BuPO(NH <sup>i</sup> Pr) <sub>2</sub> )
63	[Dy(CyPh <sub>2</sub> PO) <sub>2</sub> (H <sub>2</sub> O) <sub>5</sub> ][Br <sub>3</sub> ]
79	[Er(thd) <sub>3</sub> (bath)]; (bath = bathophenanthroline)
80	[Er(COT) <sub>2</sub> ] <sup>-</sup> ; (COT = cyclooctatetraenyl dianion)
81	[Er(COT'') <sub>2</sub> ] <sup>-</sup> ; (COT'' = 1,4-bis-(trimethylsilyl) cyclooctatetraenyl dianion)
82	[Er(COT)Cp*] <sup>-</sup> ; (Cp* = pentamethylcyclopentadienide and COT = cyclooctatetraenyl dianion)
83	[Er(N(SiMe <sub>3</sub> ) <sub>2</sub> ) <sub>3</sub> ]
84	[Er(NHPhiPr) <sub>2</sub> ](THF) <sub>2</sub>
85	[Er{N(SiMe <sub>3</sub> ) <sub>2</sub> } <sub>3</sub> Cl].2THF
85a	[Er{N(SiMe <sub>3</sub> ) <sub>2</sub> } <sub>3</sub> Cl] <sup>-</sup>
86	[Er(HL) <sub>2</sub> (NO <sub>3</sub> ) <sub>3</sub> ]; (HL = 2-methoxy-6-[(E)-phenyliminomethyl]phenol)
87	(NBu <sub>4</sub> ) <sup>+</sup> [ErPc <sub>2</sub> ] <sup>-</sup> .2DMF
88	[Er(COT) <sub>2</sub> ] <sup>-</sup>
89	[Er(trensals)]; (H <sub>3</sub> trensals = 2,2',2''-Tris-(salicylideneimino)triethylamine)
90	[Er(3-I,5-Me-trensals)]
91	[Er(5-Cl-trensals)]
92	Na[ErDOTA(H <sub>2</sub> O)].4H <sub>2</sub> O
93	[Yb(H <sub>3</sub> L) <sub>2</sub> Cl] <sub>3</sub> ; (H <sub>3</sub> L = tris(((2-hydroxy-3-methoxybenzyl)amino)ethyl)-amine)
94	Na[Yb(DOTA)(H <sub>2</sub> O)].4H <sub>2</sub> O
95	Na[Tb(DOTA)(H <sub>2</sub> O)].4H <sub>2</sub> O
96	Na[Ho(DOTA)(H <sub>2</sub> O)].4H <sub>2</sub> O
97	Na[Tm(DOTA)(H <sub>2</sub> O)].4H <sub>2</sub> O
98	[Yb(DTMA)OH <sub>2</sub> ] <sup>3+</sup>
99	[Yb(DTMA).F] <sup>2+</sup> ; Yb-F = 1.97 Å
100	[Yb(DTMA)F] <sup>2+</sup> ; Yb-F = 2.38 Å
101	[Ce{Zn(L)} <sub>2</sub> (MeOH)]BPh <sub>4</sub> ; (L = N,N,O,O-tetradentate Schiff base ligand)
102	[Li(dme) <sub>3</sub> ][Ce(COT'') <sub>2</sub> ]; (DME = dimethoxyethane, COT'' = 1,4-bis(trimethylsilyl) cyclooctatetraenyl dianion)
103	[CeCd <sub>3</sub> (Hquinha) <sub>3</sub> (n-Bu <sub>3</sub> PO) <sub>2</sub> I] <sub>3</sub> ; quinaldichydroxamic acid (H <sub>2</sub> quinha)
104	[NdCd <sub>3</sub> (Hquinha) <sub>3</sub> (n-Bu <sub>3</sub> PO) <sub>2</sub> I] <sub>3</sub> ; quinaldichydroxamic acid (H <sub>2</sub> quinha)
105	[L <sub>2</sub> Nd(H <sub>2</sub> O) <sub>5</sub> ][I <sub>3</sub> ]; (L = <sup>t</sup> BuPO(NH <sup>i</sup> Pr) <sub>2</sub> )
106	(NBu <sub>4</sub> ) <sup>+</sup> [HoPc <sub>2</sub> ] <sup>-</sup> .2dmf
107	[Ho(BcMe) <sub>3</sub> ]; ([BcMe] <sup>-</sup> = dihydrobis(methylimidazolyl)borate)
108	[Ho(BpMe) <sub>3</sub> ]; ([BpMe] <sup>-</sup> = dihydrobis(methylpyrazolyl)borate)
109	[Ho(CyPh <sub>2</sub> PO) <sub>2</sub> (H <sub>2</sub> O) <sub>5</sub> I] <sub>3</sub> ; (Cy = cyclohexyl)
110	[(Tp)Tm(COT)]; (Tp = hydrotris(1-pyrazolyl)borate; COT = cyclooctatetraenide)
111	[(Tp*)Tm(COT)]; (Tp* = hydrotris(3,5-dimethyl-1-pyrazolyl)borate)
112	[Pc <sub>2</sub> Ln] <sup>-</sup> TBA <sup>+</sup> ; (Pc = dianion of phthalocyanine; TBA <sup>+</sup> = N(C <sub>4</sub> H <sub>9</sub> ) <sub>4</sub> <sup>+</sup> )

(continued)

**Table 2** (continued)

	Structure
<b>113</b>	[Tb(BcMe) <sub>3</sub> ]
<b>114</b>	[Tb(BpMe) <sub>3</sub> ]
<b>115</b>	Li(DME) <sub>3</sub> [Tb(DAD) <sub>2</sub> ]; (DAD = ene-diamido[2,6- <i>i</i> Pr <sub>2</sub> C <sub>6</sub> H <sub>3</sub> N-CH=CH-NC <sub>6</sub> H <sub>3</sub> <i>i</i> Pr <sub>2</sub> -2,6] <sup>2-</sup> )
<b>116</b>	[(Pc)Tb]{Pc[O(C <sub>6</sub> H <sub>4</sub> )- <i>p</i> - <i>t</i> Bu] <sub>8</sub> }
<b>117</b>	[Tb{Pc[OC <sub>11</sub> H <sub>21</sub> ] <sub>4</sub> }] <sub>2</sub>
<b>118</b>	[Tb{Pc[N(C <sub>4</sub> H <sub>9</sub> ) <sub>2</sub> ] <sub>8</sub> }] <sub>2</sub>
<b>119</b>	[(Pc)Tb{Pc[N(C <sub>4</sub> H <sub>9</sub> ) <sub>2</sub> ] <sub>8</sub> }] ; {Pc[N(C <sub>4</sub> H <sub>9</sub> ) <sub>2</sub> ] <sub>8</sub> } = 2,3,9,10,16,17,23,24-octakis(dibutylamino)phthalocyaninate, Pc = phthalocyaninate }



**Fig. 4** (a, b, d, e) Molecular structures of complexes 1–4, respectively. Arrows in complex 1 and 2 (green colour) show the orientation of the principal magnetization axis. In complex 2, violet colour arrow shows direction of KD2  $g_{zz}$  axis. (c) Ab initio computed relaxation mechanism in complex 2. Colour code: central atom = Dy, red = O, dark blue/light blue = N, black/dark-brown/light-brown/white-ellipsoid shape = C, green = F and small-spherical white = H atoms. Reprinted with permission from Campbell et al. [62] Copyright@2014 American Chemical Society. Reprinted from Ungur et al. [13] with permission from John Wiley and Sons. Reprinted from Marx et al. [54], Li et al. [63] with permission from the Royal Society of Chemistry

**Table 3** List of complexes {from category A} with pertinent experimental energy barrier ( $U_{\text{eff}}$ , in  $\text{cm}^{-1}$ ), ab initio computed energy barrier ( $U_{\text{cal}}$ , in  $\text{cm}^{-1}$ ), main magnetic g factors, ground state  $M_J$  levels (major contributing) and crystallographic structural information

	$U_{\text{eff}}$	$U_{\text{cal}}$	$g_{xx}-g_{yy}$	$g_{zz}$	KD1	Type of coordinated atoms	Structure	Ref.
<b>1</b>	23.6	84.7	0.3–0.4	16.9	$\pm 13/2$	4 N, 6 O	Distorted bicapped square antiprismatic	[62]
<b>2</b>	7.6	22.3	0.06–0.14	12.64	$\pm 9/2$	( $\eta^8$ -fashion)-All C	–	[13]
<b>3</b>	35	52.3	$\sim 10^{-4}$	17.36	$\pm 13/2$	8 N	–	[54]
<b>4</b>	37.8	67.2	0.16–0.33	19.24	$\pm 11/2$	6 O, 2 N	Distorted bicapped triangular prism	[63]

alignment renders  $U_{\text{cal}}$  value of  $22.3 \text{ cm}^{-1}$  against experimental  $U_{\text{eff}}$  estimate of  $7.6 \text{ cm}^{-1}$ .

Complex **2** is composed of two  $\{\text{COT}\}^{2-}$  ligands which are bound to central  $\text{Dy}^{\text{III}}$  ion in an  $\eta^8$  fashion with one equivalent of  $[\text{K}(18\text{-crown-6})]$  counter ion. Transverse contribution to ligand field from  $\pi$  cloud of COT causes stabilization of  $|\pm M_J = \frac{9}{2}\rangle$  as ground state with partial mixing from other states. The planar COT ligands present in complex **2** exhibit strong equatorial interaction and weak axial interaction. This leads to stabilization of intermediate  $|\pm M_J\rangle$  as the ground state. This is clearly reflected in the computed CF parameters where contrary to the expected negative sign, positive crystal field parameters  $B_2^0$  and  $B_4^0$  (3.51 and 0.02, respectively) are found and this enacted as genesis for the non- $|\pm M_J = \frac{15}{2}\rangle$  ground energy level in **2** (see Fig. 4c for computed magnetization relaxation mechanism) [13].

Ab initio calculations on complex **3** (see Fig. 4d and Tables 2 and 3) led to theoretical barrier estimate of  $52.3 \text{ cm}^{-1}$  against  $U_{\text{eff}}$  value of  $35 \text{ cm}^{-1}$  (see Table 3). However, the wave function of the ground KD turns out to be:  $|\pm \frac{13}{2}\rangle$ :  $0.93 |\pm \frac{13}{2}\rangle + 0.31 |\pm \frac{15}{2}\rangle + 0.21 |\pm \frac{11}{2}\rangle$  with concomitant ground state crystal field parameter  $B_2^0$  and  $g_{zz}$  as  $-2.47$  and  $\sim 17$ , respectively, for **3** and these CF parameters are in agreement with the experimental results obtained from far-IR spectra recorded at low temperature [54]. As phthalocyanine ligands are capping the  $\text{Dy}^{\text{III}}$  ion above and below and these are not purely axial ligand that  $\text{Dy}^{\text{III}}$  enjoys, this leads to the stabilization of  $|\pm \frac{13}{2}\rangle$  as the ground state with strong mixing from the excited states. The difference in the  $U_{\text{eff}}$  and  $U_{\text{cal}}$  values is attributed to the difference in the structure employed; particularly, ab initio calculations are often performed on X-ray structure collected at 100 K while the precise spectroscopic measurements are performed at 5 K. The structural distortions, however small, are likely to influence the computed parameters and here in this example, variation of Dy-N distance by  $0.05 \text{ \AA}$  found to rationalize the difference observed. This point is particularly important as often, ab initio calculations yield barrier heights which are larger than the ones estimated from experiments. While the accuracy of the theoretical level can be improved (using dynamic correlation and expanding the reference space), often

the difference is attributed to the difference in the structure and/or intermolecular effects that are not fully captured in the calculations.

For complex **4** (see Fig. 4e and Tables 2 and 3), ab initio calculations suggest a ground state of  $|\pm M_J = \frac{11}{2}\rangle$  and this has been substantiated by the estimated  $g$ -factors:  $g_{xx} = 0.16$ ,  $g_{yy} = 0.33$  and  $g_{zz} = 19.24$ . Furthermore, **4** displayed zero-field SIM characteristics with  $U_{\text{eff}}$  value of  $37.8 \text{ cm}^{-1}$  with respect to the  $U_{\text{cal}}$  of  $67.2 \text{ cm}^{-1}$  [47, 63]. Here, the geometry around  $\text{Dy}^{\text{III}}$  ion is distorted bicapped triangular prism with  $\{\text{DyO}_6\text{N}_2\}$  core. Here, the average Dy–O distances are estimated to be  $2.323 \text{ \AA}$  while the two Dy–N bonds are at  $\sim 2.580 \text{ \AA}$  suggesting strong oxygen donations from one side. Strong oxygen donations from one side and moderate nitrogen donations from the other side lead to the stabilization of  $|\pm M_J = \frac{11}{2}\rangle$  as the ground state with concomitant mixing with other states.

### 3.1.2 Ab Initio Studies on Category B Complexes: Field-Induced $\text{Dy}^{\text{III}}$ Single Molecule Magnets Possessing $|\pm M_J = \frac{15}{2}\rangle$ Ground State

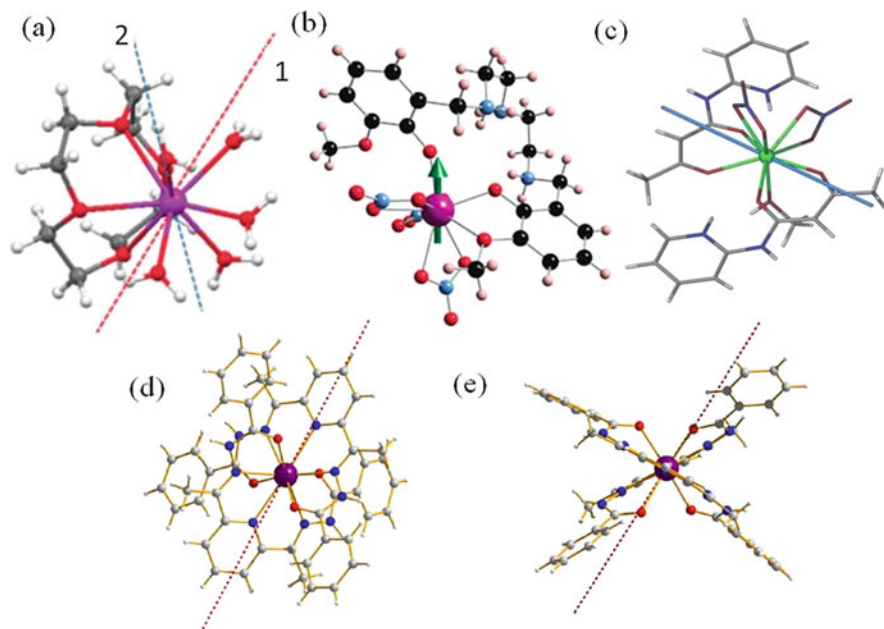
There are several  $\text{Dy}^{\text{III}}$  SIMs/SMMs reported to possess the desired  $|\pm M_J = \frac{15}{2}\rangle$  ground state. However, the lack of strong axial interactions and/or moderate equatorial interactions leads to the absence of Ising type anisotropy. In those cases, mixing of the  $|\pm M_J = \frac{15}{2}\rangle$  with the excited states is expected to yield strong QTM behaviour at the ground state. Prominent QTM within the ground KD induces fast relaxation and deters the presence of SIM/SMM behaviour in zero field. Application of static  $dc$  field quenches the QTM propensity and promotes further relaxation via higher energy excited sublevels instilling SIM behaviour. In this section, we intend to compile such literature reports which display SIM behaviour only in the presence of certain applied  $dc$  field but possess the largest  $M_J$  ground state.

The first example in this group is complex **5** (see Tables 2 and 4). Complex **5** has been characterized to possess SIM behaviour in the presence of  $1,500 \text{ Oe}$  magnetic field. Calculations postulate  $U_{\text{cal}}$  value of  $33 \text{ cm}^{-1}$  against the spectroscopically (Luminescence) dictated first excited energy level located at  $30 \pm 3 \text{ cm}^{-1}$  (see Table 4). The pronounced QTM contribution within the ground state is evident from the large calculated transverse anisotropy ( $g_{xx} = 0.90$ ,  $g_{yy} = 1.16$  and  $g_{zz} = 17.82$ ) leading to faster relaxation in zero-field conditions. Application of field instigates SIM behaviour by quenching the QTM effects [64]. Complex **5** possesses  $\text{Dy}^{\text{III}}$  ion in nine-coordinated environment with five oxygen atoms from crown ether binding weakly above the  $\text{Dy}^{\text{III}}$  ion and four oxygen atoms binding strongly below, leading to pseudocapped square antiprism geometry (see Fig. 5a and Table 4). This is likely to yield strong mixing of states and the evident transverse anisotropy.

Complex **6** also has a  $\{\text{DyO}_9\}$  core with prismatic geometry (see Fig. 5b and Tables 2 and 4) and exhibits f-SIM (using  $1,000 \text{ Oe}$ ) behaviour with  $U_{\text{eff}}$  value of  $6.1$  and  $22.2 \text{ cm}^{-1}$ . Calculations reveal substantial transverse anisotropy in the ground

**Table 4** List of complexes {from category B} with pertinent experimental energy barrier ( $U_{\text{eff}}$ , in  $\text{cm}^{-1}$ ), ab initio computed energy barrier ( $U_{\text{cal}}$ , in  $\text{cm}^{-1}$ ), main magnetic g factors and crystallographic structural information

	$U_{\text{eff}}$	$U_{\text{cal}}$	$g_{xx}-g_{yy}$	$g_{zz}$	Type of coordinated atoms	Structure	Ref.
<b>5</b>	$30\pm 3$	33	0.90–1.16	17.82	9 O	Pseudocapped square antiprismatic	[64]
<b>6</b>	6.1, 22.2	73	0.26–0.81	18.81	9 O	Prismatic	[65]
<b>7</b>	44	111.8	0.01–0.02	19.61	9 O	Between spherical capped square antiprism and muffin	[66]
<b>8</b>	22.5	44.6	0.17–0.34	17.19	6 N, 4 O	Distorted bicapped square antiprismatic	[56]
<b>9</b>	<13.2	44.1	0.25–0.65	18.78	6 N, 4 O	Distorted bicapped square antiprismatic	[56]
<b>10</b>	53	64	0.2–0.9	18.6	4 O, 4 N	Square antiprismatic	[67]
<b>11</b>	16	188.9	0.03–0.05	19.48	8 O	Triangular dodecahedron	[47]
<b>12</b>	21.1	93.0	0.02–0.07	19.26	6 O, 2 N	Distorted bicapped triangular prism	[47]
<b>13</b>	19.7	77.3	0.63–0.66	16.09	8 N	Distorted cube	[47]
<b>14</b>	24.0	75.3	0.49–0.57	16.85	8 N	Distorted cube	[47]
<b>15</b>	28.5	109.1	0.01–0.03	19.69	6 O, 2 N	Distorted square antiprismatic	[47]
<b>16</b>	17	58.7	0.02–0.03	19.69	6 N	Trigonal prismatic	[47]
<b>17</b>	17.9	41.7	0.10–0.25	18.15	9 O	–	[68]
<b>18</b>	13.5, 36	46/43	0.07–0.18	19.49/ 19.56	7 O, 2 N	Intermediate between spherical capped square antiprism and spherical tricapped trigonal prism	[69]
<b>18a</b>	14.2, 35.9	64/43	0.03–0.09	19.58/ 19.57	7 O, 2 N	Intermediate between spherical capped square antiprism and spherical tricapped trigonal prism	[69]
<b>19</b>	3.8, 4.4, 12.3	52.3	0.62–2.38	17.21	9 O	Monocapped square antiprismatic	[70]
<b>20</b>	83	91	0.02–0.04	18.82	9 O	Distorted tricapped trigonal prismatic	[71]
<b>20a</b>	16	76, 46	0.02–0.04	19.44	10 O	Distorted bicapped square antiprismatic	[71]
<b>21</b>	42.0	89.8, 106.2	0.02–0.04	18.77	8 O	Distorted square antiprismatic	[72]
<b>22</b>	11.8, 41	104.5	0.02–0.04	19.78	2 N, 6 O	Triangular dodecahedron	[73]



**Fig. 5** (a–e) Molecular structures of complexes **5–9**, respectively, exhibiting computed  $g_{zz}$  axis. Arrows in complexes show the orientation of the principal magnetization axis. In complex **5**, second arrow shows the direction of KD2  $g_{zz}$  axis. Colour code: central atom = Dy, red = O, dark blue/light blue = N, black/dark-brown/light-brown = C and white = H atoms. Reprinted from Gavey et al. [64], Ruiz et al. [65], Chilton et al. [66], Batchelor et al. [56] with permission from the Royal Society of Chemistry

KD ( $g_{xx} = 0.26$ ,  $g_{yy} = 0.81$  and  $g_{zz} = 18.81$ ) explaining the experimental observation with the estimated  $U_{\text{cal}}$  value of  $73 \text{ cm}^{-1}$  (see Table 4). The ground KD (KD1) principal  $g_{zz}$  axis of complex **6** is in close proximity to Dy–O<sub>phenolate</sub> and normal to Dy–O<sub>methoxy</sub> bond (see inset Fig. 5b) [65]. Strong transverse anisotropy dictates strong QTM at the ground state and hence an optimum field of 1,000 Oe was required to quench the observed QTM effects.

Complex **7** is also having {DyO<sub>9</sub>} core with geometry that lies between a spherical capped square antiprism and a muffin shape (see Fig. 5c and Tables 2 and 4). Despite strong axiality ( $g_{zz} = 19.61$ ,  $g_{xx} = 0.01$  and  $g_{yy} = 0.02$ ) in ground KD, complex **7** shows f-SIM (2,000 Oe) characteristics with  $U_{\text{cal}}$  and  $U_{\text{eff}}$  values estimated to be  $111.8 \text{ cm}^{-1}$  and  $44 \text{ cm}^{-1}$ , respectively [66]. The  $g_{zz}$  axis is found to lie between the  $\beta$ -diketonate ligands suggesting how coordinated nitrates play a role in determining the magnetic behaviour [66]. Presence of nitrate ions in **7** is discussed to govern the barrier for magnetization reversal.

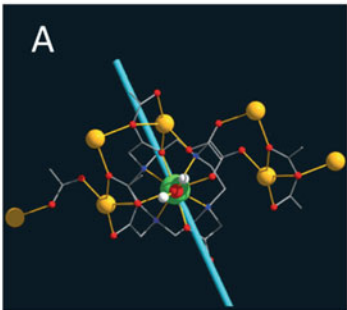
Both complexes **8** and **9** have Dy<sup>III</sup> ion in ten-coordinated distorted bicapped square antiprismatic geometry with {DyO<sub>4</sub>N<sub>6</sub>} core (see Fig. 5d, e and Tables 2 and 4). Both complexes are having almost identical structures except the deprotonated amino nitrogen of one of the ligands in complex **9**. Calculations on complexes **8** and **9** show  $U_{\text{cal}}/U_{\text{eff}}$  values of  $44.6/22.5 \text{ cm}^{-1}$  and  $44.1/13.2 \text{ cm}^{-1}$ , respectively



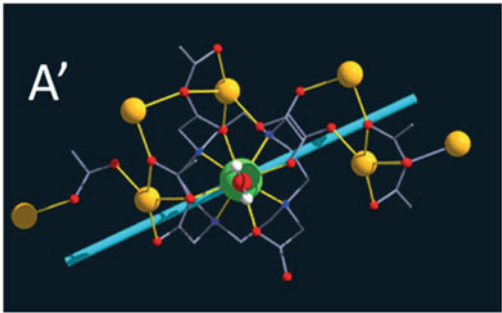
(a)

Angle of rotation H <sub>2</sub> O	Basis set	Energy gap (cm <sup>-1</sup> )	g <sub>1</sub>	g <sub>2</sub>	g <sub>3</sub>	Angle of the easy anisotropy axis
0	DZ	34	19.34	0.09	0.30	0.9
0	TZ	47	19.40	0.07	0.23	0.1
0	TZ-TZP	69	19.33	0.03	0.23	0.3
90	DZ	80	19.52	0.06	0.17	87.1
90	TZ	82	19.48	0.08	0.18	87.0
90	TZ-TZP	66	19.28	0.06	0.30	88.8



(b)



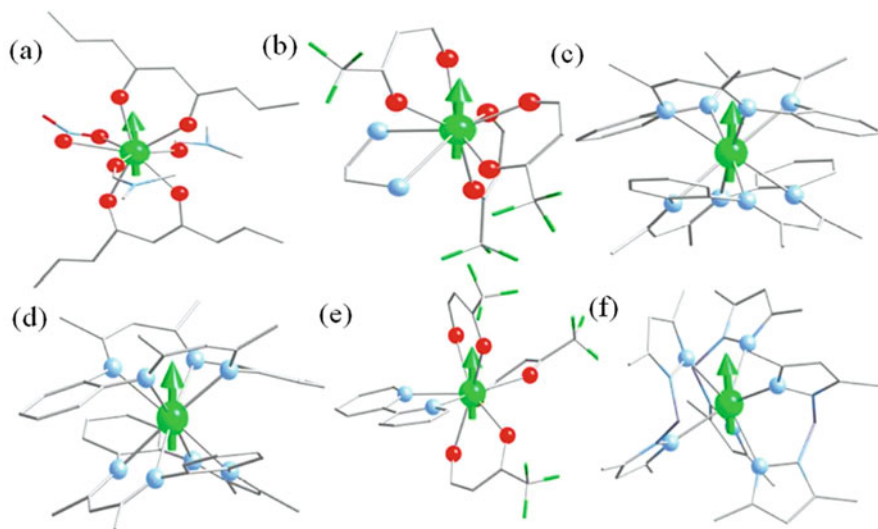
(c)

**Fig. 6** (a) Tabular compilation to show dependence of magnetic anisotropy on the rotation of coordinated second coordination sphere water molecule in **10**. (b) Complex model of [Dy(DOTA)(H<sub>2</sub>O)]<sup>+</sup> unit with three Na ions and few other modifications (model A) with their easy axis of magnetization represented by blue rod. (c) Water molecule of model A was rotated by 90° around Dy-O<sub>W</sub> axis in model A'. The corresponding blue rod indicates easy axis of magnetization. Colour code: central atom = Dy, red = O, brown = C and golden yellow = Na atoms. All the foregoing pictures were reprinted from Cucinotta et al. [67] with permission from John Wiley and Sons

[56]. Inherently two shorter bonds in **9** impose greater distortions in **9** compared to **8**. Larger transverse anisotropic components ( $g_{xx}$ ,  $g_{yy}$ ) can be ascribed to the smaller barrier in **9** compared to **8**. In **8**, the KD1- $g_{zz}$  is linked to the idealized fourfold symmetry and aligns along the coordination bond Dy-N(pyridyl). However, in **9** simple deprotonation of the ligand resulted in rotation of such orientation by 60° towards Dy-O(carbonyl) bond.

Complex **10** has a {DyO<sub>4</sub>N<sub>4</sub>} core with capped square antiprism geometry. Calculations on **10** yields  $U_{\text{cal}}$  value of 64 cm<sup>-1</sup> and absence of axial symmetry in the estimated g-tensors (see Fig. 6 and Tables 2 and 4). Calculations were undertaken on several models to appraise the genesis of different orientation of  $g_{zz}$  axis upon removal of coordinated water molecules. To profusely understand this behaviour, coordinated water molecules were rotated at different angles and several basis sets were also attempted. This revealed crucial role of second coordination sphere atoms (water molecule in **10**) to fine-tune magnetic anisotropy. This attributes to the partial charge transfer from the ligand atoms to the Dy<sup>III</sup>-5d orbitals. Furthermore, water molecule rotation could impact the relative population of Dy<sup>III</sup>-5d orbitals through  $\pi$  interaction with the O atom [67].

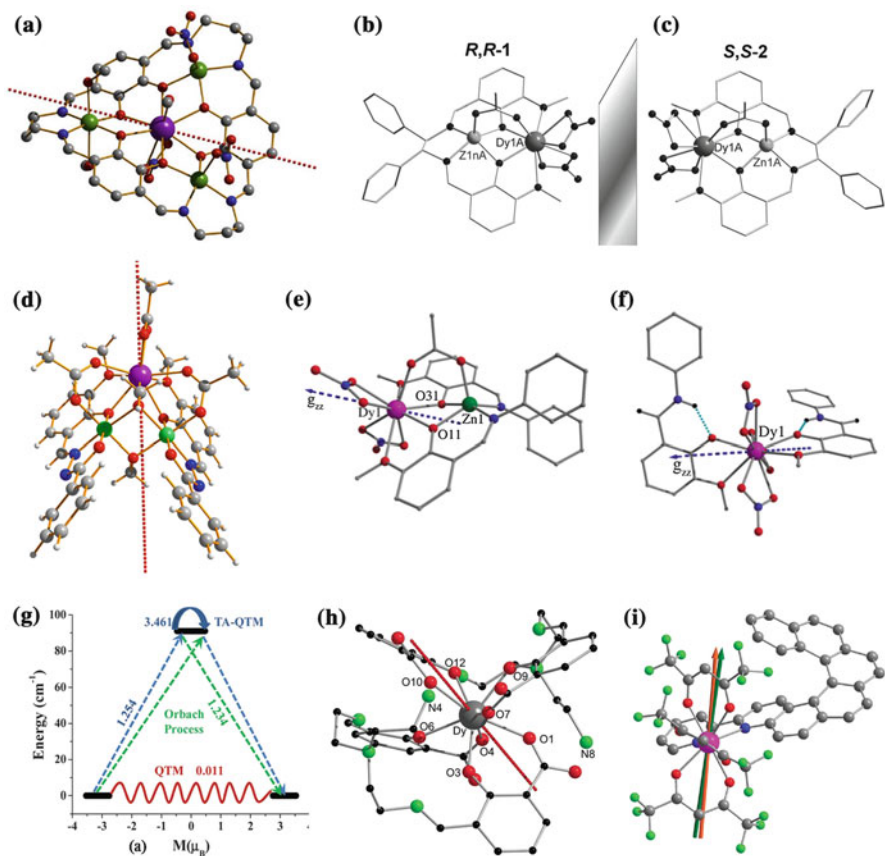
Complexes **11–16** are f-SIMs with  $U_{\text{eff}}/U_{\text{cal}}$  values 16/188.9, 21.1/93, 19.7/77.3, 24/75.3, 28.5/109.1 and 17/58.7 cm<sup>-1</sup>, respectively (see Tables 2 and 4 for



**Fig. 7** (a–f) Molecular structures of complexes **11–16**, respectively. Arrows in complexes show the orientation of the principal magnetization axis. Colour code: central atom = Dy, red = O, light blue = N, white = C and green = F atoms. Reprinted with permission from Aravena and Ruiz [47] Copyright©2013 American Chemical Society

molecular formula,  $g$ -factors and structural information) [47]. Complexes **11–15** are having eight coordination numbers around central Dy<sup>III</sup> ion with {DyO<sub>8</sub>} core in complex **11**, {DyO<sub>6</sub>N<sub>2</sub>} core in complexes **12** and **15** and {DyN<sub>8</sub>} core in complexes **13** and **14**. Complex **16** has six coordination numbers around central Dy<sup>III</sup> ion with {DyN<sub>6</sub>} core (see Fig. 7). Complexes **13** and **14** render two high-potential islands in the opposite regions of the sphere, with small potential in equatorial region due to pertinent shapes. This leads to accommodation of beta electron density in the equatorial region resulting in lower  $g_{zz}$  values (~16) (see Table 4). Complexes **13–15** are computed to possess close-lying first and second excited spin-free energies after incorporation of SOC. This is not ideal as one would require close-lying first excited state and relatively high-lying second excited spin-free energies to obtain axial  $g$ -tensors for the ground state. Due to these reasons, complexes **13–15** exhibit f-SIM behaviour [47].

The Zn<sup>II</sup> ion has an electronic configuration 3d<sup>10</sup>4s<sup>0</sup> and is non-magnetic. Hence, Zn<sup>II</sup> ion containing Dy<sup>III</sup> complexes enacts equivalent to Dy<sup>III</sup>-based mononuclear complex. Incorporation of diamagnetic ion leads to increment in barrier as they: (a) attenuate intermolecular magnetic coupling and (b) exert strong polarization effect on ligand donor atoms to impose greater negative charge. Complex **17**, in which Dy<sup>III</sup> ion is nine-coordinated, {DyO<sub>9</sub>}, is with neighbouring Dy...Dy ions that are about 10 Å apart. This large Dy...Dy separation is expected because of the presence of three diamagnetic Zn<sup>II</sup> ions in the molecule. It possesses narrower window range of eight KDs spanning within 391 cm<sup>-1</sup>. This owes to relatively longer Dy–O bonds (in avg. 2.44 Å) in **17**. KD1 in **17** is not exactly axial (substantial



**Fig. 8** (a–f, h–i) Molecular structures of complexes **17–22**, respectively and (g) ab initio calculated magnetization relaxation mechanism in **20**. Arrows in complexes show the orientation of the principal magnetization axis. In complex **22**, two arrows show the direction of experimental and computed KD1  $g_{zz}$  axis. Colour code: central atom = Dy, red = O, dark blue/light blue = N, black/dark-brown/light-brown = C and green = Zn atoms. In complexes **21** and **22**, small green balls represent nitrogen atoms. Reproduced from Long et al. [69] with permission from John Wiley and Sons. Reprinted with permission from Xue et al. [70] Copyright@2014 American Chemical Society. Reprinted with permission from Bhunia et al. [72] Copyright@2012 American Chemical Society. Reprinted from Upadhyay et al. [71], Ou-Yang et al. [73] with permission from the Royal Society of Chemistry

transverse  $g_{xx}$ ,  $g_{yy}$  components; see Table 4) and the main anisotropy axis of Dy<sup>III</sup> ion is parallel to the plane constituted by the three Zn<sup>II</sup> ions (see Fig. 8a) [68].

Next two enantiomeric complexes **18** and **18a** (R,R-1 and S,S-2, respectively) show  $U_{\text{eff}}/U_{\text{cal}}$  values of 13.5(36)/46 and 14.2(35.9)/64  $\text{cm}^{-1}$ , respectively. Both enantiomers have non-coordinated ligand field environment around Dy<sup>III</sup> ion with an intermediate geometry between a spherical capped square antiprism ( $C_{4v}$ ) and a spherical tricapped trigonal prism ( $D_{3h}$ , see Fig. 8b, c and Tables 2 and 4). The

Dy ... Dy intermolecular distance is found to be 9.21 Å. Larger transverse anisotropic components in KD1 induce relatively large transversal Zeeman splitting of the corresponding KDs that instigate QTM in **18/18a**. This justifies their pertaining f-SIM behaviour of **18** and **18a** [69]. Molecular structures for both the enantiomers show an electrical bistability up to 563 K, one of the highest reported for any molecular ferroelectric materials.

Similar to  $\text{Zn}^{\text{II}}$ ,  $\text{Co}^{\text{III}}$  is also diamagnetic and  $\text{Co}^{\text{III}}$  containing  $\text{Dy}^{\text{III}}$  complexes can also be approximated as  $\text{Dy}^{\text{III}}$ -based SIM as whole paramagnetism arises from single  $\text{Dy}^{\text{III}}$  ion. One such example is complex **19**, which has a defective cubane shaped heterometallic trinuclear  $\{\text{Co}^{\text{III}}_2\text{Dy}^{\text{III}}\}$  metallic centres (see Fig. 8d and Tables 2 and 4). Calculations on complex **19** articulate non-axial nature of ground and first excited KDs and this can be attributed to the nature of the crystal field of the ground energy multiplet. Axial crystal field parameters ( $B_2^0$ ,  $B_4^0$  and  $B_6^0$ ) are estimated to be relatively weaker than the non-axial CFPs of the ground manifold  $|M_J = \frac{15}{2}\rangle$  of the  $\text{Dy}^{\text{III}}$  centre. This provokes faster QTM within the ground KD and instigates spin flipping by direct process within ground multiplet than the Orbach process involved in the excited state. In resemblance to **17**, crystal field splitting of ground  ${}^6\text{H}_{15/2}$  multiplet of  $\text{Dy}^{\text{III}}$  is relatively narrow ( $454\text{ cm}^{-1}$ ) as a result of longer Dy-O bonds (2.41 Å). Ab initio calculated first excited state of  $\text{Dy}^{\text{III}}$  ion is located at  $\sim 50\text{ cm}^{-1}$  (see Table 4) and this is larger than the barrier height obtained from *ac* experiment ( $U_{\text{eff}}$ ). This reveals that the real thermally activated regime is out of the *ac* frequency window tested and for complex **19**, relaxation is mainly governed by quantum tunnelling. Therefore, non-axial anisotropy of  $\text{Dy}^{\text{III}}$  and intermolecular dipolar interaction between the nearest neighbours ( $d_{\text{Dy}\dots\text{Dy}} = 8.15\text{ Å}$ ) promote QTM and quench the QTM behaviour in the absence of magnetic field. This contributes to the observation of SIM behaviour in **19** only in the presence of magnetic field [70].

Complexes **20** and **20a** are heterodinuclear  $\{\text{Zn}^{\text{II}}\text{Dy}^{\text{III}}\}$  and mononuclear  $\text{Dy}^{\text{III}}$  complexes, respectively, with f-SIM behaviour. The  $U_{\text{eff}}$  for both complexes are found to be  $83\text{ cm}^{-1}$  and  $16\text{ cm}^{-1}$ , respectively. The  $\text{Dy}^{\text{III}}$  ion in both the complexes is found to have  $\{\text{DyO}_9\}$  core with distorted tricapped trigonal prismatic geometry (see Fig. 8e, f and Tables 2 and 4). KD1 of **20** and **20a** is computed to be axial in nature though it lacks pure Ising nature. Presence of diamagnetic  $\text{Zn}^{\text{II}}$  ion is found to pose increment in the magnitude of energy barrier for **20** compared to **20a**. QTM propensity within KD1 of **20a** is relatively higher than **20** due to reduced axiality in **20a**. Calculations iterate  $|M_J = \frac{13}{2}\rangle$  and  $|M_J = \frac{1}{2}\rangle$  nature of the first excited KD (KD2) in **20a** and **20**, respectively. This is further corroborated by computed transversal magnetic moment matrix element pertaining to TA-QTM within the KD2 as 3.46 and  $0.02\ \mu_{\text{B}}$  in **20** and **20a**, respectively (see Fig. 8g). Bridging phenoxo O atoms in **20** are estimated to possess higher negative charges than **20a** ( $-0.73$  vs.  $-0.30$  for **20** and **20a**, respectively). Diamagnetic  $\text{Zn}^{\text{II}}$  ion is expected to induce stronger polarization on the O atom and cumulatively instills larger electrostatic interaction on  $\text{Dy}^{\text{III}}$  ion. This causes the excited state destabilization and enhanced KD1–KD2 energy gap. This articulates the crucial presence of diamagnetic cation in

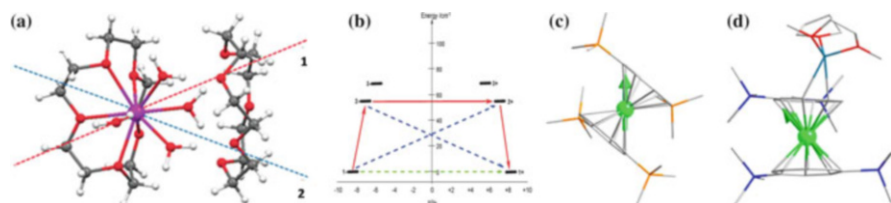
the coordination vicinity of lanthanide to promote larger energy barrier [71]. Previous studies performed by some of us suggest that diamagnetic replacement of  $\text{Co}^{\text{III}}$  ion with  $\text{K}^{\text{I}}$ ,  $\text{Zn}^{\text{II}}$  and  $\text{Ti}^{\text{IV}}$  ions induces larger formal charge on the bridging O atoms, causing large separation between ground to first excited state. Within these set of models, the ab initio analysis gives the  $U_{\text{cal}}$  values in the order of  $\text{K}^{\text{I}} > \text{Zn}^{\text{II}} > \text{Co}^{\text{III}} > \text{Ti}^{\text{IV}}$ , suggesting that with decrease in the oxidation state of the diamagnetic ion, the electronic repulsion to the bridging atoms increases, causing increase in the  $U_{\text{cal}}$  values and decrease in the QTM probability [74].

Another example for this family of molecule is complex **21**, where  $\text{Dy}^{\text{III}}$  ion is in eight-coordination environment with distorted square antiprism geometry (see Fig. 8h and Tables 2 and 4). KD1 in **21** is computed to be axial and calculations on **21** articulate that the H ion positions lead to uncertainty in the direction of anisotropy axis [72]. Intermolecular magnetic coupling constant for complex **21** is found to be very small, due to very large Dy . . . Dy separation ( $\sim 10 \text{ \AA}$ ) and the upward turn for susceptibility plot at low temperature are estimated by virtue of strong dipolar interaction.

Recently, Guennic et al. have reported a helicene based  $\text{Dy}^{\text{III}}$  single-ion magnet, complex **22** (see Fig. 8i and Tables 2 and 4). Both the racemic and enantiomerically pure forms for complex **22** are acting as SIMs in their crystalline phase. In complex **22**,  $\{\text{DyN}_2\text{O}_6\}$  core is in a triangular dodecahedron environment. KD1 in **22** shows Ising anisotropy with large  $g_{zz}$  value and this orients along the most negative charged direction of the coordination polyhedron. The computed and experimental  $g_{zz}$  lies at  $3.5^\circ$  against each other's alignment. Accounting the antiferromagnetic intermolecular dipolar coupling for **22**, nice agreements between experimental and calculated magnetic data have been demonstrated [73].

### 3.1.3 Ab Initio Studies on Category C Complexes: Zero-Field Single-Ion Magnet Complexes Possessing $|\pm M_J = \frac{15}{2}| > \text{Ground State}$ with the First Excited State Lying Within $\sim 50 \text{ cm}^{-1}$

Foregoing section demonstrated complexes showing SIM characteristics only in the presence of applied magnetic field. Here, we shift our attention towards complexes which exhibit SIM behaviour in zero field but yet have concomitant low-lying first excited state. In this regard, we have selected three reported complexes (**23–25**). Complex **23** has nine-coordinated pseudocapped square antiprismatic geometry with  $\{\text{DyO}_9\}$  core (see Fig. 9a). AC magnetic studies for complex **23** suggest two  $U_{\text{eff}}$  values for relaxation ( $34.0$  and  $19.0 \text{ cm}^{-1}$ ). Well-separated ground ( $\pm 1$ ), first ( $\pm 2$ ) and second excited ( $\pm 3$ ) states were noted through calculations on **23**. Energy gap between ground to first excited state is found to be  $58 \text{ cm}^{-1}$  which is larger than the  $U_{\text{eff}}$  value estimated. The transversal magnetic moments in **23** deviate from the Ising limit of anisotropy ( $g_{zz} = 20$ ,  $g_{xx} = g_{yy} = 0$ ) and possess transverse anisotropy. This validates the experimentally noted *ac* magnetic data of fast relaxation mechanism. The two closely lying  $U_{\text{eff}}$  values (see Tables 2 and 5) are well validated by operative



**Fig. 9** (a, b) Molecular structure for complex **23** along with its *ab initio* calculated magnetization relaxation mechanism. (c, d) Molecular structures for complexes **24** and **25**, respectively. Arrows in complexes show the orientation of the principal magnetization axis. Colour code: central atom = Dy, red = O, dark blue = N, black/dark-brown/light-brown = C, golden yellow = Si and white = H atoms. Reprinted from Gavey et al. [64] with permission from the Royal Society of Chemistry. Reprinted with permission from Aravena and Ruiz [47] Copyright©2013 American Chemical Society

**Table 5** List of complexes (from category C) with pertinent experimental energy barrier ( $U_{\text{eff}}$ , in  $\text{cm}^{-1}$ ), *ab initio* computed energy barrier ( $U_{\text{cal}}$ , in  $\text{cm}^{-1}$ ), main magnetic *g* factors and crystallographic structural information

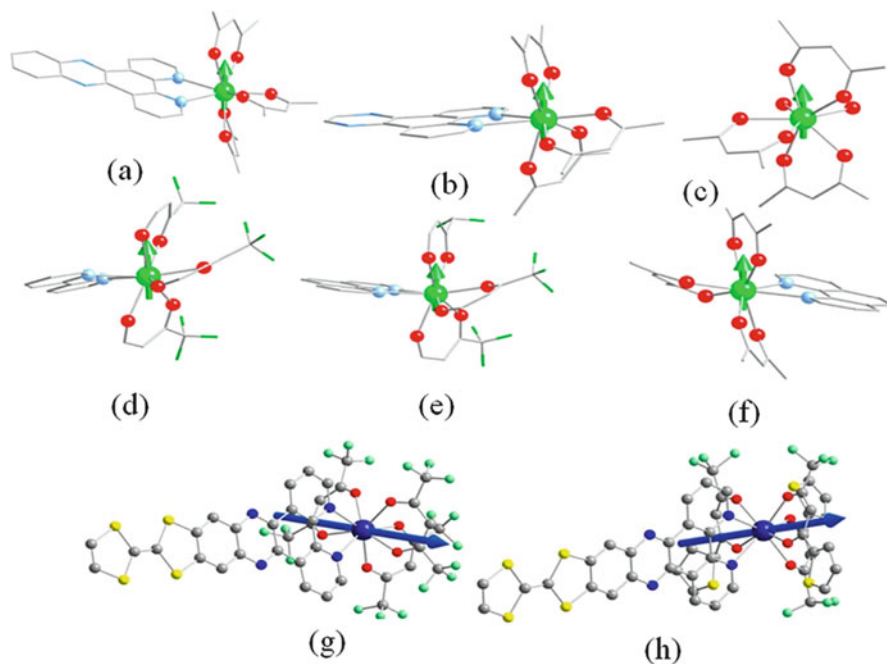
	$U_{\text{eff}}$	$U_{\text{cal}}$	$g_{xx}-g_{yy}$	$g_{zz}$	Type of coordinated atoms	Structure	Ref.
<b>23</b>	19, 34	58	0.26–0.52	17.49	9O	Pseudocapped square antiprismatic	[64]
<b>24</b>	12	36.3	0.14–0.18	15.95	(Two $\text{COT}^{2-}$ in $\eta^8$ -fashion)	–	[47]
<b>25</b>	17	45.6	0.02–0.07	16.90	(Two $\text{COT}^{2-}$ in $\eta^8$ -fashion)	–	[47]

QTM and Orbach mechanisms via KD1 and KD2, respectively (green and blue dashed lines, respectively, in Fig. 9b) [64]. In complexes **24–25**,  $\text{Dy}^{\text{III}}$  ion is sandwiched between alkyl substituted  $\eta^8$ -COT ligands (see Fig. 9c, d, respectively). Complexes **24–25** exhibit  $U_{\text{eff}}/U_{\text{cal}}$  values of 17/45.6  $\text{cm}^{-1}$ , 12/36.3  $\text{cm}^{-1}$ , respectively (see Table 5). Complexes **24–25** can be taken as an exception to *zf*-SIM complexes. The *zf*-SIM complexes are essentially known to be associated with small KD1  $g_{xx}$ ,  $g_{yy}$  components. However, contrastingly complexes **24–25** have considerable transverse anisotropy components and show low barriers which are sensitive to external *dc* magnetic field. This accentuates substantial contribution of KD1 tunneling as well as QTM contribution to the magnetic relaxation. In these two complexes, the beta electron density is accommodated in equatorial region resulting in smaller  $g_{zz}$  values for KD1 in **24–25** (~16, see Table 5) [47].



### 3.1.4 Ab Initio Studies on Category D Complexes: Zero-Field Single-Ion Magnet Complexes Possessing $|±M_J = \frac{15}{2}| > \text{Ground State}$ with First Excited State Lying Within $\sim 100 \text{ cm}^{-1}$

In this section, we intend to summarize the zf-SIMs with concomitant first excited energy multiplet located within  $\sim 100 \text{ cm}^{-1}$ . Thus, the ligand structures described here have stronger axial interactions than the ones described in the earlier section. Suitable examples of this category include complexes **26–31** (see Fig. 10 and Tables 2 and 6). KD1 of complexes **26–31** is of Ising type with  $g_{zz}$  ranging from 19.24 to 19.60 (concomitant smaller  $g_x, g_y$  values; see Table 6). Complex **28** has dodecahedron geometry with  $\{\text{DyO}_8\}$  core whereas other five complexes (**26, 27, 29–31**) are having distorted square antiprismatic geometry with  $\{\text{DyN}_2\text{O}_6\}$  core. Calculations on complex **28** rendered axially compressed shape equal to a disc with its  $g_{zz}$  being perpendicular to the beta electron plane. Complexes **26–30** estimated to possess smaller first excited and larger second excited spin-free energies (after the SOC coupling incorporation in contrary to that discussed in Sect. 3.1.2). Calculations on models of complex **28** with ligands of versatile charge distribution affirm correlation between large anisotropy of the crystal electrostatic potential and



**Fig. 10** (a–c) Molecular structure for complexes **26–28**. (d, e) Molecular structure for complexes **29a–b**. (f) Molecular structure for complex **30**. (g–h) Molecular structure for complexes **31a–b**. Reproduced from Aravena and Ruiz [47], Baldovi et al. [48] Copyright©2013 American Chemical Society. Arrows in complexes show the orientation of the principal magnetization axis. Colour code: central atom = Dy, Yellow = S, red = O, light blue = N, white = C and green = F atoms

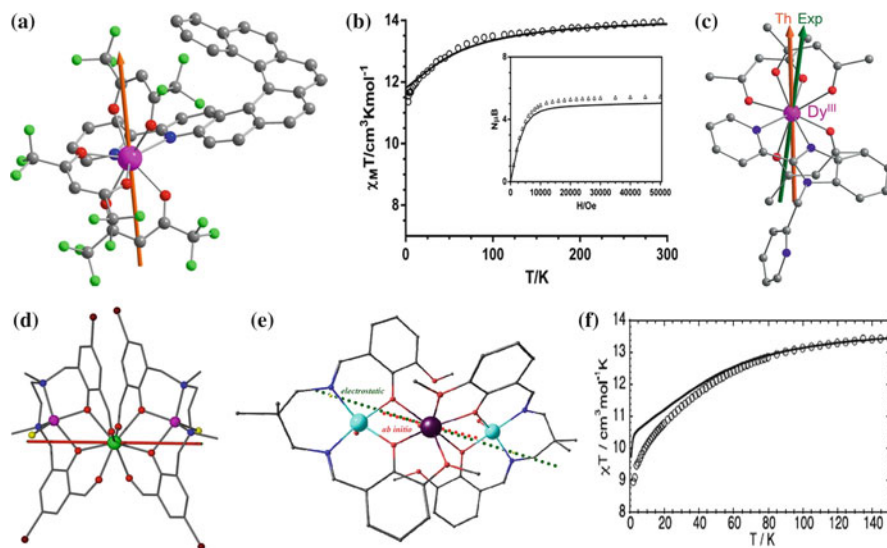
**Table 6** List of complexes (from category D) with pertinent experimental energy barrier ( $U_{\text{eff}}$ , in  $\text{cm}^{-1}$ ), ab initio computed energy barrier ( $U_{\text{cal}}$ , in  $\text{cm}^{-1}$ ), main magnetic g factors and crystallographic structural information

	$U_{\text{eff}}$	$U_{\text{cal}}$	$g_{xx}-g_{yy}$	$g_{zz}$	Type of coordinated atoms	Structure	Ref.
<b>26</b>	94	120.4	0.00–0.01	19.24	6 O, 2 N	Distorted square antiprismatic	[46]
<b>27</b>	130	146.2	0.01	19.37	6 O, 2 N	Distorted square antiprismatic	[46]
<b>28</b>	45.9	151.9	0.01	19.46	8 O	Distorted square antiprismatic	[46]
<b>29a</b>	44.4	135.8	0.00	19.39	6 O, 2 N	Distorted square antiprismatic	[46]
<b>29b</b>	40	142.6	0.00	19.60	6 O, 2 N	Distorted square antiprismatic	[46]
<b>30</b>	59	126.3	0.01	19.51	6 O, 2 N	Distorted square antiprismatic	[46]
<b>31a</b>	27.1	–	0.08–0.11	18.89	6 O, 2 N	Distorted square antiprismatic	[51]
<b>31b</b>	44.3	–	0.00	19.58	6 O, 2 N	Distorted square antiprismatic	[51]
<b>32</b>	34.8	95	0.0–0.01	18.10	4 N, 6 O	Distorted bicapped square antiprismatic	[62]
<b>33</b>	14.6, 70.2	103.6	0.01	19.66	2 N, 6 O	Triangular dodecahedron	[73]
<b>34</b>	NA	117	0.02	19.47	2 N, 6 O	Distorted square antiprismatic	[75]
<b>35</b>	97.3, 103	129.0	0.00	19.43	8 O	Distorted square antiprismatic	[46]
<b>36</b>	67.3, 89.4	92.4	0.02–0.04	19.57	9 O	Distorted muffin	[76]

heteroleptic systems (combination of charged and neutral ligands). In these desired instances, beta electron density of  $\text{Dy}^{\text{III}}-4f$  electrons have propensity to concentrate into axially compressed shape. The  $\text{Dy}^{\text{III}}-4f$  beta electron density should preferentially be located along the direction of the minimum electrostatic potential of the sphere to deter proximity with the negatively charged ligands and minimize electrostatic repulsion with them [47]. Complexes **31a–b** are having identical coordination geometry but different ligand system. Large point charge of the first neighbouring atoms causes large separation between ground to first excited state for the latter molecule compared to the former one [51].

Complex **32** is similar to complex **1** with a minor modification. Complex **32** has two imino groups instead of amine groups. KD1 in complex **32** is computed to be pure Ising type (see Table 6). Experimental magnetic data was nicely reproduced harnessing ab initio computed values. Principal magnetization axis in **32** lies along the direction perpendicular to the pseudo- $C_2$  (along the  $N-N$  bond vector) axis and





**Fig. 11** (a, c–e) Molecular structures for complexes **33–36** and (b, f)  $\chi_m T$  vs.  $T$  plot for **33** and **36**, respectively, solid line postulates calculated data. Arrows in complexes show the orientation of the principal magnetization axis. In complex **34**, two arrows show the direction of experimental and computed KD1  $g_{zz}$  axis. Colour code: central atom = Dy, red = O, dark blue/light blue = N, black/dark-brown/light-brown = C, pink = Zn and green = Cl atoms. Reprinted from Ou-Yang et al. [73] with permission from the Royal Society of Chemistry. Reproduced from Jung et al. [75], Oyarzabal et al. [46] with permission from John Wiley and Sons

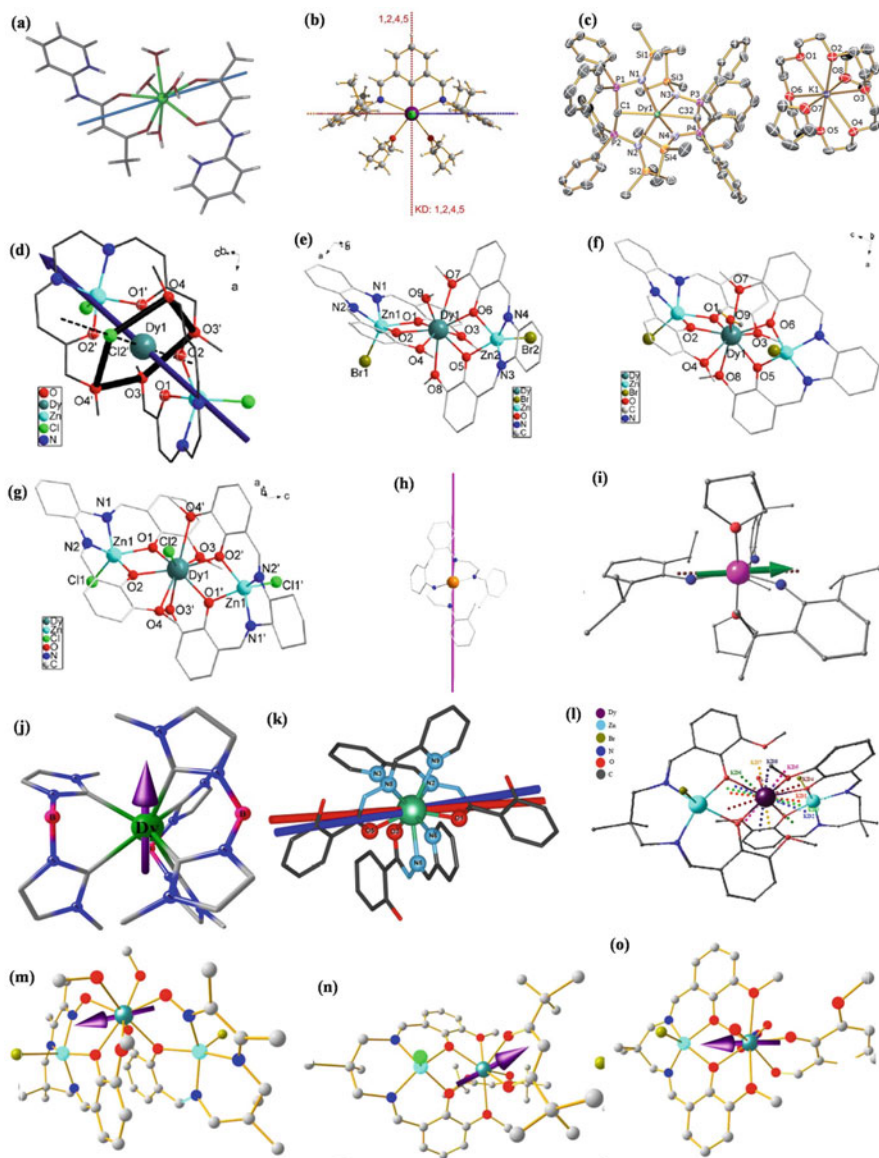
passes through the two –O atoms. Ising type ground state anisotropy in KD1 owes to shorter imine bonds (which corresponds to previous  $g_{zz}$  orientation) and the resultant stronger bonds in the axial direction cumulatively constitute favourable strong ligand field [62].

Complexes **22** and **33** are the same except that complex **22** is the racemic form whereas complex **33** is the enantiopure form. Pure Ising type anisotropy was detected in complex **33** with theoretical barrier estimated to be  $103.6 \text{ cm}^{-1}$  (see Fig. 11a and Tables 2 and 6). Accounting the positive intermolecular dipolar exchange interaction, nice agreement was found between experimental and calculated magnetic data (see Fig. 11b, contrary to its corresponding racemic analogue **22**) [73]. Complex **34** has  $\{\text{DyN}_2\text{O}_6\}$  core with distorted square antiprism geometry ( $D_{4d}$  symmetry). Easy axis of the  $\text{Dy}^{\text{III}}$  ion lies along the most negatively charged direction. Computations on complex **34** invoke pure Ising type KD1 anisotropy with  $g_{zz}$  of 19.47 (see Fig. 11c and Tables 2 and 6) [75]. Complex **35** is having square antiprism geometry with  $\{\text{DyO}_8\}$  core. KD1 is markedly axial ( $g_{zz} = 19.43$ , Fig. 11d and Tables 2 and 6) with vanishing transversal  $g$  anisotropies in compliance with  $z_f$ -SIM characteristics of **35**. Like in earlier instances, in **35** as well the calculated magnetic data matches well with the experiments. It shows zero-field SIM behaviour with  $U_{\text{eff}}$  value  $97 \text{ cm}^{-1}$  and this is smaller compared to ab initio calculated  $U_{\text{cal}}$

value ( $129 \text{ cm}^{-1}$ ).  $\text{KD1-}g_{zz}$  in **35** is located between the planes constituted by two Dy-O-Zn-O moieties and collinear with the shortest Dy-O bond ( $2.25 \text{ \AA}$ ) vectors while perpendicular to oblate shaped electron density. This reiterates the necessary requirement for axially strong coordination atmosphere to improve SIM behaviour in Dy<sup>III</sup>-based complexes. In resemblance to the earlier statement,  $\text{KD1-}g_{zz}$  is located in such direction to evade strong electrostatic repulsion. Notably, alignment of principal magnetization axis acquired via electrostatic approach [42] complies well with that computed harnessing ab initio calculations [46]. In complex **36**, central Dy<sup>III</sup> ion is surrounded by two Zn<sup>II</sup> ions. It has a nine-coordinated  $\{\text{DyO}_9\}$  core with distorted muffin geometry (Fig. 11e and Tables 2 and 6). Eight KDs in complex **36** span up to  $458 \text{ cm}^{-1}$  with subsequent excited states lying even higher in energies. KD1 is of pure Ising type and beyond this, the  $g_{zz}$  value begins to reduce until fifth KD. However, beyond fifth KD, the  $g_{zz}$  value again starts to increase and at eighth KD, the highest  $g_{zz}$  is achieved. This indicates the low-symmetry nature of complex **36**. KD1 magnetic moment lies in close proximity to the two shortest Dy-O bond and ligand donor atoms with greater electron density in compliance with the oblate–prolate model. Using the ab initio computed anisotropy and crystal field parameters, experimental magnetic data is nicely reproduced with intermolecular interaction of  $-0.0024 \text{ cm}^{-1}$  (see Fig. 11f). Ising ground state was corroborated by the transversal magnetic moment matrix element corresponding to the KD1, QTM process ( $\sim 10^{-3} \mu_B$ ). The matrix element pertaining to the direct (Orbach) process implicating  $\pm 1$  and  $\pm 2$  energy states ( $1.73 \mu_B$ ) induces relaxation via KD2 providing theoretical barrier estimate of  $92.4 \text{ cm}^{-1}$ . Wave-function analysis postulated KD1 to be predominantly  $|\pm \frac{15}{2}\rangle$ :  $0.98 |\pm \frac{15}{2}\rangle$  while KD2 is preponderantly  $|\pm \frac{13}{2}\rangle$ :  $0.37 |\pm \frac{13}{2}\rangle + 0.25 |\pm \frac{11}{2}\rangle + 0.35 |\pm \frac{9}{2}\rangle$ . DFT calculations on complex **36** articulate larger negative charges on the phenoxo O atoms as induced by the strong polarization effect of Zn<sup>II</sup> ions. In order to probe the role of secondary coordination sphere influence in  $U_{\text{cal}}$  values, water ligand coordinated to two Zn<sup>II</sup> ions in **36** was substituted by different halide ligands ( $\text{F}^-$ ,  $\text{Cl}^-$ ,  $\text{Br}^-$  and  $\text{I}^-$ ). In all the substituted models, Ising type ground multiplet was detected and  $U_{\text{cal}}$  diminishes with the expected electronegativity of the halide ion [76].

### 3.1.5 Ab Initio Studies on Category E Complexes: Zero-Field Single-Ion Magnet Complexes Possessing $|\pm M_J = \frac{15}{2}\rangle$ Ground State with First Excited State Energy Separation $> 100 \text{ cm}^{-1}$

In this category **E**, we will describe the properties of Dy<sup>III</sup> SIMs possessing  $|\pm M_J = \frac{15}{2}\rangle$  ground state with strong crystal field splitting (first excited state lying at  $> 100 \text{ cm}^{-1}$ ) and exhibiting zero-field SMM characteristics. First complex under this category is complex **37**, which has  $\{\text{DyO}_8\}$  core with trigonal dodecahedron geometry. KD1 of **37** is found to be pure Ising type with subsequent excited multiplets lying higher in energy (see  $\text{KD1-}g_{zz}$  orientation in Fig. 12a and Tables 2 and 7). The main magnetic axes of the lowest three KDs in **37** are almost parallel and are



**Fig. 12** (a–o) Molecular structures along with ground state KD orientation for complexes 37–48, 50–52, respectively. Arrows in complexes show the orientation of the principal magnetization axis. Complexes with two arrows are showing KD1 and KD2  $g_{zz}$  axis, and complexes with eight arrows are showing KD1–KD8  $g_{zz}$  axis. Colour code: central atom = Dy, red = O, dark blue/light blue = N, black/dark-brown/light-brown/white = C, cyan = Zn, light yellow = Br and green = Cl atoms. Reprinted from Chilton et al. [66], Gregson et al. [77], Sun et al. [78], Long et al. [79], Rajaraman et al. [80], Gupta et al. [81], Kishi et al. [82] with permission from the Royal Society of Chemistry. Reproduced from Lucaccini et al. [83] with permission from John Wiley and Sons. Reprinted from Liu et al. [18], Chen et al. [19], Costes et al. [84] Copyright©2016 American Chemical Society

**Table 7** List of complexes {from category E} with pertinent experimental energy barrier ( $U_{\text{eff}}$ , in  $\text{cm}^{-1}$ ), ab initio computed energy barrier ( $U_{\text{cal}}$ , in  $\text{cm}^{-1}$ ), main magnetic g factors and crystallographic structural information

	$U_{\text{eff}}$	$U_{\text{cal}}$	$g_{xx}-g_{yy}$	$g_{zz}$	Type of coordinated atoms	Structure	Ref.
37	124	249.2	0.05–0.07	16.33	8 O	Trigonal dodecahedral	[66]
38	233, 270	266	$\sim 10^{-4}$ – $10^{-3}$	19.81	2 N, 2 O, 1 C, 2 Cl	–	[55]
39	501.1, 565	515.7, 563	0.00	19.88	4 N, 2 C	–	[77]
40	299/334.3/301.6	355.6	0.00	19.96	8 O, 1 Cl	Muffin	[78]
41	161.9	351.8	0.00	19.85	9 O	Muffin	[78]
42	84.1	313.0	0.00	19.79	9 O	Spherical capped square antiprismatic	[78]
43	276.6	351.9	0.00	19.97	8 O, 1 Cl	Muffin	[78]
44	30/43/108	410.7	0.00	19.71	4 N	Tetrahedron	[79]
45	23	199.0	0.00–0.001	19.67	3 N, 2 O	Trigonal bipyramidal	[80]
46	32.8, 33.6	268.5	0.07–0.09	19.91	6 N incorporation of agostic interactions with three Hs	Trigonal prismatic; incorporation of agostic interactions with H: Tricapped trigonal prismatic	[81]
47	230	237	0.00	19.80	6 N, 3 O	Spherical capped square antiprismatic	[83]
48	102, 149.2	218.1	0.00	19.91	9 O	Distorted spherical tricapped trigonal prismatic	[76]
49	101.5, 140.7	238.5	0.00	19.94	9 O	Distorted spherical tricapped trigonal prismatic	[76]
50	82.9, 146.7	177.5	0.00	19.94	9 O	Distorted muffin	[84]
51	69.3, 111.5	159.9	0.00	19.73	8 O	Distorted biaugmented trigonal prismatic	[84]
52	44.3, 66.4	131.3	0.00	19.71	8 O	Distorted triangular dodecahedron	[84]
53	1,277	1,156	0.00	19.88	– (Sandwich type between two substituted – Cp rings)	Bent metallocene	[22]

(continued)

**Table 7** (continued)

	$U_{\text{eff}}$	$U_{\text{cal}}$	$g_{xx}-g_{yy}$	$g_{zz}$	Type of coordinated atoms	Structure	Ref.
<b>54</b>	1,223	1320.7	0.00	19.99	– (Sandwich type between two substituted – Cp rings)	Bent metallocene; approximately eclipsed two –Cp rings	[21]
<b>55</b>	66.7	362.0	0.00	19.56	2 N, 6 O	Distorted square antiprismatic	[82]
<b>56'</b>	45.2	197.0	0.01	19.44	2 N, 6 O	Distorted square antiprismatic	[82]
<b>57</b>	328.0	299	0.00	19.86	7 O	Compressed pentagonal bipyramid	[19]
<b>58</b>	377.4	276	0.00	19.88	7 O	Compressed pentagonal bipyramid	[19]
<b>58</b>	492	586	0.00	19.87	1 Cl <sup>–</sup> , 2 O, 4 N	Distorted pentagonal bipyramid	[19]
<b>59</b>	712	721	0.00	19.88	1 Br <sup>–</sup> , 2 O, 4 N	Distorted pentagonal bipyramid	[18]
<b>60</b>	305	289.9	0.00	19.87	7 O	Axial pentagonal bipyramidal	[85]
<b>61</b>	1261.4	1,220	0.00	19.89	5 N, 2 O	Distorted pentagonal bipyramid	[86]
<b>62</b>	452.4, 511.1	478.4	0.00	19.86	7 O	Distorted pentagonal bipyramid	[20]
<b>63</b>	353.1	297	0.00	19.88	7 O	Distorted pentagonal bipyramid	[87]

deviating from KD1 by  $\sim 2^\circ$  and  $1.4^\circ$ , respectively. However, the  $g$ -tensors of the two highest energy multiplets differ with respect to KD1 by  $111.4^\circ$  and  $73.6^\circ$ , respectively, and divert by  $40.3^\circ$  with respect to each other. The computed axial anisotropy is located between the two  $\beta$ -diketonate ligands and is collinear with the plane constituted by four water molecules to minimize the electrostatic repulsion with the  $U_{\text{eff}}$  value reported to be  $123 \text{ cm}^{-1}$  [66]. Next complex in this category is **38** with seven-coordinate Dy<sup>III</sup> possessing pentagonal bipyramidal geometry with two N donors, two O donors, two chloride donors and one carbon donor from the pincer ligand. The calculated main anisotropy axis passes along the main symmetry axis and is collinear with shorter Dy-C bond vector ( $2.39 \text{ \AA}$ ). Besides, the crucial role of C atom in dictating the orientation of KD1- $g_{zz}$  arises from its inherent negative charge ( $-1.17$ ) in its carbanionic form. Collinearity between the  $g_{zz}$  axes of KD1 and KD2 promotes relaxation via second excited multiplet (KD3) with  $U_{\text{cal}}$  value of  $262 \text{ cm}^{-1}$ . Furthermore, significant matrix element between  $\pm 3$  multiplets ( $3.4 \mu_{\text{B}}$ ) pertaining to the TA-QTM process corroborates the relaxation probability via that

level. Significant anisotropies in KD1 and KD2 can be supported by computed huge negative axial CFP  $B_2^0$  (−2.95). Additionally, the  $B_2^2$  term is also estimated to be large (2.09) and this explains the huge anisotropy observed in complex **38** (see the KD orientations in Fig. 12b and Tables 2 and 7). The term  $B_2^2$  is computed to be the largest when the quantization axis lies parallel to the main magnetic axis of KD3, passing along Cl-Dy-Cl bond vector [55].

Complex **39** is having six-coordinated distorted octahedral geometry with  $\{\text{DyC}_2\text{N}_4\}$  core. Linear coordination mode of the two methanediide (huge negative charge on the axis) sites in **39** assures considerable energy gap between  $|\pm M_J = \frac{15}{2}\rangle$  and other KDs. Notably, the three lowest KDs are pure  $|\pm \frac{15}{2}\rangle$ ,  $|\pm \frac{13}{2}\rangle$  and  $|\pm \frac{11}{2}\rangle$  states which are quantized along the main C=Dy=C axis. This suppresses relaxation via second and third excited KDs and promotes relaxation via higher energy levels. Wave-function analysis asserted fourth and fifth KDs to be composed of different mixed  $|\pm M_J\rangle$  levels, i.e.  $|\pm \frac{9}{2}\rangle$ ,  $|\pm \frac{7}{2}\rangle$ ,  $|\pm \frac{5}{2}\rangle$ ,  $|\pm \frac{3}{2}\rangle$  and  $|\pm \frac{1}{2}\rangle$ . Additionally, perpendicular orientation of fourth and fifth KDs  $g_{zz}$  axis with respect to ground KD preferentially induces relaxation via those states. This outlines  $U_{\text{cal}}$  value to be 516 and 563  $\text{cm}^{-1}$  (see Tables 2 and 7, and Fig. 12c for magnetization relaxation mechanism) which is very close to the estimated  $U_{\text{eff}}$  value (501  $\text{cm}^{-1}$  and 565  $\text{cm}^{-1}$ ). Besides possessing a large  $U_{\text{cal}}$  value, the molecule also characterized to possess very large blocking temperature  $T_B$  of 10 K and this is among the best blocking temperatures reported for lanthanide based SIMs [77].

Next set of complexes that are discussed are nine-coordinate  $\text{Dy}^{\text{III}}$  complexes (**40–43**, see Fig. 12d–g). Complexes **40**, **41** and **43** are having muffin geometry whereas complex **42** has spherical capped square antiprismatic geometry with  $\{\text{DyO}_8\text{Cl}\}$  core for complexes **40** and **43**, and  $\{\text{DyO}_9\}$  core for complexes **41** and **42**. Computed transverse anisotropy components for **41–42** are larger than that estimated for **40** and **43** (see Tables 2 and 7). This underscores the prominent QTM operative in **41–42** compared to **40** and **43**. This led to the following trend in the computed energy barrier and magnitude of  $g_{zz}$  values: **42** < **41** < **40** < **43** (see Table 7). The principal magnetization axis is collinear with the Zn-Dy-Zn direction and remains perpendicular to the  $C_2$  axis for **40** and **43**. The adjacent phenoxy O atoms generate huge charge density distribution rendering prominent easy-axis crystal field. Contrarily, in these complexes, four methoxy O atoms comprise hard plane. Cumulative effects from substantial negative charge distribution along easy axis in conjunction with diminished electrostatic repulsion along hard plane constitute contributing factor towards the observed magnetic anisotropy characteristics in complexes **40–43** [78].

Ab initio calculations on **44**, which is having tetrahedron geometry around  $\text{Dy}^{\text{III}}$  ion with  $\{\text{DyN}_4\}$  core, confer  $|\pm \frac{13}{2}\rangle$  nature to the first excited KD lying at 236  $\text{cm}^{-1}$  (note:  $\text{Dy}^{\text{III}}$  ion also has weakly interacting two  $\eta_2\text{-C}=\text{C}$  groups, see Fig. 12h and Tables 2 and 7). This turns out to be larger than the  $\Delta_{\text{Orbach}}$  energy barrier (30±2  $\text{cm}^{-1}$ ) procured from magnetic measurements. This infers the necessary consideration of other relaxation pathways within temperature range besides the operative Orbach relaxation phenomena. The KD1 and KD2 states have axial

character while KD3 lacks axiality instigating the relaxation process via this state. Therefore, the relaxation is likely to occur via combined effects of QTM and Raman pathways. Negligible matrix element ( $\sim 10^{-2} \mu_B$ ) pertinent to TA-QTM process within  $\pm 2$  states unleashes relaxation propensity via higher excited states. Relaxation is likely to take place via KD3 as corroborated by significant matrix element corresponding to the TA-QTM ( $0.30 \mu_B$ ) within  $\pm 3$  states. This is supported by significant matrix element of Raman process to provide  $U_{\text{cal}}$  of  $410 \text{ cm}^{-1}$  (see Table 7) in **44** [79]. Next complex in this category is **45**, which has  $\{\text{DyN}_2\text{O}_3\}$  core with trigonal bipyramidal geometry (see Fig. 12i). In complex **45**, the eight KDs span within energy window of  $790 \text{ cm}^{-1}$ . Ground state is noted to be axial with  $g_{zz} = 19.67$  and KD2 lying at  $199 \text{ cm}^{-1}$  ( $U_{\text{cal}}$ ; see Tables 2 and 7) above the KD1 state. The presence of two THF-O donor atoms in the axial positions of **45** provides favourable crystal field to yield larger  $U_{\text{cal}}$  values [80]. Complex **46** has tricapped trigonal prismatic geometry with  $\{\text{DyH}_3\text{N}_6\}$  core. Three H atoms are having agostic interaction with  $\text{Dy}^{\text{III}}$  ion (see Fig. 12j). KD1 in complex **46** is computed to be Ising type ( $g_{zz} = 19.91$ ; see Tables 2 and 7) which is well validated by large positive CFP  $B_2^0$  as 3.28. Retention of axiality of KDs is broken at fourth excited KD (KD5) rendering  $g_{xx} = 5.10$ ,  $g_{yy} = 5.30$  and  $g_{zz} = 8.00$ . This in conjunction with appreciable matrix element for the TA-QTM within  $\pm 5$  ( $1.76 \mu_B$ ) and Orbach/Raman between  $\pm 4/\pm 5$  ( $3.09 \mu_B$ ) instigates relaxation via this level to articulate  $U_{\text{cal}} = 268.5 \text{ cm}^{-1}$ . Wave-function analysis iterated KD1 to be  $|\pm \frac{15}{2}\rangle >: 99\% |\pm \frac{15}{2}\rangle >$  and KD5 to be admixture of  $56\% |\pm \frac{7}{2}\rangle > +18\% |\pm \frac{5}{2}\rangle > [81]$ .

Complex **47** has spherical capped square antiprismatic geometry with  $\{\text{DyN}_6\text{O}_3\}$  core (see Fig. 12k). KD1 is determined to be pure Ising type in **47** ( $g_{zz} = 19.80$ ) and aligned over the line which connects two carbonyl groups of the two  $\text{LH}^-$  ligands. Nice agreement between experimental and calculated data lends support to the calculated properties of **47**. KD2 turns out to be:  $71\% |\pm \frac{13}{2}\rangle > +10\% |\pm \frac{11}{2}\rangle > +10\% |\pm \frac{7}{2}\rangle >$  and this is not sufficient to provoke substantial divergence from the axiality of g-tensor. Third excited KD possesses greater mixing between various  $\pm M_J$  states. Non-collinearity of the easy axis of higher KDs increases with the KD energy and rhombicity increases with respect to KD1. The  $g_{zz}$  angle between KD1 and KD2 diverges by  $6^\circ$  and then by  $60^\circ$  with respect to the  $g_{zz}$  of KD3. In this context, magnetization relaxation occurs through Orbach two-phonon pathway via second excited state ( $U_{\text{cal}} = 237 \text{ cm}^{-1}$ , see Tables 2 and 7). Significant matrix element ( $0.54 \mu_B$ ) pertaining to TA-QTM within  $\pm 3$  in conjunction with Orbach process between states  $\pm 2$  and  $\pm 3$  ( $0.98 \mu_B$ ) further corroborates the relaxation via second excited KD [83].

Complexes **48** and **49** have distorted spherical tricapped trigonal prismatic geometries and possess analogous X-ray as well as magnetic properties (see Fig. 12l). Eight KDs in **48** and **49** span within the energy span of  $756$  and  $792 \text{ cm}^{-1}$ , respectively, with consecutive excited states lying at  $\sim 3,100 \text{ cm}^{-1}$  in both cases. KD1 is computed to be Ising type in both complexes ( $g_{zz}$  as  $19.94$  and  $19.91$  in **48–49**, respectively; see Tables 2 and 7). Relaxation occurs via first excited KD with  $U_{\text{cal}}$  value estimated as  $218$  and  $238 \text{ cm}^{-1}$  for complexes **48** and **49**, respectively, as supported by matrix

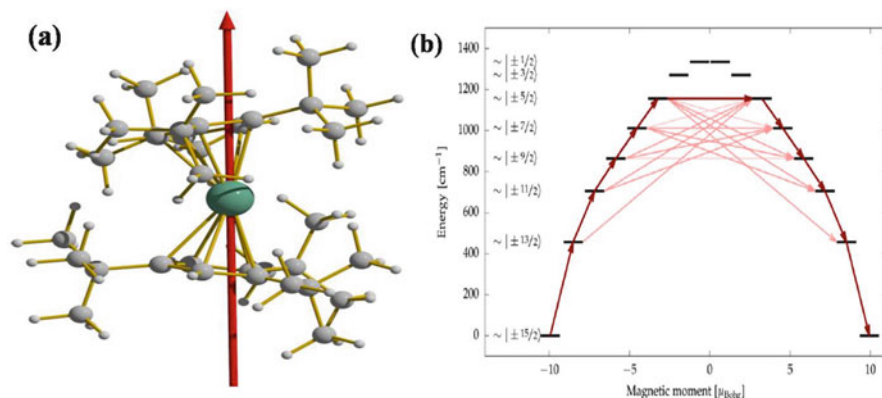


elements corresponding to TA-QTM and Orbach pathways. Axiality of the excited states gradually reduces up to sixth and seventh KD in **48–49**, respectively, with proportional enhancement in the magnetic moment along the XY-plane. Beyond these KDs, the energy levels enhance in axiality to reach nearly pure Ising type behaviour at the highest KD to reproduce KD1 observation. This sort of mirror symmetry implies the low-symmetry nature of these two compounds. To testify the accuracy of the estimated  $g_{zz}$  axis, electrostatic oblate–prolate model has been employed. Electrostatic deviation angles (angle between  $g_{zz}$  axes computed via ab initio calculations and electrostatic approach) are found to be  $0.73^\circ$  and  $3.19^\circ$  in **48–49**, respectively. This infers the propensity of principal magnetization axis to point towards the ligand donor atoms with larger electron density and shorter Dy–O bond vectors (phenoxide). This enforces Dy<sup>III</sup>-4f oblate electron density to be perpendicular to the  $g_{zz}$  axis to minimize electrostatic repulsion.

Two pairs of large negatively charged phenoxide groups with shorter Dy–O bonds in conjunction with donor O atoms deliver suitable crystal field towards achievement of larger energy barrier. Experimental magnetic data is nicely reproduced harnessing ab initio computed anisotropy parameters at intermolecular interaction of  $-0.0025$  and  $-0.0031 \text{ cm}^{-1}$  for **48** and **49**, respectively. DFT calculations imply stronger negative charges on the phenoxo O atoms as induced by the strong polarization effect of Zn<sup>II</sup> diamagnetic ion [76]. Like the foregoing discussion, complexes **50–52** (19.94, 19.73 and 19.71 for **50–52**, respectively; see Fig. 12m–o and Tables 2 and 7) also exhibit Ising type ground state anisotropy. Like in previous cases, larger Mulliken charges were noted on O atoms to impose larger barrier and KD1- $g_{zz}$  axis is found to lie along the shortest Dy–O bond vectors in both complexes. Relaxations via KD2 in **50–52** were corroborated by Orbach process as revealed by the computed matrix elements ( $1.74$ ,  $1.80$  and  $1.84 \mu_B$  for **50–52**, respectively) between  $\pm 1$  and  $\pm 2$  states. Though for all three complexes, KD1 is preponderantly  $|\pm \frac{13}{2}\rangle$ , KD2 is preferably  $|\pm \frac{13}{2}\rangle$  with minor contributions from  $|\pm \frac{9}{2}\rangle$  energy level [84].

The conventional ways to procure improved SIM/SMM behaviour is to instil axial symmetry in complexes to minimize admixture of  $|\pm M_J\rangle$  levels. In this manner, we aim to stabilize the highest angular momentum projection, i.e.  $|\pm M_J\rangle$  as ground energy state. In compliance with group-theoretical norms, point group symmetries  $C_{\infty V}$ ,  $D_{\infty h}$ ,  $S_8$ ,  $D_{4d}$ ,  $D_{5h}$ ,  $D_{6d}$  and  $D_{8d}$  exhibit disappearing off-diagonal crystal field parameters  $B_k^q$  ( $q \neq 0$ ). This forbids admixing of  $|\pm M_J\rangle$  levels and ensures stabilization of the highest  $|\pm M_J\rangle$  level. In this way, it tends to suppress QTM and lends credence towards inducing relaxation via higher energy excited multiplets. We intend to discuss such instances where simple symmetry imposition enacted as a tool to promote energy barrier. Very recently, complex **53** was reported with unprecedented barrier ( $1,277 \text{ cm}^{-1}$ , see Fig. 13 and Tables 2 and 7) and recorded the highest (to date) blocking temperature of 60 K possessing hysteresis with coercivity of 0.06 T and the sweep rate of  $3.9 \text{ mTS}^{-1}$ . Calculations inferred extraordinarily magnificent as well as first such SIM behaviour of **53** where all lower energized KDs pertain to specifically defined  $|\pm M_J\rangle$  value. Even in the higher KDs,

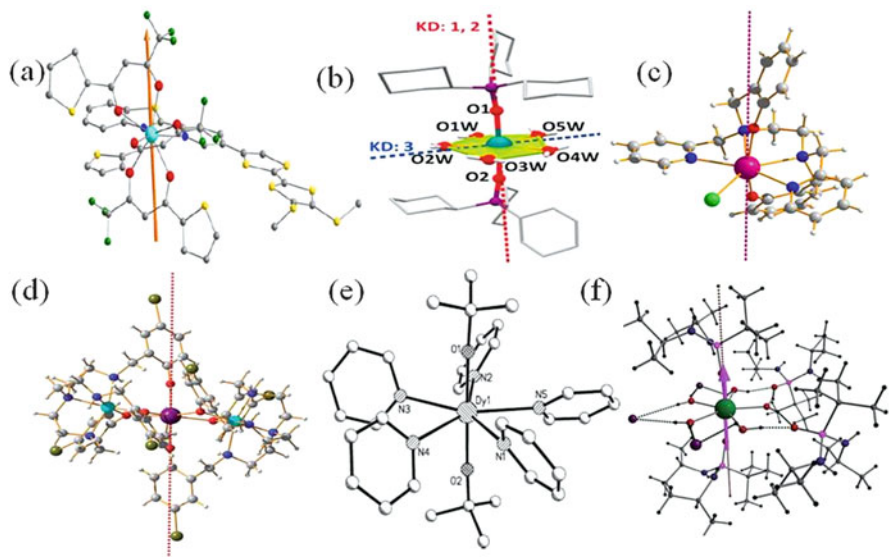




**Fig. 13** (a) Orientation of principal magnetization axis of KD1 in complex **53**. (b) Ab initio spin relaxation dynamics in complex **53**. Arrow shows the orientation of the principal magnetization axis. Colour code: central atom = Dy, light-brown = C and white = H atoms. Reprinted from Guo et al. [22] with permission from John Wiley and Sons

meagre mixing of the  $|\pm M_J\rangle$  wave functions was noted. Up to fourth KD, ideal axiality exists and high axiality retains until fifth KD ( $g_{xx} = 0.08$ ,  $g_{yy} = 0.08$  and  $g_{zz} = 9.12$  for fifth KD, see Table 7 for KD1). Beyond this level, transverse anisotropy components gradually become prominent and for the eighth KD,  $g_{xx}$ ,  $g_{yy}$  component dominates over  $g_{zz}$  components. The  $g_{zz}$  alignments of all the excited KDs lie in parallel fashion with respect to the ground KD (see Fig. 13b for the orientation) with fifth KD forming the largest deviation of  $5.6^\circ$ . All the 16 lowest energy states (8 KDs) possess huge projection on specific  $|M_J\rangle$  state. Among all, the smallest projection was computed to be 0.964 within sixth KD of  $|\pm M_J = \frac{5}{2}\rangle$ . This renders the allocation of all ligand field states of **53** onto one  $M_J$  state lacking mixing of energy states. In accordance with the matrix elements corresponding to the TA-QTM pathway and transverse anisotropic components, relaxation is likely to channel via sixth KD to render  $U_{\text{cal}}$  value of  $1,156 \text{ cm}^{-1}$  against  $U_{\text{eff}}$  value of  $1,277 \text{ cm}^{-1}$  (see Table 7). [22]

Complex **54** is a sandwich complex and the same as complex **53**. The most presumable relaxation for Orbach relaxation in **54** is likely:  $|\pm \frac{15}{2}\rangle \rightarrow |\pm \frac{13}{2}\rangle \rightarrow |\pm \frac{11}{2}\rangle \rightarrow |\pm \frac{9}{2}\rangle \rightarrow |\pm \frac{7}{2}\rangle \rightarrow |\mp \frac{5}{2}\rangle \rightarrow |\mp \frac{7}{2}\rangle \rightarrow |\mp \frac{11}{2}\rangle \rightarrow |\mp \frac{13}{2}\rangle \rightarrow |\mp \frac{15}{2}\rangle$  as per the calculations. Vibrational motions of the C–H groups on Cp<sup>III</sup> ligands induce primary ( $|\pm \frac{15}{2}\rangle \rightarrow |\pm \frac{13}{2}\rangle$ ) relaxation step. Pronounced axial ligand field lends well-defined delineation of the five low-lying KDs as  $|\pm M_J = \frac{15}{2}\rangle$ ,  $|\pm M_J = \frac{13}{2}\rangle$ ,  $|\pm M_J = \frac{11}{2}\rangle$ ,  $|\pm M_J = \frac{9}{2}\rangle$ ,  $|\pm M_J = \frac{7}{2}\rangle$ ,  $|\pm M_J = \frac{5}{2}\rangle$  levels along the Cp–Dy–Cp axis. Model calculation with variations in the coordinated ligand type postulated that: (a) equatorial H atoms, (b) bent nature of Cp–Dy–Cp and (c) eclipsed vs. staggered nature of Cp rings hardly pose impact on anisotropy. This owes to the fact that donor contribution of Cp ring originates from delocalized  $\pi$ -system of ligand and not individual carbon atoms. KD1 is estimated to be Ising



**Fig. 14** (a–f) Molecular structures along with ground state KD orientation for complexes **55–56**, **58** and **60–62**, respectively. Arrows in complexes show the orientation of the principal magnetization axis. Colour code: central atom = Dy, red = O, dark blue/light blue = N, black/dark-brown/light-brown = C, yellow = S, green = Cl and white = H atoms. Reprinted from Gupta et al. [20], Liu et al. [82], Ding et al. [85] with permission from the Royal Society of Chemistry. Reprinted from Guo et al. [55] with permission from Nature Publishing Group. Reprinted from Ding et al. [86] with permission from John Wiley and Sons. Reprinted with permission from Liu et al. [18], Chen et al. [19] Copyright©2016 American Chemical Society

type and axiality retains until fifth KD ( $g_{xy} \sim 0.01$ ) and  $g_{zz}$  alignment of KDs up to fifth KD remains parallel to that of KD1. Though substantial transverse anisotropy arises in sixth KD, smaller deviation between  $g_{zz}$  of sixth and ground KDs provokes relaxation via higher excited energy state. Significant transverse anisotropy ( $g_{xx} = 3.36$ ,  $g_{yy} = 4.30$  and  $g_{zz} = 7.46$ ) in conjunction with  $90^\circ$  divergence of seventh KD- $g_{zz}$  against KD1- $g_{zz}$  unfolds relaxation via seventh KD. This outlines  $U_{\text{cal}}$  value to be  $1,320.7 \text{ cm}^{-1}$  as well validated by the huge crystal field parameter  $B_2^0$  as  $1,226.9$  (see Table 7). Both complexes **53** and **54** show unprecedentedly the largest blocking temperature of 60 K (sweep rate of 22 Oe per second) and  $U_{\text{eff}}$  value of  $1,223 \text{ cm}^{-1}$  (see Table 7) [21]. Sandwich type complexes **53–54** near cylindrical symmetry and accommodation of  $-\text{Cp}$  ligand negative charges in the axial position had their privileges to instigate observation of such desired SIM characteristics.

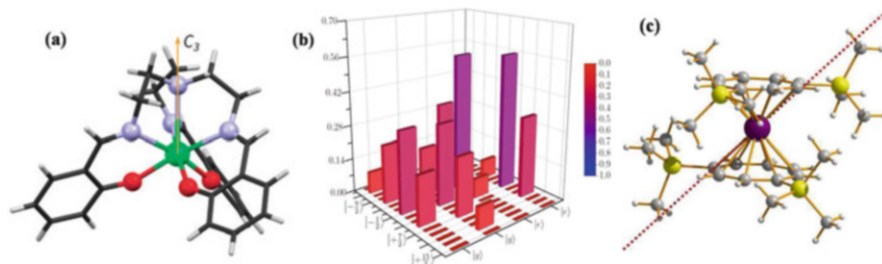
Next complexes for this category are complexes **55** and **55'** which possess distorted square antiprismatic geometry with  $\{\text{DyN}_2\text{O}_6\}$  core (see Fig. 14a). KD1 of polymorphs **55** and **55'** are pure Ising type with  $|\pm M_J| = \frac{15}{2} >$  ground state (see Tables 2 and 7). In **55** and **55'**, relaxation is expected to occur via second and first excited KD, respectively. This can be attributed to the greater matrix elements

corresponding to TA-QTM as 0.32 (within  $\pm 3$ ) and 0.13 (within  $\pm 2$ )  $\mu_B$  for **55** and **55'**, respectively. Additionally, matrix elements pertaining to Orbach process are  $\pm 2 \leftrightarrow \pm 3$  ( $2.55 \mu_B$ ) and  $\pm 1 \leftrightarrow \pm 2$  ( $1.88 \mu_B$ ) for **55** and **55'**, respectively. Large barriers in **55** and **55'** are ascribable to the desired pseudo- $D_{4d}$  symmetry around the central  $Dy^{III}$  ion accentuating the crucial role of symmetry to fine-tune barrier [82]. Complexes **56** and **57** possess identical core structural motif [ $Dy(Cy_3PO)_2(H_2O)_5$ ] $^{3+}$  with variation in anions. Five water molecules in the equatorial plane in conjunction with two  $-Cy_3PO$  ligands in the axial direction lend pseudo- $D_{5h}$  symmetry to both complexes (see Fig. 14b). This provoked relaxation via second excited KD in both the complexes to render larger barrier (see values in Table 7). Matrix element pertinent to TA-QTM within  $\pm 3$  states as 3.0 and 3.2  $\mu_B$  along with significant deviations between KD1 and KD3  $g_{zz}$  orientation provided credentials to the observed barrier. KD1- $g_{zz}$  axis is aligned along the shortest Dy-O chemical bonds as desired. KD1 axiarity as instilled by the desired ligand field symmetry was further corroborated by large negative  $B_2^0$  CFP ( $-1.80$  and  $-1.85$  for **56** and **57**, respectively). [19] Complexes **58** and **59** possess local pseudo- $D_{5h}$  symmetry, where  $Dy^{III}$  ion coordinated by 2 O in axial direction, 4 N in the equatorial plane with other equatorial site is being filled by  $Cl^-$  and  $Br^-$  for **58–59**, respectively (see Fig. 14c). KDs in complex **59** turnout to be more axial than complex **58** leading to larger barrier (see Tables 2 and 7). Additionally, larger axial ( $B_2^0$ ) CFPs and smaller non-axial ( $B_2^2$ ) CFPs in **59** explained the genesis of larger barrier in **59**. Shorter Dy-Cl bond compared to Dy-Br induced greater non-axial CFP in **58**. KD1- $g_{zz}$  is oriented along the two axially located O atoms entailing its consideration vital for anisotropy. Therefore, comparatively shorter Dy-O bond and more linear O-Dy-O angle in **59** lead to larger barrier. Like in earlier cases, significant matrix element corresponding to TA-QTM ( $1.3 \mu_B$  within  $\pm 3$ ) and Orbach processes (between  $\pm 2$  and  $\pm 3$ ;  $2.2 \mu_B$ ) promotes relaxation via  $\pm 3$ , i.e. second excited KD in **58**. However, matrix elements pertinent to TA-QTM within  $\pm 4$  ( $2.5 \mu_B$ ) and Orbach between  $\pm 3$  and  $\pm 4$  ( $2.6 \mu_B$ ) instigate magnetization blockade via third excited KD in **59** (see Tables 2 and 7 for barrier) [18]. In complex **60**, four bridging phenoxy O atoms (also coordinated to the  $Zn^{II}$  ion), one methanol terminal O in equatorial plane along with two axial phenoxy O atoms in axial direction constitutes the pseudo-pentagonal bipyramidal ( $D_{5h}$ ) geometry around  $Dy^{III}$  ion (see Fig. 14d). This ideal symmetry corresponds to pure Ising type ground state anisotropy ( $B_2^0 = -1.72$ ,  $g_{zz} = 19.87$ , see Tables 2 and 7) and leads to larger barrier by suppressing ground state QTM [85]. Large blocking temperature (14 K) in **61** can be attributed to the composite weak equatorial pyridine donor ligands combined with bis-trans-disposed tert-butoxide ligands in the axial direction. This pseudo-pentagonal bi-pyramidal ( $D_{5h}$ ) geometry and near linear O-Dy-O moiety ( $\sim 179^\circ$ ) of **61** reaffirmed the earlier statement of importance of symmetry in achieving larger barrier (see Fig. 14e and Tables 2 and 7). The lower-lying crystal field multiplets follow order  $|\pm M_J = \frac{15}{2}\rangle$ ,  $|\pm M_J = \frac{13}{2}\rangle$ ,  $|\pm M_J = \frac{11}{2}\rangle$ ,  $|\pm M_J = \frac{9}{2}\rangle$  possessing energies 0, 564, 940, 1,141  $cm^{-1}$ , respectively. The consecutive excited levels are mixed type and spread over 1,183–1,237  $cm^{-1}$ . Substantial transverse g-anisotropy

components in conjunction with matrix element pertaining to  $\pm 7$  states provoke relaxation via seventh KD to articulate  $U_{\text{cal}}$  as  $1,220 \text{ cm}^{-1}$  (see Table 7). Electro-positive ligand donor atoms (N of pyridine) in equatorial field in conjunction with electronegative donor atoms in the axial direction constitute the desired crystal field symmetry in **61** leading to a larger barrier [86]. Five water molecules in the equatorial plane and two phosphonic diamide ligands coordinated to metal through phosphorous oxygen (P=O) in the two axial site render pseudo- $D_{5h}$  symmetry around  $\text{Dy}^{\text{III}}$  ion in complex **62** (see Fig. 14f). The axial crystal field symmetry was supported by Ising type KD1 anisotropy ( $g_{zz} = 19.86$ ; see Table 6). KD1- $g_{zz}$  axis is collinear to pseudo- $C_5$  axis and is along Dy-O-P bond vector with divergence of  $4.3^\circ$ . KD2 also maintained axiality ( $g_{zz} = 17.08$ ,  $g_{x,y} = 0.02$ ) and  $g_{zz}$  is aligned almost parallel to that of KD1. Substantial transverse anisotropy ( $g_{zz} = 16.53$ ,  $g_{xx} = 0.58$  and  $g_{yy} = 3.13$ ), mixed type  $\pm M_J$  state ( $\pm \frac{1}{2}$  and  $\pm \frac{15}{2}$ ) and  $\sim 94^\circ$  deviation between KD1 and KD3  $g_{zz}$  orientation channels relaxation via KD3 state. This outlines  $U_{\text{cal}}$  value as  $478.4 \text{ cm}^{-1}$  which is in excellent agreement with the experimental barrier. [20] Complex **63** also possesses pseudo- $D_{5h}$  symmetry which is composed of five equatorial water molecules and two O atoms of  $\text{CyPh}_2\text{PO}$  ligand in the axial positions. Axial nature of KD1 (see Table 6) illustrates pronounced SIM characteristic of **63** in low temperatures. KD1- $g_{zz}$  is oriented along principal rotational axis of pseudo- $D_{5h}$  symmetry and diverges from two axial Dy-O bond vectors by  $2.9^\circ$ . Accounting the  $\sim 90^\circ$  difference between KD1 and KD2- $g_{zz}$  orientations and substantial matrix element pertinent to TA-QTM within  $\pm 2$  ( $0.76 \mu_B$ ) states, relaxation is likely to channel via KD2. This postulates  $U_{\text{cal}}$  value as  $297 \text{ cm}^{-1}$  and confirms pure Ising type ground state anisotropy (see Table 6) [87].

### 3.1.6 Ab Initio studies on Category F Complexes: $\text{Dy}^{\text{III}}$ Single-Ion Magnets with Easy Plane/Hard Axis Anisotropy Behaviour

For the molecules which are discussed in categories A–E, the magnetization axis is easy axis with  $g_{zz}$  sufficiently greater than  $g_{xx}/g_{yy}$  (negligible or small transverse anisotropy). In these cases, molecule lies in collinear fashion with respect to the direction of applied magnetic field. If the  $g_{zz}$  axis is aligned in the perpendicular direction (against the magnetic field application) to the applied field/easy axis, the resultant anisotropy can be assumed as easy plane/hard axis anisotropy. These instances are also exemplified by large concomitant transverse anisotropy components as compared to the magnitude of  $g_{zz}$  value (XY-model). First example in this category will be complex **64** where  $\text{Dy}^{\text{III}}$  ion is found to possess seven coordination numbers with  $\{\text{DyN}_4\text{O}_3\}$  core (see Fig. 15a and Table 2). The geometry around  $\text{Dy}^{\text{III}}$  ion is found to have distorted pentagonal bipyramidal geometry. The  $\chi_{\text{MT}}$  vs. T data in complex **64** can be ascribed to the depopulation of the excited sublevels. In order to assess their compatibility with the earlier reported crystal field parameters of **64**, EVALUCF software was employed to estimate the CFPs. The impact of ligand field over various energy multiplets (generated by SOC coupling) was derived through



**Fig. 15** (a, c) Molecular structures of complexes **64–65**, respectively. (b) Pictorial representation of wave-function composition in complex **64**. Arrow in complexes shows the orientation of the principal magnetization axis. Colour code: central atom = Dy, red = O, light blue = N, black/light-brown = C, yellow = Si and white = H atoms. Reprinted from Lucaccini et al. [88] with permission from the Royal Society of Chemistry. Reprinted with permission from Le Roy et al. [89] Copyright©2013 American Chemical Society

**Table 8** List of complexes {from category F} with pertinent experimental energy barrier ( $U_{\text{eff}}$ , in  $\text{cm}^{-1}$ ), ab initio computed energy barrier ( $U_{\text{cal}}$ , in  $\text{cm}^{-1}$ ), main magnetic g factors and crystallographic structural information

	$U_{\text{eff}}$	$U_{\text{cal}}$	$g_{xx}-g_{yy}$	$g_{zz}$	Type of coordinated atoms	Structure	Ref.
<b>64</b>	$7 \pm 1$	50 <sup>a</sup>	$9.4 \pm 0.5$	$1.8 \pm 0.1$	4 N, 3 O	–	[88]
<b>65</b>	17.4	15.6	10.7	1.35	Sandwich complexation (two $\text{COT}^{2-}$ in $\eta^8$ -fashion)	–	[89]

<sup>a</sup>Computed harnessing the procured crystal field parameters

crystal field parameterization within Wybourne's formalism ( $\text{Dy}^{\text{III}}$  ion is on  $C_3$  axis in **64**). This methodology does not utilize any free parameters and nicely replicate the experimental magnetic data as well as earlier reported crystal field parameters. This approach permitted direct comparison with luminescence data and allows easy inclusion of excited energy multiplets for further reference. Subsequent diagonalization rendered eigenvalues and eigenvectors of  $|J, M_J\rangle$  components by defining ground–first excited gap as  $50 \text{ cm}^{-1}$  (see Table 8). The same approach lends estimation of effective g parameters, i.e.  $g_{\perp}^{\text{eff}} = 9.6$  and  $g_{\parallel}^{\text{eff}} = 2.2$  (see Table 8) evoking easy plane type anisotropy for complex **64**. Smaller energy difference and easy plane anisotropy nature were supported by the mixed ground multiplet wave-function type as:  $8.7\% |\pm\frac{13}{2}\rangle > +24.3\% |\pm\frac{7}{2}\rangle > +33.1\% |\pm\frac{1}{2}\rangle > +20.2\% |\pm\frac{5}{2}\rangle > +5.3\% |\pm\frac{11}{2}\rangle$ . Contrary to necessary requirement of larger  $|\pm M_J\rangle$  stabilization towards achieving higher barrier, ground multiplet is dominated by the stabilization of smaller  $|\pm M_J\rangle$  components in **64**. However, first excited state wave-function composition was subjugated by larger  $|\pm\frac{3}{2}\rangle$  and  $|\pm\frac{9}{2}\rangle$  components of the energy level (see Fig. 15b) [88]. Complex **65** is a sandwich complex of  $\text{Dy}^{\text{III}}$  ion (see Fig. 15c and Table 2). Stabilization of  $|\pm M_J = \frac{1}{2}\rangle$  energy multiplet in complex **65** was exemplified by estimated g factors:  $g_{xx} = 10.67$ ,  $g_{yy} = 10.63$  and  $g_{zz} = 1.35$  (see Table 8). The  $KD1-g_{zz}$  axis point is amidst the two  $\text{COT}^{2-}$  ligands and goes through

the Dy<sup>III</sup> ion. This testifies prominent impact of the distant silyl groups over the alignment of KD1- $g_{zz}$  axis. Eighth KD in complex **65** is found to be highly axial ( $g_{zz} = 19.99$ ,  $g_{xx} = g_{yy} = 0$ ). This unfolds the fact that replacement of Dy<sup>III</sup> by Er<sup>III</sup> ion might lead to improved SIM behaviour of the same complex [89].

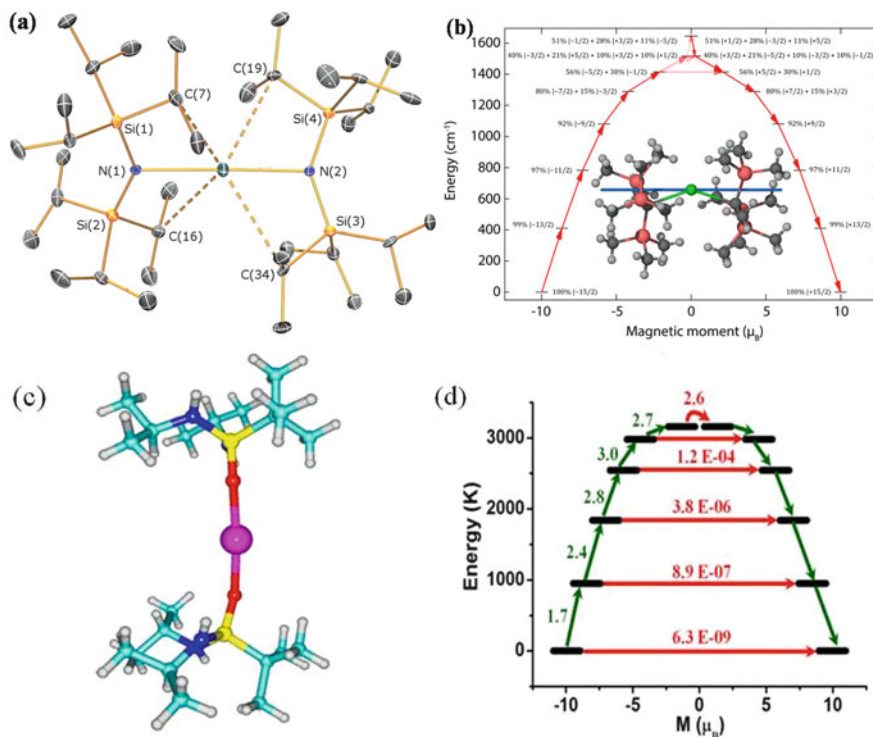
### 3.2 Model Complexes Predicted Using *Ab Initio* Calculations

To put an end to the ongoing argument of suitable geometry, symmetry, coordination number and type of metal ions towards achieving the best SIMs characteristics, calculations were carried out on several models to gain intuitive understanding and to make viable predictions. While *ab initio* calculations have proven track record to yield magnetic properties of lanthanide compounds with great accuracy, employing this methodology for predictions is at its infant stage. Here, we intend to cover such predictions and related experimental verification of the same/similar ideas, if available, already in the literature.

First of this kind here is complex **66** where originally X-ray structure is reported for the Sm<sup>III</sup> analogue and *ab initio* calculations are performed by replacing the Sm<sup>III</sup> by Dy<sup>III</sup> ion (see Fig. 16a). Calculations reveal the six lowest KDs as  $| \pm M_J \rangle = | \pm \frac{15}{2} \rangle$ ,  $| \pm \frac{13}{2} \rangle$ ,  $| \pm \frac{11}{2} \rangle$ ,  $| \pm \frac{9}{2} \rangle$ ,  $| \pm \frac{7}{2} \rangle$  where all have identical quantization axis. Accounting negligible matrix elements pertinent to QTM and TA-QTM pathways,  $U_{\text{cal}}$  can be outlined as  $\sim 1,800 \text{ cm}^{-1}$ . The barrier is one of the largest known and owes to the near linear N-Dy-N ( $\sim 176^\circ$ ) structural moiety unleashing targeted synthesis towards this direction [90]. Besides this prediction, magneto-structural correlation was performed. This discarded the need for  $\angle$ ligand-Dy-ligand to approach towards  $180^\circ$ . Instead, the essential need for two-coordinate Dy<sup>III</sup> complexes was established towards achievement of larger energy barrier. To testify this, calculations were carried out on model **67** where  $\angle$ C-Dy-C =  $137^\circ$  and  $143^\circ$ . For these geometries, the  $U_{\text{cal}}$  values were turned out to be  $\sim 1,247$  and  $1,484 \text{ cm}^{-1}$ , respectively, against the predicted of  $1,800 \text{ cm}^{-1}$  for **66** (see Fig. 16b). From both the model calculations, two-coordinate Dy<sup>III</sup> systems seem to be extremely desirable. Besides, other model calculations evoked mitigation of barrier upon coordination of solvent molecule [91]. Apart from these two coordinate models, there are also other models predicted from the existing structures. For example, **62'** modelled by the removal of five water molecules coordinated in the equatorial plane of the Dy<sup>III</sup> ion in complex **62** found to yield substantially higher barrier height (more than  $2,085 \text{ cm}^{-1}$ ). The Dy-O interactions present in **62'** are stronger than Dy-C interaction in **66** and the presence of higher symmetry quenches the tunnelling leading to very large barrier height (see Fig. 16c, d). The computed  $U_{\text{cal}}$  value for this model is one of the largest reported to date; however, these predictions are yet to be tested.

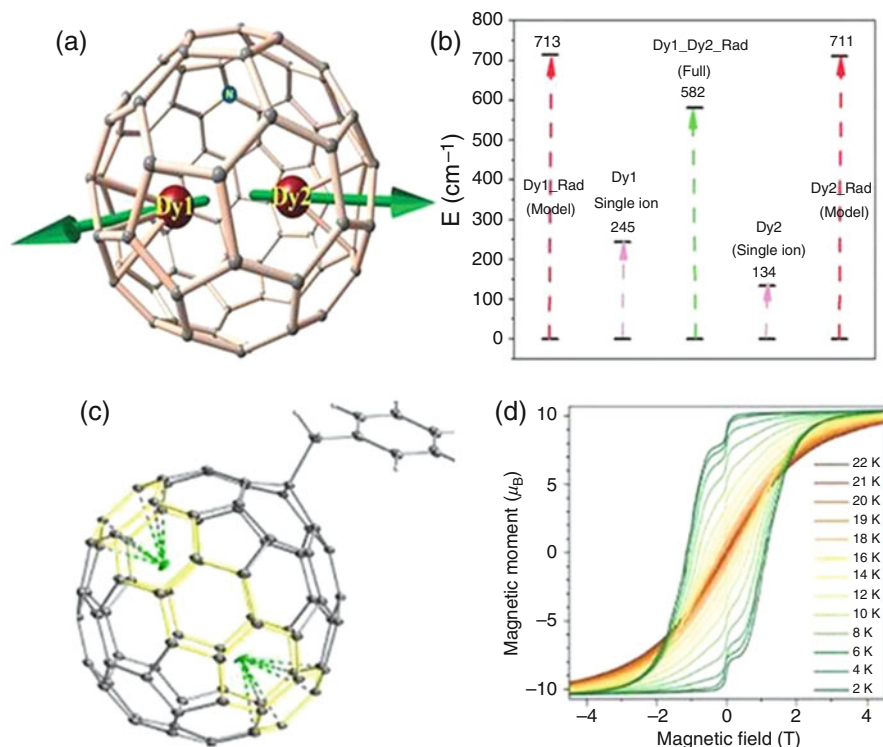
Another area where prediction seems to taken a lead in the SIMs synthesis is lanthanide encapsulated fullerene molecules that are predicted to possess interesting magnetic properties. For example, model complex **68** is an example of endohedral





**Fig. 16** (a, c) Molecular structures for complexes **66** and model **62'**, respectively. (b) Ab initio calculated relaxation dynamics for complex **67**. (d) Relaxation dynamics for model **62'**. Arrows in complexes show the orientation of the principal magnetization axis. Colour code: central atom = Dy, red = O, dark blue = N, black/dark-brown/cyan = C and white = H atoms. Reprinted from Gupta et al. [20], Chilton et al. [90] with permission from the Royal Society of Chemistry. Reprinted with permission from Chilton [91] Copyright©2015 American Chemical Society

radical hetero-metallo-fullerene molecule. Originally,  $\text{Gd}_2@C_{79}\text{N}$  has been originally reported to possess  $S = \frac{15}{2}$  ground state. Calculations that were initially performed by DFT methods reveal unusually large exchange interaction between radical and  $\text{Gd}^{\text{III}}$  ion [92]. The values are nearly by an order magnitude larger ( $400 \text{ cm}^{-1}$ ) than the radical- $\text{Gd}^{\text{III}}$  coupling known in the literature ( $27 \text{ cm}^{-1}$  reported for the recorded high exchange reported experimentally for  $\{\text{Gd}_2\text{N}_2^{3-}\}$  complex) [93, 94]. Very recently, magnetic susceptibility measurement coupled with EPR techniques verifies this prediction, where experimental  $J$  values are reported to be  $350 \pm 20 \text{ cm}^{-1}$  [95]. Additionally, calculations were performed by replacing the  $\text{Gd}^{\text{III}}$  ions by  $\text{Dy}^{\text{III}}$  ions. The Dy sites in model **68** bind in  $\eta^7/\eta^6$  fashion with the hexagonal ring to deliver the strongest predicted exchange coupling along one of the axial directions (see Fig. 17a). Additionally, another weaker coupling was noted for **68** due to the presence of second  $\text{Dy}^{\text{III}}$  centre. The eight KDs span over a window of  $837$  and  $786 \text{ cm}^{-1}$  for Dy1 and Dy2 centres, respectively. KD1 for both the sites



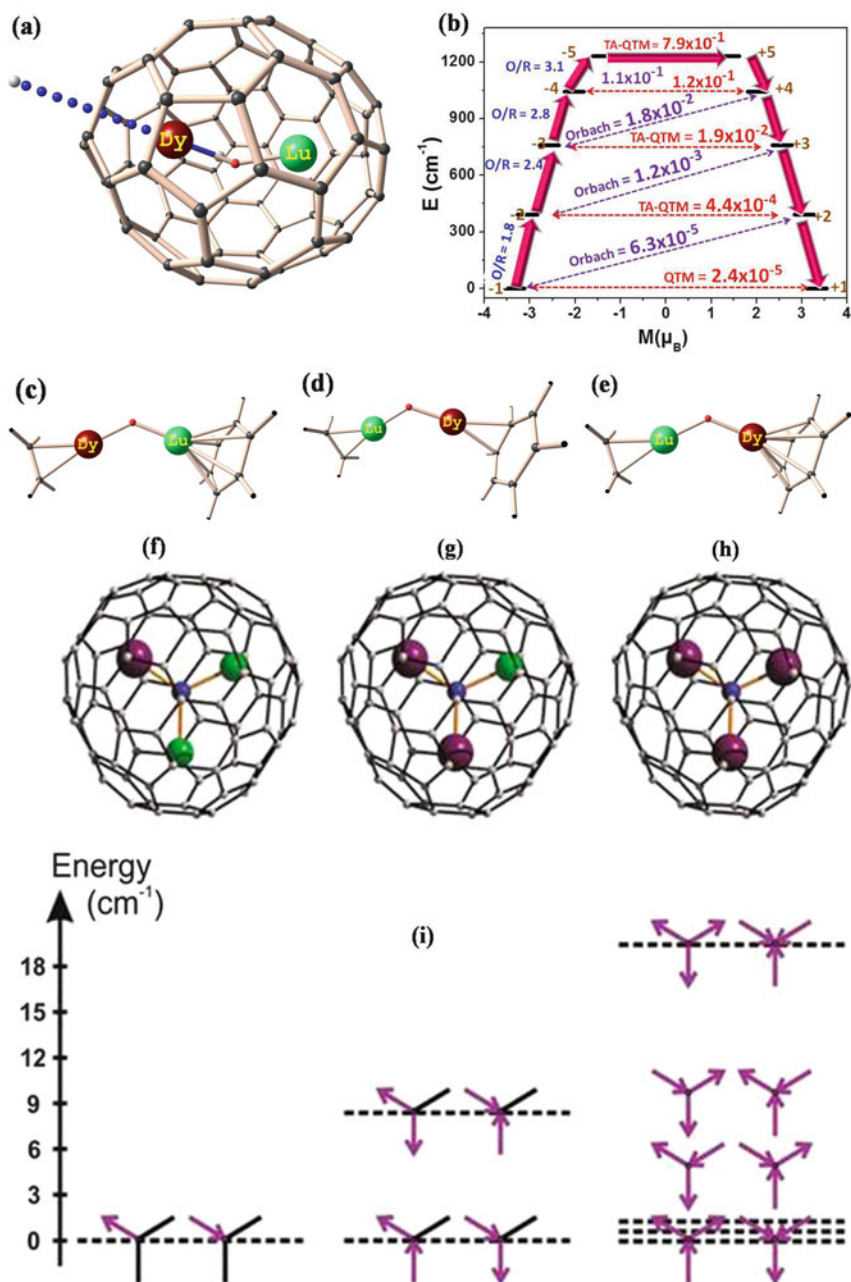
**Fig. 17** (a, c) Representative molecular structures for complexes **68** and **68'**. (b) Ab initio calculated  $U_{\text{cal}}$  for complex **68** and (d) magnetization curves measured at various temperatures with the field sweep rate of  $2.9 \text{ mTs}^{-1}$  for complex **68'**. Arrows in complex **68** show the orientation of the principal magnetization axis. Colour code: central chocolate/green atoms = Dy, blue = N, dark-brown = C and white = H atoms. Reprinted from Singh et al. [92] with permission from the Royal Society of Chemistry. Reprinted from Liu et al. [96] with permission from Nature Publishing Group

are estimated to be pure Ising type ( $g_{xx} = g_{yy} = 0$ ,  $g_{zz} = 19.98$  and  $19.88$  for Dy1 and Dy2 centres, respectively) indicating negligible QTM ( $0.0006 \mu_{\text{B}}$ ) contribution within ground multiplet.  $\text{KD1-}g_{zz}$  lies along pseudo- $\text{C}_6$  axis of the hexagonal ring. Accounting for substantial matrix element and deviation between  $g_{zz}$  axes, relaxation for both Dy sites is likely to channel via KD2. This postulates the  $U_{\text{cal}}$  value as  $244.5 \text{ cm}^{-1}$  and  $134.3 \text{ cm}^{-1}$  for Dy1 and Dy2 centres, respectively. The discrepancy between the barrier values of two Dy centres can be ascribed to the varying coordination mode with Dy1 centre interacting strongly with  $\text{C}_{79}\text{N}$  compared to the Dy2 site. Large ground–first excited level gap for the centres can be attributed to the large value of CFP  $B_2^0$  as  $-4.54$  for both centres. To have intuitive understanding of the exchange spectrum, two types of models were employed, where each of them contained one paramagnetic  $\text{Dy}^{\text{III}}$  ion along with radical hetero-fullerene, while other  $\text{Dy}^{\text{III}}$  ion is being substituted by a diamagnetic  $\text{Lu}^{\text{III}}$  ion. Ground state exchange doublets for both the models are pure Ising type with  $g_{xx} = g_{yy} \sim 10^{-8/-9}$  and



$g_{zz} = 21.9$ . In both the centres, sufficient tunnel splitting within first excited exchange doublets spurs relaxation via that level and this outlines  $U_{\text{cal}} \sim 710 \text{ cm}^{-1}$  for both centres. This increase in the energy separation between the ground to the first excited state is attributed to the very large magnetic exchange between Dy-radical centres. For more accurate model consideration, exchange spectrum containing both Dy centres and radical was constructed harnessing  $J_{\text{Dy-rad}} = +285.7 \text{ cm}^{-1}$  and  $J_{\text{DyDy}} = -0.3 \text{ cm}^{-1}$ . Considering substantial tunnel splitting,  $U_{\text{cal}}$  value from this model can be estimated as  $582 \text{ cm}^{-1}$  (see Fig. 17b). This decrease in the energy separation between the ground to the first excited state with respect to Dy-radical model is attributed to the weak magnetic exchange between both Dy-Dy centres. Hence, in all the employed exchange-coupled models,  $U_{\text{cal}}$  value is found to be larger than that for single-ion  $\text{Dy}^{\text{III}}$  ion. So, like earlier discussion, exchange is likely to play proactive role in increasing the barrier by suppressing the QTM propensity [92]. Popov and co-workers have synthesized analogous  $\text{Dy}_2@C_{80}(\text{CH}_2\text{Ph})$  EMF (**68'**) possessing very strong exchange coupling between  $\text{Dy}^{\text{III}}$  and radical fullerene cage leading to a  $U_{\text{eff}}$  value as high as  $426 \text{ cm}^{-1}$  and a reported blocking temperature of 18 K. Hetero-fullerenes are expected to have larger magnetic exchange constant value because the unpaired electrons are found to be localized between two  $\text{Dy}^{\text{III}}$  ions enhancing the charge-transfer contribution and hence the exchange coupling constants are expected to show even higher  $U_{\text{eff}}$  values (see Fig. 17c, d) [96].

Like previous one, models **69–71** exemplify three different endohedral metallofullerenes (EMF) that encapsulate  $\{\text{DyO-Lu/Sc}\}^{4+}$  unit inside  $C_{72}$ ,  $C_{76}$  and  $C_{82}$  fullerene cages, respectively (see Fig. 18a). In these studied EMFs for DyO-Lu/Sc@ $C_{76}$  (**70**) model, four different isomers were also studied to ensure the effect of different isomers of a given fullerene on anisotropic properties. In all these models,  $\text{Dy}^{\text{III}}$  ion is ligated to hexagonal/pentagonal aromatic ring inside the fullerene ring where Dy-C distances are evaluated in the range of 2.4–2.6 Å. The Dy-O distances are found to be in the range of 2.0–2.1 Å and this articulates stronger axial interaction with the O atoms. For DyOLu@ $C_{76}$ , isomer DyOLu@ $C_{76-1}$  (**70a**) is computed to possess the lowest energy (ground state,  $C_s$  symmetry). The other isomers DyOLu@ $C_{76-2}$  (**70b**), DyOLu@ $C_{76-3}$  (**70c**) and DyOLu@ $C_{76-4}$  (**70d**) are located at 6.2, 41.1 and 55.2 kJ/mol energy higher than corresponding **70a**. For complex **69**, the  $\text{Dy}^{\text{III}}$  ion and  $C_{72}$  cage exhibit  $\eta^6$  interaction with six-membered ring. However, for **70a** and **71**,  $C_{76}$  and  $C_{82}$  cages render  $\eta^2$  interaction with six-membered ring. Eight KDs in **69–71** spread within an energy window of 1,475–1,625  $\text{cm}^{-1}$  (see Fig. 18b). KD1 of  $\text{Dy}^{\text{III}}$  sites in all cases are pure Ising type ( $g_{zz} = 19.98$ ,  $g_{xx} = g_{yy} = 0$ ) with stabilization of  $|M_J = \pm \frac{15}{2}| >$  ground state. Mechanism developed suggests that the relaxation is likely to occur via KD2 in **69–70** and third excited state (KD4) in complex **71**. This renders  $U_{\text{cal}}$  value of 451.6, 396.7, 425.7, 487.0, 476.6 and 1,220.3  $\text{cm}^{-1}$  for **69**, **70a**, **70b**, **70c**, **70d** and **71**, respectively. With the increase in fullerene cage size, the equatorial interaction of aromatic ring with  $\text{Dy}^{\text{III}}$  ion is progressively minimized. This instigates mitigation of transverse anisotropic properties in conjunction with proportional enhancement in the magnitude of the barrier



**Fig. 18** (a, f–h) Representative molecular structures for complexes 69–77. (b) Spin relaxation dynamics for complex 74 (c–e) models a–c, respectively. (i) The magnetic structure of the pertinent Ising like states is reflected above with schematic local magnetic moments locating along Dy–N bonds for complexes 75–77. Arrows in complexes show the orientation of the principal magnetization axis. Colour code: central chocolate/violate atom(s) = Dy, red = O, blue = N, dark-

height. To facilitate procurement of extensive testament, three models have been developed with ethylene,  $\eta^2$ -benzene and benzene interacting with Dy<sup>III</sup> ion (models **a–c**, see Fig. 18c–e) offering different Dy- $\pi$  interactions. The models were constructed in resemblance to the lanthanide–fullerene interactions with C<sub>82</sub>, C<sub>76</sub> and C<sub>72</sub> species, respectively. For models **a–c**, as we move towards right, progressive reduction in the barrier values were detected ( $U_{\text{cal}}$  of 2,059, 1,603 and 1,424 cm<sup>-1</sup> for **a–c**, respectively). All the aforementioned **69–71** studied structures were modified by substituting Lu<sup>III</sup> with Sc<sup>III</sup> (corresponding **72–74**) to undertake detailed analysis. In the resultant modified structures, Ln-O-Sc possesses larger angles compared to Ln-O-Lu analogue owing to stronger Sc-O interaction and smaller Sc ionic radius. Like Lu<sup>III</sup> ion analogues, their corresponding Sc analogues also render pure Ising type KD1 anisotropy. Considering the foregoing contributing factors towards determining relaxation phenomena, magnetization blockade is likely to be observed via fourth excited KD in all Sc<sup>III</sup> analogues. This articulated  $U_{\text{cal}}$  value of 1,191, 1,189, 1,231, 1,341, 1,346 and 1,406 cm<sup>-1</sup> for DyOSc@C<sub>72</sub> (**72**), DyOSc@C<sub>76</sub>(a–d) (**73**) and DyOSc@C<sub>82</sub> (**74**) EMFs, respectively. To understand these observations, magneto-structural correlation was carried out on some models (model **a**, see Fig. 18c). With proportional increase of Dy-O-Lu angle, increment in  $U_{\text{cal}}$  value was noted essentially due to achievement of higher symmetry. The DyOSc@C<sub>82</sub> (**74**) EMF turns out to possess one of the highest  $U_{\text{cal}}$  values for EMF based SIMs (1,406 cm<sup>-1</sup>, see Fig. 18b) [97]. Recently, Popov and co-workers have synthesized two isomers of Dy<sub>2</sub>S@C<sub>82</sub> EMF {C<sub>3v</sub>(8) and C<sub>s</sub>(6)} with three ensuing Orbach processes having energy barriers of 7, 33 and 856 cm<sup>-1</sup> for the former isomer and with two energy barriers of 11 and 364 cm<sup>-1</sup> for the latter isomer. Oxygen is known to be a stronger ligand compared to sulphur and the axial ligand field for the former is expected to be stronger and therefore Dy<sub>2</sub>O@fullerenes are expected to be superior compared to the corresponding sulphur analogues [99].

Complexes **75–77** are series of Dy-Sc-EMFs with Dy<sub>*n*</sub>Sc<sub>3-*n*</sub>N@C<sub>80</sub> structural motif and *n* varies from 1 to 3 for **75–77**, respectively (see Fig. 18f–i). In all three structures studied, the Dy<sub>*n*</sub>Sc<sub>3-*n*</sub>N unit presents with the N atom at the centre of the triangle. KD1 of Dy<sup>III</sup> centre in **75** and two Dy<sup>III</sup> centres of **76–77** exhibit pure Ising type anisotropy. The corresponding  $g_{zz}$  values vary in the range of 19.84–19.88 with  $g_{xy}$  lying in the range of  $\sim 10^{-4/-5}$ . Even the KD2 for all Dy sites are found to be axial with the  $g_{zz} = 16.96$ –17.10 and  $g_{xx} = g_{yy} = 10^{-4/-5}$ . Such strong axiality implied pure  $|\pm M_J = \frac{15}{2} >$  and  $|\pm M_J = \frac{13}{2} >$  characters of the KD1 and KD2 level, respectively. The eight KDs span over an energy window of  $\sim 1,500$  cm<sup>-1</sup> in **75–77** and this split for atomic <sup>6</sup>H<sub>15/2</sub> multiplet is very unusual and larger compared to other Dy systems. This can be rationalized by the efficient contribution from N to the ligand field splitting of <sup>6</sup>H<sub>15/2</sub> multiplets. KD2 lies at 415, 507/393 and 555/569/



**Fig. 18** (continued) brown = C, light green = Lu, dark green = Sc and white = H atoms. Reprinted from Singh and Rajaraman [97] with permission from the Royal Society of Chemistry. Reprinted with permission from Vieru et al. [98] Copyright©2013 American Chemical Society

610  $\text{cm}^{-1}$  higher than the ground doublet for **75**, two Dy centres of **76** and three Dy centres of **77**, respectively. In order to assess the role of fullerene cage, calculations were undertaken on isolated  $[\text{DySc}_2\text{N}]^{6+}$  unit. Alleviation of Dy ligand field splitting ( $\sim 30\%$ ) was observed upon removal of the fullerene cage ( $U_{\text{cal}} = 327 \text{ cm}^{-1}$ ). The Dy-N bonds strongly interact with the fullerene cage. This has reduced the axiality of the lowest KDs and directs  $g_{zz}$  axis far from this bond vector. Strong local axiality of Dy sites, larger energy separation among ground and excited energy doublets, diminishes the coupling between the lowest KDs on Dy sites to the identical non-collinear Ising form. The Dy-Dy coupling in complexes **76** and **77** is quite significant contrasting the general notion of weaker 4f-4f interaction. The stronger exchange owes to stronger Dy-N bond, which also impinged on the larger ligand field splitting of the single-ion Dy centres. Non-Kramers exchange-coupled complex **76** shows degenerate ground exchange doublets ( $\Delta_{\text{tun}} = 10^{-10} \text{ cm}^{-1}$ ) possessing  $g_{zz} = 34.13$ . First excited exchange doublet lying at  $\sim 8 \text{ cm}^{-1}$  above also is strongly axial and degenerate ( $\Delta_{\text{tun}} = 10^{-9} \text{ cm}^{-1}$ ). Quenched QTM within ground exchange doublet invokes the occurrence of two relaxation processes in **76**. The higher temperature relaxation corresponds to relaxation via local excited levels of individual Dy centres ( $393/507 \text{ cm}^{-1}$ ) and low-temperature relaxation pertains to overcoming the exchange energy barrier ( $\sim 8 \text{ cm}^{-1}$ ). Exchange splitting in **77** ( $\sim 19 \text{ cm}^{-1}$ ) is stronger than **76** due to four additional Dy-Dy interactions in the former. All the four lowest-lying exchange doublets in **77** are strongly Ising type ( $\Delta_{\text{tun}} = 10^{-7/8} \text{ cm}^{-1}$ ). First three lowest-lying exchange doublets possess  $g_{zz} \approx 40$  while the most highly energetic fourth exchange doublet shows  $g_{zz} \approx 3$ . The three low-lying exchange doublets are quasi-degenerate with energy split over  $\sim 1 \text{ cm}^{-1}$ . This outcome is ascribable to the underlying net Ising type interaction and different magnitude of interactions between Dy2 and Dy3 centre. Such unique quasi-degeneracy of the low-lying ground exchange doublets of **77** induces magnetic frustration. This subsequently promotes QTM within the ground exchange doublet and undermines the SMM behaviour and renders the weakest SMM behaviour (than **75** and **76**) [98].

Intrusion of small magnetic units  $\{[\text{LnX}]^{-f/4+}\}$  into cages turns out to be a potential strategy towards ameliorated SMM behaviour. The distance between cage and Dy was systemically changed in a hypothetical  $[\text{DyO@C}_{60}]^+$  complex (**78**). Computational studies performed on complex **78** revealed that the *Ising* doublet eigenstates are energetically arranged chronologically in terms of both the  $M_J$  value and the energy spacing, with  $|M_J| = \frac{15}{2} >$  as the ground state doublet. The magnitudes of  $U_{\text{cal}}$ , which are subject to the Dy-O bond length, can attain a value as high as  $2,100 \text{ cm}^{-1}$  [60].

### 3.3 Review on $\text{Er}^{\text{III}}$ Containing Single-Ion Magnets

Literature perusal indicates study on  $\text{Dy}^{\text{III}}$ -based SMMs is prevalent due to very strong magnetic moment and  $|\pm M_J| = \frac{15}{2} >$  value of corresponding  $\text{Dy}^{\text{III}}$  ion. In recent years, the study of another lanthanide ion ( $\text{Er}^{\text{III}}$ ,  $^4\text{I}_{15/2}$ ) containing identical  $M_J$

value has gradually transpired.  $\text{Er}^{\text{III}}$  is a prolate type ion with axially located 4f electron density and entails strong equatorial crystal field to stabilize the highest angular momentum projection. Notably, we abstain ourselves from discussing the di-, or polynuclear  $\text{Er}^{\text{III}}$  based SMMs and are confined within SIMs with zf-SIM behaviour or likely to show zf-SIM behaviour. Series of  $\text{Er}^{\text{III}}$  complexes, **79–82** (see Table 2 for molecular formula), were theoretically investigated using ab initio calculations to check the influence of symmetry and structural distortions on the magnetic anisotropy. Complex **79** has a distorted square antiprism geometry with  $\{\text{ErN}_2\text{O}_6\}$  core. Complexes **80–82** are sandwich type structures. With single-ion anisotropic properties, nice agreement between experimental and theoretical magnetic data has been demonstrated in all the four complexes. Except for complex **79**, all three complexes possess pure Ising type ground state anisotropy. On the other hand, KD1 in **79** is axial with significant transverse anisotropic contribution.  $\text{KD1-}g_{zz}$  is aligned towards one of the  $-\text{N}$  donors of  $-\text{bath}$  ligand and deviates from  $\text{Er-N}$  bond by  $25.8^\circ$ . Two different  $U_{\text{eff}}$  values observed experimentally can be attributed to the presence of two conformations of the  $-\text{Me}$  groups present in the  $-\text{thd}$  ligands (where  $\text{thd} = (2,2,6,6\text{-tetramethyl-}3,5\text{-heptanedionate})$ ;  $\text{bath} = \text{bathophenanthroline}$ ). Concomitant transverse KD1 anisotropy promotes ground state QTM propensity as corroborated by corresponding matrix element of  $0.35 \mu_{\text{B}}$ . This pathway complies nicely with the observed fast relaxation of magnetization. However, matrix elements corresponding TA-QTM/Orbach involving  $\pm 2$  evoked relaxation via KD2 and this corresponds to the observed slow magnetization relaxation outlining  $U_{\text{cal}}$  value as  $37 \text{ cm}^{-1}$  (see Table 9). Calculations on model complex reflect no impinge of methyl group rotation on the magnitude of the barrier. In complex **80**,  $\text{KD1-}g_{zz}$  axis is directed along the main  $\text{C}_3$  axis which passes through the centre of COT ligand. The Ising type KD1 with no transverse  $g$  anisotropic components rationalized the large difference in the magnitudes of barrier height computed between **79** and **80–82**. High symmetry in **80** and **81** led to collinearity among the  $g_{zz}$  orientations up to sixth KD. However, stabilization of  $|M_J = \pm \frac{1}{2}\rangle$  state in the second excited KD of **80–81** provokes relaxation via this level. However, the absence of exact symmetry in complex **82** (**79** as well) causes prominent non-collinearity between KD1 and KD2  $g_{zz}$  axes instigating relaxation via KD2 itself (see Table 9 for estimated barrier values). The computed barrier height reflects a trend of **80** > **81** > **82** > **79** and this is in accordance with the attenuation of computed axial crystal field parameters. In order to put an end to ongoing contention of appropriate coordination number around metal ion, calculations were carried out on various  $[\text{Dy/Er}(\text{OH})_n]^{m+}$  models. Among all the appraised models, three-coordinated  $\text{D}_{3\text{h}}$  and four-coordinated  $\text{D}_{4\text{h}}$  models are computed to possess the largest barrier heights. This owes to the extensive stabilization of the equatorial crystal field for the prolate type  $\text{Er}^{\text{III}}$  ion by the favourable negatively charged  $-\text{OH}$  groups (see Fig. 19a). In similar context, calculations on  $[\text{Dy}(\text{OH})_n]^{m+}$  models indicated two-coordinated model to be most appropriate. Contrarily, two-coordinated model for  $\text{Er}^{\text{III}}$  ion does not exhibit any SMM behaviour due to lack of equatorial ligation. Model calculations affirmed crucial importance of high symmetry towards achievement of ameliorated anisotropy behaviour [118]. In

**Table 9** Complexes (79–119) with pertinent experimental energy barrier ( $U_{\text{eff}}$ , in  $\text{cm}^{-1}$ ), ab initio computed energy barrier ( $U_{\text{cal}}$ , in  $\text{cm}^{-1}$ ), main magnetic g factors and crystallographic structural information

	$U_{\text{eff}}$	$U_{\text{cal}}$	$g_{\text{xx}}$	$g_{\text{yy}}$	$g_{\text{zz}}$	Type of coordinated atoms	Structure of complex	Ref.
<b>79</b>	10.83, 15.55	37.0	0.67	1.41	14.88	2 N, 6 O	Distorted square antiprismatic	[100]
<b>80</b>	150.1	280.4	0.00	0.00	17.94	$\pi$ -coordination ( $\eta^8$ -fashion)-All C	Sandwich type	[100]
<b>81</b>	130.0	247.1	0.00	0.00	17.94	$\pi$ -coordination ( $\eta^8$ -fashion)-All C	Sandwich type	[100]
<b>82</b>	136.9	164.5	0.00	0.00	17.92	$\pi$ -coordination ( $\eta^8$ -fashion)-All C	Sandwich type	[100]
<b>82'a</b>	137	84.8	0.00	0.00	17.94	$\pi$ -coordination ( $\eta^8$ -fashion)-All C	Sandwich type	[100]
<b>82'b</b>	224	115.9	0.00	0.00	17.94	$\pi$ -coordination ( $\eta^8$ -fashion)-All C	Sandwich type	[100]
<b>83</b>	85	331	0.00	0.00	17.88	3 N	Distorted trigonal planar	[80]
<b>84</b>	–	76	0.03	0.64	16.20	3 N, 2O	Distorted trigonal bipyramidal	[80]
<b>85</b>	44	118	0.02	0.02	17.81	3 N, 1 Cl	Distorted tetrahedral	[101, 102]
<b>85a</b>	44	118	0.02	0.02	17.80	3 N, 1 Cl	Distorted tetrahedral	[101, 102]
<b>86</b>	3.6, 35.7	48.9, 104.9	1.03, 0.04	2.77, 0.07	13.99, 15.79	10 O	Distorted bicapped square antiprismatic	[103]
<b>87</b>	74	58.7	10.77	8.33	1.20	8 N	–	[54]
<b>88</b>	199	194.0	$3.5 \times 10^{-6}$	$3.5 \times 10^{-6}$	17.96	$\pi$ -coordination ( $\eta^8$ -fashion)-All C	Sandwich type	[13]
<b>89</b>	22 $\pm$ 1	54 <sup>a</sup>	1.2		13	4 N, 3 O	Distorted monocapped octahedron	[104]
<b>89 (122 K)</b>	20.54	67.58	1.85, <sup>b</sup> 2.18	1.85, 2.18	14.23, 13.81	4 N, 3 O	Distorted monocapped octahedron I	[104]
<b>89 (293 K)</b>	20.54	64.52	1.83, <sup>b</sup> 2.28	1.83, 2.28	14.26, 13.68	4 N, 3 O	Distorted monocapped octahedron	[104]

<b>90</b>	No mention	13.2, 13.5	4.96, <sup>b</sup> 5.27	4.97, 5.28	8.66, 7.79	4 N, 3 O	Distorted monocapped octahedron	[104]
<b>91</b>	No mention	21.3, 15.8	0.87, 0.53	1.30, 1.62	14.10, 13.07	4 N, 3 O	Distorted monocapped octahedron	[104]
<b>92</b>	27.1, 34.1	19.8	1.8	2.8	10.9	4 O, 4 N	Square antiprismatic	[105]
<b>93</b>	4.9	187.9	3.21	2.69	1.76	6 O	Trigonally distorted octahedron with fac-term	[106]
<b>94</b>	20.2, 24.3	197.2	0.1	1.0	6.8	4 O, 4 N	Square antiprismatic	[105]
<b>95</b>	Not SIM	1.6	0.5	2.1	12.7	4 O, 4 N	Square antiprismatic	[105]
<b>96</b>	Not SIM	4.8	1.3	3.3	6.2	4 O, 4 N	Square antiprismatic	[105]
<b>97</b>	Not SIM	4.6	0.95	1.02	12.02	4 O, 4 N	Square antiprismatic	[105]
<b>98</b>	Not performed	160	0.03	0.61	7.39	5 O, 4 N	Capped square antiprismatic	[107]
<b>99</b>	Not performed	-	4.47	4.40	0.92	4 O, 4 N, 1 F	Capped square antiprismatic	[107]
<b>100</b>	Not performed	-	3.02	3.24	1.72	4 O, 4 N, 1 F	Capped square antiprismatic	[107]
<b>101</b>	14.7	180	0.33	0.48	4.06	9 O	-; $\angle \text{ZnCeZn} = 174^\circ$	[108]
<b>102</b>	20.9	503	2.43	2.43	1.03	$\pi$ -coordination ( $\eta^8$ -fashion)-All C	Sandwich type	[108]
<b>103</b>	18.8	-	0.02	0.10	2.48	8 O	Distorted hexagonal bipyramidal	[109]
<b>104</b>	15.3	-	0.07	0.21	4.18	8 O	Distorted hexagonal bipyramidal	[109]
<b>105</b>	11.2/17.2 (zf-27.3) (field = 2000 Oe	209.9	0.02	0.02	6.29	7 O	Distorted pentagonal bipyramidal	[110]
<b>106</b>	15/19	12.9	0	0	19.16	8 N	-	[54]
<b>107</b>	Not SIM		0	0	17.10	6 N incorporation of agostic interactions with three Hs	Trigonal prismatic; incorporation of agostic interactions with H; Tricapped trigonal prismatic	[81]
<b>108</b>	Not SIM		0	0	16.92	6 N incorporation of agostic interactions with three Hs	Trigonal prismatic; incorporation of agostic interactions with H; Tricapped trigonal prismatic	[81]

(continued)

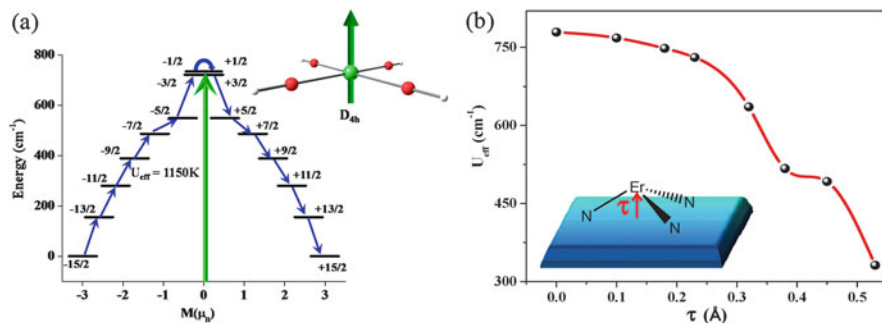
Table 9 (continued)

	$U_{\text{eff}}$	$U_{\text{cal}}$	$g_{xx}$	$g_{yy}$	$g_{zz}$	Type of coordinated atoms	Structure of complex	Ref.
<b>109</b>	237, 245	227	0	0	19.86	7 O	Distorted pentagonal bipyramidal	[111]
<b>110</b>	77.1	404.4	0	0	13.96	Three N atoms from an $\eta^3$ -coordinated tridentate pyrazolyborate anion and an $\eta^8$ -coordinated COT dianion		[112]
<b>111</b>	32.0	408.0	0	0	13.96	Three N atoms from an $\eta^3$ -coordinated tridentate pyrazolyborate anion and an $\eta^8$ -coordinated COT dianion		[112]
<b>112</b>	216					8 N, Double	Double-decker square antiprismatic	[113]
<b>113</b>	44.8, 45.2	256.36	0	0	17.93	6 N Incorporation of agostic interactions with three Hs	Trigonal prismatic; incorporation of agostic interactions with H; Tricapped trigonal prismatic	[79]
<b>114</b>	21	229.39	0	0	17.92	6 N Incorporation of agostic interactions with three Hs	Trigonal prismatic; incorporation of agostic interactions with H; Tricapped trigonal prismatic	[79]
<b>115</b>	12.2±0.5	228	0	0	17.88	4 N	Tetrahedron	[79]
<b>116</b>	652	-	-	-	-	8 N	Double-decker square antiprismatic	[114]
<b>117</b>	564	-	-	-	-	8 N	Double-decker square antiprismatic	[115]
<b>118</b>	523	-	-	-	-	8 N	Double-decker square antiprismatic	[116]
<b>119</b>	653	-	-	-	-	8 N	Double-decker square antiprismatic	[117]

<sup>a</sup>Computed harnessing the procured crystal field parameters

<sup>b</sup>First one belongs to one molecule CASSCF approach while second corresponds to one molecule embedded in five layers of point charges CASSCF approach





**Fig. 19** (a) Magnetization blockade mechanism for model  $[\text{Er}(\text{OH})_4]^-$ . Reprinted with permission from Baldoví et al. [45], Oyarzabal et al. [46], Aravena and Ruiz [47], Baldoví et al. [48–50], Pointillart et al. [51] Copyright©2014 American Chemical Society. (b) Magento-structural correlation developed by varying  $\tau$  parameter. Reproduced from Rajaraman et al. [80] with permission from the Royal Society of Chemistry

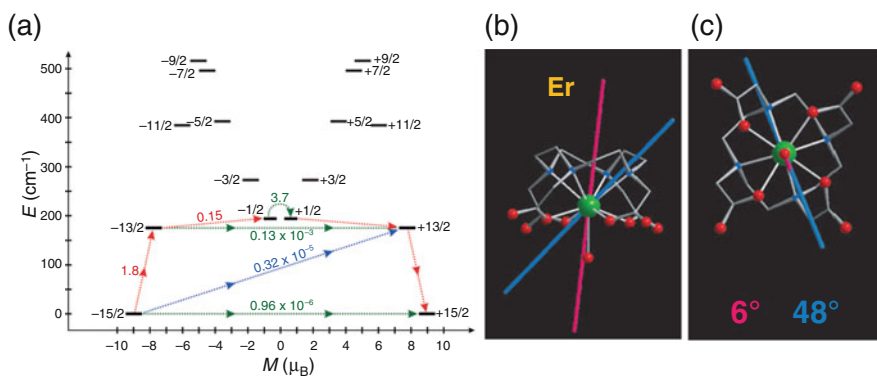
another report, another sets of calculations were carried out on two rotational conformers of complex **82** which we designate as **82'a** and **82'b** (see Table 9). Calculations on the conformers evaluated at 120 K indicate strong axially in KD1 with  $g_{xx} = g_{yy} \sim 10^{-4}$  and  $g_{zz} = 17.94$  (see Table 9). This denotes stabilization of  $|M_J = \pm \frac{15}{2}\rangle$  ground state with KD1- $g_{zz}$  lying perpendicular to the average of the planes of the two rings of COT and Cp\* ligands. Computed ground–first excited energy level separations of the two conformers, 84.8 and 115.9  $\text{cm}^{-1}$ , are lower than the  $U_{\text{eff}}$  value of 137 and 224  $\text{cm}^{-1}$  for **82'a** and **82'b**, respectively (see Table 9) [100].

In complex **83**, Er<sup>III</sup> ion is positioned above the trigonal plane of the ligand donor atoms ( $\tau$ , shift by 0.53 Å) while in **84**, in addition to the equatorial plane, two O atoms (THF) occupy the axial positions (see Table 2). In compliance with our foregoing model prejudice, zero-field SMM behaviour and lack of zero-field SMM behaviour were noted for **83** and **84**, respectively. The favourable equatorial ligand field is reflected in the Ising type KD1 state ( $\pm \frac{15}{2}$ ) of **83** while intrusion by two axial ligands in **84** deteriorated the axially with significant  $g_{xy}$  components (see Table 9). Accounting for the negligible matrix element pertinent to TA-QTM pathway, relaxation for **83** is channelled via unprecedented fourth excited KD postulating  $U_{\text{cal}}$  value as 331  $\text{cm}^{-1}$  (see Table 9). The large discrepancy between  $U_{\text{cal}}$  and  $U_{\text{eff}}$  values can be rationalized to the unavailability of dilution experiments on this complex. However, for **84**, like conventional routes, relaxation is supposedly to take place via KD2 in accordance with substantial matrix elements (see Table 9 for barrier). Out-of-plane shift parameter ( $\tau$ ) was gradually varied by moving Er<sup>III</sup> ion towards the plane of ligands. This correlation shows the largest barrier for planar structure inducing relaxation via unconventional seventh excited state (see Fig. 19b) [80].

Next complex in this category is complex **85** (see Table 2) which has distorted tetrahedral geometry with  $\{\text{ErN}_3\text{C}_{11}\}$  core. Ground states of both **85** and **85a** are

computed to be strongly axial but lack pure Ising nature. KD2 lies at 35.7 and 37.6  $\text{cm}^{-1}$  above the KD1 in **85** and **85a**, respectively. This articulates that inclusion of counter-ion and solvent molecules poses hardly any impinge on the low-lying spectrum or the  $g$ -factors. KD1- $g_{zz}$  is aligned towards the pseudo- $C_3$  axis passing through the Er-Cl bond vector. Considering the large matrix element pertinent to TA-QTM within  $\pm\frac{9}{2}$  ( $0.28 \mu_B$ ) levels, relaxation is likely to occur via third excited KD outlining  $U_{\text{cal}}$  as 118  $\text{cm}^{-1}$  for **85a**. Large discrepancy between  $U_{\text{cal}}$  and  $U_{\text{eff}}$  values attributes to intermolecular interactions/hyperfine interactions/pronounced QTM/multi-phonon relaxation pathways. Basis set assessment performed on this complex does not reveal prominent effect on barrier estimated with the increase of the proportional basis sets. Embedded cluster approach employed to account the impact of lattice and surroundings on anisotropy rendered resemblance in the anisotropic behaviour (similar to naked complex **85/85a**). Magneto-structural correlation was developed by increasing the Er-Cl distance, keeping all other structural parameters constant. Linear correspondence was reflected between increment of  $U_{\text{cal}}$  and Er-Cl bond distance. This owes to the unfavourable axial coordination of  $-\text{Cl}$  ligand with respect to  $\text{Er}^{\text{III}}$  ion and model calculation without  $\text{Cl}^-$  (only three  $-\text{N}$  donors in equatorial plane) resulted in a large  $U_{\text{cal}}$  value (557  $\text{cm}^{-1}$ ). Following up to the foregoing concept, model calculations postulated that larger Er-Cl distance and small value  $\tau$  are desired to fine-tune the local structural distortion as well as anisotropy around  $\text{Er}^{\text{III}}$  ion [101]. Model studies revealed that: (a) trigonal pyramidal or tetrahedral geometry is not appropriate geometry either for oblate/prolate ions to induce improved anisotropy and (b) trigonal pyramidal geometry is comparatively better than tetrahedral geometry for prolate ions and vice versa for oblate ions. Despite the unfavourable halide position around  $\text{Er}^{\text{III}}$  ion, effect of heavier halides on the nature of magnetic anisotropy was probed. Linear increase in  $U_{\text{cal}}$  value was observed as we move down the column (Group-17) towards the heavier halides. Enhancement of Er-halide covalency down the group-17 increases the  $\text{Er}^{\text{III}}$  vacant 5d orbital population and this directly correlates with the barrier enhancement ( $-F$  to  $-I$ ) [102]. Structural analysis of **86** indicates two molecules with identical molecular formula within the unit cell (**86a**, **86b**). Complex **86** has a distorted bicapped square antiprismatic geometry with  $\{\text{ErO}_{10}\}$  core. Greater  $\angle\text{NEr1N}$  in **86a** compared to **86b** invokes varying orientation of coordinated chelating nitrates in these two molecules. Magnetic measurements implied zero-field SIM behaviour for **86** (see Tables 2 and 9 for molecular formula and barrier, respectively). KD1 in **86a** ( $g_{xx} = 1.03$ ,  $g_{yy} = 2.77$  and  $g_{zz} = 13.99$ ) and **86b** ( $g_{xx} = 0.04$ ,  $g_{yy} = 0.07$  and  $g_{zz} = 15.78$ ) revealed axially with greater concomitant transverse anisotropy in **86a**. In both complexes, KD1- $g_{zz}$  is aligned towards one of the O atoms of the coordinated nitrate ligand. In accordance with  $g$ -factors, KD1 in both complexes are predominantly  $|M_J = \pm\frac{13}{2}\rangle$  type with extensive admixing with other higher excited states marking low-symmetry nature of both complexes. Accounting for the matrix elements and KD2 transverse anisotropy components,  $U_{\text{cal}}$  value can be predicted as 48.9 and 104.9  $\text{cm}^{-1}$  for **86a** and **86b**, respectively. The discrepancy in estimated barrier between two geometrical isomers can be ascribed to four and two O donor

ligands in the axial positions of **86a** and **86b**, respectively, along with the equatorial ligands. Additionally, greater deviation of  $\text{Er}^{\text{III}}$  ion symmetry against idealized bicapped square antiprismatic geometry in **86a** further supports the trend. Model studies articulated that in these types of complexes, removal of axial ligand/reduction in a number of axial ligands reduces the QTM tendency and proportionally enhances the energy barrier [103]. Next complex for this category is complex **87** which has square antiprismatic geometry with  $\{\text{ErN}_8\}$  core (see Table 2). Ab initio calculations on **87** led to theoretical barrier estimate of  $58.7 \text{ cm}^{-1}$  against  $U_{\text{eff}}$  value of  $74 \text{ cm}^{-1}$  (see Table 9). However, the wave function of the ground KD turns out to be:  $|\pm\frac{1}{2}\rangle > 0.99 |\pm\frac{1}{2}\rangle >$  with concomitant ground state crystal field parameter  $B_2^0$  and  $g_{zz}$  as 1.01 and  $\sim 11$  (see Table 9), respectively, for **87** [54]. KD1  $g$ -factors turn out to be completely different to earlier observations:  $g_{xx} = 10.77$ ,  $g_{yy} = 8.33$  and  $g_{zz} = 1.20$  which is a feature of  $|\pm\frac{1}{2}\rangle >$  doublet state. Contrary to its Dy analogue (complex **3**), this shows positive crystal field parameter while **3** showed negative crystal field parameter. This indicates unfavourable ligand field rendering stabilization of  $|\pm\frac{1}{2}\rangle >$  ground state with KD2 being predominantly  $|\pm\frac{3}{2}\rangle >$  [54]. Calculations on **88**, which is a sandwich type complex (see Table 2), envisioned large separation between ground and low-lying excited states. Besides, KD1 and KD2 are computed to be strongly axial with collinearity between KD1 and KD2 principal magnetization axis alignment. Negligible transverse anisotropies for KD1 and KD2 suppress QTM and TA-QTM within KD1 and KD2, respectively, as corroborated by pertinent matrix elements of  $\sim 10^{-6}$  and  $\sim 10^{-3} \mu_{\text{B}}$ , respectively. Accounting the collinearity between KD1 and KD2  $g_{zz}$  axis, magnetization blockade is likely to be observed at KD3 which is supported by significant matrix element ( $3.7 \mu_{\text{B}}$ ) corresponding to TA-QTM process (see Table 9 and Fig. 20a). The Dy analogue (complex **2**) of **88** showed smaller energy barrier and weak SMM property. This reverse behaviour is



**Fig. 20** (a) Magnetization blockade mechanism developed for complex **88**. Reprinted with permission from Ungur et al. [13] Copyright 2014 Wiley-VCH. Computed (blue) and experimental (pink) easy axis of magnetization orientation for **92** viewed (b) perpendicular and (c) parallel to the pseudo-fourfold symmetry axis of the molecule. Colour code: Er = green, O = red, N = blue and C = grey. Reprinted with permission from Boulon et al. [105] Copyright 2013 Wiley-VCH

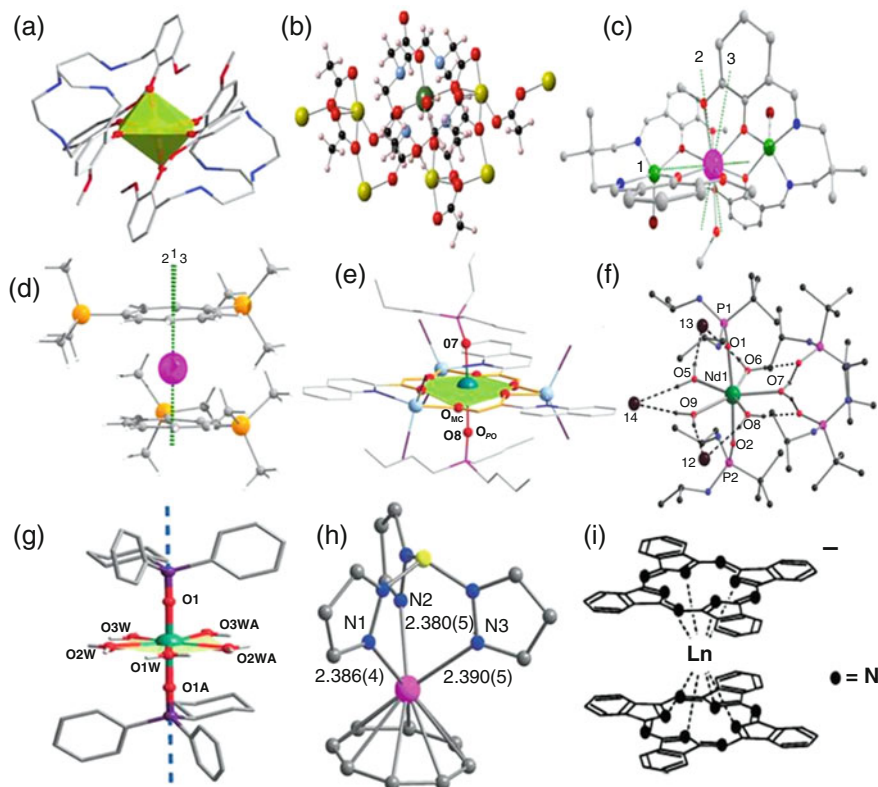
essentially ascribable to the positive and negative CFP  $B_2^0$  for **2** (0.35) and **88** ( $-1.52$ ), respectively. This also is connected to the stabilization of  $|\pm \frac{9}{2}\rangle$  and  $|\pm \frac{15}{2}\rangle$  ground state in **2** and **88**, respectively [13]. Next three complexes (**89–91**) of this category are trigonal in geometry with  $\{\text{ErN}_4\text{O}_3\}$  core. Ground–first excited gap in **89** turns out to be  $54 \text{ cm}^{-1}$  (see Table 9). This resulted in effective  $g$  parameters, i.e.  $g_{\perp}^{\text{eff}} = 1.2$  and  $g_{\parallel}^{\text{eff}} = 13.0$  (see Table 9) evoking easy-axis type anisotropy for **89** contrary to the easy plane behaviour for Dy analogue. Easy-axis anisotropy nature was supported by the ground multiplet wave-function type as predominantly  $|\pm \frac{13}{2}\rangle$ :  $68.4\% |\pm \frac{13}{2}\rangle + 5\% |\pm \frac{7}{2}\rangle + 10.4\% |\pm \frac{1}{2}\rangle + 11.6\% |\mp \frac{13}{2}\rangle$ . This indicates lesser energy level admixture compared to Dy analogue [88]. Ab initio calculations were undertaken on complex **89** utilizing the measured crystal structures at 122 and 293 K. For **90** and **91**, the measured crystal structures at 122 K and room temperature were used. All these endeavours were aimed to compare the crystal field procured from the previously published optical spectra [101]. In this work, in addition to the CASSCF calculations, Madelung potential was approximated via five layers of point charges in order to appraise the impact of ligand field atmosphere (Madelung potential) on low-lying energy states. This delivers realistic charge distribution within the ligand field atmosphere composed by the underlying neutral molecules. All the point charges were positioned at the Cartesian position of every atom pertinent to crystal environment. The charges imposed on every atom in the ground state were adopted from foregoing CASSCF steps of the individual molecule. The ab initio computed first excited energy levels for the complex **89** at temperature 122 K resulted ground–first excited energy separation of  $67 \text{ cm}^{-1}$  ( $B_2^0 = -1.05$ ) and  $58 \text{ cm}^{-1}$  ( $B_2^0 = -0.96$ ) for bare molecule and for molecule embedded in five layers of point charges, respectively. Similarly, calculations at 293 K structure using bare molecule and molecule embedded in five layers of point charges led to the energy separation of  $64 \text{ cm}^{-1}$  ( $B_2^0 = -0.99$ ) and  $52 \text{ cm}^{-1}$  ( $B_2^0 = -0.88$ ), respectively. All of these aforementioned energy levels acquired harnessing different approaches are in nice agreement with the energy extracted from Luminescence spectra ( $54 \text{ cm}^{-1}$ ). Even the computed higher energy excited doublets also agree well with the Luminescence energies. The  $g$ -values of the ground state procured from fitted Stevens parameters and ab initio calculations are noted as:  $g_{\parallel} = 11.9/13.68$  and  $g_{\perp} = 3.36/2.29$ , respectively (see Table 9 for details). The overestimation of the  $g$  values can be ascribed to the underlying easy plane type anisotropy of the first excited energy level ( $g_{\parallel} = 2.87$  and  $g_{\perp} = 7.62$ ). This articulates efficient impact of crystal field variation on the anisotropy of ground level which has low-lying first excited energy level (like in this case). The ab initio calculated energies along with  $g$ -factors of the ground multiplet of **90–91** are summarized in Table 9 [104]. Following up to this work, in another work,  $g$ -factors of complex **89** were estimated by different approaches. Due to the pseudo- $C_3$  symmetry in **89**, orientation of main magnetic axis procured from ab initio and electrostatic approaches resembles each other. However, electrostatic point-charge models render highly axial  $g$ -tensor values, contrasting the experimental observation. Additionally, harnessing the anisotropy data procured via aforementioned electrostatic approaches could neither reproduce the experimental

susceptibility or magnetization data. In similar context, minimum CASSCF+RASSI-SO approach with standard active space, considering the effects of Madelung potential and dynamic electron correlation offered energy level splitting equivalent to 75% of the experimental value. The remaining 25% of the ligand field splitting can be recovered via missing features of dynamic electron correlation and Madelung potential. The indispensability of ab initio calculations corresponds to its flexible nature as it permits mixing between metal and attached ligand orbitals, providing covalent contributions to the ligand field. As metal–ligand covalency is underestimated in the CASSCF approach, possibility of improving the accuracy to enhance splitting of the crystal field levels was probed. Inclusion of dynamic electron correlation (performing CASPT2 along with CASSCF) in conjunction with electrostatic Madelung potential of the crystal resulted computed magnetic data which is in agreement with experiments. Additionally, increase of active space by incorporating  $5p^6$ ,  $5d^0$ ,  $6p^0$  and  $5f^0$  orbitals (either by CASSCF or RASSCF approach) was found to impose prominent improvement of the energy level splitting [26].

Complex **92** is having a square antiprismatic geometry with  $\{\text{ErN}_4\text{O}_4\}$  core (see Table 2). KD1 of **92** possesses significant rhombic anisotropy as evident from the values  $g_{xx} = 1.8$ ,  $g_{yy} = 2.8$  and  $g_{zz} = 10.9$ . Easy axis of magnetization for KD1 in **92** is almost collinear (deviation by  $\sim 6^\circ$ ) to the Er–O<sub>w</sub> bond and the axial direction in the capped square antiprismatic geometry (see Fig. 20b, c). Despite this orientation, large discrepancy was detected between the computed and experimental anisotropy axis. This can be attributed to the considerable impact of incorporation of dynamic correlation on Er<sup>III</sup> single-ion anisotropy. [35] f-SIM behaviour was noted for **92** with  $U_{\text{eff}}$  value of 27.1 (34.1)  $\text{cm}^{-1}$ . The calculated ground–first excited energy state difference of 19.8  $\text{cm}^{-1}$  agrees well with the experimental value. The eight KDs of **92** spread within an energy window up to 427  $\text{cm}^{-1}$  [105].

### 3.4 Review on Unconventional Ln<sup>III</sup> Containing Single-Ion Magnets

Although the most common lanthanides (Dy<sup>III</sup>, Er<sup>III</sup> and to some extent Tb<sup>III</sup>) remain pervasive, study of other uncommon lanthanides (Yb<sup>III</sup>, Ce<sup>III</sup>, Nd<sup>III</sup>, Ho<sup>III</sup> and Tm<sup>III</sup>) also has gradually begun to transpire [119]. Particularly, Tb<sup>III</sup> ion based SIMs are widely studied and the first SIM reported based on lanthanides is, in fact,  $[\text{Tb}(\text{Pc})_2]^-$  complex possessing very large  $U_{\text{eff}}$  value and attractive blocking temperature [113]. Here, we present selected examples of SIMs based on not only Tb<sup>III</sup> ion but also other lanthanides. The Yb<sup>III</sup>, Ce<sup>III</sup>, Nd<sup>III</sup>, Ho<sup>III</sup>, Tm<sup>III</sup> and Tb<sup>III</sup> are represented by their term symbols as  $^2F_{7/2}$ ,  $^2F_{5/2}$ ,  $^4I_{9/2}$ ,  $^5I_8$ ,  $^3H_6$  and  $^7F_6$ . Among these, Ce<sup>III</sup>, Nd<sup>III</sup>, Ho<sup>III</sup> and Tb<sup>III</sup> are oblate and Yb<sup>III</sup> and Tm<sup>III</sup> are prolate ions, respectively. In this section, we intend to cover the ab initio calculations on Ln<sup>III</sup>-based SIMs. Besides, as on date, no zero-field SIM feature been reported for Pr<sup>III</sup>/Sm<sup>III</sup> complexes, and



**Fig. 21** (a–i) Molecular structures of complexes **93**, **94**, **101**, **102**, **103**, **105**, **109**, **110** and **112**, respectively. Arrows/dashed lines in complexes show the orientation of the principal magnetization axis. Complexes with more than one arrow are showing  $g_{zz}$  axis for the same numbers of KD states. Colour code: central atom(s) = Dy, red = O, dark-blue/light-blue = N, black/dark-brown/light-brown = C, dark green = Na, golden yellow = Si, yellow = S and white = H atoms. Reprinted from Li et al. [109], Gupta et al. [110] with permission from the Royal Society of Chemistry. Reprinted from Boulon et al. [105], Singh et al. [108], Chen et al. [111], Meng et al. [112] with permission from John Wiley and Sons. Reprinted with permission from Ishikawa et al. [113] Copyright©2003 American Chemical Society. Reprinted with permission from Liu et al. [106] Copyright©2012 American Chemical Society

therefore those are also discarded from our confined study. First complex of this category is complex **93** which has trigonally distorted octahedron geometry with  $\{\text{YbO}_6\}$  core (see Fig. 21a and Table 2 for molecular formula). Complex **93** was noted as the first  $\text{Yb}^{\text{III}}$ -based complex showing easy plane anisotropy. Complex **93** exhibited f-SIM behaviour with  $U_{\text{eff}}$  of  $4.9 \text{ cm}^{-1}$  (see Table 9). KD1 in **93** possesses large transverse anisotropy as evident in the estimated values  $g_{xx} = 3.21$ ,  $g_{yy} = 2.69$  and  $g_{zz} = 1.76$  (see Table 9). KD1 rhombicity promotes strong QTM within the ground state, discarding the possibility of SIM behaviour in the absence of external applied field. Eigenfunctions of the KD1 can be represented as:  $-0.02 | \frac{7}{2} \rangle > -0.02 |$



$-\frac{7}{2} > +0.65 \frac{5}{2} > +0.67 |-\frac{5}{2} > -0.26 | \frac{1}{2} > +0.25 |-\frac{1}{2} >$ . This reveals that **93** does not comply with the requirement of the largest  $|M_J = \pm \frac{7}{2} >$  as the ground state. Rather, contribution from  $|M_J = \pm \frac{7}{2} >$  is meagre, with extensive mixing from other energy levels. This was further corroborated by the KD1  $g_{zz}$  value which is far from the expected  $g_{zz}$  value of KD8 for the stabilized  $|M_J = \pm \frac{7}{2} >$  level. KD2 is located at  $187.9 \text{ cm}^{-1}$  higher in energy and remains far from experimental value. Therefore, slow magnetization relaxation in **93** corresponds to direct process while Orbach relaxation pathway is discarded completely [106]. Next set of complexes for this category is complexes **94–97** (Yb<sup>III</sup> (**94**), Tb<sup>III</sup> (**95**), Ho<sup>III</sup> (**96**) and Tm<sup>III</sup> (**97**), see Fig. 21b). They have {LnO<sub>4</sub>N<sub>4</sub>} core with square antiprism geometry. Among these four complexes, only complex **94** shows field-induced SMM behaviour. KD1 of **94** has improved axiality compared to **93**, with  $g_{xx} = 0.1$ ,  $g_{yy} = 1.0$  and  $g_{zz} = 6.8$ . Easy axis of magnetization for KD1 in **94** is almost collinear (deviation by  $\sim 12^\circ$ ) to the Yb–O<sub>w</sub> bond and the axial direction in the capped square antiprismatic geometry. f-SIM behaviour was noted for **94** with  $U_{\text{eff}}$  value of  $20.2 \text{ cm}^{-1}$ . The calculated ground–first excited energy state difference is estimated as  $197.2 \text{ cm}^{-1}$ . The eight KDs of **94** spread within an energy window of  $416 \text{ cm}^{-1}$  with larger  $g_{zz}$  value corresponds to  $|M_J = \pm \frac{7}{2} >$  ground state [105]. SIM behaviour was missing for complexes **95–97**.

Easy axis of magnetization for KD1 in **95** is perpendicular (deviation by  $\sim 85^\circ$ ) to the Tb–O<sub>w</sub> bond and the axial direction in the capped square antiprismatic geometry. Considering the non-Kramers nature of the Tb<sup>III</sup>, Ho<sup>III</sup> and Tm<sup>III</sup> in **95**, **96** and **97**, respectively, tunnel splitting ( $\Delta_{\text{tun}}$ ) within the ground energy multiplets acts as dictating factor for SIM behaviour ( $\Delta_{\text{tun}} = 1.6, 4.8$  and  $4.6 \text{ cm}^{-1}$  were evaluated for **95**, **96** and **97**, respectively). Within the ground energy multiplet, this large separation precludes the presence of magnetic bistability deterring SIM behaviour in all these three complexes. Besides, KD1 in all three complexes possess significant transverse anisotropy inducing magnetization blockade within ground states itself [105]. Easy axis to easy plane type ground state anisotropy transformation was noted upon changing the axial water ligand from **98** to axial fluoride ligand in **99/100**. All these three complexes have capped square antiprismatic geometry. Complexes **99** and **100** possess identical coordination environment, with {LnO<sub>4</sub>N<sub>4</sub>F<sub>1</sub>} core, except the Yb–F bond length which is  $1.97 \text{ \AA}$  and  $2.38 \text{ \AA}$  for **99** and **100**, respectively. The KD1 main magnetic factors for **98–100** nicely corroborated the change of anisotropy behaviour (see Table 9). This ascribes to the weaker equatorial crystal field of employed DTMA (diethylene triamine penta acetic acid) ligand which stabilizes the prolate  $|M_J = \pm \frac{7}{2} >$  state. Coordination of the F<sup>−</sup> over the fourfold axis creates prevalent axial crystal field unfavourable for prolate ions. This instigates stabilization of  $|M_J = \pm \frac{1}{2} >$  as the ground state. Compared to the neutral water ligand, replacement by negatively charged fluoride in axial direction is found to be detrimental for the SIM behaviour [107]. Complexes **101** and **102** are Ce<sup>III</sup> ion based SIMs, with former complex having nine oxygen atoms coordinated to Ce<sup>III</sup> ion whereas latter is having  $\pi$ -coordination ( $\eta^8$ -fashion) – where C atoms coordinated to Ce<sup>III</sup> ion (see Fig. 21c, d). Complex **101** shows axial type KD1 anisotropy with

stabilization of  $|M_J = \pm\frac{5}{2}\rangle$  state, substantiating zero-field SIM behaviour (see Table 9). KD1- $g_{zz}$  is aligned towards one of the O donors of the bridging ligands and diverged from Ce-O bond vector/Zn-Ce-Zn axis by  $11^\circ/20.8^\circ$ , respectively. Accounting for matrix elements and  $g$ -factors of KD2, relaxation is likely to channel via KD2 outlining  $U_{\text{cal}}$  value as  $180\text{ cm}^{-1}$  (see Table 9). Model calculations revealed that intermolecular interaction (point charges) and increase of active space/basis set have no significant role on the nature of anisotropy. The eight KDs in **101** and **102** span over an energy window of  $488$  and  $1,036\text{ cm}^{-1}$ , respectively. This infers the presence of stronger metal–ligand covalent interaction in **102**. However, larger transverse component with small  $g_{zz}$  values of KD1 stabilizes  $|M_J = \pm\frac{1}{2}\rangle$  state in **102** and rationalized by the presence of stronger equatorial ligand field. This corresponds to stronger QTM within ground state (matrix element =  $0.79\ \mu_B$ ) and entails the need of application field ratifying its f-SIM feature (see Table 9). Stabilization of  $|M_J = \pm\frac{5}{2}\rangle$  and  $|M_J = \pm\frac{1}{2}\rangle$  in **101** and **102**, respectively, was nicely endorsed by computed CFP  $B_2^0 = -23.35$  and  $+17.61$ , respectively. Complex **101** shows ideal crystal field but lacks symmetry whereas **102** with higher symmetry is devoid of suitable ligand field. This articulates the simultaneous need of ideal symmetry and crystal field to achieve improved SIM behaviour. Model calculations indicated that lower coordination number [120] and coordination no 5/7 possessing trigonal bipyramidal or pentagonal bipyramidal geometries are appropriate to procure larger barrier [108].

Complexes **103–104** have distorted hexagonal bipyramidal geometry around central metal ion with  $\{\text{LnO}_8\}$  core (see Fig. 21e and Table 2). Complex **103** is having  $\text{Ce}^{\text{III}}$  paramagnetic ion and complex **104** has analogous  $\text{Nd}^{\text{III}}$  paramagnetic ion. KD1 for complex **103** is computed to compose of:  $96\% | \pm\frac{3}{2}\rangle$  (f-SIM) with predominant  $g_{zz}$  values and negligible transverse anisotropy (See Table 9). The ground–first excited energy separation ( $303\text{ cm}^{-1}$ ) is larger than the reported  $U_{\text{eff}}$  value (see Table 9) discarding the relaxation probability via Orbach process. This articulates that predominant relaxation pathway is likely to be Raman process with direct process involved in substantial fields and QTM pathway prevails in zero field. Complex **104** (f-SIM) is isostructural with **103** with KD1 representation as:  $71\% | \pm\frac{9}{2}\rangle + 29\% | \pm\frac{3}{2}\rangle$ . Here as well, due to larger ground–first excited level gap ( $104\text{ cm}^{-1}$ ), underlying relaxation mechanism delineation resembles to that discussed for **103**. Experimental data postulated that the  $g_{zz} \sim 5\text{--}5.5$  for axial type KD1 in **104** which is larger than computed one (see Table 9). It is notable that harnessing computed anisotropy properties are in nice agreement with experiments [109]. Complex **105** is seven-coordinated  $\text{Nd}^{\text{III}}$  complex with  $\{\text{NdO}_7\}$  core (see Fig. 21f). Five KDs pertaining to  $^4I_{9/2}$  ground level of  $\text{Nd}^{\text{III}}$  in complex **105** spread within an energy window of  $416\text{ cm}^{-1}$ . KD1 is found to be axial (see Table 9) with stabilization of  $|M_J = \pm\frac{9}{2}\rangle$  state. KD1- $g_{zz}$  lies in proximity to the O of (O=P–) atom of the phosphonic amide ligand (along  $C_5$  axis but deviated by  $\sim 5^\circ$ ). KD2 possesses large transverse anisotropy ( $g_{xx} = 0.10$ ,  $g_{yy} = 0.42$  and  $g_{zz} = 5.10$ ) implying possible relaxation via this state (see Table 9). Wave-function analysis postulated KD2 as mixture of  $|M_J = \pm\frac{5}{2}\rangle$  and  $|M_J = \pm\frac{1}{2}\rangle$  levels. CASSCF LoProp



charges showed prominently larger negative charges on the axial O atoms compared to their equatorial congeners rendering  $|M_J = \pm \frac{9}{2}\rangle$  as the ground state [110]. Complex **106** is isostructural to complex **87** but with Ho<sup>III</sup> ion instead of Dy<sup>III</sup> ion. KDI is calculated to have  $g_{zz} = 19.16$  and  $B_2^0 = -0.85$  (see Table 9). Considering integer angular momentum quantum number of Ho<sup>III</sup> ion, all the energy states are found to be strongly mixed [54]. The ab initio calculated ground–first excited gap ( $12.9 \text{ cm}^{-1}$ ) agrees well with that procured from the crystal field approach ( $15/19 \text{ cm}^{-1}$ ; see Table 9) [54].

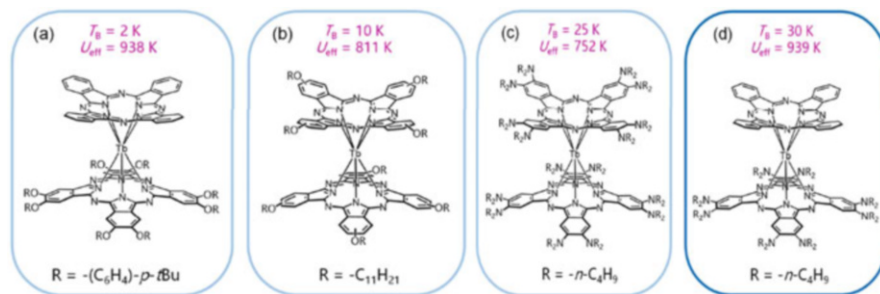
Like complex **106**, next three complexes are (**107–109**) also Ho<sup>III</sup> ion based SIMs with the energy spectrum for 17 energy levels (seven pseudo-doublets and three singlets) of the ground  $^5I_8$  multiplet for the Ho<sup>III</sup> ion shows showing energy span of 204 and  $207 \text{ cm}^{-1}$  for **107** and **108**, respectively. Complexes **107** and **108** are trigonal prismatic in geometry with three agostic interaction between Ln and H atoms. Complex **109** has distorted pentagonal bipyramidal geometry with {HoO<sub>7</sub>} core (see Fig. 21g). Ground pseudo-doublets of **107** and **108** are Ising type with  $g_{zz}$  of 17.10 and 16.92, respectively. Wave-function analysis articulates predominantly  $|\pm M_J = 7\rangle$  type ground state with mixing from other higher states and this was corroborated by the  $g_{zz} = 17.5$  expected for pure  $|\pm M_J = 7\rangle$  state. The  $\Delta_{\text{tun}}$  is noted as 0.04 and  $0.07 \text{ cm}^{-1}$  for **107** and **108**, respectively, precluding magnetic bistability and SIM behaviour. Positive value of ground state CFP  $B_2^0 = 1.00$  and 0.93 for **107** and **108**, respectively, endorses for unfavourable crystal field and completely suppressed SIM behaviour [81]. Complex **109** is a rare zero-field SIM where compressed pseudo-D<sub>5h</sub> environment around Ho<sup>III</sup> reduces its inherent QTM probability as well as mixing of different  $|\pm M_J\rangle$  levels. KDI possesses  $g_{zz}$  of 19.86 (see Table 9) and approaches towards that expected for pure  $|\pm M_J = 8\rangle$  state of 20. The  $\Delta_{\text{tun}} = \sim 10^{-4} \text{ cm}^{-1}$  was noted within ground pseudo-doublets provoking possible relaxation via higher excited energy levels. Though the  $\Delta_{\text{tun}}$  within first excited pseudo-doublet was considerable enough, transition moment matrix element corresponding to the  $\pm 1$  and  $\pm 2$  was not pronounced. Substantial  $\Delta_{\text{tun}}$  within  $\pm 3$  in conjunction with matrix elements within  $\pm 2$  and  $\pm 3$  spurs relaxation via this state (see Table 9) [111].

Complexes **110–111** are Tm<sup>III</sup> ion based complexes with three N atoms from an  $\eta^3$ -coordinated tridentate pyrazolylborate anion and  $\eta^8$ -coordinated COT dianion (see Fig. 21h). Complex **111** is the same as complex **110** except methyl substitution in Tp\*. Dynamic magnetization experiments revealed slow magnetization relaxation for **110** and **111** in applied static *dc* magnetic field whereas corresponding diluted samples exhibit relaxation even at zero field. Both **110** and **111** exhibit nearly degenerate ground states with  $\Delta_{\text{tun}} = 0.01$  and  $0.02 \text{ cm}^{-1}$ , respectively, denoting faster QTM in **111**. Non-coincidence between ground and first excited pseudo-doublets indicated plausible magnetization blockade via this first excited level ( $128.8^\circ$  and  $85.9^\circ$  for **110** and **111**, respectively). Additionally, huge  $\Delta_{\text{tun}}$  of 19.36 and  $2.93 \text{ cm}^{-1}$  in **110** and **111**, respectively, necessitates relaxation to be channelled via this state (see Table 9). The larger ground–first excited gap can be attributed to the differences between 4f charge density of ground  $|\pm M_J = 6\rangle$  and  $|\pm$

$M_J = 5 >$  states. The improved barrier of **110** corresponds to better molecular symmetry (see Table 9) and steric hindrance arose from  $-\text{Me}$  groups in **111**. Due to this, comparatively longer Tm-N bonds in **111** exert inherently weaker crystal field. Further, ground pseudo-doublet wave-function analysis for **110** and **111** as:  $0.96 | \pm 6 > + 0.03 | \pm 3 >$  and  $0.92 | \pm 6 > + 0.04 | \pm 4 > + 0.02 | \pm 2 >$ , respectively, reinforced better SIM behaviour in **110** [112].

The highly anisotropic ground states of the  $\text{Tb}^{\text{III}}$  ion, which are oblate in nature and prefer strongly axial ligand fields, can be stabilized in sandwich complexes. Ishikawa and co-workers, in 2003, have reported first  $\text{Ln}^{\text{III}}$ -based mononuclear sandwich complexes,  $[\text{TbPc}_2]^-$  complex (where Pc = phthalocyanine) (**112**), with very large barrier height for spin reversal ( $216 \text{ cm}^{-1}$ ) which surpassed all the records of barrier heights reported for any mono-/polynuclear transition metal complexes at that point in time. It has to be noted that phthalocyanine/porphyrin type macrocycles are not considered as classical  $\eta$ -type capping ligands because their coordination mode is more  $\sigma$ -type, similar to the multidentate chelating ligands. Therefore, the CF symmetry of such a ligand can be regarded as pseudo  $C_4$  [113]. Next three complexes (**113–115**) are  $\text{Tb}^{\text{III}}$  ion based SMMs with  $\{\text{TbN}_6\text{H}_3\}$  core for the **113** and **114** and  $\{\text{TbN}_4\}$  core for the complex **115**. The energy spectrum for 13 energy states (six pseudo-doublets and one singlet) of ground  $^7\text{F}_6$  atomic multiplet of  $\text{Tb}^{\text{III}}$  in **113** and **114** spans within an energy window up to  $590$  and  $515 \text{ cm}^{-1}$ , respectively. The ground pseudo-doublets are pure Ising type (see Table 9) and approaching towards that expected for pure  $| \pm M_J = 6 >$  state of  $\sim 18$ . The ground pseudo-doublets are detected with  $\Delta_{\text{tun}} = 0.02$  and  $0.05 \text{ cm}^{-1}$  for **113** and **114**, respectively, entailing f-SIM behaviour in both complexes. However, significant  $\Delta_{\text{tun}} = 0.03$  and  $0.04 \text{ cm}^{-1}$  within first excited pseudo-doublet of **113** and **114**, respectively, inevitably blocks magnetization via this state (see Table 9 for barrier values) [81]. Ab initio calculations on complex **115** confer  $| \pm M_J = 6 >$  as the ground pseudo-doublet possessing  $\Delta_{\text{tun}}$  of  $0.03 \text{ cm}^{-1}$ . This large intrinsic tunnelling gap necessitates use of external static  $dc$  applied magnetic field to quench QTM and observe SIM behaviour. Now, first excited pseudo-doublet lying at  $\sim 228 \text{ cm}^{-1}$  with  $\Delta_{\text{tun}}$  of  $0.65 \text{ cm}^{-1}$  undoubtedly spurs relaxation via this state. This turns out to be larger than the  $\Delta_{\text{Orbach}}$  energy barrier ( $12.2 \pm 0.5 \text{ cm}^{-1}$ ) procured from magnetic measurements. This infers the necessary consideration of other relaxation pathways within temperature range. Therefore, the relaxation is likely to occur via combined effects of QTM, direct and Raman pathways which is reminiscent of the mechanism discussed for its Dy analogue (complex **44**) [79].

Next four set of complexes for this category are  $\text{Tb}^{\text{III}}$  double-decker complex with  $\{\text{TbN}_8\}$  core and square antiprismatic geometry (**116–119**, see Fig. 22). Complexes **116** and **119** are heteroleptic whereas complexes **117** and **118** are homoleptic in nature. Inclusion of the bulky strong electron-donating (dibutylamino) groups on the periphery positions of either phthalocyanine ligands offers strong ligand field with unsymmetrical molecular structure and radical-4f interactions. These factors result in appearance of both large energy barrier and high magnetic blocking temperatures [114–117].



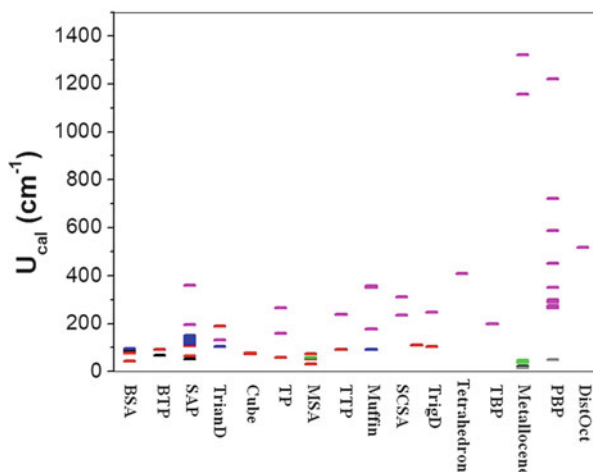
**Fig. 22 (a–d)** Molecular structures along with blocking temperature and effective energy barrier for complexes **116–119**, respectively. Reprinted with permission from Chen et al. [117] Copyright©2017 American Chemical Society

## 4 Conclusions

Controlling ligand geometry and point group symmetry could help chemists to aim appropriate complexes with significantly large magnetization blockade barrier. In spite of the progress made till date, it is clear that thorough theoretical calculations are required to predict promising molecular systems that are worth to synthesize using experimental means. Designing ligands with appropriate symmetry is extremely important to fine-tune the  $U_{\text{eff}}$  and also to enhance  $T_B$  beyond liquid  $N_2$  temperatures. As the stabilization of the largest  $M_J$  level as the ground state and the crystal field splitting of the  $M_J$  levels are the most desired characteristics of lanthanide based SMMs, we have summarized various  $Dy^{III}$  SIMs based on their ground state  $|\pm M_J\rangle$  levels and the computed crystal field splitting to six different categories that are discussed above (A to F). We have also considered  $Er^{III}/Tb^{III}$  SIMs with f-SIM or zf-SIM properties reported for our analysis.

To summarize, we have plotted all the different geometries of  $Dy^{III}$  complexes (along  $x$ -axis) from all the six categories with respect to their  $U_{\text{cal}}$  values reported (y axis, see Fig. 23). Out of 16 geometries studied, pentagonal bipyramidal geometry found to yield both large as well as small  $U_{\text{cal}}$  values based on its axial and equatorial ligand field strength. Those molecules with strong axial ligand field with weak equatorial ligand field yield very large  $U_{\text{cal}}$  values with attractive blocking temperatures. However, if the ligand field strength is reversed, i.e. strong equatorial ligation and weak axial ligation yields smaller  $U_{\text{cal}}$  values. This particular geometry clearly illustrates how important it is to design the strength of the donor ligands to obtain attractive magnetic properties.

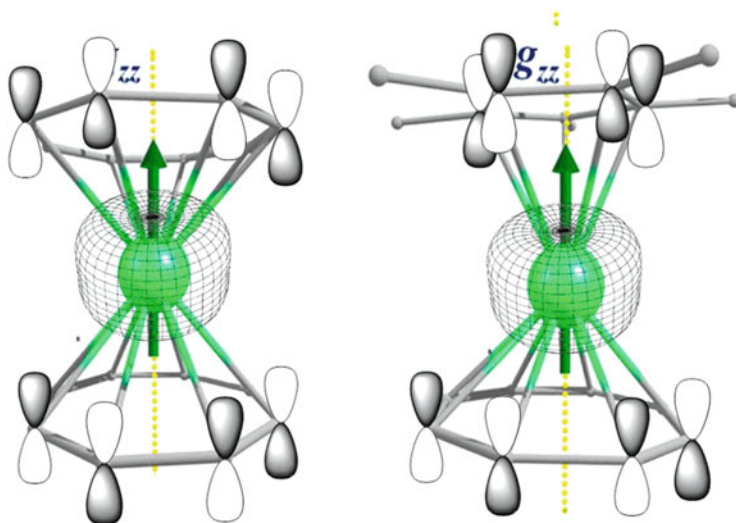
The second category is  $Dy^{III}$  ion based metallocene complexes; here as well, both smaller and larger  $U_{\text{cal}}$  values are possible depending on the nature of the coordinating ring. Sandwich complexes with large aromatic rings interact with the equatorial electron density of the  $Dy^{III}$  ion leading to smaller  $U_{\text{cal}}$  values as one can witness in  $[Dy(\text{COT})_2]$  complexes. Whereas, sandwich complexes with small aromatic rings, such as  $\text{Cp}^*$ , are found to yield very large  $U_{\text{cal}}$  values due to strong axial



**Fig. 23** Plot representing  $U_{cal}$  values for different complexes of all six categories with respect to their geometries. Colour code for categories: black = A, red = B, green = C, blue = D, magenta = E and grey = F. *BSA* bicapped square antiprismatic, *BTP* bicapped triangular prism, *SAP* square antiprismatic, *TrianD* triangular dodecahedron, *TP* trigonal prismatic, *MSA* monocapped square antiprismatic, *TPP* tricapped trigonal prismatic, *SCSA* spherical capped square antiprismatic, *TrigD* trigonal dodecahedron, *TBP* trigonal bipyramidal, *PBP* pentagonal bipyramidal, *DistOct* distorted octahedral

ligand field exerted by this ligand in stabilizing  $| \pm M_J = \frac{15}{2} \rangle$  ground state and destabilizing the  $| \pm M_J = \frac{1}{2} \rangle$  state (see Fig. 24). Besides, higher symmetry helps to quench the tunnelling leading to relaxation via higher excited state resulting in a very large  $U_{cal}$  values. If the ring sizes of the sandwich complexes are chosen aptly, this can lead to a significant breakthrough as has been witnessed with a blocking temperature of 60 K. However, one of the main issues with such systems is stability of these organometallic SMMs under ambient conditions as this is desired in the next logical step of fabricating devices from these molecules.

Tetrahedron is another possible geometry where one can get high  $U_{cal}$  value. Perfect octahedral complexes are found to relax via ground state KD. But, if the structures are distorted significantly, this found to yield large  $U_{cal}$  values. Bicapped square antiprismatic, bicapped triangular prism, cube and monocapped square antiprismatic geometries are not the desired ones as they yield very low  $U_{cal}$  values, independent of the choice of the donor ligands. Based on the studied examples, one can achieve  $U_{cal}$  value of  $95 \text{ cm}^{-1}$ ,  $93 \text{ cm}^{-1}$ ,  $75 \text{ cm}^{-1}$  and  $73 \text{ cm}^{-1}$ , respectively, for these geometries. Many examples are reported in the literature where complexes with these geometries are found to exhibit not even f-SIM characteristics. Remaining nine geometries (see Fig. 23) are found to yield mixture of both large as well as small  $U_{cal}$  values based on the distortion and ligand field strength. For square antiprismatic geometries, one can achieve a max  $U_{cal}$  value as high as  $362 \text{ cm}^{-1}$ . For this geometry, among our studied complexes, the minimum reported  $U_{cal}$  value is  $52 \text{ cm}^{-1}$ . In the same way, for remaining eight geometries, triangular dodecahedron,

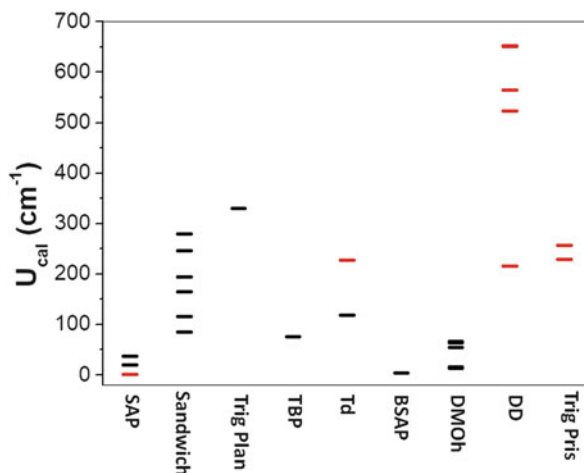


**Fig. 24** Pictorial presentation of two different molecules with: (a) two  $C_8$  rings around  $Dy^{III}$  ion and (b) one  $C_8$  and second  $C_5$  ring around  $Dy^{III}$  ion along  $|\pm M_J = \frac{15}{2}\rangle$  charge distribution suggesting strong axial ligand field geometry maintained for the second molecule with a  $C_5$  ring with respect to the first molecule with  $C_8$  rings

trigonal prismatic, tricapped trigonal prismatic, muffin, trigonal dodecahedron, spherical capped square antiprismatic, tetrahedron and trigonal bipyramidal, the maximum to minimum reported  $U_{cal}$  are found to be 104/189, 59/267, 91/239, 92/356, 105/249, 237/313 and 199/199  $cm^{-1}$ , respectively. For a given geometry, it is preferable to have oxygen donor ligands along the axial directions than nitrogen donors as the former exerts stronger crystal field interaction than the latter. This is one of the desired conditions when we have mixed N, O donor ligands, to obtain large  $U_{cal}$  values in  $Dy^{III}$  SIMs.

We have plotted all different studied geometries of  $Er^{III}$  and  $Tb^{III}$  complexes (along  $x$ -axis) with respect to their  $U_{cal}$  values reported ( $y$  axis, see Fig. 25). Out of all the studied geometries for  $Er^{III}$  complexes, trigonal planar is found to yield the highest  $U_{cal}$  value (331  $cm^{-1}$ ) because of strong equatorial ligand field around  $Er^{III}$  ion with no ligation along axial direction. The  $Er^{III}$  sandwich complexes can yield both large as well as small  $U_{cal}$  values (85–280  $cm^{-1}$ ) based on the size of the ring and whether it exerts axial or equatorial ligand field? Those molecules with strong equatorial ligand field in the presence or absence of weak axial ligand field found to yield larger  $U_{cal}$  values and this is eventually translated into attractive blocking temperatures. However, if the ligand field strength is reversed, this yield smaller not desired  $U_{cal}$  values.  $Er^{III}$  complexes with tetrahedral geometry are found to achieve  $U_{cal}$  value as high as 118  $cm^{-1}$ . Besides,  $Er^{III}$  ion in the distorted monocapped octahedron geometry is found to yield  $U_{cal}$  value between 16 and 54  $cm^{-1}$ . Remaining three geometries (square antiprism, trigonal bipyramidal and bicapped square antiprismatic) yield  $U_{cal}$  values smaller than 50  $cm^{-1}$ .

**Fig. 25** Plot representing  $U_{\text{cal}}$  values for different complexes of  $\text{Er}^{\text{III}}$  and  $\text{Tb}^{\text{III}}$  with respect to their geometries. Colour code: black =  $\text{Er}^{\text{III}}$  and red =  $\text{Tb}^{\text{III}}$ . *SAP* square antiprismatic, *Trig Plan* trigonal planar, *TBP* trigonal bipyramidal, *Td* tetrahedral, *BSAP* bicapped square antiprismatic, *DMOH* distorted monocapped octahedron, *DD* double decker, *Trig Pris* trigonal prismatic



Out of all the geometries studied for  $\text{Tb}^{\text{III}}$  complexes, double-decker complexes are found to yield very high  $U_{\text{cal}}$  value ( $653 \text{ cm}^{-1} \leq U_{\text{cal}} < 216 \text{ cm}^{-1}$ ). Tetrahedral and trigonal prismatic geometries also found to yield high  $U_{\text{cal}}$  value such as  $228 \text{ cm}^{-1}$  and  $257 \text{ cm}^{-1}$ , respectively. The  $\text{Tb}^{\text{III}}$  ion square prismatic geometries are found to be not suitable for obtaining large  $U_{\text{cal}}$  values as the relaxation in most of the instances occurs through ground state or through first excited state, which is found to be very close to the ground state.

Besides these coordination complexes based on lanthanide ions, there are also other classes of SMMs where the role of theory in predicting potential targets is well highlighted. This includes synthesis and characterization of various  $\text{Dy}^{\text{III}}$  ion based endohedral fullerene molecules. Several such molecules are predicted to possess attractive magnetic properties and recently some of those molecules are synthesized and characterized. Experiments essentially confirm the predictions at least in three reported cases, and this highlights the role of ab initio calculations in the design and development of lanthanide based SIMs.

## 4.1 Future Outlook

In this section, we intend to describe the future outlook in the area of ab initio calculations and how one could possibly solve the existing issues? The limitations and accuracy of the methodology employed are already described; while some work to correct such problems are undertaken already, this area still needs to catch with the parallel development on new theoretical methods. Here, we highlight a few issues which could be targeted in the near future:

1. One of the limitations of the widely employed CASSCF methodology is the restriction on the reference space employed. While this methodology is highly successful for lanthanide based systems, employing these methods for radical-4f and {3d-4f} clusters is challenging as computations are often limited by the number of orbitals/electrons that can be considered within the chosen reference space.
2. For polynuclear lanthanide complexes, often fragment approach is employed where individual lanthanide ion anisotropies are computed and eventually coupled together using Lines model to derive relaxation mechanism. While this approach has been employed successfully for several systems, if the number of exchange interaction increases, this generates the familiar problem of over parameterization in fitting procedure. Thus, one has to adapt other possible theories such as density matrix renormalization group (DMRG or DMRG-PT2) or multi-reference coupled cluster (MR-CCSD(T)) methods where there is a possibility to perform calculations on full systems. While these methodologies are already available and are tested for various systems, applications in lanthanide based SIMs/SMMs are yet to be carried out.
3. While the relaxation mechanism derived from ab initio calculations are very useful, the accuracy of the relaxation mechanism needs to be improved tremendously to have a meaningful comparison with experimental observations. Modelling spin–spin, spin–lattice and other relaxation processes are of utmost importance to bridge the gap and to make robust predictions. Employing Pauli master equation to derive other mechanistic features has been highlighted recently in several examples [21, 121, 122], and further work in this direction needs to be carried out on a priority basis to improve our understanding of the mechanism of relaxation.
4. Estimation of blocking temperature and relaxation time for SIMs/SMMs is extremely important. The blocking temperatures in lanthanide SMMs are often unpredictable and there is a large difference between the  $U_{\text{eff}}$  and  $T_B$  values. At present,  $T_B$  values are obtained only by experimental means and computing this parameter is very intricate and one has to go beyond molecular calculations to accurately reproduce such important parameters. Development in this direction is desired.
5. While it is known that spin is a dynamic quantity, calculations are often performed on static structure and there are only a few instances where the structural dynamics of the complexes are taken into account [121]. This is fundamentally important problem, as many of the molecules reported have fluxional behaviour and thus are expected to fluctuate significantly even at low temperatures. Methodologies coupling molecular dynamics and ab initio calculations are to be developed to further enhance our understanding.
6. Viable predictions from the calculations offer important clues to the experimentalist to design and develop new generation SMMs. Predictions often need accurate geometries and these are (albeit limited) often performed at present using density functional methods. While it is known that DFT has inherent problems in addressing degenerate states, methodologies which are superior

need to be adapted to offer accurate structures which in turn will lead to reliable predictions.

**Acknowledgments** G.R. thanks the SERB (EMR/2014/00024) and INSA for funding. MKS thanks UGC-India for fellowship. TG thanks UGC for a fellowship.

## References

1. Miller JS, Epstein AJ (2000) *MRS Bull* 25:21–30
2. Yamashita M, Katoh K (2017) *Molecular magnetic materials*. Wiley-VCH Verlag GmbH, KGaA, Weinheim, pp 79–101
3. Aldoshin SM, Korchagin DV, Paliy AV, Tsukerblat BS (2017) *Pure Appl Chem* 89:1119
4. Cornia A, Costantino AF, Zobbi L, Caneschi A, Gatteschi D, Mannini M, Sessoli R (2006) In: Winpenny R (ed) *Single-molecule magnets and related phenomena*. Springer, Berlin, Heidelberg, pp 133–161
5. Coulon C, Miyasaka H, Clerac R (2006) *Single-molecule magnets and related phenomena*, vol 122. Springer, Berlin, Heidelberg, pp 163–206
6. Gatteschi RSD, Villain J (2006) *Molecular nanomagnets*. Oxford University Press, Oxford
7. Pedersen KS, Vindigni A, Sessoli R, Coulon C, Clérac R (2017) *Molecular magnetic materials*. Wiley-VCH Verlag GmbH, KGaA, Weinheim, pp 131–159
8. Gao S (2015) *Molecular nanomagnets and related phenomena*. Springer, Berlin, Heidelberg
9. Benelli C, Gatteschi D (2015) *Introduction to molecular magnetism*. Wiley-VCH Verlag GmbH, KGaA, Weinheim, pp I–VII
10. Kahn O (1993) *Molecular magnetism*. VCH Publishers, Orsay
11. Ruiz E, Alvarez S, Rodriguez-Fort A, Alemany P, Pouillon Y, Massobrio A (2001) In: Miller JS, Drillon M (eds) *Magnetism: molecules to material*, vol 2. Wiley-VCH, Weinheim, p 227
12. Clemente-Juan JM, Coronado E, Gaita-Ariño A (2015) *Lanthanides and actinides in molecular magnetism*. Wiley-VCH Verlag GmbH, KGaA, Weinheim, pp 27–60
13. Ungur L, Le Roy JJ, Korobkov I, Murugesu M, Chibotaru LF (2014) *Angew Chem Int Ed Engl* 53:4413–4417
14. Luzon J, Sessoli R (2012) *Dalton Trans* 41:13556–13567
15. Sessoli R, Powell AK (2009) *Coord Chem Rev* 253:2328–2341
16. Jiang S-D, Wang B-W, Gao S (2014) In: Gao S. (ed) *Molecular nanomagnets and related phenomena*, Springer, Berlin, pp 1–31
17. Tang J, Zhang P (2015) *Lanthanide single molecule magnets*. Springer, Berlin
18. Liu J, Chen Y-C, Jia J-H, Liu J-L, Vieru V, Ungur L, Chibotaru LF, Lan Y, Wernsdorfer W, Gao S, Chen X-M, Tong M-L (2016) *J Am Chem Soc* 138:5441–5450
19. Chen Y-C, Liu J-L, Ungur L, Liu J, Li Q-W, Wang L-F, Ni Z-P, Chibotaru LF, Chen X-M, Tong M-L (2016) *J Am Chem Soc* 138:2829–2837
20. Gupta SK, Rajeshkumar T, Rajaraman G, Murugavel R (2016) *Chem Sci* 7:5181–5191
21. Goodwin CAP, Ortu F, Reta D, Chilton NF, Mills DP (2017) *Nature* 548:439–442
22. Guo F-S, Day BM, Chen Y-C, Tong M-L, Mansikkamäki A, Layfield RA (2017) *Angew Chem Int Ed* 56:11445–11449
23. Meng Y-S, Jiang S-D, Wang B-W, Gao S (2016) *Acc Chem Res* 49:2381–2389
24. Liddle ST, van Slageren J (2015) *Chem Soc Rev* 44:6655–6669
25. Dreiser J (2015) *J Phys Condens Matter* 27:183203
26. Ungur L, Chibotaru LF (2017) *Chem Eur J* 23:3708–3718
27. Chibotaru L (2015) *Theoretical understanding of anisotropy in molecular nanomagnets*. In: Gao S (ed) *Molecular nanomagnets and related phenomena*, vol 164. Springer, Berlin, Heidelberg, pp 185–229



28. Ungur L, Chibotaru LF (2015) Lanthanides and actinides in molecular magnetism. Wiley-VCH Verlag GmbH, KGaA, Weinheim, pp 153–184
29. Aquilante F, Autschbach J, Carlson RK, Chibotaru LF, Delcey MG, De Vico L, Fdez Galván I, Ferré N, Frutos LM, Gagliardi L, Garavelli M, Giussani A, Hoyer CE, Li Manni G, Lischka H, Ma D, Malmqvist PÅ, Müller T, Nenov A, Olivucci M, Pedersen TB, Peng D, Plasser F, Pritchard B, Reiher M, Rivalta I, Schapiro I, Segarra-Martí J, Stenrup M, Truhlar DG, Ungur L, Valentini A, Vancoillie S, Veryazov V, Vysotskiy VP, Weingart O, Zapata F, Lindh R (2016) *J Comp Chem* 37:506–541
30. Aquilante F, De Vico L, Ferre N, Ghigo G, Malmqvist PA, Neogrady P, Pedersen TB, Pitonak M, Reiher M, Roos BO, Serrano-Andres L, Urban M, Veryazov V, Lindh R (2010) *J Comp Chem* 31:224–247
31. Duncan JA (2009) *J Am Chem Soc* 131:2416–2416
32. Swerts B, Chibotaru LF, Lindh R, Seijo L, Barandiaran Z, Clima S, Pierloot K, Hendrickx MFA (2008) *J Chem Theory Comput* 4:586–594
33. Veryazov V, Widmark PO, Serrano-Andres L, Lindh R, Roos BO (2004) *Int J Quantum Chem* 100:626–635
34. Karlstrom G, Lindh R, Malmqvist PA, Roos BO, Ryde U, Veryazov V, Widmark PO, Cossi M, Schimmelpennig B, Neogrady P, Seijo L (2003) *Comput Mater Sci* 28:222–239
35. Malmqvist PA, Roos BO, Schimmelpennig B (2002) *Chem Phys Lett* 357:230–240
36. Chibotaru LF, Ungur L (2012) *J Chem Phys* 137:064112–064122
37. Chibotaru LF, Ungur L (2006) MOLCAS SINGLE\_ANISO routines. University of Leuven, Belgium
38. Douglas M, Kroll NM (1974) *Ann Phys* 82:89–155
39. Hess BA (1985) *Phys Rev A* 32:756–763
40. Heß BA, Marian CM, Wahlgren U, Gropen O (1996) *Chem Phys Lett* 251:365–371
41. Ungur L, Chibotaru LF. <http://www.molcas.org/documentation/manual/node105.html>
42. Chilton NF, Collison D, McInnes EJJ, Winpenny REP, Soncini A (2013) *Nat Commun* 4:2551
43. Rinehart JD, Long JR (2011) *Chem Sci* 2:2078–2085
44. Sievers J (1982) *Z Phys B: Condens Matter Quanta* 45:289–296
45. Baldoví JJ, Clemente-Juan JM, Coronado E, Gaita-Ariño A (2014) *Inorg Chem* 53:11323–11327
46. Oyarzabal I, Ruiz J, Seco JM, Evangelisti M, Camón A, Ruiz E, Aravena D, Colacio E (2014) *Chem Eur J* 20:14262–14269
47. Aravena D, Ruiz E (2013) *Inorg Chem* 52:13770–13778
48. Baldoví JJ, Borrás-Almenar JJ, Clemente-Juan JM, Coronado E, Gaita-Arino A (2012) *Dalton Trans* 41:13705–13710
49. Baldoví JJ, Cardona-Serra S, Clemente-Juan JM, Coronado E, Gaita-Ariño A, Palií A (2012) *Inorg Chem* 51:12565–12574
50. Baldoví JJ, Cardona-Serra S, Clemente-Juan JM, Coronado E, Gaita-Ariño A, Palií A (2013) *J Comput Chem* 34:1961–1967
51. Pointillart F, Jung J, Berraud-Pache R, Le Guennic B, Dorcet V, Golhen S, Cador O, Maury O, Guyot Y, Decurtins S, Liu S-X, Ouahab L (2015) *Inorg Chem* 54:5384–5397
52. Lines ME (1971) *J Chem Phys* 55:2977–2984
53. Ungur L, Chibotaru LF (2007) POLY\_ANISO program. KU Leuven, Belgium
54. Marx R, Moro F, Dorfel M, Ungur L, Waters M, Jiang SD, Orlita M, Taylor J, Frey W, Chibotaru LF, van Slageren J (2014) *Chem Sci* 5:3287–3293
55. Guo Y-N, Ungur L, Granroth GE, Powell AK, Wu C, Nagler SE, Tang J, Chibotaru LF, Cui D (2014) *Sci Rep* 4:5471
56. Batchelor LJ, Cimatti I, Guillot R, Tuna F, Wernsdorfer W, Ungur L, Chibotaru LF, Campbell VE, Mallah T (2014) *Dalton Trans* 43:12146–12149

57. Bernot K, Luzon J, Bogani L, Etienne M, Sangregorio C, Shanmugam M, Caneschi A, Sessoli R, Gatteschi D (2009) *J Am Chem Soc* 131:5573–5579
58. Gupta T, Rajaraman G (2016) *Chem Commun* 52:8972–9008
59. Zhang P, Zhang L, Tang J (2015) *Dalton Trans* 44:3923–3929
60. Ungur L, Chibotaru LF (2016) *Inorg Chem* 55:10043–10056
61. Orbach R (1961) *Proc R Soc Lond A* 264:485–495
62. Campbell VE, Bolvin H, Rivière E, Guillot R, Wernsdorfer W, Mallah T (2014) *Inorg Chem* 53:2598–2605
63. Li DP, Wang TW, Li CH, Liu DS, Li YZ, You XZ (2010) *Chem Commun* 46:2929–2931
64. Gavey EL, Al Hareri M, Regier J, Carlos LD, Ferreira RAS, Razavi FS, Rawson JM, Pilkington M (2015) *J Mater Chem C* 3:7738–7747
65. Ruiz J, Mota AJ, Rodriguez-Dieguez A, Titos S, Herrera JM, Ruiz E, Cremades E, Costes JP, Colacio E (2012) *Chem Commun* 48:7916–7918
66. Chilton NF, Langley SK, Moubarak B, Soncini A, Batten SR, Murray KS (2013) *Chem Sci* 4:1719–1730
67. Cucinotta G, Perfetti M, Luzon J, Etienne M, Car PE, Caneschi A, Calvez G, Bernot K, Sessoli R (2012) *Angew Chem Int Ed Engl* 51:1606–1610
68. Feltham HLC, Lan Y, Klöwer F, Ungur L, Chibotaru LF, Powell AK, Brooker S (2011) *Chem Eur J* 17:4362–4365
69. Long J, Rouquette J, Thibaud J-M, Ferreira RAS, Carlos LD, Donnadiou B, Vieru V, Chibotaru LF, Konczewicz L, Haines J, Guari Y, Larionova J (2015) *Angew Chem Int Ed* 54:2236–2240
70. Xue S, Ungur L, Guo Y-N, Tang J, Chibotaru LF (2014) *Inorg Chem* 53:12658–12663
71. Upadhyay A, Singh SK, Das C, Mondol R, Langley SK, Murray KS, Rajaraman G, Shanmugam M (2014) *Chem Commun* 50:8838–8841
72. Bhunia A, Gamer MT, Ungur L, Chibotaru LF, Powell AK, Lan Y, Roesky PW, Menges F, Riehn C, Niedner-Schatteburg G (2012) *Inorg Chem* 51:9589–9597
73. Ou-Yang JK, Saleh N, Fernandez Garcia G, Norel L, Pointillart F, Guizouarn T, Cador O, Totti F, Ouahab L, Crassous J, Le Guennic B (2016) *Chem Commun* 52:14474–14477
74. Vignesh KR, Langley SK, Murray KS, Rajaraman G (2017) *Inorg Chem* 56:2518
75. Jung J, da Cunha TT, Le Guennic B, Pointillart F, Pereira CLM, Luzon J, Golhen S, Cador O, Maury O, Ouahab L (2014) *Eur J Inorg Chem* 2014:3888–3894
76. Costes JP, Titos-Padilla S, Oyarzabal I, Gupta T, Duhayon C, Rajaraman G, Colacio E (2015) *Chem Eur J* 21:15785–15796
77. Gregson M, Chilton NF, Ariciu A-M, Tuna F, Crowe IF, Lewis W, Blake AJ, Collison D, McInnes EJJ, Winpenny REP, Liddle ST (2016) *Chem Sci* 7:155–165
78. Sun W-B, Yan P-F, Jiang S-D, Wang B-W, Zhang Y-Q, Li H-F, Chen P, Wang Z-M, Gao S (2016) *Chem Sci* 7:684–691
79. Long J, Shestakov BG, Liu D, Chibotaru LF, Guari Y, Cherkasov AV, Fukin GK, Trifonov AA, Larionova J (2017) *Chem Commun* 53:4706–4709
80. Rajaraman G, Singh SK, Gupta T, Shanmugam M (2014) *Chem Commun* 50:15513–15516
81. Gupta T, Velmurugan G, Rajeshkumar T, Rajaraman G (2016) *J Chem Sci* 128:1615–1630
82. Kishi Y, Pointillart F, Lefevre B, Riobe F, Le Guennic B, Golhen S, Cador O, Maury O, Fujiwara H, Ouahab L (2017) *Chem Commun* 53:3575–3578
83. Lucaccini E, Briganti M, Perfetti M, Vendier L, Costes J-P, Totti F, Sessoli R, Sorace L (2016) *Chem Eur J* 22:5552–5562
84. Costes JP, Titos-Padilla S, Oyarzabal I, Gupta T, Duhayon C, Rajaraman G, Colacio E (2016) *Inorg Chem* 55:4428–4440
85. Liu J-L, Chen Y-C, Zheng Y-Z, Lin W-Q, Ungur L, Wernsdorfer W, Chibotaru LF, Tong M-L (2013) *Chem Sci* 4:3310–3316
86. Ding Y-S, Chilton NF, Winpenny REP, Zheng Y-Z (2016) *Angew Chem Int Ed* 55:16071–16074

87. Chen Y-C, Liu J-L, Lan Y, Zhong Z-Q, Mansikkamäki A, Ungur L, Li Q-W, Jia J-H, Chibotaru LF, Han J-B, Wernsdorfer W, Chen X-M, Tong M-L (2017) *Chem Eur J* 23:5708–5715
88. Lucaccini E, Sorace L, Perfetti M, Costes J-P, Sessoli R (2014) *Chem Commun* 50:1648–1651
89. Le Roy JJ, Jeletic M, Gorelsky SI, Korobkov I, Ungur L, Chibotaru LF, Murugesu M (2013) *J Am Chem Soc* 135:3502–3510
90. Chilton NF, Goodwin CAP, Mills DP, Winpenny REP (2015) *Chem Commun* 51:101–103
91. Chilton NF (2015) *Inorg Chem* 54:2097–2099
92. Singh MK, Yadav N, Rajaraman G (2015) *Chem Commun* 51:17732–17735
93. Rinehart JD, Fang M, Evans WJ, Long JR (2011) *Nat Chem* 3:538–542
94. Rajeshkumar T, Rajaraman G (2012) *Chem Commun* 48:7856–7858
95. Hu Z, Dong B-W, Liu Z, Liu J-J, Su J, Yu C, Xiong J, Shi D-E, Wang Y, Wang B-W, Ardavan A, Shi Z, Jiang S-D, Gao S (2017) *J Am Chem Soc*
96. Liu F, Krylov DS, Spree L, Avdoshenko SM, Samoylova NA, Rosenkranz M, Kostanyan A, Greber T, Wolter AUB, Büchner B, Popov AA (2017) *Nat Commun* 8:16098
97. Singh MK, Rajaraman G (2016) *Chem Commun* 52:14047–14050
98. Vieru V, Ungur L, Chibotaru LF (2013) *J Phys Chem Lett* 4:3565–3569
99. Chen C-H, Krylov DS, Avdoshenko S, Liu F, Spree L, Yadav R, Alvertis A, Hozoi L, Nenkov K, Kostanyan A, Greber T, Wolter AUB, Popov AA (2017) *Chem Sci* 8:6451–6465
100. Boulon ME, Cucinotta G, Liu SS, Jiang SD, Ungur L, Chibotaru LF, Gao S, Sessoli R (2013) *Chem Eur J* 19:13726–13731
101. Flanagan BM, Bernhardt PV, Krausz ER, Lüthi SR, Riley MJ (2001) *Inorg Chem* 40:5401–5407
102. Singh SK, Pandey B, Velmurugan G, Rajaraman G (2017) *Dalton Trans* 46:11913–11924
103. Das C, Upadhyay A, Vaidya S, Singh SK, Rajaraman G, Shanmugam M (2015) *Chem Commun* 51:6137–6140
104. Pedersen KS, Ungur L, Sigrist M, Sundt A, Schau-Magnussen M, Vieru V, Mutka H, Rols S, Weihe H, Waldmann O, Chibotaru LF, Bendix J, Dreiser J (2014) *Chem Sci* 5:1650–1660
105. Boulon ME, Cucinotta G, Luzon J, Degl’Innocenti C, Perfetti M, Bernot K, Calvez G, Caneschi A, Sessoli R (2013) *Angew Chem Int Ed* 52:350–354
106. Liu J-L, Yuan K, Leng J-D, Ungur L, Wernsdorfer W, Guo F-S, Chibotaru LF, Tong M-L (2012) *Inorg Chem* 51:8538–8544
107. Blackburn OA, Chilton NF, Keller K, Tait CE, Myers WK, McInnes EJJ, Kenwright AM, Beer PD, Timmel CR, Faulkner S (2015) *Angew Chem* 127:10933–10936
108. Singh SK, Gupta T, Ungur L, Rajaraman G (2015) *Chem Eur J* 21:13812–13819
109. Li Q-W, Wan R-C, Chen Y-C, Liu J-L, Wang L-F, Jia J-H, Chilton NF, Tong M-L (2016) *Chem Commun* 52:13365–13368
110. Gupta SK, Rajeshkumar T, Rajaraman G, Murugavel R (2016) *Chem Commun* 52:7168–7171
111. Chen Y-C, Liu J-L, Wernsdorfer W, Liu D, Chibotaru LF, Chen X-M, Tong M-L (2017) *Angew Chem Int Ed* 56:4996–5000
112. Meng Y-S, Qiao Y-S, Zhang Y-Q, Jiang S-D, Meng Z-S, Wang B-W, Wang Z-M, Gao S (2016) *Chem Eur J* 22:4704–4708
113. Ishikawa N, Sugita M, Ishikawa T, Koshihara SY, Kaizu Y (2003) *J Am Chem Soc* 125:8694
114. Ganivet CR, Ballesteros B, de la Torre G, Clemente-Juan JM, Coronado E, Torres T (2013) *Chem Eur J* 19:1457–1465
115. Mannini M, Bertani F, Tudisco C, Malavolti L, Poggini L, Misztal K, Menozzi D, Motta A, Otero E, Ohresser P, Sainctavit P, Condorelli GG, Dalcanale E, Sessoli R (2014) *Nat Commun* 5:4582
116. Chen Y, Ma F, Chen X, Dong B, Wang K, Jiang S, Wang C, Chen X, Qi D, Sun H, Wang B, Gao S, Jiang J (2017) *Inorg Chem Front* 4:1465
117. Chen Y, Ma F, Chen X, Dong B, Wang K, Jiang S, Wang C, Chen X, Qi D, Sun H, Wang B, Gao S, Jiang J (2017) *Inorg Chem* 56:13889–13896

118. Singh SK, Gupta T, Rajaraman G (2014) *Inorg Chem* 53:10835–10845
119. Pointillart F, Cadour O, Le Guennic B, Ouahab L (2017) *Coord Chem Rev.* <https://doi.org/10.1016/j.ccr.2016.1012.1017>
120. Gupta T, Rajaraman G (2014) *J Chem Sci* 126:1569–1579
121. Lunghi A, Totti F, Sessoli R, Sanvito S (2017) *Nat Commun* 8:14620
122. Vignesh KR, Soncini A, Langley SK, Wernsdorfer W, Murray KS, Rajaraman G (2017) *Nat Commun* 8:1023. <https://doi.org/10.1038/s41467-017-01102-5>

# Complete Active Space Wavefunction-Based Analysis of Magnetization and Electronic Structure



Frédéric Gendron, H el ene Bolvin, and Jochen Autschbach

## Contents

1	Introduction .....	356
2	Theoretical Methods .....	357
3	Case Studies: From Transition Metals to Actinides .....	366
3.1	A Trigonal Cobalt(II) Complex: $\text{Co}(\text{Tp})_2$ .....	367
3.2	A High-Spin Fe(II) Complex: $\text{FeLCl}$ .....	370
3.3	Zero-Field Splitting in an Octahedral Ni(II) Complex .....	372
3.4	Linear Ln(III) Complexes: $\text{Ln}(\text{COT})_2^-$ .....	376
3.5	An Octahedral Np(VI) Complex: $\text{NpF}_6$ .....	381
3.6	Trigonal U(IV) Complexes: $\text{Ar}_3\text{U-X}$ with $\text{Ar} = \text{aryl}$ .....	383
3.7	The $[\text{U}(\text{Tp}^{\text{Me}_2})_2(\text{bipy})]\text{I}$ Complex .....	387
4	Summary .....	388
	References .....	388

**Abstract** A theoretical framework for the generation of natural orbitals, natural spin orbitals, as well as orbital- and spin-magnetizations, from multi-configurational ab initio wavefunction calculations including spin-orbit coupling is presented. Selected case studies show how these computational orbital and magnetization tools can be used to interpret and rationalize the magnetic properties of complexes containing transition metals, lanthanides, and actinides.

**Keywords** Electron spin Hamiltonian · Magnetization · Natural orbitals · Spin Hamiltonian · Spin orbit coupling · Wavefunction calculations · Zeeman interaction

---

F. Gendron and J. Autschbach (✉)  
Department of Chemistry, University at Buffalo, State University of New York, Buffalo, NY,  
USA  
e-mail: [jochena@buffalo.edu](mailto:jochena@buffalo.edu)

H. Bolvin  
Laboratoire de Physique et de Chimie Quantiques, Universit e Toulouse 3, Toulouse, France

## Units, Notation, and Acronyms

The reader is assumed to be familiar with basic concepts of quantum mechanics and computational chemistry. SI or Hartree atomic units (au) are employed. Nuclear motion is ignored in the discussion. The symbols  $\cdot$  and  $\times$  indicate inner and outer products, respectively, for vectors and matrices or tensors. Bold-italic notation such as  $\mathbf{r}$ ,  $\hat{\mathbf{S}}$ ,  $\boldsymbol{\mu}$  is used for vectors and vector quantum operators. Upright-bold such as  $\mathbf{a}$ ,  $\mathbf{G}$ ,  $\boldsymbol{\mu}$  is used for matrices and rank-2 tensors. The EPR pseudo-spin operator is denoted as  $\hat{S}$ .

The following acronyms are used in the text:

3D	Three-dimensional
AO	Atomic orbital (orbital of an atom, or AO basis function)
CAS	Complete active space
CF	Crystal field
DFT	Density functional theory (“pure” and generalized KS variants)
EPR	Electron paramagnetic resonance
ES	Excited state
GS	Ground state
HF	Hartree-Fock
HOMO	Highest occupied molecular orbital
KD	Kramers doublet
KS	Kohn-Sham
LF	Ligand field
LR	Linear response
MO	Molecular orbital
NMR	Nuclear magnetic resonance
NR	Nonrelativistic (calculation excluding any relativistic effects)
PV	Principal value (of a tensor)
PAS	Principal axis system (of a tensor)
QM	Quantum mechanical (e.g., in reference to Dirac, Schrödinger Eqs.)
SMM	Single-molecule magnet
SO	Spin-orbit (SO calculation usually also includes SR effects)
SOC	SO coupling
SR	Scalar relativistic (relativistic calculation without SO effects)
TIP	Temperature-independent paramagnetism
WFT	Wavefunction theory
ZFS	Zero-field splitting

## 1 Introduction

Metal complexes with interesting magnetic properties tend to have complicated open-shell electronic structures that require a multi-configurational (multi-reference) wavefunction description, often including relativistic effects. Regarding the latter, one usually distinguishes between scalar relativistic (SR) effects and spin-orbit

(SO) coupling. In the context of this chapter, the SO level of calculation is meant to include both SR and SO effects.

The complete active space (CAS) wavefunction theory (WFT) framework, whereby one performs a full configuration interaction within a chosen active space of orbitals [1, 2], restricted or generalized active space methods, or CAS-like approaches utilizing the density matrix renormalization framework [3–5], are the methods of choice for treating systems with complicated open shells, because such electronic states are generally not well described by single-configuration methods such as Kohn-Sham density functional theory (KS-DFT) or standard coupled-cluster methods. However, SO multi-reference wavefunctions are complex, in the usual meaning of complicated or intricate, as well as in the mathematical sense. Therefore, such wavefunctions have traditionally not been as amenable to an intuitive analysis in terms of real orbitals as, for instance, SR DFT electronic states.

In recent years, analysis tools in terms of orbitals that are familiar to chemists have been used increasingly to dissect the electron density as well as spin-densities, and magnetization densities that arise from the orbital angular momentum, based on sophisticated SO multi-reference wavefunction calculations. Furthermore, the magnetization densities arising from the spin and orbital angular momentum in SO CAS calculations can be visualized. In combination with the orbitals and their associated populations, detailed numerical as well as qualitative chemical information can be extracted from *ab initio* calculations about how calculated magnetic susceptibilities and electronic magnetic moments (*g*-factors) are ultimately related to the geometry and chemical bonding of a metal complex.

In Sect. 2, some theoretical aspects underlying these analyses are discussed. Section 3 presents a variety of case studies involving complexes with *3d*, *4f*, and *5f* metals.

## 2 Theoretical Methods

We assume that the metal complex of interest is oriented within the laboratory coordinate frame such that its principal magnetic axes *X*, *Y*, and *Z* coincide with the *x*, *y*, and *z* direction. We therefore use these notations interchangeably. The alignment can be achieved, for instance, by first calculating the magnetic susceptibility tensor in its Cartesian  $3 \times 3$  matrix representation (components *xx*, *xy* = *yx*, *xz* = *zx*, *yy*, *yz* = *zy*, *zz*). Diagonalization of the tensor gives its principal values (the eigenvalues) and the principal axis system (PAS, the eigenvectors). The metal complex is then rotated such that the PAS coincides with the unit vectors of the Cartesian laboratory coordinate frame. Furthermore, the components of degenerate or weakly split degenerate states can be chosen to diagonalize the Zeeman operator for the magnetic field along a selected magnetic axis, as described, for instance, in [6].

Static homogeneous external magnetic fields can usually be described well by the corresponding nonrelativistic orbital and spin Zeeman operators, even if the

electronic structure calculation of the complex requires a treatment of relativistic effects. The reason for this is that the Zeeman operators sample the spatial valence and outer core atomic regions where “kinematic” terms that modify the relativistic perturbation operators relative to their nonrelativistic counterparts do not make a large difference. (In contrast, nuclear magnetic hyperfine operators sample the electronic structure in the vicinity of the nuclei and are – for heavy atoms – strongly impacted by relativistic effects [7].) Therefore, the familiar nonrelativistic operators for an external magnetic field are used in the following. The magnetic moment operator describing the interaction of the electrons with a magnetic field in direction  $u \in \{x, y, z\}$  is in this “nonrelativistic with spin” formalism given by

$$\begin{aligned}\widehat{\mu}_u &= -\mu_B \widehat{M}_u \quad \text{with} \\ \widehat{M}_u &= \widehat{L}_u + g_e \widehat{S}_u\end{aligned}\tag{1}$$

Here,  $\mu_B = e\hbar/(2m_e)$  is the Bohr magneton, and  $g_e \simeq 2$  is the free electron  $g$ -value. Small deviations of the free electron  $g$ -value from 2 are due to quantum electrodynamics (QED) corrections to the Dirac relativistic treatment. The operators  $\widehat{L}_u$  and  $\widehat{S}_u$  are the dimensionless one-electron operators for the  $u$ -component of the orbital angular momentum and the spin angular momentum, respectively.

Let  $\psi$  be an electronic ground or excited state wavefunction of a metal complex, or a component of the respective state if it is degenerate. Based on Eq. (1), orbital and spin magnetizations can be defined as follows:

$$m_u^L(\mathbf{r}) = \int \psi^* \widehat{L}_u \psi d\tau' \tag{2a}$$

$$m_u^S(\mathbf{r}) = g_e \int \psi^* \widehat{S}_u \psi d\tau' \tag{2b}$$

The notation  $d\tau'$  indicates an integration over all electron spin degrees of freedom, and all but one electron position degrees of freedom. The resulting functions therefore depend on a single electron coordinate. The procedure for calculating the magnetizations is similar to how the electron density  $\rho$  is defined in terms of the wavefunction:

$$\rho(\mathbf{r}) = N \int \psi^* \psi d\tau' \tag{2c}$$

In the equation for the electron density,  $N$  is the number of electrons of the system.

The three functions,  $m_u^L(\mathbf{r})$ ,  $m_u^S(\mathbf{r})$ , and  $\rho(\mathbf{r})$ , are real functions of 3D space and therefore they can be visualized easily, for example in cut-planes or as 3D isosurfaces. The volume integrals of these functions space give

$$\int m_u^L(\mathbf{r}) dV = \langle L_u \rangle \tag{3}$$



$$\int m_u^S(\mathbf{r}) dV = g_e \langle S_u \rangle \quad (4)$$

$$\int \rho(\mathbf{r}) dV = N \quad (5)$$

The integral over the electron density gives the electron number. In the other two cases, the integration gives the expectation value of a component of the orbital or spin angular momentum (times  $g_e$  for the latter). We write  $g_e$  in the equations, but in our numerical calculations of the spin magnetization the QED corrections are neglected, i.e.,  $g_e = 2$  is used. Per Eq. (1), the magnetic moment expectation value is obtained from the magnetizations via

$$\langle \mu_u \rangle = -\mu_B \langle M_u \rangle \quad \text{with} \quad \langle M_u \rangle = \int [m_u^L(\mathbf{r}) + m_u^S(\mathbf{r})] dV \quad (6)$$

If  $\psi$  is a component of a degenerate state of interest in a computational study of a paramagnetic metal complex, then arbitrary unitary transformations among the state components can be applied without loss of generality. However, the functions  $m_u^L(\mathbf{r})$  and  $m_u^S(\mathbf{r})$  may not be invariant under such transformations. The electron density  $\rho(\mathbf{r})$  for the individual components of orbitally degenerate states may also not transform as one of the irreducible representations (“irreps”) of the complex’s symmetry point group if this is not enforced in the calculations. Many quantum chemistry programs do not support non-abelian symmetry groups.

For example, for a complex with linear metal coordination, the quantum number  $m_\ell$  for the projection of the orbital angular momentum onto a quantization axis can be used to classify the orbitals at the SR level, as long as the principal rotational symmetry axis is of order  $>2\ell$ . Here,  $\ell = 2$  or  $3$  is the angular momentum quantum number for a  $d$  or  $f$  orbital, respectively. (When the SO coupling is included in the theoretical treatment, the corresponding quantum number  $m_j$  for the projection of the total angular momentum can be used instead.) That is, when the order of the principal symmetry axis is sufficiently high, the orbitals behave the same as if the symmetry were fully linear, as in the  $C_{\infty v}$  or  $D_{\infty h}$  point groups. Accordingly, the calculated electronic structure should reflect the rotational symmetry. The  $d$  and  $f$  orbitals can then be classified as  $\sigma$ ,  $\pi$ ,  $\delta$ ,  $\phi$ , with respect to the rotational axis, corresponding to  $|m_\ell| = 0, 1, 2, 3$ . (This notation is often convenient even when the actual symmetry is lower.) The usual textbook expressions for the  $d$  and  $f$  orbitals corresponding to these symmetries, for a quantization axis in  $z$  direction, are:  $d_\sigma = d_{z^2}$ ,  $f_\sigma = f_{z^3}$ .  $d_\pi = d_{xz}$  and  $d_{yz}$ ;  $f_\pi = f_{xz^2}$  and  $f_{yz^2}$ .  $d_\delta = d_{xy}$  and  $d_{x^2-y^2}$ ;  $f_\delta = f_{xyz}$  and  $f_{z(x^2-y^2)}$ .  $f_\phi = f_{x(x^2-3y^2)}$  and  $f_{y(3x^2-y^2)}$ . The  $\pi$ ,  $\delta$ , and  $\phi$  orbitals are doubly degenerate. Single (or triple) occupations of these orbitals correspond to a spatially (orbitally) degenerate electronic state. In order for each state component to have a rotationally symmetric electron density individually, the degenerate orbitals must be evenly occupied (e.g., 0.5 each for a  $d^1$  or  $f^1$  configuration, which requires at least two configurations = determinants in the wavefunction) if they are the usual real  $d$  or  $f$  orbitals. However, NR and SR CAS calculations for

such a nonbonding degenerate  $d^1$  or  $f^1$  example will likely produce two state components in which one of the real  $d$  or  $f$  orbitals is occupied and the counterpart of the same symmetry is unoccupied. As a consequence, the rotational symmetry is broken in the individual state components.

Well-defined spin and orbital magnetization densities can be generated easily after a subsequent treatment of the SO interaction, which generally requires complex wavefunction coefficients anyway. The components of the degenerate state are then chosen to diagonalize the magnetic moment operator matrix for a given field direction. In the case studies of Sect. 3, we diagonalize the  $u$  component of the magnetic moment operator prior to generating  $m_u^L(\mathbf{r})$  and  $m_u^S(\mathbf{r})$ . Unless stated otherwise, the resulting state component with the most positive  $\langle S_u \rangle$  is then chosen for further analysis. For axial complexes, the procedure tends to generate linear combinations of the SR states such that, for the  $d^1$  or  $f^1$  example, equal occupations of  $\pi$ ,  $\delta$ , or  $\phi$  metal orbitals are achieved, which corresponds to forming the angular momentum eigenfunctions from the real  $d$  or  $f$  metal orbitals. There is also the possibility to diagonalize the magnetic moment operator component  $u$  in the basis of the state components, and then visualize  $m_v^L(\mathbf{r})$  and  $m_v^S(\mathbf{r})$  with  $v \neq u$ , but we are not referring to such cases in Sect. 3 unless noted explicitly.

When NR or SR calculations generate spin eigenfunctions with well-defined quantum numbers  $S$  and  $M_S$ , then  $\langle S_u \rangle = M_S$  if  $u$  is the chosen projection quantization axis. In quantum chemistry,  $u = z$  is the default choice. The function  $m_z^S$  is then nothing but the familiar *spin density*. When the magnetic moment operator for a degenerate state is diagonalized, the direction of the magnetic field defines the quantization axis for the spin and the orbital angular momentum. In relativistic calculations where the effects from spin-orbit (SO) coupling are included in the wavefunctions, spin and orbital angular momentum cease to be good quantum numbers. Of course, the corresponding expectation values can still be calculated, and they are meaningful because of their contributions to the magnetic moment.

When an atomic orbital (AO) basis set  $\{\chi_\mu\}$  with real functions is used, as it is customary in quantum chemistry, the electron density and the spin magnetization can be expressed in the AO basis in terms of the elements of density matrices:

$$\rho = \sum_{\mu\nu} \chi_\mu \chi_\nu D_{\nu\mu}^\rho \quad (7a)$$

$$m_u^S = \sum_{\mu\nu} \chi_\mu \chi_\nu D_{u,\nu\mu}^S \quad (7b)$$

It is important to note that the action of the spin operator is fully considered in Eq. (2b), and that subsequently all spin degrees of freedom are integrated over. Therefore, there are no spin degrees of freedom explicitly contained in  $m_u^S$  anymore. The function implicitly depends on the action of the spin operator because of Eq. (2b). The matrices  $\mathbf{D}^\rho$  and  $\mathbf{D}_u^S$  which are formed by the elements  $D_{\nu\mu}^\rho$  and  $D_{u,\nu\mu}^S$ , respectively, are real and symmetric, and therefore they can be diagonalized in order to reduce the double sums in Eqs. (7a) and (7b) to single sums:

$$\rho(\mathbf{r}) = \sum_p n_p [\varphi_p(\mathbf{r})]^2 \quad \text{with} \quad \sum_p n_p = N \quad \text{and} \quad \int [\varphi_p(\mathbf{r})]^2 dV = 1 \quad (8a)$$

$$m_u^S(\mathbf{r}) = \sum_p n_{u,p}^S [\varphi_{u,p}^S(\mathbf{r})]^2 \quad \text{with} \quad \sum_p n_{u,p}^S = g_e \langle S_u \rangle \quad \text{and} \quad \int [\varphi_{u,p}^S(\mathbf{r})]^2 dV = 1 \quad (8b)$$

The orbitals (one-electron functions)  $\varphi_p$  are the natural orbitals (NOs), and the numbers  $n_p$  are the corresponding populations (or occupations). We refer to the eigenfunctions  $\varphi_{u,p}^S$  of the spin magnetization components as natural spin orbitals (NSOs). The numbers  $n_{u,p}^S$  are the corresponding spin populations. The orbitals are chosen to be ortho-normal. The populations of the NOs add up to the total number of electrons, and the sum of the spin populations gives  $g_e \simeq 2$  times the expectation value for spin component  $u$ . Furthermore, the orbitals are chosen to be real such that for metal  $d$  and  $f$  orbitals they resemble the orbitals familiar from textbooks.

Examples for how the NO and NSO populations can help with the analysis of complicated electronic structures are provided in Sect. 3. For a single, real, closed-shell or restricted-open-shell Slater-determinant wavefunction, the NO occupations are 1 or 2 and indicate how often a spin-orbital appears in the determinant (if an orbital does not appear in the Slater determinant, it is called unoccupied). The NSO spin populations are +1 for  $\alpha$ -spin ( $\uparrow$ ) and  $-1$  for  $\beta$ -spin ( $\downarrow$ ) orbitals in this case and add up to the excess of  $\alpha$  vs.  $\beta$  spin electrons. More generally, however, the NO and NSO populations are not integers, because the wavefunction may be composed of several, or even very many, Slater determinants, due to a combination of static and dynamic correlation and SO coupling.

The diagonalization leading to Eqs. (8a) and (8b) does not in itself produce well-defined linear combinations of orbitals with identical populations. This includes the whole set of unoccupied orbitals and – in CAS calculations – the set of inactive occupied orbitals as well as active orbitals with equal populations. Additional criteria, for example based on the degree of localization or simply aesthetics, may be applied in order to select specific linear combinations within a set of equally populated orbitals.

The orbital magnetization requires additional consideration, because of the derivative term in the (dimensionless) one-electron orbital angular momentum component operator

$$\widehat{L}_u = -i \sum_{k=1}^N [\mathbf{r}_k \times \nabla_k]_u \quad (9)$$

The notation indicates that the component  $u$  of the vector  $\mathbf{r}_k \times \nabla_k$  is used to construct  $\widehat{L}_u$ . The operator  $\widehat{L}_u$  is imaginary, self-adjoint for square-integrable functions, and spin-independent. It is possible to construct, from a many-electron wavefunction, a one-particle density matrix  $\mathbf{D}^J$  that can be used to calculate the expectation value of an imaginary operator such as  $\widehat{L}_u$  as follows:

$$\langle L_u \rangle = -i \sum_{\mu\nu} \langle \chi_\mu | [\mathbf{r} \times \nabla]_u | \chi_\nu \rangle D_{\nu\mu}^J \quad (10)$$

The matrix formed by the integrals  $\langle \chi_\mu | [\mathbf{r} \times \nabla]_u | \chi_\nu \rangle$  over the real AO basis is real and antisymmetric, i.e., upon multiplication with the factor  $-i$  one obtains a purely imaginary Hermitian matrix. Likewise, the matrix  $\mathbf{D}^J$  is imaginary and antisymmetric, such that the expectation value is real. We use a superscript  $J$  for this matrix in order to associate it with the paramagnetic current density defined below, as it is not specific to the orbital angular momentum. The matrix  $\mathbf{D}^J$  with elements  $D_{\nu\mu}^J$  can be used to calculate expectation values of any spin-independent quantum operator that is imaginary and has an antisymmetric matrix representation in the AO basis. Since the matrix  $\mathbf{D}^J$  is Hermitian, it can be diagonalized to give a set of complex eigenfunctions  $\varphi_p^J$ , chosen to be ortho-normal, and real eigenvalues  $n_p^J$ , such that the double sum of Eq. (10) reduces to:

$$\begin{aligned} \langle L_u \rangle &= -i \sum_p n_p^J \int \varphi_p^{J*} [\mathbf{r} \times \nabla]_u \varphi_p^J dV \\ &= -\frac{i}{2} \sum_p n_p^J \int \left( \varphi_p^{J*} [\mathbf{r} \times \nabla]_u \varphi_p^J - \varphi_p^J [\mathbf{r} \times \nabla]_u \varphi_p^{J*} \right) dV \end{aligned} \quad (11)$$

The antisymmetrized form in the second line of Eq. (11) is more commonly used when the orbital magnetization is re-cast in terms of the paramagnetic current density. The latter is defined in the context of the present discussion as the real-valued vector field

$$\mathbf{j}(\mathbf{r}) = -\frac{i}{2} \sum_p n_p^J \left( \varphi_p^{J*} \nabla \varphi_p^J - \varphi_p^J \nabla \varphi_p^{J*} \right) \quad (12)$$

In terms of the paramagnetic current density, the orbital magnetization is given as

$$m_u^L = [\mathbf{r} \times \mathbf{j}]_u = \sum_p n_p^J [\mathbf{r} \times \mathbf{j}_p]_u \quad (13)$$

A per-orbital paramagnetic current density can be defined accordingly as

$$\mathbf{j}_p(\mathbf{r}) = -\frac{i}{2} \left( \varphi_p^{J*} \nabla \varphi_p^J - \varphi_p^J \nabla \varphi_p^{J*} \right) \quad (14)$$

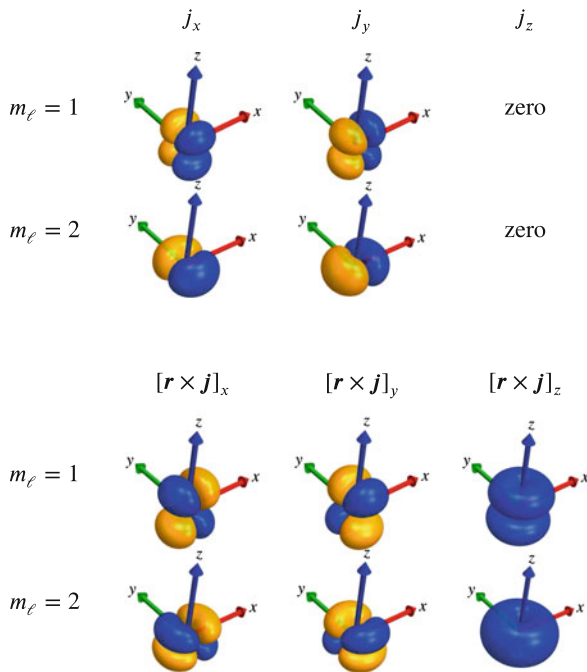
The numbers  $n_p^J$  do not have as specific of a definition as the NO and NSO populations, because they need to be combined with the action of a spin-independent imaginary operator in order to correspond to an expectation value or magnetization density, as in Eqs. (11) or (13).

Löwdin [8] defined natural (spin) orbitals as the eigenfunctions of the full one-particle density matrix in the molecular spin-orbital basis. The NOs, NSOs, and the orbitals used to construct the current density, as described in this section, are

based on related concepts but defined in the AO basis, and they are not dependent on the electron spins. (The signs of the NSO populations indicate  $\alpha$  vs.  $\beta$  spin.) The restricted active space self-consistent field (RASSCF) [9] and restricted active space state-interaction (RASSI) [10] programs of the Molcas quantum chemistry software suite [11] have for a long time included modules to calculate matrix elements of various kinds of operators in a basis of spin-free (SF) SR many-electron wavefunctions, which are subsequently transformed to the basis of SO wavefunctions. A key feature of this code is that it generates only the necessary SR density matrix information needed for matrix elements of (1) spin-free real operators (e.g., multipole moments, EFGs), (2) spin-free real operators multiplied by  $\hat{S}_x$ ,  $\hat{S}_y$ , or  $\hat{S}_z$  and the spin operators themselves, (3) spin-free imaginary operators (e.g., orbital angular momentum components), or (4) spin-free imaginary operators multiplied by  $\hat{S}_x$ ,  $\hat{S}_y$ , or  $\hat{S}_z$ . This code was rearranged [12, 13] in such a manner that the corresponding density matrices for cases (1) to (4) are constructed explicitly for the SO wavefunctions first, while the contraction with the operator AO integral matrices is the very last step of the calculation. This approach gives access both to the operator matrix elements for the SO wavefunctions, and the related (single-state or transition-) density matrices and their eigenfunctions (orbitals). The NOs of this section are related to type (1). The NSOs are related to type (2), and the eigenfunctions of  $\mathbf{D}^f$  are related to type (3).

Often, the magnetic properties of a metal complex are intimately tied to formally nonbonding  $d$  or  $f$  orbitals at the metal center (and magnetic couplings between metal centers, in multi-nuclear complexes or solids). The NOs and NSOs determined from ab initio calculations then often appear as textbook examples of  $d$  or  $f$  orbitals, with varying degrees of covalency involving the ligands. Furthermore, when the orbital angular momentum magnetization is caused by a single or a few nonbonding metal  $d$  or  $f$  orbitals, the resulting magnetization  $m_u^L$  may easily reveal the underlying contributions from the components of the magnetization density  $\mathbf{r} \times \mathbf{j}$  of individual orbitals. For reference, Figs. 1 and 2 display isosurfaces of the paramagnetic current density components, and the components of the magnetization density, for  $d$  and  $f$  angular momentum eigenfunctions with different  $m_\ell$ .

In the discussion in Sect. 3, the NOs and NSOs correspond to the usual *real*  $d$  and  $f$  orbitals. For a degenerate pair of these orbitals of  $\pi$ ,  $\delta$ , or  $\phi$  symmetry, a spatial doublet state arises if there is a single electron or a single hole in the level, i.e., for a combined population of 1 or 3. For rotational symmetry-adapted state components, the real NOs then have occupations of 0.5 or 1.5 each. As alluded to above, such an occupation pattern can be viewed as having formed complex linear combinations of the real NOs, with equal weight, to form angular momentum eigenfunctions with a given positive or negative  $m_\ell$  value, and this tends to happen when the magnetic moment operator is diagonalized in the basis of the components of a spatially degenerate state. (This is the reverse process of the textbook case where real atomic orbitals are formed from the complex eigenfunctions of  $\hat{L}_z$ .) In this case, the expectation value for the associated orbital angular momentum component, calculated separately for the state components, is nonzero. A linear combination of the

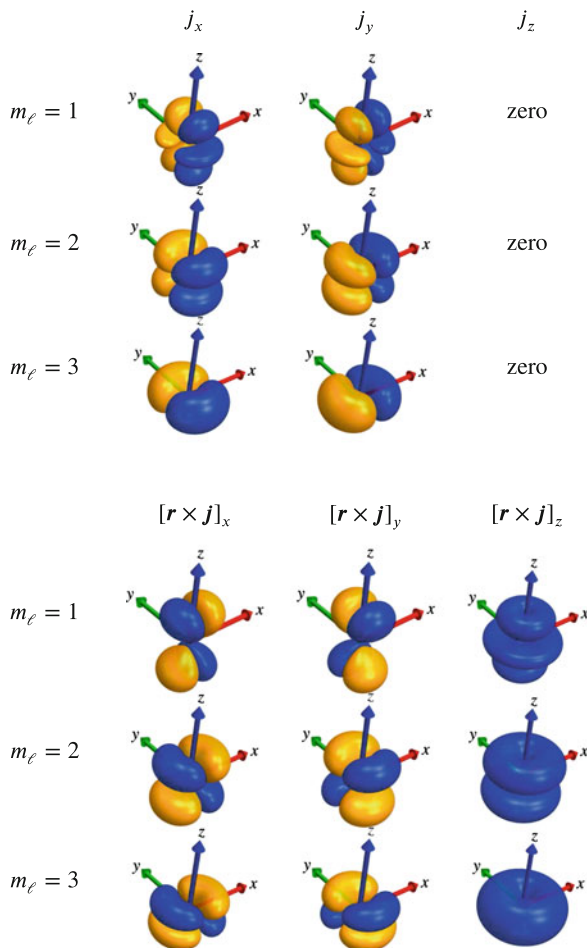


**Fig. 1** Isosurfaces ( $\pm 0.005$  au) for the components of the paramagnetic current density  $\mathbf{j}$  and the components of the orbital magnetization  $m_u^L = [\mathbf{r} \times \mathbf{j}]_u$  generated from analytic expressions of the spherical harmonic angular functions  $Y_\ell^{m_\ell}$  for  $d$  orbitals, i.e.,  $\ell = 2$  and  $m_\ell = 1 - 2$ , multiplied with a normalized  $3d$  Slater-type radial function  $r^2 \exp(-\zeta r)$  with an exponent  $\zeta = 2$ . There are no contributions from the  $m_\ell = 0$   $d_\sigma$  orbital. Blue/dark shading indicates positive, orange/light shading indicates negative, function values. The isosurfaces for negative  $m_\ell$  have the same shapes but the functions have the opposite sign patterns. The magnetization quantization axis is  $z$  in all cases

state components that shifts the single occupation or hole dominantly or fully to one of the real NOs breaks rotational symmetry of the state components, which may result in vanishing orbital angular momentum expectation values. The angular momentum is then “hidden” in the off-diagonal angular momentum operator matrix elements between two different state components. In cases of lower symmetry than linear, near-degeneracies may lead to similar scenarios: A state with quenched orbital angular momentum at the SF level may be very close in energy to its rotational symmetry parentage counterpart, such that strong SO coupling between these states leads to a partial de-quenching.

All calculations discussed in Sect. 3 were carried out with the Molcas software [11], employing the complete active-space self-consistent field (CASSCF) method and when necessary the CAS second-order perturbation theory (CASPT2) for the dynamic electron correlation [9, 14], along with ANO-RCC basis sets and the second-order Douglas-Kroll-Hess (DKH2) all-electron scalar relativistic Hamiltonian [15]. The SO interaction was treated with atomic mean-field integrals (AMFI) and the restricted active space state-interaction (RASSI) approach [10]. For brevity,

**Fig. 2** Isosurfaces ( $\pm 0.003$  au) for the components of the paramagnetic current density  $\mathbf{j}$  and the components of the orbital magnetization  $m_u^L = [\mathbf{r} \times \mathbf{j}]_u$  generated from analytic expressions of the spherical harmonic angular functions  $Y_\ell^{m_\ell}$  for  $f$  orbitals, i.e.,  $\ell = 3$  and  $m_\ell = 1 - 3$ , multiplied with a normalized  $4f$  Slater-type radial function  $r^3 \exp(-\zeta r)$  with an exponent  $\zeta = 2$ . There are no contributions from the  $m_\ell = 0 f_\sigma$  orbital. Blue/dark shading indicates positive, orange/light shading indicates negative, function values. The isosurfaces for negative  $m_\ell$  have the same shapes but the functions have the opposite sign patterns. The magnetization quantization axis is  $z$  in all cases

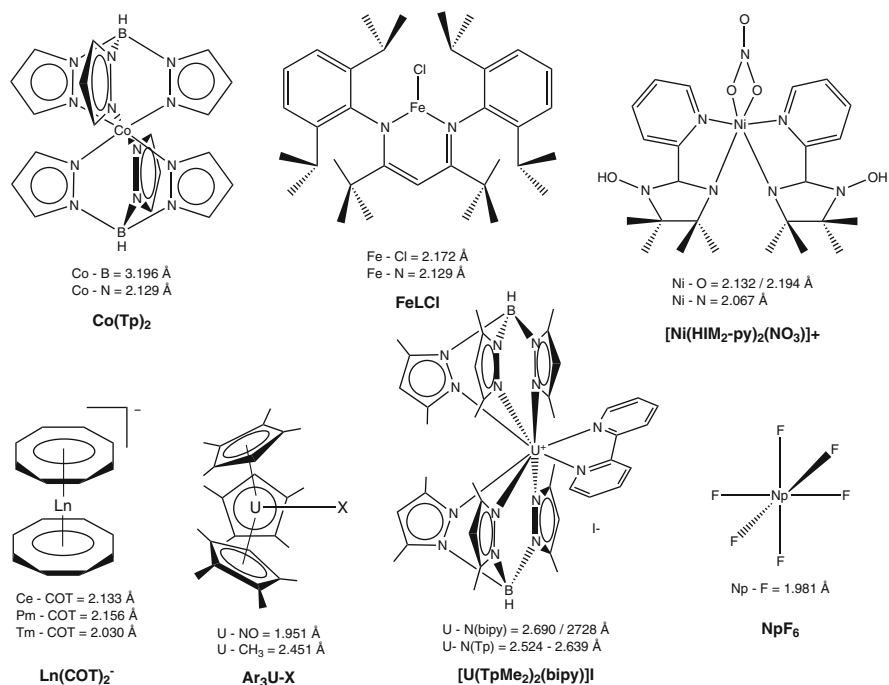


the scalar relativistic (SR, i.e., pre-RASSI) and SO CASSCF and CASPT2 calculations are denoted as SCF-SR, SCF-SO, PT2-SR, and PT2-SO in the following. Magnetic properties were calculated according to [6, 16–18]. Single-crystal experimental structures or optimized structures from density functional theory were used for the calculations. Further details, and reasons for the active space choices if they are not minimal (open  $d$  or  $f$  shells only), are provided in the references provided in the following. Important ligand-metal interactions may take place in orbitals that are not part of the active space (“inactive orbitals,” which are also optimized during the CAS-calculations), while in other cases a suitable description of the magnetic properties requires active orbitals beyond the open shell. The calculations for  $\text{Co}(\text{Tp})_2$  were carried out for this work using similar computational details as those of Ridier et al. [19], with an active space comprising the  $3d$  and  $3d'$  orbitals as well as two ligand orbitals of  $\sigma$  symmetry (CAS(11,12)). For the  $\text{FeLCl}$  complex, a CAS(12,13) active

space including the five  $3d$  and the correlation  $3d'$  orbitals as well as three bonding orbitals was used with CASPT2 energies. 5 quintet, 15 triplet, and 10 singlet states were considered.  $[\text{Ni}(\text{HIM}_2 - \text{py})_2(\text{NO}_3)]^+$  is described using a CAS(12,12) active space including two bonding  $e_g$  orbitals, the five  $3d$  orbitals and a second  $3d'$  shell with CASPT2 energies [20] and 10 triplet and 15 singlet states.  $\text{NpF}_6$  is described by a RAS (37/18;7;18)SCF calculation. RAS1 comprises the 18  $2p$  orbitals, RAS2 the 7  $5f$  orbitals, and RAS3 the 18 antibonding/correlation counterparts of the orbitals of RAS1. Two holes/particles were allowed in RAS1/3. SOC was calculated with CASPT2 energies [21] and seven doublet states. The  $[\text{U}(\text{Tp}^{\text{Me}_2})_2(\text{bipy})]\text{I}$  complex is described using a CAS(3,7) ( $5f$  orbitals) with CASPT2 energies and 35 quartet and 40 doublet states. The NOs and NSOs and magnetization plots were generated according to [11, 12, 22, 23].

### 3 Case Studies: From Transition Metals to Actinides

Chemical structure drawings of the metal complexes discussed in this section are provided in Fig. 3 along with selected bond distances.



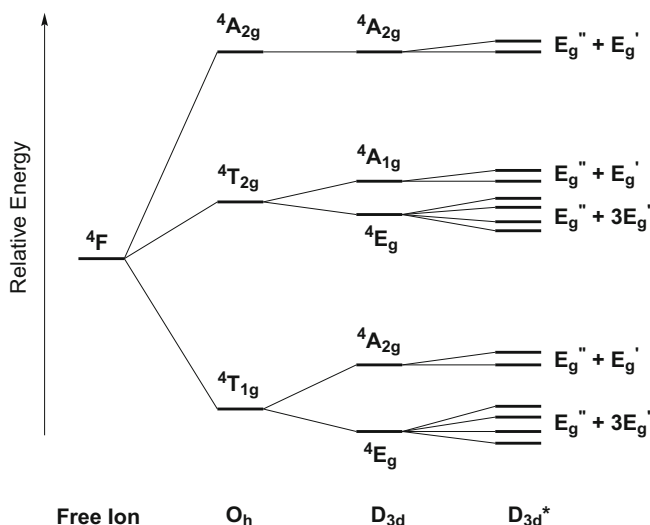
**Fig. 3** Chemical structures of the complexes used as examples for the orbital analysis in this chapter. Selected bond distances in Å. For details about the structural data of these complexes, the reader is referred to the original articles [20–22, 24–27] for  $\text{Co}(\text{Tp})_2$ ,  $\text{FeLCl}$ ,  $[\text{Ni}(\text{HIM}_2 - \text{py})_2(\text{NO}_3)]^+$ ,  $\text{Ln}(\text{COT})_2^-$ ,  $\text{Ar}_3\text{U-X}$ ,  $[\text{U}(\text{Tp}^{\text{Me}_2})_2(\text{bipy})]\text{I}$ , and  $\text{NpF}_6$ , respectively



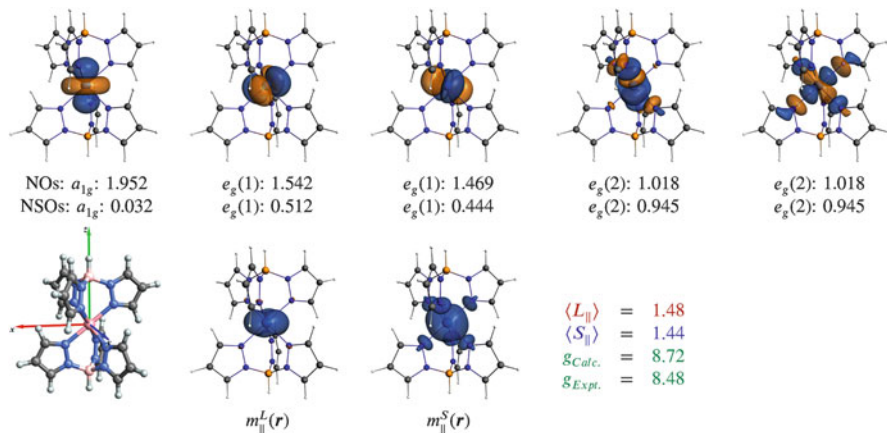
### 3.1 A Trigonal Cobalt(II) Complex: $\text{Co}(\text{Tp})_2$

The magnetic properties of the approximately  $D_{3d}$ -symmetric  $\text{Co}^{\text{II}}(\text{Tp})_2$  complex (Tp = trispyrazolylborate) were investigated by Tierney et al. using EPR and NMR spectroscopy [24, 28]. Due to its interesting magnetic properties, we decided to perform calculations for this complex. The EPR measurements revealed a strong axial magnetic anisotropy characterized by  $g_{\parallel} = 8.48$  and  $g_{\perp} = 1.02$ , with  $g_{\parallel}$  being in the direction of the threefold principal axis of symmetry. The electronic structures of trigonal Co(II) complexes were rationalized theoretically already in the early 1950s by Abragam and Pryce [29], and then revisited by Jesson and McGarvey in 1970s [30, 31]. It is beneficial to consider the (approximate)  $D_{3d}$  point group symmetry of the complex as a trigonal distortion from an  $O_h$  parent coordination. As seen in Fig. 4, the  $3d^7$  configuration of the  $\text{Co}^{2+}$  ion leads to the spectroscopic  $LS$ -ground term  ${}^4F$ . The excited  ${}^4P$  term is much higher in energy and therefore not discussed here. The sevenfold orbital degeneracy of the ground term is split by an octahedral ligand-field (LF) into the spin quartets  ${}^4T_{1g}$ ,  ${}^4T_{2g}$ , and  ${}^4A_{2g}$ . The  $O_h$  ground state (GS)  ${}^4T_{1g}$  is then split by the trigonal LF distortion into a spin quartet  ${}^4E_g$  and a spin quartet  ${}^4A_{2g}$ . The zero-field splitting (SO interaction) finally breaks the fourfold spin- and twofold orbitally-degenerate SR GS into four Kramers doublets (KDs).

The EPR  $g$ -factors of  $\text{Co}(\text{Tp})_2$  were calculated from CAS wavefunctions. The  $3d$  NOs for the SO GS are shown in Fig. 5, along with the orbital and spin magnetizations. At the SCF-SO level, the GS doublet derives very dominantly from



**Fig. 4** Schematic energy diagram of the lowest electronic states deriving from the splitting of the  ${}^4F$  term of the  $\text{Co}^{2+}$  ion by an octahedral ( $O_h$ ) and a trigonal ( $D_{3d}$ ) crystal-field.  $D_{3d}^*$  is the corresponding double group in which the SO states are classified



**Fig. 5** Top row: Isosurfaces ( $\pm 0.03$  au) and occupations of selected natural orbitals (NOs) of the SO GS of  $\text{Co(Tp)}_2$ . The spin populations of the corresponding natural spin orbitals (NSOs, for  $\parallel$  magnetization quantization axis) are also given for comparison. The NSOs isosurfaces appear to be very similar to those of the NOs and are therefore not shown. Bottom row: Orientation of the principal magnetic axes, isosurfaces ( $\pm 0.001$  au) of the orbital ( $m_{\parallel}^L(r)$ ) and spin ( $m_{\parallel}^S(r)$ ) magnetizations, and  $g$ -factors for the SO GS of  $\text{Co(Tp)}_2$ . Doublet components with  $\langle S_{\parallel} \rangle > 0$ . SCF-SO Results

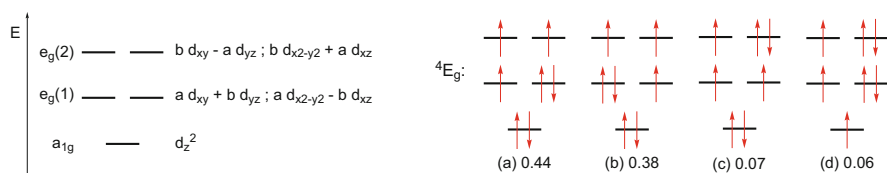
the SR GS  ${}^4E_g$  (98%). It is separated from the first excited state (ES) by  $220 \text{ cm}^{-1}$ . As the EPR measurements were performed at 3.6 K, only the GS is thermally populated, and hence, the electronic  $g$ -factors can be rationalized with a pseudo-spin  $\mathbb{S} = 1/2$  and the following spin Hamiltonian:

$$\widehat{\mathcal{H}}_S = \mu_B \left[ g_{\parallel} B_{\parallel} \widehat{\mathbb{S}}_{\parallel} + 2g_{\perp} (B_{\perp} \widehat{\mathbb{S}}_{\perp}) \right] \quad (15)$$

The SCF-SO calculation gives for the GS  $g_{\parallel} = 8.72$  and  $g_{\perp} = 1.01$ . The large magnitude of the magnetic moment along the  $\parallel$  magnetic axis results from a large un-quenched orbital angular momentum, and from the reinforcement of  $\langle L_{\parallel} \rangle$  and  $\langle S_{\parallel} \rangle$  (Fig. 5). One can notice that the calculated spin expectation value of  $\langle S_{\parallel} \rangle = 1.44$  is close to the expected value for the  $M_S = 3/2$  component of an SR spin quartet, which is evidence of the relatively weak mixing of SR states in the SO GS. Nonetheless,  $\langle S_{\perp} \rangle$  is 0.23 and thus it is responsible for most of  $g_{\perp}$  ( $\langle L_{\perp} \rangle$  is only 0.05), whereas it would be zero for an SR spin quartet. Introduction of the dynamic correlation at the PT2-SO level does not improve the calculated  $g$ -factors ( $g_{\parallel} = 8.77$  and  $g_{\perp} = 0.84$ ). The deviations from the experimental data can be attributed to a number of factors, among which are: (1) The dipolar spin-spin interactions, which are not included in our calculations, are known to contribute to the ZFS in transition metals [32]. (2) The active space is still relatively small. (3) The measurement was done for the solid state but the calculation is for the isolated complex.

The large magnitude of  $\langle L_{\parallel} \rangle$  and  $\langle S_{\parallel} \rangle$  in  $\text{Co}(\text{Tp})_2$  can be related to the populations of the NOs and NSOs of the SO GS. The fivefold degeneracy of the  $3d$  orbitals is split by the trigonal CF into a nondegenerate  $a_{1g}$  (using  $D_{3d}$  symmetry labels), and two sets of degenerate  $e_g$  orbitals. The  $a_{1g}$  orbital essentially corresponds to the real  $3d_{z^2}$  orbital ( $d_{\sigma}, m_{\ell} = 0$ ), whereas the  $e_g$  orbitals correspond to real linear combinations of the complex  $3d$  orbital angular momentum eigenfunctions with  $m_{\ell} = \pm 1$  and  $\pm 2$  [33]. As seen in Fig. 5, the deviation from a perfect  $D_{3d}$  symmetry in  $\text{Co}(\text{Tp})_2$  leads to slightly nonequivalent  $e_g$  orbitals with different NO and NSO populations and an approximately  $100 \text{ cm}^{-1}$  energy difference of the corresponding canonical MOs.

For an idealized  $D_{3d}$   $\text{Co}(\text{Tp})_2$  complex, the wavefunction of the SR GS  ${}^4E_g$  component with  $M_S = 3/2$  would be an admixture of equal weight of the configurations (a) and (b) shown in Fig. 6. Due to the dominant contribution of the SR GS in the SO GS, the SO NO occupations (very close to  $a_{1g}^2 e_g(1)^3 e_g(2)^2$ ) arise directly from these two configurations. For an electronic state component with even weights of configurations (a) and (b), we would expect an occupation of 1.5 for each of the  $e_g(1)$  metal orbitals, and a calculated  $\langle S_{\parallel} \rangle$  of 1.5 which results from contributions due to both sets of  $e_g$  orbitals. The  $a_{1g}$  orbital is doubly occupied, and hence, does not contribute to the spin angular momentum. Its corresponding NSO spin population (Fig. 5) is close to zero, accordingly. The  $e_g(1)$  set shares one unpaired electron and each orbital contributes to 0.5 to  $2\langle S_{\parallel} \rangle$ , whereas the  $e_g(2)$  orbitals are both singly occupied and each contribute approximately to 1 to  $2\langle S_{\parallel} \rangle$ . These contributions from both  $e_g$  sets give a tangerine-shaped  $m_{\parallel}^S(\mathbf{r})$  isosurface at the cobalt center. The calculated  $\langle S_{\parallel} \rangle = 1.44$  results principally from this description. However, the symmetry breaking leads to an SR GS  ${}^4E_g$  with admixtures of additional configurations (c) and (d) of Fig. 6. These configurations, in combination with the SO interaction, affect the populations of the  $a_{1g}$  and  $e_g(1)$  NOs and NSOs. Furthermore, sizable spin-magnetization is also seen on the ligand-nitrogen atoms. This effect is associated with the  $e_g(2)$  orbitals (see Fig. 5), which are seen to afford Co–N antibonding interactions. In reference to the orbital diagram of Fig. 6, the ligands donate electron density to the metal  $e_g(2)$  shell, but only with  $\downarrow$  spin because the  $\uparrow$  spin metal  $3d$  orbitals are filled. This donation is reflected by NO populations of 1.018, slightly larger than the idealized value of 1, and by NSO spin populations slightly below 1 due to the contributions from  $\downarrow$  spin in the  $e_g(2)$  shell.



**Fig. 6** Left: Splitting of the  $3d$  orbitals in the  $D_{3d}$  symmetry point group. Right: Composition of the SR ground state wavefunction  ${}^4E_g$ . Only the configurations with a weight larger than 5% are shown

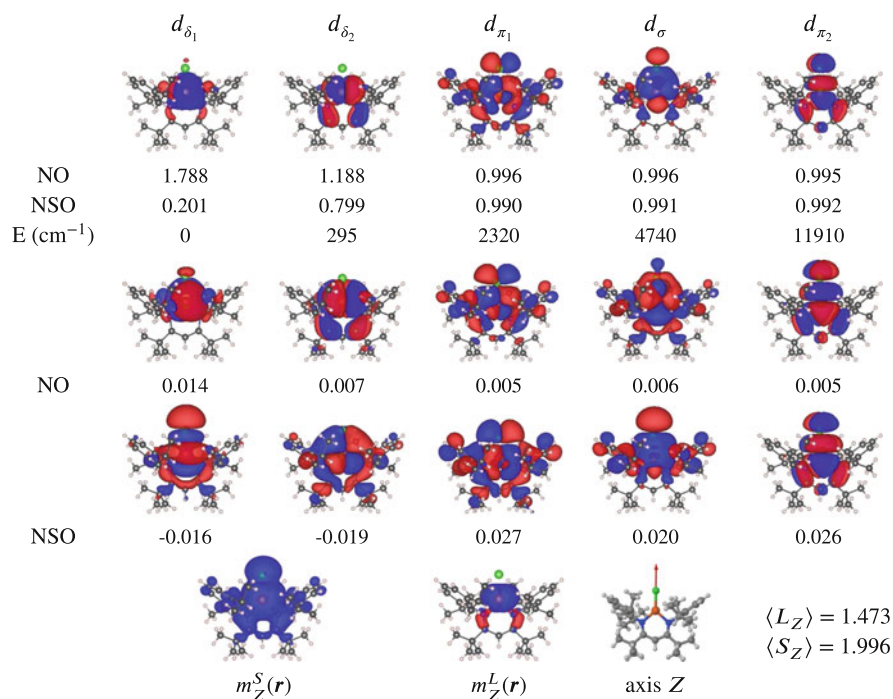
$\langle L_{\parallel} \rangle$  and the associated orbital magnetic moment results essentially from contributions of the  $e_g(1)$  orbitals (approximately  $d_{\delta}$ ). The  $a_{1g}$  orbital does not contribute to  $\langle L_{\parallel} \rangle$ , whereas the contributions from the  $e_{1g}(2)$  orbitals (approximately  $d_{\pi}$ ) to the orbital angular momentum cancel: Due to their single occupations, their contributions to  $\langle L_{\parallel} \rangle$  correspond to a sum of two  $\widehat{L}_{\parallel}$  eigenfunctions, with eigenvalues  $+m_{\ell}$  and  $-m_{\ell}$ . For the  $e_g(1)$  shell, the electronic occupation of ca. 3/2 in each orbital allows to maximize their contributions to  $\widehat{L}_{\parallel}$ . In this case, one can make a linear combination of the two real orbitals to obtain approximate  $\widehat{L}_{\parallel}$  eigenfunctions with  $\pm m_{\ell}$ , one of each being occupied in the two components of the degenerate GS. The composition of the  $e_g(1)$  orbitals in terms of the real 3d orbitals calculated for  $\text{Co}(\text{Tp})_2$  is the following, with  $z$  coinciding with the threefold symmetry axis

$$\begin{aligned} e_{1g}(1)_a &= -0.74d_{xy} + 0.35d_{yz} + 0.40d_{xz} + 0.42d_{x^2-y^2} \\ e_{1g}(1)_b &= 0.44d_{xy} + 0.42d_{yz} + 0.33d_{xz} + 0.73d_{x^2-y^2} \end{aligned} \quad (16)$$

The presence of the  $d_{\pi}$  ( $xz$  and  $yz$ ) contributions reflects the tilting of the two orbitals of approximate  $d_{\delta}$  symmetry with respect to the  $z$  axis, whereas the mixing of  $xy$  and  $x^2 - y^2$  mainly simply reflects the arbitrary choice of the ligand azimuth positions relative to the coordinate axes. Using the above expressions for  $e_g(1)_a$  and  $e_g(1)_b$ , and equal populations of 1.5, one can make a linear combination that would lead to an orbital angular momentum expectation value of  $\langle L_{\parallel} \rangle = 1.73$ . This linear combination is responsible for the oblate  $m_{\parallel}^L(\mathbf{r})$  visible in Fig. 5. Refer to Fig. 1: The two orbitals in question are approximately of  $d_{\delta}$  ( $|m_{\ell}| = 2$ ) symmetry. The corresponding orbital magnetization for an  $m_{\ell} = \pm 2$  angular momentum eigenfunction affords the ‘‘doughnut’’ shape in the bottom right of the figure, which is quite similar to the actual calculated  $m_{\parallel}^L$  isosurface. The lowering of symmetry from linear to trigonal causes the model to deviate from the expected  $\langle L_{\parallel} \rangle = \pm 2$  for a  $d_{\delta}$  hole by hybridization with  $d_{\pi}$ . The model  $\langle L_{\parallel} \rangle$  value is not far from the CASSCF result of  $\langle L_{\parallel} \rangle = 1.48$ . The deviation between the model and the ab initio data is also attributed to the geometrical distortions in  $\text{Co}(\text{Tp})_2$ , which cause the magnitude of the orbital angular momentum to decrease further, via an uneven population of  $e_g(1)_a$  and  $e_g(1)_b$ .

### 3.2 A High-Spin Fe(II) Complex: FeLCl

In the  $[\text{FeLCl}]$  complex with  $L = \beta$ -diketimate, the Fe(II) center is in a  $3d^6$  high-spin configuration with a spin quintet ground state. EPR measurements in the  $X$  band reveal a quasi-degenerate  $M_S = \pm 2$  ground doublet with an axial  $g = 10.9$  and a small energy splitting of  $0.35 \text{ cm}^{-1}$  of the doublet components. The next component of the spin quintet was estimated to be higher than  $150 \text{ cm}^{-1}$  [25]. In a pure spin quintet, the  $M_S = \pm 2$  components have a  $g$ -factor of 8; the experimental value shows that there is a substantial orbital magnetization contribution due to only



**Fig. 7** Top row: Isosurfaces and occupation numbers of selected NOs for the two lowest SO states of [FeLCl]. The spin populations of the corresponding NSOs along the magnetic axis and the energy of the corresponding canonical orbitals are given for comparison. Second row: Isosurfaces and occupation numbers of additional NOs. Third row: Isosurfaces and spin populations of additional NSOs. Bottom row: Isosurfaces of the spin and orbital magnetizations along the Z magnetic axis. Isosurface values:  $\pm 0.07$  au for orbitals;  $\pm 0.0001$  au for magnetization

partial quenching of the orbital angular momentum and a low lying SR excited state. This is confirmed by CASPT2 calculations which show that the first excited state lies at  $516 \text{ cm}^{-1}$  above the GS. With the SO coupling, the spin quintet splits into five components by  $0.34$ ,  $118$ ,  $132$ , and  $180 \text{ cm}^{-1}$  [34]. The spin Hamiltonian is either written for the non-Kramers doublet GS with a small ZFS and a large anisotropic  $g$ -factor, or by a pseudo-spin  $S = 5$  with a large ZFS splitting and a nearly isotropic  $g$  tensor. The following analysis is performed based on the non-Kramers doublet (non-KD) perspective.

For a non-KD, only one component of the  $g$  tensor is nonzero. In the [FeLCl] complex, the magnetic axis of the ground doublet is parallel to the  $C_2$  symmetry axis of the molecule, which is taken to be along the Z direction and coinciding with the quantization axis. The two  $d_{\delta}$  orbitals are nonbonding with the chlorine atom and have the lowest energy, while the  $d_{\pi}$  and  $d_{\sigma}$  are antibonding and destabilized. The two  $d_{\delta}$  are split by  $300 \text{ cm}^{-1}$  due to a differential interaction with the L ligand (cf Fig. 7). The  $d_{\pi_2}$  orbital is more antibonding than the  $d_{\sigma}$  due to a strong  $\pi$  interaction with the ligand L. The two low lying SR states correspond to

configurations  $(d_{\delta_1})^2 d_{\delta_2} d_{\pi_1} d_{\pi_2} d_{\sigma}$  and  $d_{\delta_1} (d_{\delta_2})^2 d_{\pi_1} d_{\pi_2} d_{\sigma}$  respectively, and the orbital moment is quenched. These states are strongly coupled by SO coupling due to the small energy gap, leading to a mixing of 80% and 20%; this strong mixing leads to the partial de-quenching of the orbital moment, to the large splitting of the spin quintet, and to the large magnetic anisotropy of the ground doublet.

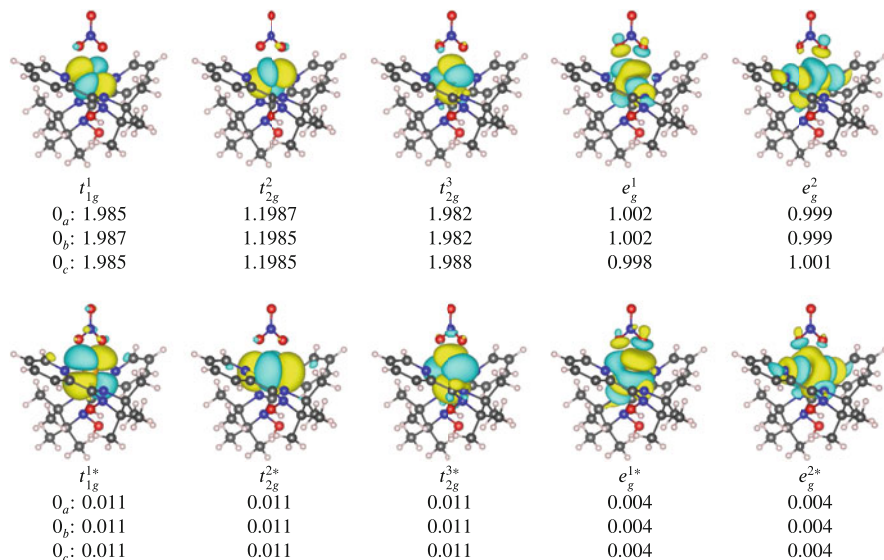
NOs and NSOs for the ground doublet are shown in Fig. 7. While for a non-Kramers doublet the NO populations might be different for the two components, they are almost identical here with 1.8 electrons in  $d_{\delta_1}$  and 1.2 in  $d_{\delta_2}$  as expected from the SO coupling mixing. The mixing by SO coupling is much smaller for the other three components of the quintet, and the populations of  $d_{\delta_1}$  and  $d_{\delta_2}$  lie in the ranges 1.89–1.98 and 1.08–0.99, respectively. There is one correlation orbital per occupied  $d$  orbital. The largest correlation is obtained for the  $d_{\delta_1}$  orbital, which is the most populated one.

In a non-KD, NSOs are only defined along the magnetic axis. The spin population follows the electronic configuration, as it appears as a complement to 2 to the electron occupancy of the orbitals. The correlation NSOs are shown in the third row of Fig. 7 and have a spin population of ca.  $\pm 0.02$ . There is a delocalization of the  $\alpha$ -spin density in the  $\pi$  and  $\sigma$  symmetries and a spin polarization with the appearance of a  $\beta$ -spin density on the ligands in the orbitals of  $\delta$  symmetry. However, the  $\beta$ -spin density is hardly visible in the plot of the spin magnetization at the chosen isosurface value. The spin delocalization onto the ligands is readily visible in  $m_Z^S(\mathbf{r})$ . Finally, as shown in the last row of Fig. 7, the orbital magnetization for the  $Z$  magnetic axis is approximately cylindrical, in accordance with Fig. 1. Interestingly, the magnetization spreads out onto the lower part of the L ligand and exhibits a sign change, meaning that the covalent interactions between the metal and the ligand induce an orbital magnetization on the ligand that is of opposite sign to that on the metal. The orbital contributing the most to the orbital magnetization is  $d_{\delta_1}$ .

For this complex, the NOs and NSOs permit a visualization of the strong mixing of two SR states by SO coupling which, by partially de-quenching the orbital magnetic moment, leads to a strong magnetic anisotropy. Furthermore, the “secondary” (weakly populated) NOs and corresponding NSOs permit to quantify the effects of dynamical correlation and of spin-delocalization and spin-polarization.

### 3.3 Zero-Field Splitting in an Octahedral Ni(II) Complex

The complex  $[\text{Ni}(\text{HIM}_2 - \text{py})_2(\text{NO}_3)]^+$  is a six-coordinate complex of Ni(II) where the two bidentate  $\text{HIM}_2 - \text{py}$  ligands (2-(2-pyridyl)-4,4,5,5-tetramethyl-4,5-dihydro-1H-imidazolyl-1-hydroxy) and the nitrate ion form a deformed octahedral coordination sphere [35]. The SR GS is a spin triplet arising from the  $(t_{2g})^6(e_g)^2 O_h$  parentage metal configuration. The SOC mixes this SR GS with the excited states, in particular with a triplet arising from the  $(t_{2g})^5(e_g)^3$  configuration, and removes the degeneracy of the three components of the ground triplet, leading to zero-field



**Fig. 8** Isosurfaces ( $\pm 0.02$  au) and occupation numbers (populations) for selected NOs of the three components ( $0_a$ ,  $0_b$ , and  $0_c$ ) derived from the GS spin-triplet of  $[\text{Ni}(\text{HIM}_2 - \text{py})_2(\text{NO}_3)]^+$

splitting. The magnetic anisotropy of the ground triplet may be characterized by a spin Hamiltonian whose canonical form is

$$\begin{aligned} \hat{\mathcal{H}}_S = & \mu_B (g_X B_X \hat{S}_X + g_Y B_Y \hat{S}_Y + g_Z B_Z \hat{S}_Z) \\ & + D \left( \hat{S}_Z^2 - \frac{1}{3} \mathbb{S}(\mathbb{S} + 1) \right) + E (\hat{S}_X^2 - \hat{S}_Y^2) \end{aligned} \quad (17)$$

The ZFS parameters  $D$  and  $E$  and the three  $g$ -factors have been determined by High-Field High-Frequency spectroscopy with:  $D = -10.1 \text{ cm}^{-1}$ ,  $E/D = 0.24$ ,  $g_X = g_Y = 2.20$ , and  $g_Z = 2.27$ . This is nicely reproduced by the CASPT2 calculations using a CAS(13,13) active space including two bonding  $e_g$  orbitals and a second  $d$  shell [20].

As it is usually the case in transition metals, the anisotropic magnetic behavior is borne by the ZFS of the ground spin state, and the large negative  $D$  value leads to an axial magnetization. The three components of the ground spin triplet are nondegenerate and consequently, the expectation value of the magnetic moment vanishes. Magnetic properties arise from the coupling between the three components by the Zeeman operator; the closer the two components are in energy, the more magnetic the corresponding direction is [20, 34].

The two lowest components denoted  $0_a$  and  $0_b$ , are close in energy,  $1.8 \text{ cm}^{-1}$ , while the third one,  $0_c$ , has a larger energy gap of  $12.1 \text{ cm}^{-1}$ . The NOs of the three components are depicted in Fig. 8. They are very similar to each other, since the

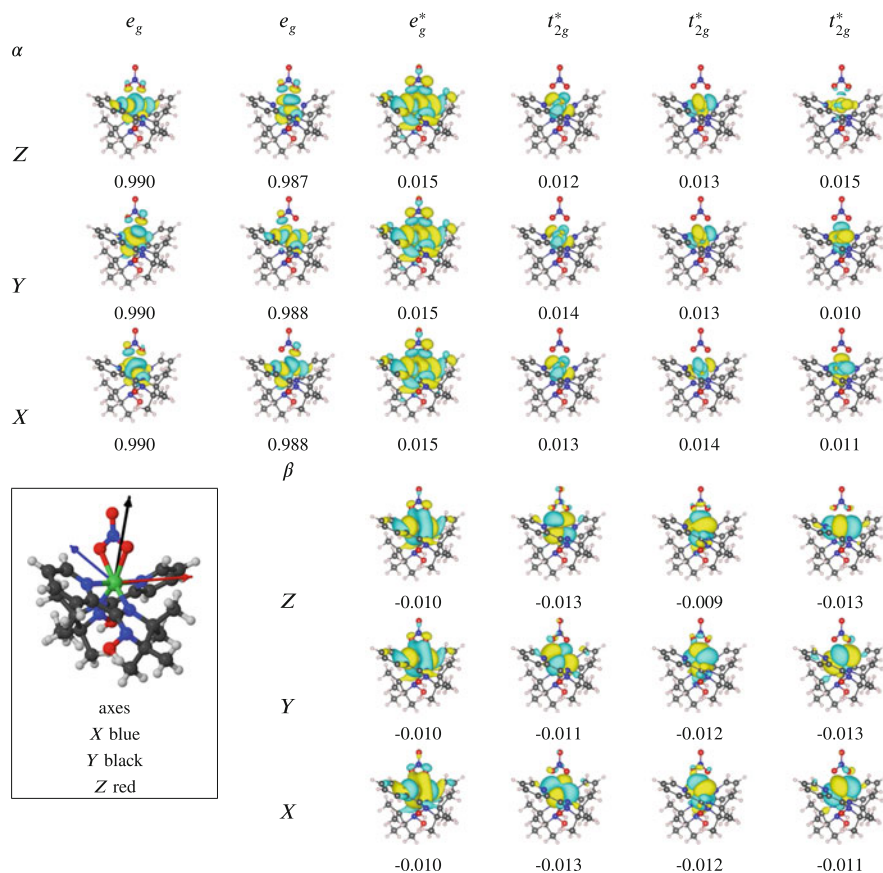


three components arise from the same spin triplet and the SO effects are small, but their occupations differ slightly. The magnetic anisotropy arises precisely from these small differences. The negative  $D$  value can be rationalized by the energetic ordering of the  $d$  orbitals, and mostly from the splitting of the two  $e_g$  orbitals, which is due to the difference of  $\sigma$  donation of the ligands to the metal [20]. Referring to Fig. 8, the three  $t_{2g}$ -like orbitals have a population that is slightly smaller than 2 due to the dynamic electron correlation. The two  $e_g$ -like orbitals have occupations close to 1, one below and one above. The  $e_g^1$  has a  $d_{z^2}$  shape and points towards two nitrogen atoms of the  $\text{HIM}_2 - \text{py}$  ligands while  $e_g^2$  is the  $d_{xy}$  orbital and points towards the two other nitrogen atoms and the two oxygen atoms of the nitrate. Since the  $\text{HIM}_2 - \text{py}$  ligands are better  $\sigma$  donors than the nitrate, the  $e_g^1$  orbital is more antibonding and more destabilized than  $e_g^2$ . As a consequence, in the two lowest  $0_a$  and  $0_b$  components, the population of the most stabilized  $e_g$  is larger than one while it is less than one for the  $0_c$  component. The populations of the correlation  $t_{2g}^*$  NOs are about 0.01 each, which corresponds roughly to the depletion in the  $t_{2g}$  shell. The correlation in the  $e_g$  shell is less important since the orbitals are singly occupied, and the population of the correlation  $e_g^*$  NOs is slightly less than half those of the  $t_{2g}^*$  ones.

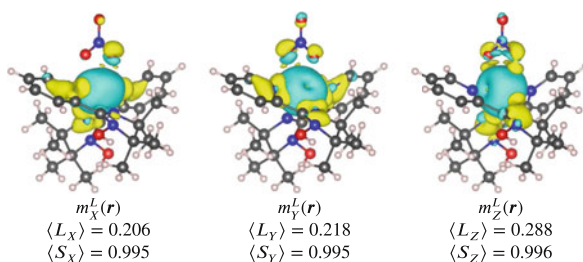
Magnetic properties arise from the coupling between two components of the split ground triplet. The coupling between  $0_a$  and  $0_b$  is the largest, since these components are the closest in energy. This coupling defines the direction of the axial magnetization, denoted  $Z$ . The NSOs for this quantization direction are shown in Fig. 9 in comparison to those in directions  $X$  and  $Y$  obtained from the coupling between  $0_b$  and  $0_c$  and between  $0_a$  and  $0_c$ , respectively. In the calculations, the respective pair of split-triplet components was chosen to diagonalize the magnetic moment operator for magnetic axis  $U$  prior to generating the NSOs. The spin magnetization is mostly borne by the  $e_g$  orbitals with a spin population close to 1, as expected, but it should be noted that one of the  $e_g$  has a larger spin population, namely the  $d_{yz}$  when the magnetic axis is along  $U = X, Y, Z$ . Spin polarization appears with both  $\alpha$  and  $\beta$  densities through  $\sigma$  ( $e_g$ -type orbitals) and  $\pi$  ( $t_{2g}$ -like orbitals) bonding schemes. The  $\alpha$  and  $\beta$  populations of the  $t_{2g}$  NSOs are both 0.038. The  $\beta$ -spin density is more delocalized on the ligands leading to spin polarization through the  $\pi$  bonding network. There is a small anisotropy, since the orbital with the lobes perpendicular to the  $U$  axis has the lowest  $\beta$ -spin density. For the  $e_g$ -like correlation NSOs, the  $\alpha$ -spin density is slightly larger than the  $\beta$ -spin one (0.015 against 0.01), the  $\alpha$  one being more delocalized on the ligands. This spin delocalization through the  $\sigma$  bonding is permitted by the half-filled  $e_g$  shell while the  $t_{2g}$  shell is completely filled as in the case for the  $\text{FeLCl}$  complex in Sect. 3.2.

The orbital magnetization densities for the three magnetic axes are shown in Fig. 10. In this complex, the orbital moment is quenched in the GS as long as the SO coupling is not considered. The SO coupling with the excited states gives rise to small orbital angular momentum contributions that play a key role for the anisotropic properties. The largest contribution is along the  $Z$  axis. The orbital magnetization in direction  $U$  forms a doughnut shape around the  $U$  axis, indicative of  $d_\delta$ -like





**Fig. 9** Isosurfaces ( $\pm 0.02$  au) and spin populations for selected NSOs for the three coupled states derived from the triplet GS of  $[\text{Ni}(\text{HIM}_2 - \text{py})_2(\text{NO}_3)]^+$  for the three principal magnetic axes X, Y, and Z. See text for details



**Fig. 10** Isosurfaces of the orbital magnetization ( $m_u^L(\mathbf{r})$ ) ( $\pm 5.10^{-5}$  au) for the state components generated from the triplet GS of  $[\text{Ni}(\text{HIM}_2 - \text{py})_2(\text{NO}_3)]^+$  for a quantization axis along the three principal magnetic axes X, Y, and Z. The expectation values for the orbital ( $\langle L_U \rangle$ ) and spin ( $\langle S_U \rangle$ ) angular momentum are given for comparison

contributions along the quantization axis, per Fig. 1, but with a somewhat more cylindrical shape that is indicative of some  $d_\pi$  contributions. The orbital magnetization spreads onto the ligands perpendicular to the  $U$  axis.

For this complex, we have shown that when a pure spin triplet is split by the SO coupling with excited states, the NOs permit to quantify the small differences between the three components and to visualize the effects of correlation. The magnetic axes are defined by the coupling between two of the components arising from the triplet, with corresponding NSOs and orbital magnetization. It turns out that the spin density is slightly anisotropic and that there is some spin delocalization in the  $\sigma$  bonding scheme and spin polarization in the  $\pi$  one. The orbital magnetization is a current around the considered axis and originates mainly from a  $d_\delta$  like orbital in the coupled state, with some  $d_\pi$  admixture, where  $\delta$  and  $\pi$  refer to the symmetry with respect to the magnetization quantization axis.

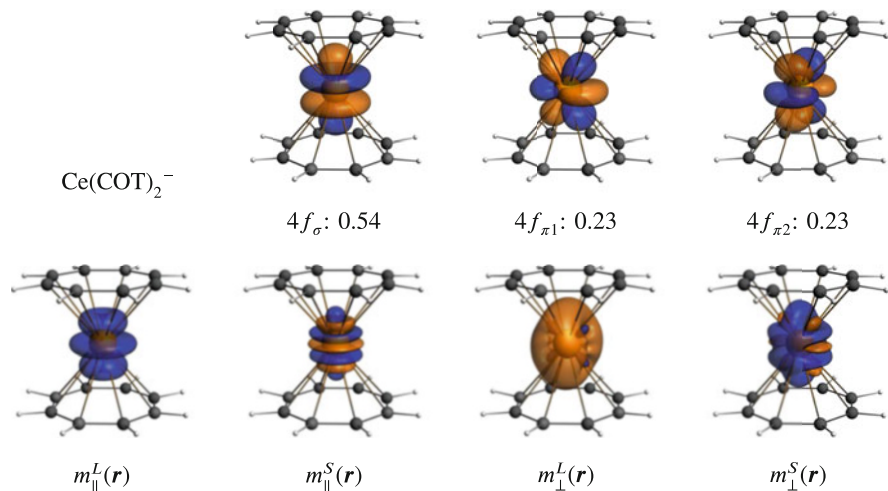
### 3.4 Linear Ln(III) Complexes: $\text{Ln}(\text{COT})_2^-$

In  $\text{Ce}(\text{COT})_2^-$  ( $4f^1$  configuration), the linear crystal-field lifts the sevenfold degeneracy of the cerium  $4f$  orbitals to give rise to an SR  ${}^2\Sigma$  ground state when using labels for rotational symmetry, which is appropriate because  $M_\ell$  for the  $4f$  shell is a good quantum number in the presence of an eightfold symmetry axis. Introduction of the SO interaction mixes the  $\uparrow$  and  $\downarrow$  spin components of the SR GS and the excited  ${}^2\Pi$  state. The SO GS corresponds then to a KD of  $M_J = \pm\frac{1}{2}$  parentage which originates from the spectroscopic level  ${}^2F_{5/2}$  of the  $\text{Ce}^{3+}$  ion [22]. The EPR  $g$ -factors associated with the GS were characterized experimentally by Walter et al. and revealed a planar magnetic anisotropy, with  $g_{\parallel} = 1.12$  and  $g_{\perp} = 2.27$  [36]. These observed  $g$ -factors somewhat differ from the idealized values of  $g_{\parallel} = 0.86$  and  $g_{\perp} = 2.57$  for a  $J = \frac{1}{2}$ ,  $M_J = \pm\frac{1}{2}$  ion micro-state. The deviations between the observed and CF  $g$ -factors result from a different admixture of the SR  ${}^2\Sigma$  and  ${}^2\Pi$  states. This admixture is characterized in the GS wavefunction  $|\psi\rangle$  by real coefficients  $A$  and  $B$ , with

$$|\psi\rangle = A({}^2\Sigma) + B({}^2\Pi) \quad (18)$$

For the  $\text{Ce}^{3+}$  ion micro-state, values of 0.65 and 0.76 would be expected for  $A$  and  $B$ , respectively.

The electronic structure of  $\text{Ce}(\text{COT})_2^-$  was calculated at the SCF-SO level with a minimal active space containing the seven  $4f$  orbitals [22]. The resulting natural orbitals of the SO GS are shown in Fig. 11. As expected, the unpaired electron is shared between the  $4f_\sigma$  and the  $4f_\pi$  orbitals, with the occupation numbers corresponding to 0.74 and 0.68 for the real wavefunction coefficients  $A$  and  $B$ , respectively. (For this effective one-electron system, the  $\sigma$  and combined  $\pi$  NO occupations are the squares of  $A$  and  $B$ , respectively.) The calculated  $g_{\parallel} = 1.08$  and  $g_{\perp} = 2.35$  are in good agreement with the experiment. The planar magnetic



**Fig. 11** Top row: Isosurfaces ( $\pm 0.03$  au) and occupations of selected natural orbitals of the SO GS of  $Ce(COT)_2^-$ . Bottom row: Isosurfaces ( $\pm 0.001$  au) of the orbital ( $m_u^L(\mathbf{r})$ ) and spin ( $m_u^S(\mathbf{r})$ ) magnetizations of  $Ce(COT)_2^-$  for the  $\parallel$  and  $\perp$  magnetic axes. Doublet components with  $\langle S_u \rangle > 0$ . SCF-SO results

anisotropy can be related to the orbital and spin magnetizations shown in Fig. 11. Using Eqs. (2a) and (2b), the orbital and spin magnetizations along the parallel magnetic axis of  $Ce(COT)_2^-$  are given for the model wavefunction of Eq. (18) as follows:

$$\begin{aligned}
 m_{\parallel}^S(\mathbf{r}) &= \frac{1}{2} [A^2 Y_3^0 Y_3^0 + B^2 Y_3^1 Y_3^{-1}] \\
 &= \frac{A^2}{2} f_\sigma^2 - \frac{B^2}{4} [f_{\pi+}^2 + f_{\pi-}^2]
 \end{aligned} \tag{19}$$

$$\begin{aligned}
 m_{\parallel}^L(\mathbf{r}) &= -B^2 Y_3^1 Y_3^{-1} \\
 &= \frac{B^2}{2} [f_{\pi+}^2 + f_{\pi-}^2]
 \end{aligned} \tag{20}$$

Here,  $Y_\ell^{m_\ell}$  are spherical harmonics, and the  $f_{|m_\ell|\pm}$  correspond to the  $\ell = 3$  tesseral harmonics which are real linear combinations of the complex  $Y_3^{m_\ell}$  with the same  $|m_\ell|$ .

As seen in Eq. (19), the spin magnetization corresponds to positive contributions from the  $f_\sigma^2$  density and to negative contributions from the  $f_\pi^2$  densities, giving the alternating blue and orange lobes for  $m_{\parallel}^S(\mathbf{r})$  in Fig. 11. The blue lobes represent the positive contributions from  $f_\sigma$  and integrate to  $A^2/2 = 0.27$ , while the orange lobes correspond to the contributions related to  $f_\pi$  and integrate to  $-2B^2/4 = -0.23$ . Therefore, the two contributions are almost equal and with opposite sign, leading to a very small spin expectation value  $\langle S_{\parallel} \rangle = 0.04$ . This value is far from the expected value for an SR spin doublet  $\langle S \rangle = 1/2$  and reflects the importance of SO

coupling in the  $4f$  shell. The orbital magnetization is simpler to analyze. Due to the lack of orbital angular momentum from the  $4f_\sigma$  orbital along the  $\parallel$  magnetic axis, only the  $4f_\pi$  orbitals contribute to  $m_\parallel^L(\mathbf{r})$ . This is visible in Fig. 11 where the orbital magnetization corresponds simply to a linear combination of each  $f_\pi^2$  densities. The isosurface of  $m_\parallel^L$  is also essentially identical to the idealized one for  $m_\ell = 1$  in Fig. 2. Integration of the magnetization results an orbital angular momentum expectation value  $\langle L_\parallel \rangle = 0.46$ . Along the parallel axis the magnitude of the magnetic moment is driven by the orbital contribution from the  $4f_\pi$  orbitals. In turn, the occupation of these orbitals is a consequence of the SO interaction, mixing the SR  $^2\Sigma$  GS components with the  $^2\Pi$  state components of opposite spin projection. Overall, the electronic  $g_\parallel$ -factor remains relatively small due to a quenching of the spin magnetic moment.

A similar approach can be used to analyze the magnetization densities along the perpendicular magnetic axis. As already mentioned in Sect. 2, the wavefunction components used for the analysis diagonalize the operator  $\widehat{L}_\perp + g_e \widehat{S}_\perp$ . In the model, this is achieved by taking a linear combination of the initial wavefunction  $|\psi_\parallel\rangle$  and of its Kramers conjugate  $|\bar{\psi}_\parallel\rangle$ :

$$\begin{aligned} |\psi_\parallel\rangle &= AY_3^0 - BY_3^{-1} \\ |\bar{\psi}_\parallel\rangle &= AY_3^0 - BY_3^{-1} \end{aligned}$$

to give

$$|\psi_\perp^\pm\rangle = \frac{1}{\sqrt{2}}(|\psi_\parallel\rangle \pm |\bar{\psi}_\parallel\rangle) \quad (21)$$

Substituting Eq. (21) into Eqs. (2a) and (2b), the orbital and spin magnetizations along the  $\perp$  magnetic axis for the  $\langle S_\perp \rangle > 0$  component of the doublet can be written as:

$$\begin{aligned} m_\perp^S(\mathbf{r}) &= \frac{A^2}{2}[Y_3^0 Y_3^0] - \frac{B^2}{4}[Y_3^1 Y_3^1 + Y_3^{-1} Y_3^{-1}] \\ &= \frac{A^2}{2}f_\sigma^2 - \frac{B^2}{4}[f_{\pi^-}^2 - f_{\pi^+}^2] \end{aligned} \quad (22a)$$

$$\begin{aligned} m_\perp^L(\mathbf{r}) &= -AB\sqrt{3}[Y_3^0 Y_3^0] + \frac{AB\sqrt{3}}{2}[2 \cdot Y_3^1 Y_3^{-1} + Y_3^1 Y_3^1 + Y_3^{-1} Y_3^{-1}] \\ &= -AB\sqrt{3}[f_\sigma^2 + f_{\pi^+}^2] \end{aligned} \quad (22b)$$

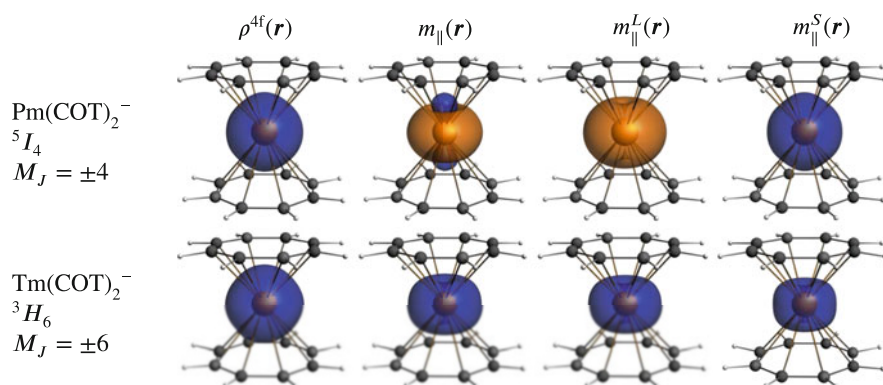
The isosurfaces of the corresponding magnetizations calculated ab initio are shown in Fig. 11. The spin magnetization corresponds to a dominant positive (blue isosurface) contribution which arises from the addition of the positive contributions of the  $f_\sigma^2$  and  $f_{\pi^+}^2$  densities, which integrates to 0.38 (i.e.  $A^2/2 + B^2/4$ ). This positive contribution is counterbalanced by a smaller negative contribution integrating to  $-0.11$ . The negative contribution is characterized by the orange lobes

in  $m_{\perp}^S(\mathbf{r})$  and results from the  $f_{\pi-}^2$  density. As seen in Eq. (22b), the orbital magnetization results from the reinforcing contributions of the  $f_{\sigma}^2$  and  $f_{\pi+}^2$  densities. This leads to a large calculated expectation value for the orbital angular momentum  $\langle L_{\perp} \rangle = -1.72$ , characterized in Fig. 11 by a large orange lobe. Therefore, the origin of the planar magnetic anisotropy in  $\text{Ce}(\text{COT})_2^-$  resides in the large magnitude of the orbital magnetization for a field along the perpendicular magnetic axis, which is only to a small extent canceled by the spin magnetization.

Of particular interest are the relationships that may exist between the electron density generated by the 4f orbitals ( $\rho^{4f}(\mathbf{r})$ ) and the orbital and spin magnetizations, and hence the magnetic moments. Comparisons of  $\rho^{4f}(\mathbf{r})$  and of  $m_{\parallel}^{L/S}(\mathbf{r})$  calculated for the SO GSs of  $\text{Pm}(\text{COT})_2^-$  and  $\text{Tm}(\text{COT})_2^-$  are provided in Fig. 12 [22].

It is clear that the orbital and spin magnetization are only indirectly related to the 4f electron density, because the electron density itself contains no information about the magnetic properties. In the case of  $4f^n$  complexes with  $n \leq 7$ , the spin magnetization tends to resemble the electron density. For instance, in  $\text{Pm}(\text{COT})_2^-$  ( $4f^4$  configuration), both  $\rho^{4f}(\mathbf{r})$  and  $m_{\parallel}^S(\mathbf{r})$  have a prolate shape due to similar NO occupations and NSO spin populations, respectively. Here the four unpaired electrons are equally shared among the  $4f_{\sigma}$ ,  $4f_{\pi}$ ,  $4f_{\delta}$ , and  $4f_{\phi}$  NOs (or NSOs).

In the case of  $4f^n$  systems with  $n > 7$ , on the other hand,  $m_{\parallel}^S(\mathbf{r})$  tends to represent the unpaired electron(s), or the electron hole(s). For example, the electronic occupation of the SO GS of  $\text{Tm}(\text{COT})_2^-$  ( $4f^{12}$  configuration) is  $4f_{\sigma}^2 4f_{\pi}^2 4f_{\delta}^3 4f_{\phi}^3$ , which leads to a mainly prolate 4f electron density due to the lack of occupations in the  $\delta$  and  $\phi$  orbitals. The spin magnetization is oblate, however, because the two unpaired spins are associated with the  $4f_{\delta}$  and  $4f_{\phi}$  orbitals. Similar to the spin magnetization,  $\rho^{4f}(\mathbf{r})$  is not directly related to the orbital magnetization. For instance, the very similar appearance of the 4f electron density isosurfaces calculated for the GS of  $\text{Pm}(\text{COT})_2^-$  and  $\text{Tm}(\text{COT})_2^-$  goes along with drastically different orbital



**Fig. 12** Comparison of the ab initio 4f electron density ( $\rho^{4f}(\mathbf{r})$ ), orbital ( $m_{\parallel}^L(\mathbf{r})$ ), spin ( $m_{\parallel}^S(\mathbf{r})$ ), and total  $m_{\parallel}(\mathbf{r})$  magnetizations for the SO GS of  $\text{Pm}(\text{COT})_2^-$  and  $\text{Tm}(\text{COT})_2^-$ . Doublet components with  $\langle S_{\parallel} \rangle > 0$ . SCF-SO Results. Isosurfaces at  $\pm 0.001$  au

magnetizations. For  $\text{Pm}(\text{COT})_2^-$ , a relatively large oblate  $m_{\parallel}^L(\mathbf{r})$  with opposite sign to  $m_{\parallel}^S(\mathbf{r})$  is calculated. The associated expectation values  $\langle L_{\parallel} \rangle = -5.73$  and  $\langle S_{\parallel} \rangle = 1.73$  lead to a GS with a sizable magnetic anisotropy with  $g_{\parallel} = 4.50$  and  $g_{\perp} = 0.00$ . For  $\text{Tm}(\text{COT})_2^-$ , a positive oblate  $m_{\parallel}^L(\mathbf{r})$  is calculated with  $\langle L_{\parallel} \rangle = 5.00$ . As for all the complexes of the second half of the series, the orbital and spin magnetization reinforce each other in  $\text{Tm}(\text{COT})_2^-$  to give a very large magnetic anisotropy with  $g_{\parallel} = 13.98$  and  $g_{\perp} = 0.00$ .

The large orbital angular momenta in  $\text{Pm}(\text{COT})_2^-$  and  $\text{Tm}(\text{COT})_2^-$  can be rationalized with the help of the electronic occupation of the  $4f$  orbitals. As already mentioned, when a single electron or a single hole is equally shared in degenerate orbitals with the same  $|m_{\ell}|$ , one can generate an occupied linear combination of the two orbitals that is an  $\widehat{L}_{\parallel}$  eigenfunction with an eigenvalue  $\pm m_{\ell}$ , and hence maximize the contribution to the orbital angular momentum. For example, the two unpaired electrons in  $\text{Tm}(\text{COT})_2^-$  are equally shared in the  $4f_{\delta}$  and  $4f_{\phi}$  orbitals such that the orbital angular momentum is essentially the sum of the two  $m_{\ell} = \pm 2$  and  $\pm 3$ .

The largest orbital angular momentum for an  $f$ -element in an axial environment would therefore be associated with  $\sigma^n \pi^1 \delta^1 \phi^1$  and  $\sigma^n \pi^3 \delta^3 \phi^3$  configurations. For the former case, the  $f$ -shell is less than half filled and the spin and orbital angular momenta would not reinforce each other. Accordingly, the latter case would lead to the overall largest magnetic moment (with  $\sigma^1$  maximizing the spin magnetic moment). Such configurations are potentially accessible in linear environments with the  $\text{Dy}^{3+}$  and  $\text{Er}^{3+}$  ions, leading to a  $|J = 1/2, M_J = \pm 1/2\rangle$  KD GS, and with the  $\text{Ho}^{3+}$  ion leading to a non-Kramers doublet  $|J = 8, M_J = \pm 8\rangle$  [37]. The  $|1/2, \pm 1/2\rangle$  doublet was characterized both experimentally and theoretically for the  $\text{Er}(\text{COT})_2^-$  complex [22, 38], whereas the pentagonal-bipyramidal  $[\text{Ho}(\text{CyPh}_2\text{PO})_2(\text{H}_2\text{O})_5]\text{I}_3$  complex affords an almost perfect  $M_J = \pm 8$  GS, therefore being very close to the theoretical ceiling of the magnetic moment of a single  $f$  ion [39, 40]. It is worth mentioning that the single-molecule magnet (SMM) with the largest relaxation barrier characterized so far is the  $[\text{Dy}(\text{C}_5\text{H}_2\text{tBu}_3)_2][\text{B}(\text{C}_6\text{F}_5)_4]$  complex with a  $|J = 1/2, M_J = \pm 1/2\rangle$  GS separated from the lowest ES by  $488 \text{ cm}^{-1}$  [41].

To obtain larger magnetic moments, one would need to reach the even larger orbital angular momenta  $m_{\ell} = \pm 4$  and  $\pm 5$  associated with  $g$ - and  $h$ -shells, couple orbital angular momenta from different centers, and/or create a large number of strongly coupled unpaired spins. Instead of trying to access exotic and unstable elements with partially filled shells of  $\ell \geq 4$  [42], one could potentially use small metal clusters to generate magnetic superatoms [43]. For instance, transition metal clusters such as  $\text{Pb}_{12}^{2-}$ ,  $\text{Sn}_{12}^{2-}$ , or the doped versions  $[\text{M Pb}_{12}]^q$  ( $\text{M} = \text{U}, \text{Pu}, \text{Am}, \text{Cm}$ ) exhibit superatomic molecular orbitals that resemble atomic  $g$  and  $h$  orbitals [44]. The partial filling of these superatomic orbitals could lead to potentially gigantic orbital angular momenta. However, Hund's rules do not necessarily apply to unsupported metallic clusters because of potentially large Jahn-Teller distortions, which may break the high degeneracy and favor complexes with quenched magnetic moments [45].

### 3.5 An Octahedral $Np(VI)$ Complex: $NpF_6$

$NpF_6$  crystallizes as a molecular crystal; the molecule is octahedral with a  $5f^4$  configuration. Its magnetic properties have been characterized by EPR and magnetic susceptibility measurements [46, 47]. The ground state is a KD with a negative  $g$ -factor of  $-0.604$ . This is well reproduced by CASPT2 calculations using a CAS(13/13) active space including the  $5f$  orbitals of the neptunium and six  $2p$  orbitals of the ligands [21]. The strong deviation of  $g$  from 2 is caused by an orbital angular momentum due to SO-induced mixing of nonbonding and bonding  $5f$  orbitals, as explained below, and therefore the calculation describes the balance of SO coupling and ligand-metal bonding well. There are also covalent interactions of the ligand with the Np  $6d$  shell, but these orbitals are not essential in the active space to describe the ground-state magnetism.

In  $O_h$  symmetry, the seven  $5f$  orbitals split in three sets: the nonbonding and nondegenerate  $f_{xyz}$  orbital belonging to the  $a_{2u}$  irrep, the three  $\pi$  antibonding  $f_{x(z^2-y^2)}$ ,  $f_{y(z^2-x^2)}$ , and  $f_{z(x^2-y^2)}$  orbitals of  $t_{2u}$  symmetry, and the three  $t_{1u}$   $\sigma$ -antibonding orbitals  $f_{x^3}$ ,  $f_{y^3}$ , and  $f_{z^3}$ . The SO GS of the molecule is a KD of symmetry  $E_{5/2}$  corresponding to a single electron in a  $e_{5/2}$  spinor, which is a mixture of the  $a_{2u}$  and  $t_{2u}$  orbitals under the SO coupling interaction. Due to the high symmetry, only two parameters are required to describe this mixing, as explained in [21]. The two components of the KD are accordingly, for a quantization axis along  $z$ ,

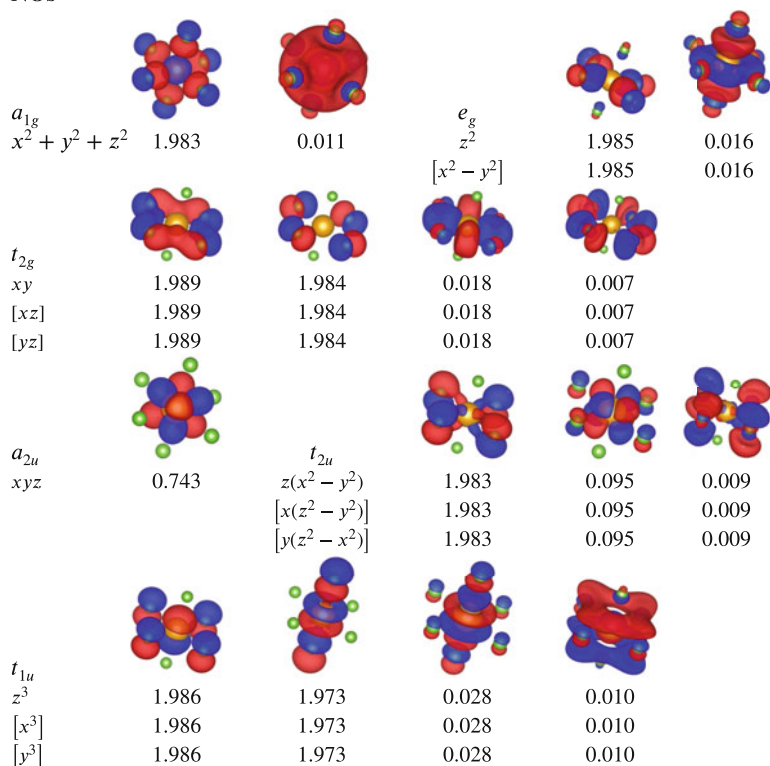
$$\begin{aligned} |\psi\rangle &= A|f_{xyz}; \alpha\rangle + B\frac{1}{\sqrt{3}}\left(|f_{z(x^2-y^2)}; \alpha\rangle + |f_{x(z^2-y^2)}; \beta\rangle + i|f_{y(z^2-x^2)}; \beta\rangle\right) \\ |\bar{\psi}\rangle &= A|f_{xyz}; \beta\rangle + B\frac{1}{\sqrt{3}}\left(|f_{z(x^2-y^2)}; \beta\rangle - |f_{x(z^2-y^2)}; \alpha\rangle + i|f_{y(z^2-x^2)}; \alpha\rangle\right) \end{aligned} \quad (23)$$

where  $A$  and  $B$  are real coefficients depending on the crystal-field splitting between the  $a_{2u}$  and  $t_{2u}$  orbitals and the SO coupling. When the quantization axis is along  $x$  or  $y$ , the Kramers partners are obtained from Eq. (23) by circular permutation  $x \rightarrow y \rightarrow z$  and  $x \rightarrow z \rightarrow y$ , respectively. Without SO coupling, the SR GS is orbitally nondegenerate and the orbital moment is quenched. From Eq. (23) one can derive three contributions to the  $g$ -factor: (1) a spin contribution  $2 - 4B^2/3$ ; the deviation from 2 arises from the admixture of a  $\beta$ -spin component through SO coupling, (2) a first order orbital angular momentum contribution  $-8AB/\sqrt{3}$  due to the partial de-quenching of the angular momentum by SO coupling, and (3) a second order orbital angular momentum contribution  $2B^2/3$  corresponding to the contribution of the  $t_{2u}$  orbitals.

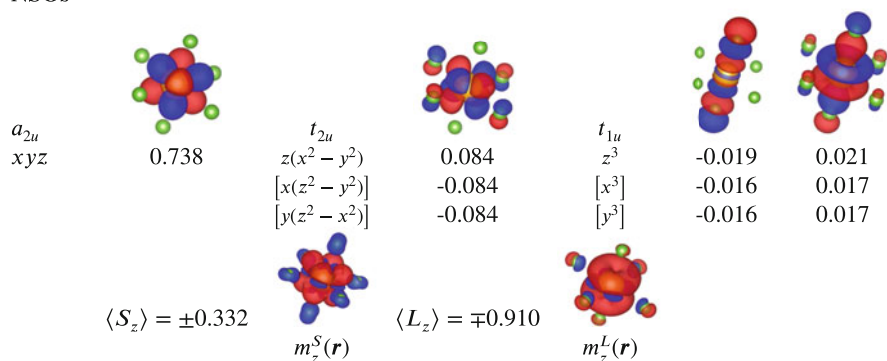
In order to describe properly the interactions between the metal and the ligands, all fluorine  $2p$  bonding combinations were included in the active space, along with their antibonding counterparts. The ligand combinations of  $g$  and  $u$  symmetry mix with the  $6d$  and  $5f$ , respectively. The NOs of the ground KD are shown in Fig. 13. As expected from Eq. (23), the  $f_{xyz}$  orbital and the  $f_{x(z^2-y^2)}$ ,  $f_{y(z^2-x^2)}$ , and  $f_{z(x^2-y^2)}$  orbitals



## NOs



## NSOs



**Fig. 13** Isosurfaces of selected NOs, and NSOs for the  $z$  quantization axis (vertical tilted), and corresponding populations. One orbital per degenerate irrep is shown, along with the AO labels [in brackets for the orbitals that are not shown]. The NSOs for the  $x$  and  $y$  quantization axes are obtained by circular permutation as explained in the text. Isosurface values:  $\pm 0.04$  au for orbitals,  $\pm 0.0008$  au for magnetization



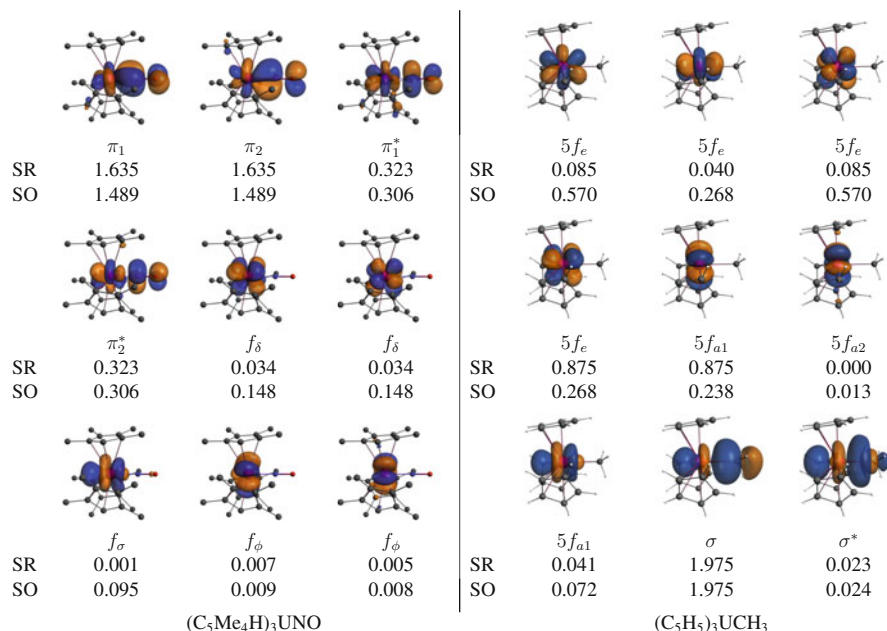
are partially occupied with respective populations of  $A^2 = 0.74$  and a combined population of  $B^2 = 0.28$ . The dynamical correlation occurs equivalently in all the irreps, either  $g$  or  $u$ , with a depletion in the bonding orbital in favor of the corresponding antibonding one. The NSOs along the  $z$  axis with the largest spin population are in accordance with Eq. (23) (slight numerical deviations from the simple model occur, of course): an  $\alpha$  spin population of  $A^2$  in orbital  $f_{xyz}$  and  $1/3 B^2$  in orbital  $f_{z(x^2-y^2)}$  and a  $\beta$  spin population of  $1/3 B^2$  in orbitals  $f_{x(z^2-y^2)}$  and  $f_{y(z^2-x^2)}$ . Spin correlation is the largest through  $t_{1u}$  orbitals with a  $\alpha$  spin population in the metallic  $t_{1u}$  orbitals in favor of a  $\beta$  population in the corresponding orbitals  $t_{1u}^*$  mostly localized on the ligands. Spin correlation occurs as well in the  $g$  orbitals but to a lesser extent. The spin polarization appears clearly on the total spin magnetization with some  $\beta$ -spin magnetization on all fluorine atoms. Spin densities for a magnetic field applied along another axis are obtained by circular permutations.

As expected from the analysis of the  $g$ -factor, there is an important contribution from orbital magnetization. Indeed, the expectation values of the orbital and spin angular momentum are  $\mp 0.91$  and  $\pm 0.33$ , respectively. The orbital magnetization for the field along  $z$  is cylindrical around  $z$  and resembles the  $m_\ell = 2$  “double doughnut” shape in Fig. 2, i.e.,  $f_\delta$  with respect to the quantization axis, but there is also a signature of magnetization contributions from  $f_\pi$  ( $|m_\ell| = 1$ ) visible. The orbital magnetization shape isosurface is consistent with the qualitative analysis of the wavefunction, and – like the orbitals contributing to  $m_z^S$  – it shows contributions from the fluorine ligands.

In this case, NOs and NSOs permit the visualization of electron and spin densities according to the wavefunction deduced from crystal field theory. Furthermore, they permit to see the spin polarization on the fluorine ligands as well as an extent of magnetic coupling between the metal and the ligands that shows up in the orbital magnetization.

### 3.6 Trigonal $U(IV)$ Complexes: $Ar_3U-X$ with $Ar = aryl$

The electronic structure of  $(C_5Me_4H)_3UNO$  ( $5f^2$  configuration) was rationalized with the help of KS-DFT and wavefunction calculations [26]. This complex represents one of the few examples of  $U^{IV}$  complexes that exhibit temperature-independent paramagnetism (TIP) at room temperature [48]; usually, the onset of temperature-dependent magnetism occurs at much lower temperatures. For  $(C_5Me_4H)_3UNO$ , the SR GS corresponds to the nondegenerate singlet state  $^1A_1$  in the  $C_{3v}$  symmetry point group, with the lowest SR triplet state lying above the GS at  $4 \cdot 10^3 \text{ cm}^{-1}$ . The energy gap is so large because the unpaired electrons at  $U^{IV}$  form a quite strong double bond with the nitrosyl ligand, as explained below, leading to a stable closed-shell SR GS. The natural orbitals of the SR GS calculated at the CAS(4,9)SCF-SO level are shown in Fig. 14. The NOs from the SO calculations are very similar, and therefore not shown, while the occupations for the SO case, provided in Fig. 14, notably differ from the SR calculation.



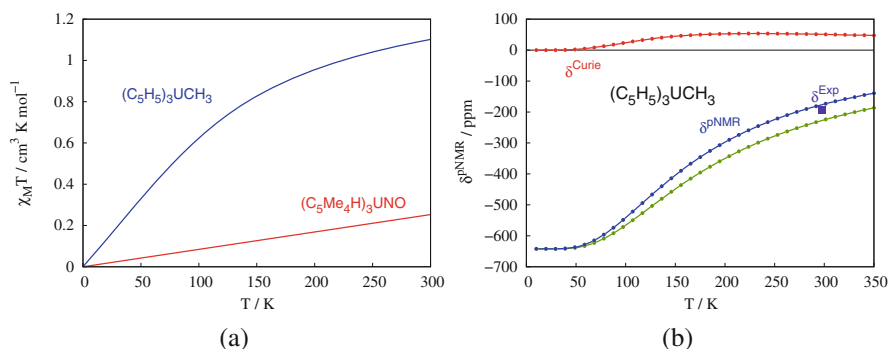
**Fig. 14** Selected SR NOs and occupations for the SR and SO GS of  $(C_5Me_4H)_3UNO$  (left) and  $(C_5H_5)_3UCH_3$  (right). CAS(4,9)SCF Results. Isosurfaces ( $\pm 0.03$  au). For a sake of clarity, hydrogen atoms have been removed in  $(C_5Me_4H)_3UNO$ . The SO NOs appear very similar to the SR NOs; the main difference between the SR and SO calculations is seen in the occupation numbers

It is helpful to consider the bonding in terms of an  $Ar_3U(III)$  ( $Ar = aryl$ ) fragment and the axial NO ligand. Electron transfer conceptually creates  $[Ar_3U(IV)]^+$  and  $NO^-$ , with two unpaired electrons each in orbitals of  $\pi$  symmetry. Strong anti-ferromagnetic coupling of the two electron pairs then gives two covalent  $\pi$  bonds and a singlet GS. The electronic structure of  $(C_5Me_4H)_3UNO$  therefore results from strong bonding, but also antibonding, interactions between singly occupied  $5f_\pi$  orbitals of the  $U(C_5Me_4H)_3$  fragment with the two singly occupied  $\pi^*$  orbitals of the nitrosyl ligand. The bonding combinations correspond to the HOMO and HOMO-1 of the complex. As seen in Fig. 14, the occupations of these bonding  $\pi$  orbitals differ significantly from 2. Indeed, the SR GS is strongly multi-configurational in character and cannot be simply described just by the  $|\pi_1^2\pi_2^2\pi_1^{*0}\pi_2^{*0}|$  “DFT configuration”. In fact, this configuration represents only 14% of the GS wavefunction. The major configuration (20%) corresponds to a double excitation among the  $\pi$  orbitals ( $|\pi_1^\uparrow\pi_2^\uparrow\pi_1^{*\downarrow}\pi_2^{*\downarrow}|$ ), while configurations corresponding to single excitations among the  $\pi$  orbitals also have sizable weights. This strongly correlated wavefunction leads to a GS with an effective U–N bond order (EBO) of 1.3 instead of 2 for the U–NO  $\pi$  bond, as determined qualitatively from the occupations of the bonding vs. antibonding NOs. Introduction of the SO coupling mixes the SR GS with the lowest excited SR triplet states, leading to a nondegenerate GS with ca. 35% of SR spin triplet character. This admixture leads

to a sizable decrease in the occupations of the  $\pi$  (and to a lesser degree of the  $\pi^*$ ) NOs. This goes along with an increase of the occupation numbers of the  $5f_\delta$  orbitals, which arise formally from the SO coupling between the  $5f_\pi$  and the  $5f_\delta$  orbitals at the metal center, shifting electron density at the metal from  $f_\pi$  to  $f_\delta$ . Since the  $5f_\delta$  are nonbonding, the EBO is slightly reduced by SO coupling, to below 1.2.

The calculated magnetic susceptibility  $\chi$  for  $(C_5Me_4H)_3UNO$  was calculated using the Van Vleck equation. The result is shown in Fig. 15a. The agreement with the experiment (not shown) is satisfactory [26]. The reader is reminded that the magnitude of  $\chi$  according to the Van Vleck equation depends on two terms for each electronic state, namely the Curie term and a linear response (LR) term. The former is explicitly temperature dependent ( $1/T$ ) and is present for degenerate magnetic states, whereas the latter is temperature-independent and arises from contributions due to the magnetic coupling between different electronic states [49]. A more complicated behavior of  $\chi$  may arise via a  $T$ -dependent Boltzmann LR and Curie terms average of the low-energy electronic state. The calculated  $\chi T$  for  $(C_5Me_4H)_3UNO$  reveals a linear increase with temperature, i.e., the susceptibility itself is constant. This TIP over such a large temperature range is due to the large energy gap (calculated as being over  $3000\text{ cm}^{-1}$ ) between the nondegenerate SO GS and the first excited magnetic doublets. At room temperature, the lowest magnetic ESs are not populated to a significant degree, and therefore only the LR term for the GS contributes to the magnetic susceptibility.

The replacement of the axial nitrosyl ligand in  $(C_5Me_4H)_3UNO$  by a methyl in  $(C_5H_5)_3UCH_3$  leads to the formation of a  $\sigma$  bond between a fragment orbital of the  $CH_3$  radical ligand and a (mainly)  $6d_\sigma/6p_\sigma$  hybrid orbital of the  $(C_5H_5)_3U$  fragment. The bonding combination is formally doubly occupied, whereas the antibonding one is vacant. Conceptually, starting with  $Ar_3U(III)$  and a methyl radical, electron transfer creates  $[Ar_3U(II)]^+$  and a closed-shell  $CH_3^-$  ligand that forms a donation bond by donating into the  $6d_\sigma/6p_\sigma$  hybrid orbital, leaving two singly occupied



**Fig. 15** (a) Calculated magnetic susceptibility times the temperature,  $\chi T$  ( $\text{cm}^3\text{ K mol}^{-1}$ ), as a function of  $T$  (K) for  $(C_5Me_4H)_3UNO$  and  $(C_5H_5)_3UCH_3$ . (b) Calculated temperature-dependence of the  $^1\text{H}$  pNMR shift  $\delta^{\text{pNMR}}$  (ppm) for  $(C_5H_5)_3UCH_3$  and individual LR and Curie contributions. The experimental shift at room temperature is also indicated

uranium  $5f$  orbitals. As seen in the right panel of Fig. 14, the  $5f$  orbitals do not strongly interact with the  $\text{CH}_3$  orbitals and remain principally nonbonding. Therefore, the SR GS corresponds to an orbitally degenerate spin triplet  ${}^3E$  in which the two unpaired electrons occupy mainly the  $5f_{a_1}$  and the  $5f_e$  orbitals. The  $5f_\pi$  and  $5f_\delta$  orbitals of the  $C_{\infty h}$  point group belong to the same irreducible representation ( $e$ ) in the  $C_{3v}$  symmetry, leading to  $5f_e$  orbitals which are linear combinations of  $5f_\pi$  and  $5f_\delta$ . The SO interaction mixes the SR GS with the lowest excited SR triplet states and gives a nondegenerate GS. Due to the strong mixing of states, the SO GS only contains 14 wt.% of the SR GS, and derives principally (42%) from the lowest SR ES  ${}^3A_1$ . Thus, the SO occupation numbers of the nonbonding NOs differ significantly from the ones calculated for the SR GS. As for the nitrosyl complex, the SR and SO NOs of  $(\text{C}_5\text{H}_5)_3\text{UCH}_3$  themselves are very similar, and only the SR set is shown in Fig. 14.

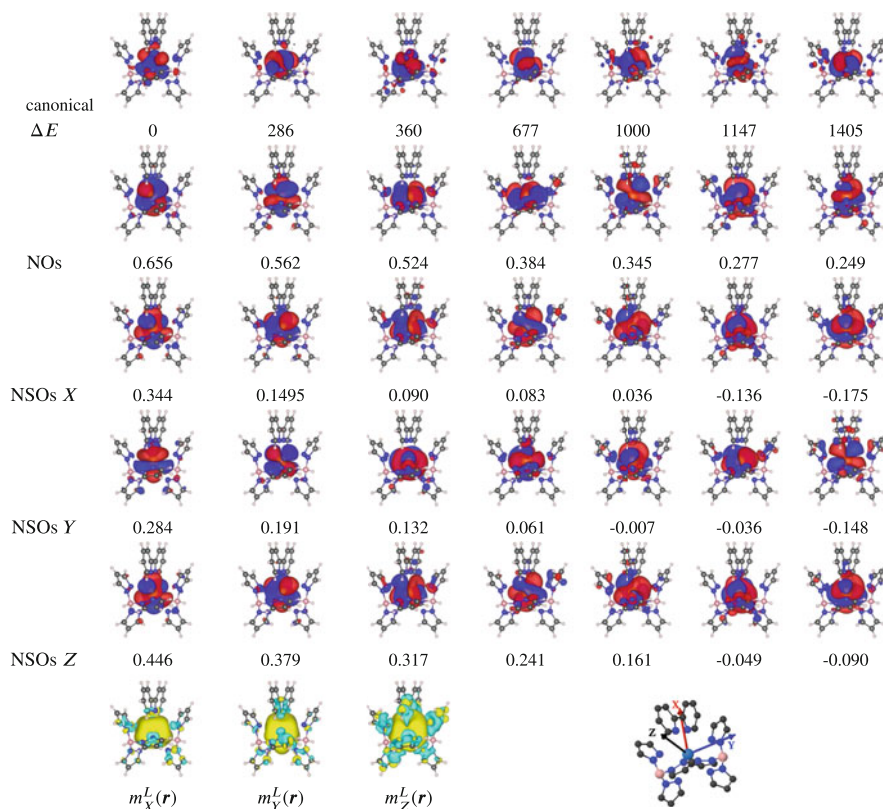
The calculated  $\chi T$  for  $(\text{C}_5\text{H}_5)_3\text{UCH}_3$  is shown in Fig. 15a and reveals a very different magnetic behavior than  $(\text{C}_5\text{Me}_4\text{H})_3\text{UNO}$ . At low  $T$ ,  $\chi T$  increases linearly with  $T$ . This is the TIP regime and it is the result of the magnetic coupling that takes place between the nondegenerate GS and the two lowest magnetic ESs. These ESs are calculated at 192 and 347  $\text{cm}^{-1}$  above the GS and are therefore not populated at low  $T$ . Above ca. 60 K, however, the thermal population of the lowest ESs becomes nonnegligible. The Curie term contributions to the magnetic susceptibility increase and  $\chi$  becomes temperature-dependent. This behavior is typical for U(IV) complexes [50].

The magnetic behavior of  $(\text{C}_5\text{H}_5)_3\text{UCH}_3$  was also characterized experimentally with the help of  ${}^1\text{H}$  NMR spectroscopy. The NMR spectrum reveals that the proton chemical shifts exhibit strong paramagnetic effects. In reference to tetramethylsilane (TMS), the methyl protons have a paramagnetic NMR shift ( $\delta_{\text{pNMR}}^{\text{H}}$ ) of  $-195$  ppm at room temperature [51]. The  ${}^1\text{H}$  pNMR shifts were calculated fully ab initio, using restricted active space self-consistent field (RASSCF) wavefunctions as described in [52]. The resulting temperature-dependence of  $\delta_{\text{pNMR}}^{\text{H}}$  is shown in Fig. 15b. If one assumes that the pNMR ligand shifts, with respect to an analogous diamagnetic system, are principally due to contributions that arise from the low-lying paramagnetic metal-centered states, then the isotropic ligand pNMR shifts can be calculated from the metal-centered low-energy states only, using the Soncini and van den Heuvel (SvH) equation [53, 54]. Similar to the Van Vleck susceptibility [55], the SvH equation contains Curie and LR terms to represent the explicitly temperature-dependent and temperature-independent contributions, respectively, to the NMR shifts. As seen in Fig. 15b, the methyl proton pNMR shift in  $(\text{C}_5\text{H}_5)_3\text{UCH}_3$  is constant at low  $T$ . This behavior arises from the LR term of the nondegenerate GS. Despite the fact that the paramagnetic electronic states are not populated at these temperatures, the very strong magnetic coupling between the GS and the lowest ESs renders the methyl proton shifts highly unusual. At higher  $T$ , the thermal population of the excited states causes  $1/T$ -dependent contributions to  $\delta_{\text{pNMR}}^{\text{H}}$  from the Curie terms, but they remain relatively small, while the LR contributions to the shift decrease in magnitude with increasing  $T$ . At room temperature, a methyl proton shift of  $-182$  ppm is calculated, in quite good agreement with the experiment.

### 3.7 The $[U(\text{Tp}^{\text{Me}_2})_2(\text{bipy})]\text{I}$ Complex

$[U(\text{Tp}^{\text{Me}_2})_2(\text{bipy})]\text{I}$  where  $\text{Tp}^{\text{Me}_2} = \text{hydrotris}(3,5\text{-dimethylpyrazolyl})\text{borate}$  is a complex of U(III) with a  $5f^3$  configuration exhibiting SMM behavior [27]. The ground KD presents a roughly axial magnetization in a direction close to the pseudo  $C_2$  symmetry axis ( $g_z = 3.4$ ,  $g_x = 1.3$ ,  $g_y = 0.7$ ). The first excited KD is  $138 \text{ cm}^{-1}$  above the ground state.

NOs for the ground KD are depicted in Fig. 16. All  $5f$  orbitals participate in this state, with an occupation varying from 0.65 to 0.25. For the sake of comparison, the CASSCF canonical orbitals are also shown in Fig. 16. The splitting of the  $5f$  orbitals is more than  $1,000 \text{ cm}^{-1}$ ; the more destabilized orbitals show a stronger delocalization in the  $\pi$  system of the ligands due to a stronger antibonding interaction. The



**Fig. 16**  $[U(\text{Tp}^{\text{Me}_2})_2(\text{bipy})]\text{I}$ . Top row: Isosurfaces and energies ( $\text{cm}^{-1}$ ) of the  $5f$  canonical orbitals. Second row: Isosurface and occupation number of selected NOs. Third to fifth row: Isosurfaces and spin population of NSOs for the three magnetic axes. Bottom row: Isosurfaces of the orbital magnetization  $m_i^L(r)$  for the three magnetic axes and representation of the magnetic axes. NOs and NSOs are calculated for the component of the ground KD with  $\langle S_U \rangle > 0$ . Isosurface values:  $\pm 0.04 \text{ au}$  for orbitals,  $\pm 0.0001 \text{ au}$  for magnetization

trend is the same for the NSOs: The more delocalized orbitals are less populated since they are higher in energy.

In direction  $Z$  with the largest magnetic moment,  $g_Z = 3.4$  with respective orbital and spin contributions of  $g_Z^L = 6.23$  and  $g_Z^S = -2.81$ . These two contributions have opposite signs, and the orbital one is the largest, which is reminiscent of the free ion where, according to the third Hund rule,  $J = L - S$  with  $L = 6$  and  $S = 3/2$ . Five NSOs have an important  $\alpha$ -spin contribution, while the  $\beta$ -spin contributions are almost negligible. The total spin magnetization for  $Z$  direction appears quite spherical. Along  $X$  and  $Y$ ,  $g_X^L = 1.50$ ,  $g_X^S = -0.78$ ,  $g_Y^L = 2.24$ , and  $g_Y^S = -0.96$ . In these directions, the  $\beta$  contribution to the spin magnetization is not negligible. In all directions, the orbital magnetization is mostly a ring around the corresponding axis, but also spreads on the ligands perpendicular to this axis.

In this case of a nonsymmetric actinide complex with three “magnetic electrons,” wavefunctions are difficult to analyze since they are strongly multi-reference, dynamical correlation plays an important role, and the SO coupling mixes many of the SF states. The analysis tools still provide a useful and complementary way in order to gain physical and chemical insight and to analyze the magnetic properties of the ground state.

## 4 Summary

Magnetic molecules tend to have complicated electronic states. Nonetheless, different sets of orbitals and their populations, generated from the complex many-determinant wavefunctions, can provide chemically intuitive insight into the chemical bonding and the resulting magnetic behavior. Additionally, the total spin and orbital magnetizations provide information about the magnetic behavior and, for instance, whether the ligands of an open-shell metal center contribute directly to it.

**Acknowledgments** J.A. acknowledges support of his research on EPR and NMR parameters of actinide complexes, and theoretical method developments, by the U.S. Department of Energy, Office of Basic Energy Sciences, Heavy Element Chemistry program, under grant DE-SC0001136.

## References

1. Roos BO (2009) Multiconfigurational quantum mechanics (QM) for heavy element compounds. In: Encyclopedia of Inorganic Chemistry. Wiley
2. Malrieu JP, Caballol R, Calzado CJ, de Graaf C, Guihéry N (2014) Chem Rev 114:429
3. Chan GKL, Sharma S (2011) Annu Rev Phys Chem 62:465
4. Knecht S, Hedegård ED, Keller S, Kovyrshin A, Ma Y, Muolo A, Stein C, Reiher M (2016) Chimia 70:244
5. Knecht S, Keller S, Autschbach J, Reiher M (2016) J Chem Theory Comput 12:5881
6. Chibotaru LF, Ungur L (2012) J Chem Phys 137:064112

7. Autschbach J (2012) *J Chem Phys* 136:150902
8. Löwdin PO (1955) *Phys Rev* 97:1475
9. Roos BO, Taylor PR, Siegbahn PEM (1980) *Chem Phys* 48:157
10. Malmqvist PA, Roos BO, Schimmelpfennig B (2002) *Chem Phys Lett* 357:230
11. Aquilante F, Autschbach J, Carlson RK, Chibotaru LF, Delcey MG, Vico LD, Galván IF, Ferré N, Frutos LM, Gagliardi L, Garavelli M, Giussani A, Hoyer CE, Manni GL, Lischka H, Ma D, Malmqvist PÅ, Müller T, Nenov A, Olivucci M, Pedersen TB, Peng D, Plasser F, Pritchard B, Reiher M, Rivalta I, Schapiro I, Segarra-Martí J, Stenrup M, Truhlar DG, Ungur L, Valentini A, Vancoillie S, Veryazov V, Vysotskiy VP, Weingart O, Zapata F, Lindh R (2016) *J Comput Chem* 37:506
12. Gendron F, Páez-Hernández D, Notter FP, Pritchard B, Bolvin H, Autschbach J (2014) *Chem Eur J* 20:7994
13. Pritchard B (2014) Calculation of magnetic properties of paramagnetic molecules. PhD thesis, University at Buffalo, State University of New York
14. Andersson K, Malmqvist PÅ, Roos BO, Sadlev AJ, Wolinski K (1990) *J Phys Chem* 94:5483
15. Wolf A, Reiher M, Hess BA (2002) *J Chem Phys* 117(20):9215
16. Bolvin H (2006) *ChemPhysChem* 7:1575
17. Vancoillie S, Malmqvist PA, Pierloot K (2007) *ChemPhysChem* 8:1803
18. Vancoillie S, Neese F, Rulisek L, Pierloot K (2009) *J Phys Chem A* 113:6149
19. Ridier K, Mondal A, Boileau C, Cador O, Gillon B, Chaboussant G, Le Guennic B, Costuas K, Lescouëzec R (2016) *Angew Chem Int Ed* 55:3963
20. Charon H, Malkin E, Rogez G, Batchelor LJ, Mazerat S, Guillot R, Guihèry N, Barra AL, Mallah T, Bolvin H (2017) *Chem Eur J* 22:1
21. Notter FP, Bolvin H (2009) *J Chem Phys* 130(18):184310
22. Gendron F, Pritchard B, Bolvin H, Autschbach J (2015) *Dalton Trans* 44:19886
23. Autschbach J (2016) *Comments Inorg Chem* 36:215
24. Myers WK, Duesler EN, Tierney DL (2008) *Inorg Chem* 47:6701
25. Andres H, Bominaar EL, Smith JM, Eckert NA, Holland PL, Münck E (2002) *J Am Chem Soc* 124:3012
26. Gendron F, Le Guennic B, Autschbach J (2014) *Inorg Chem* 53:13174
27. Coutinho JT, Antunes MA, Pereira LCJ, Bolvin H, Marçaloa J, Mazzanti M, Almeida M (2012) *Dalton Trans* 41:13568
28. Myers WK, Scholes CP, Tierney DL (2009) *J Am Chem Soc* 131:10421
29. Abragam A, Pryce MHL (1951) *Proc R Soc Lond A* 206:173
30. Jesson JP (1966) *J Chem Phys* 45:1049
31. McGarvey BR (1970) *J Chem Phys* 53:86
32. Neese F (2006) *J Am Chem Soc* 128:10213
33. McGarvey BR, Telsler J (2012) *Inorg Chem* 51:6000
34. Bolvin H, Autschbach J (2017) In: Liu W (ed) *Handbook of relativistic quantum chemistry*. Springer, Berlin, pp 725–763
35. Rogez G, Rebilly JN, Barra AL, Sorace L, Blondin G, Kirchner N, Duran M, van Slageren J, Parsons S, Ricard L, Marvilliers A, Mallah T (2005) *Angew Chem* 44:1876
36. Walter MD, Booth CH, Lukens WW, Andersen RA (2009) *Organometallics* 28(3):698
37. Rinehart JD, Long JR (2011) *Chem Sci* 2:2078
38. Meihaus KR, Long JR (2013) *J Am Chem Soc* 135:17952
39. Chen YC, Liu JL, Wernsdorfer W, Liu D, Chibotaru LF, Chen XM, Tong ML (2017) *Angew Chem Int Ed* 56:4996
40. Kajwara T (2017) *Angew Chem Int Ed* 56. <https://doi.org/10.1002/anie.201703022>
41. Goodwin CAP, Ortu F, Reta D, Chilton NF, Mills DP (2017) *Nature* 458:439
42. Dognon J, Pykkö P (2017) *Angew Chem Int Ed* 56:10132
43. Reveles JU, Clayborne PA, Reber AC, Khanna SN, Pradhan K, Sen P, Pederson MR (2009) *Nat Chem* 1:310

44. Pyykkö P, Clavaguéra C, Dognon J (2015) In: Dolg M (ed) *Computational methods in lanthanide and actinide chemistry*. Wiley, Chichester
45. Zhang X, Wang Y, Wang H, Lim A, Gantefoer G, Bowen KH, Reveles JU, Khanna SN (2013) *J Am Chem Soc* 135:4856
46. Hutchison CAJ, Weinstock B (1960) *J Chem Phys* 32:56
47. Hutchison CAJ, Tsang T, Weinstock B (1962) *J Chem Phys* 37:555
48. Siladke NA, Meihaus KR, Ziller JW, Fang M, Furche F, Long JR, Evans WJ (2012) *J Am Chem Soc* 134:1243
49. Kahn O (1993) *Molecular magnetism*. VCH, New York
50. Kindra DR, Evans WJ (2014) *Chem Rev* 114:8865
51. Marks T, Seyam AM (1972) *J Am Chem Soc* 94(18):6545
52. Gendron F, Autschbach J (2016) *J Chem Theory Comput* 12:5309
53. Van den Heuvel W, Soncini A (2013) *J Chem Phys* 138:054113
54. Soncini A, Van den Heuvel W (2013) *J Chem Phys* 138(2):021103
55. Autschbach J (2015) In: Dixon DA (ed) *Annual reports in computational chemistry*, vol 11. Elsevier, Amsterdam, pp 3–36



# Magnetism of Actinide Coordination Compounds



Jan van Leusen, Manfred Speldrich, and Paul Kögerler

## Contents

1	Introduction .....	392
2	Challenges in Interpreting the Magnetic Behavior .....	392
3	A Theoretical Model for Magnetic Properties of Actinide Coordination Compounds .....	395
4	Examples .....	396
4.1	A $U^{4+}$ Coordination Compound with $C_{3v}$ Site Symmetry .....	397
4.2	Trivalent Actinide Chlorides in $D_{3h}$ Site Symmetry .....	398
4.3	The $5f^7$ Compounds $CmCl_3/Cm^{3+}:LaCl_3$ and $Bk^{4+}:CeF_4$ .....	404
4.4	Exchange Interactions in a $Bk^{4+}$ Dimer .....	407
5	Outlook .....	409
	References .....	409

**Abstract** The magnetochemical interpretation of actinide ions in ligand environments represents a complex challenge, since the approximations and simplifications that are commonly employed in transition metal and lanthanide coordination compounds cannot be applied in the case of  $5f^N$  systems. We herein aim to deconvolute the various contributions to the magnetic characteristics of such systems, and we demonstrate how to construct appropriate microscopic model Hamiltonians. The approach to account for all relevant intrinsic effects is finally showcased by a number of examples.

**Keywords** Actinide coordination compounds · Ligand field theory · Magnetism · Magnetochemistry · Molecular actinide compounds

---

J. van Leusen, M. Speldrich, and P. Kögerler (✉)

Institute of Inorganic Chemistry, RWTH Aachen University, Aachen, Germany

e-mail: [paul.koegerler@ac.rwth-aachen.de](mailto:paul.koegerler@ac.rwth-aachen.de)

## 1 Introduction

Actinide coordination compounds feature remarkable chemistry and magnetism. They exhibit a wide range of stable oxidation states compared to the usually trivalent lanthanides, unlocking a variety of chemical reactivities for f shell elements, which are in particular complementary to that of 3d transition metals. Therefore, recent years have seen a renaissance in the design of catalysts based on actinides, and – due to significant improvement of computational resources – in the field of the magnetism of actinide coordination compounds [1–9]. However, there is a worrisome tendency to neglect a careful application of theory, i.e., a comprehensive quantum chemical approach, to explain the experimental data and to quantify the magnetic properties of such compounds. This is often a direct consequence of the intrinsic challenges involved in interpreting and analyzing the magnetic behavior of 5f compounds compared to those of, e.g., lanthanide compounds. For example, the average radii of the partly filled shells of 3d, 4f, and 5f atoms are 0.8–0.9 Å, 0.5 Å, and 0.7 Å, respectively [10]. Thus, the actinide atoms fill less space than the elements of the first transition metal series and more than the lanthanides, benefiting, in principle, from the advantages of both worlds. This results in multiple consequences: In comparison to their lighter 4f homologues, 5f metal ions and their ligands may form bonds with a significant degree of covalent character since the shielding of the 5f electrons by the respective outer 5d shell electrons is weaker. This also allows for coordination modes and numbers that are almost unique and rarely encountered within lighter lanthanide or transition metal compounds. In addition, any change to the valence electron states will have a larger impact on the physical properties of actinides when compared to lanthanides. While the general composition of the electronic ground multiplets of 4f and 5f compounds is to some degree similar for a given coordination environment and number of f electrons, the splitting of the energy states and the mixing of the corresponding wave functions are very different. In addition to the valence electron–electron interactions, these observations are caused by the ligand field, whose total splitting is about twice as large for actinides as for lanthanides, and by spin-orbit coupling, which increases with the atomic number and which for actinides reaches approximately twice the magnitude of lanthanides [11].

## 2 Challenges in Interpreting the Magnetic Behavior

As a consequence, interelectronic repulsion ( $\approx 10^4 \text{ cm}^{-1}$ ), spin-orbit coupling ( $\approx 10^3 \text{ cm}^{-1}$ ), and ligand field potential ( $\approx 10^3 \text{ cm}^{-1}$ ) energies are roughly of the same order of magnitude for actinide coordination compounds, and  $L$  (angular momentum quantum number),  $S$  (spin quantum number), and  $J$  (total angular momentum quantum number) are no longer “good” quantum numbers. Therefore, all these effects have to be considered simultaneously, and the magnetism of actinide compounds cannot be meaningfully described in terms of perturbation theory or models

**Table 1** Relative order of energetic contributions [11, 12]

System	Order of energetic contributions	Coupling scheme
$3d^N$	$H_{ee} > H_{lf} > H_{so}$	Weak field
	$H_{lf} > H_{ee} > H_{so}$	Strong field
	$H_{lf} \approx H_{ee} > H_{so}$	Intermediate field
$4f^N$	$H_{ee} > H_{so} > H_{lf}$	Strong field lanthanide system
	$H_{ee} > H_{so} \gg H_{lf}$	Weak field lanthanide system (except $\text{Sm}^{3+}$ , $\text{Eu}^{3+}$ : $H_{so} \approx H_{lf}$ )
$5f^N$	$H_{ee} \approx H_{so} \approx H_{lf}$	Inappropriate for actinide coordination compounds in terms of perturbation theory

**Table 2** Comparison of energetic effects for  $nd^N$ ,  $4f^N$ , and  $5f^N$  centers [11, 12]

Effect	System	Energy equivalent wavenumber/cm <sup>-1</sup>
Interelectronic repulsion $H_{ee}$	3d, 4d, 5d	$3d > 4d > 5d \approx 10^4$
	4f, 5f	$4f > 5f \approx 10^4$
Spin-orbit coupling $H_{so}$	3d, 4d, 5d	$3d < 4d < 5d \approx 10^3$
	4f, 5f	$4f < 5f \approx 10^3$
Ligand field potential $H_{lf}$	3d, 4d, 5d	$3d < 4d < 5d \approx 2 \times 10^4$
	4f	$\approx 10^2$
	5f	$\approx 10^3$
Exchange interactions $H_{ex}$	d–d	$\leq 10^2$
	4f–4f	$< 1$
	4f–nd	$< 10$
Magnetic field $H_{mag}$		$\approx 0.5$ (1 T)

based on it. This is in stark contrast to the situation for transition metal and lanthanide compounds (see Tables 1 and 2). For the former, in particular for the first-row transition metals,  $L$ ,  $S$ , and  $J$  are “good” quantum numbers, and the “spin-only” approximation works reasonably well for most octahedral, tetrahedral, or square planar coordination geometries. For the latter, only  $J$  remains as a “good” quantum number, and the electronic structure can be approximately derived using the Russell-Saunders coupling scheme.

For example, paramagnetic uranium centers are reported in a growing number of varied synthetic systems [5–7]. However, the analysis for unraveling and understanding their magnetic properties often stops at an unsatisfactory stage due to the lack of simple (or reasonably simplified) theoretical models that allow for an accurate description of, e.g., the magnetic susceptibility as a function of field and temperature. Consider the trivalent uranium ion  $\text{U}^{3+}$  with its three unpaired electrons within the 5f valence shell. Following the Russell-Saunders coupling scheme, a  $^4I_{9/2}$  ground multiplet would be expected, derived from the  $^4I$  ( $S = 3/2$ ,  $L = 6$ ) ground state and a total angular momentum of  $J = 9/2$ . However, strong spin-orbit coupling induces distinct mixing of the states, in particular, of other  $J = 9/2$  states into the  $^4I_{9/2}$  ground multiplet. Thus, spectroscopic studies of  $\text{U}^{3+}$  ions [13] revealed that there is a significant  $^2H_{9/2}$  contribution of 15.2% to the “free ion” ground state besides  $^4I_{9/2}$ . The Russell-Saunders coupling scheme is therefore not an adequate scheme to fully

identify the ground state. Beyond that, the mixing of states causes – and their significant extent even enhances – the difficulties in modeling the temperature-dependent molar magnetic susceptibility ( $\chi_m$ ).

Describing the electronic structure of the  $U^{3+}$  ion following the order of effects as above (first coupling of the spins and coupling of orbital momenta, then spin-orbit coupling, and finally mixing of  $J$  states) is known as the intermediate coupling scheme. Instead of starting from the more familiar Russell-Saunders coupling scheme, the electronic structure of an actinide compound could be equally well described by starting with the  $j$ - $j$  coupling scheme (the spin and the orbital angular momentum of each individual electron couple to form the total angular momentum  $j$  of that electron). Then the interelectronic repulsions are considered and finally the mixing of  $J$  states. Since neither coupling scheme (Russell-Saunders,  $j$ - $j$  coupling) for itself accurately describes the electronic structure of actinide coordination compounds, an intermediate coupling scheme (or equivalent) is the best approximation. Adding ligands to a free actinide ion has a significantly larger impact on their electronic characteristics than on corresponding lanthanide compounds due to the aforementioned greater radial extent of the 5f orbitals. Dependent on the symmetry of the ligand field, the already (partially) removed  $(2J + 1)$ -fold degeneracy of the ground state, induced by spin-orbit coupling, may be further removed. This results in  $2J + 1$  sublevels identified by the “crystal quantum number”  $m_J$  according to Hellwege [14]. Furthermore, the eigenvalues of these  $m_J$  sublevels are affected by the symmetry, orientation, and strength of the ligand field. While not causing the mixing of states, the ligand field, however, considerably contributes to this mixing since the relative strengths of the so-called single-ion effects (interelectronic repulsion, spin-orbit coupling, ligand field) determine the degrees of mixing. This can produce highly complex electronic structures in actinide coordination compounds due to the similar magnitudes of those effects. Additionally, the energies of the lowest sublevels are usually smaller than  $k_B T$  at ambient temperature (about  $210 \text{ cm}^{-1}$ ), which causes the effective magnetic moment,  $\mu_{\text{eff}}$ , or the product  $\chi_m T$  to be distinctly temperature dependent. This may also obscure other simultaneous effects, such as magnetic exchange coupling between centers and saturation effects caused by applied magnetic field. For example, while the oxidation state of a metal center can be estimated from the value of the effective magnetic moment  $\mu_{\text{eff}}$  at ambient temperature for most isolated 3d and 4f metals, oxidation states derived from this specific value are ambiguous in case of actinide compounds. The respective  $\mu_{\text{eff}}$  values of, e.g.,  $U^{5+}$  and  $U^{4+}$  centers can thus be very similar depending on the ligand field strength.

While the complexity of the electronic structure can be frustrating in terms of its effects on the magnetic properties, it is also exciting due to the large range of variations with respect to these properties. For example, a large single-ion anisotropy could cause a large energy barrier between the ground-state spins of the center. Such a coordination compound could represent a single-ion magnet with a high blocking temperature. Alternatively, multiple of such centers could couple via exchange interactions, potentially forming single-molecule magnets.

Recapitulating, employing simple models as the Curie-Weiss law would be meaningless for properly considering all single-ion effects of actinide coordination

compounds. Since a perturbation theory approach is not adequate for accurately describing their magnetic properties, almost all effective models fail to describe the magnetic properties of actinide compounds without introducing vast numbers of parameters with potential interdependencies. Therefore, a Hamiltonian taking all single-ion effects simultaneously into account must be considered, which needs then be applied to a sufficiently large basis set.

### 3 A Theoretical Model for Magnetic Properties of Actinide Coordination Compounds

The relative energies, i.e., the splitting of the relevant multiplet energy levels, rather than the total energies, are of importance when analyzing the magnetic properties of molecular actinide compounds. Moreover, only the effects of the valence electrons are considered, since the effects of the inner closed shells can be neglected in a good approximation. The corresponding Hamiltonian, representing the single-ion contributions, reads

$$\begin{aligned} \hat{H}_{\text{Sl}} = & \underbrace{\sum_{i=1}^N \left[ -\frac{\hbar^2}{2m_e} \nabla_i^2 + V(r_i) \right]}_{\hat{H}_0} + \underbrace{\sum_{i>j}^N \frac{e^2}{r_{ij}}}_{\hat{H}_{\text{ee}}} + \underbrace{\sum_{i=1}^N \xi(r_i) \kappa \hat{\mathbf{l}}_i \cdot \hat{\mathbf{s}}_i}_{\hat{H}_{\text{so}}} \\ & + \underbrace{\sum_{i=1}^N \sum_{k=0}^{\infty} \left\{ B_0^k C_0^k(i) + \sum_{q=1}^k \left[ B_q^k \left( C_{-q}^k(i) + (-1)^q C_q^k(i) \right) + i B_q^k \left( C_{-q}^k(i) - (-1)^q C_q^k(i) \right) \right] \right\}}_{\hat{H}_{\text{lf}}} \\ & + \underbrace{\sum_{i=1}^N \mu_B (\kappa \hat{\mathbf{l}}_i + g_e \hat{\mathbf{s}}_i) \cdot \mathbf{B}}_{\hat{H}_{\text{mag}}} \end{aligned}$$

The sum index  $i$  here runs over all  $N$  valence electrons. The operator  $\hat{H}_0$  represents the energy in the central field approximation. Since it describes a constant shift of the total energy, we neglect this contribution in the following discussions. The remaining operators  $\hat{H}_{\text{ee}}$ ,  $\hat{H}_{\text{so}}$ ,  $\hat{H}_{\text{lf}}$ , and  $\hat{H}_{\text{mag}}$  denote interelectronic repulsion, spin-orbit coupling, electrostatic effect of the ligands (ligand field), and Zeeman effect of an external magnetic field  $\mathbf{B}$ , respectively. The interelectronic repulsions can be parameterized in terms of, e.g., Slater-Condon ( $F^2$ ,  $F^4$ ,  $F^6$  for f systems) parameters and the spin-orbit coupling in terms of, e.g., the one-electron spin-orbit coupling parameter  $\zeta$  and the orbital reduction factor  $\kappa$ . In  $\hat{H}_{\text{lf}}$ , the  $C^k q = \sqrt{4\pi/(2k+1)} Y^k q$  represent the spherical tensors, which are directly related to the spherical harmonics  $Y^k q$ . The  $B^k q$  are the (real) ligand field parameters according to Wybourne's notation [15]. The spherically symmetric terms  $B_0^0 C_0^0(i)$  are neglected in the following as they exclusively cause a shift of the total energy. In addition to a well-defined Hamiltonian, we require a basis set that is sufficiently large to cover all relevant effects, particularly for actinides due to the significant mixing of

excited states into the ground state. Such a basis set is, e.g., the “full” basis of microstates [16] that incorporates all  $(2(2l + 1))!/[N! \cdot (2(2l + 1) - N)!]$  states of the valence electron configuration ( $l$ , orbital angular quantum number of the  $N$  valence electrons). These states may be illustrated in terms of the familiar orbital diagrams of the valence electrons, e.g., for an  $f^1$  system:  $\boxed{\uparrow | | | | | | |}$ ,  $\boxed{| \uparrow | | | | | |}$ ,  $\boxed{| | \uparrow | | | | |}$ , etc. This model is also referred to as “full model.”

Besides calculating the energy levels and corresponding wave functions, further physical quantities such as the magnetic susceptibility can be derived from the Hamiltonian. For example, the molar magnetic susceptibility in the specific direction  $\alpha$  of an applied magnetic field  $\mathbf{B}$  can be usually calculated from  $\chi_{m,\alpha} = \mu_0 M_{m,\alpha}/|\mathbf{B}|$ , if the molar magnetization  $M_{m,\alpha}$  is calculated by the fundamental equation [11] employing Boltzmann statistics:

$$M_{m,\alpha} = N_A \frac{\sum_n \mu_{n,\alpha} \exp(-E_{n,\alpha}/k_B T)}{\sum_n \exp(-E_{n,\alpha}/k_B T)}$$

The component of the magnetic moment  $\mu_{n,\alpha} = \boldsymbol{\mu}_n \cdot \mathbf{B}/|\mathbf{B}|$  of the  $n$ th state (with energy  $E_{n,\alpha}$ ) can be obtained by considering the magnetic moment operator  $\hat{\boldsymbol{\mu}}$  in connection with the application of the Zeeman operator  $\hat{H}_{\text{mag}} = -\hat{\boldsymbol{\mu}} \cdot \mathbf{B}$ .

In case of non-isolated magnetic centers, two or more centers may interact either directly or via superexchange ligands. Thus, the corresponding exchange interactions have to be additionally considered besides the single-ion effects of each center. The most successful model in describing the exchange interactions for molecular compounds is the phenomenological model of Heisenberg [17]. Originally, Heisenberg postulated that isotropic nearest-neighbor spin-spin interactions characterize the exchange interactions by effective exchange energies  $J_{ij}$ . For each pair of centers  $i$  and  $j$ , the exchange interactions are represented by

$$\hat{H}_{\text{ex},ij} = -2J_{ij} \hat{\mathbf{S}}_i \cdot \hat{\mathbf{S}}_j$$

If the centers are anisotropic, which is typically the case for actinide coordination compounds, the exchange interactions may become also anisotropic. By application of the “full model,” potential anisotropies are automatically taken into account. This can be managed by considering all effects causing anisotropy such as spin-orbit coupling or the ligand field in the resulting spin matrices of the respective actinide centers. This, however, also means that we lose any remaining “good” (spin) quantum numbers.

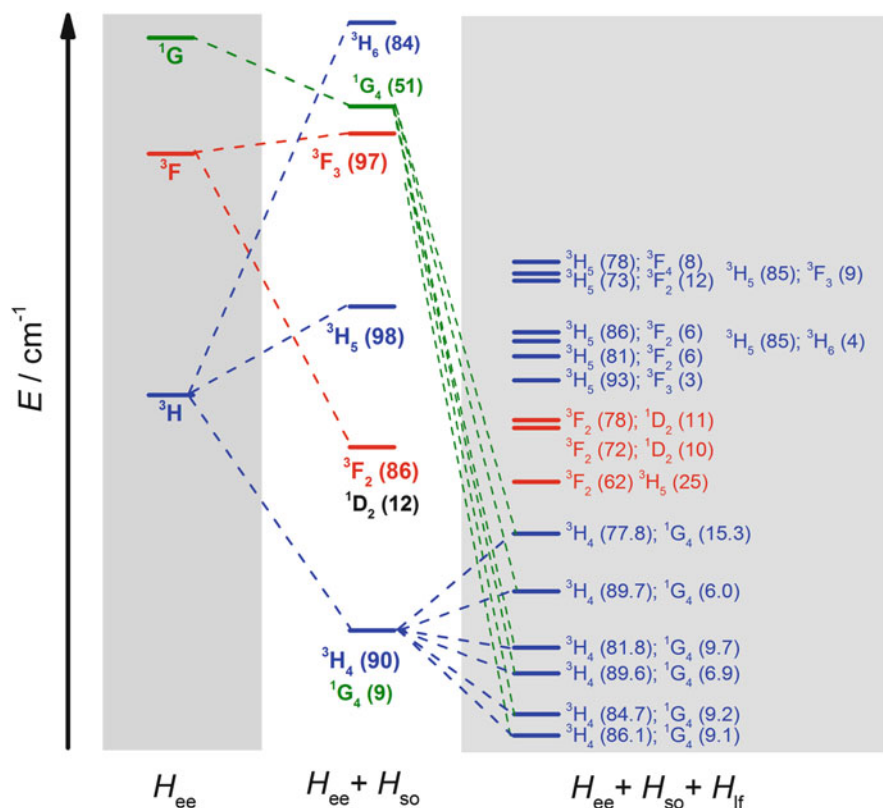
## 4 Examples

A software solution that covers all aspects of the “full model” is the computational framework CONDON [18–20]. All calculations for the examples discussed in the following sections employ this framework.

### 4.1 A $U^{4+}$ Coordination Compound with $C_{3v}$ Site Symmetry

As a first example, we study the contributions of the single-ion effects for actinide compounds on the basis of an isolated  $U^{4+}$  center residing in a  $C_{3v}$ -symmetric environment, based on the experimental data of tris( $\eta^5$ -cyclopentadienyl) uranium (IV) [21]. Employing the “full model,” we extract the respective parameter set from the spectroscopic data. To confirm the validity of the following discussion, we were able to reproduce the results of the work of Amberger et al. [21] by using this experimentally determined parameter set employing the “full model.” Following the Russell-Saunders scheme, the interelectronic repulsion ( $H_{ee}$ ) splits the  $5f^2$  electron configuration yielding the energetically lowest three terms  $^3H$ ,  $^3F$ , and  $^1G$  (see Fig. 1, left).

Neglecting all further effects, the characteristics of actinide and lanthanide compounds are the same. The introduction of spin-orbit coupling splits these terms with



**Fig. 1** Effects of interelectronic repulsion ( $H_{ee}$ ), spin-orbit coupling ( $H_{so}$ ), and electrostatic ligand field ( $H_{lf}$ ) on the energy states arising for a  $5f^2$  configuration based on a  $U^{4+}$  complex with  $C_{3v}$  symmetry [21]; numbers in brackets indicate percentage of contribution

respect to the total angular momentum  $J$  ( $H_{\text{ce}} + H_{\text{so}}$ , Fig. 1, center). In case of the  $\text{U}^{4+}$  model compound, the ground multiplet  ${}^3H_4$  is about  $6,000 \text{ cm}^{-1}$  below the  ${}^3F_2$  multiplet. However, instead of exhibiting only a small mixing of the excited states into the ground multiplet as observed for  $\text{Pr}^{3+}$  centers (less than 5%), the mixing is much stronger for  $\text{U}^{4+}$  centers (more than 10%) due to distinctly larger spin-orbit coupling contributions ( $\zeta(\text{Pr}^{3+}) = 758 \text{ cm}^{-1}$  vs.  $\zeta(\text{U}^{4+}) = 1,740 \text{ cm}^{-1}$ ). Introducing the ligand field complicates the situation in case of the actinide compound because of the almost equal magnitudes of all three contributions ( $H_{\text{ce}} + H_{\text{so}} + H_{\text{lf}}$  Fig. 1, right). Due to the large mixing and the relatively small energetic difference of the ground ( ${}^3H_4$ ) and the respective excited multiplet ( ${}^1G_4$ ), the substates of the ground multiplet cannot be meaningfully characterized in terms of an effective total angular momentum, not to mention of an effective spin.

## 4.2 Trivalent Actinide Chlorides in $D_{3h}$ Site Symmetry

The following analysis of the magnetic properties of trivalent actinide compounds was motivated by investigations of actinide [22] and lanthanide compound spectra [23]. In the latter, the authors concluded that the spectral data could be sufficiently interpreted in terms of an effective operator model, which reproduces the entire electronic structure of the  $f^N$  configurations using 15 effective parameters in addition to the parameters for electron interrepulsion, spin-orbit coupling, and the ligand field. Due to energetic similarity of the individual single-ion effects for actinide coordination compounds (shown in Tables 1 and 2), the effective operator model used for  $4f^N$  systems is inadequate to model the spectra of the  $5f^N$  compounds. A sufficient expansion of that model was found by introduction of a few further effective parameters. To model the magnetic properties of the trivalent actinide compounds, we employ the “full model” requiring thus significantly fewer independent parameters (8) than the effective model (17). We model the spectroscopic data of the trivalent actinide chlorides presented in the work of Carnall [22] and the references therein. For comparison, we also model the spectrum of the compound  $\text{Bk}^{4+}:\text{CeF}_4$  ( $C_{2v}$  symmetry) presented in the work of Liu et al. [24]. The Slater-Condon parameters ( $F^2, F^4, F^6$ ), the one-electron spin-orbit coupling parameters ( $\zeta$ ), and the ligand field parameters ( $B_q^k$ ) extracted from the experimental spectra are shown in Table 3.

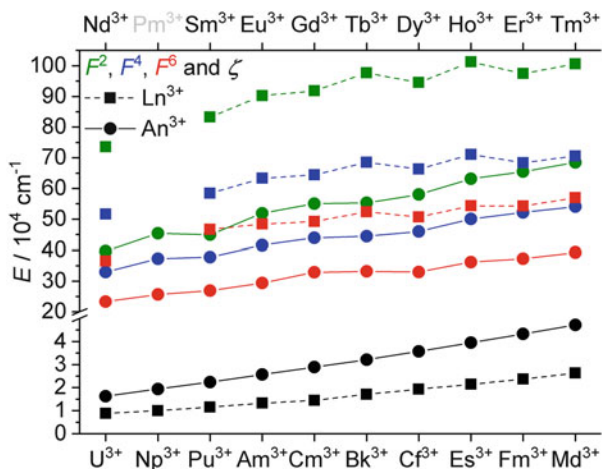
The Slater-Condon parameters and the spin-orbit coupling parameters for the actinide chlorides are used as calculated in [22], thus yielding a slightly worse fit ( $SQ$ , relative root mean squared error) for the  $\text{Bk}^{3+}$ ,  $\text{Cf}^{3+}$ , and  $\text{Es}^{3+}$  derivatives. The parameters are also shown in a graphical representation in Fig. 2. Roughly, the Slater-Condon parameters and the spin-orbit coupling parameters continuously increase with the number of  $f$  valence electrons. However, the differences of both contributions for the  $5f$  compounds are noticeably smaller than for their  $4f$  analogs, consistent with the general values shown in Table 2.



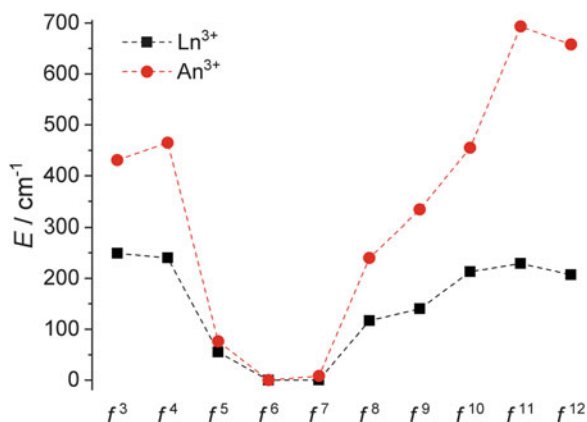
**Table 3** Energy level parameters for An<sup>3+</sup>:LaCl<sub>3</sub> and Bk<sup>4+</sup>:CeF<sub>4</sub> in cm<sup>-1</sup>

	U <sup>3+</sup>	Np <sup>3+</sup>	Pu <sup>3+</sup>	Am <sup>3+</sup>	Cm <sup>3+</sup>	Bk <sup>4+</sup>	Bk <sup>3+</sup>	Cf <sup>3+</sup>	Es <sup>3+</sup>	Fm <sup>3+</sup>	Md <sup>3+</sup>
	5f <sup>3</sup>	5f <sup>4</sup>	5f <sup>5</sup>	5f <sup>6</sup>	5f <sup>7</sup>	5f <sup>7</sup>	5f <sup>8</sup>	5f <sup>9</sup>	5f <sup>10</sup>	5f <sup>11</sup>	5f <sup>12</sup>
F <sup>2</sup> [22]	39,611	45,382	48,679	51,900	55,055	57,697	60,464	63,174	65,850	68,454	39,611
F <sup>4</sup> [22]	32,960	37,242	39,333	41,600	43,938	45,969	48,026	50,034	52,044	54,048	32,960
F <sup>6</sup> [22]	23,084	25,644	27,647	29,400	32,876	32,876	34,592	36,199	37,756	39,283	23,084
ζ [22]	1,626	1,937	2,242	2,564	2,889	3,210	3,572	3,944	4,326	4,715	5,114
B <sub>0</sub> <sup>2</sup>	474	149	193	242	280	1,170	302	254	248	305	306
B <sub>2</sub> <sup>2</sup>	-	-	-	-	-	48	-	-	-	-	-
B <sub>0</sub> <sup>4</sup>	-722	-597	-759	-582	-884	-3,560	-914	-891	-985	-1,062	-1,061
B <sub>2</sub> <sup>4</sup>	-	-	-	-	-	1,425	-	-	-	-	-
B <sub>4</sub> <sup>4</sup>	-	-	-	-	-	-2,410	-	-	-	-	-
B <sub>0</sub> <sup>6</sup>	-1,639	-1,515	-1,581	-1,887	-1,293	-1,020	-780	-2,068	-1,454	-1,444	-1,442
B <sub>2</sub> <sup>6</sup>	-	-	-	-	-	1,300	-	-	-	-	-
B <sub>4</sub> <sup>6</sup>	-	-	-	-	-	-820	-	-	-	-	-
B <sub>6</sub> <sup>6</sup>	870	1,006	1,093	1,122	990	1,560	868	1,928	759	943	941
SQ (%)	0.01	1.56	0.01	1.02	0.9	1.2	3.98	4.15	4.30	0.01	0.12

**Fig. 2** Comparison of the Slater-Condon parameters ( $F^2$ ,  $F^4$  and  $F^6$ ) and spin-orbit coupling parameter  $\zeta$  (in  $\text{cm}^{-1}$ ) for trivalent lanthanide and actinide compounds  $M^{3+}:\text{LaCl}_3$  ( $M = \text{Ln}$  [22] and  $\text{An}$  [23])

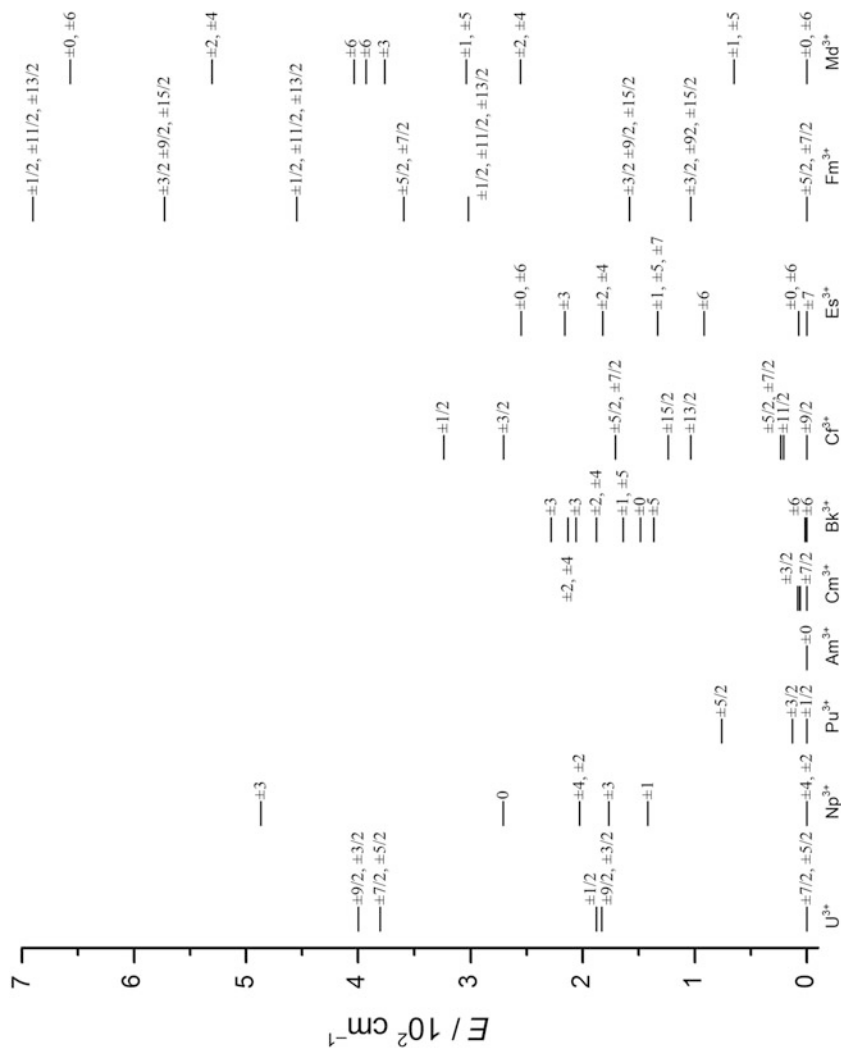


**Fig. 3** Comparison of the total ground multiplet splitting for  $M^{3+}:\text{LaCl}_3$  ( $M = \text{Ln}$  [22] and  $\text{An}$  [23])



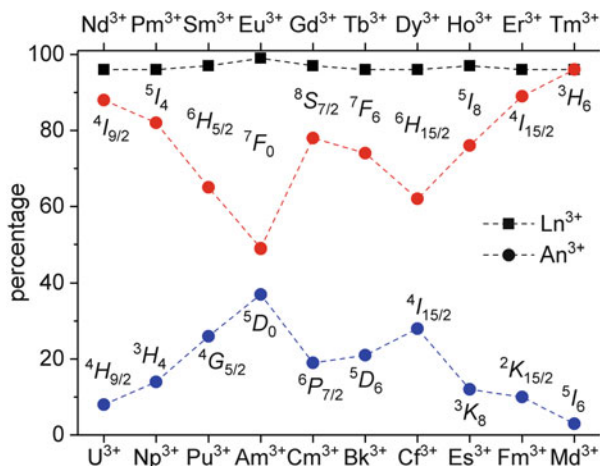
Additionally, for  $\text{Ln}^{3+}$  and  $\text{An}^{3+}$  ions in  $D_{3h}$ -symmetric ligand fields, in Fig. 3, we show the total splitting of the  $2J + 1$  states emerging from the ground multiplet. Figure 4 details this for the  $\text{An}^{3+}$  systems in more detail and depicts all substates. There are two striking observations: First, the overall splittings of the actinide ground multiplets span energy ranges that are about two to three times larger than the respective ranges of the corresponding lanthanide analogs. Second, the substates are significantly mixed states for the actinide chlorides as indicated by the  $m_j$  values in Fig. 4.

This is also evident from the term composition of the ground multiplets (Fig. 5). The lanthanide chlorides exhibit ground multiplets that are slightly mixed, but the main component is represented by a single term to at least 96%. In contrast, the ground multiplets of the actinide chlorides are characterized by significant mixing of two (or more) terms with very strong mixing for the  $\text{Am}^{3+}:\text{LaCl}_3$  and the  $\text{Cf}^{3+}:\text{LaCl}_3$  compounds.



**Fig. 4** Comparison of the ground multiplet splittings of An<sup>3+</sup>:LaCl<sub>3</sub> [22]. The m<sub>j</sub> values of each substate are indicated to the right of the corresponding energy level

**Fig. 5** Comparison of the calculated ground multiplet compositions for  $M^{3+}:\text{LaCl}_3$  ( $M = \text{An}$  and  $\text{Ln}$ ). Only the main components of the multiplet wave functions are shown



The latter results are summarized in Table 4. For comparison, the fitted overall splittings of the ground multiplets are also given. We expand the table with the corresponding ambient temperature values of a characteristic magnetic parameter: the effective magnetic moment  $\mu_{\text{eff}}$  (and, for convenience, converted to  $\chi_m T$ ). These values are distinctly different from the values found for the corresponding lanthanide analogs, which are usually (except for  $\text{Sm}^{3+}$  and  $\text{Eu}^{3+}$  coordination compounds) close to the free ion values approximated as  $g_J \sqrt{J(J+1)} \mu_B$  ( $g_J$ , Landé factor;  $J$ , total angular momentum).

The temperature dependence of the effective magnetic moments at an applied field of 0.1 T calculated according to the parameters of Table 3 is shown in Fig. 6. At 290 K, all  $\mu_{\text{eff}}$  values are as tabulated in Table 4. Each curve reveals a distinct decrease of  $\mu_{\text{eff}}$  with temperature unambiguously demonstrating the invalidity of the Curie-Weiss law for the actinide chlorides. Even for  $\text{Cm}^{3+}:\text{LaCl}_3$  with a  $5f^7$  valence electron configuration, there is a clear deviation from spin-like behavior, i.e., constant  $\mu_{\text{eff}}$ , for  $T < 30$  K.

These features are also revealed in the representation of the data as the inverse molar susceptibility  $\chi_m^{-1}$  vs.  $T$  (Fig. 7). For all electron configurations but  $5f^7$  ( $\text{Cm}^{3+}$ ), there are deviations from linearity for  $T > 20$  K, which are exclusively caused by the single-ion effects. Interpreting these deviations in corresponding experimental data sets as errors from data recording is therefore usually wrong. In addition, employing the Curie-Weiss law to the nearly linear parts of the  $\chi_m^{-1}$  vs.  $T$  curves yields Weiss temperatures different from zero, which is obviously meaningless since we here discuss non-coupled centers.

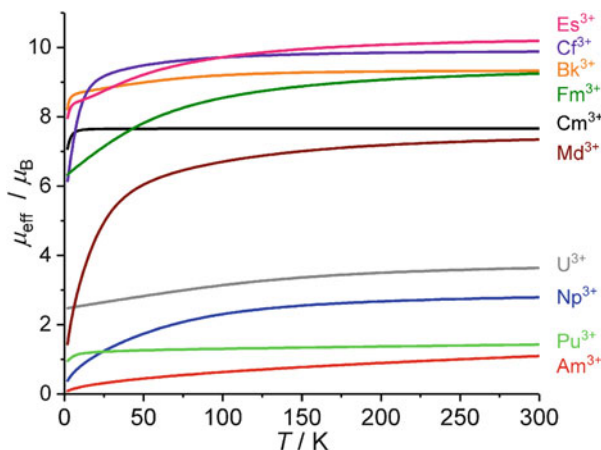
**Table 4** Trivalent actinide chlorides in  $D_{3h}$  site symmetry ( $An^{3+} \cdot LaCl_3$ ): term symbol, one-electron spin-orbit coupling parameter  $\zeta$ , composition of the ground multiplet, overall splitting of the ground multiplet, and  $\mu_{eff}$  and  $\chi_m T$  values at ambient temperature

$An^{3+}$	$f^N$	$2S + 1L_J^a$	$\zeta/cm^{-1}$	Composition/% <sup>b</sup>	$\Delta E_{exp}/cm^{-1c}$	$\Delta E_{calc}/cm^{-1}$	$\mu_{eff}/\mu_B$	$\chi_m T/cm^3 K mol^{-1}$
$U^{3+}$	$f^3$	$4I_{9/2}$	1,626	$4I_{9/2}$ (88), $4H_{9/2}$ (8)	431 [249]	400	3.64	1.66
$Np^{3+}$	$f^4$	$5I_4$	1,937	$5I_4$ (82), $3H_4$ (14)	465 [240]	480	2.79	0.97
$Pu^{3+}$	$f^5$	$6H_{5/2}$	2,242	$6H_{5/2}$ (65), $4G_{5/2}$ (25)	76 [55]	80	1.43	0.26
$Am^{3+}$	$f^6$	$7F_0$	2,564	$7F_0$ (49), $5D_0$ (37)	0 [0]	0	1.09	0.15
$Cm^{3+}$	$f^7$	$8S_{7/2}$	2,889	$8S_{7/2}$ (78), $6P_{7/2}$ (19)	8 [0.2]	8	7.66	7.33
$Bk^{3+}$	$f^8$	$7F_6$	3,210	$7F_6$ (74), $5G_6$ (21),	240 [117]	227	9.33	10.88
$Cf^{3+}$	$f^9$	$6H_{15/2}$	3,572	$6H_{15/2}$ (62), $4I_{15/2}$ (28)	334 [140]	324	9.88	10.21
$Es^{3+}$	$f^{10}$	$5I_8$	3,944	$5I_8$ (76), $3K_8$ (22)	455 [213]	451	10.19	12.96
$Fm^{3+}$	$f^{11}$	$4I_{15/2}$	4,326	$4I_{15/2}$ (89), $2K_{15/2}$ (10)	693 [229]	690	9.25	10.69
$Md^{3+}$	$f^{12}$	$3H_6$	4,715	$3H_6$ (96), $5I_6$ (3)	658 [207]	656	7.34	6.75

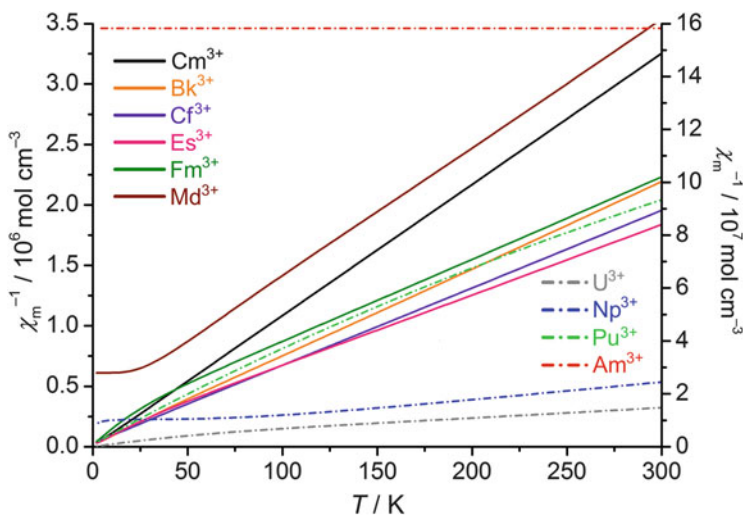
<sup>a</sup>Ground multiplet according to Hund's rules

<sup>b</sup>Composition of the ground multiplet (main components)

<sup>c</sup>Overall splitting of the ground multiplet [22]; numbers in brackets: values for the corresponding  $Ln^{3+}$  compounds [23]



**Fig. 6** Calculated temperature dependence of  $\mu_{\text{eff}}$  at 0.1 T of  $\text{An}^{3+}:\text{LaCl}_3$  ( $D_{3h}$  site symmetry) and  $\text{Bk}^{4+}:\text{CeF}_4$  ( $C_{2v}$  site symmetry) based on the parameters in Table 3



**Fig. 7** Calculated temperature dependence of the inverse molar magnetic susceptibility  $\chi_m^{-1}$  at 0.1 T of  $\text{An}^{3+}:\text{LaCl}_3$  ( $D_{3h}$  site symmetry) based on the parameters in Table 3 (left ordinate for solid lines, right ordinate for dashed-dotted lines, SI units)

### 4.3 The $5f^7$ Compounds $\text{CmCl}_3/\text{Cm}^{3+}:\text{LaCl}_3$ and $\text{Bk}^{4+}:\text{CeF}_4$

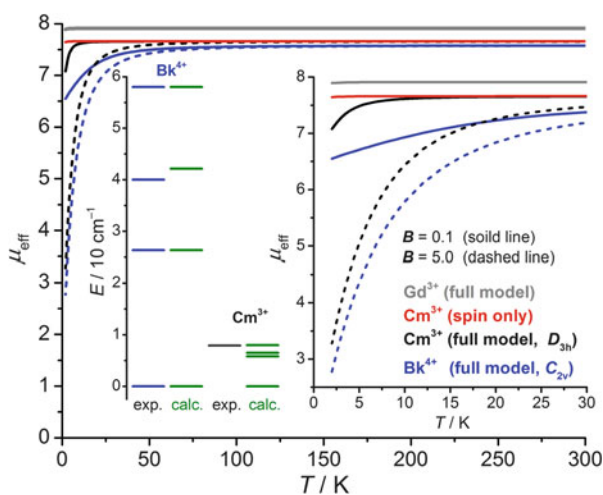
In this section, we focus on actinide compounds that are characterized by a half-filled subshell, i.e., a valence electron configuration of  $f^7$  with a seemingly simple electronic situation. We consider the compounds  $\text{CmCl}_3/\text{Cm}^{3+}:\text{LaCl}_3$  and  $\text{Bk}^{4+}:\text{CeF}_4$

representing the  $5f^7$  compounds in two different ligand fields [9] and, for comparison, the free  $Gd^{3+}$  ion as  $4f^7$  representative, for which the impact of the ligand field is very small. For the calculations, we use the parameters listed in Table 3 and from Condon and Shortley [16] for the free  $Gd^{3+}$  ion.

The ligand field potential on its own does not split a degenerate  ${}^8S$  term, which would be the expected ground state for a  $f^7$  system according to Hund's rules. However, the additional presence of spin-orbit coupling causes a splitting of the degenerate state and potentially introduces mixing of the states. Although being very small in case of  $4f^7$  systems, this effect is well-known even for isolated  $Gd^{3+}$  centers [25]. Modeling the free  $Gd^{3+}$  ion as a representative example for a  $4f^7$  center shows a splitting of the assumed  ${}^8S_{7/2}$  ground multiplet of about  $0.2\text{ cm}^{-1}$ . This is due to a small but observable mixing of states yielding a ground multiplet composed of 97%  ${}^8S_{7/2}$  and 2.7%  ${}^6P_{7/2}$  terms (and further, smaller contributions). In terms of magnetic properties, the observations are a  $g$  factor of 1.993, which is slightly smaller than the value of the free electron  $g_e \approx 2.0023$ , and a value of  $\mu_{\text{eff}} = 7.91\ \mu_B$  at ambient temperature (see Fig. 8, gray lines), which is less than the value  $7.94\ \mu_B$  determined from  $g_J \sqrt{J(J+1)}\ \mu_B$ .

A much stronger spin-orbit coupling, a reduced interelectronic repulsion, and a larger ligand field potential drastically change the situation for actinide compounds. While the amount of (excited) states mixed into the  ${}^8S_{7/2}$  multiplet forming the ground multiplet is almost uniform at a value of 3% for most  $Gd^{3+}$  centers, the amount is larger for actinides and distinctly changes from center to center depending on the strength of the single-ion effects. For both examples, about 22% ( $\text{Cm}^{3+}:\text{LaCl}_3/\text{Cm}^{3+}:\text{LaCl}_3$ ) and 26% ( $\text{Bk}^{4+}:\text{CeF}_4$ ), respectively, of the ground multiplet originate from multiplets other than  ${}^8S_{7/2}$ . Due to the nature of these other multiplets, the effective magnetic moments at ambient temperature are reduced to  $7.66\ \mu_B$  ( $\text{Cm}^{3+}$ ) and  $7.59\ \mu_B$  ( $\text{Bk}^{4+}$ ), respectively, as are the  $g$  factors to 1.9261 and 1.9241, respectively. Since the ligand field has a significant impact on the magnetism

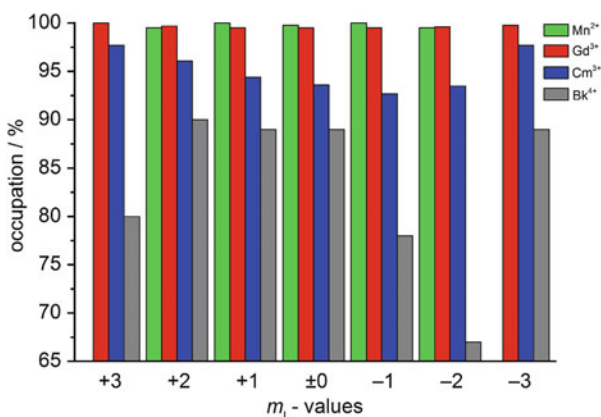
**Fig. 8** The temperature dependence [9] of  $\mu_{\text{eff}}$  of  $\text{Cm}^{3+}:\text{LaCl}_3$ ,  $\text{Bk}^{4+}:\text{CeF}_4$ , and a free  $\text{Gd}^{3+}$  ion at two applied magnetic fields ( $B = 0.1$  and  $5.0\text{ T}$ ). The  $\text{Gd}^{3+}$  ion is used as reference. Inset: low-temperature range in detail (right) and splitting of the four lowest energy doublets – experimental (blue or dark gray) and calculated (green) energy levels of  $\text{Cm}^{3+}:\text{LaCl}_3$  and  $\text{Bk}^{4+}:\text{CeF}_4$  (center)



of actinide compounds, the  $\mu_{\text{eff}}$  vs.  $T$  curves for both example compounds are different: Below 25 K, the  $\text{Cm}^{3+}$  center in a  $D_{3h}$ -symmetric environment shows less temperature dependence compared to the  $\text{Bk}^{4+}$  center in its  $C_{2v}$ -symmetric environment, which starts to display temperature-dependent deviations already below 75 K (see inset Fig. 8). Consistently, the eight substates of the ground multiplet form four doublets, which split over different energy ranges (Fig. 8, center); this range is significantly smaller for  $\text{CmCl}_3/\text{Cm}^{3+}:\text{LaCl}_3$  with  $8\text{ cm}^{-1}$  in comparison to  $58\text{ cm}^{-1}$  for  $\text{Bk}^{4+}:\text{CeF}_4$ . Note that these deviations from spin-like behavior are again easily misinterpreted: Due to inappropriately using the Curie-Weiss law, the low-temperature variations of  $\mu_{\text{eff}}$  are often misinterpreted as effects of exchange interactions or of low-lying excited energy multiplets.

Another remarkable property of the  $5f^7$  compounds is revealed in Fig. 9. In this figure, the occupations of the spin-up components are assigned to the complex  $m_l$  orbitals for the ground states of half-filled shell systems. Due to an almost fully quenched orbital momentum and a very small splitting of the ground multiplet,  $4f^7$  centers (represented by  $\text{Gd}^{3+}$ ) and high-spin  $3d^5$  centers (represented by an arbitrary octahedral  $\text{Mn}^{2+}$  complex) show Curie behavior down to very low temperatures, even down to 2 K and lower. Note that the small variation of  $\mu_{\text{eff}}$  at  $T < 5\text{ K}$  in Fig. 8 (gray line) is almost exclusively caused by the Zeeman effect of the applied field ( $B = 0.1\text{ T}$ ). This observation is also reflected by the occupation of the spin-up components of both ground states, which add up to more than 99% of the number of valence electrons, i.e., 5 ( $\text{Mn}^{2+}$ ) and 7 ( $\text{Gd}^{3+}$ ), respectively. For the actinide compounds, the occupations of the spin-up components distinctly differ for both examples and vary in a wider range between 67 and 97%. In other words, non-negligible parts of the electrons occupy the spin-down components of the orbitals characterized by  $m_l$ . This also implies a loss of the spherical symmetry of the f electron distribution when going from  $4f^7$  to  $5f^7$ . Therefore, analyses of magnetic properties of actinides based on a comparison of actinide and lanthanide compounds with the same  $f^N$  electron configuration can easily lead to a misinterpretation of the

**Fig. 9** Electron distribution of the ground states of  $\text{Mn}^{2+}$  (green),  $\text{Gd}^{3+}$  (red),  $\text{Cm}^{3+}$  (blue,  $D_{3h}$ ), and  $\text{Bk}^{4+}$  (gray,  $C_{2v}$ ) centers. Shown are the occupations of the spin-up components with respect to the complex  $m_l$  orbitals





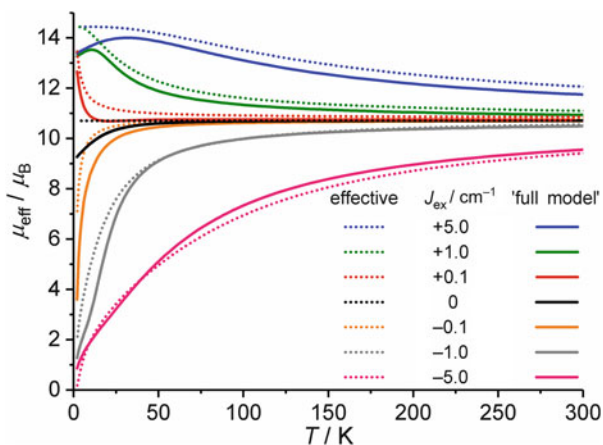
experimental data, since the electronic situations are significantly different between  $4f^N$  and  $5f^N$  compounds and readily tuned by the ligand field for the latter.

#### 4.4 Exchange Interactions in a $Bk^{4+}$ Dimer

Now that the single-ion contributions of the seemingly simple  $5f^7$  examples were presented, we discuss the effects of Heisenberg exchange interactions between such ions. Since we like to highlight the key characteristics of the interactions, we chose a hypothetical dimeric unit consisting of two  $Bk^{4+}$  centers, i.e., a homodinuclear complex. Due to the lack of experimental data, we will model the compound as two interacting  $Bk^{4+}$  centers based on the above discussed data of the compound  $Bk^{4+}:\text{CeF}_4$ , i.e., with the  $5f^7$  centers in  $C_{2v}$ -symmetric ligand fields [24]. We employ the parameters tabulated for  $Bk^{4+}$  in Table 3, and we only vary the exchange interaction parameter  $J_{\text{ex}}$  and the applied magnetic field.

Starting with a very small field of  $B = 0.01$  T, thus suppressing the contributions of the Zeeman effect, six different strengths of exchange interactions represented by  $J_{\text{ex}} = \pm 0.1 \text{ cm}^{-1}$ ,  $\pm 1.0 \text{ cm}^{-1}$ , and  $\pm 5.0 \text{ cm}^{-1}$  are taken into account, in addition to the values of two non-coupled  $Bk^{4+}$  centers. In Fig. 10, the corresponding temperature dependences of  $\mu_{\text{eff}}$  employing the “full model” and, for comparison, an effective spin model (using  $g = 1.9241$ ,  $S = 7/2$  per center) are shown. As already indicated in Fig. 8, the two isolated  $Bk^{4+}$  centers (black solid line) reveal a significant temperature dependence for temperatures below 70 K in contrast to the expectations according to the effective spin model (black dotted line). In addition to these single-ion contributions, the presence of exchange interactions distinctly influences the shape of the  $\mu_{\text{eff}}$  vs.  $T$  plot. In general, a ferromagnetic interaction ( $J_{\text{ex}} > 0 \text{ cm}^{-1}$ ) between both centers increases the values of  $\mu_{\text{eff}}$ , while an antiferromagnetic

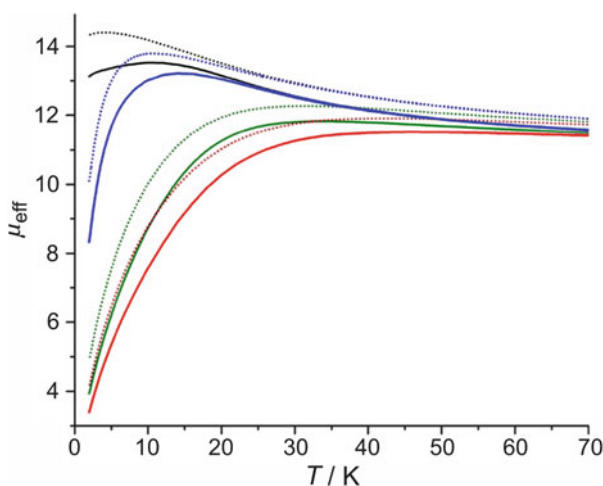
**Fig. 10** Variation  $\mu_{\text{eff}}$  vs.  $T$  at 0.01 T of a dinuclear  $5f^7$  unit based on  $Bk^{4+}:\text{CeF}_4$ , simulated for different exchange coupling energies  $J_{\text{ex}}$ : “full model” (solid lines) vs. effective spin model (dotted lines)



interaction ( $J_{\text{ex}} < 0 \text{ cm}^{-1}$ ) decreases  $\mu_{\text{eff}}$  compared to the reference value  $10.74 \mu_{\text{B}}$  ( $= \sqrt{2}\mu_{\text{eff}}(\text{Bk}^{4+} : \text{CeF}_4)$ ) for the two isolated centers at ambient temperature.

At this temperature, the values increase (ferromagnetic coupling) or decrease (antiferromagnetic coupling), respectively, with increasing magnitude of the exchange energy  $J_{\text{ex}}$ . Even at the strongest interactions ( $J_{\text{ex}} = \pm 5 \text{ cm}^{-1}$ ), the estimated effective magnetic moments are roughly similar for both models:  $13.98 \mu_{\text{B}}$  vs.  $14.43 \mu_{\text{B}}$  and  $9.55 \mu_{\text{B}}$  vs.  $9.41 \mu_{\text{B}}$  (“full model” vs. effective spin model). By lowering temperature, in particular below 100 K, these similarities vanish due to the single-ion contributions. This becomes most evident in case of the ferromagnetic examples with  $J_{\text{ex}} = +1.0 \text{ cm}^{-1}$  and  $+ 5.0 \text{ cm}^{-1}$ , for which maxima occur and subsequent values of  $\mu_{\text{eff}}$  decrease (“full model” calculations in Fig. 10). In contrast, the effective spin model calculations reach a plateau at lowest temperatures. Thus, estimating the nature of an exchange interaction by a simple subtraction of experimental data and single-center contributions modeled by a simple effective spin Hamiltonian can easily result in false interpretations if the analysis is primarily based on the lower-temperature range.

The situation gets more complicated if the Zeeman effect has to be additionally considered. As example, we show in Fig. 11 the  $\mu_{\text{eff}}$  vs.  $T$  curves for  $J_{\text{ex}} = +1.0 \text{ cm}^{-1}$  in presence of four different applied magnetic fields at  $T < 70 \text{ K}$ . The larger the fields, the less pronounced are the characteristic maxima of ferromagnetic interactions, vanishing above  $B = 7.0 \text{ T}$ . In addition, besides revealing the respective maximum at different temperatures, the  $\mu_{\text{eff}}$  values according to the effective spin model are larger than the values according to the “full model.” Note that this effect of the effective spin model calculations cannot be corrected by a simple shift of the  $\mu_{\text{eff}}$  values, since such a shift would yield a different  $g$  factor, which in turn generates a



**Fig. 11** Zeeman effect on the temperature dependence of  $\mu_{\text{eff}}$  of a dinuclear  $5f^7$  unit based on  $\text{Bk}^{4+}$ :  $\text{CeF}_4$  interacting with  $J_{\text{ex}} = +1.0 \text{ cm}^{-1}$ : Solid lines correspond to the “full model” and dotted lines to the effective spin model;  $B = 0.1 \text{ T}$  (black),  $1.0 \text{ T}$  (blue),  $5.0 \text{ T}$  (green), and  $7.0 \text{ T}$  (red)

mismatch with the data for the isolated  $\text{Bk}^{4+}$  center. Again, neglecting the single-ion effects of actinide coordination compounds, even for the “simple”  $5f^7$  systems, may easily lead to wrong conclusions about the analyzed compound.

## 5 Outlook

While we herein introduced a model that is, in general, capable to analyze and describe the magnetic properties of actinide compounds, the model is semiempirical and thus relies on complementary data, e.g., from spectroscopy experiments. This allows us to handle, to a certain degree, the electron correlation issues, among other aspects. In addition, the corresponding data are rather scarce and thus must usually be collected in parallel to, e.g., SQUID magnetometry measurements. Therefore, the desire for simply calculating the magnetic properties with ab initio methods is even stronger than for transition metal or lanthanide compounds. However, when it comes to the magnetic properties of molecular actinide compounds, even the most promising ab initio approaches such as CASSCF (complete active space self-consistent field) including its perturbative expansions (e.g., CASPT2) or DFT (density functional theory) very frequently fail in reproducing the data [20]. There are only a few examples in literature for which CAS or DFT results are reasonable from a magnetic point of view, presumably due to the rather small energy scales characterizing magnetic properties in these specific cases. The situation unfortunately worsens for actinide molecular compounds, since in particular perturbation theory approaches here are intrinsically unsuitable models. Hence, there still is significant headroom for method development ahead of us.

## References

1. Lukens WW, Beshouri SM, Bloesch LL, Andersen RA (1996) *J Am Chem Soc* 118:901
2. Fox AR, Bart SC, Meyer K, Cummins CC (2008) *Nature* 455:341
3. Arnold PL, Mansell SM, Maron L, McKay D (2012) *Nat Chem* 4:668
4. Cooper O, Camp C, Pécaut J, Kefalidis CE, Maron L, Gambarelli S, Mazzanti M (2014) *J Am Chem Soc* 136:6716
5. Schilder H, Speldrich M, Lueken H, Sutorik AC, Kanatzidis MG (2004) *J Alloys Compd* 374:249
6. Lukens W, Speldrich M, Yang P, Duignan TJ, Autschbach J, Kögerler P (2016) *Dalton Trans* 45:11508
7. Meihaus KR, Long JR (2015) *Dalton Trans* 44:2517
8. Silver MA, Cary SK, Johnson JA, Baumbach RE, Arico AA, Luckey M, Urban M, Wang JC, Polinski MJ, Chemey A, Liu G, Chen K-W, Van Cleve SM, Marsh ML, Eaton TM, van de Burgt LJ, Gray AL, Hobart DE, Hanson K, Maron L, Gendron F, Autschbach J, Speldrich M, Kögerler P, Yang P, Braley J, Albrecht-Schmitt TE (2016) *Science* 353:888

9. Silver MA, Cary SK, Garza AJ, Baumbach RE, Arico AA, Galmin GA, Chen K-W, Johnson JA, Wang JC, Clark RJ, Chemey A, Eaton TM, Marsh ML, Seidler K, Galley SS, van de Burgt L, Gray AL, Hobart DE, Hanson K, Van Cleve SM, Gendron F, Autschbach J, Scuseria GE, Maron L, Speldrich M, Kögerler P, Celis-Barros C, Páez-Hernández D, Arratia-Pérez R, Ruf M, Albrecht-Schmitt TE (2017) *J Am Chem Soc* 139:13361
10. Robinson JM (1979) *Phys Rep* 51:1
11. Lueken H (1999) *Magnetochemie*. Teubner, Stuttgart
12. Williams AF (1979) *A Theoretical approach to inorganic chemistry*. Springer, Berlin
13. Carnall WT, Wybourne BG (1964) *J Chem Phys* 40:3428
14. Hellwege KH (1948) *Ann Phys* 439:95
15. Weybourne BG (1965) *Spectroscopic properties of rare earths*. Wiley, New York
16. Condon EU, Shortley GH (1970) *The theory of atomic spectra*. Cambridge University Press, Cambridge
17. Heisenberg W (1928) *Z Phys* 49:619
18. Schilder H, Lueken H (2004) *J Magn Magn Mater* 281:17
19. Speldrich M, Schilder H, Lueken H, Kögerler P (2011) *Isr J Chem* 51:215
20. van Leusen J, Speldrich M, Schilder H, Kögerler P (2015) *Coord Chem Rev* 289–290:137
21. Amberger H-D, Reddmann H, Edelstein N (1988) *Inorg Chim Acta* 141:313
22. Carnall WT (1992) *J Chem Phys* 96:8713
23. Carnall WT, Goodman GL, Rajnak K, Rana RS (1989) *J Chem Phys* 90:3443
24. Liu GK, Carnall WT, Jursich G, Williams CW (1994) *J Chem Phys* 101:8277
25. Sytsma J, Murdoch KM, Edelstein NM, Boatner LA, Abraham MM (1995) *Phys Rev B* 52:12668

## Correction to: Cobalt(II) Complexes as Single-Ion Magnets



**Shalini Tripathi, Atanu Dey, Maheswaran Shanmugam,  
Ramakirushnan Suriya Narayanan, and Vadapalli Chandrasekhar**

**Correction to:**  
**Chapter “Cobalt(II) Complexes as Single-Ion Magnets” in:**  
**S. Tripathi et al., Topics in Organometallic Chemistry,**  
**DOI: [10.1007/3418\\_2018\\_8](https://doi.org/10.1007/3418_2018_8)**

In the Chapter opener page, the spelling of the author is inadvertently misspelt as Vadapalli Chandrsekhar, which is now corrected as Vadapalli Chandrasekhar.

## Correction to: Cobalt(II)/(III)–Lanthanide(III) Complexes as Molecular Magnets



Atanu Dey, Shalini Tripathi, Maheswaran Shanmugam,  
Ramakirushnan Suriya Narayanan, and Vadapalli Chandrasekhar

**Correction to:**  
**Chapter “Cobalt(II)/(III)–Lanthanide(III) Complexes  
as Molecular Magnets” in: A. Dey et al.,  
Topics in Organometallic Chemistry,  
DOI: [10.1007/3418\\_2018\\_9](https://doi.org/10.1007/3418_2018_9)**

In the Chapter opener page, the spelling of the author is inadvertently misspelt as Vadapalli Chandrsekhar, which is now corrected as Vadapalli Chandrasekhar.

# Index

## A

Ab initio calculations, 43, 112, 163, 194, 232, 281, 355, 409  
Actinide chlorides, 398  
Actinides, coordination compounds, 366, 391  
Aminophenol, 101  
Anisotropy, magnetic, 3, 7, 37, 102, 177, 184, 192, 291  
ANO-RCC, 364  
Arenes, 268–270  
Atomic mean-field integral (AMFI), 284, 364  
Atomic natural orbitals (ANOs), 289  
Axial clusters, 242

## B

Berkelium (Bk), 398, 404–409

## C

CASPT2, 282, 286, 364, 373, 381, 409  
CASSCF, 46, 67, 87, 112, 128, 184, 281, 287, 364, 370, 387, 409  
Ce(COT), 376  
CeF<sub>4</sub>, 404  
Charge transfer (CT), 2, 25, 178, 303  
Charge-transfer induced spin-crossover (CTIST), 25  
Cluster complexes, 77  
CmCl<sub>3</sub>, 404  
CN-bridged networks, organic–inorganic, 1  
Co(Tp)<sub>2</sub>, 367  
Cobalt complexes, 35, 77, 93, 239, 242, 367  
Coercivity, 48, 85, 266, 273, 318

Complete active space self-consistent field (CASSCF), 281  
Constitutional (structural) isomerism, 215  
Coordination compounds, 101, 104, 163, 183, 254, 391  
  geometry, 3, 39, 42, 97, 144, 191, 205–222, 258, 310, 393  
  numbers, 72, 173, 191–222, 237, 282, 304, 322, 331, 342  
  sphere, 6–10, 19, 39, 72, 102, 117, 163, 184, 195, 303, 312, 372  
Crystal field theory, 231, 285, 383  
  splitting, 283  
Curie term, 385, 386, 406  
Curie-Weiss constant/law, 40, 394, 402, 406  
Cyanide ligands, 1, 2, 22  
Cyanidometallates, 17  
Cyclic alkyl amino carbene (CAAC), 256  
Cycloheptatrienyl, 254, 271, 272  
Cyclooctatetraenyl, 253–255, 272  
Cyclopentadienyl, 253, 258, 272, 275, 276, 397

## D

Dilanthanides, 267  
Dinuclear systems, 241  
DMRG, 349  
Donor-acceptor type dyads, nitrogen-based, 173  
Douglas–Kroll–Hess (DKH), 284  
  second-order (DKH2), 364  
Dysprosium, 93, 215, 240, 253, 266  
  metallocenes, 259  
  SIMs, 281

**E**

Electron paramagnetic resonance (EPR), 35  
Electron spin Hamiltonian, 355  
Endohedral metallofullerenes (EMF), 327  
Er(COT), 380  
Erbium, 233, 240, 253–278

**F**

FeLCl, 370  
Frequency-domain magnetic-resonance spectroscopic (FDMRS), 235  
Fullerenes, 324, 327, 330, 348

**G**

Gadolinium (Gd), 19, 79–92, 119–153, 164, 266, 325, 405  
Guest ions/molecules, 1, 23, 26, 28, 69

**H**

Hall-bar sensor, 235  
Hartree–Fock (RHF), 288  
Heisenberg exchange, 244, 287, 407  
Hexacyanidometallate, 10  
High-frequency electron paramagnetic resonance (HFEP), 235  
Hyperfine interaction, 51, 64, 78, 112, 163, 171, 230, 246, 336

**I**

Irreducible tensor operator (ITO), 284  
Ising anisotropy, 46, 55, 72, 178, 184, 228, 241, 245, 300, 307, 329  
Ising exchange, 287  
Isomerism, *cis-trans*, 216, 222

**K**

Kohn-Sham density functional theory (KS-DFT), 357  
Kramers doublets, 43, 85, 104, 150, 170, 179, 194, 239, 294, 367

**L**

LaCl<sub>3</sub>, 404  
Lanthanides, 77, 101, 163, 192, 281  
Lanthanide single-molecule magnets (Ln-SMMs), 191  
Ligand field theory, 191, 391, 395

Light induced excited spin state trapping (LIESST), 11

Lines model, 286, 287, 349  
Ln(COT)<sub>2</sub>, 376  
Long-range magnetic ordering (LRMO), 8  
Luminescence, 1, 12, 17–19, 101, 107, 164, 185, 236

**M**

Magnetic anisotropy, 255  
axes, 233  
Magnetic chains, 8, 243–245  
Magnetic clusters, 4, 228  
Magnetic coupling, 2, 8, 131, 228–232, 266, 287, 363, 383–386  
Magnetic hysteresis, 102, 181, 208, 238, 266  
Magnetic layers, 10  
Magnetic sponges, 2, 11, 21, 25  
Magnetization-induced second harmonic generation (MSHG), 3  
Magnetization, reversal, 36, 47, 62–65, 102, 108, 123, 135, 282, 291, 302  
slow relaxation, 9, 17, 38, 50, 61–69, 77, 83, 102–153, 191, 212, 219, 239, 277  
Magnetochemistry, 391  
Magneto-chiral dichroism (MChD), 3  
Mannich ligands, 101–153  
Metallofullerenes, 327  
endohedral (EMF), 327  
Metal-to-metal charge transfer (MMCT), 11, 14  
Micro-SQUID, 235  
Molecular actinide compounds, 391  
Molecular engineering, 163, 227, 245  
Molecular magnetism, 2, 102, 191, 227, 253, 275  
Molecular orbitals (MOs), 3, 210, 237, 287, 291, 380  
Multifunctionality, 1, 17, 164, 182  
Multi-switchable spin-crossover (SCO), 2

**N**

Nanomagnets, 102, 114, 254  
Natural orbitals (NOs), 355, 361, 368, 376, 383  
Natural spin orbitals (NSOs), 361, 368  
Neptunium (Np) complexes, 366, 381, 399, 403  
Nickel (Ni) complexes, 7, 80, 372

**O**

Octacyanidometallates, 5, 23, 27  
Octacyanidomolybdate (IV), 5



- Octacyanidonioate (IV), 22  
Octacyanidostate (IV), 5  
Orbach process/route, 38, 43, 67, 93, 107, 127, 143, 170, 175, 209, 256  
Orbital hybridization, 238
- P**  
Pentadecanuclear clusters, 5  
Perturbation theory, 16, 289, 364, 392, 395, 409  
Phosphacyclopentadienyl, 277  
Photomagnetism, 1, 3, 5, 11  
Plutonium (Pu), 399, 403  
Pm(COT), 380  
Point-charge electrostatic (PCE) model, 285  
Predominant bond, 191, 222  
Principal axis system (PAS), 357  
Prussian blue analogues (PBAs), 2, 10, 11, 25, 28
- Q**  
Quantum electrodynamics (QED), 358  
Quantum tunnelling of magnetization (QTM), 43, 78, 102, 208, 256, 282
- R**  
Racah operators, 230, 231  
Radicals, 65, 243, 266  
Relaxation, mechanism, 281  
    magnetization, slow, 9, 17, 38, 50, 61–69, 83, 102–153, 212, 219, 239, 277  
Restricted active space self-consistent field (RASSCF), 288, 363  
Restricted active space state-interaction (RASSI), 363  
    with spin-orbit coupling (RASSI-SO), 281  
Russell-Saunders coupling, 393, 397  
    multiplet mixing, 231
- S**  
Sandwich complexes, 70, 207, 253–277, 319, 337, 344–347  
Scalar relativistic (SR) effects, 356  
Single-chain magnets (SCMs), 1, 3, 9, 17, 282  
Single-ion anisotropy, 227  
Single-ion effects, 394–398, 402, 405  
Single-ion magnets (SIMs), 35  
    zero-field, 45, 47, 58, 294, 300, 307–312, 339, 342
- Single-molecule magnets (SMMs), 77, 101, 163, 227, 253  
    zero-field, 80–83, 88, 123, 134, 137, 147, 176, 201, 293, 300, 335  
Single-molecule toroids (SMTs), 114  
Singly occupied molecular orbital (SOMO), 3  
Slater-Condon parameters, 395, 398  
Slow relaxation of magnetization, 9, 17, 38, 50, 61–69, 83, 102–153, 191, 212, 219, 239, 277  
Solvatomagnetism, 1, 21–25  
Spin-crossover (SCO), 2, 3  
    charge-transfer induced (CTIST), 25  
    switchable, 2  
    thermal, 15  
Spin Hamiltonian (SH), 35, 39, 43, 72, 229, 282, 289, 355, 408  
Spin-orbit coupling, 67, 282, 355  
Stark sublevels, 193  
Stevens formalism/operator, 193, 283  
Susceptibility tensors, 233–242, 357
- T**  
Temperature-independent paramagnetism (TIP), 383  
Terbium (Tb), 18, 239, 253, 255–267, 290, 298, 339–348  
Tetrathiafulvalene, 163–185  
Tm(COT), 379  
Trispyrazolylborate, 367
- U**  
Uranium complexes, 383, 394–398
- V**  
Valence bond (VB), 285
- W**  
Wavefunctions, 210–212, 240, 355–388  
    calculations, 355  
    ground-state, 129  
    theory (WFT), 357  
Wybourne formalism, 193, 323, 395
- X**  
X-ray diffraction, 35, 42, 54

**Y**

Ytterbium, 17, 164

**Z**Zeeman effect/interactions, 37, 63, 178, 230,  
284, 289, 355, 395, 406

Zeeman operators, 357, 373, 396

Zero-field quantum tunneling of magnetization,  
48, 90, 112, 113, 116, 208, 261Zero-field splitting (ZFS), 37, 64, 66, 104, 230,  
291, 367, 372

Zero-field tunneling, 63, 107